STRUCTURE MEASUREMENTS IN A SYNTHETIC TURBULENT BOUNDARY LAYER

Thesis by

Jaywant H. Arakeri

In Partial Fulfillment
of the Requirements for the Degree of
Doctor of Philosophy

California Institute of Technology
Pasadena, California

1987
(Submitted 22 May 1987)

To my mother, and to the memory of my father

ACKNOWLEDGMENTS

I learned a lot from Professor D. Coles, and I am deeply grateful to him. His expertise in experimental fluid mechanics and his insight into turbulent boundary layers were major contributing factors in this research.

Special thanks goes to Kathy Eriksen for her friendship and help. Her always cheerful presence made a difference.

The help received from Raghu Madhaven and Harry Robey in the completion of the thesis is appreciated. Finally I am grateful for the support I recieved from everyone at GALCIT and for making this a second home to me.

This research was supported by the National Science Foundation, grant no. MEA-8315402.

ABSTRACT

Extensive hot-wire measurements have been made to determine the structure of the large eddy in a synthetic turbulent boundary layer on a flat-plate model. The experiments were carried out in a wind tunnel at a nominal free-stream velocity of 12 m/s. The synthetic turbulent boundary layer had a hexagonal pattern of eddies and a ratio of streamwise scale to spanwise scale of 3.2:1. The measured celerity of the large eddy was 84.2 percent of the free-stream velocity. There was some loss of coherence, but very little distortion, as the eddies moved downstream. Several mean properties of the synthetic boundary layer were found to agree quite well with the mean properties of a natural turbulent boundary layer at the same Reynolds number.

The large eddy is composed of a pair of primary counter-rotating vortices about five δ long in the streamwise direction and about one δ apart in the spanwise direction, where δ is the mean boundary-layer thickness. The sense of the primary pair is such as to pump fluid away from the wall in the region between the vortices. A secondary pair of counter-rotating streamwise vortices, having a sense opposite to that of the primary pair, is observed outside of and slightly downstream from the primary vortices. Both pairs of vortices extend across the full thickness of the boundary layer and are inclined at a shallow angle to the surface of the flat plate. The data show that the mean vorticity vectors are not tangential to the large-eddy vortices. In fact, the streamwise and normal vorticity components that signal the presence of the eddy are of the same order of magnitude. Definite signatures are obtained in terms of the mean skin-friction coefficient and the mean wake parameter averaged at constant phase. Velocities induced by the vortices are partly responsible for entrainment of irrotational fluid, for transport of momentum, for generation of Reynolds stresses, and for maintenance of streamwise and normal vorticity in the outer flow. A stretching mechanism is important in matching spanwise vorticity close to the wall to variations in turbulent shearing stress. Regions where the stretching term is large coincide with regions of large wall shearing stress and large turbulence production.

TABLE OF CONTENTS

List of Figures

LIST OF SYMBOLS

Symbol	Description
A , B	constants in hot wire calibration
C_f	skin friction coefficient, $\tau_w/1/2\rho u_\infty^2$
h	distance between centers of the wires in an X-wire probe
n	exponent in King's law
p	static pressure
q	turbulent energy
Re_δ	Reynolds number based on boundary-layer thickness, $u_\infty\delta/\nu$
Re_{δ^*}	Reynolds number based on displacement thickness, $u_\infty\delta^*/\nu$
Re_θ	Reynolds number based on momentum thickness, $u_\infty\theta/\nu$
t	time (sec)
T	temporal period of disturbance (sec)
u_τ	friction velocity, $\sqrt{\tau_w/\rho}$
x	streamwise coordinate, measured from plate leading edge (cm)
y	normal coordinate, measured from plate surface (cm)
z	spanwise coordinate, measured from plate centerline
α	angle made by probe with free stream (deg)
β	angle made by hot-wire sensor with probe axis
δ	boundary-layer thickness; outer scale
δ^*	displacement thickness, $\int_o^\infty (1 - \frac{u}{u_\infty})\, dy$
ΔT	temperature difference between hot-wire sensor and ambient, $T_w - T_\infty$
γ	intermittency
λ	constant in hot-wire calibration
λ_x	streamwise period of disturbance (cm)
λ_z	spanwise period of disturbance (cm)

ν	kinematic viscosity
ν/u_τ	one wall unit; inner scale
ω_x	streamwise component of vorticity
ω_y	normal component of vorticity
ω_z	spanwise component of vorticity
ρ	air density
τ_ω	wall shearing stress
$< >$	ensemble mean at constant phase
$\tilde{}$	ensemble mean of the periodic component
$\bar{}$	global mean
$'$	random component

Chapter 1

Introduction

It is now generally believed that coherent structures are fundamental to the dynamics of all turbulent shear flows, and recent reviews emphasize this point (Cantwell 1981, Hussain 1983). Various definitions that have been proposed for the term coherent structure (Coles 1987) all refer to an organized motion that is characteristic of a particular flow. The general definition adopted here is that coherent structure is any flow pattern that survives the operation of ensemble averaging over realizations having a common phase reference in some suitable moving frame. Certain free shear flows, such as mixing layers, have easily identifiable coherent motions. However, the situation for the turbulent boundary layer is less transparent. The coherent structures in turbulent boundary layers are three-dimensional, and they occur randomly in space and time and at various stages of devlopment. It will be argued later that the small growth rates of turbulent boundary layers imply a relatively weak structure. All of these factors make the detection and definition of coherent structures in turbulent boundary layers difficult. In any case, it is essential that an eventual definition of these structures be consistent with the two commonly accepted similarity laws (the law of the wall and the law of the wake) and with other observed features, such as the small growth rate.

In this thesis, most of the discussion refers to turbulent boundary layers on smooth walls at constant pressure. Two distinct scales are recognized in turbulent boundary layers; the sublayer (or inner) scale ν/u_τ and the overall (or outer) scale δ. Several coherent structures are supposed to exist in turbulent boundary layers; the ones most widely investigated include sublayer streaks, turbulent bursts, and large-scale outer eddies. They are best categorized as inner or outer, based on their scale; however, such a distinction is not always possible. The present research is directed primarily at the large-scale outer eddy.

1.1. Coherent Structures in Turbulent Boundary Layers.

Sublayer streaks -- so called because of the tendency for dye, introduced through a slot on the surface, to accumulate into long thin lines (Kline, Reynolds, Schraub, and Runstadler 1967) -- are related to coherent motions having the inner scale. Flow visualization and hot-wire/hot-

film measurements all lead to a consistent view of the sublayer streaks. They are about 1000 wall units long in the streamwise direction, are spaced about 100 wall units apart in the spanwise direction, and contain fluid having relatively small values for the streamwise component of velocity. The most characteristic feature of sublayer streaks is their ubiquity. They seem to be a basic feature of all smooth-wall turbulent shear flows, including turbulent spots (Cantwell, Coles, and Dimotakis 1978). It has sometimes been assumed (Coles 1978), and there is some experimental evidence (Kastrinakis and Eckelmann 1979), that low-speed streaks are associated with pairs of counter-rotating streamwise vortices in the sublayer. A Taylor-Görtler type of instability, driven by the outer flow, has been proposed as a possible mechanism by which the sublayer vortices might be generated (Coles 1978). Recently, however, a Navier-Stokes solution of turbulent channel flow by Kim and Moin (1986) has revealed regions of strong streamwise vorticity in the sublayer that are only about 100 wall units long and form the legs of a horse-shoe type vortex.

Turbulent bursts are the most intensively investigated coherent structures in boundary layers and are also the least well understood. Traditionally, bursting has been connected with the sublayer. The bursting process in turbulent boundary layers was originally defined in terms of liftup and subsequent violent oscillation of a sublayer streak (Kline et al. 1967). It is now believed that the bursting process is composed of two phases that can occur either together or independently of each other. One component, known as the sweep, involves transport of high-speed fluid toward the wall. The other component, known as ejection, involves transport of low-speed fluid away from the wall. Both components are associated with large values of the Reynolds shearing stress close to the wall (Lu and Willmarth 1973). Two schemes have commonly been applied to detect bursts, using hot-wire or hot-film probes. The VITA technique of Blackwelder and Kaplan (1976) recognizes large local gradients in the streamwise component of velocity. If the sign of the gradient is negative, the motion detected is a sweep followed by an ejection; if the sign is positive, the motion detected is an ejection followed by a sweep. A second scheme applied to detect bursts, the quadrant technique of Lu and Willmarth, looks for large values of the instantaneous shearing stress $u'v'$. A positive value of the associated normal component of velocity, v, indicates an ejection, and a negative value indicates a sweep. Bogard and Tiederman (1986) investigated the relative merits of various

burst-detection schemes and concluded that an ejection as determined by the quadrant method correlates best with liftup of a low-speed streak as determined by flow visualization. They also found that ejections sometimes tend to appear in rapid succession, and they consider these ejections to be part of a single burst.

Bursting events appear to be of small spatial scale and short duration. An outstanding feature of bursts is that are well separated in space or time; the mean time period between bursts is typically several times δ/u_∞, where δ is the boundary-layer thickness. It is not completely clear whether the frequency of occurrence of bursts scales with inner or outer variables. A related and unresolved question is whether a burst is essentially an instability that is characteristic of the sublayer, or whether a burst is a signature of the passage of a large outer eddy. Guezennec (1985), after collecting data for a large number of turbulent boundary layers on flat plates, concluded that the bursting frequency scales with inner variables. It is therefore significant that phases of sweep and ejection have also been observed in turbulent boundary layers over rough walls, where the sublayer is radically different (Grass 1971). Narasimha and Kailas (1987) investigated bursts in atmospheric boundary layers, which have significantly higher Reynolds numbers than boundary layers in the laboratory, and concluded that the bursting frequency cannot scale with inner variables.

The large-eddy structure in turbulent boundary layers has received far less attention and is not well defined. The main difficulty seems to be that the large eddy is weak and is imbedded in a highly turbulent background flow. Kovasznay, Kibens, and Blackwelder (1970) obtained space-time correlation maps for streamwise and normal components of velocity as well as intermittency in the outer region of a turbulent boundary layer. Relatively large separations in space and time were used, in order to find the permanent features of the large-scale motion. The correlation maps suggest a large eddy occupying the full height of the boundary layer and extending about four δ in the streamwise direction and one δ in the spanwise direction. Fukunishi (1984) used a hot-wire probe in the outer region of a turbulent boundary layer to detect low values for the streamwise component of velocity. The conditionally-averaged flow field associated with this low-speed fluid resembled a horse-shoe vortex having the scale of the boundary-layer thickness. Fukunishi also suggested that a hierarchy of sizes of such eddies

exists in the turbulent boundary layer. Head and Bandyopadhyay (1981), using smoke for flow visualization, concluded that the outer portion of a turbulent boundary layer is composed of a forest of hairpin eddies inclined at 45 degrees to the wall and extending across the height of the boundary layer. It should be noted that one principal axis of the mean strain field is also inclined at 45 degrees to the wall.

A number of studies have tried to investigate the link between events in the inner region and events in the outer region of a turbulent boundary layer. Brown and Thomas (1977) made correlation measurements of the wall shearing stress and the streamwise velocity component at various heights from the wall, and suggested an organized structure inclined at an angle of 18 degrees to the wall and occupying much of the boundary-layer thickness. They also suggested that regions of large wall shearing stress and regions of large fluctuations in wall shearing stress coincide at the upstream end of the structure. Finally, Guezennec (1985) has successfully linked the bursting signature at the wall with the presence of large counter-rotating eddy pairs.

It is important to note that the research reported here is concerned with motions of large scale, and not with flow in the sublayer. It is likely that the present results will be useful in attempts to understand the difficult problem of the sublayer, but these applications lie in the future.

1.2. The Synthetic Turbulent Boundary Layer.

From the discussion above, it is clear that coherent structures do exist in turbulent boundary layers, although their specific nature and role are not clear. The difficulty is one of detecting a three-dimensional structure whose signature is unknown. The results that are obtained are necessarily biased by the detection criterion used. The problem is further exacerbated if probes capable only of single-point measurements are used.

As a possible means for circumventing these difficulties, Coles and Barker (1975) proposed the concept of a synthetic turbulent boundary layer. The objective is to create a flow whose mean properties are essentially identical to those of a natural turbulent boundary layer under similar conditions, except that the large eddies in the synthetic boundary layer are ordered. In particular, the eddies have a known phase reference, so that ensemble averages at constant

phase can be obtained without *a priori* knowledge of the signature of the large eddy.

In practice, a synthetic turbulent boundary layer is produced by generating a regular array of turbulent spots in the laminar boundary layer near the leading edge of a flat plate. In the present experiments, as in the the experiments of Coles and Barker (1975) and Savas and Coles (1985), the spots were generated in a hexagonal pattern. The pattern has a streamwise period, λ_x, which depends on the frequency of the disturbance, and a spanwise period, λ_z, which depends on the mechanical scale of the generator in the spanwise direction. The main assumptions of the present research are that the genesis of the large eddies is in these spots, and that the structure of the large eddies in a synthetic turbulent boundary layer is similar to the structure of the randomly occurring large eddies in a natural turbulent boundary layer.

So far, only two external papers on the synthetic turbulent boundary layer have appeared in the literature, by Chambers (1985) and Goodman (1985). Both papers describe flows having relatively large values of the ratio λ_x/λ_z, and both were motivated by the conjecture that such a flow might have lower surface friction than a natural boundary layer at the same Reynolds number. If this conjecture is right, then the premise of the present research is wrong, since the two flows are here supposed to have similar properties, including the value of the surface friction. Fortunately for the present research, the papers cited did not show any significant differences.

The work on coherent structure at the Graduate Aeronautical Laboratories, California Institute of Technology (GALCIT) has been executed in two stages, the first being concerned with the term "coherent" and the second being concerned with the term "structure". The objective in the first stage, which was carried out by Savas (Savas and Coles 1985), was to identify a synthetic boundary layer that is suitable for detailed study. Savas generated synthetic boundary layers having a wide range of streamwise and spanwise scales for the hexagonal pattern, and observed the modulation of the mean intermittency at constant phase in the outer flow at various downstream stations. He found that the pattern of eddies was most persistent (the flow remained coherent) for certain values of the streamwise and spanwise periods. If the spots were closely packed, then the flow rapidly became incoherent, in the sense that modulation of the mean intermittency at constant phase fell below a useful threshold. A

synthetic boundary layer with a ratio of streamwise scale to spanwise scale of about 3.2:1 was recommended as optimum for detailed structural measurements.

The present work is concerned with the second stage; namely, "structure". Extensive measurements of the velocity field have been carried out with an X-wire probe in a synthetic boundary layer having the recommended scales. Most of the measurements were made in two traverses. The first traverse, along the centerline of the flat-plate model, includes velocity measurements at several distances normal to the wall at several downstream stations. For this traverse, the X-wire probe was oriented to measure the streamwise and normal components of velocity. These measurements are used in chapter 4 to obtain the celerity of the large eddies in the synthetic boundary layer and also to study the development of the large eddies with increasing downstream distance. In order to establish that the synthetic and natural flows are closely related, certain time-averaged mean properties of the synthetic boundary layer on the plate centerline, such as the mean skin-friction coefficient and the mean wake parameter, are compared with the corresponding mean properties of natural turbulent boundary layers.

The second traverse was concerned with the main issue, the structure of the synthetic large eddy, and includes measurements of the three components of velocity at several spanwise locations at one streamwise station. Slightly more than one cycle of the periodic pattern is covered in the spanwise direction. The structure of the large eddy in the synthetic boundary layer is described in chapter 5 in terms of the large-scale mean velocity, mean vorticity, and turbulence fields as functions of phase. The overall signature of the eddy is also displayed in terms of mean skin-friction coefficient, mean wake parameter, and boundary-layer thickness as functions of phase.

Out of necessity, the concept of Reynolds averaging is retained in the data presentation. It is by now well understood that this concept, with its attendant loss of phase information, has become a serious obstacle to understanding of turbulent flow. However, the averaging process is applied here at a lower level, retaining phase information for the motions of largest scale. It is possible, and even probable, that other structural mechanisms operate at smaller scales than the scale observed here. If so, they are more likely to be discovered by numerical than by experimental methods.

The results are mostly presented as contour maps of the various variables after averaging at constant phase in the $t-y$, $t-z$ or $z-y$ planes. (A definition of the coordinate system is given below.) In describing the structure of the eddy, the streamwise coordinate x is effectively treated as $-ct$, where c is the celerity or phase velocity of the eddy. This approximation is commonly referred to as Taylor's hypothesis. The alternative strategy, of making a spanwise traverse at several different x stations, would have required an order-of-magnitude increase in the already massive amount of data, which is about 3 Gbytes.

1.3. Coordinate System.

A right-hand coordinate system is used throughout, with x measured downstream from the leading edge of the flat-plate model, y measured normal to the surface, and z measured in the spanwise direction from the centerline of the plate. The velocity components in the x, y, and z directions are denoted by u, v, and w, respectively. The time coordinate t usually refers to time measured from a particular reference state for the disturbance generator. In the present experiments, this reference state is taken to be the index pulse from a 200-line encoder on the camshaft described in chapter 2.

1.4. Ensemble Averages.

The structure of the large eddy is defined by its properties evaluated at constant phase. It is necessary to define several types of ensemble averages used in this thesis. In view of the doubly-periodic property of the mean flow, any quantity f in the synthetic boundary layer can be decomposed in two ways;

$$f = \langle f \rangle + f'$$

or

$$f = \bar{f} + \tilde{f} + f'$$

where $\langle f \rangle$ is the ensemble mean at constant phase, f' is the random component, $\bar{f}$ is the global mean, and $\tilde{f}$ is the mean of the periodic component at constant phase. Both

decompositions were introduced for a somewhat different purpose by Reynolds and Hussain (1972) and have since been used for description of coherent structures in turbulent flows by several authors (see, for example, Cantwell and Coles 1983 and Hussain 1983). By definition, it follows in the doubly-periodic flow that

$$<f>(x, y, z, t) = <f>(x, y, z + m\lambda_z, t + nT)$$

where m and n are integers, and where λ_z and T refer to the spanwise period and the time period, respectively, of the hexagonal pattern. The mean at constant phase, $<f>$, is calculated by summing all samples of the quantity f at fixed phase,

$$<f>(x, y, z, t) = \frac{1}{MN} \sum_{m=1}^{M} \sum_{n=1}^{N} f(x, y, z + m\lambda_z, t + nT)$$

In the present experiments, $M = 1$ (data were taken over one cycle in the spanwise direction) and $N = 2000$ (data were taken for 2000 cycles in time). The global mean is calculated by averaging the ensemble mean at constant phase over one cycle in both of the two directions, t and z;

$$\bar{f}(x, y) = \frac{1}{\lambda_z T} \int_0^{\lambda_z} \int_0^{T} <f>(x, y, z, t)\, dt\, dz$$

In practice, since data were obtained only at discrete points in the $t-z$ plane, the quantity $\bar{f}$ is evaluated as a double summation. Note that the global mean is a function only of the variables x and y. In chapter 4, reference will be made to a quantity called the time mean, which is calculated by averaging over one cycle in the time direction only. The time mean is therefore a function of the spanwise coordinate, z, in addition to the coordinates x and y.

It follows from the definitions that $\bar{\tilde{f}} = 0$ (the periodic component has zero global mean); that $<f'> = 0$ (the random fluctuations have zero mean at constant phase); and that $\overline{\tilde{f}f'} = 0$ (the periodic and random motions are uncorrelated).

Chapter 2

Experimental Arrangement

The Merrill wind tunnel at GALCIT was used for the experiments. The length of the test section is 265 cm; the width increases from 114.5 cm at the entrance to 117.4 cm at the exit; and the height increases from 81.6 cm to 82.8 cm. The flat-plate model is shown in plan view in figure 2.1. The plate is 264.2 cm long and was mounted in a horizontal plane at approximately mid-height in the test section. The leading edge is half of a 10:1 ellipse. The plate spanned the width of the test section, with inflatable seals along the sides. The pressure-coefficient distribution was constant to within ± 0.01 over the working area of the plate. The free-stream turbulence level in the tunnel at a free-stream velocity of 1200 cm/s was determined from hot-wire measurements to be about 0.006 u_∞ at x = 117.8 cm, y = 8 cm, and z = 0 cm.

Figure 2.2, taken from Savas and Coles (1985), shows some details of the mechanism used for generating the synthetic flow. A camshaft below the plate at x = 22.9 cm displaced small pins momentarily into the laminar flow to produce a regular pattern of turbulent spots. The diameter of the active part of the pin is 0.10 cm, and the displacement of the pin is 0.165 cm. Two lobes of the cam, 180 degrees apart, are retained at each active pin location. Alternate active cams along the cam shaft are displaced by 90 degrees, thus producing a hexagonal pattern of spots in the (z, t) plane when the camshaft is rotating. The period λ_z in the spanwise direction is determined by the cam spacing and is 12.19 cm in the present experiments. The period T in time is half the period of shaft rotation and is 0.032 seconds (the camshaft rotates at 937.5 rpm).

2.1. Temperature Control.

The tunnel is of the return-circuit type. Until the present research, it had no provision for cooling. The tunnel temperature increased about 3 °C per hour at a free-stream velocity of 12 m/s. Better temperature stability was needed for precision hot-wire and hot-film measurements. A finned-tube heat exchanger was therefore installed in the vertical leg of the diffuser section, upstream of the propeller. The cross section at this location is octagonal, with each of the eight sides measuring approximately 80 cm. The tubes (Heat Exchange Applied Technology) are

90/10 cupronickel with an O.D. of 1.59 cm and a wall thickness of 0.125 cm. The height of the copper fins is 0.95 cm and the fin spacing is 0.25 cm. The length of the tubes varies from 87.9 cm to 162.3 cm to accomodate the octagonal section. The total number of tubes is twenty and the spacing between the tubes is about 8 cm. The tubes are supported by the tunnel walls and by a central bridge. All of the plumbing connections are outside of the tunnel. Stiffeners are installed between adjacent tubes to reduce resonant vibration of the heat exchanger caused by vortex shedding.

Chilled water is used as the cooling liquid. The water circuit has two sections in parallel to give maximum uniformity in temperature downstream of the heat exchanger. The mixing action of the propeller is also effective in this regard. Valves and a flow meter are used to control and monitor the flow rate of the chilled water, which is limited at present to 0.19 litres/sec with the valves fully open. For the experiments reported here, the tunnel speed was nominally 1200 cm/s and a typical run was four hours long. Under these conditions, the test-section temperature could be held constant to within $\pm$ 0.2 °C.

2.2. Traversing System.

A second major modification to the tunnel for the present experiments was the installation of a three-dimensional computer-controlled traverse (Aerotech, stepping motor drives SA/4005/10KR/DO/R/SM-O/FP/TW/BR and tables ATS-424/300SMW, ATS-412/200SMW, and ATS-406/200SMW) and probe support. A welded steel frame mounted on top of the test section supports the traverse system. A streamlined strut attached to the vertical traverse supports the hot-wire probe. The range of travel in the x, y, and z directions is 60.96 cm, 15.24 cm, and 30.48 cm, respectively. Each traverse can be controlled either from a local panel or from a computer through the IEEE 488 bus.

The tunnel ceiling was modified to accomodate probe movement in three directions and at the same time maintain an adequate seal at the point of entry of the streamlined strut. A 119.4-cm by 33.0-cm cutout in the ceiling allows measurement from x = 83.8 cm to x = 198.1 cm and from $z = -$ 15 cm to z = 15 cm. An aluminum plate, 0.2 cm thick, covers the cutout at all times and moves with the probe in the x-direction. The moving plate is mounted in guides attached to the underside of a 2-cm thick plywood frame that comprises the fixed part of

the ceiling. Teflon-coated tape between the sliding plate and the guides provides smooth movement. The sliding plate is independently attached to the x-traverse to avoid any load on the probe strut. A spanwise slot, 3.8 cm by 30.5 cm, in the sliding plate allows movement of the probe in the z or spanwise direction. The slot itself is covered by a sliding mylar strip 0.01 cm thick which is held taut by two constant-force springs, identical to the ones used in tape measures, at either end of the slot. The streamlined tube passes through a matching hole in the mylar strip. Figure 2.3 is a photograph showing some details of the experimental arrangement above the test section.

2.3. Hot-Wire Probes.

The probe support consists of a vertical streamlined tube, 3.00 cm by 1.27 cm by 0.089-cm wall thickness, 72.4 cm long. A 0.635-cm diameter rod, 79.9 cm long, passes through the tube and through brass plugs brazed to the streamlined tube at either end. The streamlined tube also carries cables from the hot-wire probe to the anemometer circuits. The hot-wire probe itself is mounted on a brass bracket clamped to the central rod as shown in figure 2.4. The probe may be yawed in the $x-z$ plane by rotating the rod. A lever arm attached to the rod at the top is spring-loaded into a series of notches, allowing the yaw angle to be accurately set at thirteen discrete values, – 30(5)30 degrees. The hot wires are positioned on the axis of the rod so that yawing the probe does not displace the sensing elements in the spanwise direction. The probe body is inclined at 5 degrees to the surface of the flat plate to minimize probe interference for measurements close to the wall.

Two types of commercial hot-wire probes were used for the present experiments. One is a single-wire probe (Thermo Systems 1260Y-T1.5) and the other is an X-wire probe (1248AU-T1.5 or 1248BK-T1.5). There was no breakage of the hot wires of any of the probes during the experiments. The X-wire probes were used to measure either the u and v or the u and w components of velocity. During calibration, the probe was oriented to measure u and w, so that it could be yawed in its own plane. If the probe was to be used to measure u and v, the probe had to be rotated 90 degrees about its axis for calibration and then rotated back. This operation was done accurately and quickly with the aid of a square sleeve (0.4 cm long and 0.18 cm square) epoxied to the probe stem. The sleeve was carefully aligned with the plane of the

X-wire and was a close fit in a matching socket on the probe holder. Figure 2.5 shows X-wire probes with and without the square sleeve.

The vertical distance between the probe and the wall was determined by measuring the distance between the probe needles and their images in the flat plate. A cathetometer (Gaertner M101AT telescope and M940-303 micrometer slide) mounted outside the test section was used for this purpose. The measurements were accurate to better than 0.005 cm.

2.4. Hot-Wire Circuits.

The constant-temperature hot-wire anemometer circuit is based on the design of Perry and Morrison (1971). The overheat ratio for the hot-wire probes was nominally set at 1.7, corresponding to a wire operating temperature of about 200 $^{\circ}C$. The bridge inductance and voltage offset were adjusted to optimize the frequency response of the system, as determined by a standard square-wave test. The frequency response was flat to about 15 kHz.

Intermittency was one of the variables measured. The settings on the intermittency circuit were determined using the procedure described by Savas and Coles (1985). The fluctuating component of the hot-wire signal was amplified (100 times) and bandpass filtered (2.5 kHz - 8 kHz) before being processed by the intermittency circuit.

2.5. Temperature and Free-Stream Velocity Measurement.

The dynamic pressure in the test section was measured by a pitot-static probe (United Sensor PDC-12-g-10-KL) connected to a 100-mm Hg differential electronic manometer (Datametrics Barocel pressure sensor 511-11 and electronic manometer 1014A). The pitot-static probe was mounted from one window of the test section. A thermistor probe (Omega 44034), mounted near the pitot-static probe, and a mercury thermometer were used to measure the tunnel temperature. The calibration of the thermistor probe was stable throughout the experiments, and the difference between the temperatures indicated by the two thermometers was typically less than 0.2 °C.

Chapter 3

Experiments

3.1. Selection of Flow for Detailed Study.

Savas and Coles (1985) constructed a number of synthetic boundary layers having various imposed scales and recommended (see figure 3.1, reproduced from their figure 13) that a flow suitable for detailed study should have the scales

$$\frac{\lambda_z}{\delta} = 2.5\,, \quad \frac{u_\infty T}{\delta} = 8$$

where λ_z is the spanwise period and T is the time period of the periodic pattern. Given a nondimensional celerity $c = 0.842\ u_\infty$ (see below), the desired streamwise wavelength λ_x is obtained as $\lambda_x/\delta = cT/\delta = 6.7$. This value refers to flow parameters far downstream, where loss of coherence is so severe as to be unacceptable.

It was decided for the present investigation to use essentially the recommended ratio of streamwise to spanwise scales but to study the upstream region of the flow, so as to stay well within the coherent regime. What is important is that the original turbulent spots should have grown to a size where they are definitely in contact; there should be no vestiges of the laminar boundary layer. The spanwise period λ_z is 12.2 cm and the time period T is 0.032 sec. The free-stream velocity is nominally 1200 cm/sec. At the upstream station, x = 117.8 cm, where the bulk of the measurements were made, the global mean boundary-layer thickness $\overline{\delta}$ is 1.77 cm. The streamwise wavelength, $\lambda_x = cT$, is 32.3 cm. Thus $\lambda_x/\lambda_z = 2.65$, $\lambda_z/\overline{\delta} = 7.0$, and $\lambda_x/\overline{\delta} = 18.6$. The latter two values should decrease by a factor of two to three within the coherent regime. The parameters corresponding to the present flow are marked in Savas's coherence diagram (figure 3.1).

3.2. Experiments.

Most of the measurements were made in two primary traverses:

(1) profiles of u, v were obtained at 11 streamwise locations at $z = 0$ and $x =$ 117.8(4.0)157.8 cm.

(2) profiles of u, v and u, w were obtained at 29 spanwise locations at $x = 117.8$ cm and $z = -7.0(0.5)7.0$ cm.

A profile is 15 data points at standard values of y ranging from $y = 0.15$ cm to $y = 3.4$ cm. The 15 y locations are listed in table 1.

A separate spanwise traverse was made at $x = 117.8$ cm, $y = 1.93$ cm, $z = -$ 14.5(0.5)14.5 cm to verify the periodicity of the eddy pattern by observing the mean intermittency at a fixed distance from the surface over the full spanwise range of the traverse. Figure 3.2 shows a contour plot, obtained from this traverse, of the mean intermittency at constant phase in the $t-z$ plane. The pattern is nearly homogenous, and the spots produced by the different pins and lobes of the cam mechanism are quite similar to each other.

Additional measurements were also made with wall-shear gauges at several values of z, and with a single hot wire at $y^+ = 15$ and $z = -7(0.5)7$ cm ($y^+ = y\sqrt{\tau_w/\rho}/\nu$, where τ_w is wall shearing stress and ρ and ν are fluid density and kinematic viscosity). The single-wire measurements can be used to study the bursting phenomenon in the synthetic boundary layer. The results of these measurements, however, are not included in this thesis.

The first traverse was intended to establish a value for the celerity of the large eddies in the synthetic boundary layer, and also to observe the flow development with downstream distance. The second traverse and the other measurements were intended to establish the structure of the large eddy and its various signatures.

3.3. Data Acquisition.

The data acquisition system is essentially the same as the one described by Savas (1979). It consists of an HP-2100 computer, a 15-bit, 16-channel analog-to-digital converter (ADC), cartridge disc, and tape drive. Generally, outputs from two hot-wire anemometers, one surface hot-film gauge, a pitot-static probe, and a thermistor were connected to five channels of the A-D converter to be digitized and transferred to the computer. A binary intermittency signal was

recorded in the least significant bit of each ADC word and recovered by software during data reduction. The ADC data were left-justified for this purpose. The hot-wire and hot-film data were recorded on magnetic tape without processing. The data from the thermistor and the pitot-static probe were averaged 100 samples at a time before transfer to the tape.

Sampling was controlled by a clock that also served as the command signal to a phase-locked loop driving the camshaft motor (Printed Motors Inc. U16M4). The other input to the phase-locked loop is from a 200-line optical encoder mounted on the camshaft. The clock sampling frequency is 3.125 kHz. The period T of the periodic pattern is 0.032 seconds, which corresponds to half a camshaft revolution. Therefore, during each cycle of 0.032 seconds, 100 samples of data were recorded from each hot-wire channel. At each probe position, data were recorded for 2000 cycles; i.e., for 64 seconds. The sampling rate for the single-wire measurements in the sublayer was increased to 25 kHz in order to allow application of the VITA technique (Blackwelder and Kaplan 1976).

3.4. Experimental Procedure.

A typical run included four profiles lasting about four hours. The wind tunnel and the chilled water for the heat exchanger were turned on about fifteen minutes before the start of a run. During the experiment, the tunnel temperature and the flow rate of the chilled water were continually monitored. Typically, variations in tunnel temperature of less than $\pm$ 0.2 °C were achieved by close regulation of the cooling-water flow rate.

The hot-wire probes were calibrated at the beginning and at the end of each run. During calibration the X-wire probe was at x = 117.8 cm, y = 8.0 cm, and z = 0 cm, and the probe was yawed in its own plane at various free-stream velocities. The cam mechanism was turned off during the probe calibration, and the boundary layer was laminar. Each calibration included 35 points, consisting of seven yaw angles (– 30(10)30 degrees) for the probe and five free-stream speeds ranging from 500 cm/s to 1300 cm/s. If the probe was oriented to measure the u and w components of velocity, the tunnel could be kept running during the calibration. In order to measure the u and v components of velocity, the probe had to be rotated 90 degrees about its axis for calibration and then rotated back. The tunnel was turned off during the latter operations.

The hot-wire probe was positioned by the computer-controlled traverse described earlier. Measurements for each profile started at y = 3.4 cm. After every 8 data points in a profile, data were also recorded at two standard positions. One was outside the boundary layer, at x = 117.8 cm, y = 8.0 cm, z = 0 cm, and the other was in a region of intermittent turbulence, at x = 117.8 cm, y = 1.93 cm, z = 0 cm. The purpose was to record drift in any aspect of the experiment, during a run as well as between runs, and to verify that the camshaft mechanism was not subject to serious wear. The stability of the data was found to be excellent.

3.5. Preliminary Data Reduction.

The two components of velocity in the plane of the X-wire, u and w (or v), are calculated using the equations (see appendix A)

$$u = \frac{q_{e_1}A_{2w} - q_{e_2}A_{1w}}{A_{1u}A_{2w} - A_{2u}A_{1w}} \tag{1}$$

$$w = -\frac{q_{e_1}A_{2u} + q_{e_2}A_{1u}}{A_{1u}A_{2w} - A_{2u}A_{1w}}$$

where the effective velocities q_{e_1} and q_{e_2} are related to the hotwire voltages E_1 and E_2 by

$$q_{e_i} = \left[\frac{\frac{E_i^2}{\Delta T_i} - A_i}{B_i}\right]^{1/n_i} \qquad i = 1, 2 \tag{2}$$

Calculation of velocity from the hot-wire data involved conversion of about 460 million voltage pairs to velocity vectors. A look-up table was essential to speed up this process. Inversion was done in two steps. For each voltage pair (E_1, E_2) the corresponding effective-velocity pair (q_{e_1}, q_{e_2}) was obtained from a look-up table generated with the aid of equations (2). The lookup table contained values for effective velocities q_e for each wire for a thousand values of $E^2/\Delta T$ in the range from 0.08 to 0.24 volt$^2/°C$; the corresponding range in output voltage was approximately from 4 to 7 volts. Thus the average resolution is 3 millivolts, representing an

average resolution of about 3 cm/s in q_e. The second step was calculation of the velocity-vector components u and w (or v) from equations (1).

In the inversion process it is the calculation of effective velocities from equations (2) that is computationally time consuming. The constants A_{1u}, A_{2u}, A_{1w}, A_{2w} in equation (1) are functions of calibration constants λ_1, β_1, λ_2, and β_2. Of the five calibration constants A, B, n, β, and λ for each of the wires, only A and B changed appreciably between the beginning and end of a four-hour run, which began and ended with a wire calibration. Typically, the change in A was less than one percent and the change in B was less than half of one percent. To obtain the best results possible, it was decided to incorporate these small changes by interpolating the constants A and B. A run typically involves measurements at 80 positions of the X-wire probe and contains 80 files, one for each position. The constants A and B for each of the wires were calculated by interpolation for each file and were kept constant during the conversion of the 200,000 voltage pairs in that file to velocity vectors. Thus the lookup tables for q_e had to be regenerated each time the constants A and B were adjusted. A more standard method, of obtaining the components of velocity directly from voltage pairs, using a look-up table with the same resolution, would require a 1000 by 1000 array. The associated 500-fold increase in storage requirement would not be compensated by a corresponding improvement in speed of computation.

Ensemble averages were calculated for the velocity components $<u>$, $<v>$, $<w>$; the Reynolds stresses $<u'u'>$, $<u'v'>$, $<v'v'>$, $<u'w'>$, $<w'w'>$; and the intermittency $<\gamma>$. The Reynolds stress $<v'w'>$ was not accessible. The calculation was done in in two passes. In the first pass, the digitized voltages from the hot-wire anemometers were converted to velocity components, and the ensemble means of the velocities were calculated. The raw velocity components were stored on the computer disc. In the second pass, the fluctuating velocity components were calculated from the stored raw values and the known mean values of the velocity components. At the same time, the Reynolds stresses at constant phase were calculated. This procedure avoids the error arising out of subtraction of two large numbers, as would be required in a single-pass calculation of the stresses.

For the streamwise traverse, both velocities and Reynolds stresses are restricted to the $x-y$ plane. Initially, 200 values were obtained per camshaft revolution for each of the ensemble-averaged quantities. The 200 values in each revolution were averaged five at a time, and then the two cycles in each revolution were superposed. Thus there are 20 phase intervals per cycle, and the number of samples per phase is 10000. This operation was effective in reducing scatter, especially in the Reynolds stresses. The frequency content in the ensemble-averaged quantities was low enough to justify the five-point averaging.

Further processing was necessary for the data from the spanwise traverse. The spanwise velocities $<w>$ had to be corrected for the error caused by the gradient of the streamwise velocity normal to the wall, as explained in appendix A. The velocity component normal to the wall at constant phase, $<v>$, is everywhere less than half of one percent of u_∞. Because the measured values of $<v>$ were found to be unusable, due perhaps to probe interference from the wall, the continuity equation was used to calculate this velocity component. The procedures used to obtain the spanwise and vertical components of velocity at constant phase are described in appendix A.

Finally, profile parameters $<\delta>$, $<\Pi>$, and $<C_f>$ corresponding to the 20 phases were inferred from a fit to the ensemble-mean velocity $<u>$ at each of the 11 centerline stations and the 29 spanwise stations. The procedure for obtaining these parameters is described in the next chapter.

3.6. The Condense Operation.

It was possible to exploit the doubly-periodic property of the flow to further reduce scatter in the data, especially in the mean spanwise component of velocity and in the Reynolds stresses. That the flow is indeed closely doubly periodic is verified by the contour plot of the intermittency $<\gamma>$ at constant phase already shown in figure 3.2. Five pins and ten cam lobes are involved in the figure, and they are seen to be essentially interchangeable. The various eddies can usefully be superposed, say by associating a rectangular area with each, to increase the sample population and normalize the image of the large eddy. The rectangular area in question will be referred to as a tile. Finally, the data can be folded along the centerline to exploit the spanwise symmetry. The effect is to reduce the storage requirements for a complete

description of the flow to a rectangular region $\lambda_x/2$ by $\lambda_z/2$ by about $2\,\delta$. In hindsight, it would have been better for this purpose to synchronize the spanwise data stations with the pin spacing, rather than to use a fixed increment of 0.5 cm, especially as the probe position was controlled by the computer. Another tile shape might be more graphic but would not have the obvious advantage of the rectangular storage array. In any event, the flow is fully described if information is available from half a period in the t and z directions, running from phase N to phase N + 10 and from $z = 0$ cm to $z = 6.1$ cm. (One cycle in t is 20 phases and one cycle in z is 12.2 cm.) For any variable $<f>$, data from four such half-tiles can be combined using the following property for a doubly periodic flow;

$$
\begin{aligned}
& f(\text{phase}, z/z_0) && \text{1st quadrant} \\
&= \pm f(\text{phase}, -z/z_0) && \text{2nd quadrant} \\
&= f(\text{phase} + 10, -(1 - z/z_0)) && \text{3rd quadrant} \\
&= \pm f(\text{phase} + 10, (1 - z/z_0)) && \text{4th quadrant}
\end{aligned}
$$

where the time variable or phase varies from 1 to 10, and the spanwise variable z/z_0 varies from 0 to 1/2. The $+$ sign is for variables that are symmetric about $z = 0$ and the $-$ sign is for variables that are antisymmetric. Data from the four quadrants were combined into the first quadrant according to these rules. The data were then smoothed by subtracting the means, fitting a four-term Fourier series in the z direction at each phase, and then fitting a four-term Fourier series in the t direction at each z. Four terms were found to be adequate to represent low-frequency fluctuations for all of the variables. This whole operation of combining and smoothing the data is called the condense operation. All of the ensemble-averaged variables, such as velocity and Reynolds stresses at each y and the profile parameters $<\delta>$, $<C_f>$, and $<\Pi>$ at the wall, were condensed in this fashion. Figure 3.3 shows contour plots of the skin-friction coefficient at constant phase, $<C_f>$, before and after the condense operation.

Chapter 4

Celerity and Mean Properties

The contents of this chapter fall into two areas. The first area deals with the celerity of the large eddy in the synthetic turbulent boundary layer and with the general development with downstream distance of the flow in the plane of symmetry. The second area deals with the time-mean properties of the synthetic turbulent boundary layer in terms of the streamwise component of velocity, $\langle u \rangle$, the skin-friction coefficient, $\langle C_f \rangle$, the wake parameter, $\langle \Pi \rangle$, and the Reynolds stresses. These quantities are compared with the mean properties of a natural (i.e., carefully tripped) turbulent boundary layer at similar Reynolds numbers.

The celerity, or phase velocity, is an important quantity for several reasons. One is the need to establish a moving coordinate system in which the ensemble-averaged flow field is steady, or nearly steady. This need is acute in discussions of dynamics, because streamwise transport (or any other quantity that involves directly the velocity $\langle u \rangle$, rather than its derivatives) cannot otherwise be evaluated correctly. A second reason is the desirability of avoiding distortion in plan-view or side-view presentations of data when x and t are treated as equivalent variables.

4.1. Similarity Laws.

Two similarity laws, the law of the wall and the law of the wake (see, for example, Coles 1969), have been developed for natural turbulent boundary layers. In the present research, these laws were found to be valid also for the mean velocity $\langle u \rangle$ at constant phase in the synthetic boundary layer. This fact was decisive in determining the celerity of the large eddy. As will be established in the next chapter, it also provided a useful basis for describing the general structure of the flow.

The mean velocity $\langle u \rangle$ in the stream direction at constant phase was decomposed into wall and wake components using the following formula;

$$\frac{<u>}{<u_\tau>} = \frac{1}{\kappa} \log_e \left[\frac{y<u_\tau>}{\nu} \right] + c + \frac{2<\Pi>}{\kappa} \sin^2 \left[\frac{\pi}{2} \frac{y}{<\delta>} \right] \qquad (4.1)$$

where $<u_\tau>$, $<\Pi>$, and $<\delta>$ are the friction velocity, wake parameter, and boundary-layer thickness, respectively, all at constant phase. The universal constants c and κ are taken as $c = 5.0$ and $\kappa = 0.41$ (this constant c should not be confused with the celerity, which is represented by the same symbol). The three profile parameters were obtained from a least-squares fit to equation (4.1). Following the recommendation by Coles (1969), data close to the wall and data near the edge of the boundary were omitted, and the fitting operation was carried out for data in the range from $y/<\delta> = 0.1$ to $y/<\delta> = 0.75$. The fit is uniformly excellent, and the difference between the measured and fitted mean velocities, $<u>$, is typically less than about 0.2 percent of the free-stream velocity, u_∞. Figure 4.1 shows ensemble-mean velocity profiles at $x = 117.8$ cm at the twenty phases, with curves fitted according to equation (4.1). The lowest curve is the profile of the time-averaged mean, $\bar{u}$. The three profile parameters $<u_\tau>$, $<\Pi>$, and $<\delta>$ were thus obtained as functions of phase for each of the 11 centerline stations of the first traverse and for each of the 29 spanwise stations of the second traverse (see chapter 3 for a description of the two traverses). The same fitting operation was carried out for the profile averaged over one cycle in time to obtain $\bar{\delta}$, $\bar{u}_\tau$, and $\bar{\Pi}$. These values cannot be distinguished, for any practical purpose, from the mean of the 20 averages at constant phase; i.e., $<\bar{\delta}>$, etc. Henceforth, no distinction is made between the two types of average.

4.2. Celerity and Loss of Coherence.

Data obtained at the 11 centerline stations, $x = 117.8\,(4.0)\,157.8$ cm, were used to establish the celerity of the large eddies in the synthetic boundary layer and to study loss of coherence as the eddies move downstream.

Figure 4.2 shows the distribution of the Reynolds number, $<R_\delta> = u_\infty<\delta>/\nu$, as a function of phase. The modulation in $<R_\delta>$ for the lowest curve ($x = 117.8$ cm) is about 30 percent, and the modulation decreases monotonically with increasing downstream distance. However, there is no noticeable difference in the shape of the curves corresponding to the different x-

stations. Similar sets of curves for the wake parameter (figure 4.3) and the skin-friction coefficient (figure 4.4) at constant phase also display waveforms that move downstream with decreasing amplitude but without significant change in shape. To establish the celerity, the phases corresponding to the maximum, the minimum, and the two crossings of the mean value are plotted in figures 4.5, 4.6, and 4.7 in the form of an $x-t$ diagram for each of the variables $<R_\delta>$, $<\Pi>$, and $<C_f>$. A similar plot for $<R_Y>$, where $<R_Y>$ is based on Y, the distance from the wall at which the intermittency, $<\gamma>$, is equal to 0.5, is not shown. The average of the sixteen slopes, four for each variable, is 0.842, with an rms deviation of 0.02. The straight lines in the figures all have the same slope, corresponding to the the celerity $c = 0.842\, u_\infty$, but their intercepts are determined by the least-squares fit. Two important conclusions may be drawn. The different variables give essentially the same value for celerity, and this celerity is constant, at least over the 40-cm length investigated. The implication is that each eddy travels as a single entity. In terms of the global mean-velocity profile, the celerity corresponds to the physical velocity at about $y/\bar{\delta} = 0.25$.

It is apparent in figures 4.2 to 4.4 that the coherence, as measured by the amplitude of modulation of the three variables, $<R_\delta>$, $<\Pi>$, and $<C_f>$, decreases with increasing downstream distance. This observation is made quantitative in figure 4.8, which shows plots of the maximum, minimum, and mean, at each of the 11 centerline stations, of the variables $<R_\delta>$, $<\Pi>$, and $<C_f>$ as functions of the time-mean Reynolds number based on momentum thickness, $\bar{R}_\theta$. Note the relatively small modulation in $<C_f>$ when compared with the other two variables, $<R_\delta>$ and $<\Pi>$. The amplitude of modulation of all three profile parameters decreases by about a factor of 1/2 in a downstream distance of one spatial period (cT = 32.3 cm). Figure 4.9, showing this reduction, is a plot of normalized peak-to-peak modulation of the variables $<R_\delta>$, $<\Pi>$, and $<C_f>$ plotted against downstream distance (note the logarithmic scale of the ordinate). The observed loss of coherence is not necessarily due to a real reduction in the strength of the large-eddy motion, but may be due to dispersion which smoothes the ensemble averages at constant phase. This hypothesis could only be tested by resorting to a second stage of conditional averaging to remove the jitter due to different arrival times of different eddies, and this has so far not been done in the present study.

4.3. Mean Properties of the Synthetic Boundary Layer.

The main premise of the present research is that the structures in the synthetic flow and the natural flow are similar. In the synthetic boundary layer, the large eddies are ordered; in the natural turbulent boundary layer, they occur randomly. A comparison of certain mean properties, such as skin-friction coefficient and wake parameter, under similar conditions, is important in verifying this premise.

Figure 4.10a shows a plot of Reynolds number based on boundary-layer thickness, R_δ, against Reynolds number based on momentum thickness, R_θ. The figure includes a plot of the time-mean quantity $\bar{R}_\delta$ against $\bar{R}_\theta$ at the 11 centerline stations as well as plots of time trajectories of $<R_\delta>$ versus $<R_\theta>$ at $x = 117.8$ cm and $x = 169.8$ cm. Recall that the time mean of a quantity is formed by averaging that quantity in the time direction at constant z. The point corresponding to the global mean (the average over one cycle in the two directions, t and z, for the doubly-periodic flow) at $x = 117.8$ cm is shown by a cross. The global mean is calculated using data from the spanwise traverse described in chapter 3. The $R_\delta - R_\theta$ curve obtained in a natural turbulent boundary layer at constant pressure is also shown for comparison. Figure 4.10b is a similar plot of the wake parameter, Π, and figure 4.10c is a similar plot of the skin-friction coefficient, C_f. The time trajectories of $<R_\delta>$, $<C_f>$, and $<\Pi>$ are double-valued at a given R_θ and suggest the non-equilibrium nature of the local flow. In spite of the decreasing amplitude, the trajectories remain essentially congruent as the eddies move downstream. The trajectory of $<R_\delta>$ seems to agree more closely with the time-mean values $\bar{R}_\delta$, indicating a more predictable dependence of $<R_\delta>$ on $<R_\theta>$.

The global means in the synthetic boundary layer can be compared with corresponding quantities in natural boundary layers. The properties of the natural flow were determined using the formulas recommended by Coles (1969), with the addition of an empirical formula for Π; namely,

$$\Pi = 0.62 - 1.21\, e^{-\delta^+/290}$$

This formula was obtained from a fit to the data of Wieghardt (see Coles 1969) for a natural

turbulent boundary layer at constant pressure. The difference between the synthetic flow and the natural flow in terms of mean properties is about 8 percent in the case of R_δ, 3 percent in the case of C_f, and 15 percent in the case of Π (note that Π represents only about ten percent of the mean-velocity variation). These differences are quite acceptable for the purposes of the present study.

Figure 4.11 shows the global means of four Reynolds stresess, $\overline{\langle u'v' \rangle}$, $\overline{\langle u'u' \rangle}$, $\overline{\langle v'v' \rangle}$, and $\overline{\langle w'w' \rangle}$, all normalized by $\overline{u_\tau^2}$ and plotted as functions of $y/\overline{\delta}$, where $\overline{u_\tau}$ and $\overline{\delta}$ are the global means of the friction velocity and the boundary-layer thickness, respectively. The stress distributions resemble the corresponding distributions in natural turbulent boundary layers (see, for example, Klebanoff 1955). One unexplained discrepancy arises in the case of the turbulent shearing stress $\overline{\langle u'v' \rangle}$. Close to the wall, but outside the sublayer, the value of this stress should approach the wall shearing stress; i.e., the value of the normalized turbulent shearing stress plotted in figure 4.11 should be near unity near the wall, but is actually about 0.85. Similar discrepancies have sometimes been reported in the literature by various investigators using similar instrumentation (see, for example, Alfredsson and Johansson 1984).

Chapter 5

Structure

5.1. Introduction.

As stated in chapter 1, the main aim of this research is to identify and describe the structure of the large eddy in a turbulent boundary layer at constant pressure. It is instructive to look at some known characteristics of turbulent boundary layers to establish the role that these eddies must play.

For two-dimensional boundary layers at constant pressure, laminar or turbulent, the total mean vorticity per unit length is given to a good approximation by $\int(\partial u/\partial y)dy$ and thus is equal to the constant free-stream velocity u_∞. The difference between laminar and turbulent boundary layers is that most of the mean vorticity in a turbulent flow is concentrated close to the wall, with the remaining vorticity distributed in a long tail away from the wall. One consequence of the concentration of vorticity near the wall is the large wall shearing stress observed in the turbulent boundary layer. Figure 5.1 shows expected vorticity distributions, $-\omega_z = \partial(u/u_\infty)/\partial y$, against y for two hypothetical turbulent boundary layers having $R_\theta = 1559$ and $R_\theta = 3357$, where R_θ is Reynolds number based on momentum thickness. These flow parameters correspond to the conditions of the present experiment. For the boundary layer at $R_\theta = 1559$, the vorticity at the wall $\partial(u/u_\infty)/\partial y$ is -14.7 per cm, whereas for the boundary layer with $R_\theta = 3357$, this value drops only to -12.0 per cm, even though the boundary-layer thickness has increased by more than a factor of two. The growth of a turbulent boundary layer is thus mainly by extension of the vorticity tail (see also Lighthill 1963). This behavior is related to the existence of two length scales in turbulent boundary layer. One is the inner viscous length scale, ν/u_τ, and the other is the outer scale or boundary-layer thickness, δ. The viscous scale increases slowly with downstream distance, roughly like $x^{1/10}$, in contrast to the boundary-layer thickness, which increases roughly like $x^{4/5}$. Any model for a turbulent boundary layer must adequately represent this feature.

Viscous diffusion of vorticity is important in the sublayer, where the gradient normal to the wall of the mean spanwise vorticity is large. Viscous diffusion by itself results in a boundary

layer whose thickness increases like $x^{1/2}$. As indicated above, the sublayer in a turbulent boundary layer grows at the much slower rate of $x^{1/10}$. Thus, to account for the smaller growth rate of the sublayer, a part of the vorticity propagation away from the wall due to viscous diffusion in the sublayer must be opposed by turbulent transport by sublayer vortices and, to a lesser extent, transport by large-scale eddies. Besides playing a role in maintaining the spanwise mean vorticity close to the wall, the large eddies must be responsible for the growth of the long tail of vorticity referred to above. In addition, the large eddies must also be at least partly responsible for entrainment of irrotational fluid, which is then made rotational by viscous diffusion.

Most of the turbulence production in a turbulent boundary layer occurs near the wall, and much of this is dissipated locally. The rest of the turbulence is transported away from the wall by a process often called turbulent diffusion. Figure 5.2, taken from Hinze (1975), shows these features. As will be argued below, there is in addition a certain amount of transport of turbulence by the large eddies.

Turbulent boundary layers are also distinguished by their slow recovery from disturbances introduced into the outer portions of the boundary layer (see, for example, Clauser 1956). Another relevant property of boundary layers at constant pressure is their small growth rate. The dimensionless growth rate with downstream distance, $d\delta/dx$, is about 1/100. As pointed out above, the growth of the viscous length scale, ν/u_τ, is much slower. Both of these features point to a weak large eddy. This behavior is in strong contrast with the behavior of rapidly growing free turbulent flows like the jet or mixing layer, where the coherent structures are energetic and are in fact the flow. For example, the rate of growth of a mixing layer is about 1/4.

Thus, the large eddy in a turbulent boundary layer can be expected to be a weak structure responsible for transport of certain quantities such as turbulence and spanwise vorticity in the outer regions of the boundary layer, for entrainment of irrotational fluid, and probably for maintaining spanwise vorticity close to the wall. However, no one has so far succeeded in establishing the role of the large eddy in the creation and maintenance of the ubiquitous sublayer streaks that are found next to the wall in turbulent boundary layers.

5.2. Presentation of Results.

The results in this chapter are presented in numerous contour plots and vector plots in the three planes $z-y$, $t-z$, or $t-y$. In all of the contour plots, the contour line corresponding to the zero level is omitted. The contour interval is stated in the first figure title in each of the contour plots. Contours corresponding to negative values for the variables are shown as dashed lines; contours corresponding to positive values are shown as solid lines. The variables plotted are ensemble averages at constant phase or perturbations at constant phase (variations of the ensemble mean from the global mean). The global mean of the boundary-layer thickness, $\overline{\delta}$, and the ratio $\overline{\delta}/u_\infty$ are used as length and time scales to normalise the plotted variables. The variable t is shown increasing from right to left to give the impression of a flow moving from left to right. In all of the plots, the length scale is indicated by a line segment representing the global mean of the boundary-layer thickness, 1.77 cm. The plots in the $z-y$ and the $t-z$ planes have identical scales in the horizontal and vertical directions. The spanwise locations of the pins used to generate the turbulent spots are indicated in the $z-y$ plane, with the size of the pins to scale. The plots in the $t-y$ plane usually have the scale in the stream direction compressed by a factor of five to emphasize the structure of the flow, which is highly elongated in the streamwise direction. The edge of the boundary layer observed at constant phase, $<\delta>$, is shown in the $z-y$ plane and the $t-y$ plane.

Variables observed at constant phase in the synthetic boundary-layer flow fall into two categories. The first category is associated with the strong background flow, which is conceptually different from the global mean flow. Certain variables, such as the mean-velocity component in the stream direction, have large gradients in the direction normal to the wall and have a non-zero global mean in the $t-z$ plane at any y. They are weakly modulated with respect to the global mean, typically by no more than a few percent. It is sometimes instructive to plot perturbation quantities (variations from the global mean) for these variables. Other variables, such as the spanwise component of mean velocity, $<w>$, are part of the coherent structure, belong to the second category, and normally have zero global mean.

5.3. Preview.

The data presented in this chapter are from the spanwise traverse at the station $x = 117.8$ cm (see chapter 3). Flow parameters and global means of certain quantities at this station, such as the skin-friction coefficient, are listed in table 2.

Early in the data analysis, it became clear that the flow consists of a strong background component on which a weak large-eddy structure is superposed. The background flow is essentially two-dimensional in the mean and is characterized by large spanwise vorticity, large horizontal shear, large Reynolds stresses, and large turbulence production. All of these quantities have maximum values near the wall and decrease to zero as the edge of the boundary layer is approached. The principal axes of strain are at 45 degrees to the wall. In contrast, the outstanding feature of the large-eddy structure is three-dimensionality in the mean. There are concentrations of streamwise and normal mean vorticity through the full depth of the boundary layer, with magnitudes small compared to the background spanwise vorticity. However, it appears that this weak structure is responsible for sustenance of the flow. These aspects of the flow will be discussed in more detail at the end of the present chapter, but it is useful to keep them in mind in the following discussion.

The Reynolds-averaged equations of motion for momentum, vorticity, and turbulence energy at constant phase are given in appendix B. Terms in the equations that play an important role in the dynamics of the flow are cited here as the need arises. The equations are written in a coordinate system moving in the downstream direction with a constant speed equal to the celerity, c, of the large eddies, which is 84.2 percent of u_∞. An important question that needs to be answered is how, in spite of the large shearing strain, a large eddy can move at a fixed speed without substantial distortion. The same question can be asked for Tollmien-Schlichting instability waves, or for the turbulent free shear layer, but at least the shear layer does not have the strong background component that is present in the boundary layer. In the absence of distortion and growth, all ensemble-averaged flow properties must be constant in the moving coordinate system; i.e., $\partial \langle f \rangle / \partial t = 0$, where f is any variable such as velocity or vorticity. The equations in appendix B are therefore written in the form $\partial \langle f \rangle / \partial t =$ (various terms). There must be a balance of the terms on the right-hand sides of these equations, much

as in a shock wave, where steepening effects due to non-linearity are balanced by viscous effects. In the present flow, of course, there is growth in the direction normal to the wall. Thus there is some distortion, and $\partial<f>/\partial t$ can be only approximately zero. As a quantitative measure, the data of figure 4.8 (or alternatively the data of table 2 of Savas and Coles 1985) show that the global mean thickness of the synthetic boundary layer increases by about 25 percent in one streamwise period of 32 cm centered on the main data station.

Terms that are common to all of the equations of motion in appendix B are the convective terms, $-(<u>-c)\,\partial f/\partial x$, $-v\,\partial f/\partial y$, and $-w\,\partial f/\partial z$, where f is any transportable quantity. The transport term due to the streamwise flow, $-(<u>-c)\,\partial f/\partial x$, can be important away from regions where $u = c$. Note that this term is a direct measure of distortion caused by the large shearing strain, $\partial<u>/\partial y$, referred to above. Near the edge of the boundary layer, any transportable quantity overtakes the eddy. Close to the wall, it is left behind by the eddy. The convective term due to the vertical component of velocity, $-<v>\,\partial<f>/\partial y$, can be important in transport of background-flow quantities having large gradients normal to the wall. Such background quantities include the streamwise momentum, $<u>$, the spanwise component of vorticity, $<\omega_z>$, the turbulent stresses, and the turbulence energy, $<q>$. The third convective term, $-<w>\,\partial f/\partial z$, is generally of second order and does not contribute much to the dynamics of the flow. The other terms in the equations are unique to the variable in question; e.g., the tilting terms in the equations for the three components of vorticity. Thus general statements are not possible for these other terms.

Quantitative estimates of such quantities as entrainment are difficult, primarily because of the use of Taylor's hypothesis, but also because of the weakness of the coherent structure. However, a study of the various terms in the equations indicates the important interactions and contributes to understanding of the behavior of the flow.

5.4. Signatures.

The structure of the large eddy can be described mainly in terms of its mean-velocity components, its large-scale mean vorticity, and its turbulent stresses, all evaluated at constant phase. The profile parameters $<\delta>$, $<C_f>$, and $<\Pi>$ are useful signatures, and are taken as the starting point in describing the structure of the flow.

Figure 5.3 shows contour plots of $<C_f>$, $<R_\delta>$, and $<\Pi>$ in the $t-z$ plane. Regions of large $<R_\delta>$ indicate bulges of turbulence in the outer parts of the boundary layer, bulges that could be made visible by flow visualization using smoke or dye. These bulges coincide with regions of large streamwise vorticity. Low values of Π mean fuller profiles, and thus indicate enhanced mixing. Note that $<R_\delta>$ and $<\Pi>$ are strongly modulated but that $<C_f>$ is not.

For convenience, the discussion will refer mostly to eddies on the center line, $z = 0$. The most striking feature of figure 5.3 is the highly structured distributions for the variables $<C_f>$ and $<\Pi>$. The peak in $<C_f>$ is located under the nose of the eddy. This result is in contrast to the result for the isolated turbulent spot (Wygnanski, Sokolov, and Friedman 1976), where there are two peaks in $<C_f>$ in the plane of symmetry. One peak occurs near the leading edge of the spot and the other, larger, peak occurs near the trailing edge. The latter must be associated with thinning of the spot at the rear and eventual reversion to laminar flow. The valley in $<\Pi>$, indicating a region of greater mixing, leads the eddy slightly but lags the peak in $<C_f>$. Regions away from the eddy are characterized by small $<R_\delta>$, small $<C_f>$, and large $<\Pi>$, and, as will be seen below, also by negligible amounts of mean streamwise and normal vorticity. This region, lying roughly between phases 5 and 15 near $z = 0$ (or between phases 15 and 5 near $z = \pm 6.1$ cm), is the region referred to here as the passive or background region. This passive region is inactive only in a relative sense; for example, the value of $<C_f>$ in the passive region is only about five percent lower than the peak value of $<C_f>$.

5.5. Vorticity Field.

It is convenient to take the ensemble-averaged streamwise and vertical components of vorticity, $<\omega_x>$ and $<\omega_y>$, as primary variables, since these quantities are zero for the global mean and for the hypothetical background flow. Other aspects of the flow, including mean-velocity components, turbulence quantities, and turbulence production, can generally be interpreted on the basis of these primary variables. The spanwise component of vorticity, $<\omega_z>$, is largely concentrated near the wall and is part of the background flow.

5.5.1 Streamwise Vorticity. Figure 5.4 shows contour plots of streamwise vorticity at the

twenty phases, starting from phase 13. Attention should focus on the eddy on the centerline. At phase 18, regions of vorticity first appear near the edge of the boundary layer on either side of the line of symmetry. These regions first grow and then eventually become flatter and move closer to the wall. The peak vorticity initially increases with distance upstream (increasing phase). By about phase 6, these regions have almost disappeared. The sense of this vortex pair is such as to pump fluid away from the wall along the centerline. We think of these as the primary streamwise vortices. At phase 17, a secondary pair of strong streamwise-vorticity regions appears, having a sense opposite to that of the primary pair. This secondary pair is probably induced by the primary vortices and displays a similar behavior, starting near the edge of the boundary layer and moving closer to the wall with increasing distance upstream. However, unlike the vortices in the primary pair, the vortices in the secondary pair move towards each other slightly with increasing phase. By about phase 2 the secondary pair has almost disappeared.

Contour plots of the same streamwise vorticity component in the t–y plane for z = 0(0.5)7.0 cm are shown in figure 5.5. The scale in the y-direction is five times the scale in the t-direction. The primary-vorticity regions are clearly seen from $z = 0.5$ cm to $z = 2.5$ cm for the center-line eddy. They are attached to the wall at their upstream end, are inclined in the streamwise direction, and have their maximum intensity at about $z = 1.0$ cm, where they extend across the full thickness of the boundary layer. The secondary streamwise vorticity regions lie slightly downstream from the primary ones and are strongest from $z = 2.0$ cm to $z = 3.5$ cm.

Finally, figure 5.6 shows contour plots of the same vorticity component $<\omega_x>$ in the t–z plane at the 15 y-measurement locations. This figure reveals especially large values of streamwise vorticity close to the wall (e.g., at $y = 0.150$ cm) that are associated with the secondary streamwise vortices.

A perspective view of the primary and secondary streamwise-vorticity regions is shown in figure 5.7. The three axes have nearly identical scales. The surface represents a non-dimensional streamwise vorticity equal to 0.01. This is the central figure of the present research, and it will be referred to often in the following discussion. The figure covers half a

cycle in the t-direction, from phase 16 to phase 6, and a full cycle in the spanwise direction, from $z = -6.1$ cm to $z = +6.1$ cm. This is the area that is referred to as a tile and contains the basic largest entity of the flow -- the large eddy. The synthetic boundary layer is composed of a continuous distribution of such tiles (eddies) arranged in a hexagonal pattern, as shown in the upper right corner of figure 5.7. There is some interaction between neighboring eddies. For example, in the figure the tile corresponding to the centerline eddy contains, from phase 16 to phase 18, tails of the off-centerline eddies. However, the interaction between neighboring eddies is believed to be small in the present flow. If the interaction is indeed small, then it is not necessary that the eddies be produced in a hexagonal pattern; for example, a rectangular array of eddies should equally well satisfy the requirements of the present type of study. However, only an experiment can determine whether any pattern is adequately stable.

5.5.2. Normal Vorticity. The existence of a normal component of vorticity, $<\omega_y>$, in the large eddy is one of the key findings of the present research. The most significant feature is that regions of large streamwise vorticity and large normal vorticity occur close to each other, and in fact nearly coincide. The importance of this fact will become apparent later, when the question of maintenance of the eddy as a single entity in a highly sheared and highly turbulent background flow is addressed. The vertical component of vorticity, $<\omega_y>$, is shown in figures 5.8, 5.9, and 5.10 as sets of contour plots in the $z-y$, $t-y$ and $t-z$ planes. Again two pairs of vortices are observed, at approximately the same locations as the streamwise vortices. For the primary vortices the peak value of the normal component, $<\omega_y>$, is somewhat higher than the peak value of the streamwise component, $<\omega_x>$. The opposite is true for the secondary vortices. As in the case of $<\omega_x>$, the primary regions of the normal component of vorticity extend across the thickness of the boundary layer and are inclined at a shallow angle to the wall. The sense of the normal vorticity for the primary pair of vortices is such as to slow fluid near the center line. As in the case of the streamwise vortices, the sense of the normal vorticity in the secondary vortices is opposite to that of the primary vortices.

The term "vortices" is used loosely here to mean any region where there is a concentration of vorticity and where the mean instantaneous stream paths are close to being closed curves rather than parallel lines (see figure 5.15 below). To clarify this point, figure 5.11 shows the

vorticity vectors in the $t-y$ plane at $z = 1.0$ cm and at $z = 2.5$ cm. The primary and secondary vorticity regions are centered at approximately these z locations (cf. figure 5.9). This particular figure has the same scale in both directions, and only phases 16 to 6 are shown. Even though vorticity in the streamwise and normal directions is concentrated at about the same locations, a single vortex tube at a steep angle to the wall is not consistent with the figure.

5.5.3. Spanwise Vorticity. Primarily because of the term $\partial<u>/\partial y$ in the definition of $<\omega_z>$, the spanwise component of vorticity is part of the strong background flow discussed above. The value of $<\omega_z>$ at the measurement location closest to the wall, $y = 0.15$ cm, is negative and of order unity. Near the edge of the boundary layer it diminishes to about -0.1. For comparison, the peak values observed for the streamwise and normal components of vorticity are about 0.05. However, the maximum modulation in $<\omega_z>$ away from the global mean $\overline{\omega_z}$ is about 0.1, and is therefore of the same order of magnitude as the peak values for $<\omega_x>$ and $<\omega_y>$. Contour plots of the perturbation of the spanwise component of vorticity away from the global mean are shown in figures 5.12, 5.13, and 5.14. These plots are instructive in discerning the structure of the flow. Maximum values of $-<\omega_z>$ close to the wall occur where large values of the skin-friction coefficient, $<C_f>$, are observed. This coincidence is not surprising, since in the log region of the boundary layer the gradient is given by $\partial<u>/\partial y = (1/\kappa)\,<u_\tau>/y$. Very close to the wall, for values of y less than 0.2 cm, $-<\omega_z>$ is observed to have a peak at about phase 6 for $z = 0$ (see figure 5.14), a vicinity where low values of $<C_f>$ also occur. This anomaly may be caused by uncertainty in the differentiation process required to calculate $<\omega_z>$. Also, in the outer regions of the boundary layer, local peaks in $-<\omega_z>$ are observed that can be associated with peaks in the boundary layer thickness, $<\delta>$. The shape of these regions, especially near $y = 0.7$ or 0.9 cm, is agreeably similar to the shape of a turbuelnt spot. As discussed below, the structure of the spanwise vorticity distribution seems to be determined mostly by the stretching term in the equation for the spanwise component of vorticity.

It will be argued later that interactions among the three components of vorticity are strong, and that each of the components is essential to the overall dynamics of the flow.

5.6. Velocity Field.

The streamwise component of velocity at constant phase, $<u>$, belongs to the background flow. There are large gradients normal to the wall and weak modulations in the t and z directions at a given distance from the wall. The maximum modulation in $<u>$ occurs at about half the boundary-layer thickness and is about five percent of u_∞. The normal velocity component, $<v>$, and the spanwise velocity component, $<w>$, however, are part of the large-eddy structure and are well correlated with the streamwise and normal vorticity components described in the previous section. The magnitudes of the velocity components $<v>$ and $<w>$ are small (less than $0.01\ u_\infty$), in agreement with the hypothesis of a weak large eddy. The normal component of velocity is important in entrainment of irrotational fluid and in transport of various background-flow quantities, such as streamwise momentum and turbulence energy. In addition, the normal component of velocity enters as the gradient $\partial<v>/\partial z$ in the dominant tilting term in the equation for the normal vorticity, $<\omega_y>$. The main importance of the spanwise component of velocity seems to in the stretching term, $<\omega_z>\partial<w>/\partial z$, in the equation for the spanwise vorticity (see section 5.9 below).

5.6.1. Velocity Vector Diagrams. Figure 5.15 shows the velocity vectors in the $t-y$ plane at z = 0(0.5)7 cm as they appear to an observer moving in the streamwise direction at the celerity c. The plots are compressed by a factor of five in the t-direction with respect to the y-direction, to reveal the structure. The lengths of the vector components parallel to the wall are similarly compressed, so that the vectors do not represent the true angles. The most striking features are the large shear in the stream direction and the small value of the normal component of velocity compared to the streamwise component. No definitely closed streamlines are observed in the $t-y$ plane, a result in contrast to that for an isolated turbulent spot, which contains closed streamlines in its plane of symmetry (Cantwell, Coles, and Dimotakis 1978). Relatively strong upward flow occurs at phase 2 near z = 0 cm and downward flow occurs at phase 12 near z = 4.0 cm.

The main purpose of figure 5.15 is to show the large horizontal shearing-strain rates that exist in the $t-y$ plane. The difference between the streamwise components of velocity at the edge of the boundary layer and at y = 0.15 cm (the measurement location closest to the wall) is

about 0.35 u_∞. Thus a line of particles initially perpendicular to the wall and extending between y = 0.15 cm and the edge of the boundary layer would have an average inclination of less than 45 degrees to the wall by the time the eddy travels a distance of only $3\,\overline{\delta}$. Since the large eddy is travelling at a fixed speed without a substantial change in shape, fluid must pass through or possibly around the eddy.

Figure 5.16 shows velocity vectors in the $z-y$ plane at successive phases, starting at phase 13. The scale for the lengths of the velocity vectors is also shown, to make plain that the velocity magnitude in this plane is everywhere less than 0.01 u_∞. Figure 5.16 is probably the one figure that epitomizes of the important features of the large eddy in the synthetic boundary layer. Note that the peaks in streamwise vorticity do not always fall on points where the $<v>$ and $<w>$ components of velocity are simultaneously zero, as would be the case, for example, for an isolated two dimensional vortex. Relatively strong upward flow is induced between the primary vortices near the plane of symmetry, and downward and inward flow is induced from about phase 18 to about phase 2 at $z = \pm$ 2 cm. A highly structured and relatively strong spanwise flow is observed along the entire length of the eddy (phase 16 to phase 4). At about phase 15, flow associated with the secondary streamwise vortices is being formed; this flow becomes stronger and then eventually dies out at about phase 1. In the passive region, phases 13 and 14 near z = 0, there is not much activity near the centerline away from the wall. Close to the wall, a fairly strong flow away from the centerline is observed, at least part of which is due to the influence of the off-centerline eddies (which are 180 degrees out of phase with the centerline eddy). Points at which $<v> = 0$ and $<w> = 0$ are observed on the center line near the edge of the boundary layer at phases 13 to 18. These points are not stagnation points, because $<u>$ is not equal to zero even in the moving coordinate system; the flow is simply parallel to the wall at these points (see also figure 5.15).

Velocity vectors in the $t-z$ plane at different y-locations, shown in figure 5.17, offer a different point of view. The vector components in the streamwise direction are those corresponding to the perturbation of the velocity component $<u>$ from the global mean, $\overline{u}$. In the outer portions of the boundary layer (between $y = 0.5$ cm and $y = 1.8$ cm), regions associated with the primary pair of normal vortices (see figure 5.10) are clearly seen. Within

the eddy the fluid is slowed down; outside of the eddy the fluid has a relatively higher speed. The suggestion of closed streamlines is only apparent, as it is perturbation values for the streamwise component of velocity that are plotted. The flow closer to the wall is more complicated and not readily described.

5.6.2. Normal Velocity Component. Figures 5.18 and 5.19 are contour plots of the normal component of velocity in the $z-y$ and $t-z$ planes, respectively. As argued earlier, no quantitative estimates of entrainment are possible. However, entrainment of irrotational fluid can be expected wherever there is downflow near the edge of the boundary layer; e.g., near $z = \pm 2$ cm from phase 17 to phase 2 in figure 5.18. Similarly, any flow away from the wall can be expected to transport quantities such as streamwise momentum, spanwise vorticity, and turbulence energy into the outer portions of the boundary layer. Such outflow is observed near the centerline from phase 19 to phase 12. The positive normal-velocity components from phases 9 to 11 near $z = 0$ are due to the combined influence of the two off-centerline eddies, located from phases 6 to 16. All of these features may be seen in figure 5.16 or in figure 5.19.

Positive values for the normal component of velocity result in the transport of fluid having low streamwise momentum away from the wall; negative values bring fluid having high streamwise momentum closer to the wall. Therefore, a correlation may be expected between the streamwise and normal components of mean velocity. Contour plots of the perturbation in the streamwise component of velocity, $<u> - \bar{u}$, are shown for the $z-y$, $t-z$, and $t-y$ planes in figures 5.20, 5.21 and 5.22. The correlation mentioned above is conspicuous in the plots in the $z-y$ plane (figure 5.20). Attention should focus on the centerline eddy. Regions of deficit in the streamwise component of velocity are observed from about phase 19 to about phase 5. These regions coincide with regions of flow away from the wall (see figure 5.18). Similarly, regions of excess streamwise momentum coincide with regions of flow toward the wall; e.g., at phase 19 and $z = \pm 2$ cm. Close to the wall (y = 0.15 cm), regions with relatively higher streamwise momentum coincide with regions of high wall shearing stress (compare figures 5.21 and 5.3). This result is to be expected, as the wall shearing stress was determined from a fit to the mean-velocity component $<u>$ (see chapter 4).

5.6.3. Spanwise Velocity Component. The spanwise component of velocity, $\langle w \rangle$, is shown in the form of contour maps in the $z-y$ and $t-z$ planes in figures 5.23 and 5.24. The outstanding features are the relatively large values obtained near the wall for $\langle w \rangle$ and for the strain rate $\partial\langle w \rangle/\partial z$ (see, especially, figure 5.24).

5.6.4. Secondary Flow. The flow associated with the secondary pair of streamwise vortices (see, for example, figures 5.7 and 5.16) is most conveniently described in terms of the continuity equation for the mean velocity at constant phase. A study of the continuity equation sometimes provides a different, useful point of view to explain certain properties of a flow. To appreciate this point, consider the $z-y$ plane. If the velocity gradient normal to this plane, $\partial\langle u \rangle/\partial x$, has values small compared with values of the in-plane velocity gradients $\partial\langle v \rangle/\partial y$ and $\partial\langle w \rangle/\partial z$, then the flow may be considered to be roughly two-dimensional locally in the $z-y$ plane. This same argument also applies to the $t-z$ or the $t-y$ plane. Contour plots of the velocity gradients $\partial\langle u \rangle/\partial x$, $\partial\langle v \rangle/\partial y$, and $\partial\langle w \rangle/\partial z$ in the $z-y$ plane are shown in figures 5.25, 5.26, and 5.27, and plots of the gradient $\partial\langle w \rangle/\partial z$ in the $t-z$ plane are shown in figure 5.28. The region from about phase 13 to about phase 17 near the centerline has small values for the velocity gradient $\partial\langle v \rangle/\partial y$, compared with values of the other two terms in the continuity equation. That the flow in this region is roughly parallel to the wall is confirmed by the velocity-vector diagrams (figure 5.16). The secondary flow begins at about phase 15, downstream of the nose of the eddy (see figure 5.16). Consider the flow in the coordinate system moving in the streamwise direction with the celerity of $0.842\, u_\infty$. In the outer portions of the boundary layer, the fluid inside the eddy has relatively smaller values of the streamwise velocity component (figure 5.17). The faster-moving fluid outside of the eddy closes in on the nose of the eddy; therefore, flow in the outer half of the boundary layer is toward the plane of symmetry at phases 15 to 17. The flow toward the plane of symmetry from phases 18 to 3 is mainly due to the primary vortices. Close to the wall, the fluid is slowed down (in the moving coordinate system) in the streamwise direction by the relatively high wall shearing stress (figure 5.3) near phase 17 and $z = 0$. The flow in the negative x–direction diverges downstream of the high shearing-stress region; i.e., the flow in the lower half of the boundary layer is away from the centerline at phases 15 and 16. This divergence of the flow close to the wall, and the

convergence of the flow farther from the wall, are responsible for the secondary streamwise vortices that are clearly seen in figure 5.16. Dynamics always determines the flow, but dynamics is not always needed to explain certain features of the flow. The secondary flow above is a case in point. The formation of the primary vortices, however, could not be explained as simply from continuity considerations alone.

5.7. Turbulence Quantities.

The Reynolds stresses and the turbulent energy, $\langle q \rangle$, at constant phase represent contributions from smaller eddies. It is important to know the distribution of these quantities relative to the location of the large eddy. The other quantity of interest related to the random turbulence is the intermittency at constant phase, $\langle \gamma \rangle$. Figure 5.29 is a set of contour plots of the variable $\langle \gamma \rangle$ in the $t-y$ plane. The contour levels vary from 0.1 to 0.9. The band of the intermittent region is spread roughly evenly about the edge of the boundary layer. However, the lines of constant intermittency are less modulated than is the boundary-layer thickness. This difference is probably an experimental artifact, and is related to the fact that the raw intermittency data were not edited before calculation of the ensemble mean and also the fact that a constant hold time of one millisecond was used in the one-shot in the intermittency circuit. In one millisecond, fluid elements in the free stream travel about 1.2 cm, which is of the order of the boundary-layer thickness. In any case, it is clear from figure 5.29 that the instantaneous corrugations normal to the wall of the outer edge of the boundary layer have a smaller scale, about $0.4\ \overline{\delta}$, than the length of the eddy in the streamwise direction, about $5\ \overline{\delta}$. Flow-visualization pictures of turbulent boundary layers and isolated turbulent spots are consistent with this observation, revealing instantaneous undulations in the outer edge of the boundary layer on the scale of the boundary-layer thickness.

Of the accessible Reynolds stresses, $\langle u'u' \rangle$, $\langle u'v' \rangle$, $\langle v'v' \rangle$, $\langle w'w' \rangle$, and $\langle u'w' \rangle$, only the first four are important. Like the spanwise component of vorticity, these stresses belong to the background flow, in that they are weakly modulated in the t and z directions and have large gradients normal to the wall. Another important characteristic of the stresses is that they all give the impression of being in local equilibrium.

Contour plots at constant phase of the four Reynolds stresses $\langle u'u' \rangle$, $\langle u'v' \rangle$, $\langle v'v' \rangle$, and $\langle w'w' \rangle$ in the $t-y$ plane are shown in figures 5.30 to 5.33. Note that the contour intervals for the different stresses are not the same. All of the plots show essentially similar features. Lines joining the loci of the maximum or minimum values of the stress at different values of y are inclined at a shallow angle to the wall. The most significant difference between the distributions of the different stresses is in the streamwise locations of the maximum stress near the wall. The contours in the outer regions of the boundary layer follow closely the curve $y = \langle \delta \rangle$. See, especially, the plot of the stress $\langle u'v' \rangle$ in figure 5.30, where the choice of contour levels makes the top contour almost exactly coincident with the edge of the boundary layer. This coincidence is remarkable, in view of the fact that the boundary-layer thickness was determined by a profile fit to the mean velocity $\langle u \rangle$ and is thus totally independent of the measured turbulent stresses.

Figures 5.34, 5.35, and 5.36 show contour plots of the perturbation shear stress $\langle u'v' \rangle - \overline{u'v'}$ in the $z-y$, $t-z$ and $t-y$ planes. Consider the plots in the $t-y$ plane, figure 5.36. The region of primary streamwise vorticity lies between the regions of maximum and minimum perturbation-stress contours. The peaks in the shearing stress $-\langle u'v' \rangle$ near the wall lie close to the regions of high wall shear (compare figures 5.36 and 5.3). The greatest modulation in the shearing stress occurs on the centerline, and the least modulation is observed midway between adjacent pins; e.g., near $z = 3$ cm.

Figures 5.37, 5.38, and 5.39 show that the ensemble-averaged streamwise fluctuations $\langle u'u' \rangle - \overline{u'u'}$ in the three planes, plotted as a perturbation from the global mean, behave in much the same way as $\langle u'v' \rangle - \overline{u'v'}$. The main difference between these two stresses is in the location of their peak values close to the wall; the peak value in $\langle u'v' \rangle$ occurs somewhat upstream of the peak value in $\langle u'u' \rangle$. This property is readily apparent when comparing the plots for the two stresses in the plane of symmetry, $z = 0$. Figures 5.40 to 5.42 and 5.43 to 5.45 are similar plots of the stresses $\langle v'v' \rangle - \overline{v'v'}$ and $\langle w'w' \rangle - \overline{w'w'}$. The stress $\langle u'w' \rangle$ was measured, but is small. A contour plot with the same contour intervals as for $\langle u'v' \rangle$ would be completely blank. This stress is therefore omitted from the data presentation.

The outstanding feature common to all of the Reynolds stresses is that regions of low or high values of the perturbation stress are highly elongated in the streamwise direction and are inclined at a shallow angle to the wall. It should be emphasized again that the compression of the horizontal scale for plots in the $t-y$ plane presents a distorted picture, and that the structures are much flatter than they appear to be in the figures.

The distribution of each of the Reynolds stresses in the outer regions of the boundary layer is correlated with vertical components of velocity that are induced by the large eddy. As an example, consider the plots of the perturbation stress $<u'u'> - \overline{u'u'}$ in the $z-y$ plane (figure 5.37). From about phase 19 to phase 4, regions of higher stress in the outer half of the boundary layer can be clearly associated with upflow near the plane of symmetry. From about phase 18 to about phase 2, regions of lower stress near $z = 0$ in the lower half of the boundary layer can be associated with flow toward the wall (compare figures 5.36, 5.16 and 5.18). This clear correlation between stress level and the vertical component of velocity exists for the other stresses, $<u'v'>$, $<v'v'>$, and $<w'w'>$, as well.

Evidently, the structures of all of the Reynolds stresses are similar. To make this point quantitatively, the ratios of the shearing stress $-<u'v'>$ to each of the other stresses, $<u'u'>$, $<v'v'>$, and $<w'w'>$, are plotted against the dimensionless distance $y/<\delta>$ in figures 5.46 to 5.48. Each of the figures contains two parts, a and b . Part a has four plots, each representing phases 16 to 6, at the spanwise positions z = 0(1.0)3.0 cm. Part b is similar except that each plot represents phases 6 to 16. Thus part a corresponds to the region containing the large eddy, and part b corresponds to the passive region referred to earlier. Note that a complete tile is represented in the figures. Values corresponding to global means are drawn as solid lines in the plots. The data collapse fairly well for all of the ratios, especially for values of $y/<\delta>$ less than 1. The collapse is not quite as good for the ratio $-<u'v'>/<w'w'>$ as it is for the other quantities. Besides indicating the the degree of similarity between the various stresses, these ratios are in some sense a measure of the active component -- the shear-producing part -- of the turbulence. The inactive part may be considered to consist of irrotational fluctuations and fluctuations associated with the large-scale vorticity in the outer flow (Bradshaw 1967). There is a tendency for the shearing stress $<u'v'>$

to be lower, compared with values of $\langle v'v' \rangle$ and $\langle w'w' \rangle$, in the region containing the eddy than in the passive region. This observation may be an indication that the large eddy contains a relatively larger proportion of irrotational fluctuations. With increasing distance from the edge of the boundary layer, the shear stress $-\langle u'v' \rangle$ goes to zero faster than the normal stresses $\langle u'u' \rangle$, $\langle v'v' \rangle$, and $\langle w'w' \rangle$. Note that there are extensive regions within the boundary layer where the ratios $-\langle u'v' \rangle / \langle u'u' \rangle$ and $-\langle u'v' \rangle / \langle w'w' \rangle$ are nearly constant; however, the ratio $-\langle u'v' \rangle / \langle v'v' \rangle$ increases monotonically from a small value outside the boundary layer to a value of about unity as the wall is approached.

The similarity in the distributions of the Reynolds stresses suggests that contributions to these stresses come from eddies of small or medium scale. The reaction times of these eddies are short enough so that all of the stresses are in local equilibrium. Probably there is a connection between this observation and the fact that the log law is valid locally everywhere in this flow.

5.8. Turbulence Production.

The dominant term in the equation for turbulence energy is the term $-\langle u'v' \rangle \partial \langle u \rangle / \partial y$. This term represents work done by the Reynolds shearing stress against the mean rate of shearing strain, $\partial \langle u \rangle / \partial y$, to produce turbulence energy. As stated earlier, a large fraction of the turbulence energy thus produced is dissipated locally. The term $-\langle u'v' \rangle \partial \langle u \rangle / \partial y$ belongs to the background-flow structure, and it is more useful to look at perturbations of this quantity from the global mean. Figures 5.49 to 5.51 show contour plots of the perturbation of the production term in the $z-y$, $t-z$, and $t-y$ planes. As in the case of the Reynolds stresses, regions of higher and lower turbulence production are inclined in the flow direction at a quite shallow angle to the wall (see, e.g., figure 5.51). More important, regions of high turbulence production close to the wall are associated with regions of high wall shear (compare figures 5.50 and 5.3). As will be shown below, these regions are also close to regions where the stretching term is large in the equation for the spanwise component of vorticity.

5.9. Overview.

It is possible at this point to define the large eddy and to comment on the role it plays and the mechanisms by which it is maintained. In the coordinates used here, the large-scale features

of the flow are frozen when viewed in a coordinate system moving at the celerity of the eddy.

5.9.1. Role of the Structure. The large eddy appears to contain two regions -- primary and secondary -- where relatively large values of streamwise and normal vorticity are observed. The perspective view showing regions of streamwise vorticity greater than 0.01 (figure 5.7) suggests that the primary pair of vortices is about five $\overline{\delta}$ long in the streamwise direction and inclined at a shallow angle to the wall. The centers of the two vortices are separated by about one $\overline{\delta}$ in the spanwise direction. The secondary regions are about two $\overline{\delta}$ long and are separated by two $\overline{\delta}$ in the spanwise direction. As indicated earlier, the normal component of vorticity also is concentrated in these same primary and secondary regions (see figure 5.8).

A positive normal velocity is induced between the primary vortices. This upward flow results in transport away from the wall of low-momentum fluid, of turbulent stresses, and of spanwise vorticity. Thus there is a correlation in the outer regions of the boundary layer between regions of upward flow and regions with relatively small values of $<u>$, and between regions of upward flow and regions of relatively high turbulent stresses. However, regions of large spanwise vorticity and regions of upward flow are not always correlated, primarily because of the domination of the stretching term in the equation for the spanwise component of vorticity (see below). Downward and inward flow is found between the primary and secondary vortices and results in transport of high-momentum fluid and fluid with low values for the turbulent stresses towards the wall and toward the plane of symmetry of the structure.

Large strain rates in the spanwise direction, $\partial<w>/\partial z$, are observed near the wall as a consequence of variable spanwise velocities induced by the eddy. Depending on the sign of $\partial<w>/\partial z$, these strain rates strengthen or weaken the spanwise vorticity through the stretching term $<\omega_z>\partial<w>/\partial z$. Together with transport of $<\omega_z>$ by the normal component of velocity, stretching seems to be the primary mechanism by which vorticity remains concentrated close to the wall. Figures 5.52 and 5.53 show contour maps in the $z-y$ plane of the stretching term $<\omega_z>\partial<w>/\partial z$ and the transport term $-<v>\partial<\omega_z>/\partial y$.

The stretching term appears to be intimately connected with the wall shearing stress. Regions of large negative values of $<\omega_z>\partial<w>/\partial z$ are observed near $z = 0$ cm from phase

14 to phase 16, and near $z = \pm 2$ cm from phase 18 to phase 2 (figure 5.51). Both of these regions become less extensive in the y direction with increasing distance upstream. Peak values in $<C_f>$ at the wall coincide with regions of large spanwise stretching, although there is a slight phase difference; peaks in $<C_f>$ lie upstream of peaks in $<\omega_z> \partial<w>/\partial z$. This observation is probably related to the tendency, referred to above, for peak regions in $<\omega_z> \partial<w>/\partial z$ to move toward the wall with increasing upstream distance. Similarly, regions of low $<C_f>$ are related to areas where large positive values of $<\omega_z> \partial<w>/\partial z$ occur. It should be pointed out that the strain rate $\partial<w>/\partial z$ is the controlling factor in the stretching process, since $<\omega_z>$ is part of the background flow, is large everywhere, and is only weakly modulated at a given y. The fact that $\partial<w>/\partial z$ is large wherever $<C_f>$ is large is important to the overall machinery of the eddy, because that is the only means by which higher diffusion of spanwise vorticity associated with higher $<C_f>$ can be countered.

It may be noted that the vortex-stretching process can account for the well-known rapid adjustment of flow near the wall to perturbations in the boundary conditions, compared with the slow adjustment of the outer flow. Whether or not stretching is involved in maintenance of the streamwise vortices in the sublayer is an open question, since the origin of these vortices is not understood. Finally, stretching provides a mechanism by which a constant shearing stress normal to the wall can be maintained for a changing outer flow without the agency of pressure gradients.

The transport term due to the normal component of velocity, $-<v> \partial<\omega_z>/\partial y$, is important between the legs of the primary vortices (figure 5.7). It is strongest between phase 20 and phase 4 near $z = 0$. The convective term due to the streamwise component of velocity, $-(<u> - c)\, \partial<w>/\partial x$, is only important close to the wall, where vorticity is left behind by the eddy. The role, if any, that this residual vorticity plays in the passive region (near phase 13 and $z = 0$) is not clear.

The dominant viscous diffusion term, $\nu\, \partial^2<\omega_z>/\partial y^2$, in the equation for $<\omega_z>$ is large close to the wall compared with the stretching and transport terms discussed above. Thus the rest of the diffusion term is balanced by smaller eddies, which show up as the turbulence correlation terms. (See equation (B2), appendix B.) However, the mechanism of vorticity

maintenance close to the wall by the small eddies must be essentially the same as that of the large eddy; namely, intensification of vorticity by stretching of vortex lines as they approach the wall (cf. Lighthill 1963).

5.9.2. Maintenance. The streamwise and normal components of vorticity are critical to the large eddy. It is therefore important to identify the dominant terms in the equations for $<\omega_x>$ and $<\omega_y>$. The large gradient of streamwise velocity normal to the wall, $\partial<u>/\partial y$, determines which of the tilting terms in the vorticity equations for $<\omega_x>$ and $<\omega_y>$ are dominant. The gradient $\partial<u>/\partial y$ appears either as a term responsible for tilting or as part of the spanwise component of vorticity, $<\omega_z>$, that is being tilted. The convective term due to the streamwise component of velocity is important near the wall and near the edge of the boundary layer. If only these dominant terms and the unknown turbulence terms are retained, equation (B.2) for $<\omega_x>$ becomes

$$\frac{\partial<\omega_x>}{\partial t} \approx -(<u>-c)\frac{\partial<\omega_x>}{\partial x} + \frac{\partial<u>}{\partial y}<\omega_y> + \frac{\partial<u>}{\partial z}<\omega_z> + \text{turbulence terms}$$

Of the two tilting terms, the first is dominant, and the equation becomes, after the vorticity components are expressed in terms of velocity derivatives,

$$\frac{\partial<\omega_x>}{\partial t} \approx -(<u>-c)\frac{\partial<\omega_x>}{\partial x} + \frac{\partial<u>}{\partial y}\left[-\frac{\partial<w>}{\partial x}\right] + \text{turbulence terms} \qquad (5.1)$$

The term $-\partial<w>/\partial x$ is part of the vertical component of vorticity that is being tilted by $\partial<u>/\partial y$.

Figure 5.54 shows the convective term, $-(<u>-c)\,\partial<\omega_x>/\partial x$, as a series of contour plots in the $z-y$ plane, starting at phase 13. Figure 5.55 shows the same variable in the $t-y$ plane. This term is important close to the wall, since relatively large values of $<\omega_x>$ exist near the wall. Contributions due to secondary streamwise vorticity (see figure 5.4) are seen from phase 1 to phase 5 close to the wall. Part of the primary streamwise vorticity is left

behind between phases 5 and 8 near the wall. This residual vorticity must be balanced by the turbulence terms, as the streamwise vorticity is negligible in these regions. Some contribution from the convective term is also observed near the edge of the boundary layer between phases 18 and 20 near the centerline. The more important tilting term, shown in figures 5.56 and 5.57, has contributions at approximately the same locations where the streamwise vorticity $<\omega_x>$ has large values. This may be seen by comparing figure 5.56 with figure 5.4, which shows the streamwise vorticity contours. The value of any mean quantity at constant phase, including streamwise vorticity, $<\omega_x>$, should not change appreciably as seen by an observer following the eddy, as explained in section 5.3. It follows that the sum of the convective term due to the streamwise component of velocity and the tilting term must be balanced by the turbulence terms, since these are the only remaining terms in the equation for streamwise vorticity. Figure 5.58 shows the sum of the convective and tilting terms of equation (5.1) as a set of contour plots in the $z-y$ plane. This figure indicates the magnitude of the turbulence terms, which appear to be of the order of the tilting term. It is difficult to judge which turbulence terms in the equation are dominant (see equation B2). But it is clear experimentally that tilting of the normal component of vorticity is the mechanism by which the streamwise vorticity is sustained in the primary and secondary regions of the eddy.

The equation for the normal component of vorticity, $<\omega_y>$, with only the dominant terms, is

$$\frac{\partial<\omega_y>}{\partial t} \approx -(<u>-c)\frac{\partial<\omega_y>}{\partial x} + \frac{\partial<v>}{\partial z}<\omega_z> + \text{turbulence terms}$$

The convective term, $-(<u>-c)\,\partial<\omega_y>/\partial x$, shown in figures 5.59 and 5.60, is important near the edge of the boundary layer for phases 16 to 18. These are contributions from the primary normal component of vorticity (see figure 6) which has been carried downstream by the faster-moving fluid in the outer regions of the boundary layer. Again, as in the case of $<\omega_x>$, the convected normal component of vorticity, $<\omega_y>$, cannot be sustained in steady flow (in the moving frame) and must be balanced by the turbulence and tilting terms. The tilting of the spanwise component of vorticity to produce the normal component, measured by

$(\partial \langle w \rangle / \partial x)\ \langle \omega_z \rangle$, is shown in figures 5.61 and 5.62. Comparison of figures 5.8 and 5.16 shows that regions of large contributions from the tilting term and regions of large $\langle \omega_y \rangle$ roughly coincide. To get an indication of the importance of the turbulence terms, the sum of the convective and tilting terms is shown in figure 5.63. Again, as in the case of the streamwise component of vorticity, the turbulence terms seem to be important in the equation for the normal component of vorticity and to act as a sink for the mean normal vorticity at constant phase, $\langle \omega_y \rangle$. Again, tilting seems to be the mechanism that balances the changes due to convection and turbulence and thus sustains the normal vorticity.

The interaction among the three components of vorticity is depicted in the sketch below. Consider the top part of the figure. Part of the normal component of vorticity, $\langle \omega_y \rangle$, is tilted by $\partial \langle u \rangle / \partial y$ to generate $\langle \omega_x \rangle$ (shown as path A in the figure). The streamwise component of vorticity, $\langle \omega_x \rangle$, induces a large strain in the spanwise direction, $\partial \langle w \rangle / \partial z$, which through the stretching term $(\partial \langle w \rangle / \partial z) \langle \omega_z \rangle$ intensifies the spanwise component, $\langle \omega_z \rangle$ (shown as path B in the figure). The gradient $\partial \langle v \rangle / \partial z$ in $\langle \omega_x \rangle$ is responsible for tilting the spanwise component $\langle \omega_z \rangle$ to generate the normal component of vorticity, $\langle \omega_y \rangle$ (shown as path C in the figure). The intensification of the spanwise component component, $\langle \omega_z \rangle$, by the strain rate $\partial \langle w \rangle / \partial z$ coincides with regions of large wall shear and large turbulence production. The normal components of velocity induced by the large eddy seem to be partly responsible for entrainment of irrotational fluid and also for transport across the outer regions of the boundary layer of quantities such as streamwise momentum. The lower part of the figure, labelled kinematics, shows pictorially the tilting mechanisms responsible for the generation of streamwise and spanwise vorticity.

5.10. Comparison with Results from Natural Turbulent Boundary Layers.

It is necessary to establish that the large-eddy structures observed in the synthetic turbulent boundary layer and the natural turbulent boundary layer are similar. This issue can, at least in part, be clarified by determining whether or not the structure of the large eddy observed in the synthetic boundary layer is consistent with results from investigations in natural boundary layers. It has already been demonstrated in chapter 4 that the two boundary layers compare well in terms of their mean properties.

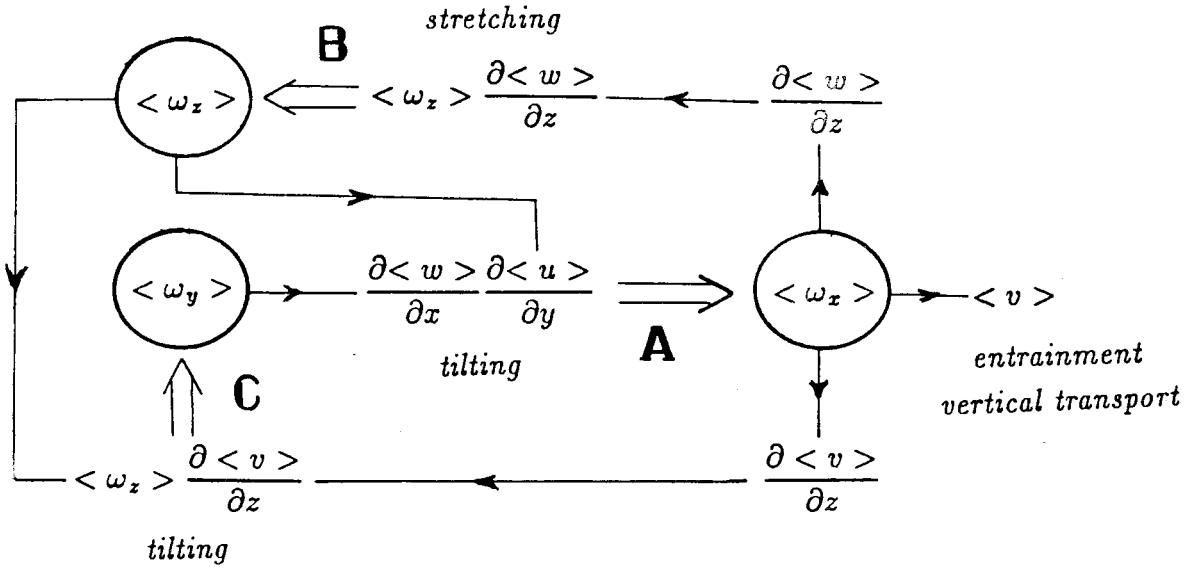
stretching
B
$< \omega_z >$
$< \omega_z > \frac{\partial < w >}{\partial z}$
$\frac{\partial < w >}{\partial z}$
$< \omega_y >$
$\frac{\partial < w >}{\partial x} \frac{\partial < u >}{\partial y}$
tilting
A
$< \omega_x >$
$< v >$
entrainment
vertical transport
C
$< \omega_z > \frac{\partial < v >}{\partial z}$
$\frac{\partial < v >}{\partial z}$
tilting

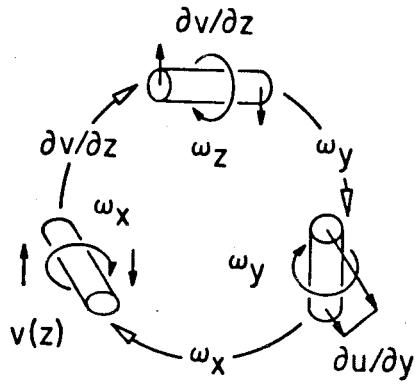
∂v/∂z
∂v/∂z
ωz
ωy
ωx
ωy
v(z)
ωx
∂u/∂y

KINEMATICS

The paper by Kovasznay, Kibens, and Blackwelder (1970) was the first serious attempt to detect large-eddy structure, and employed space-time correlation functions involving the streamwise and normal components of velocity as well as the intermittency. Figure 5.64 shows a typical space-time autocorrelation function obtained for the streamwise component of velocity. The signals used to calculate the correlation function are from two hot-wire probes separated in space. One probe is fixed at a height of $0.5\ \delta$ from the wall, and a second probe is positioned at various locations in a $z-y$ plane at a distance of $3.8\ \delta$ downstream from the first probe. A unique interpretation of these results is not possible, but a large eddy about four δ long in the streamwise direction, about one δ wide, and inclined at shallow angle to the wall is suggested. These numbers agree very well with the dimensions of the large eddy in the synthetic boundary layer. Even though a direct comparison is not a simple matter, there is a striking similarity between the correlation map in figure 5.64 and the contours of constant streamwise velocity in the outer regions of the synthetic boundary layer (see figure 5.21). Both of these figures indicate that regions of low streamwise momentum are highly elongated in the stream direction. The value of the celerity for the large eddies obtained from these correlation maps is about $0.93\ u_\infty$, compared with the measured celerity of $0.842\ u_\infty$ in the synthetic boundary layer.

Fukunishi (1984) concluded that a large horse-shoe vortex, shown in figure 5.65, is associated with slowly moving fluid in the outer part of a turbulent boundary layer. The perturbation-velocity vectors associated with the vortex, shown in the same figure, are similar to the perturbation-velocity vectors in the synthetic boundary layer (see, for example, figure 5.17 at $y = 0.9$ cm). Fukunishi inferred the horse-shoe geometry from a sequence of velocity-vector diagrams of the type shown in figure 5.65 at various values of y. He also found that the large eddy (the vortex) tends to lean downstream as it moves, unlike the large eddy in the synthetic boundary layer, which travels downstream with little distortion.

Neither of the studies cited above indicates the presence of a pair of secondary vortices like the ones associated with the large eddy in the synthetic boundary layer. However, Guizennec (1985) discovered two types of counter-rotating pairs of streamwise vortices connected with bursting events in a natural (tripped) turbulent boundary layer. Figure 5.66a shows a pair of

what Guizennec calls "rollers", containing relatively large values for the streamwise and normal vorticity and coinciding with the ejection (Q2) event. Fluid is ejected between these rollers much as in the case of the primary vortices of the large eddy in the synthetic boundary layer. Figure 5.66b shows a similar plot of a pair of vortices or rollers coinciding with the sweep (Q4) event. The Q4 vortices are shorter in length in the streamwise direction than the Q2 vortices and also are of opposite sense. Thus the Q4 vortices are similar to the secondary vortices in the synthetic boundary layer. However, the present experiments show that the two types of vortices occur together and are, in fact, part of the same eddy. Guizennec determines a value of 0.65 u_∞ for the convection velocity of the vortices, in contrast with the higher value obtained for the large eddy in the synthetic boundary layer.

Even though some discrepancies remain, especially with regard to the value of the celerity of the large eddy and with regard to distortion of the eddy with distance downstream, it is apparent that the large-eddy structure in the synthetic boundary layer explains and is consistent with many of the observed features of natural turbulent boundary layers. One discrepancy worth noting concerns the universality of the ensemble-averaged velocity profile when this profile is conditioned on detection of a bursting event (Blackwelder and Kaplan 1976). If the location of bursting events is random on a scale smaller than the scale of the large eddies, this discrepancy cannot be resolved within the scope of the sampling techniques used here.

Chapter 6

Concluding Remarks

Several new and important results have been obtained for the structure of the large eddy in the turbulent boundary layer. As demonstrated in chapter 5, the main features of the large eddy in the present synthetic boundary layer are entirely consistent with features found in various investigations of natural turbulent boundary layers in the literature.

6.1. Key Findings.

First, the coherent velocity field that defines the large eddy involves weak variations from the global mean flow, of at most a few percent of the free-stream velocity. Moreover, the structure of the eddy has to be educed from a noisy background of random (i.e., incoherent) fluctuations that are an order of magnitude larger than the coherent signal itself.

Thus the boundary layer is characterized by a strong background flow in which the large eddy enters only as a weak modulation. The idea of a coherent structure as a weak eddy is consistent with the small growth rate of turbulent boundary layers, as pointed out in the introductory section of chapter 5. In chapter 5, the main signatures of the large eddy are established in terms of the quantities $<R_\delta>$, $<\Pi>$, and $<C_f>$. Associated with the eddy are bulges of turbulence into the outer flow, as indicated by large values of $<\delta>$; regions of increased mixing, as indicated by low values of $<\Pi>$; and small local peaks in the shearing stress at the wall. The peak region of $<C_f>$ lies close to the nose of the eddy.

The large eddy in the synthetic turbulent boundary layer moves with a celerity of $0.842\, u_\infty$ without much distortion. The eddy is highly three-dimensional. It is composed of two regions -- primary and secondary -- characterized by relatively large streamwise and normal components of vorticity. The primary region consists of a pair of counter-rotating streamwise vortices, separated by about one δ in the spanwise direction. The vortices are about five δ long in the streamwise direction and occupy much of the boundary-layer thickness. The sense of the primary vortices is such as to pump fluid away from the wall and to slow down fluid between the two vortices of the pair. The secondary region consists of another pair of counter-rotating streamwise vortices, whose sense is opposite to that of the primary vortices. The secondary

vortices are about three δ long in the streamwise direction and lie outboard of and slightly downstream from the primary vortices. Both the primary and secondary pairs are inclined at quite shallow angles to the wall. The vortices just described are regions where the instantaneous stream paths in a plane looking upstream (the $z-y$ plane) are close to being closed curves.

Upflow induced between the primary vortices is at least partly responsible for transport of background-flow quantities, including spanwise vorticity, streamwise momentum, and turbulence energy, away from the wall. The growth of the boundary layer; i.e., the extension of the long tail of vorticity referred to in chapter 5, is due to this transport. Entrainment of irrotational fluid is at least partly associated with flow toward the wall in adjacent regions of the boundary layer.

Relatively large values of the velocity gradient $\partial<w>/\partial z$ are induced close to the wall, and result in either stretching or compression, depending on the sign of the gradient, of spanwise vorticity close to the wall. Intensification of the spanwise vorticity occurs near regions of high wall shear and large turbulence production, and suggests the mechanism by which variations in wall shear are sustained. Similarly, a weakening of spanwise vorticity associated with compression occurs near regions of small wall shear.

The eddy can be visualized as an equilibrium configuration. The observed mean streamwise and normal components of vorticity are generated and sustained by tilting mechanisms, with a strong interaction among the three components of vorticity. Coincidence of regions of relatively large streamwise and normal vorticity is necessary for the tilting mechanisms to operate.

6.2. General Conclusions.

The following remarks, some speculative, are derived from the present observations in the synthetic turbulent boundary layer.

(1) It appears that stretching plays a key role in maintaining large values of spanwise vorticity close to the wall in turbulent boundary layers and probably also during transition of laminar boundary layers. Only streamwise vortices can produce stretching of spanwise vorticity; such a mechanism would not be possible for a two-dimensional spanwise vortex. It is, perhaps, significant that secondary vortices, similar to the ones associated with the large eddy in the synthetic boundary layer, have been discovered recently in a simple horse-shoe vortex generated in a laminar boundary layer (Acarlar and Smith 1987). Finally, transition to turbulence in boundary layers is preceded by the appearance of three dimensionality and lambda vortices (Klebanoff, Tidstrom, and Sargent 1962). Kovasznay, Komoda and Vasudeva (1962) recognized that stretching of spanwise vorticity must be the only mechanism by which the rapid redistribution of vorticity observed during transition can take place. In contrast, amplification of two-dimensional Tollmien-Schlichting waves is governed by a balance between diffusion and convection of vorticity, and does not lead directly to breakdown to turbulence.

(2) Large-eddy break-up devices (LEBU's) have recently been used, with some success, to reduce skin-friction drag in turbulent boundary layers. From the present investigation of the structure of the large eddy, an estimate can be obtained of the amount of drag reduction that is possible. The peak value in surface friction associated with the large eddy is only about four percent larger than the global mean value, and about seven percent larger than the surface friction in passive regions of the flow. Thus, if the large eddies in a turbulent boundary layer were disabled, only a modest reduction in skin friction could be expected, a reduction near the value already achieved using LEBU's.

(3) An isolated turbulent spot has some properties in common with the turbulent boundary layer; for example, the log law for the mean-velocity profile seems to hold in both flows. One of the most important features of the turbulent spot is that the growth rate in the streamwise and spanwise directions is much greater than the growth rate in the normal direction. Even though the whole spot can usefully be viewed as a single horse-shoe vortex (Cantwell et al. 1978), the spot may in fact contain multiple eddies that scale with the thickness of the spot. The present findings suggest that these eddies may be similar in structure to the large eddy in the synthetic boundary layer.

6.3. Future Work.

Numerous important questions are raised by the present research but remain unanswered. Some of these questions can be explored by analysis of of some hot-wire and surface-gauge measurements already at hand but not discussed here. The most important question deals with the degree and nature of interactions between the wall flow and the outer flow, and requires a study of the bursting phenomenon in the synthetic boundary layer using the VITA technique. This analysis will determine whether a preferred location exists in the eddy where bursts are most likely to occur. As stated earlier, it has been established for turbulent boundary layers and turbulent channel flows that the hairpin vortices found in these flows tend to align themselves at 45 degrees to the wall; i.e, along the principal axis of strain. It remains to show, by a closer study of data like those in figure 5.11, that this type of alignment also occurs in the synthetic boundary layer.

Granted that the present study is useful in clarifying some aspects of coherent structure in turbulent boundary layers, it raises other questions of equal or greater difficulty. The large-eddy structure is defined here as the Reynolds-averaged periodic response of the flow to a periodic disturbance; i.e., as the difference between the doubly-periodic flow and the global mean. There are problems with this point of view.

What may be wanted, especially if the large eddy is ever to be interpreted as the product of an instability, is the difference between the doubly-periodic flow and the hypothetical background flow. The latter is presumably represented in some sense by the mean flow outside the large eddies. This flow is essentially two-dimensional in the mean and is unstructured at the scale examined here, but is otherwise possessed of all the properties established long ago for time-averaged turbulent flow. These include a high fluctuation level, large gradients of several mean variables normal to the wall, and conformity with accepted similarity laws. In particular, the background flow has a large wake component, a property now interpreted to mean relatively poor mixing and the absence of coherent structure of large scale. The transport mechanism in the background flow is therefore not clear, although it is nearly as effective as the mechanism of the coherent motion.

One point of view that might preserve the connotations of the term "wake component" is that the background flow is continuously being processed by coherent structures as a result of relative motion. The same process would then have to operate in wakes, and further evidence should be sought there. In any event, it seems that it is now the background flow that has to be explained.

Appendix A

Hot-Wire Analysis

A.1. X-wire Calibration.

For each of the wires in an X-wire probe (figure A1), King's law is assumed to apply in the form

$$\frac{E_i^2}{\Delta T_i} = A_i + B_i (q_{e_i})^{n_i} \qquad i = 1, 2 \tag{A1}$$

where E is the anemometer output voltage, ΔT is the temperature difference between the wire and the fluid, and q_e is an effective velocity. In the literature, various definitions have been proposed for this effective velocity. In the present study, for the sake of preserving linear relationships among various velocity components, the following definition was used :

$$q_e = q_n + \lambda q_p \tag{A2}$$

where q_n is the velocity component normal to the wire and q_p is the component parallel to the wire. From equation (A1),

$$q_{e_i} = \left[\frac{\frac{e_i^2}{\Delta T_i} - A_i}{B_i} \right]^{\frac{1}{n_i}} \tag{A3}$$

and from equation (A2) and figure A1,

$$q_{e_i} = U\, A_{1u} + W\, A_{1w}$$

$$q_{e_2} = U\, A_{2u} + W\, A_{2w} \tag{A4}$$

where $A_{1u} = \sin\beta_1 + \lambda_1 \cos\beta_1$, $A_{1w} = -\cos\beta_1 + \lambda_1 \sin\beta_1$, $A_{2u} = \sin\beta_2 + \lambda_2 \cos\beta_2$, and $A_{2w} = \cos\beta_2 - \lambda_2 \sin\beta_2$, with β_1 and β_2 the angles that the wires make with the probe axis. Thus if A, B, n, β, and λ are known for each of the wires, u and w can be expressed parametrically in terms of $E_1^2/\Delta T_1$ and $E_2^2/\Delta T_2$ using equations (A3);

$$u = \frac{q_{e_1} A_{2_w} - q_{e_2} A_{1_w}}{A_{1_u} A_{2_w} - A_{2_u} A_{1_w}} \tag{A5}$$

and

$$w = -\frac{q_{e_1} A_{2_u} + q_{e_2} A_{1_u}}{A_{1_u} A_{2_w} - A_{2_u} A_{1_w}}$$

Calibration is carried out by placing the probe in a uniform stream and varying the stream velocity and the yaw angle. The five unknown parameters A, B, n, β and λ for each wire are obtained by a least-squares fit. Values obtained in a typical calibration are shown in table A1. The values for n and β are close to those generally reported in the literature. Figure A2 shows the calibration points and the fitted curves.

TABLE A1

Typical Calibration Constants for an X-wire Probe

	wire 1	wire 2
A (volt^2/°C)	0.0654	0.0670
B (volt^2/°C)/(cm/sec)	0.0430	0.0384
η	0.429	0.443
β (deg)	47.38	47.67
λ	0.010	0.012

A.2. Gradient Correction.

Large gradients of the streamwise velocity u in the direction normal to the wall are characteristic of turbulent boundary layers. A relatively large correction was found to be required to account for this gradient in the measurement of the spanwise or w component of velocity in the non-uniform flow. Consider an X-wire probe oriented to measure the u and w components of velocity, as shown in figure A1. In coordinates (x, y, z), the center of wire 1 is at $(0, h, 0)$ and the center of wire 2 is at $(0, -h, 0)$. This configuration is defined to be a right-hand probe. A left-hand probe is one for which h is negative; i.e., wire 1 is lower than wire 2. If $\partial u/\partial y \neq 0$, then the two wires see different stream velocities on the average, and the effective velocities for the two wires are given by

$$q_{e_1} = \left[u + h\frac{\partial u}{\partial y} \right] A_{1_u} + w\, A_{1_w}$$

and

$$q_{e_2} = \left[u - h\,\frac{\partial u}{\partial y} \right] A_{2_u} + w\, A_{2_w}$$

where A_{1_u}, A_{1_w}, A_{2_u}, and A_{2_w} are the same as in equations (A4).

Solution for u and w gives

$$u = \frac{q_{e_1}A_{2_w} - q_{e_2}A_{1_w}}{DEN} - \frac{h\,\dfrac{\partial u}{\partial y}\,(A_{1_u}A_{2_2} + A_{1_w}A_{2_u})}{DEN} = u_{uncorr} - h\,\frac{\partial u}{\partial y}\,C_u$$

$$w = \frac{-q_{e_1}A_{2_u} + q_{e_2}A_{1_u}}{\mathrm{DEN}} + h\,\frac{\partial u}{\partial y}\,\frac{2(A_{1_u}A_{2_u})}{\mathrm{DEN}} = w_{uncorr} + h\,\frac{\partial u}{\partial y}\,C_w$$

where $\mathrm{DEN} = A_{1_u}A_{2_w} - A_{2_u}A_{1_w}$. For X-wire probes, $C_u = 0$ and $C_w = 1$. For the present

purposes, therefore, u was not corrected, but w was calculated from

$$w = w_{uncorr} + h_{eff} \frac{\partial u}{\partial y} + w_0 \tag{A6}$$

The effective half-distance, h_{eff}, incorporates C_w and any irregularities in probe geometry. The constant w_0 is an offset that is independent of $\partial u/\partial y$.

In a plane of symmetry in the synthetic boundary layer, $\overline{w}$ and $<w>$ are identically zero. Thus

$$\overline{w} = \overline{w}_{uncorr} + h_{eff} \frac{\partial \overline{u}}{\partial y} + w_0 = 0$$

In practice, w_0 was set equal to $-\overline{w}_{uncorr}$ at $y = 3.4$ cm, which is nearly two $\overline{\delta}$ ($\overline{\delta}$ = 1.77 cm; see chapter 4). There is no question that $\overline{w} = 0$ for y = 3.4 cm and $\pm z$ = 0, 3.05, 6.10, 9.15... cm, because of the symmetry of the flow. The condition was therefore applied everywhere. Then h_{eff} was determined by a least-squares fit to the data on the centerline. The gradient was determined analytically from global-mean profile parameters obtained by measurement of $\overline{u}$ on the centerline. If $\overline{u}$ varies like $\log y$, for example, then $\partial\overline{u}/\partial y$ varies like $1/y$. Figure A3 shows uncorrected and corrected values of $\overline{w}$ on the centerline at various y. The value for h_{eff} was determined to be 0.0292 cm, close to the value 0.025 cm quoted by the probe manufacturer. The correction is quite substantial, amounting to about 0.02 u_∞ for the data point closest to the wall. It should be noted that the maximum value of $<w>$ in the synthetic boundary layer is less than 0.01 u_∞.

To verify the analysis just given for the gradient error, a left-hand X-wire probe was obtained from the manufacturer on special order, and u–w measurements were made in the same flow with both probes on the center line and also at $z = -3$ cm and $z = +3$ cm. Figure A4 also shows the uncorrected and corrected values of $\overline{w}$ for the left-hand probe. The effective distance, h_{eff}, was determined to be -0.0244 cm. As expected, the sign of the correction is reversed but the magnitude is essentially the same.

The bulk of the measurements were carried out with the right-hand X-wire probe. The w-component of velocity at constant phase, $<w>$, was obtained using formula (A6) everywhere in the flow. A value of 0.0292 cm was used for h_{eff} throughout, and w_0 was taken as $-w(x, y_0, z)$, where $y_0 = 3.4$ cm, the farthest point from the wall where measurements were made. The gradient $\partial<u>/\partial y$ was obtained from

$$\frac{\partial<u>}{\partial y} = \frac{<u_\tau>}{\kappa y} + \frac{<\Pi><u_\tau>\pi}{\kappa<\delta>} \sin\left[\frac{\pi y}{<\delta>}\right]$$

where $<u_\tau>$, $<\Pi>$, and $<\delta>$ were evaluated as described in chapter 4.

For the spanwise traverse described in chapter 3, measurements were made on both sides of the plane of symmetry, $z = 0$. The spanwise component of velocity $<w>$ is antisymmetric about this plane; i.e., $<w>(x, y, z) = -<w>(x, y, -z)$. The streamwise component, $<u>$, and thus the correction term, $\partial<u>/\partial y$, are symmetric. There was evidence of a need for further symmetric corrections, which are of second order. The condense operation, described in section 3.6, effectively removes these symmetric errors. The condense operation uses the doubly-periodic property of the flow in t and z and combines ensemble-averaged data into one half cycle in each direction.

Figure A4 shows the corrected-condensed $<w>/u_\infty$ plotted against the corrected $<w>/u_\infty$ for $z = 0.5\,(1.0)\,4.5$ cm. The corrected $<w>$ is calculated from equation (A6). The data would be evenly scattered about the 45-degree line if the error were purely random. However, there is some bias; for example, at $z = 0.5$ cm a majority of the points lie below the 45-degree line. That this bias is mainly due to second-order symmetric error can be seen by plotting the corrected-condensed $<w>/u_\infty$ against $(<w>(+z)-<w>(-z))/2u_\infty$ as in figure A5. The bias and scatter are substantially reduced.

Finally, the corrected ensemble velocities $<w>/u_\infty$ at $z = \pm 3$ cm, as obtained from the right-hand and left-hand probes, are plotted as a function of t/T for various values of y in figure A6. The corrected and condensed values of $<w>/u_\infty$ from the right-hand probe are also shown. Except for points very near the wall ($y = 0.15$ cm and $y = 0.175$ cm), data from the

right-hand and left-hand probes agree well.

The error in the final corrected condensed values of $<w>$ presented in this thesis is estimated to be no more than $\pm 0.001\, u_\infty$. This accuracy is quite sufficient to justify the use of the continuity equation to calculate v from the measured u and w, and thus sufficient to resolve the main structural features of the large eddy in the synthetic boundary layer.

A.3. Calculation of $<v>$.

Continuity was invoked in the calculation of the normal component of velocity, $<v>$, at constant phase. The measured values of $<v>$ were found to be unusable, because the error due to probe interference near the wall was of the same order as the expected values of $<v>$. No correction scheme could be devised for calculation of the normal component of velocity of the type just described for calculation of the spanwise component, $<w>$. From continuity, the normal component of velocity is

$$<v> = -\int_0^y \frac{\partial <w>}{\partial z}\, dy - \int_0^y \frac{\partial <u>}{\partial x}\, dy$$

Measurements during the spanwise traverse (see chapter 3) were carried out only at one value of the downstream distance x. Therefore, the derivative $\partial <u>/\partial x$ could not be obtained directly. It was necessary to invoke Taylor's hypothesis and write the stream coordinate x as ct, where c is the celerity of the large eddy in the synthetic boundary layer. Experimentally, $c = 0.842\, u_\infty$ (see section 4.2). The equation for $<v>$ then becomes

$$<v> = -\int_0^y \frac{\partial <w>}{\partial z}\, dy + \int_0^y \frac{\partial <u>}{\partial (ct)}\, dy \qquad \text{(A7)}$$

The values used for the quantities $\partial <w>/\partial z$ and $\partial <u>/\partial (ct)$ in equation A7 were the ones obtained after the condense operation described in section 3.6; the values used for $<u>$ in this processing were the measured ones, not the fitted ones (see section 4.1). The use of Taylor's hypothesis is justified by the fact that the large eddy in the synthetic boundary layer travels with a constant celerity, has a small growth rate for the thickness, and does not exhibit much

distortion with downstream distance. The values obtained for the velocity component $<v>$ using equation (A7) can only be approximately correct. For example, the global mean of the normal component of velocity, $\bar{v}$, is necessarily zero. Of course, this value is not zero for the actual synthetic boundary layer, which grows at a rate of 1/100 for $d\delta/dx$ as x increases. The estimated global mean of $\bar{v}$ at the edge of the boundary layer is about 0.001, whereas the maximum experimental value of $<v>$ is 0.005 when inferred for the synthetic boundary layer by the method just described.

Appendix B

Equations of Motion

In the synthetic turbulent boundary layer, any measured quantity f may be decomposed as

$$f = \langle f \rangle + f' \tag{B1}$$

where f' is the random component and $\langle f \rangle$ is the ensemble mean at constant phase. The synthetic boundary layer flow is doubly periodic in the time and spanwise directions. The global mean $\bar{f}$ is the quantity obtained by averaging the quantity f in t and z over one cycle. The governing equations for mean momentum, vorticity, Reynolds stress, and turbulence energy, all evaluated at constant phase, are given in the following sections. The equations are written in a coordinate system moving in the downstream direction with a constant speed equal to $c\,u_\infty$. A mixed notation is used for the sake of brevity and clarity. The terms are ordered starting at the top; i.e., terms I appear in the first line in the equation, and so on.

B.1. Momentum.

$$I \quad \frac{\partial \langle u_i \rangle}{\partial t} = -(\langle u \rangle - c)\frac{\partial \langle u_i \rangle}{\partial x} - \langle v \rangle \frac{\partial \langle u_i \rangle}{\partial y} - \langle w \rangle \frac{\partial \langle u_i \rangle}{\partial z} \tag{B2}$$

$$II \quad -\frac{\partial \langle u_i' u_j' \rangle}{\partial x_j}$$

$$III \quad -\frac{1}{\rho}\frac{\partial \langle p \rangle}{\partial x_i}$$

$$IV \quad +\nu \frac{\partial^2 \langle u_i \rangle}{\partial x_i \partial x_j}$$

where $i = 1, 2, 3$ and $u_1 = u$, $u_2 = v$, and $u_3 = w$. Term I is convective transport of momentum, term II is Reynolds stress at constant phase, term III is the pressure gradient, and term IV represents viscous diffusion of momentum.

B.2. Vorticity.

$$I \quad \frac{\partial <\omega_i>}{\partial t} = -(<u> - c)\frac{\partial <\omega_i>}{\partial x} - <v>\frac{\partial <\omega_i>}{\partial y} - <w>\frac{\partial <\omega_i>}{\partial z} \tag{B3}$$

$$II \quad + <\omega_x>\frac{\partial <u_i>}{\partial x} + <\omega_y>\frac{\partial <u_i>}{\partial y} + <\omega_z>\frac{\partial <u_i>}{\partial z}$$

$$III \quad + \frac{\partial}{\partial x_j}(<u'_i\omega'_j> - <u'_j\omega'_i>)$$

$$IV \quad + \nu\frac{\partial^2 <\omega_i>}{\partial x_j \partial x_j}$$

where $i = 1, 2, 3$ and $\omega_1 = \omega_x$, $\omega_2 = \omega_y$ and $\omega_3 = \omega_z$. Term I is transport of vorticity by the mean velocity at constant phase, term II represents stretching and tilting of the vorticity components, term III is the contribution from the random turbulence, and term IV is viscous diffusion of vorticity.

B.3. Reynolds Stresses.

$$I \quad \frac{\partial <u'_i u'_j>}{\partial t} = -(<u> - c)\frac{\partial <u'_i u'_j>}{\partial x} - <v>\frac{\partial <u'_i u'_j>}{\partial y} - <w>\frac{\partial <u'_i u'_j>}{\partial z}$$

$$II \quad - <u'_i u'_k>\frac{\partial <u_j>}{\partial x_k} - <u'_j u'_k>\frac{\partial <u_i>}{\partial x_k}$$

$$III \qquad -\frac{\partial}{\partial x_k}\langle u'_i u'_j u'_k\rangle$$

$$IV \qquad -\frac{1}{\rho}\left\langle u'_i\,\frac{\partial p'}{\partial x_j} + u'_j\,\frac{\partial p'}{\partial x_i}\right\rangle$$

$$+\nu\left[\frac{\partial^2\langle u'_i u'_j\rangle}{\partial x_k \partial x_k}\right] - 2\nu\left\langle\frac{\partial u'_i}{\partial x_k}\,\frac{\partial u'_j}{\partial x_k}\right\rangle$$

Term I is transport by mean velocity at constant phase, term II is stress production due to mean velocity gradient, term III represents turbulent diffusion; term IV is sometimes called pressure diffusion, and term V is the viscous term.

B.4. Turbulence Energy.

$$I \qquad \frac{\partial\langle q\rangle}{\partial t} = -(\langle u\rangle - c)\,\frac{\partial\langle q\rangle}{\partial x} - \langle v\rangle\,\frac{\partial\langle q\rangle}{\partial y} - \langle w\rangle\,\frac{\partial\langle q\rangle}{\partial z}$$

$$II \qquad -\langle u'_i u'_j\rangle\,\frac{\partial\langle u_i\rangle}{\partial x_j}$$

$$III \qquad -\frac{\partial}{\partial x_j}\langle u'_j q\rangle$$

$$IV \qquad -\frac{1}{\rho}\,\frac{\partial}{\partial x_j}\langle u'_j\, p'\rangle$$

$$V \qquad +\nu\,\frac{\partial}{\partial x_j}\left\langle u'_i\left[\frac{\partial u'_i}{\partial x_j} + \frac{\partial u'_j}{\partial x_i}\right]\right\rangle$$

$$VI \qquad -\nu \left\langle \left[\frac{\partial u'_i}{\partial x_i} + \frac{\partial u'_j}{\partial x_j} \right] \left[\frac{\partial u'_i}{\partial x_j} + \frac{\partial u'_j}{\partial x_i} \right] \right\rangle$$

Term I is transport by mean velocity at constant phase, term II is turbulence production, term III is turbulent diffusion, term IV is pressure transport, term V is reversible viscous work, and term VI is turbulence dissipation.

References

Acarlar, M.S. and Smith, C.R. (1987) A study of hairpin vortices in a laminar boundary layer. Part 1. Hairpin vortices generated by a hemisphere protuberance. J. Fluid Mech. **175**, 1-41.

Alfredsson, P.H. and Johansson, A.V. (1984) On the detection of turbulence-generating events. J. Fluid Mech. **139**, 325-345.

Blackwelder, R.F. and Kaplan, R.E. (1976) On the wall structure of the turbulent boundary layer. J. Fluid Mech. **76**, 89-112.

Bogard, D.G. and Tiederman, W.G. (1986) Burst detection with single-point velocity measurements. J. Fluid Mech. **162**, 389-413.

Bradshaw, P. (1967) 'Inactive' motion and pressure fluctuations in turbulent boundary layers. J. Fluid Mech. **30**, 241-258.

Brown, G.L. and Thomas, A.S.W. (1977) Large structure in a turbulent boundary layer. Phys. Fluids **20**, S243-S252.

Cantwell, B.J. (1981) Organized motion in turbulent flow. Ann. Rev. Fluid Mech. **13**, 457-515.

Cantwell, B. and Coles, D. (1983) An experimental study of entrainment and transport in the turbulent near wake of a circular cylinder. J. Fluid Mech. **136**, 321-374.

Cantwell, B., Coles, D., and Dimotakis, P. (1978) Structure and entrainment in the plane of symmetry of a turbulent spot. J. Fluid Mech. **87**, 641-672.

Chambers, F.W. (1985) Synthetically generated turbulent boundary layer development and structure. AIAA Paper 85-0534.

Clauser, F. (1956) The turbulent boundary layer. Adv. Appl. Mech. **4**, 1-51.

Coles, D. (1969) The young person's guide to the data. In "Computation of Turbulent Boundary Layers" (Coles, D. and Hirst, E.A., eds.), Vol. II, Stanford Univ., 1-45.

Coles, D. (1978) A model for flow in the viscous sublayer. In "Coherent Structure of Turbulent Boundary Layers" (Smith, C.R. and Abbott, D.E., eds.), Lehigh Univ., 462-475.

Coles, D. (1987) Coherent structures in turbulent boundary layers. In "Perspectives in Turbulence Studies" (Meier, H.U. and Bradshaw, P., eds.), Springer-Verlag, 93-114.

Coles, D. and Barker, S.J. (1975) Some remarks on a synthetic turbulent boundary layer. In "Turbulent Mixing in Nonreactive and Reactive Flows" (Murthy, S.N.B., ed.), Plenum, 285-292.

Fukunishi, Y. (1984) Influence of ordered motions on the structure of outer region of the turbulent boundary layer. In "Turbulence and Chaotic Phenomena in Fluids" (Tatsumi, T., ed.), Elsevier, 371-376.

Goodman, W.L. (1985) Emmons spot forcing for turbulent drag reduction. AIAA J. **23**, 155-157.

Grass, A.J. (1971) Structural features of turbulent flow over smooth and rough boundaries. J. Fluid Mech. **50**, 233-255.

Guezennec, Y.G. (1985) Documentation of large coherent structures associated with wall events in turbulent boundary layers. Ph.D. Thesis, Illinois Institute of Technology.

Head, M.R. and Bandyopadhyay, P. (1981) New aspects of turbulent boundary-layer structure. J. Fluid Mech. **107**, 297-338.

Hinze, J.O. (1975) *Turbulence* (2nd ed.). McGraw-Hill.

Hussain, A.K.M.F. (1983) Coherent structures - reality and myth. Phys. Fluids **26**, 2816-2850.

Kastrinakis, E.G. and Eckelmann, H. (1983) Measurement of streamwise vorticity fluctuations in a turbulent channel flow. J. Fluid Mech. **137**, 165-186.

Kim, J. and Moin, P. (1986) The structure of the vorticity field in turbulent channel flow. Part 2. Study of ensemble-averaged fields. J. Fluid Mech. **162**, 339-363.

Klebanoff, P.S. (1955) Characteristics of turbulence in a boundary layer with zero pressure gradient. NACA Rep. 1247.

Klebanoff, P.S., Tidstrom, K.D., and Sargent, L.M. (1962) The three-dimensional nature of boundary-layer instability. J. Fluid Mech. **12**, 1-34.

Kline, S.J., Reynolds, W.C., Schraub, F.A., and Runstadler, P.W. (1967) The structure of turbulent boundary layers. J. Fluid Mech. **30**, 741-773.

Kovasznay, L.S.G., Komoda, H., and Vasudeva, B.R. (1962) Detailed flow in transition. Proc. 1962 Heat Transfer and Fluid Mech. Inst., 1-26.

Kovasznay, L.S.G., Kibens, V., and Blackwelder, R.F. (1970) Large-scale motion in the intermittent region of a turbulent boundary layer. J. Fluid Mech. **41**, 283-325.

Lighthill, M.J. (1963) In "Laminar Boundary Layers" (Rosenhead, L., ed.), Oxford, 46-113.

Lu, S.S. and Willmarth, W.W. (1973) Measurements of the structure of the Reynolds stress in a turbulent boundary layer. J. Fluid Mech. **60**, 481-511.

Narasimha, R. and Kailas, S. (1987) Energy events in the atmospheric boundary layer. In "Perspectives in Turbulence Studies" (Meier, H.U. and Bradshaw, P., eds.), 188-222.

Perry, A.E. and Morrison, G.L. (1971) A study of the constant-temperature hot-wire anemometer. J. Fluid Mech. **47**, 577-599.

Reynolds, W.C. and Hussain, A.K.M.F. (1972) The mechanics of an organized wave in turbulent shear flow. Part 3. Theoretical models and comparisons with experiments. J. Fluid Mech. **54**, 263-288.

Savas, O. (1979) Some measurements in synthetic turbulent boundary layers. Ph.D. Thesis, California Institute of Technology.

Savas, O. and Coles, D. (1985) Coherence measurements in synthetic turbulent boundary layers. J. Fluid Mech. **160**, 421-446.

Wygnanski, I.J., Sokolov, M., and Friedman, D. (1976) On a turbulent 'spot' in a laminar boundary layer. J. Fluid Mech. **78**, 785-819.

TABLE 1

Probe Positions Normal to the Surface of the Plate

Point	y (cm)
1	0.15
2	0.175
3	0.20
4	0.25
5	0.30
6	0.40
7	0.50
8	0.70
9	0.90
10	1.10
11	1.40
12	1.80
13	2.20
14	2.60
15	3.40

TABLE 2

Global Mean Parameters for the
Synthetic Boundary Layer at $x = 117.8$ cm

Parameter	Value
$u_\infty (cm/s)$	1200
$\nu (cm^2/s)$	0.155
$\overline{\delta} (cm)$	1.77
$\overline{C}_f$	0.00388
$\overline{\Pi}$	0.38
$\overline{R}_\theta$	1400
$\overline{R}_{\delta^*}$	1800

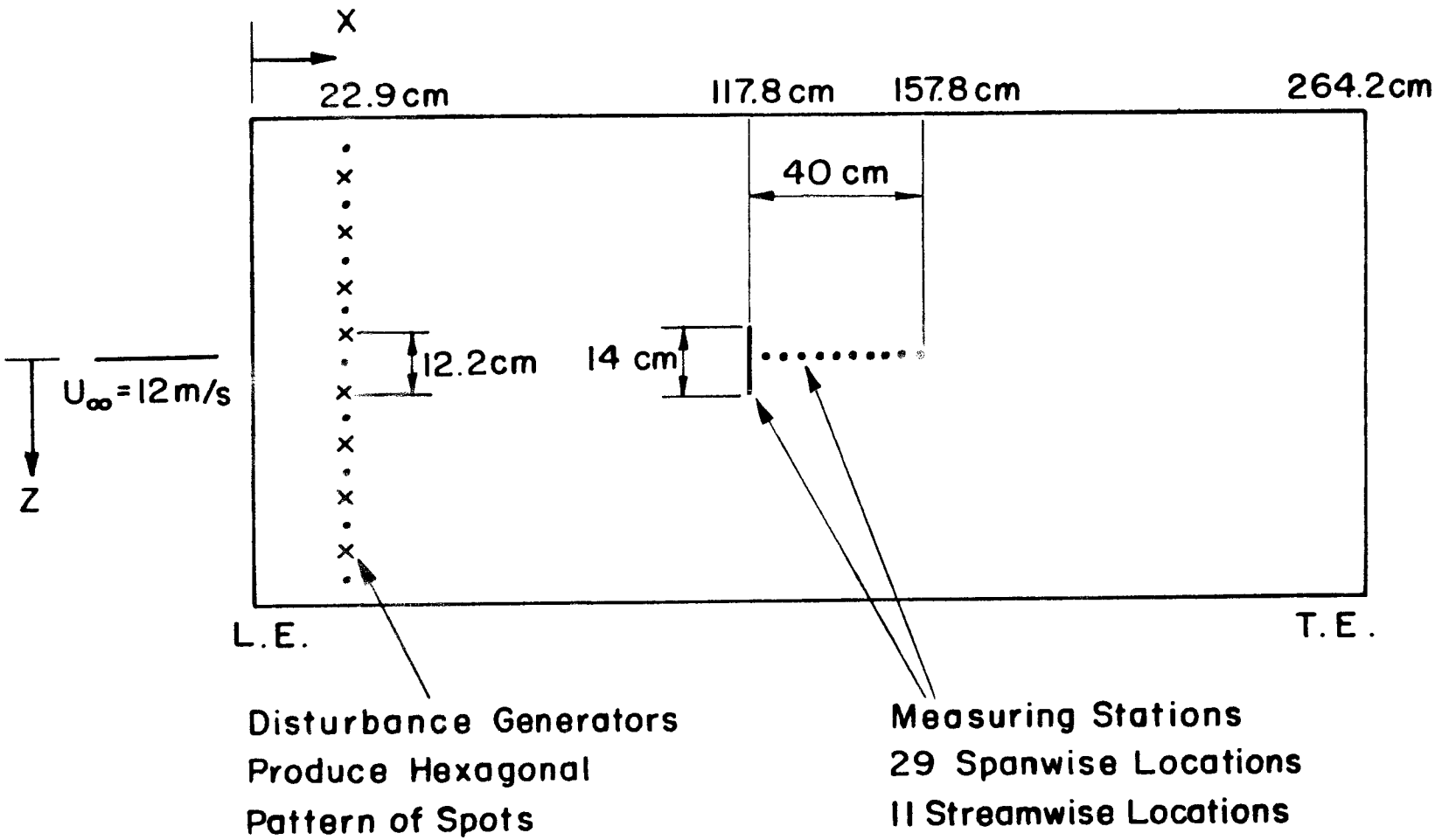

Figure 2.1. The flat-plate model.

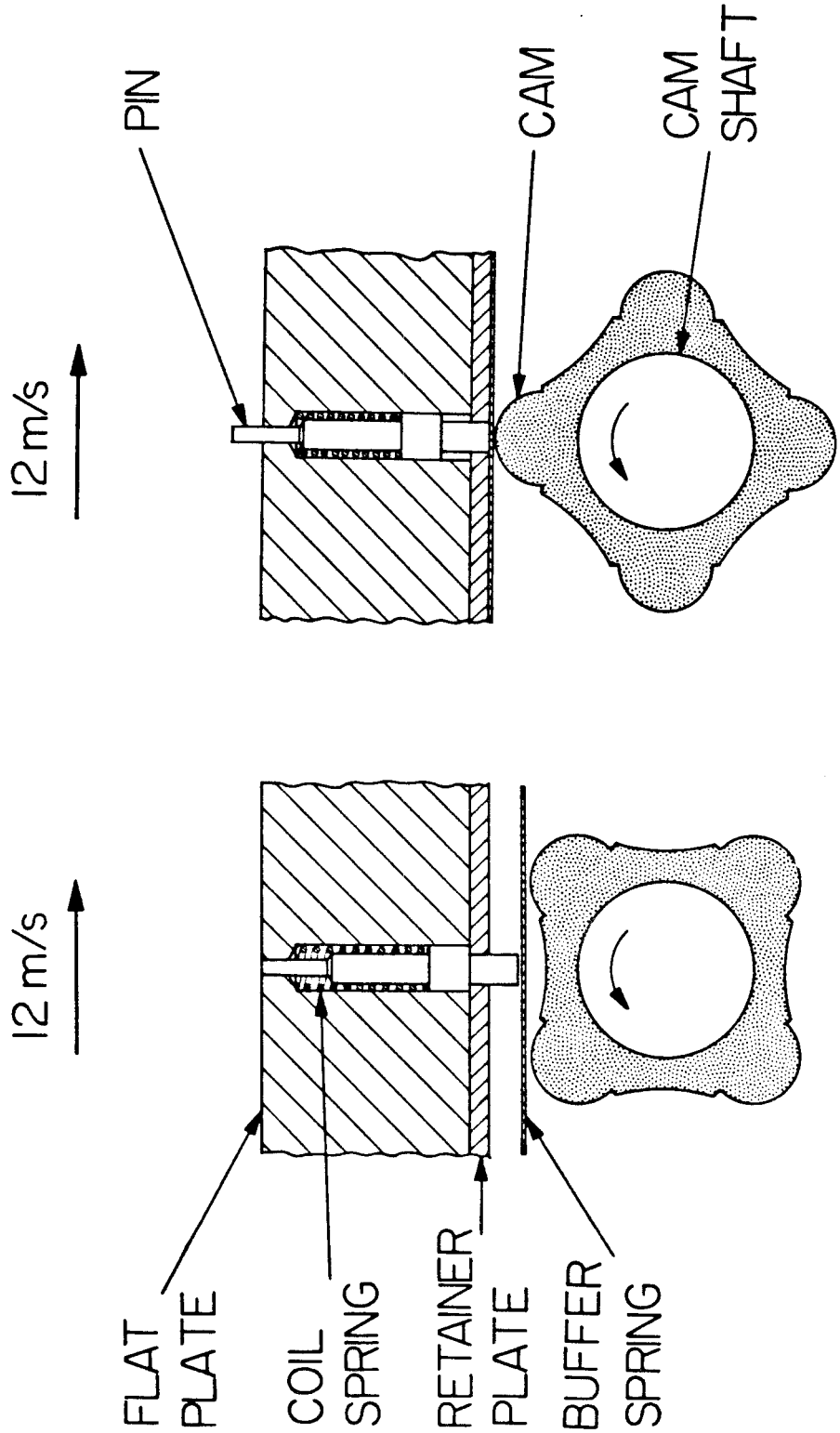

Figure 2.2. Detail of disturbance-generator mechanism looking in the spanwise or z direction (from Savas 1979). Left: pin retracted. Right: pin displaced into boundary layer.

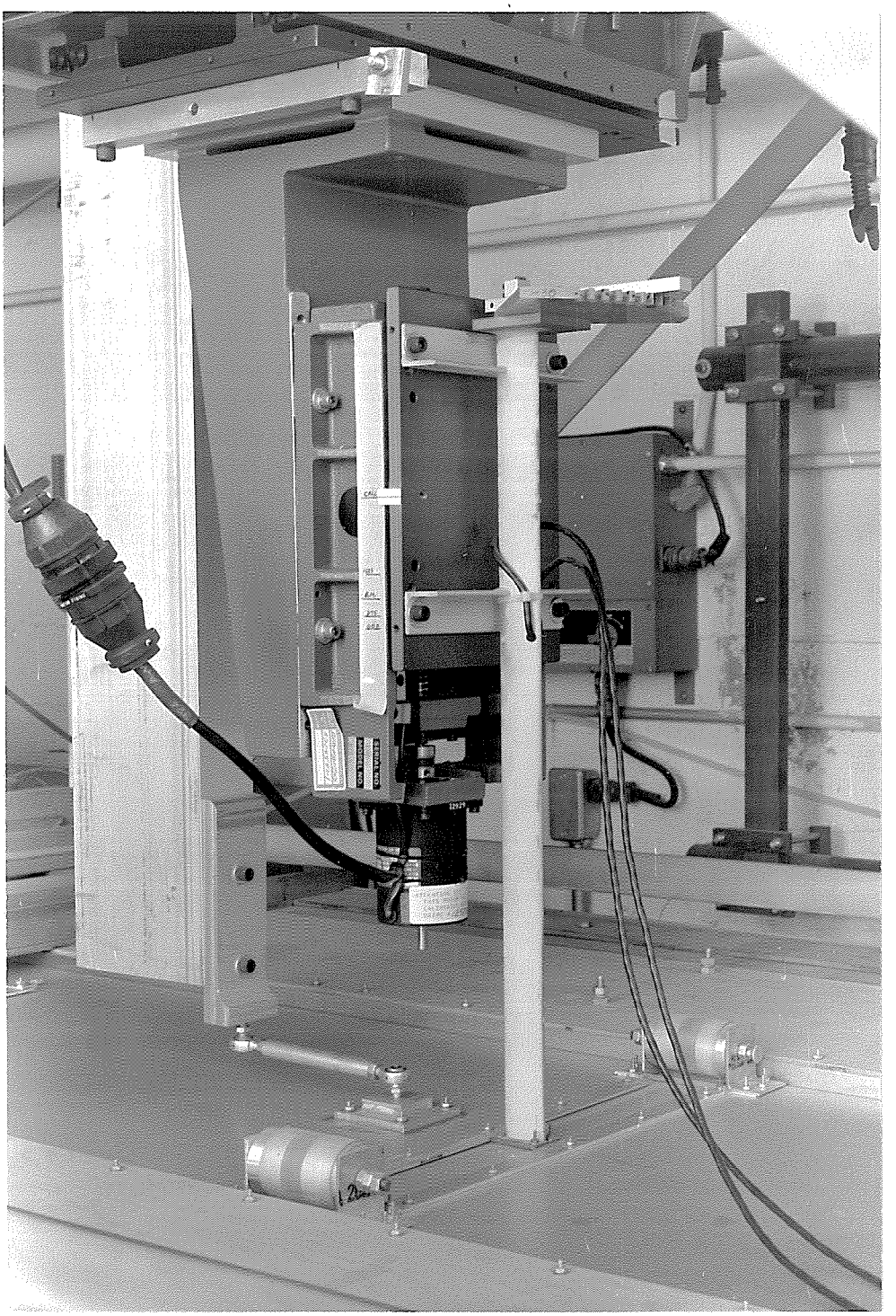

Figure 2.3. Traverse and probe-holder strut above test section.

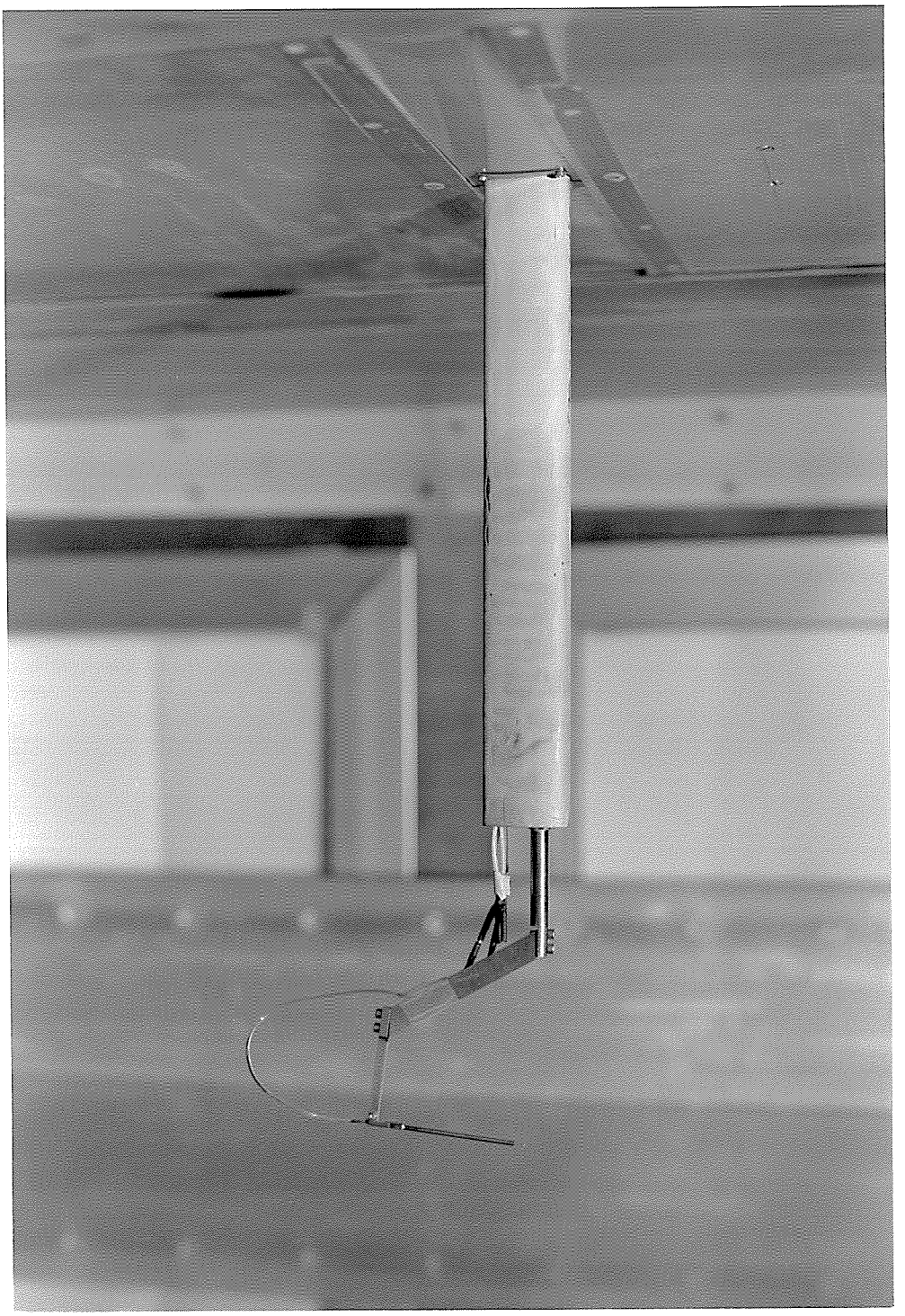

Figure 2.4. Probe mounted on streamlined support.

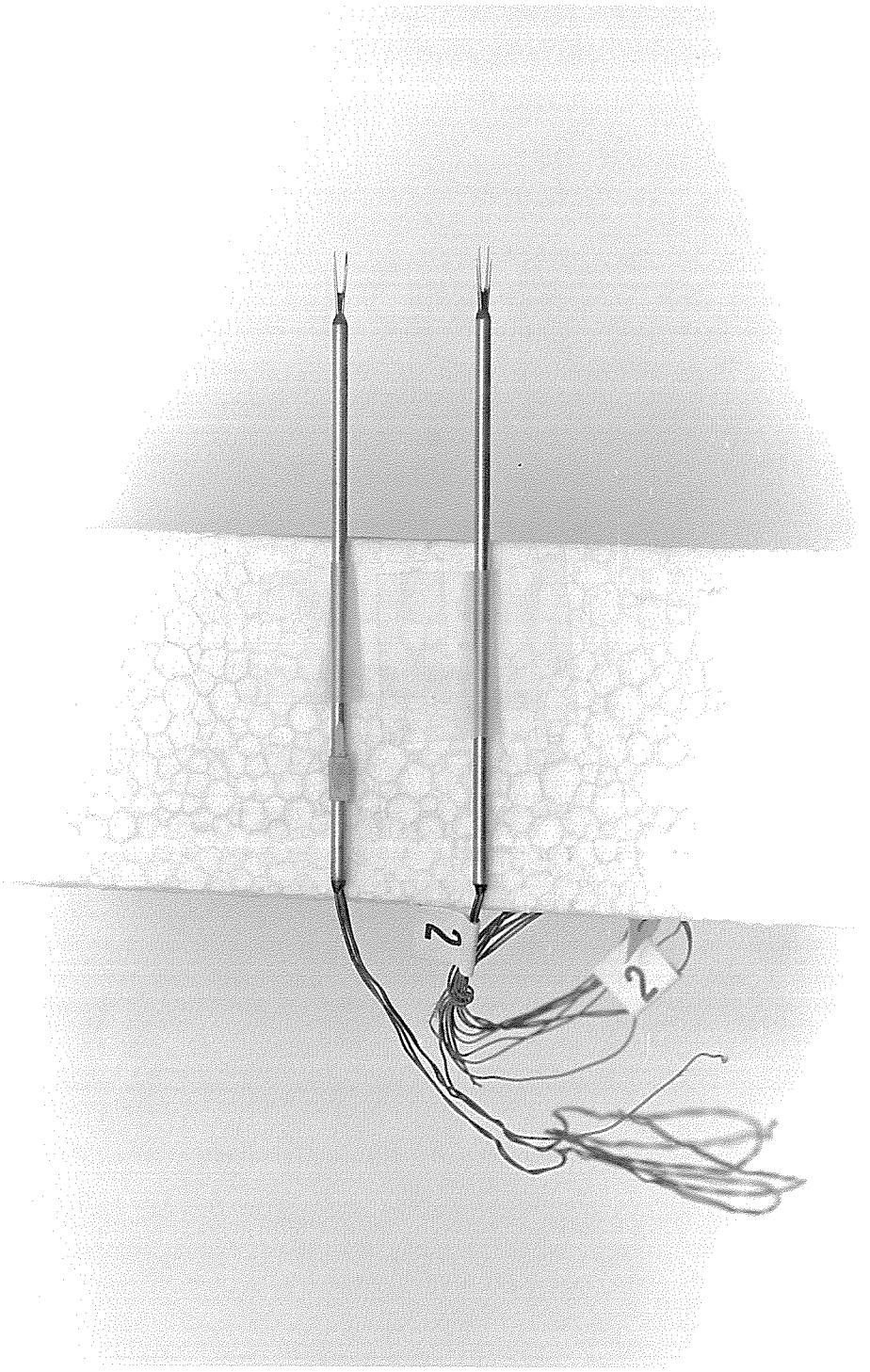

Figure 2.5. X-wire probes with and without square sleeve.

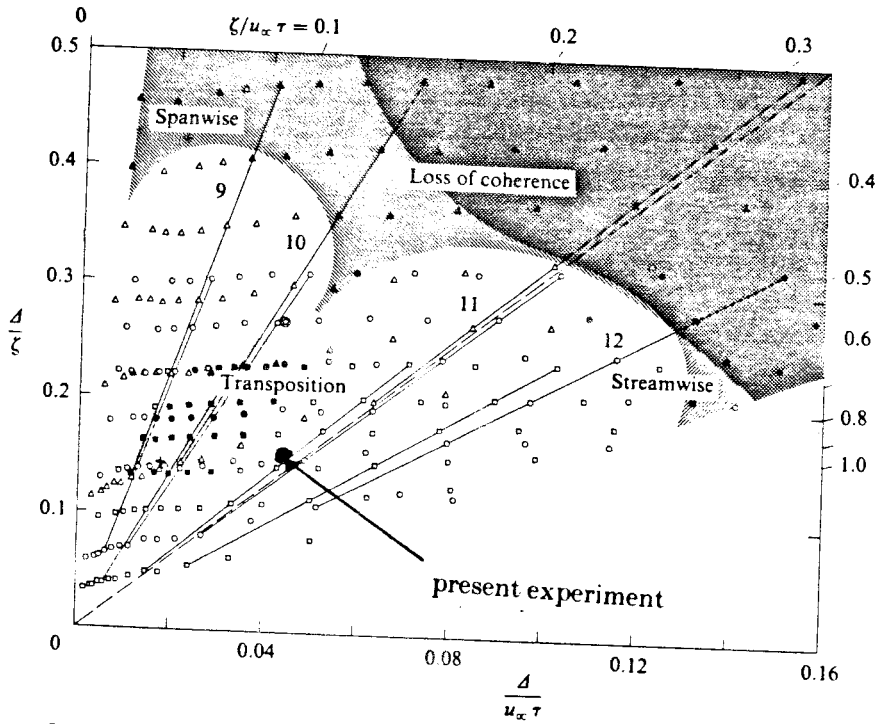

Coherence diagram for synthetic turbulent boundary layer. Open symbols, coherent pattern; solid symbols and shading, loss of coherence (or transposition); □, 12.2 cm cam; ○, 9.1 cm cam; △, 6.1 cm cam; labelled groups of lines, see figures 9–12; dashed line, $\zeta/u_\infty \tau = 0.32$; star, flow studied by Coles & Barker (1975); +, flows studied by Chambers (1982).

Figure 3.1 (from Savas and Coles 1985). Dot indicates flow studied in present experiment. Δ = height at which $\bar{\gamma} = 0.4$; ζ = spanwise period, same as λ_z; τ = time period, same as T.

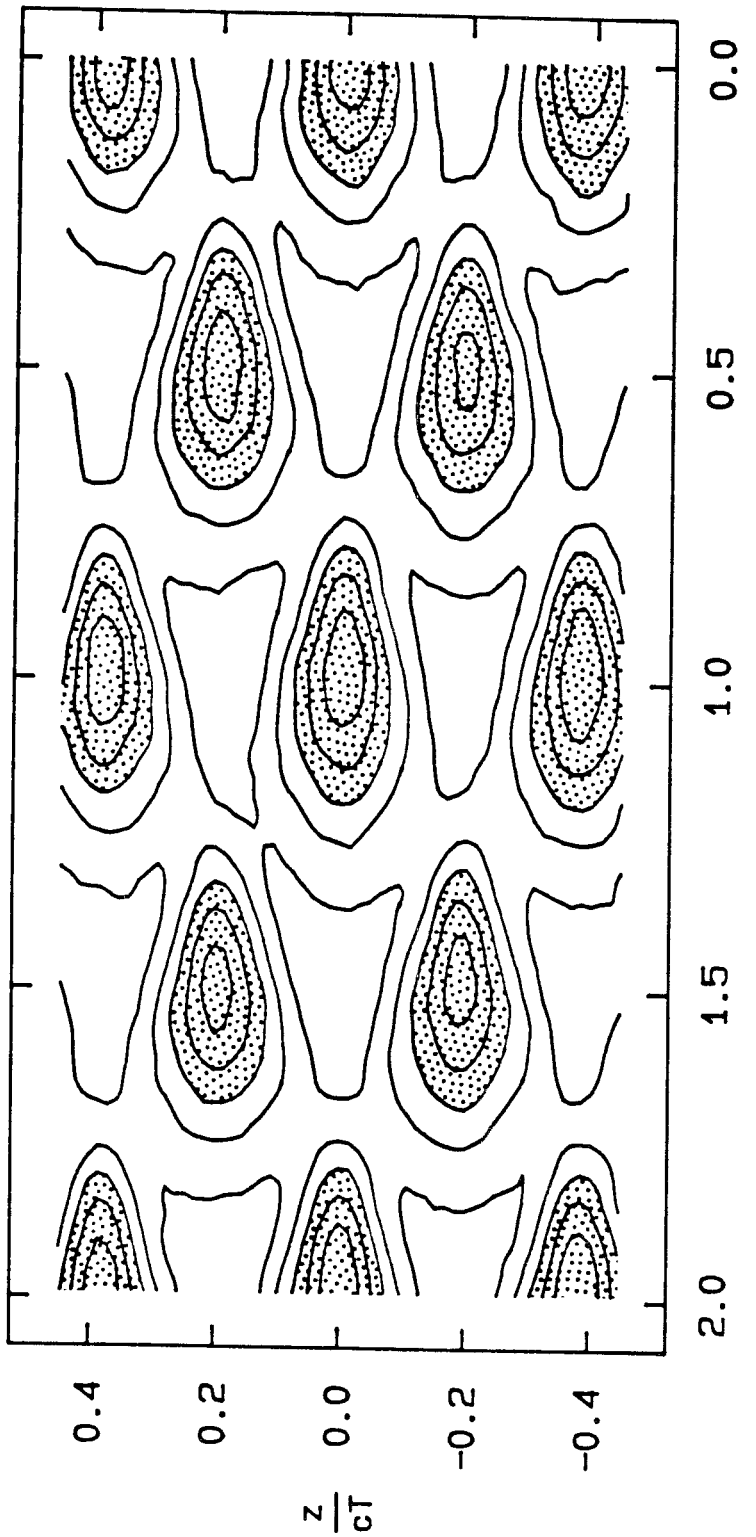

Figure 3.2. Contour plot of $\langle\gamma\rangle$ in plan view at x = 117.8 cm, y = 1.93 cm, for one full camshaft revolution. Scales for z and $x = ct$ are matched. Contour levels are 0.1(0.1)0.5. Shaded area corresponds to $\langle\gamma\rangle \geq 0.3$.

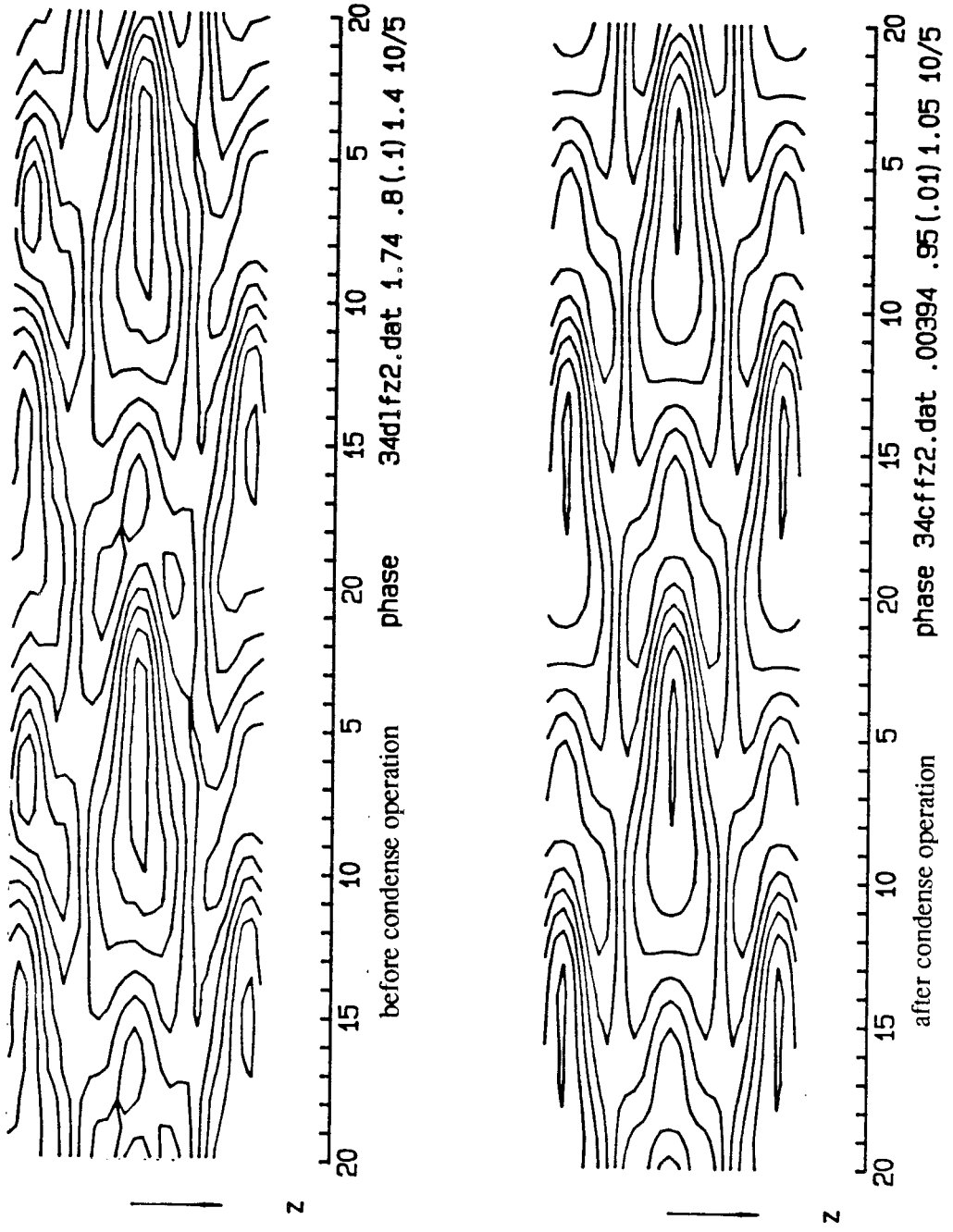

Figure 3.3. $<C_f>$ before and after condense operation.

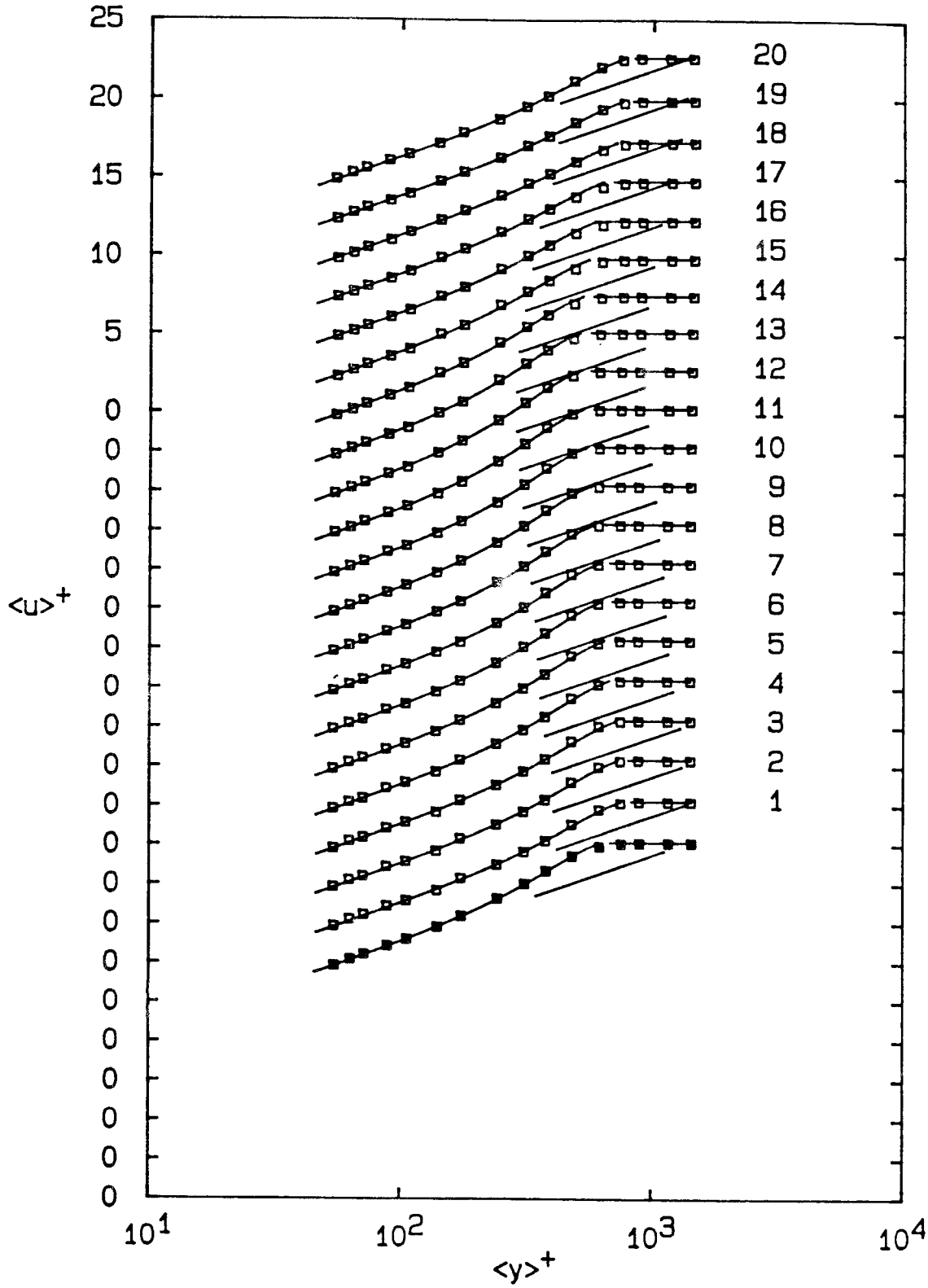

Figure 4.1. Ensemble-mean velocity profiles; phases 1-20 at x = 117.8 cm, z = 0 cm. Solid symbols are time average.

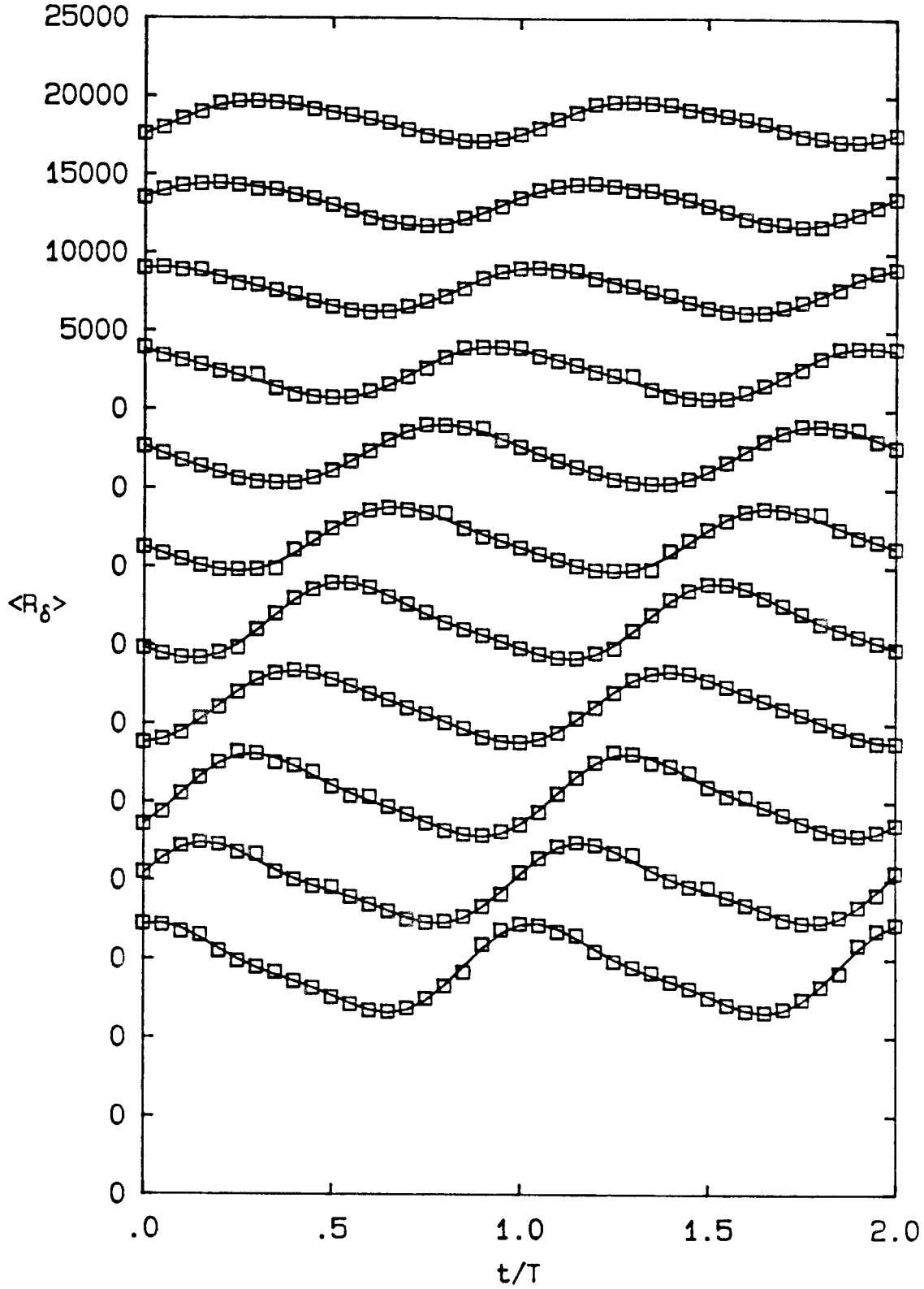

Figure 4.2. From bottom to top, variation of $\langle R_\delta \rangle$ with phase at x = 117.8(4)157.8 cm.

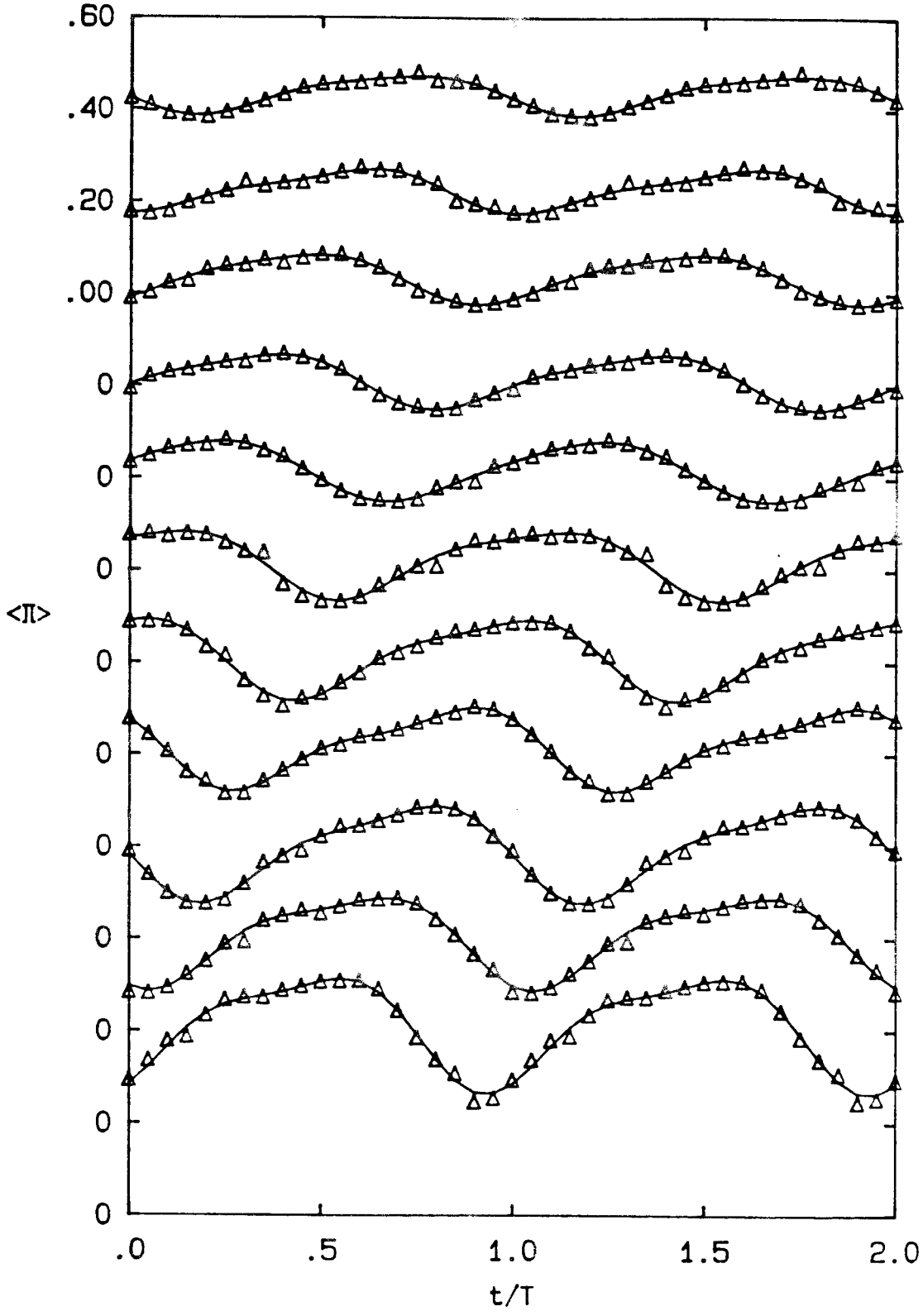

Figure 4.3. From bottom to top, variation of <Π> with phase at x = 117.8(4)157.8 cm.

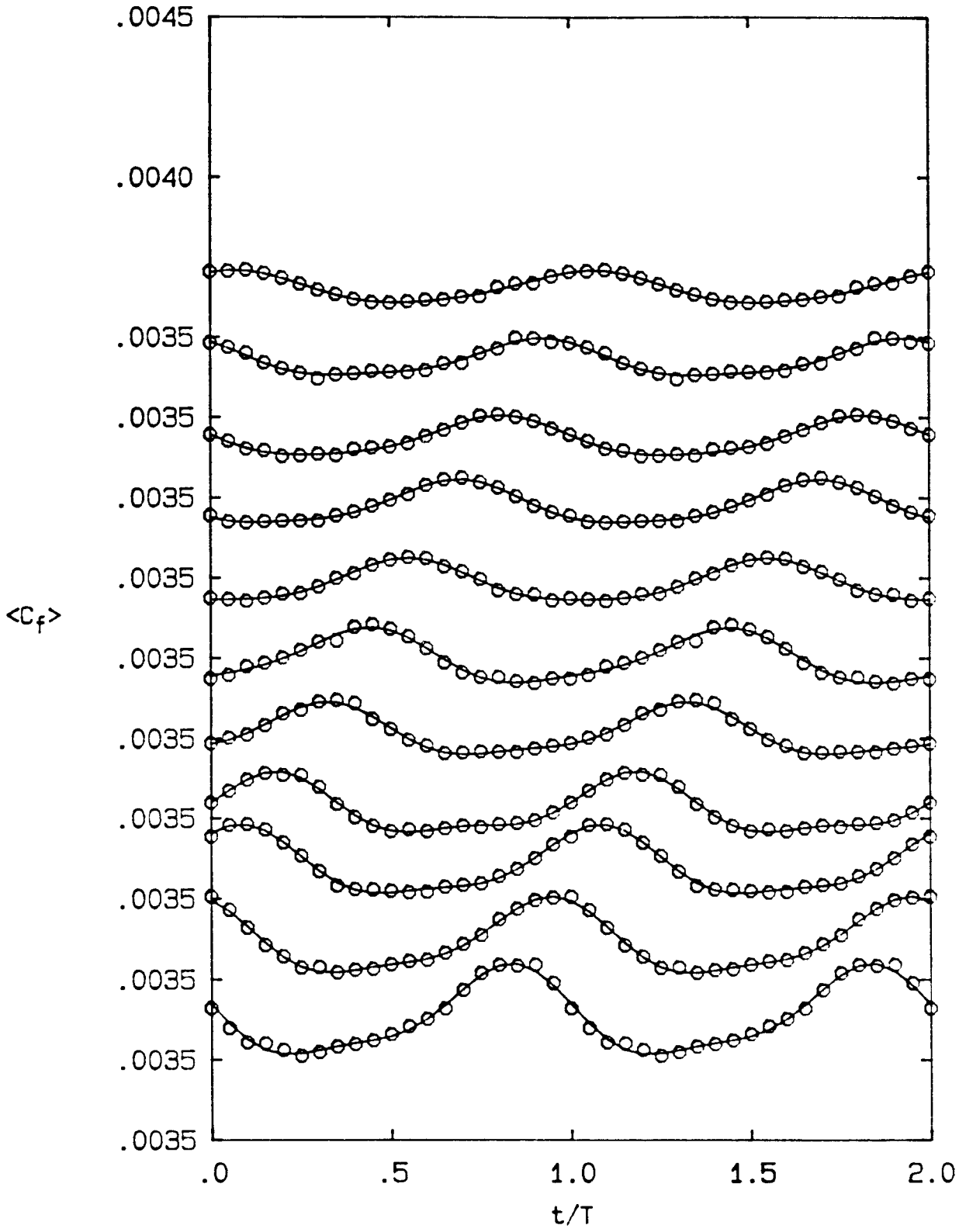

Figure 4.4. From bottom to top, variation of $<C_f>$ with phase at x = 117.8(4)157.8 cm.

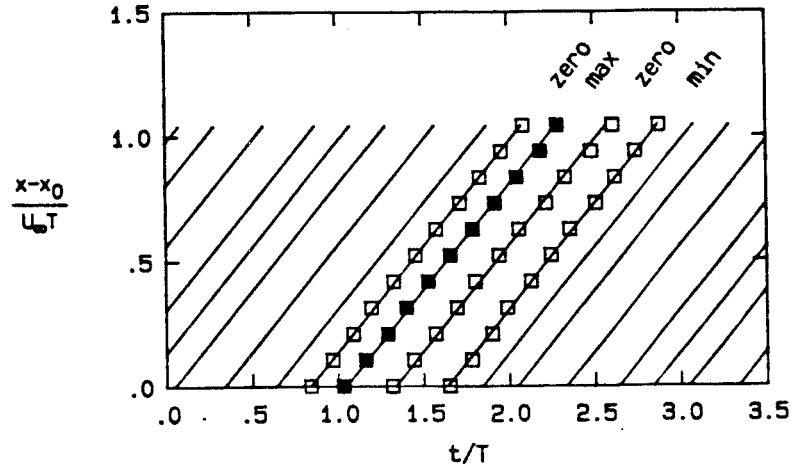

Figure 4.5. Experimental $x-t$ diagram for $<R_\delta>$.

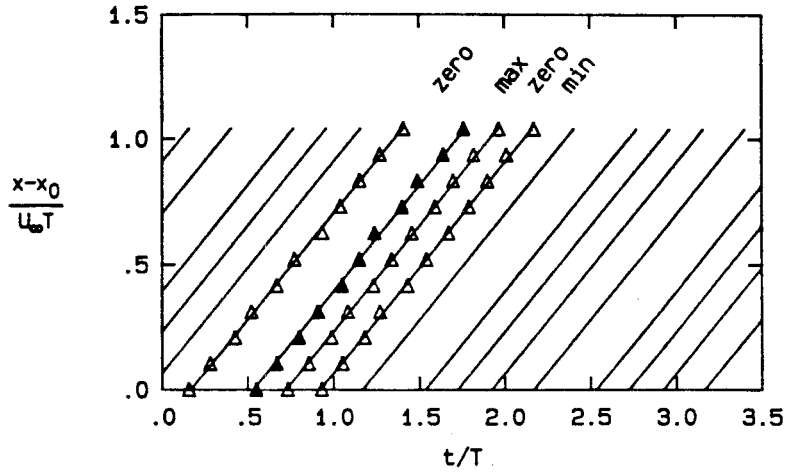

Figure 4.6. Experimental $x-t$ diagram $<\Pi>$.

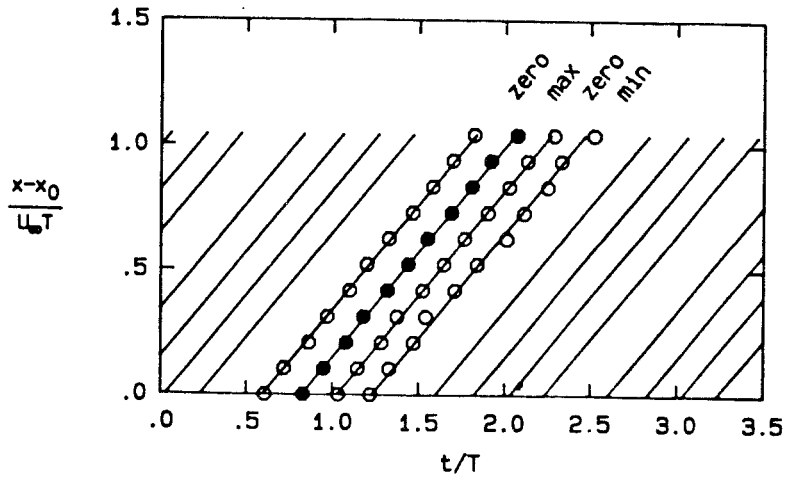

Figure 4.7. Experimental $x-t$ diagram for $<C_f>$.

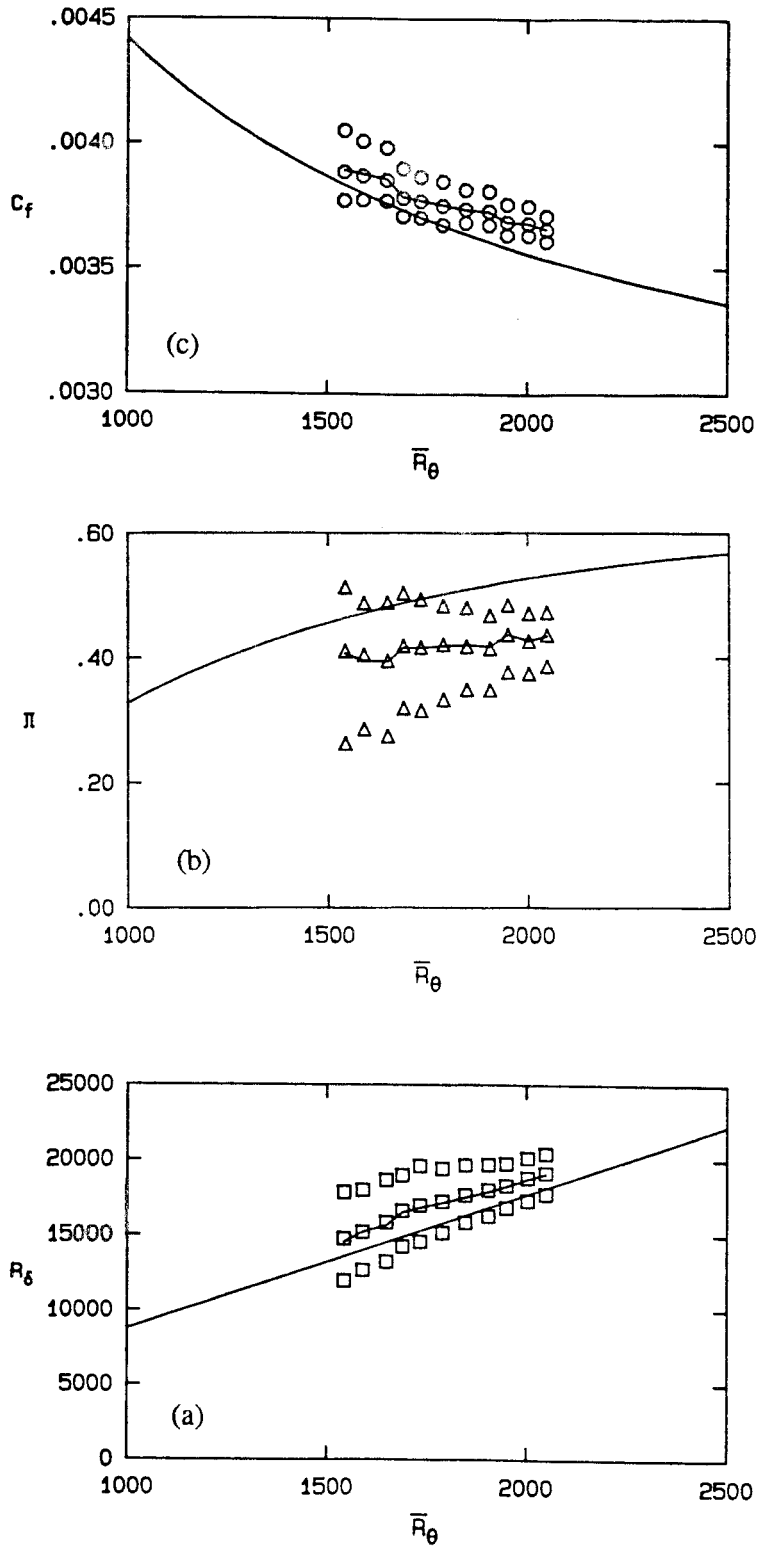

Figure 4.8. Maximum, minimum, and time mean of (a) $<R_\delta>$; (b) $<\Pi>$; and (c) $<C_f>$ as functions of time-mean momentum thickness $\overline{R}_\theta$.

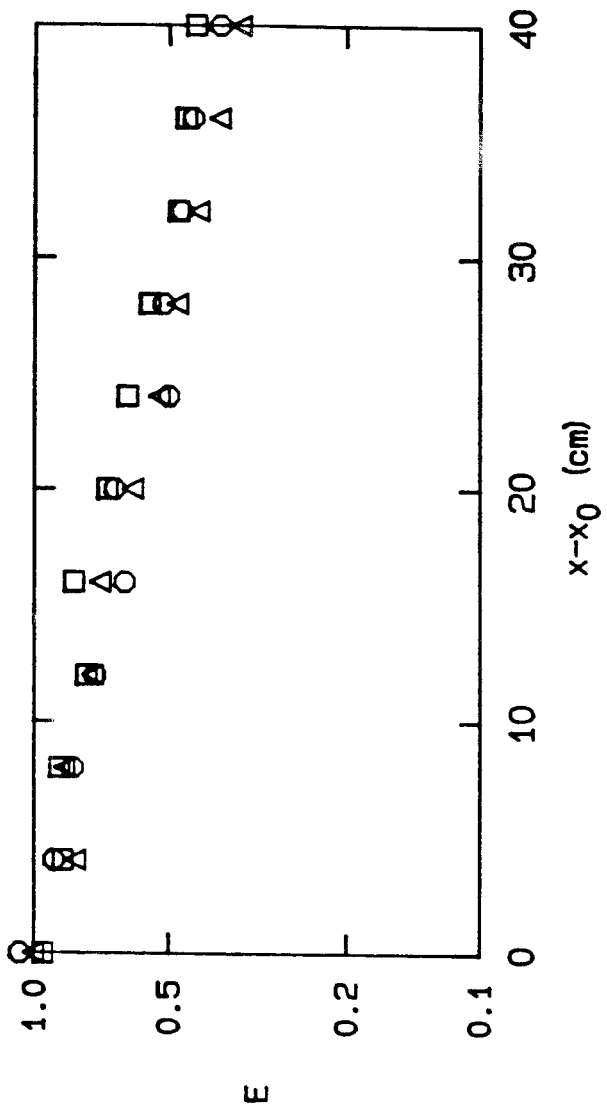

Figure 4.9. Loss of coherence with increasing downstream distance as measured by peak-to-peak amplitude E in figure 4.8. Note logarithmic scale for ordinate.

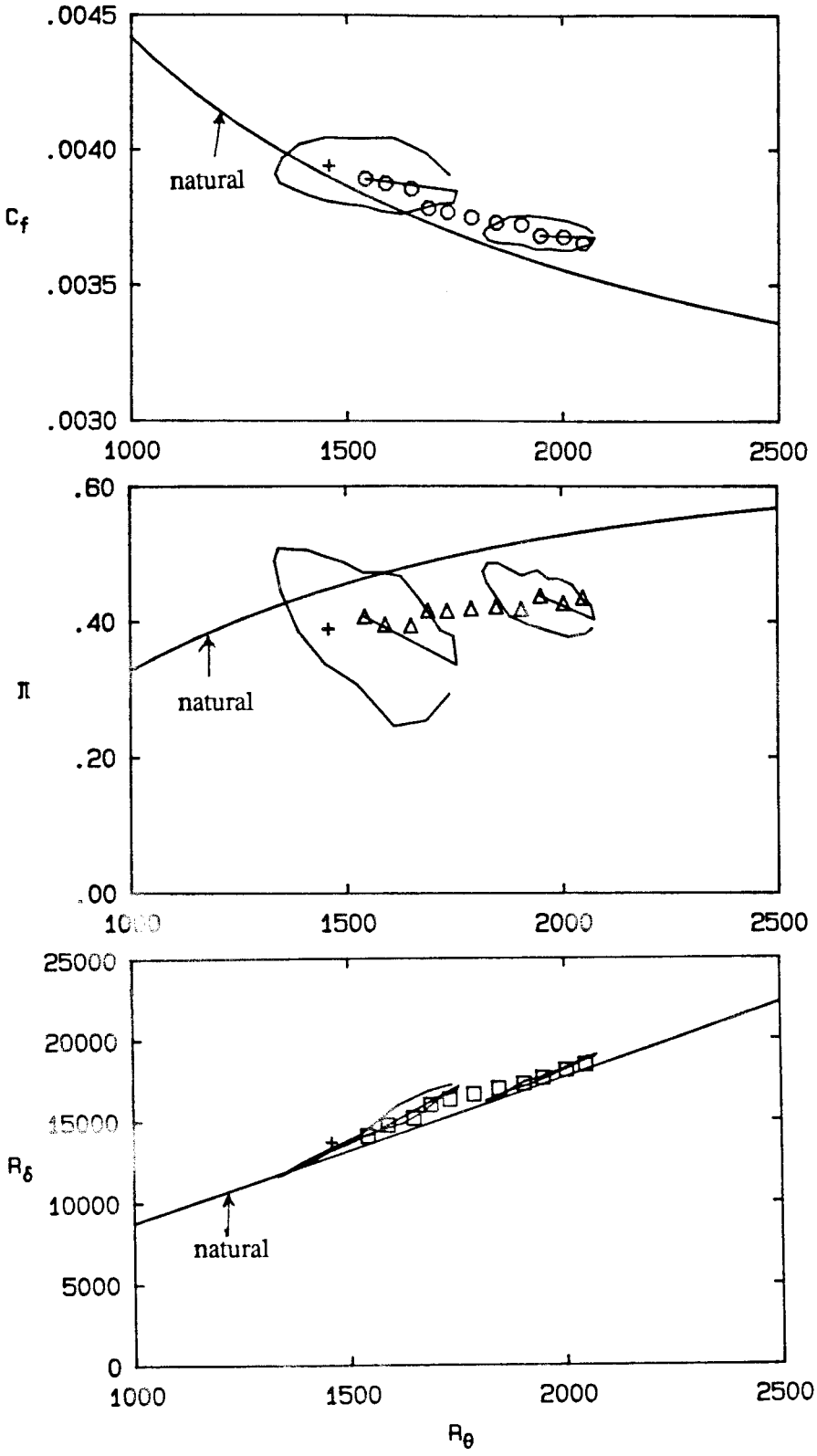

Figure 4.10. Profile parameters in synthetic and natural boundary layers. open symbols , time mean at x = 117.8 cm, z = 0 cm; +, global mean at x = 117.8 cm; –, average at constant phase at x = 117.8 cm, 147.8 cm, z = 0 cm.

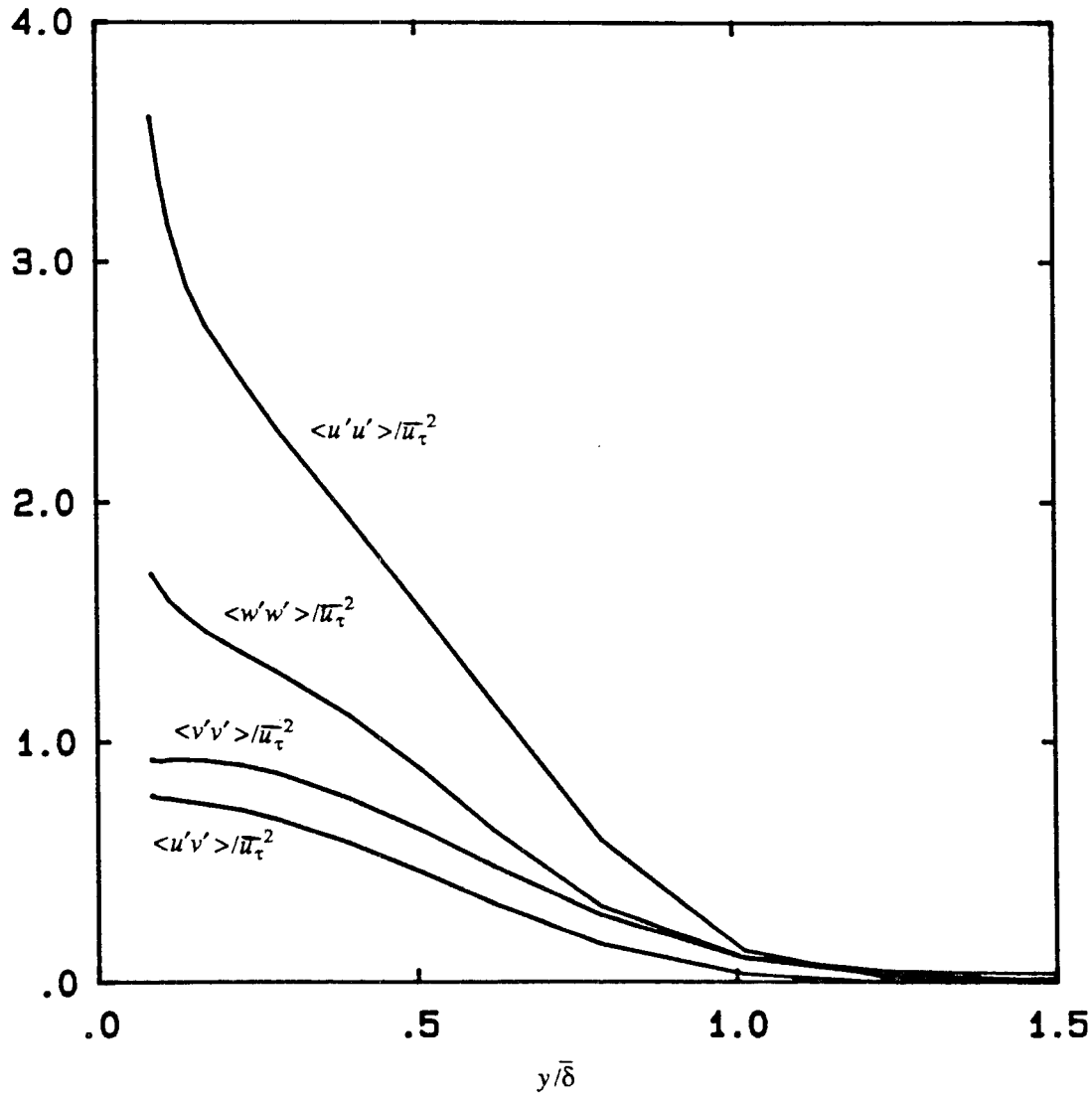

Figure 4.11. Reynolds stresses in synthetic boundary layer; global averages at x = 117.8 cm.

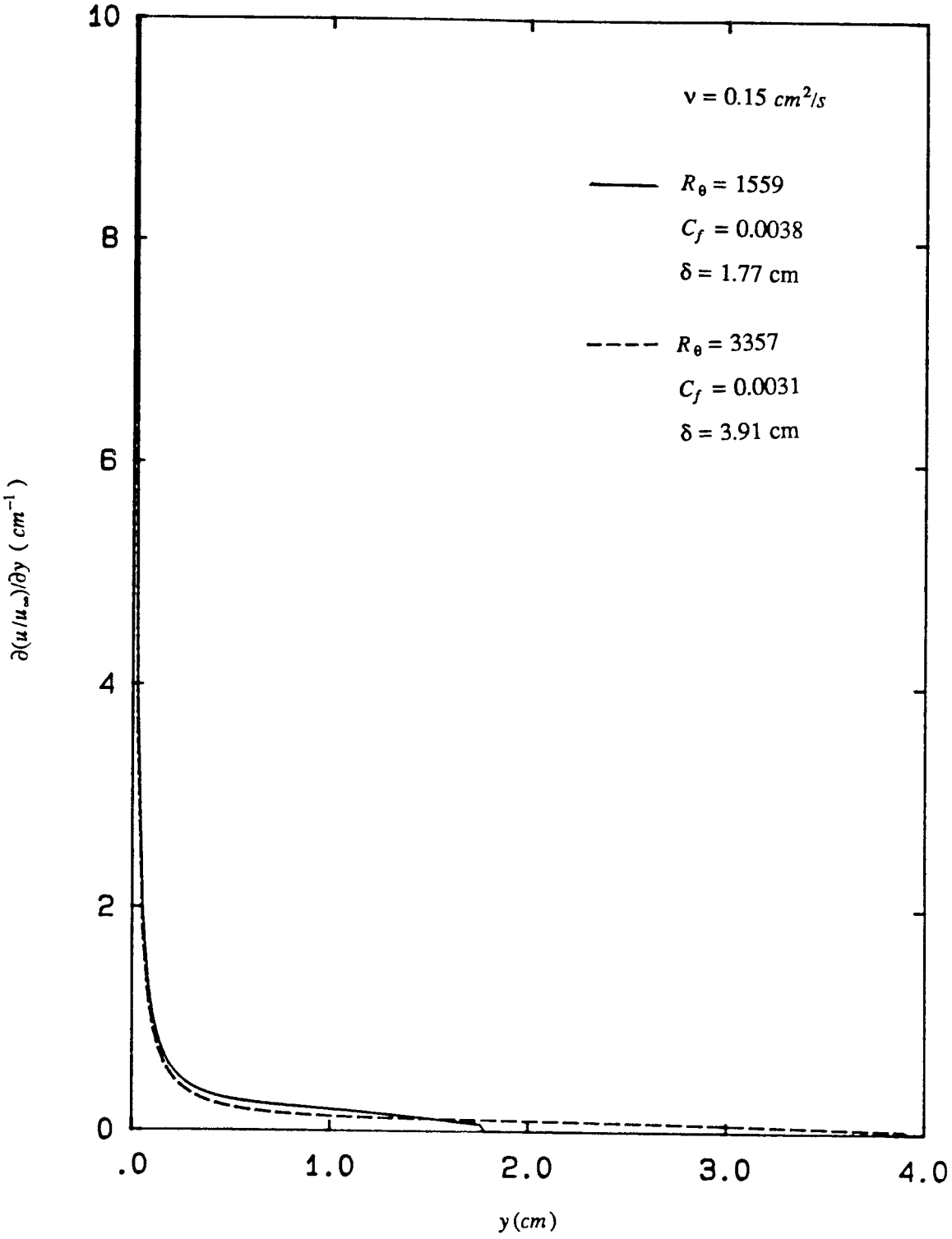

Figure 5.1. Mean vorticity distributions in hypothetical turbulent boundary layers at two Reynolds numbers.

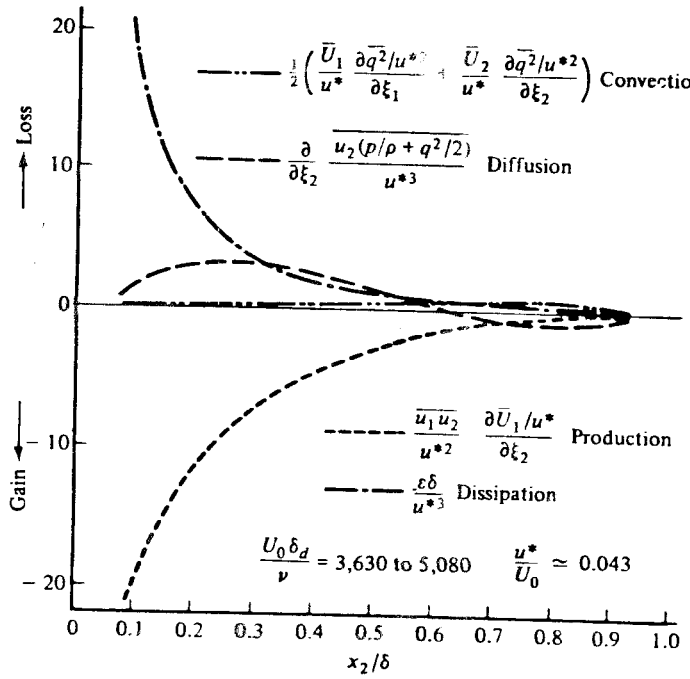

Energy balance in the boundary layer along a smooth wall with zero pressure gradient.

Figure 5.2. Energy balance in a turbulent boundary layer (from Hinze 1975).

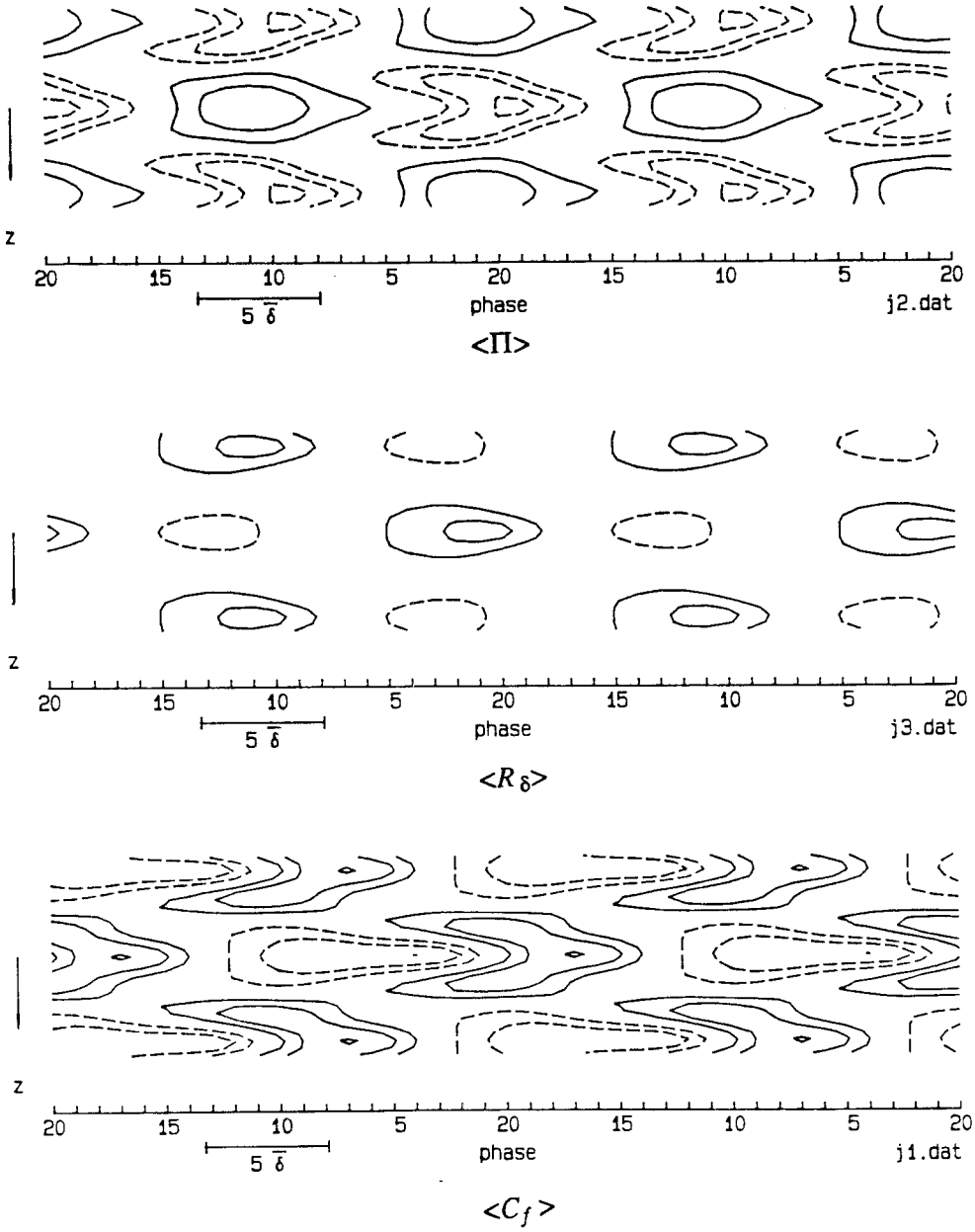

Figure 5.3. Contours of $\langle C_f \rangle$, $\langle R_\delta \rangle$, $\langle \Pi \rangle$ in the $t-z$ plane. Contour intervals: for $\langle C_f \rangle$, 0.01 $\overline{C_f}$; for $\langle R_\delta \rangle$, 0.1 $\overline{R}_\delta$; for $\langle \Pi \rangle$, 0.1 $\overline{\Pi}$.

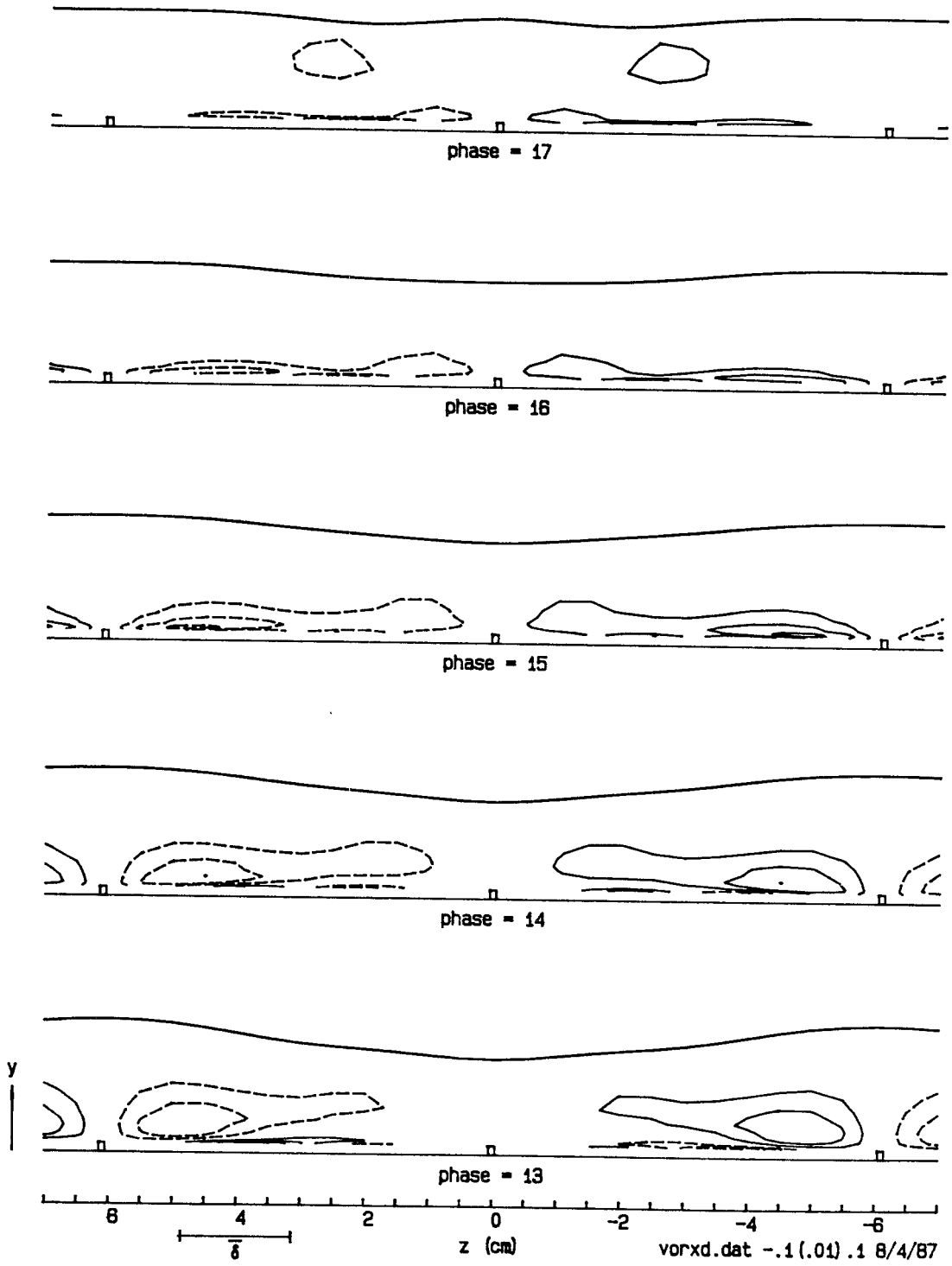

Figure 5.4. Streamwise vorticity $<\omega_x>$ in the $z-y$ plane. Contour interval 0.01.

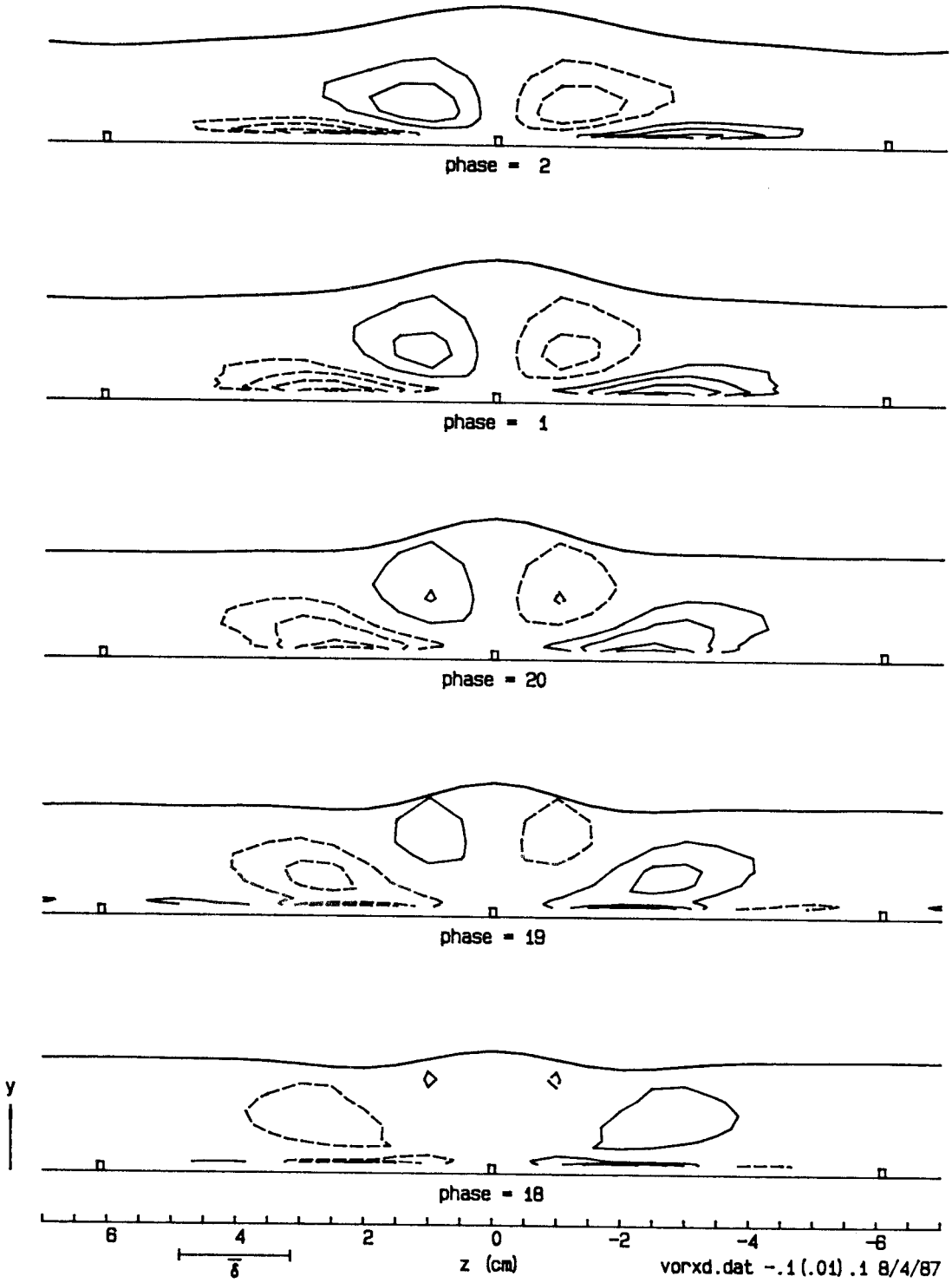

Figure 5.4 (cont'd.). Streamwise vorticity $<\omega_x>$ in the $z-y$ plane.

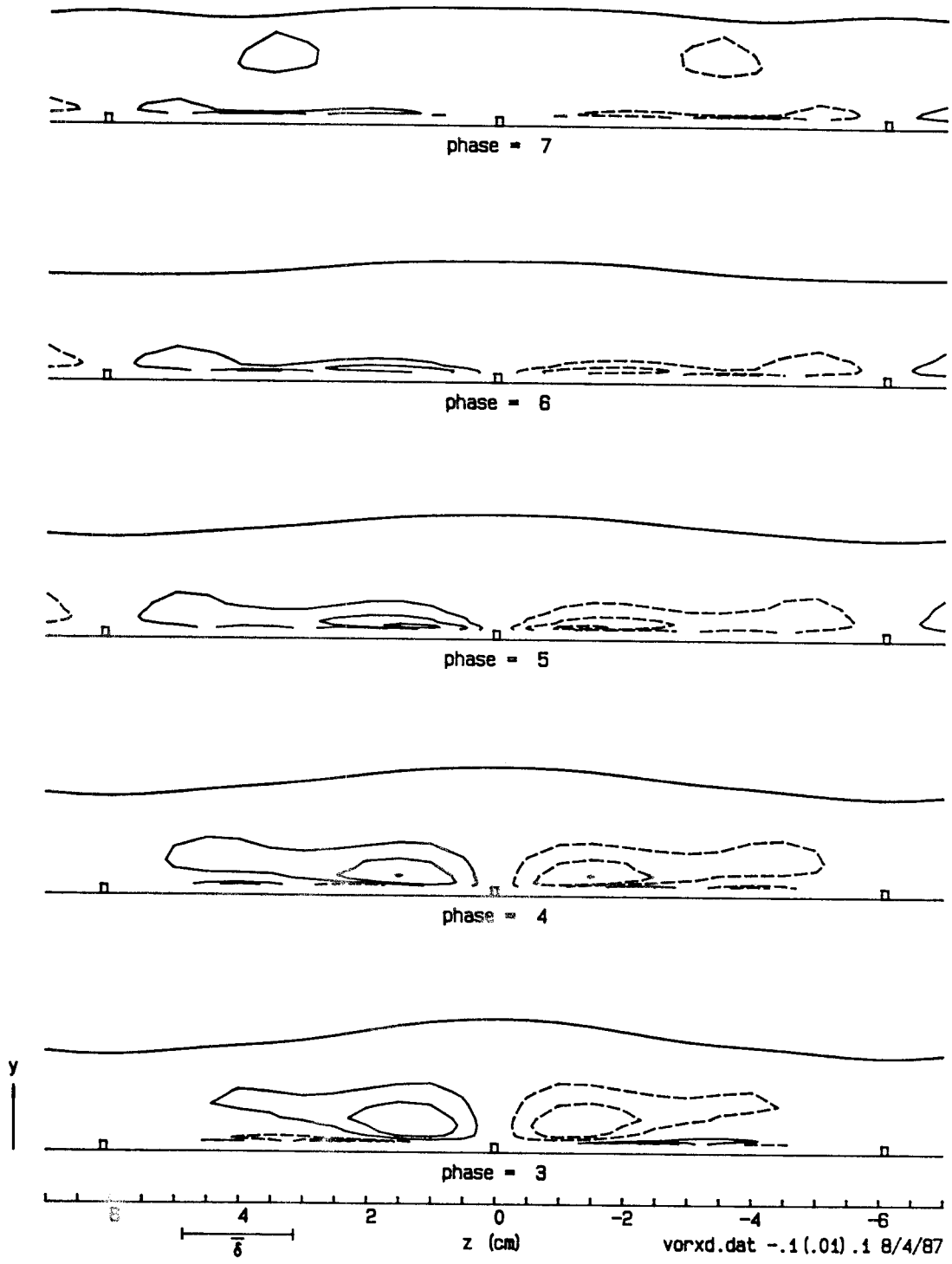

Figure 5.4 (cont'd.). Streamwise vorticity $<\omega_x>$ in the $z-y$ plane.

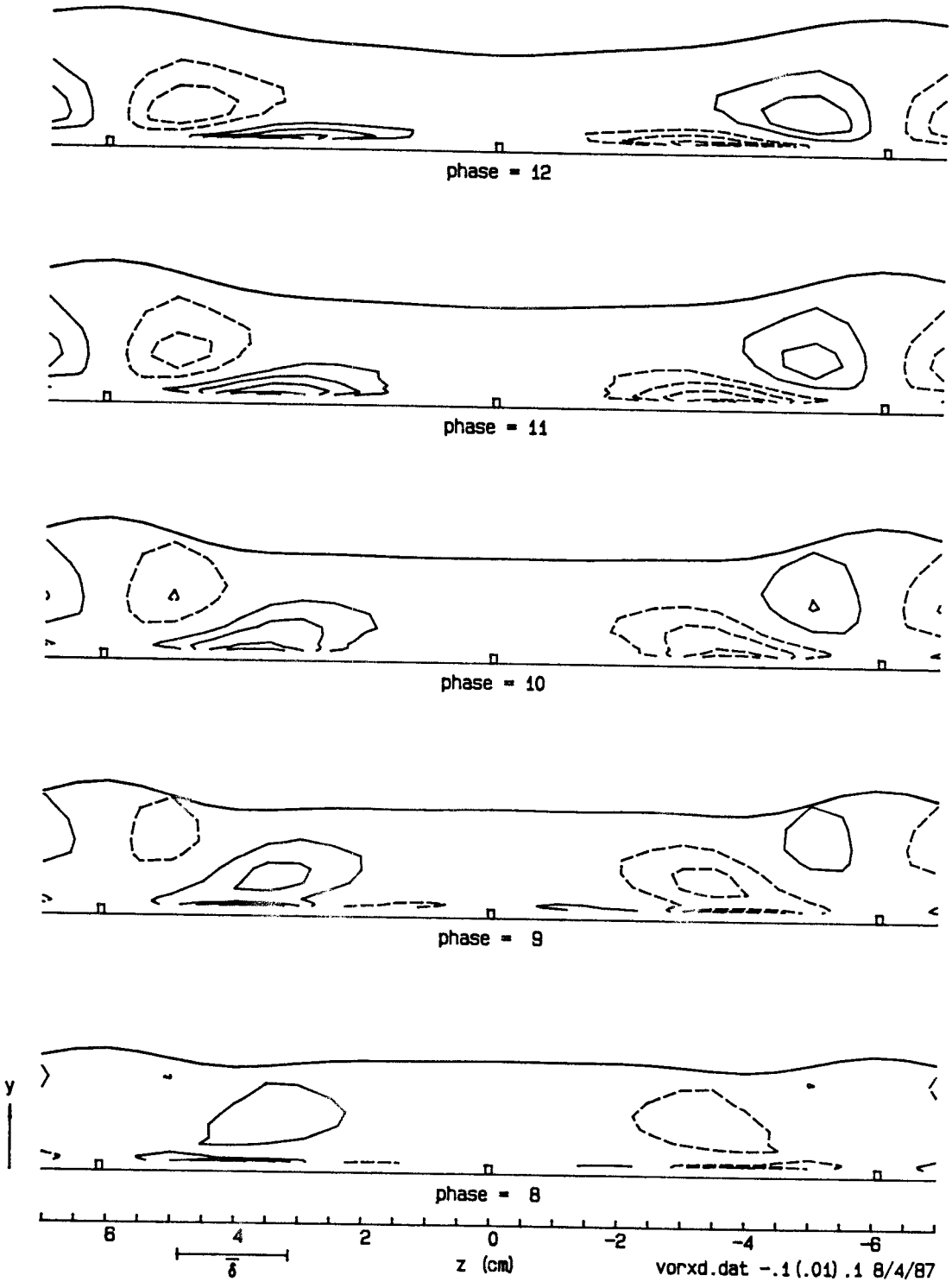

Figure 5.4 (cont'd.). Streamwise vorticity $<\omega_x>$ in the $z-y$ plane.

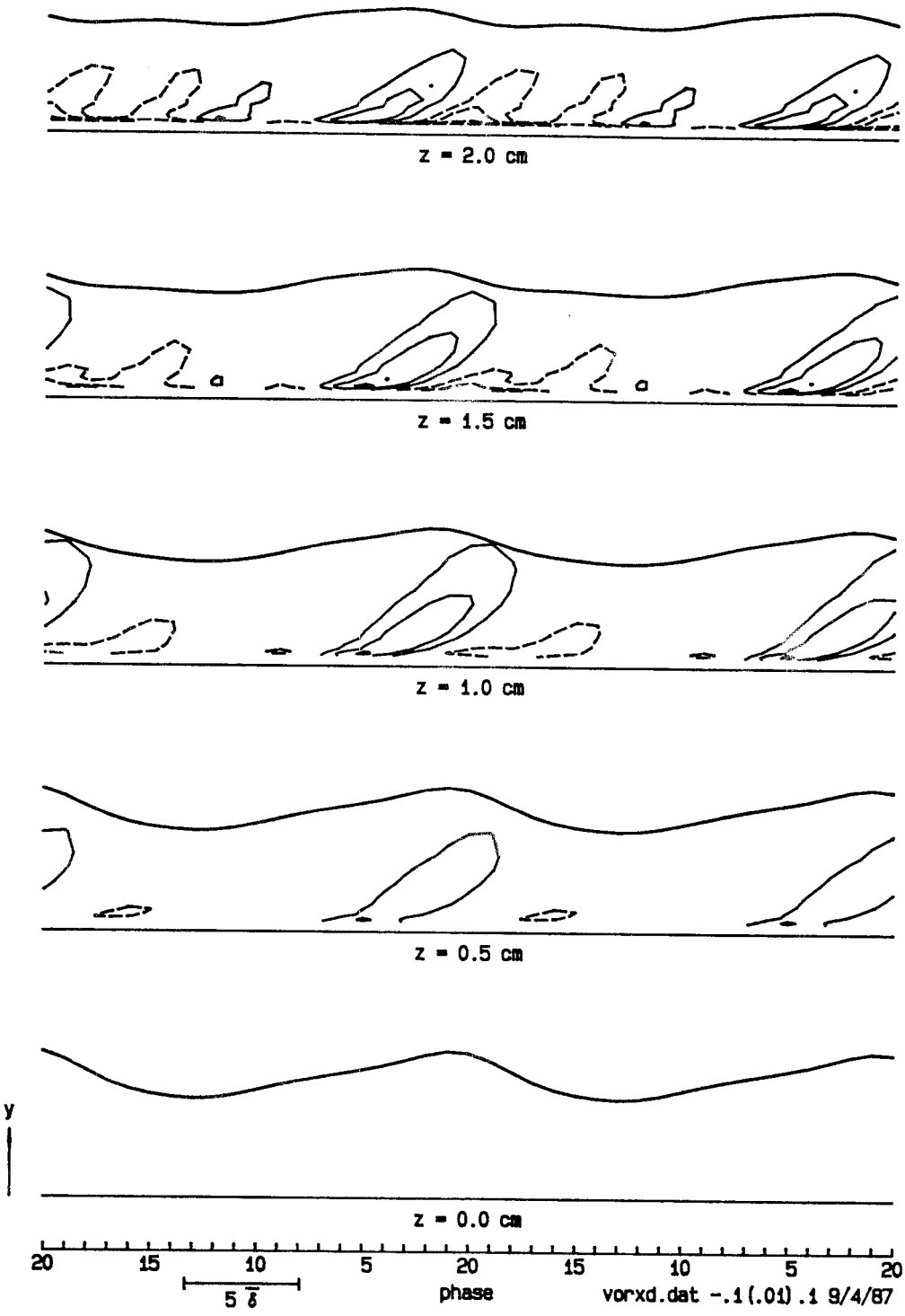

Figure 5.5. Streamwise vorticity $<\omega_x>$ in the $t-y$ plane. Contour interval 0.01.

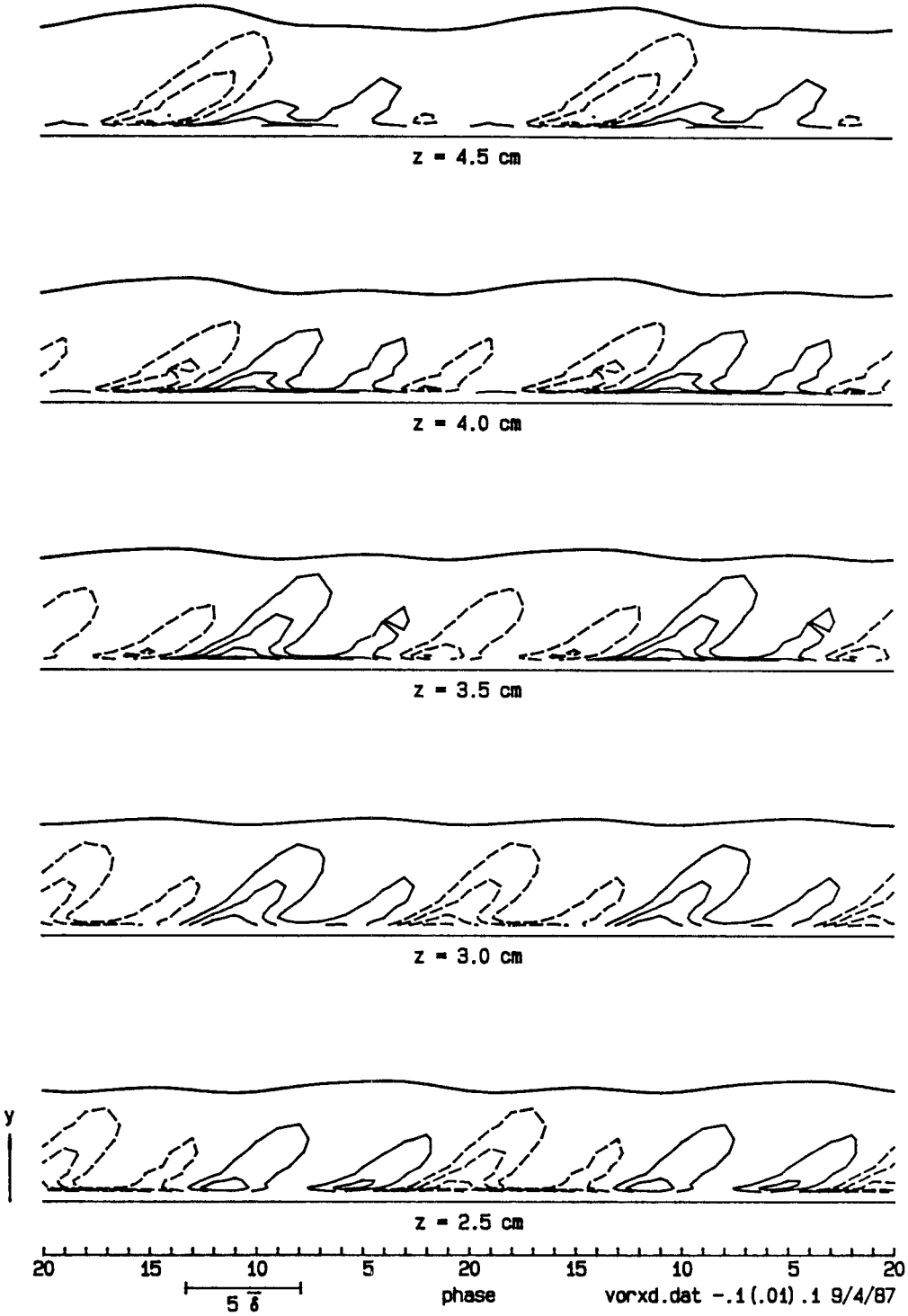

Figure 5.5 (cont'd.). Streamwise vorticity $<\omega_x>$ in the $t-y$ plane.

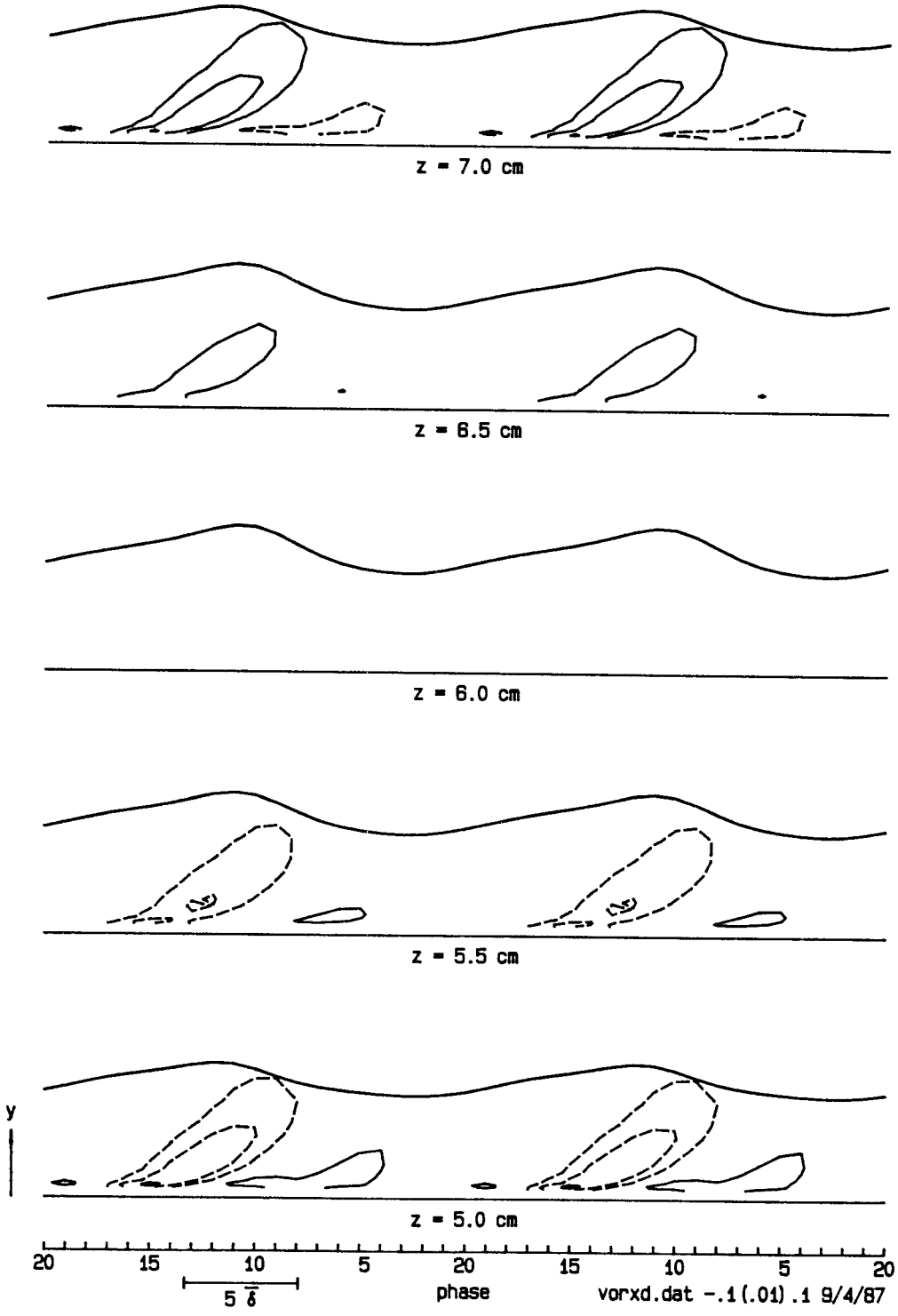

Figure 5.5 (cont'd.). Streamwise vorticity $<\omega_x>$ in the $t-y$ plane.

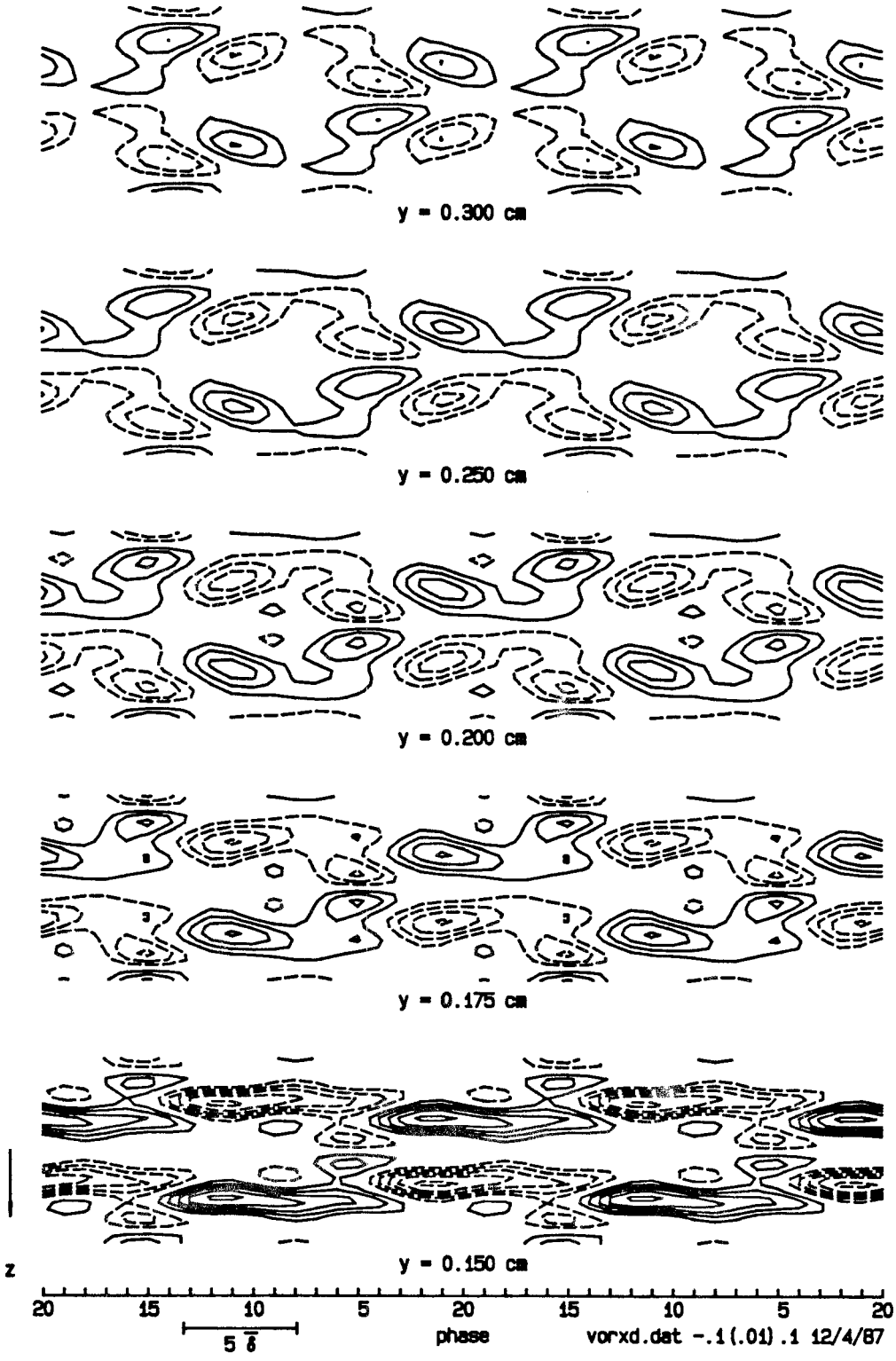

Figure 5.6. Streamwise vorticity $<\omega_x>$ in the $t-z$ plane. Contour interval 0.01.

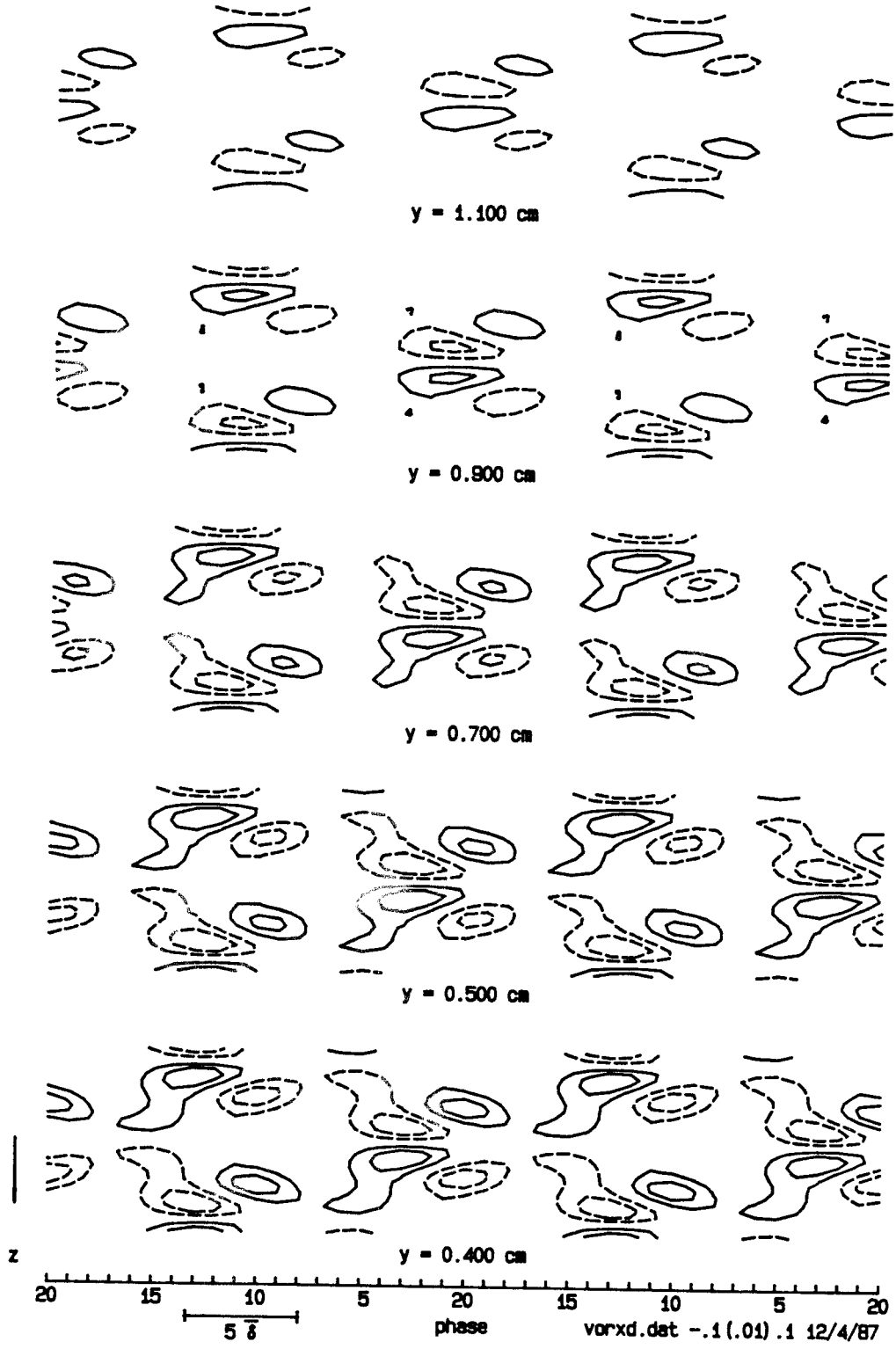

Figure 5.6 (cont'd). Streamwise vorticity $<\omega_x>$ in the $t-z$ plane.

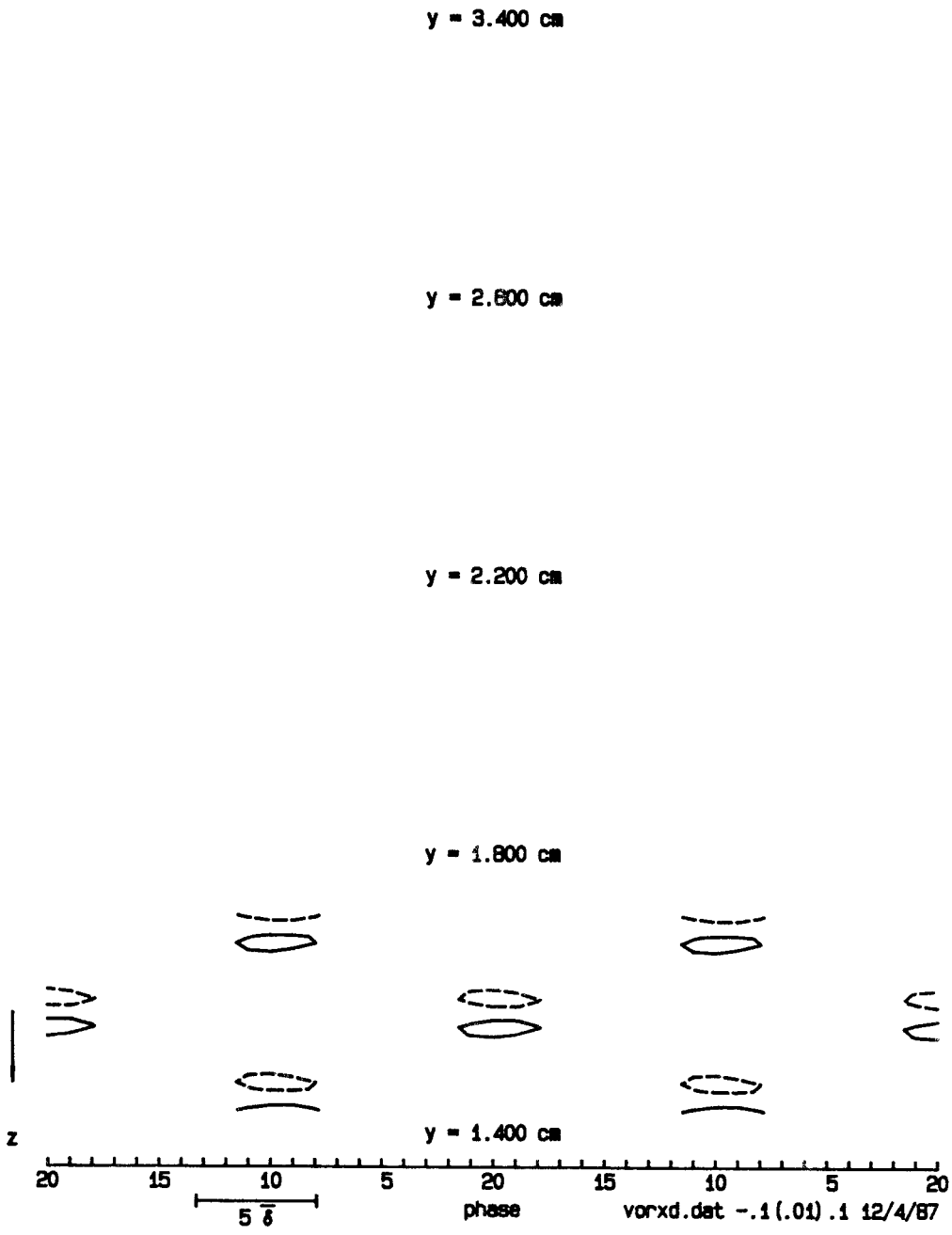

Figure 5.6 (cont'd). Streamwise vorticity $<\omega_x>$ in the $t-z$ plane.

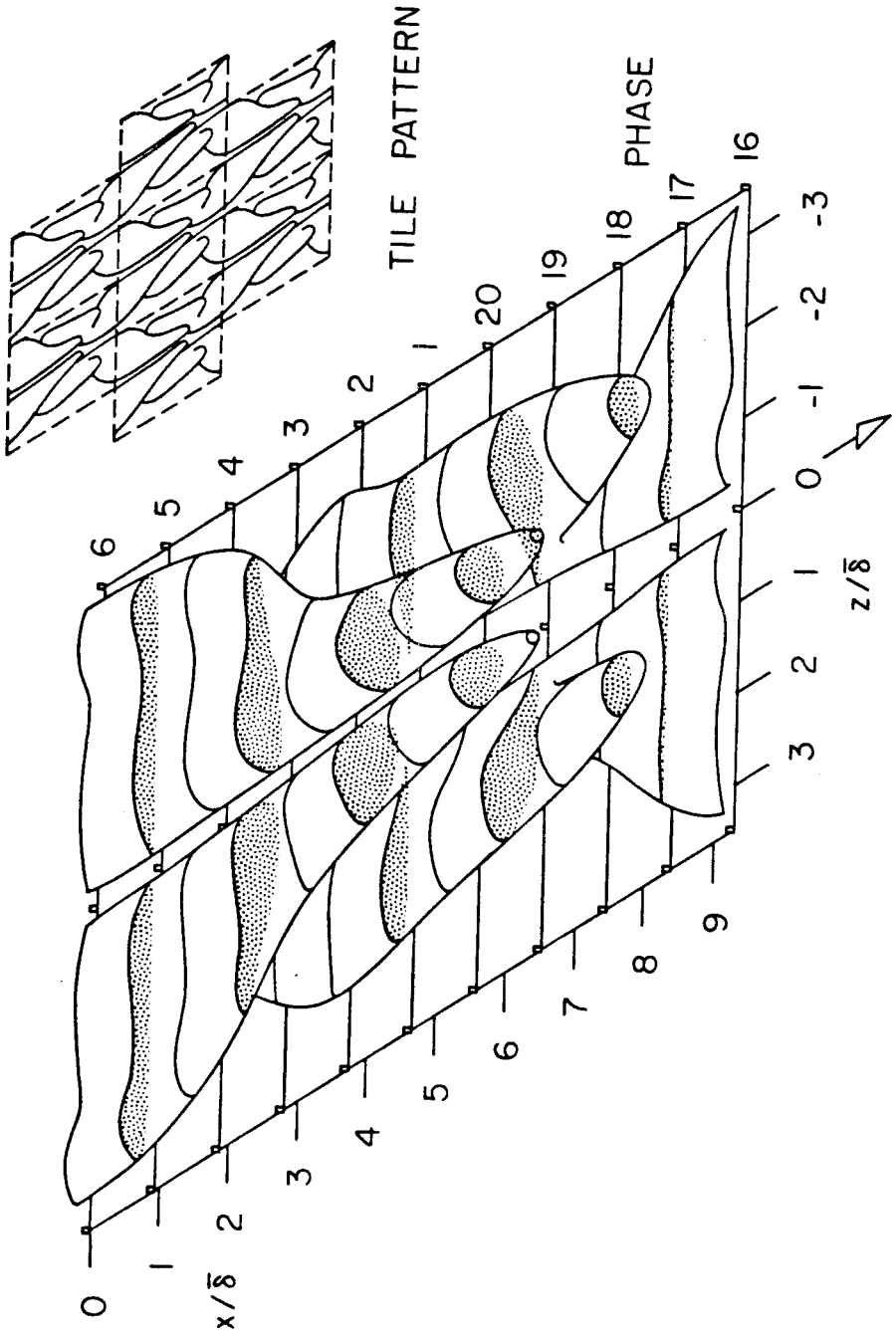

Figure 5.7. Perspective view of streamwise vorticity $<\omega_x>$.

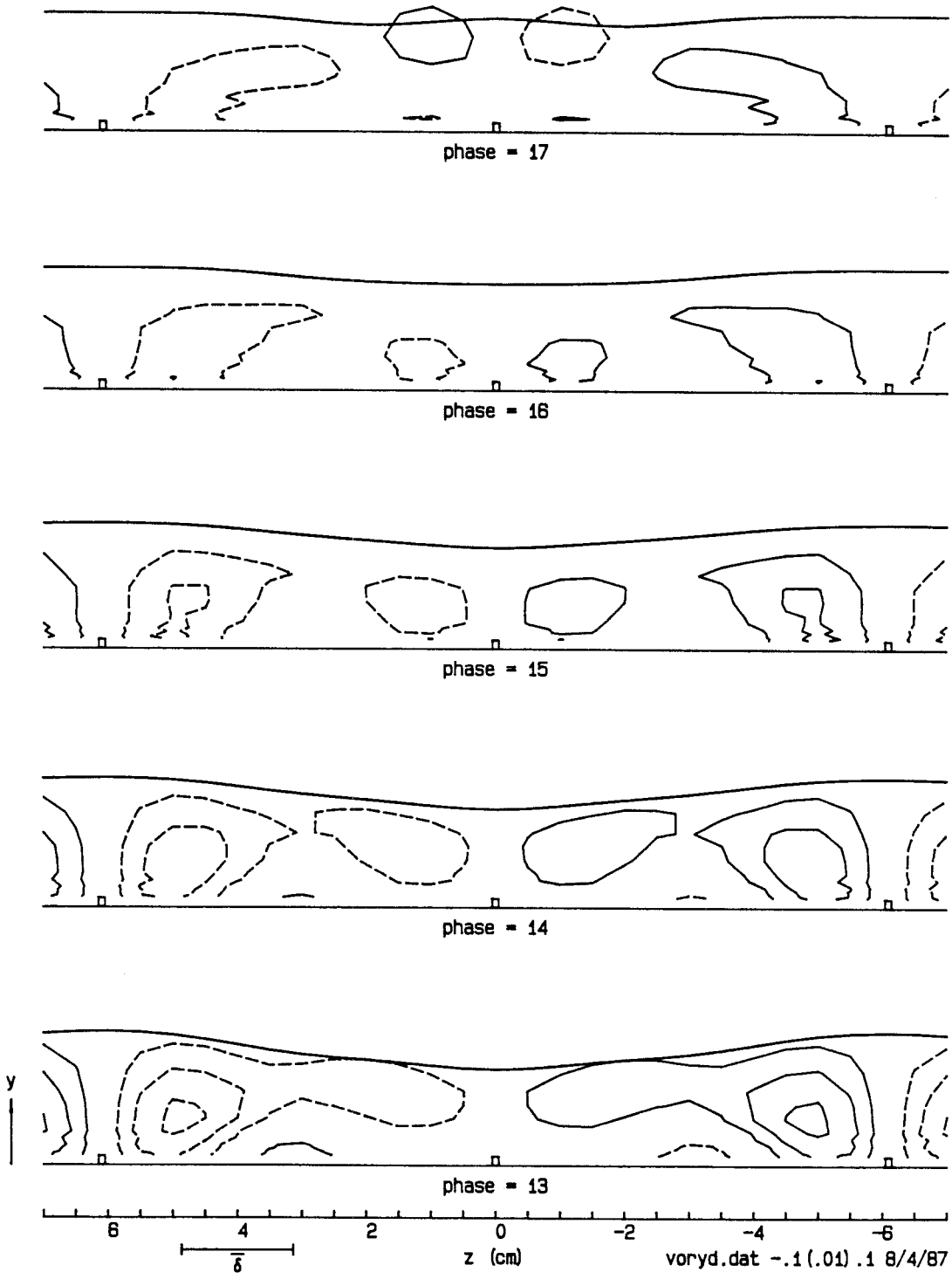

Figure 5.8. Normal vorticity $<\omega_y>$ in the $z-y$ plane. Contour interval 0.01.

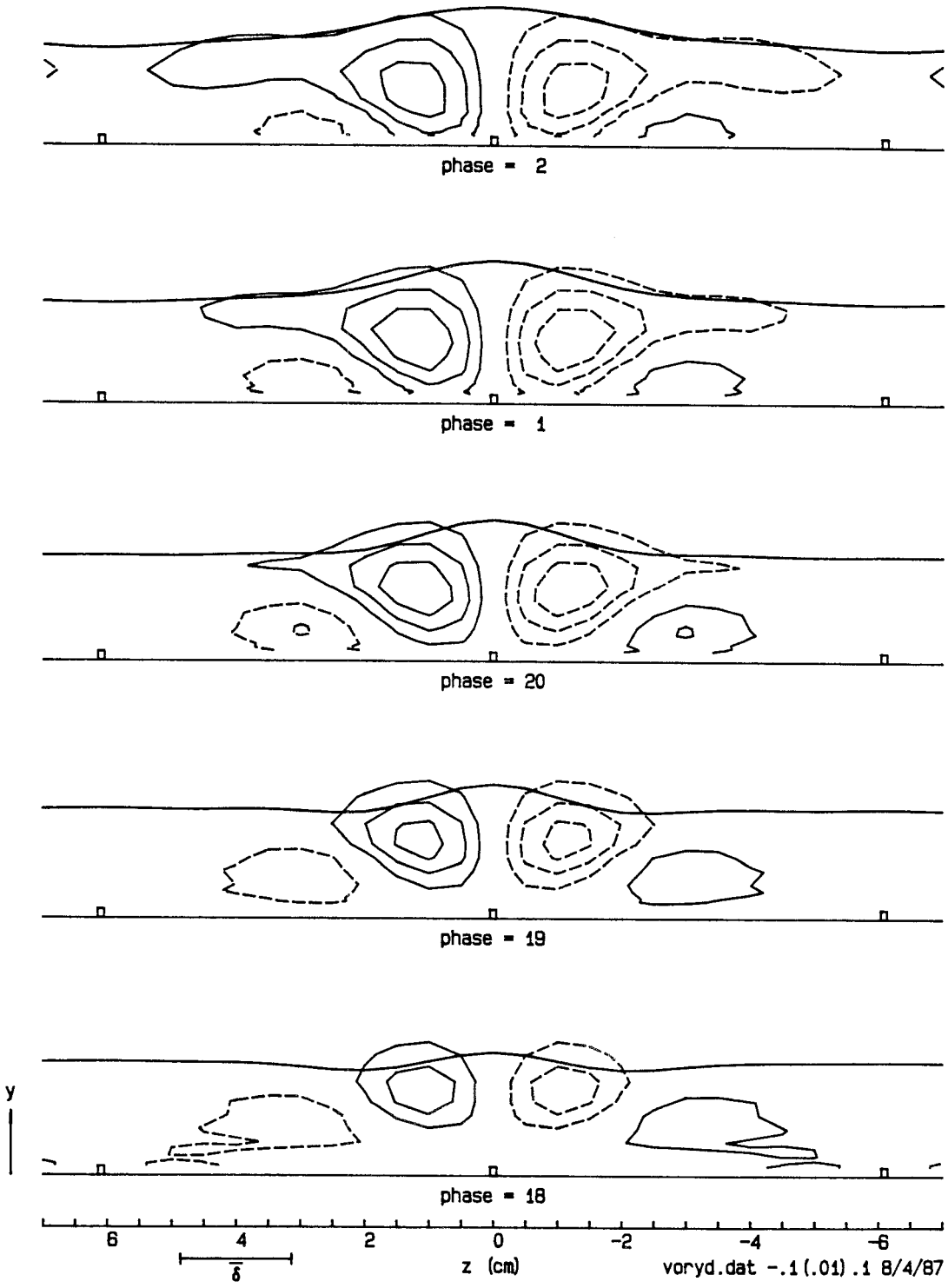

Figure 5.8 (cont'd.). Normal vorticity $<\omega_y>$ in the $z-y$ plane.

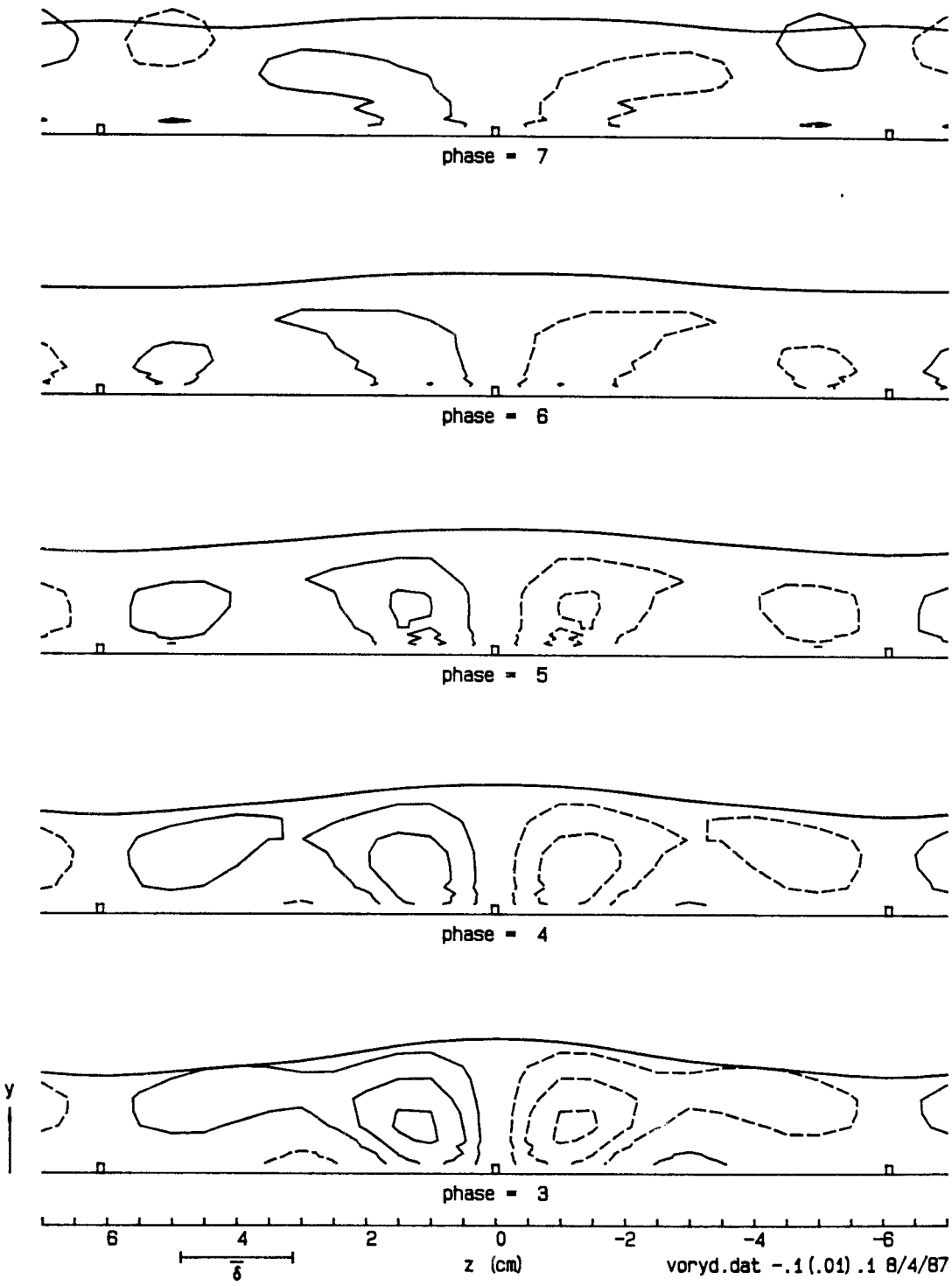

Figure 5.8 (cont'd.). Normal vorticity $<\omega_y>$ in the $z-y$ plane.

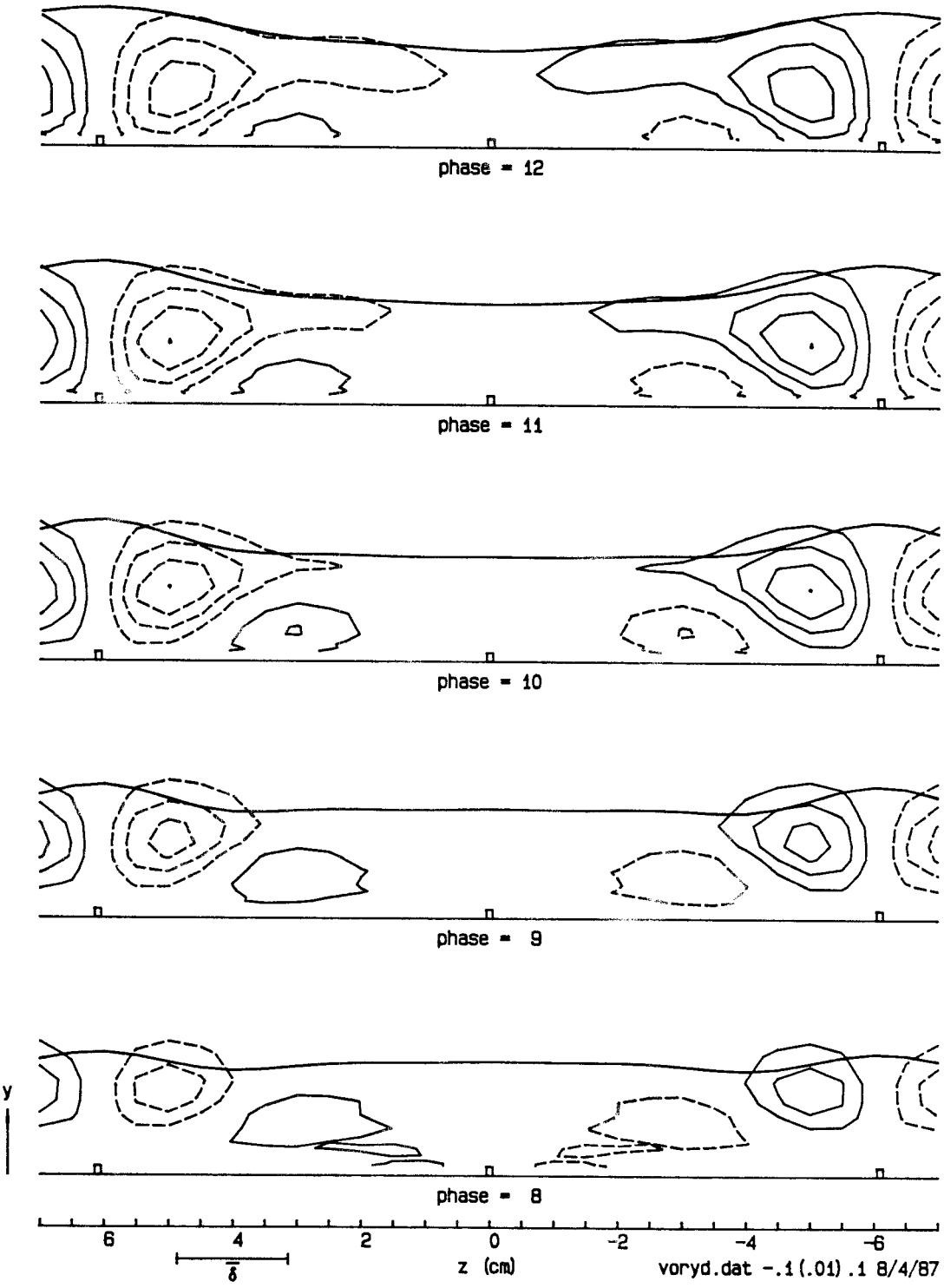

Figure 5.8 (cont'd.). Normal vorticity $<\omega_y>$ in the $z-y$ plane.

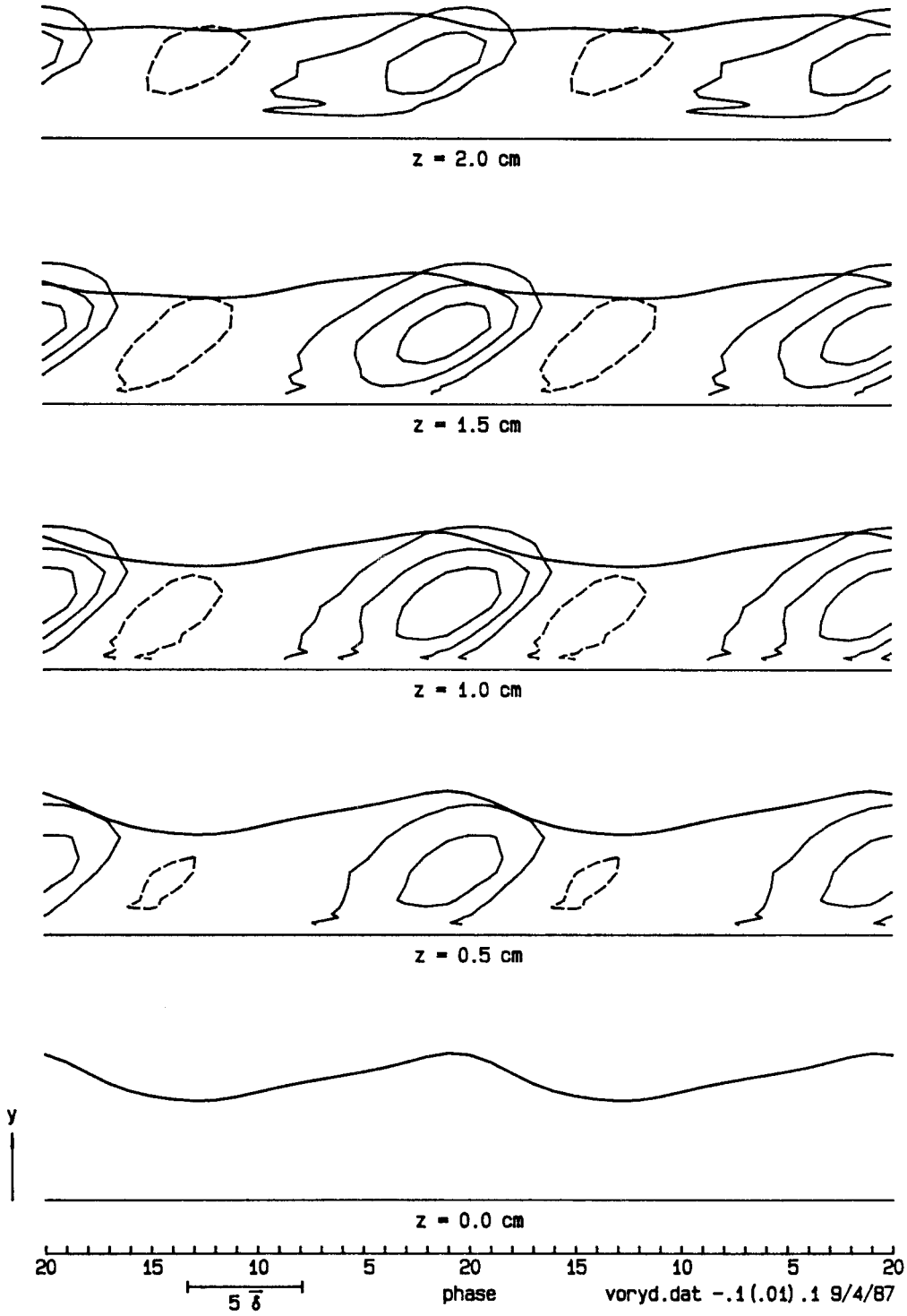

Figure 5.9. Normal vorticity $<\omega_y>$ in the t–y plane. Contour interval 0.01.

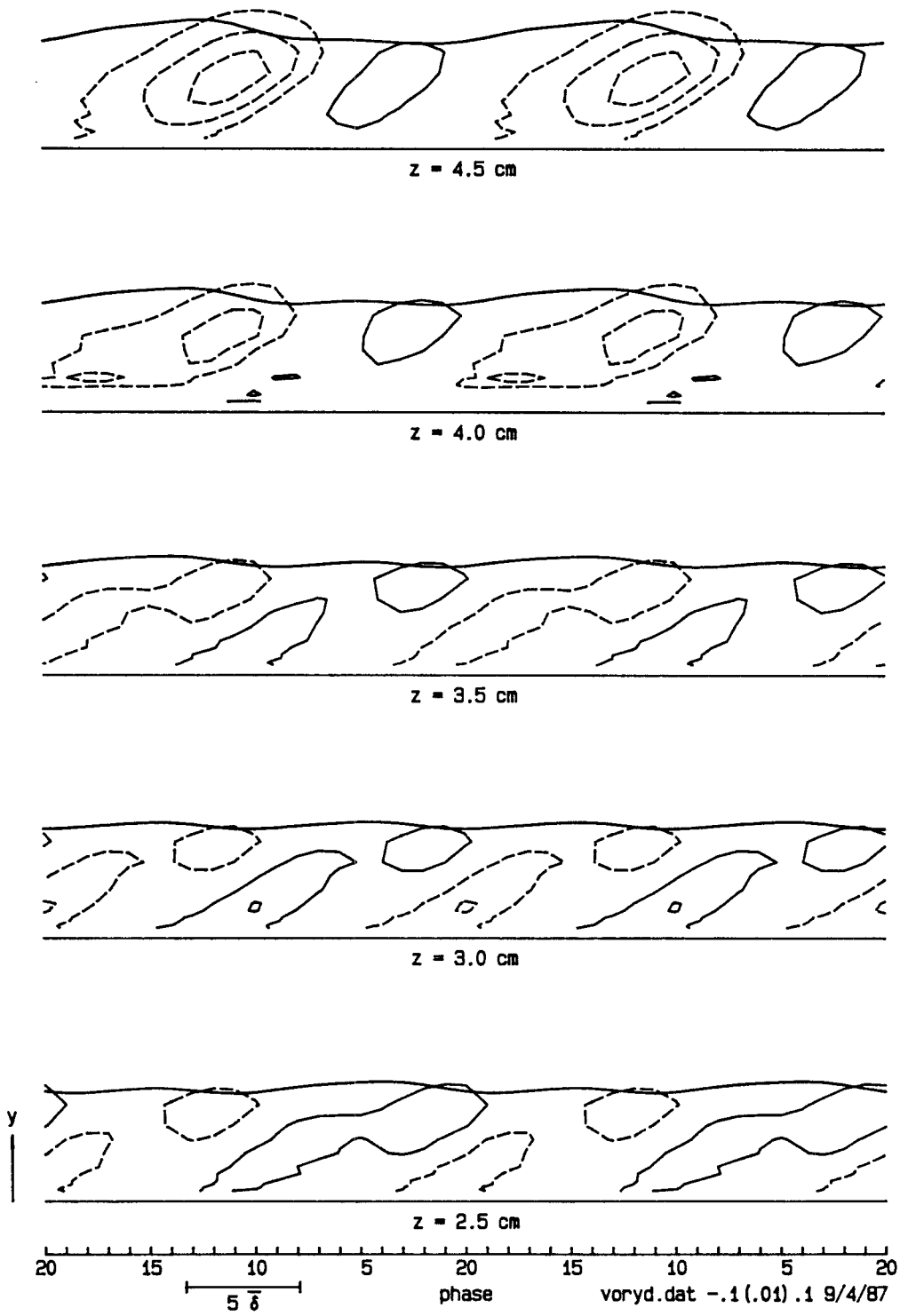

Figure 5.9 (cont'd.). Normal vorticity $\langle\omega_y\rangle$ in the $t-y$ plane.

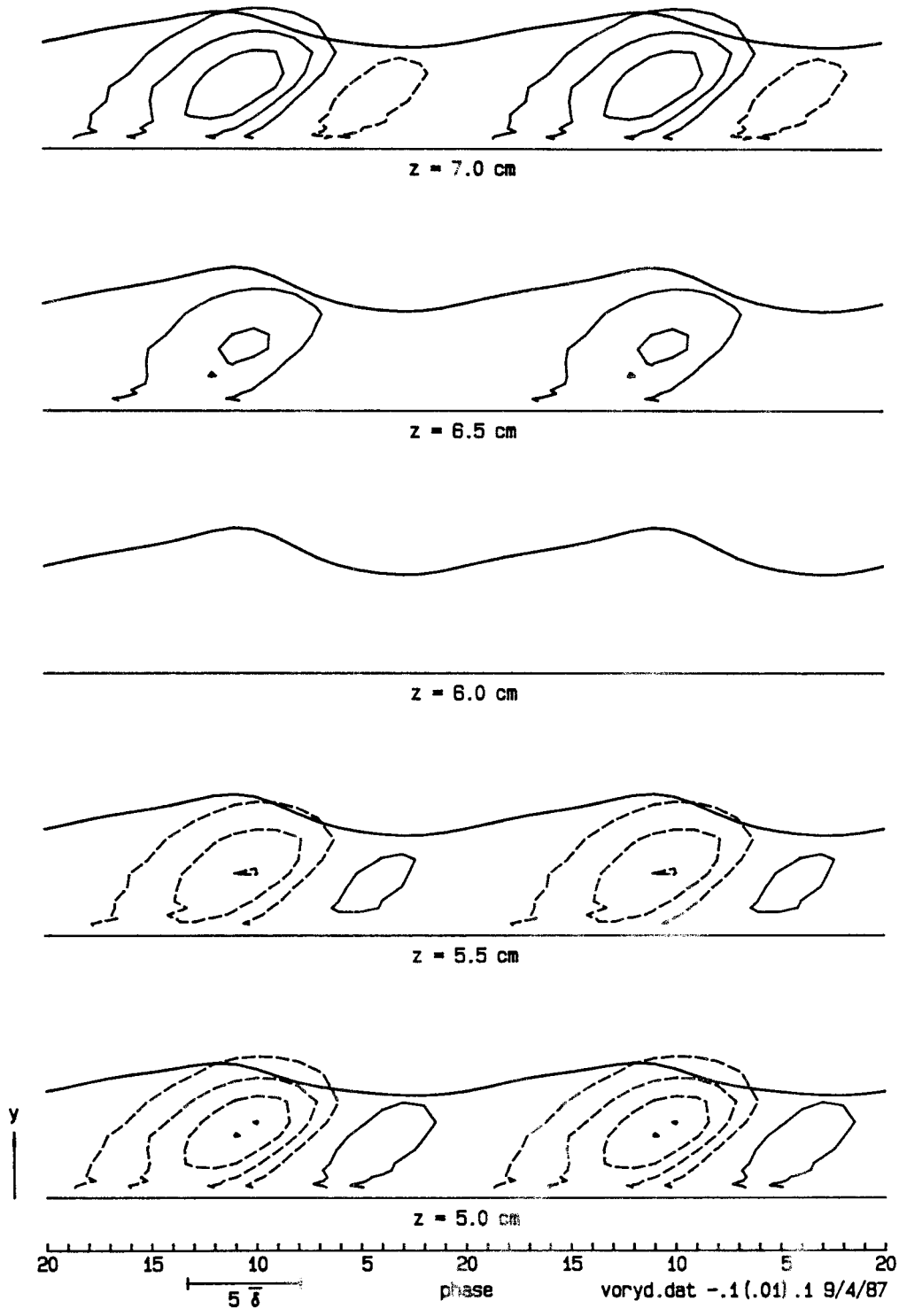

Figure 5.9 (cont'd). Normal vorticity $\langle \omega_y \rangle$ in the t–y plane.

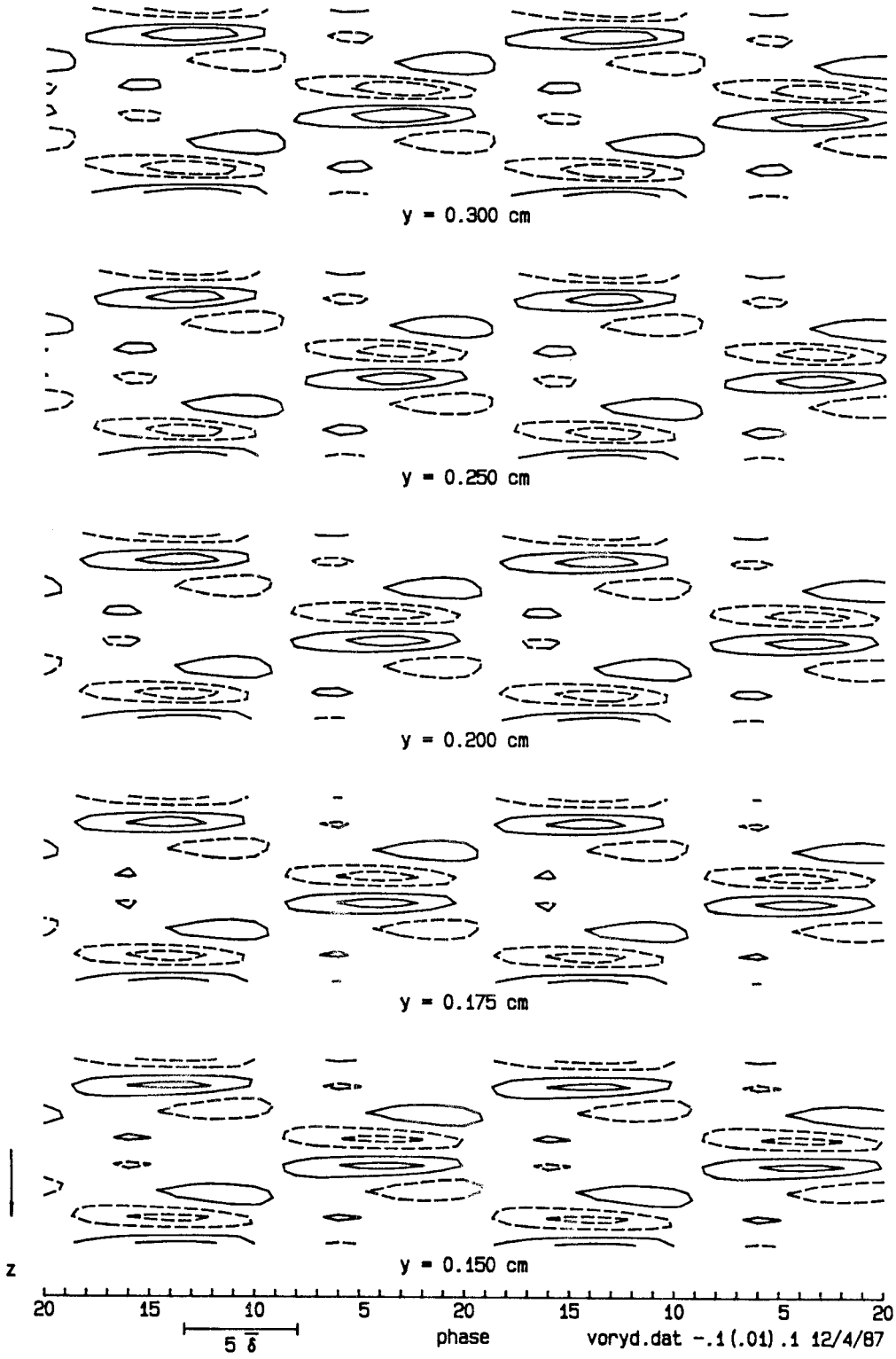

Figure 5.10. Normal vorticity $<\omega_y>$ in the $t-z$ plane. Contour interval 0.01.

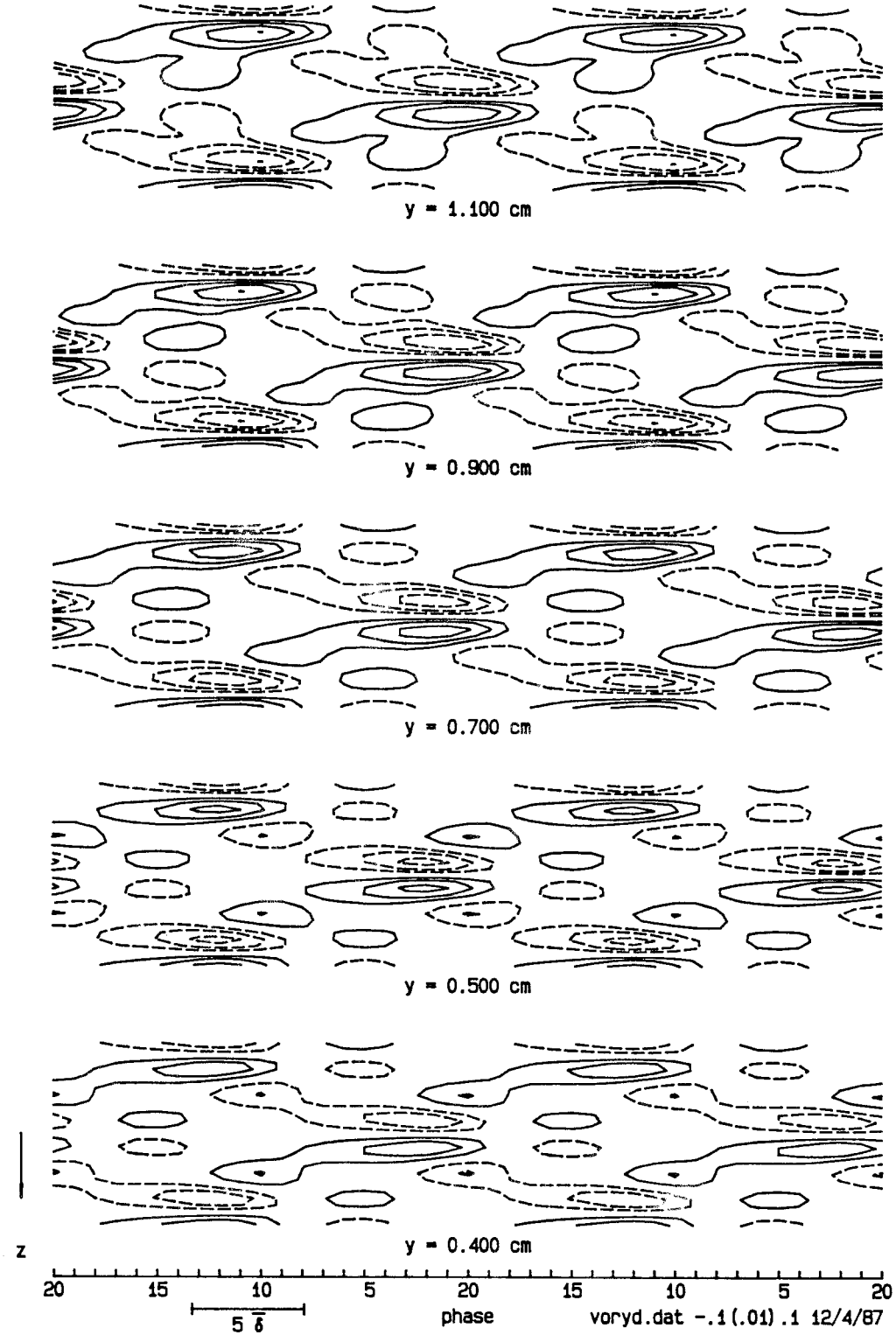

Figure 5.10 (cont'd.). Normal vorticity $<\omega_y>$ in the $t-z$ plane.

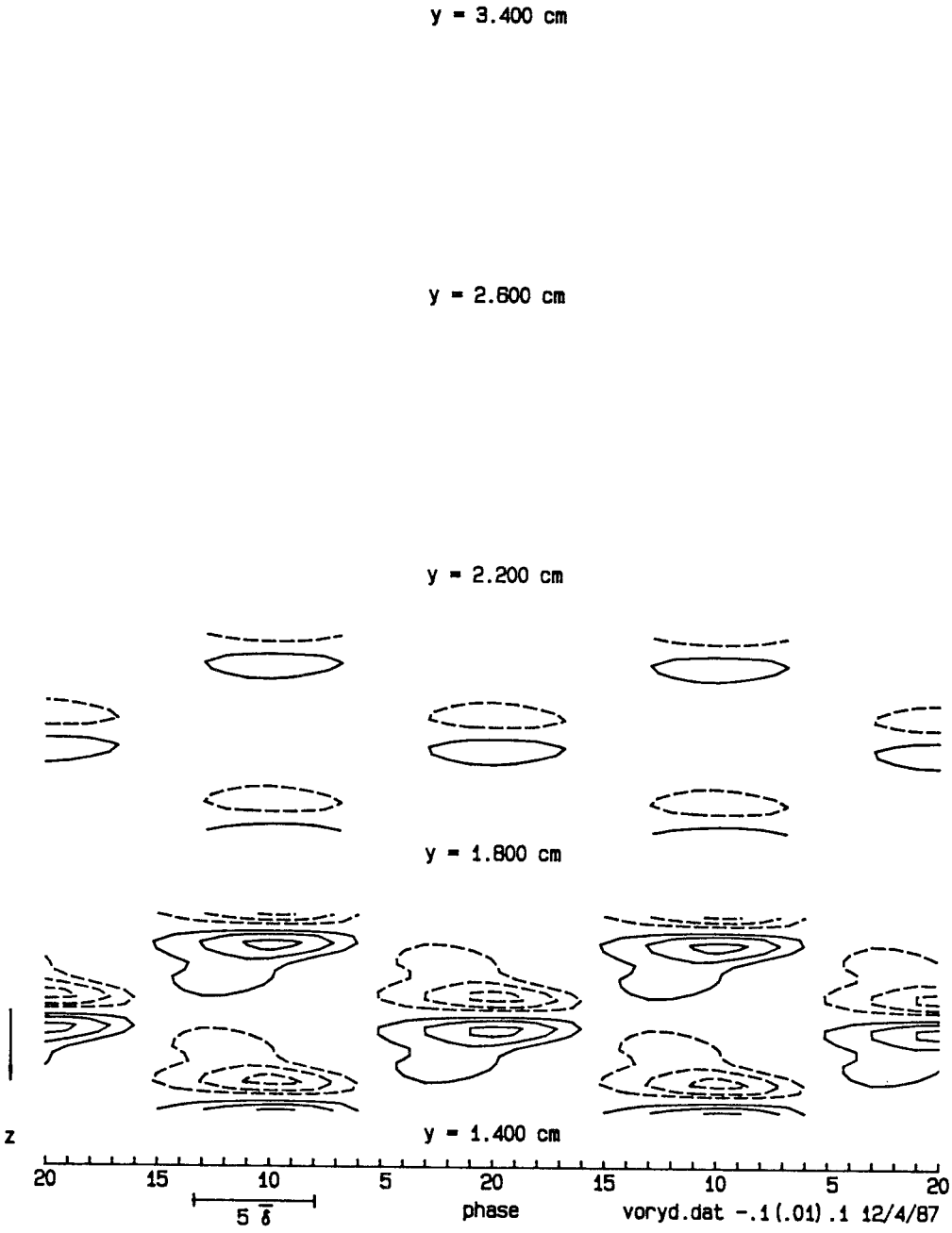

Figure 5.10 (cont'd.). Normal vorticity $\langle\omega_y\rangle$ in the $t-z$ plane.

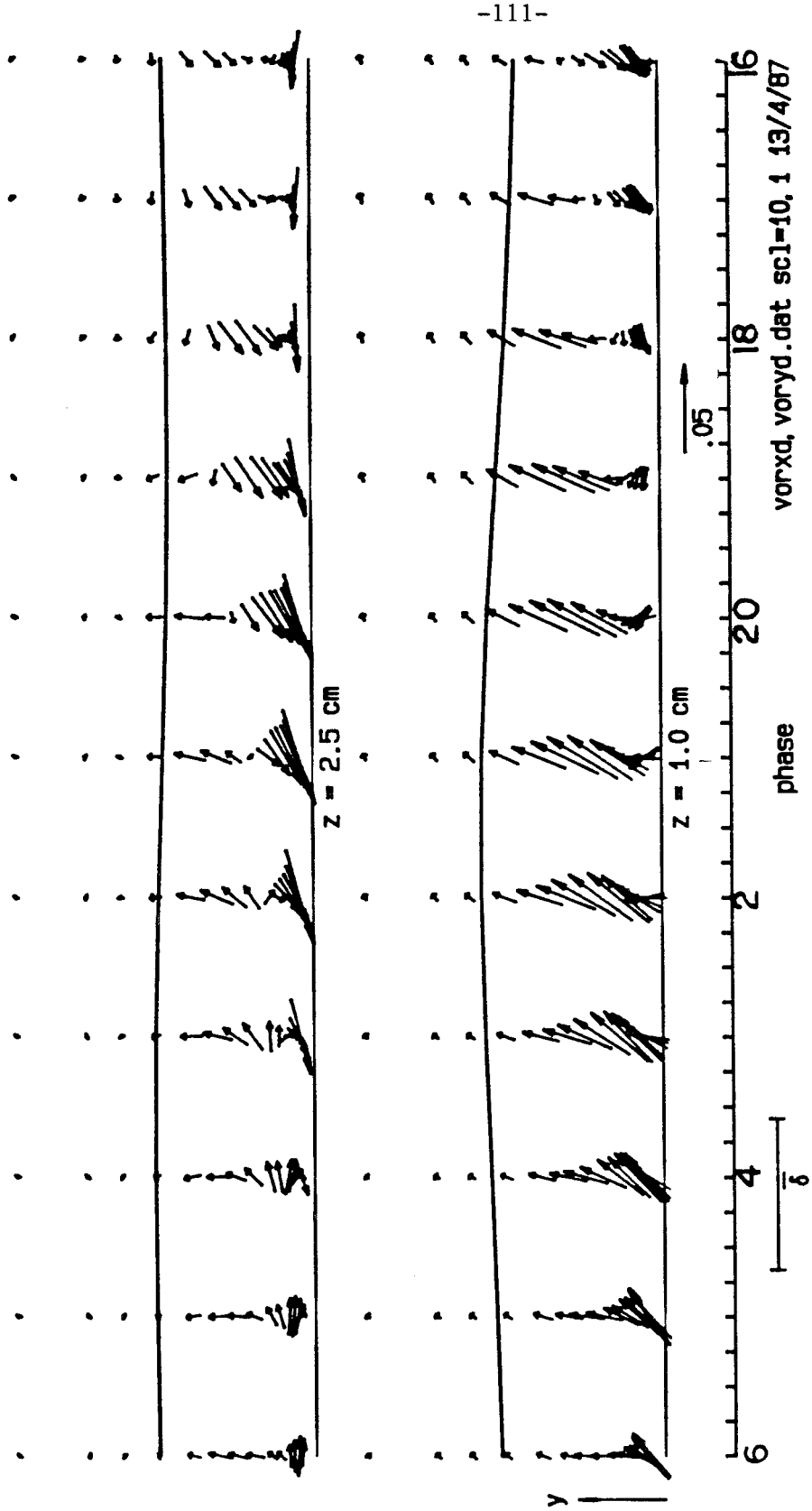

Figure 5.11. Vorticity vectors in the t–y plane at z = 1.0 cm and 2.5 cm for phases 16-6. The two axes have same scale.

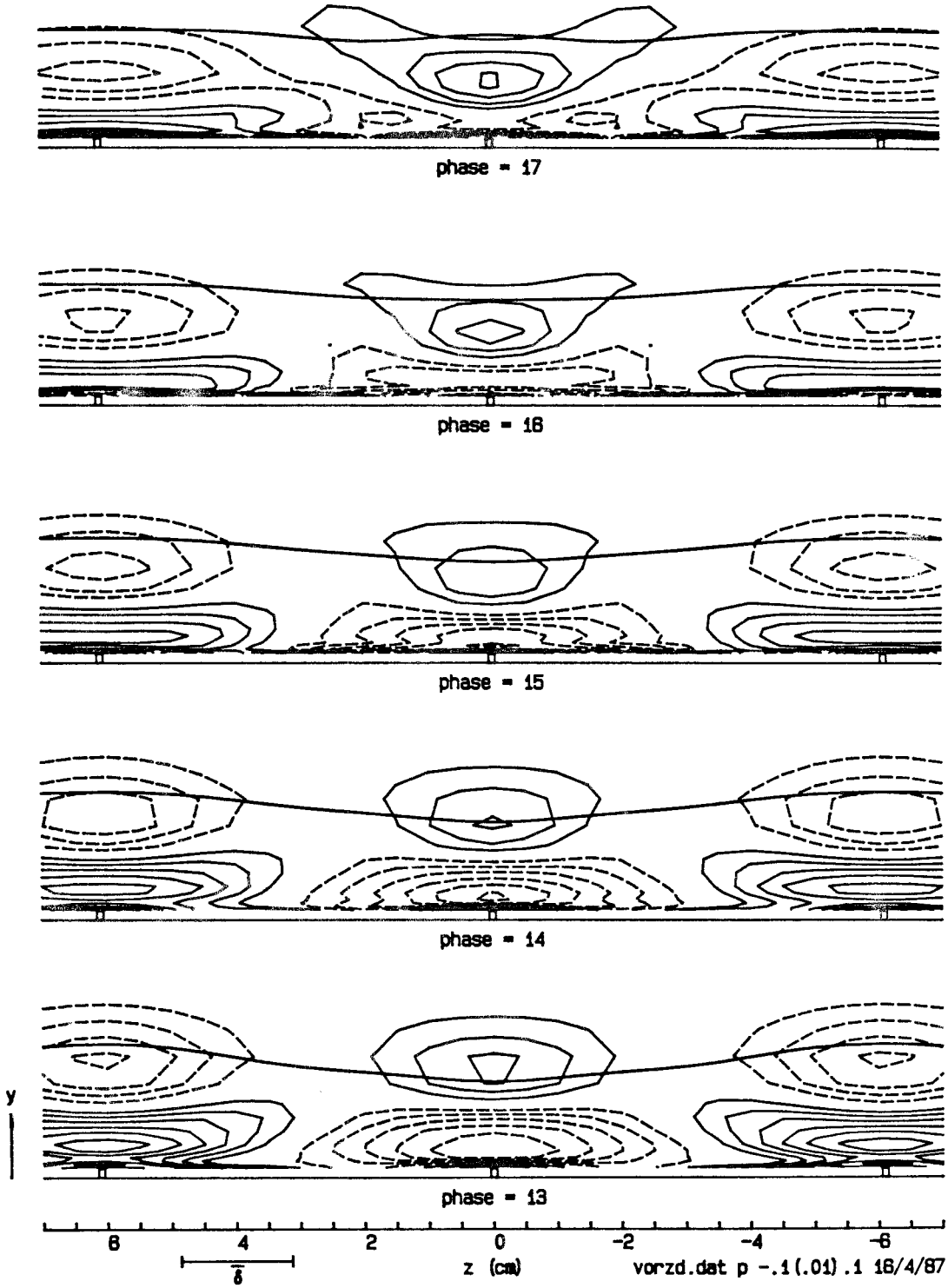

Figure 5.12. Spanwise vorticity perturbation $<\omega_z> - \overline{\omega_z}$ in the $z-y$ plane. Contour interval 0.01.

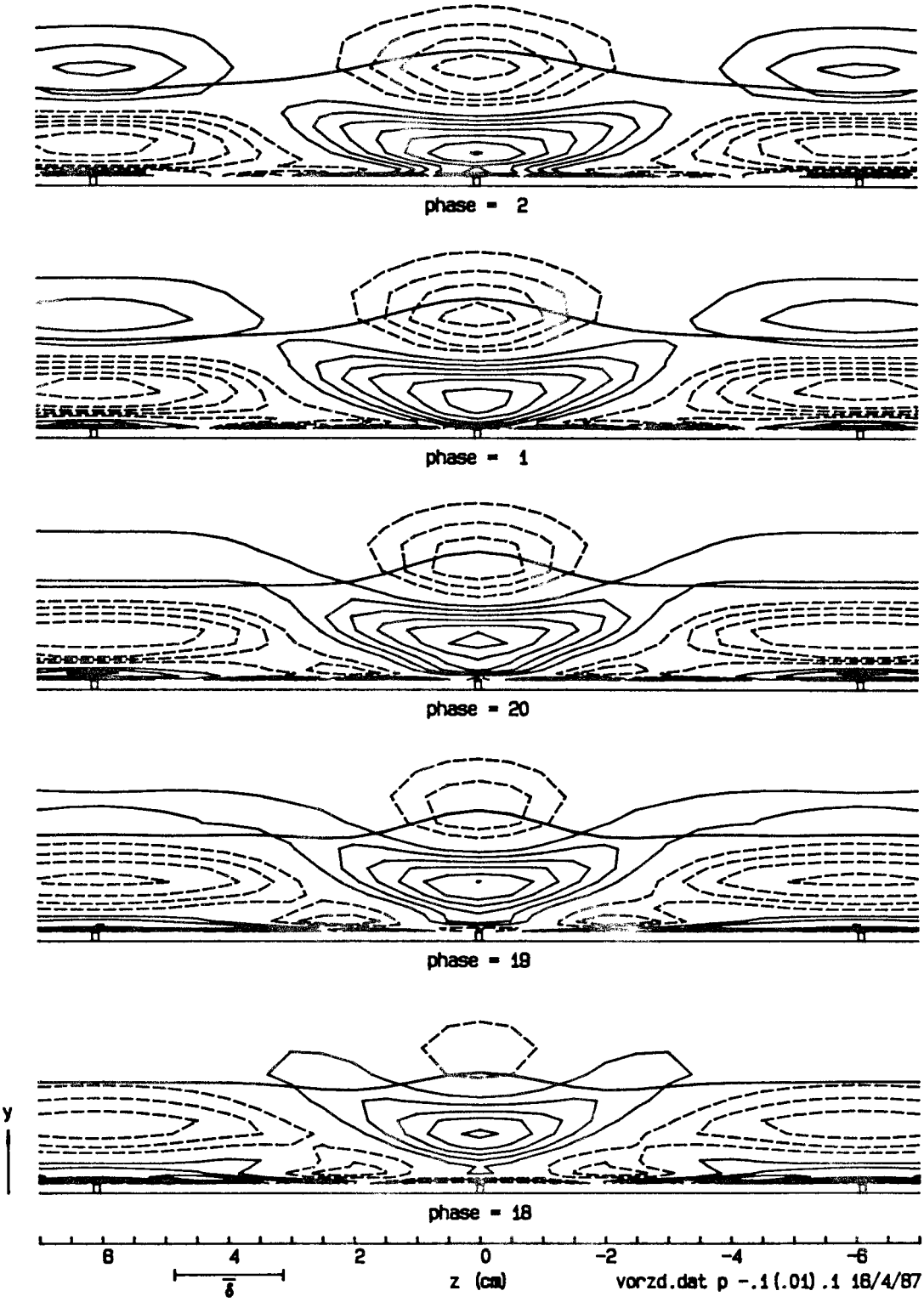

Figure 5.12 (cont'd.). Spanwise vorticity perturbation $<\omega_z> - \overline{\omega_z}$ in the $z-y$ plane.

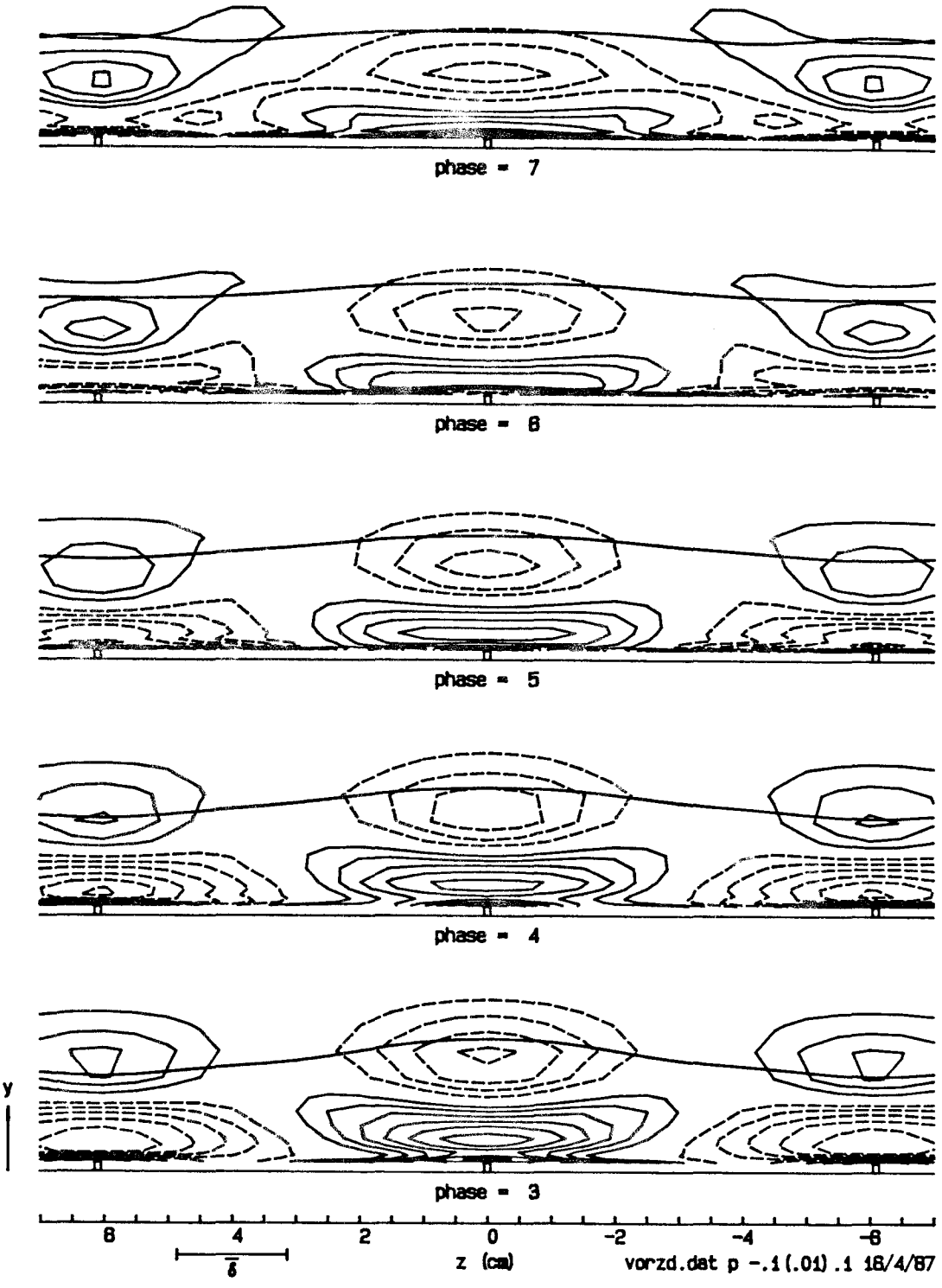

Figure 5.12 (cont'd.). Spanwise vorticity perturbation $<\omega_z> - \overline{\omega_z}$ in the $z-y$ plane.

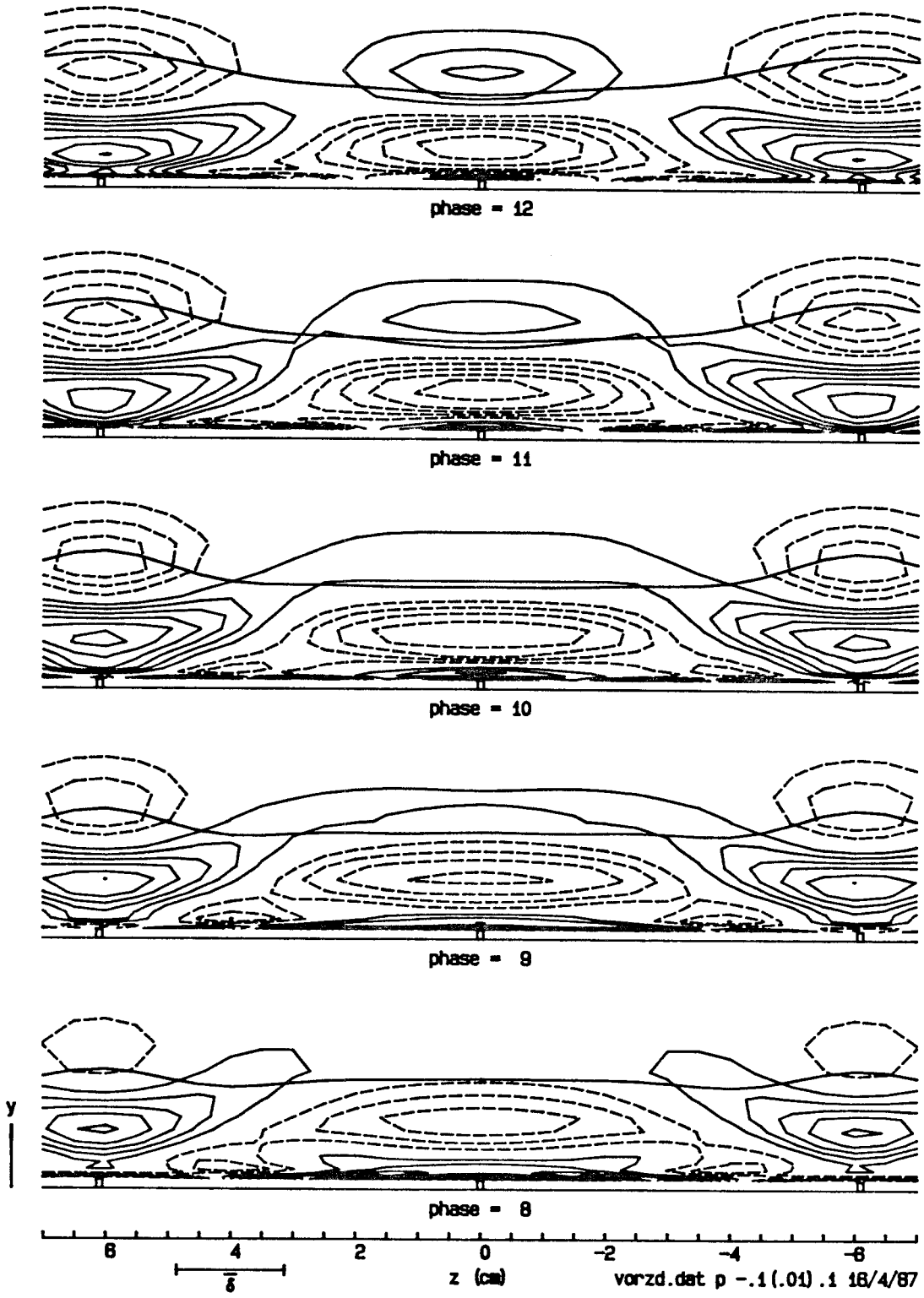

Figure 5.12 (cont'd.). Spanwise vorticity perturbation $<\omega_z> - \overline{\omega_z}$ in the $z-y$ plane.

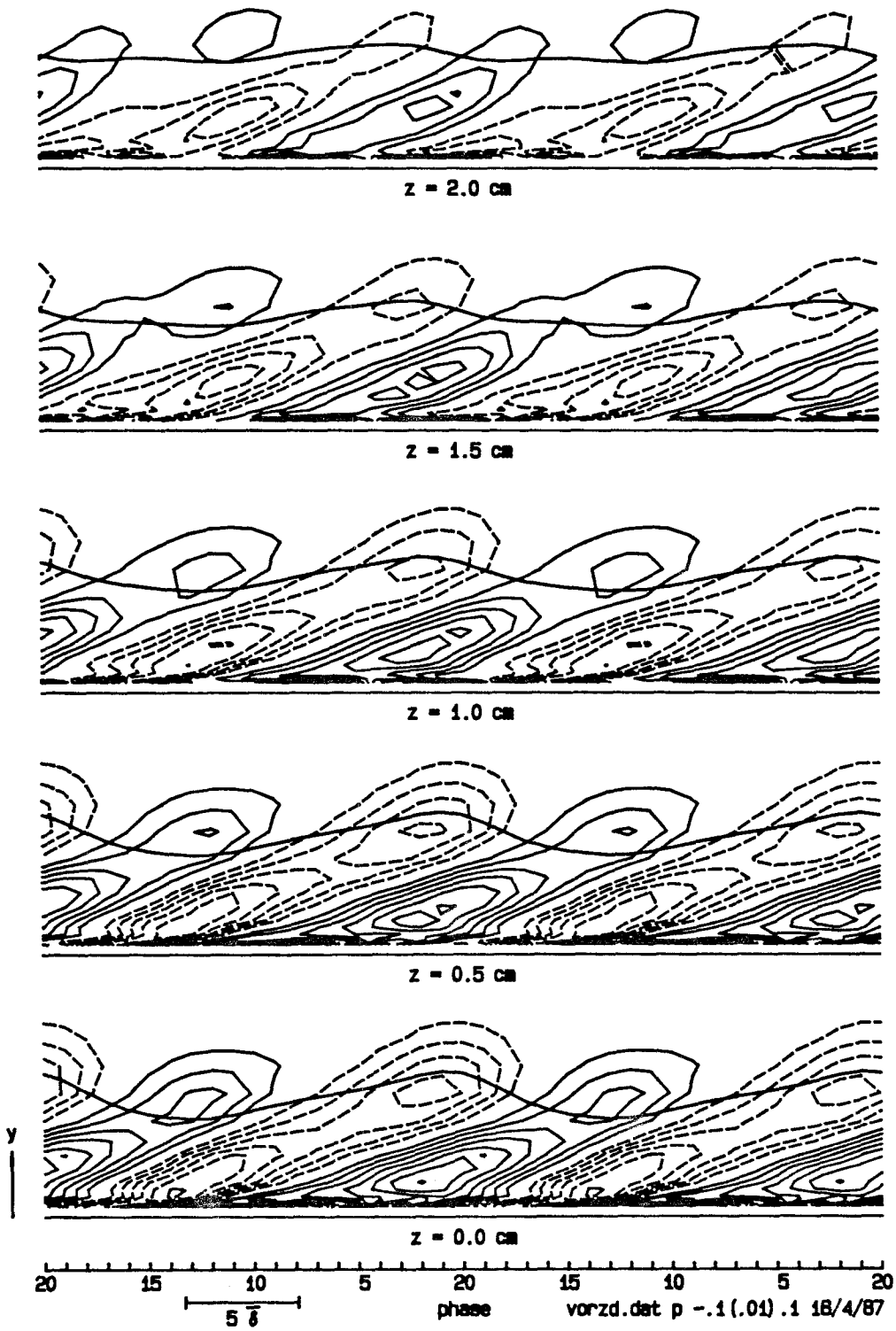

Figure 5.13. Spanwise vorticity perturbation $<\omega_z> - \overline{\omega_z}$ in the t–y plane. Contour interval 0.01.

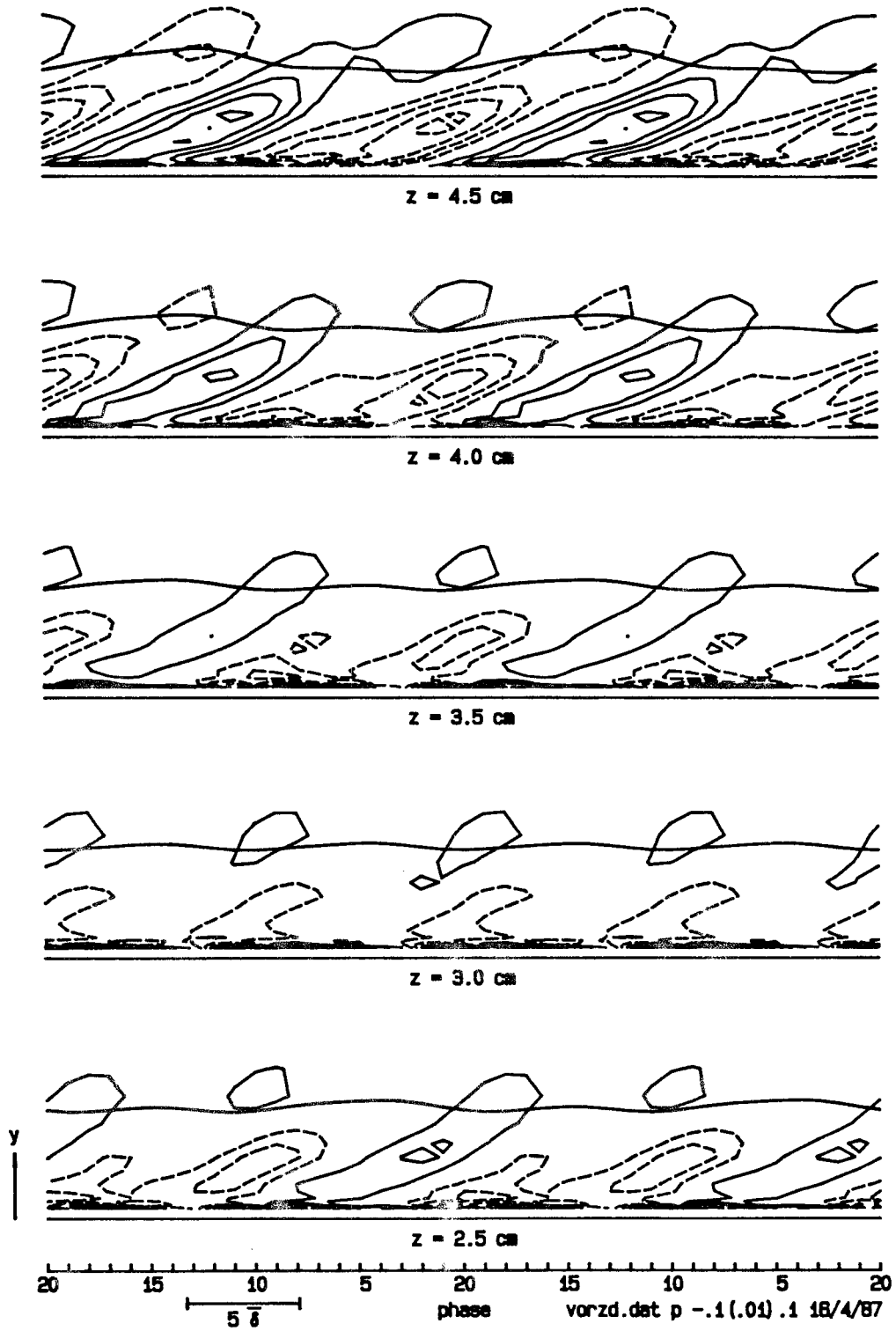

Figure 5.13 (cont'd.). Spanwise vorticity perturbation $<\omega_z> - \overline{\omega_z}$ in the $t-y$ plane.

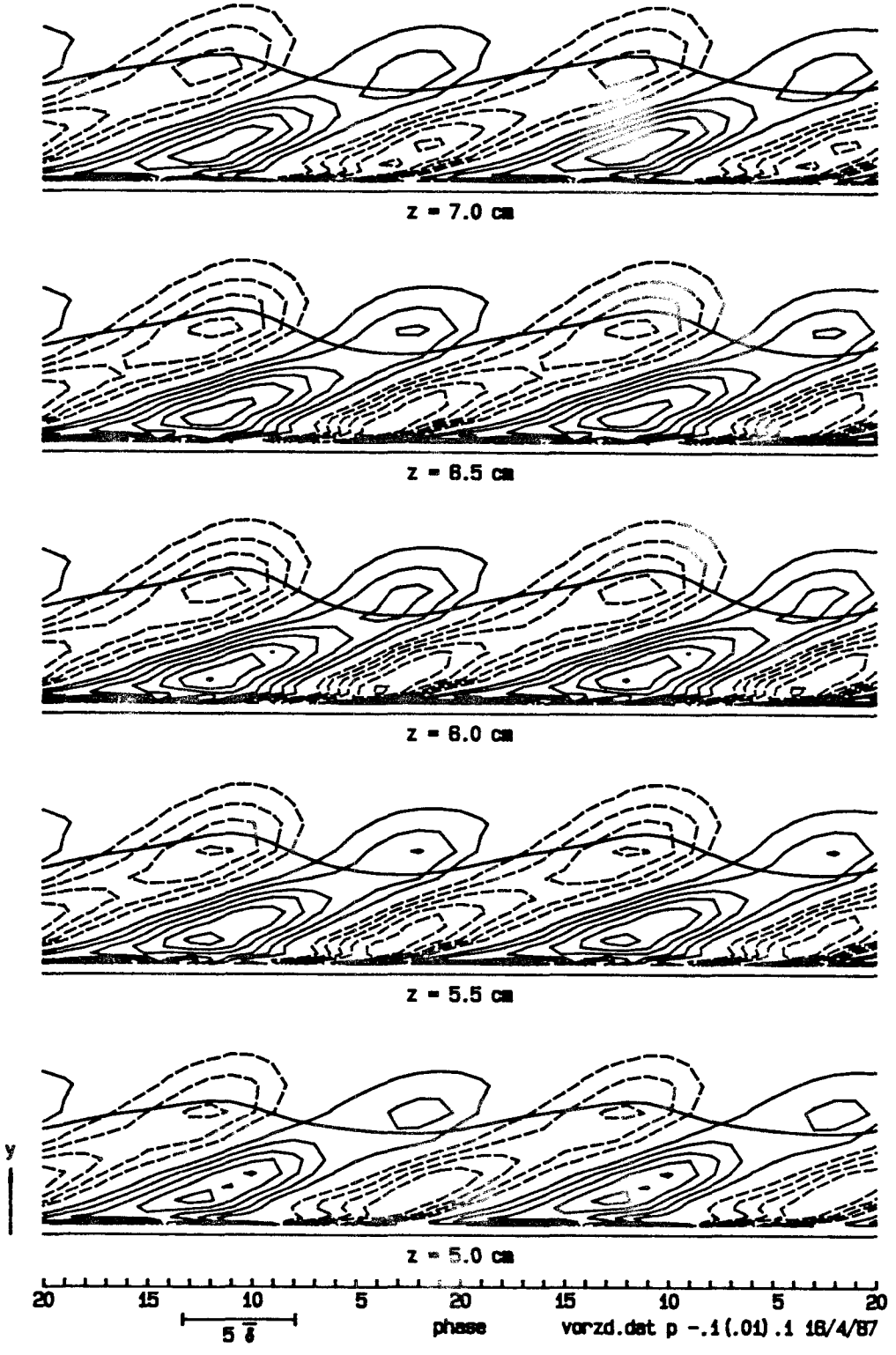

Figure 5.13 (cont'd.). Spanwise vorticity perturbation $<\omega_z> - \overline{\omega_z}$ in the $t-y$ plane.

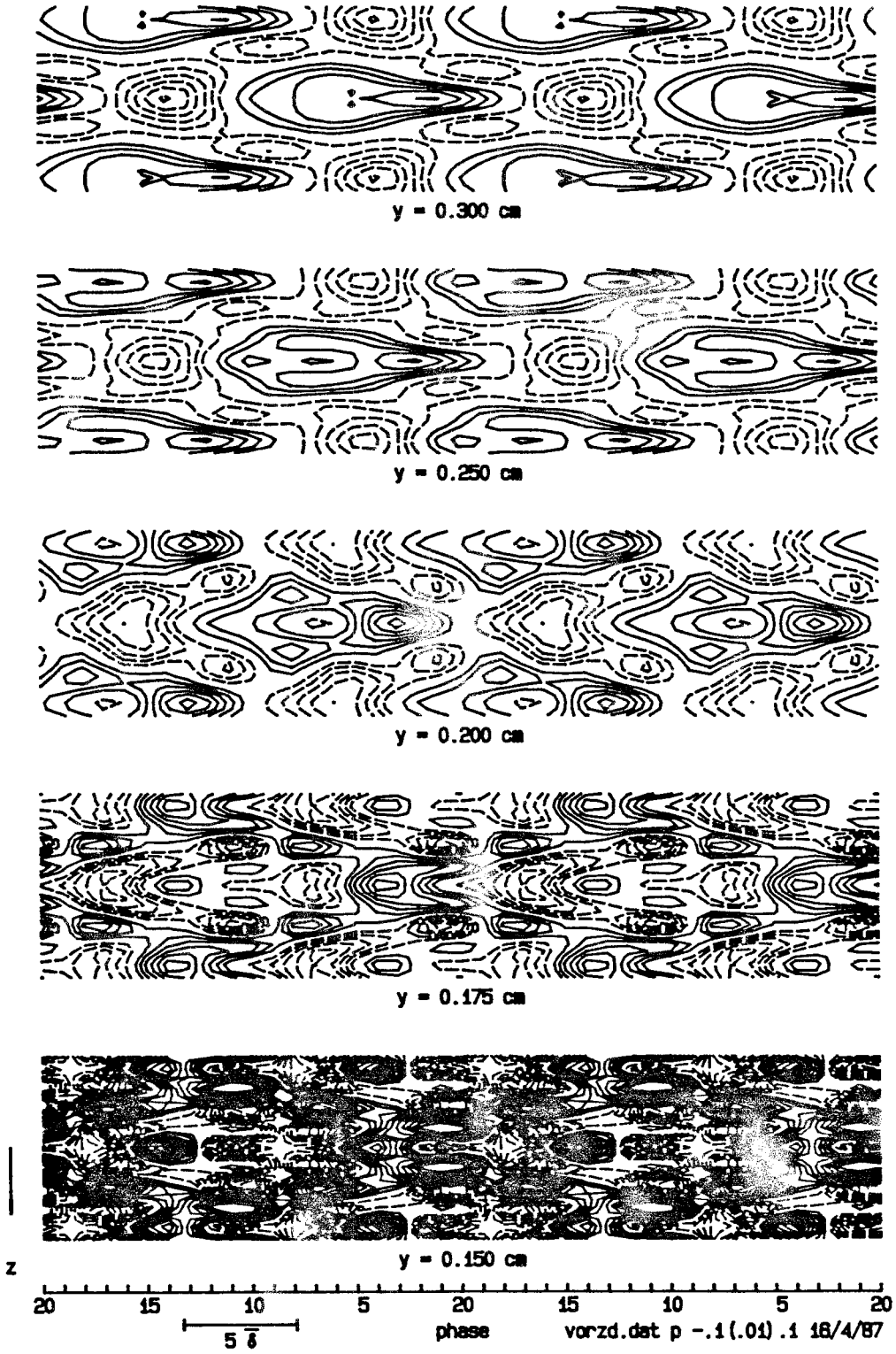

Figure 5.14. Spanwise vorticity perturbation $<\omega_z> - \overline{\omega_z}$ in the $t-z$ plane. Contour interval 0.01.

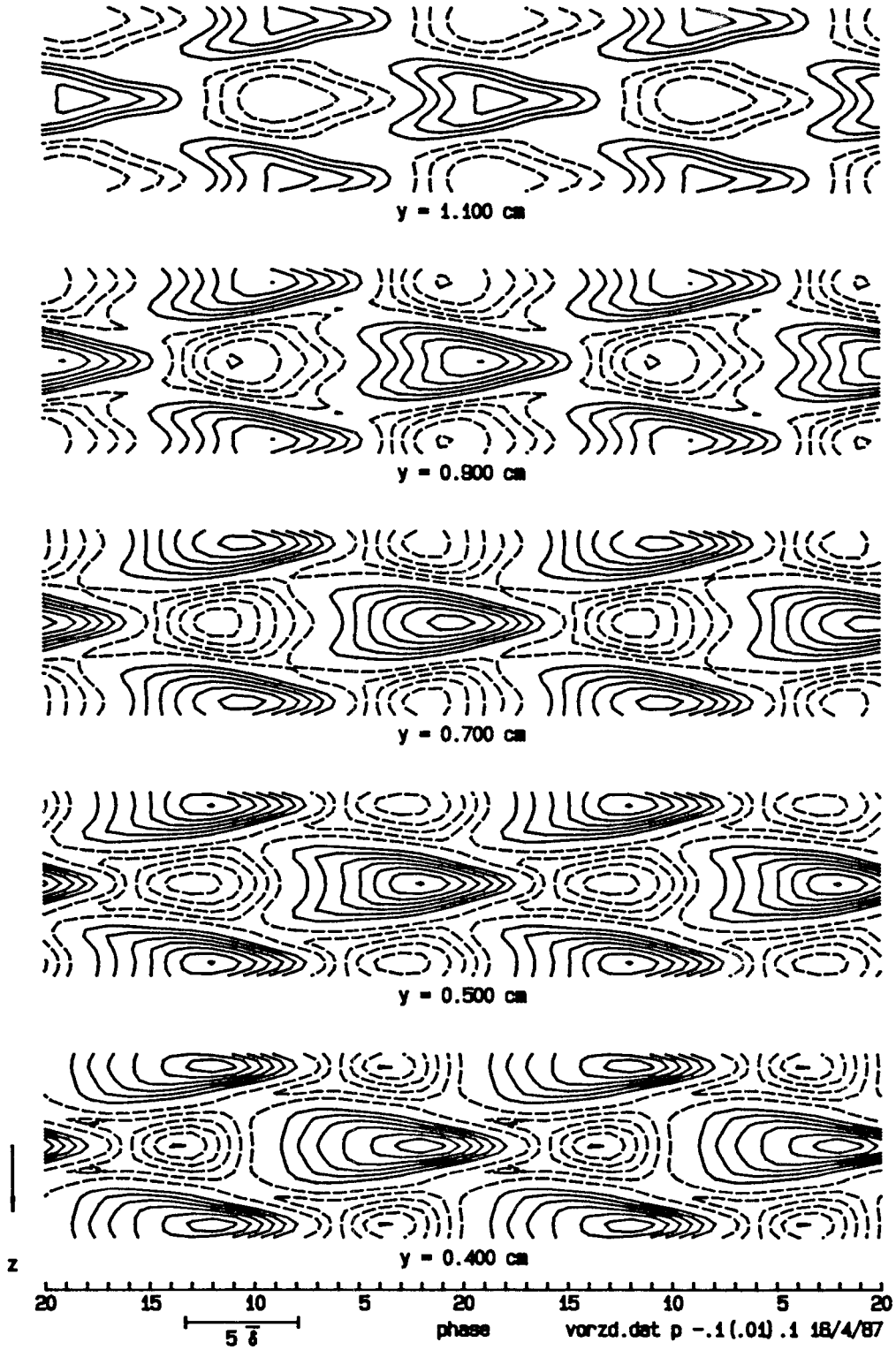

Figure 5.14 (cont'd.). Spanwise vorticity perturbation $<\omega_z> - \overline{\omega_z}$ in the $t-z$ plane.

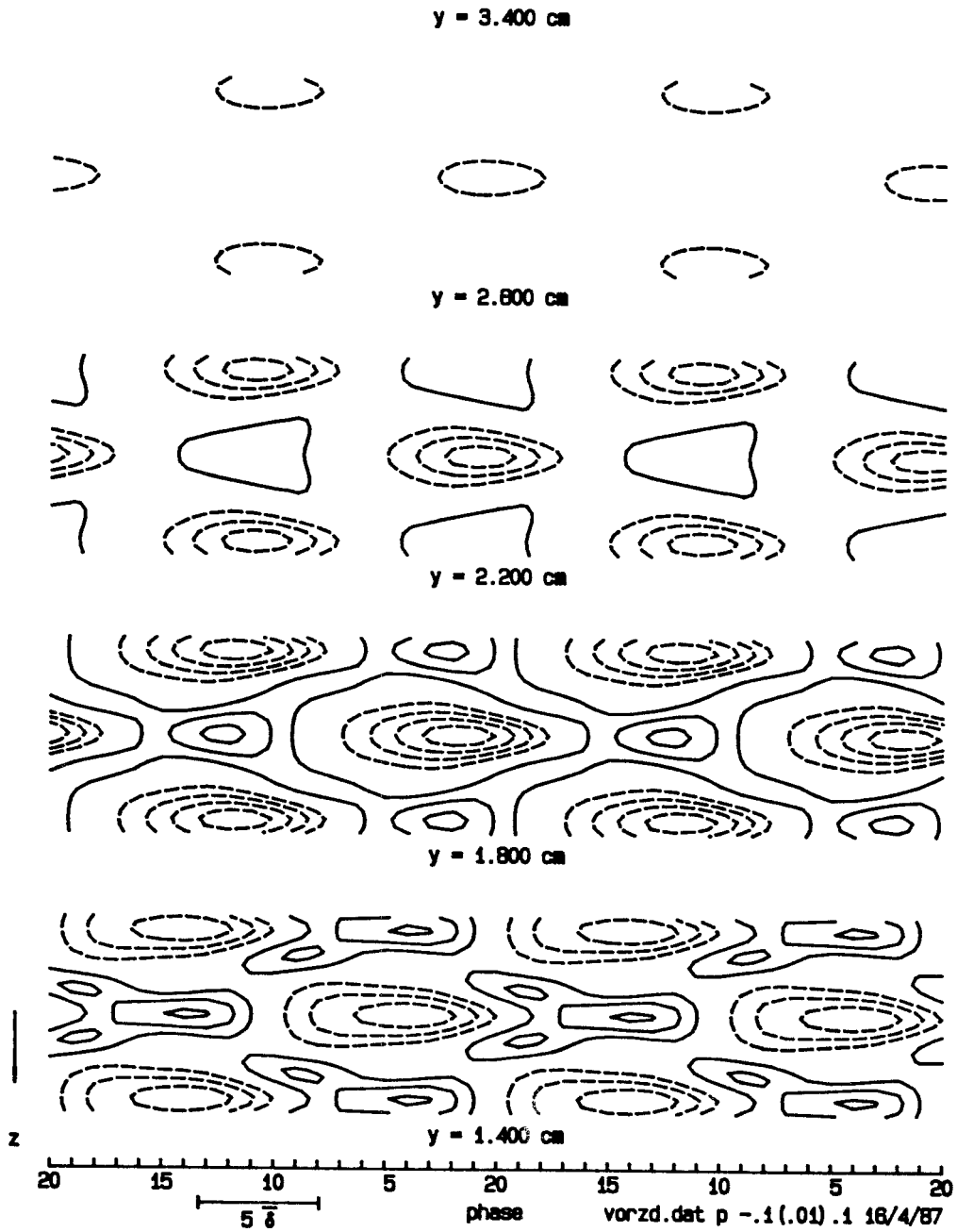

Figure 5.14 (cont'd.). Spanwise vorticity perturbation $<\omega_z> - \overline{\omega_z}$ in the $t-z$ plane.

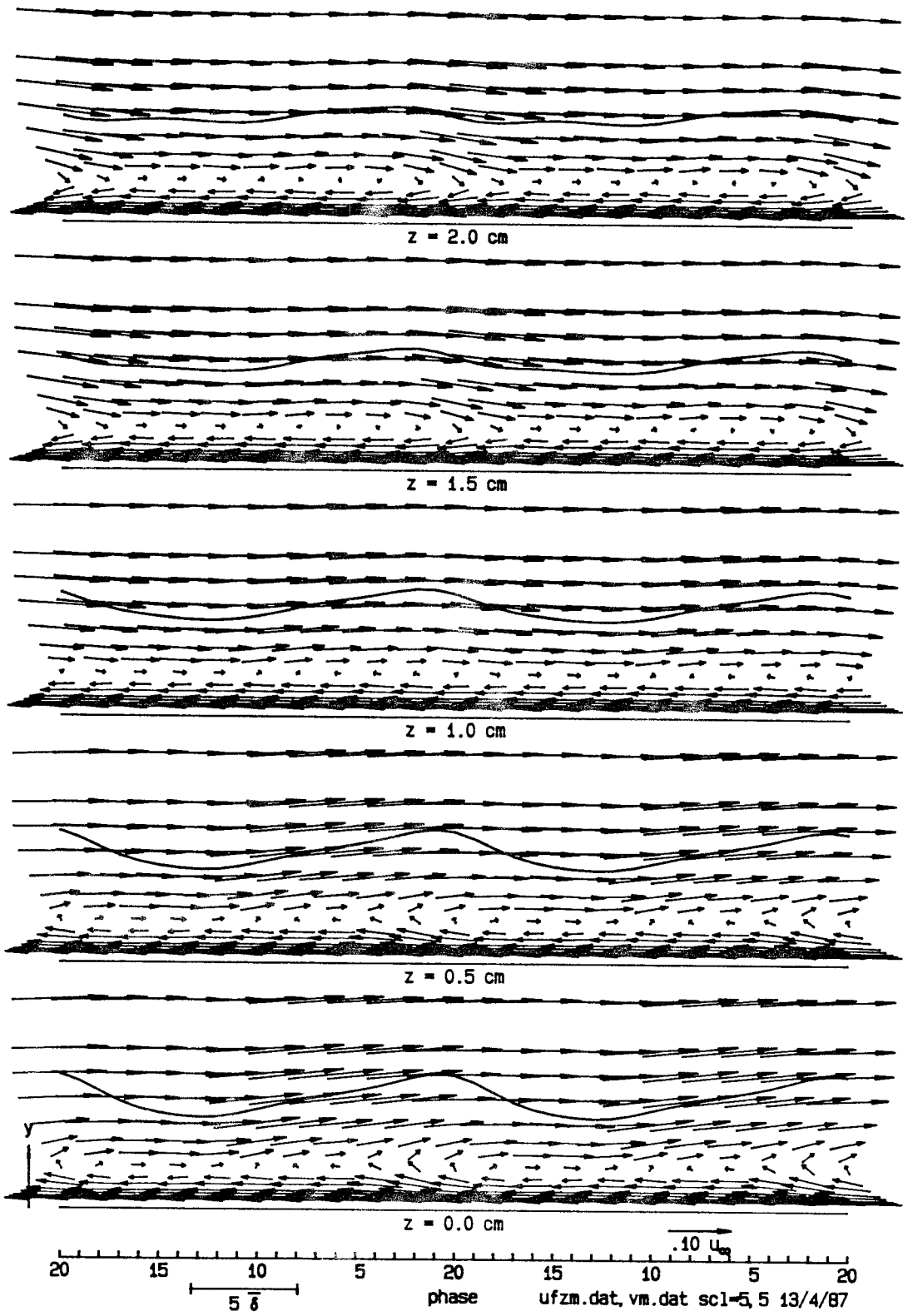

Figure 5.15. Velocity vectors $<u>$, $<v>$.

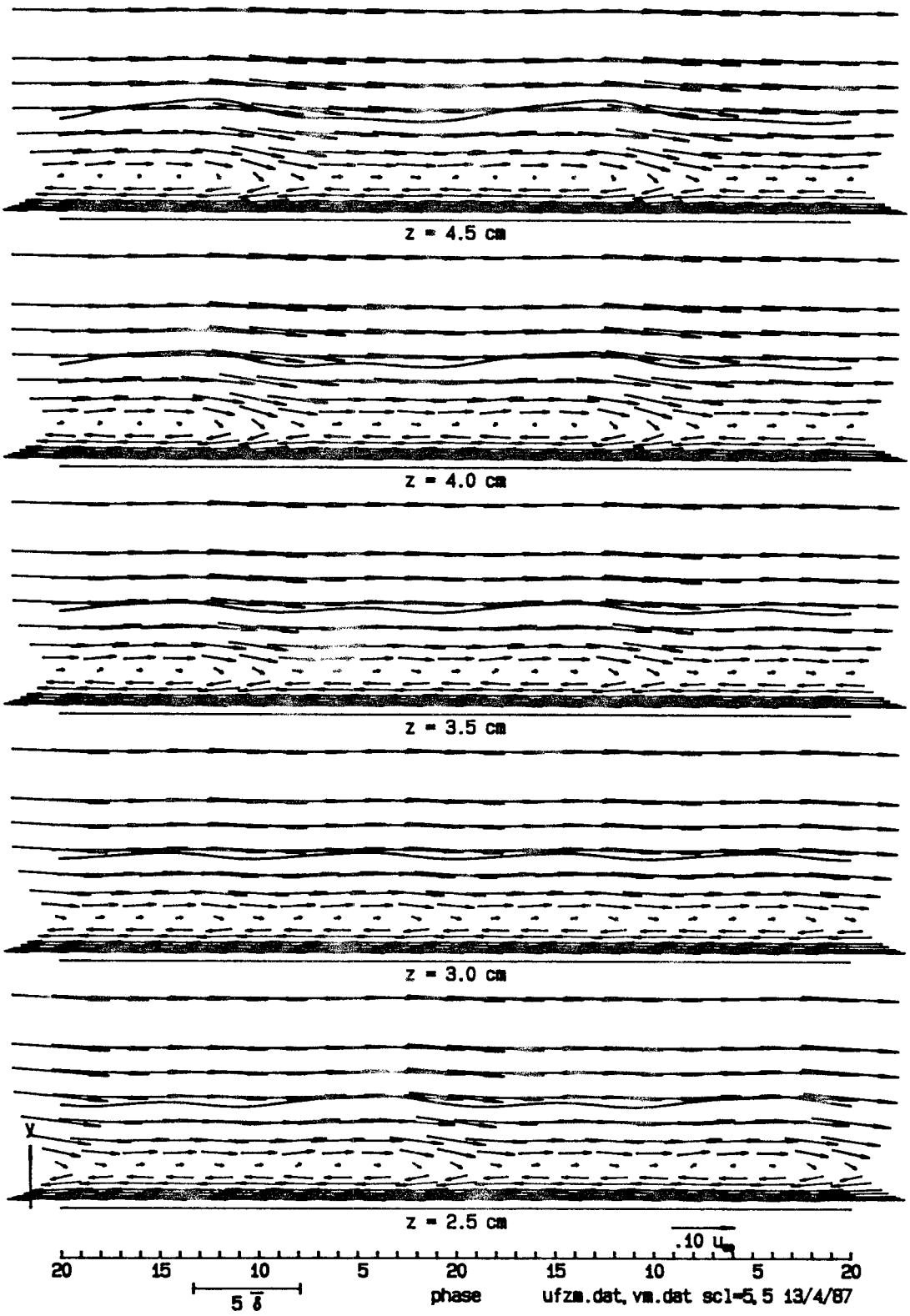

Figure 5.15 (cont'd.). Velocity vectors $\langle u \rangle$, $\langle v \rangle$.

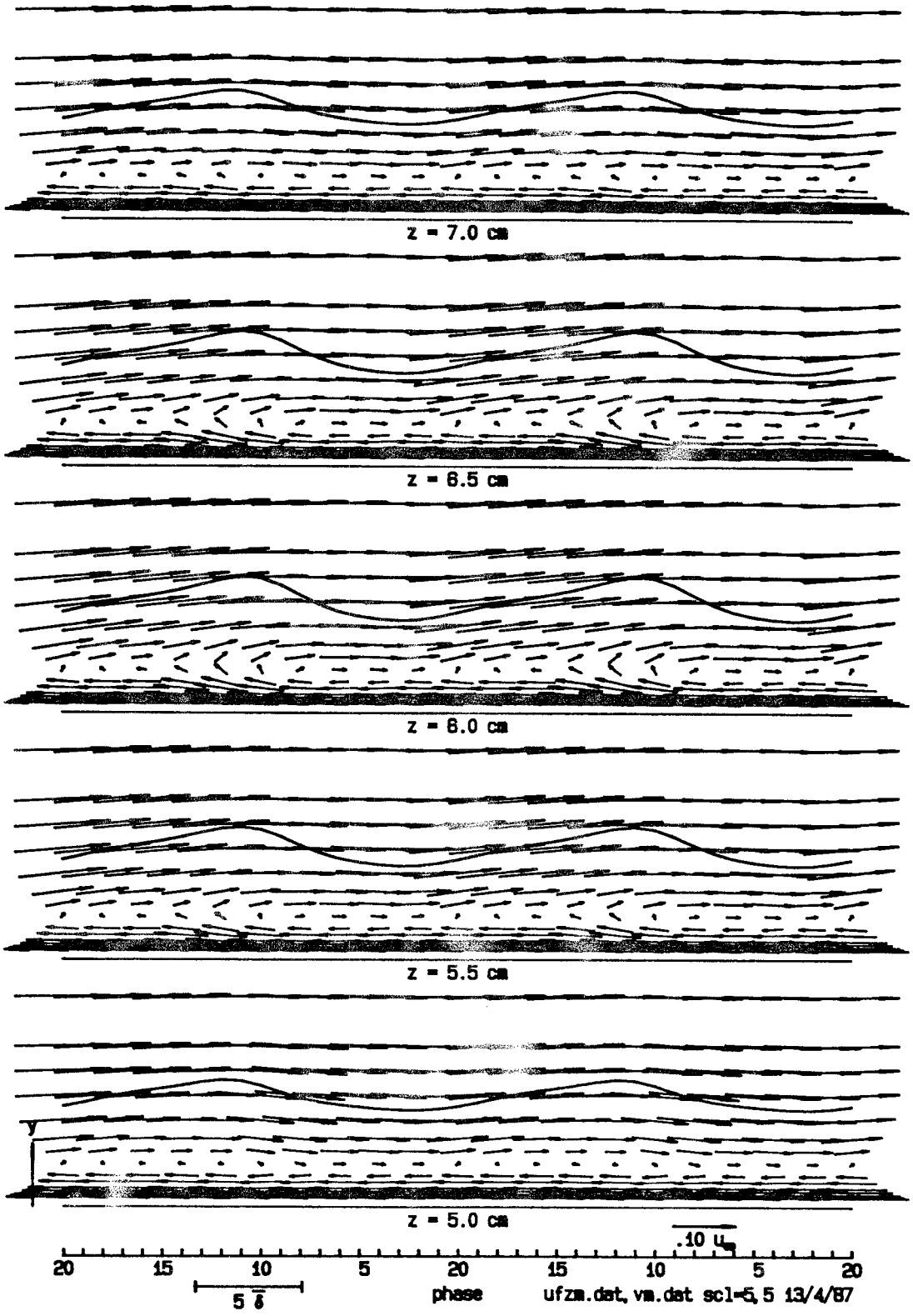

Figure 5.15 (cont'd.). Velocity vectors $\langle u \rangle$, $\langle v \rangle$.

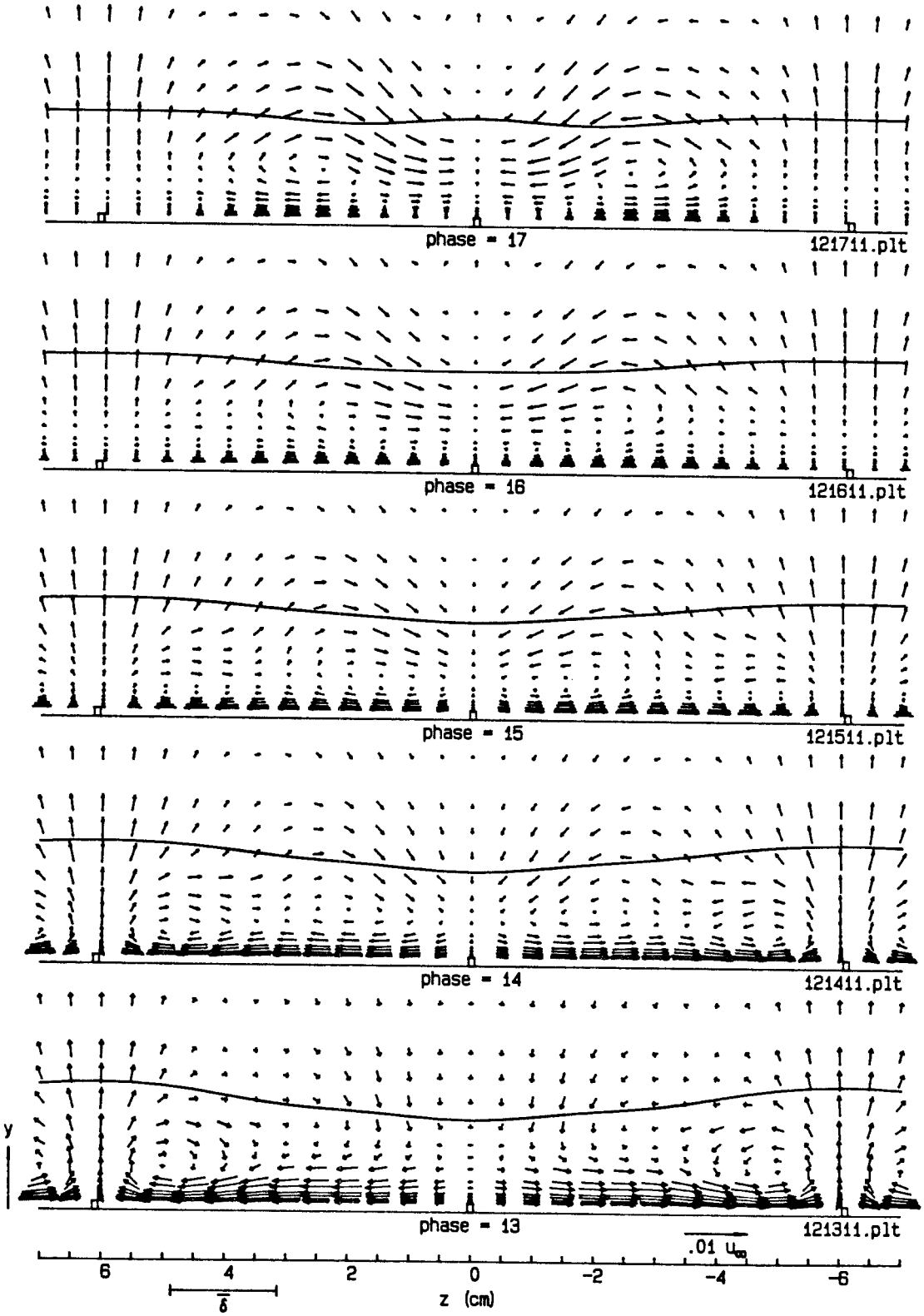

Figure 5.16. Velocity vectors $\langle w \rangle$, $\langle v \rangle$.

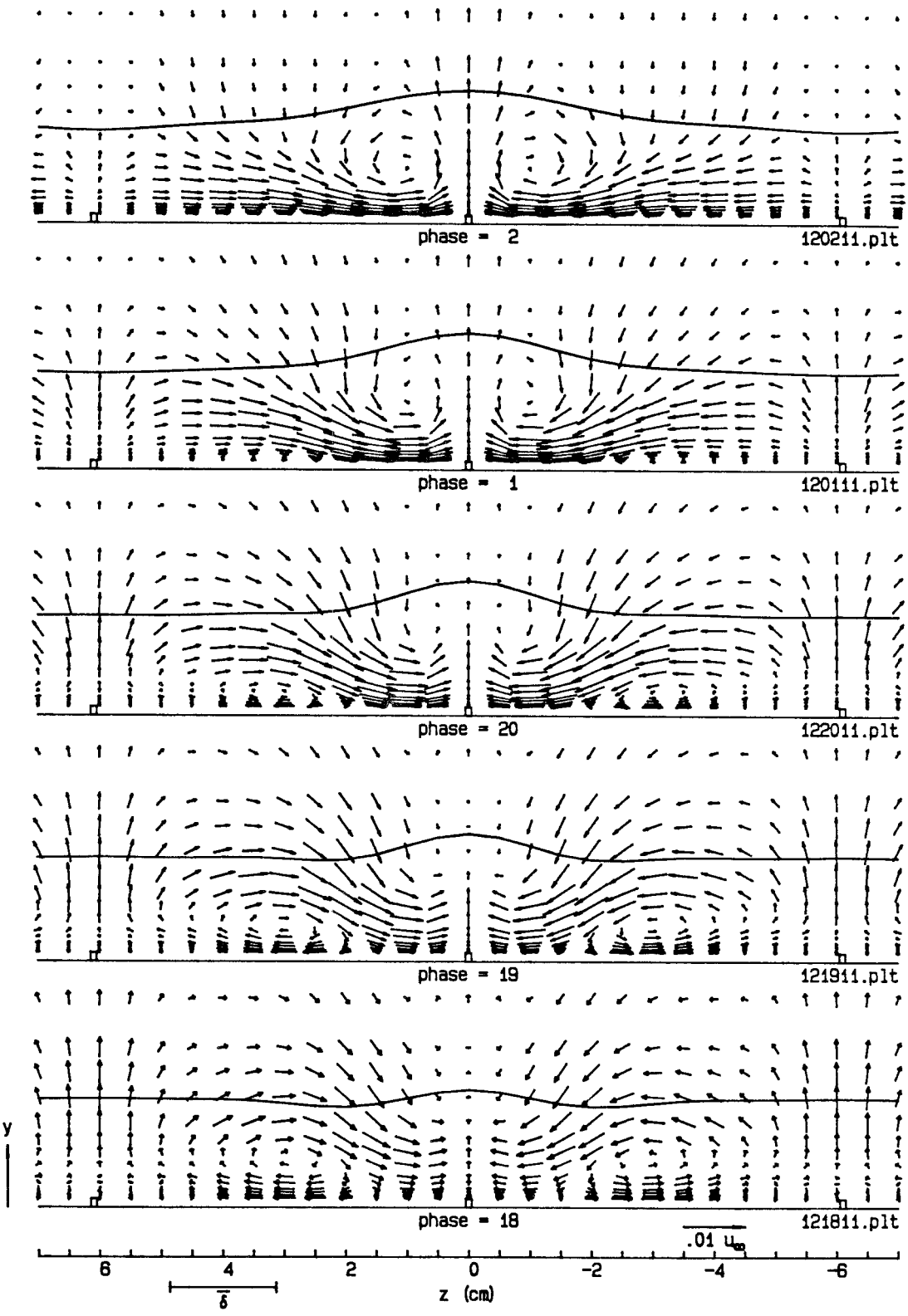

Figure 5.16 (cont'd.). Velocity vectors $\langle w \rangle$, $\langle v \rangle$.

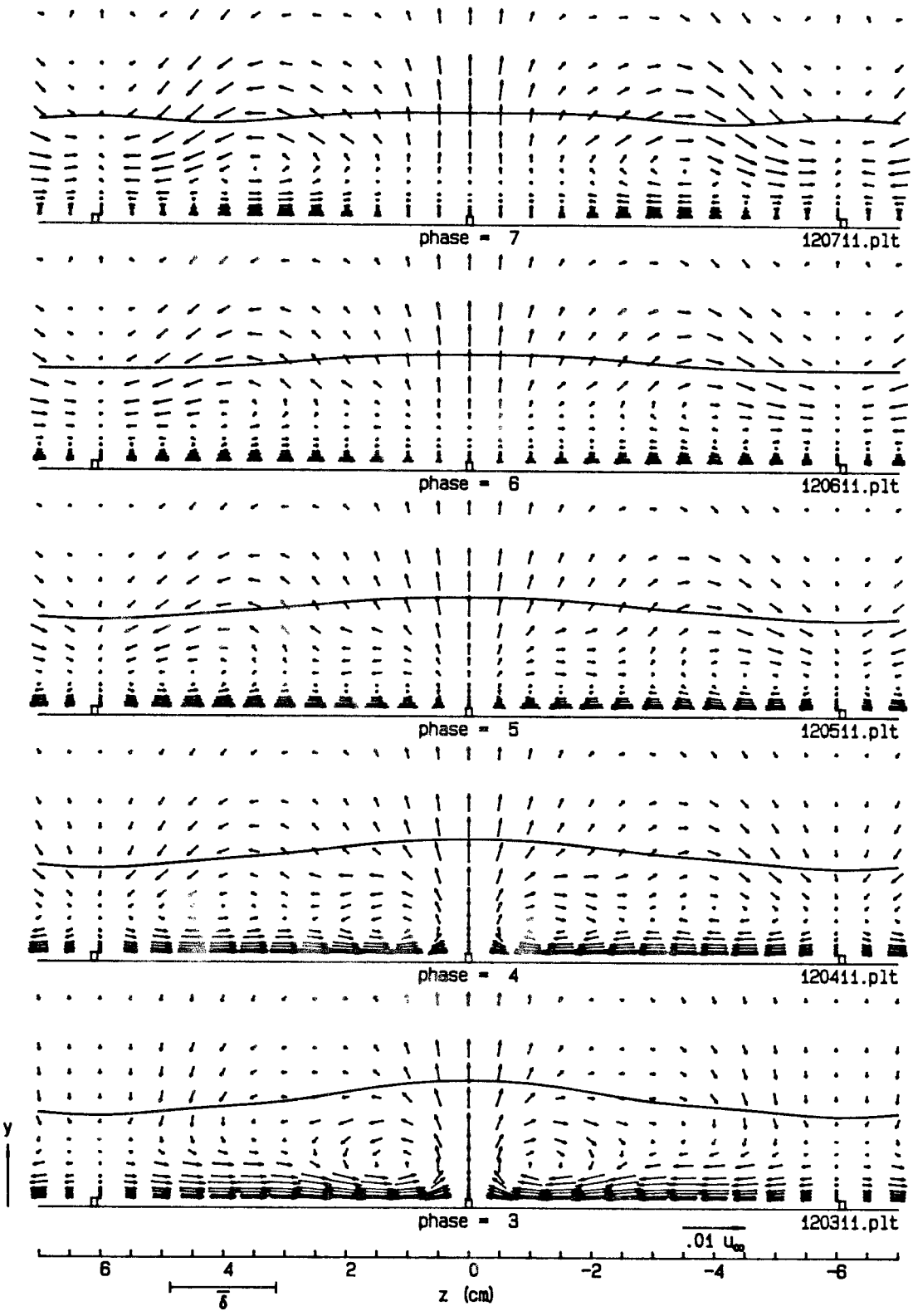

Figure 5.16 (cont'd.). Velocity vectors $\langle w \rangle$, $\langle v \rangle$.

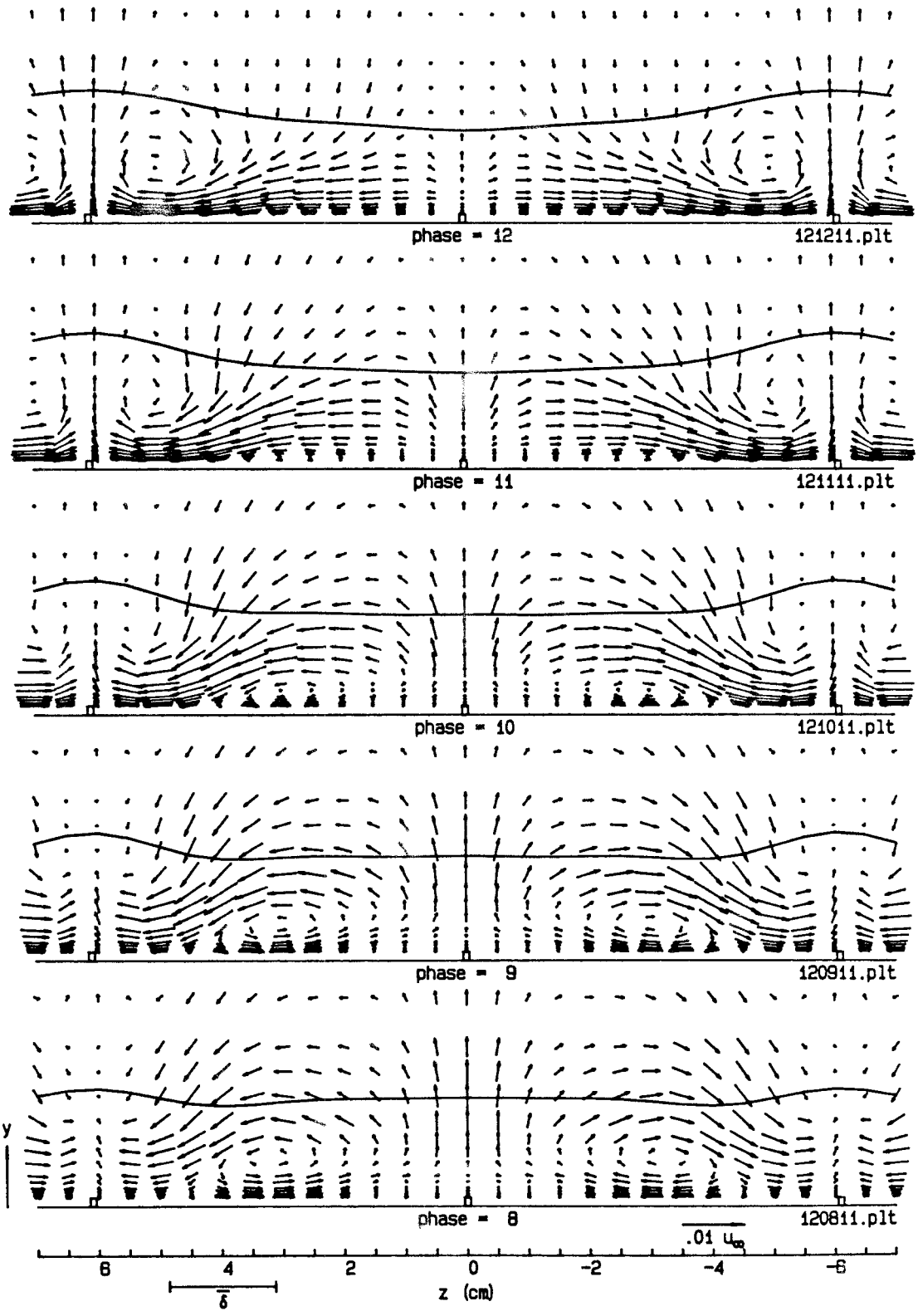

Figure 5.16 (cont'd.). Velocity vectors $\langle w \rangle$, $\langle v \rangle$.

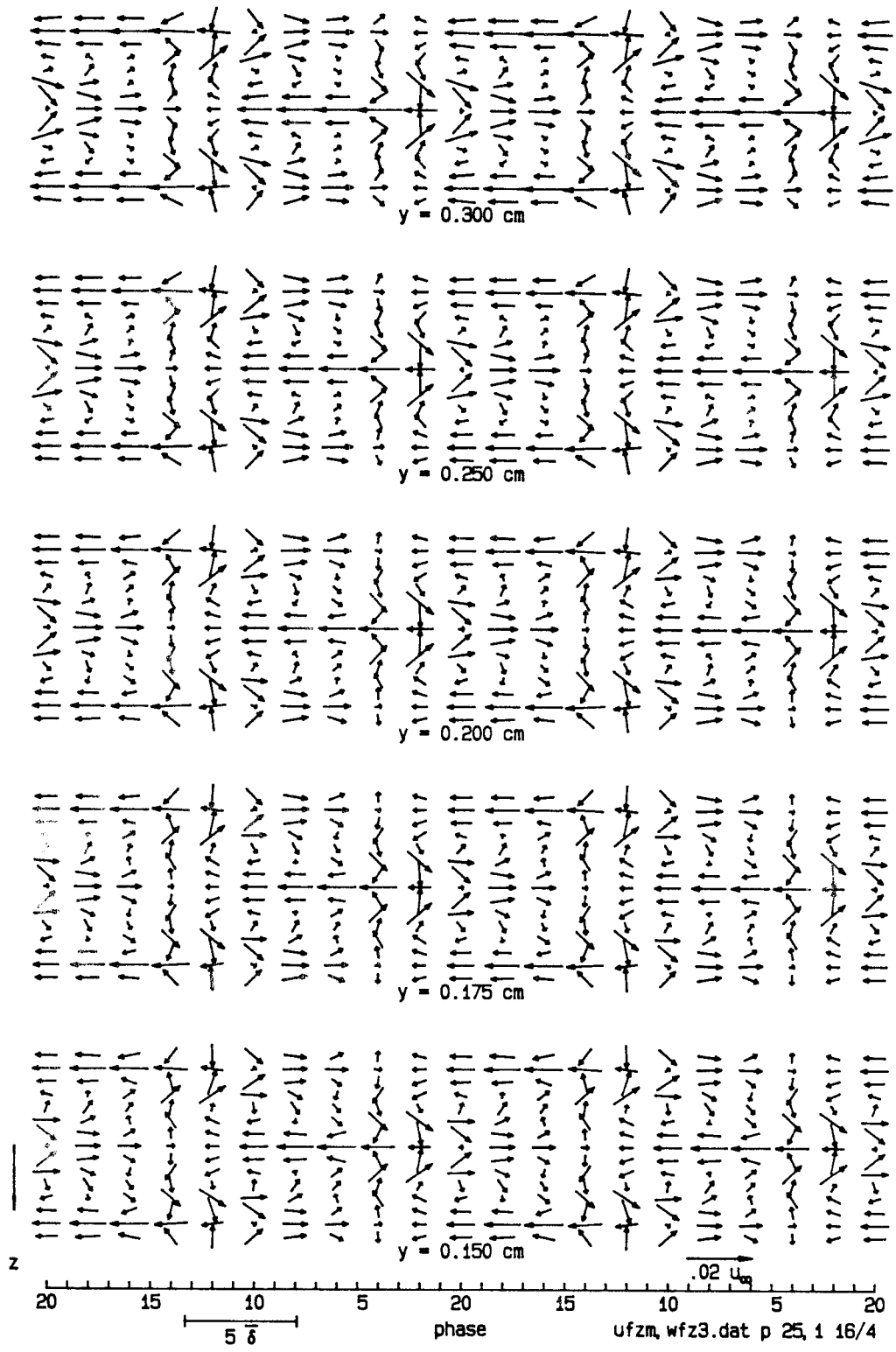

Figure 5.17. Velocity vectors $(\langle u \rangle - \bar{u})$, $\langle w \rangle$.

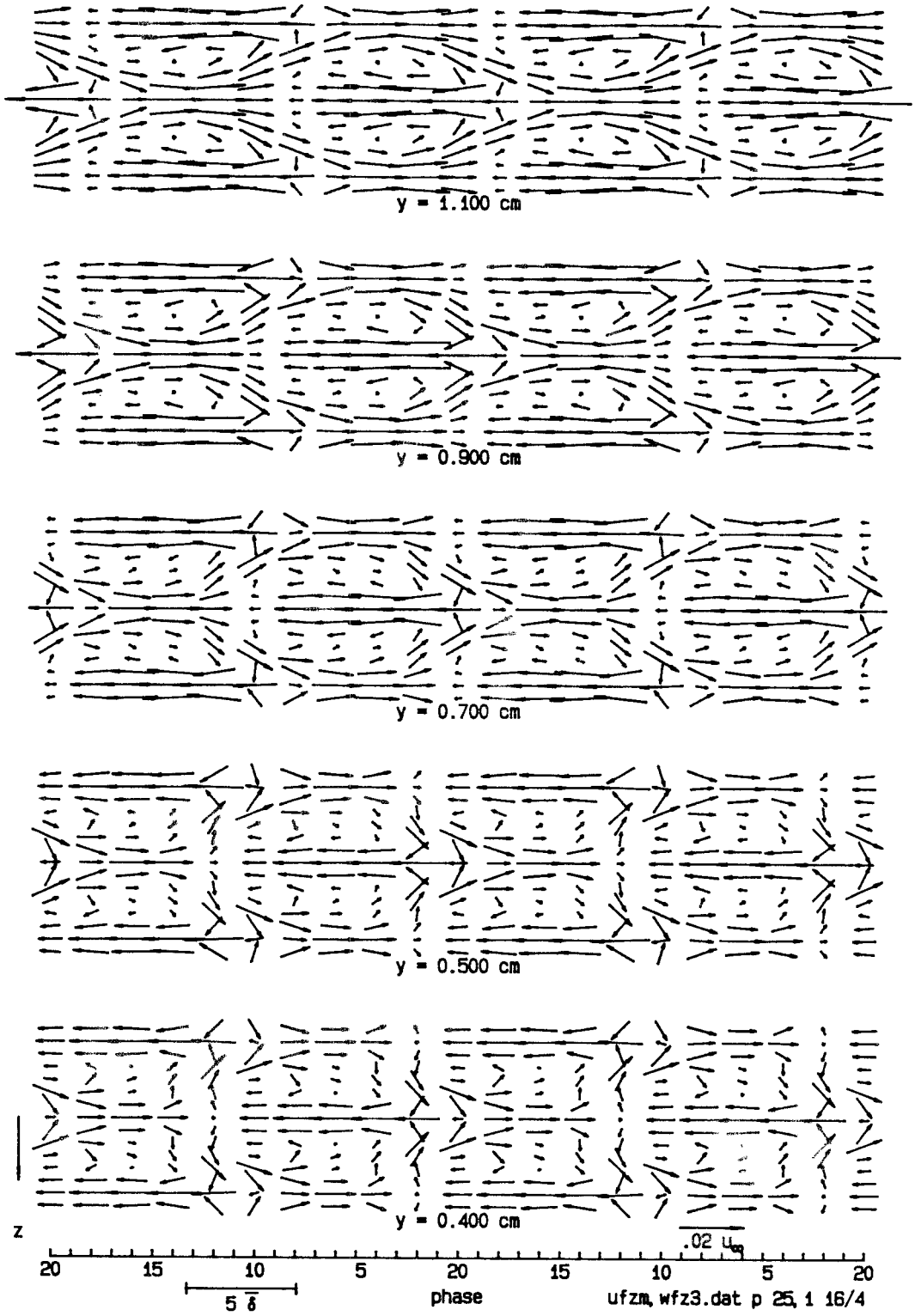

Figure 5.17 (cont'd.). Velocity vectors $(<u> - \overline{u})$, $<w>$.

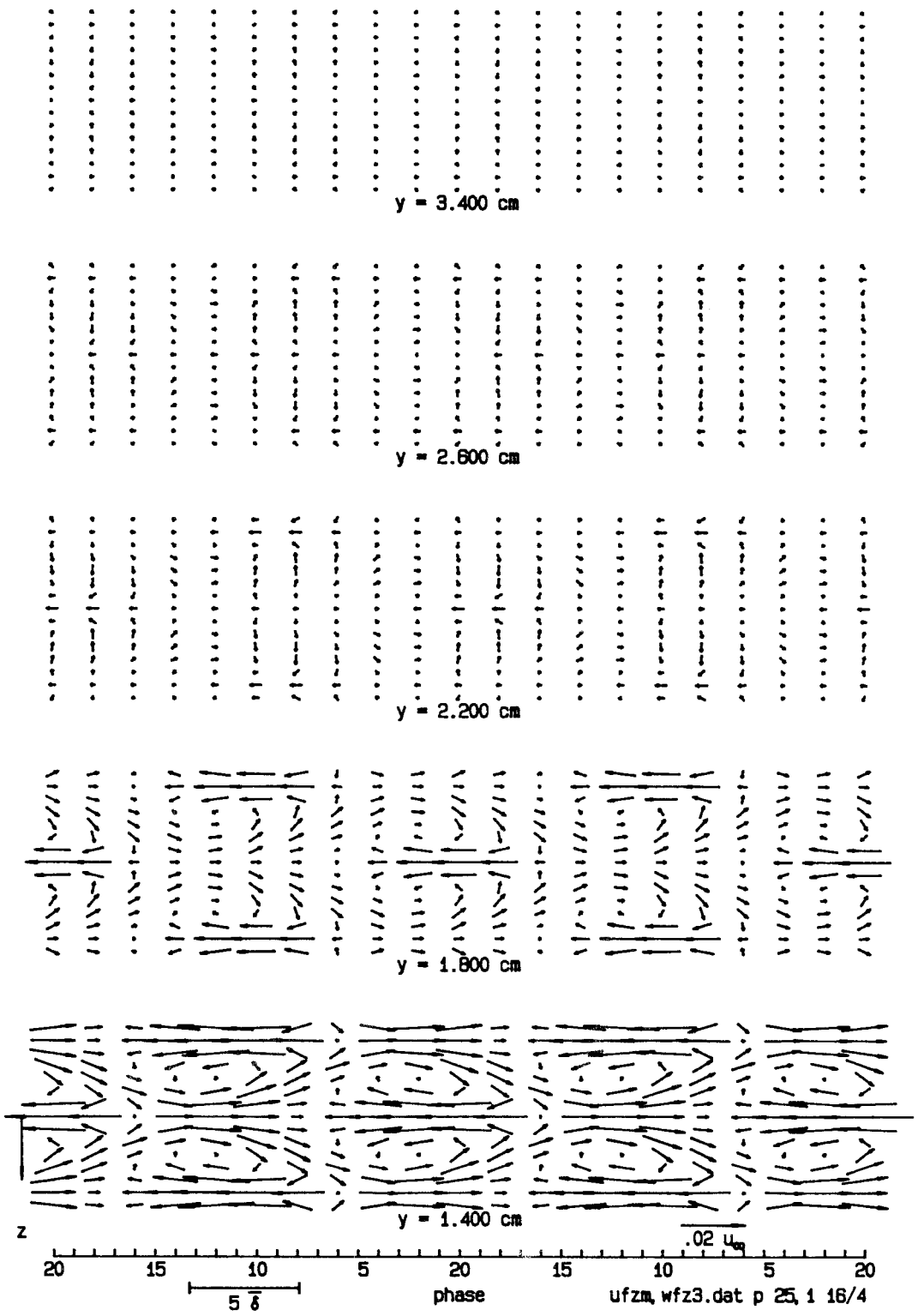

Figure 5.17 (cont'd.). Velocity vectors $(\langle u \rangle - \bar{u})$, $\langle w \rangle$.

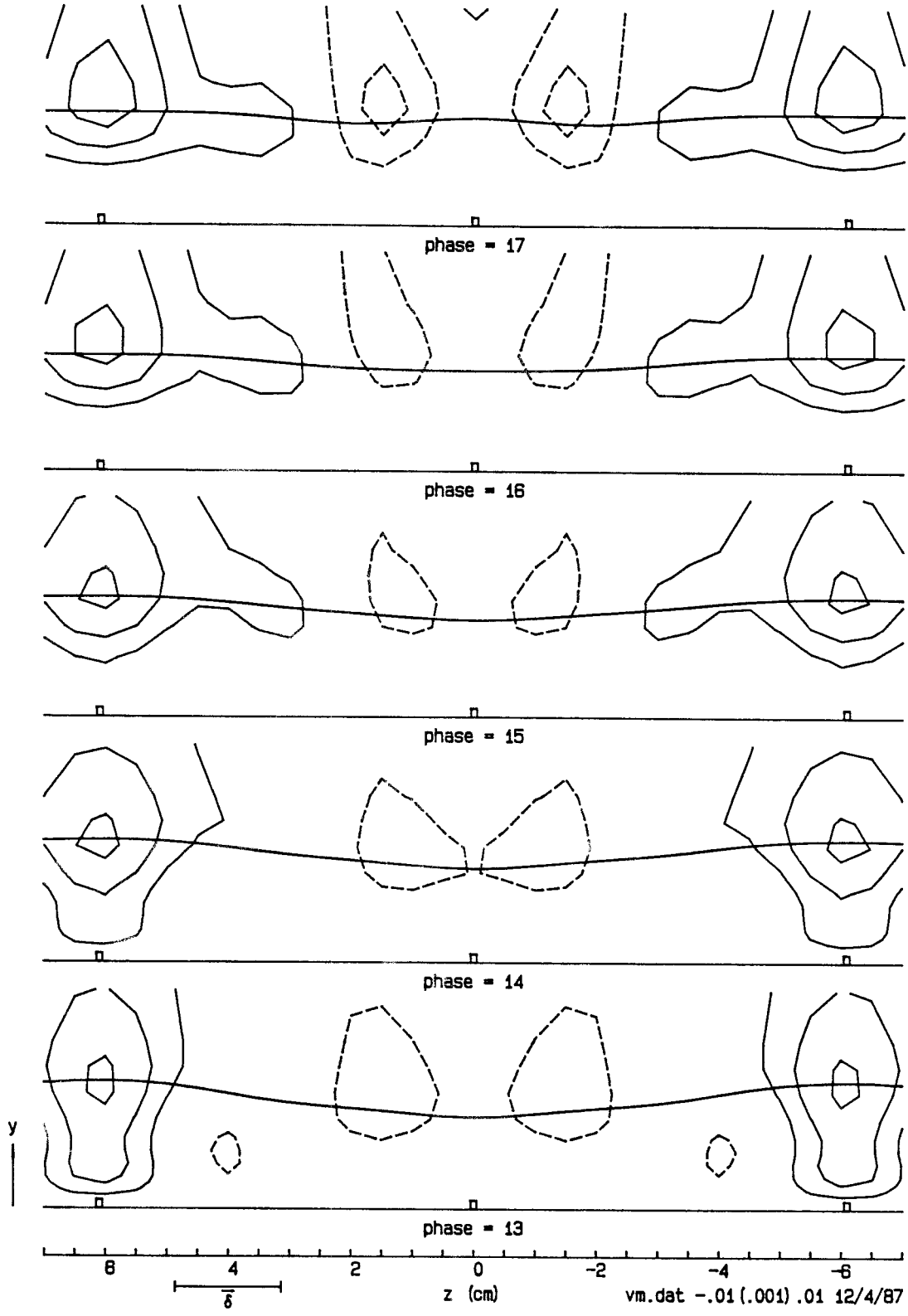

Figure 5.18. Normal velocity $<v>$ in the $z-y$ plane. Contour interval 0.001.

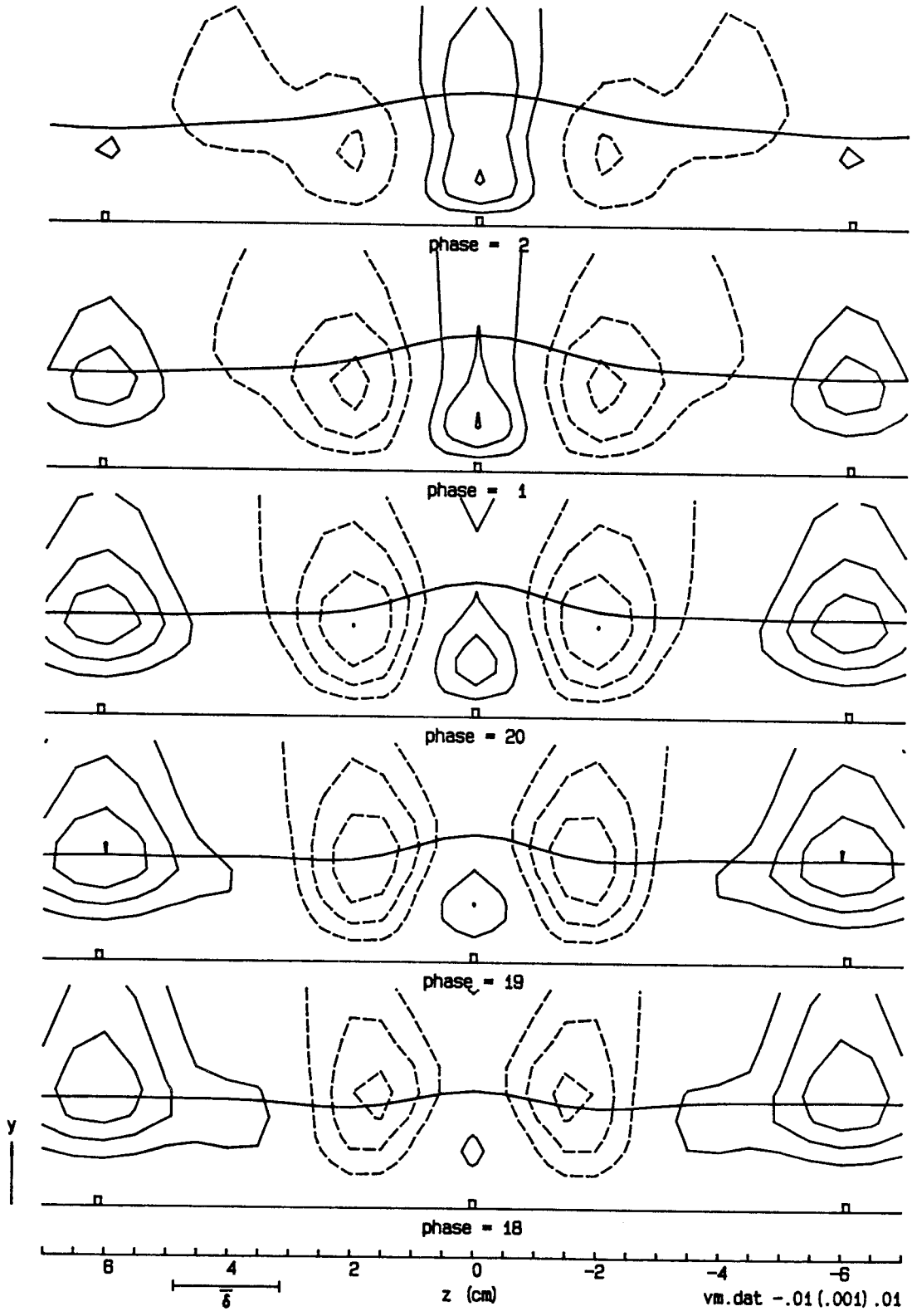

Figure 5.18 (cont'd.). Normal velocity $<v>$ in the $z-y$ plane.

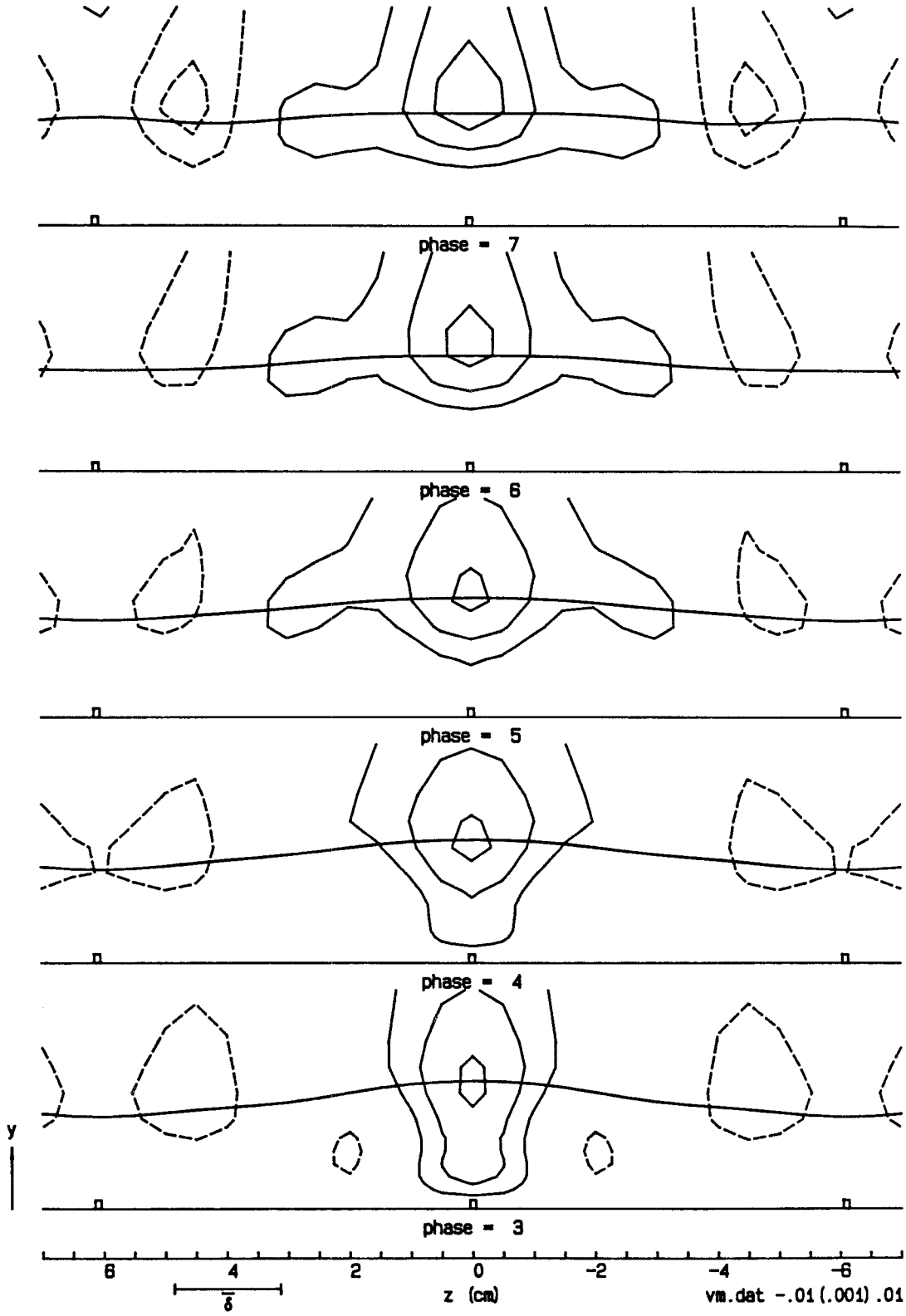

Figure 5.18 (cont'd.). Normal velocity $<v>$ in the $z-y$ plane.

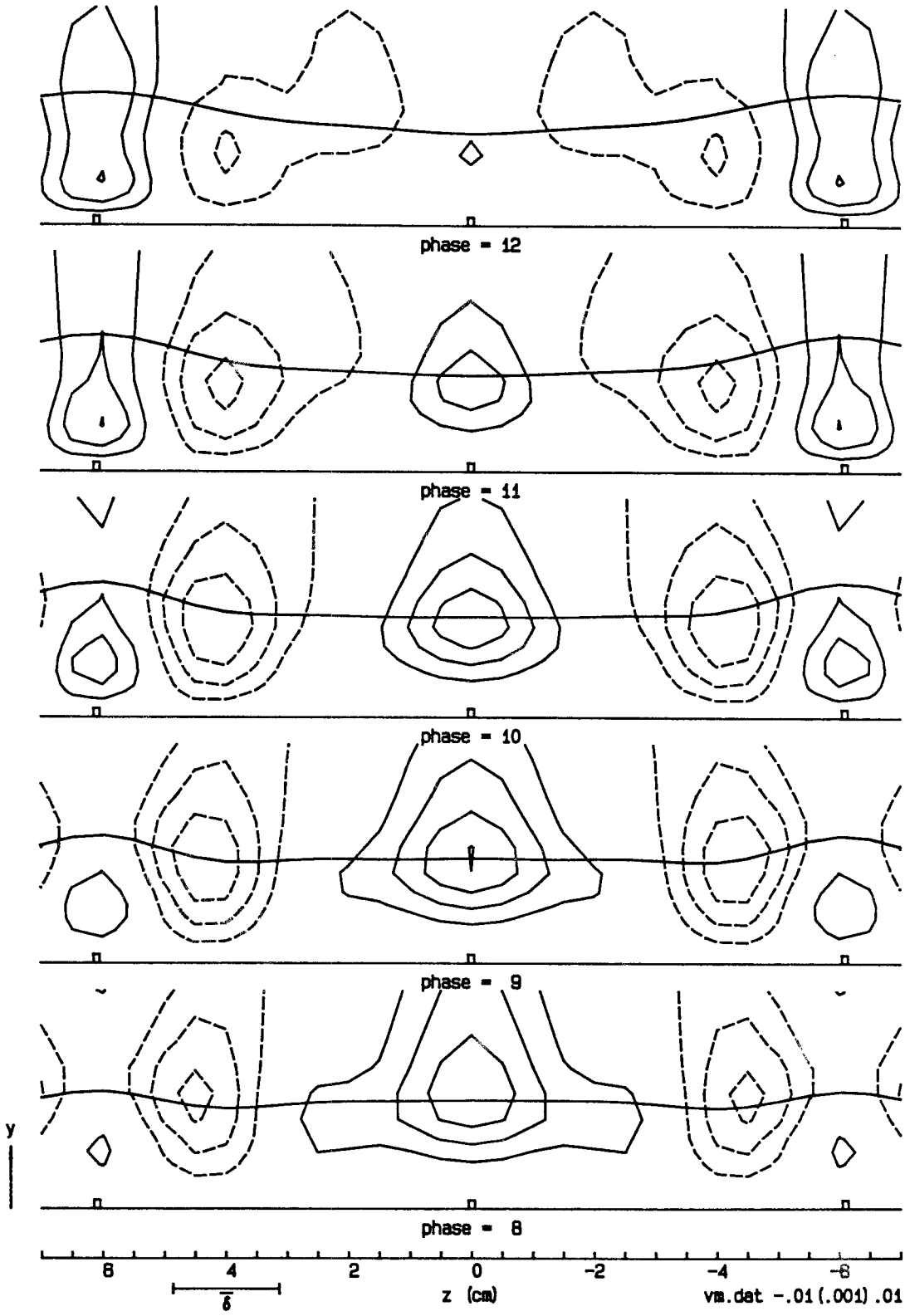

Figure 5.18 (cont'd.). Normal velocity $<v>$ in the $z-y$ plane.

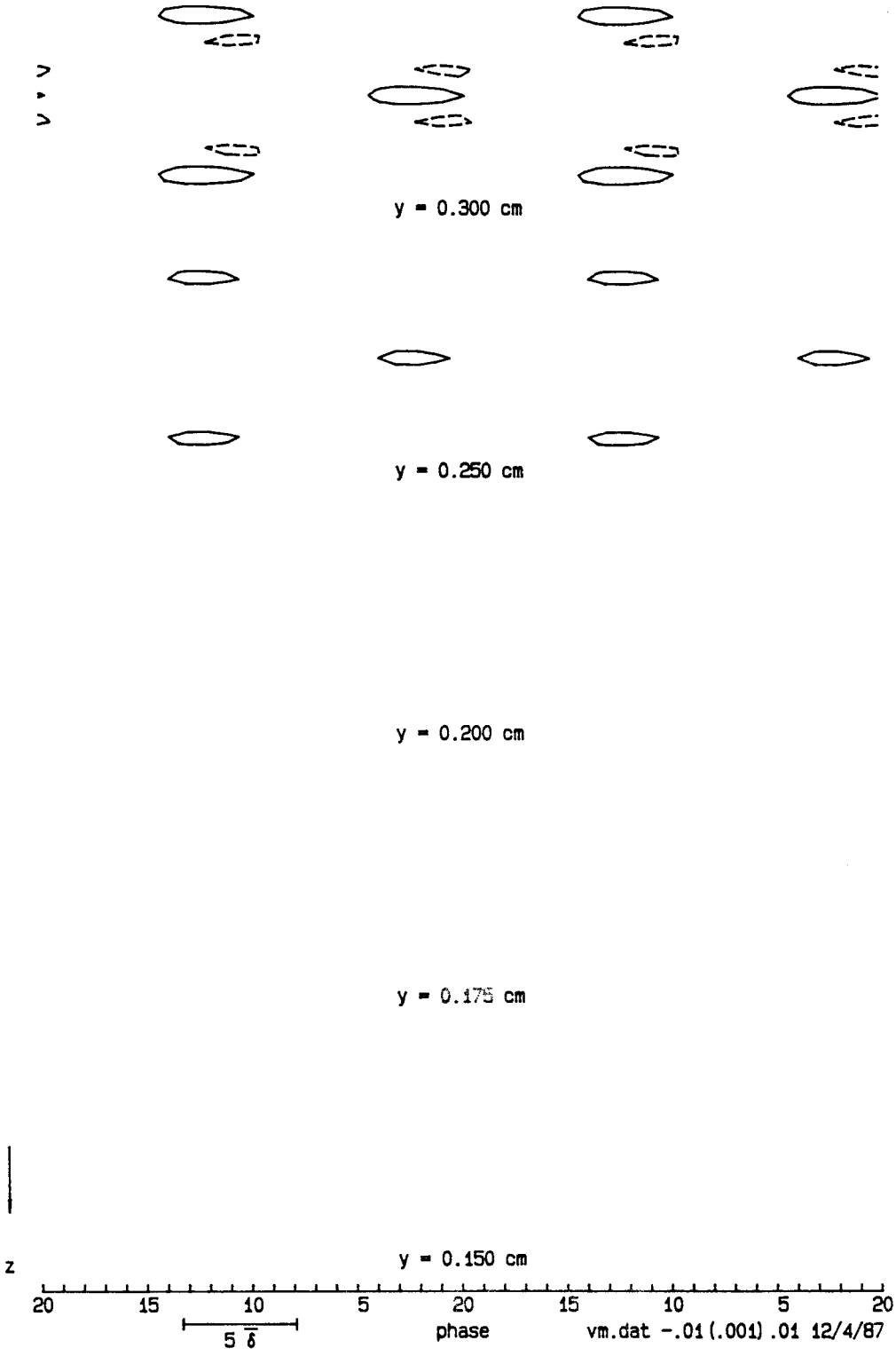

Figure 5.19. Normal velocity $<v>$ in the $t-z$ plane. Contour interval 0.001.

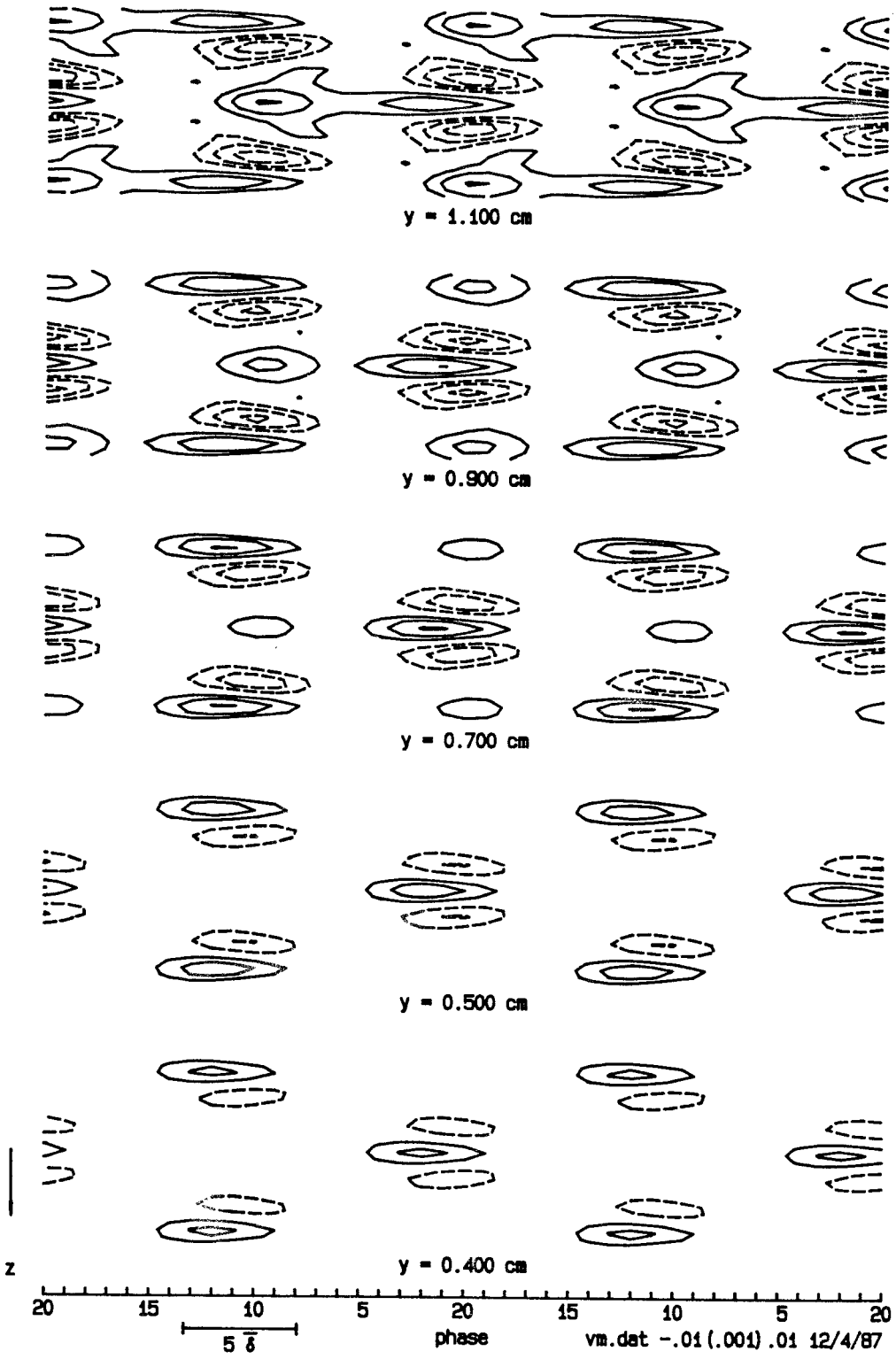

Figure 5.19 (cont'd.). Normal velocity $\langle v \rangle$ in the $t-z$ plane.

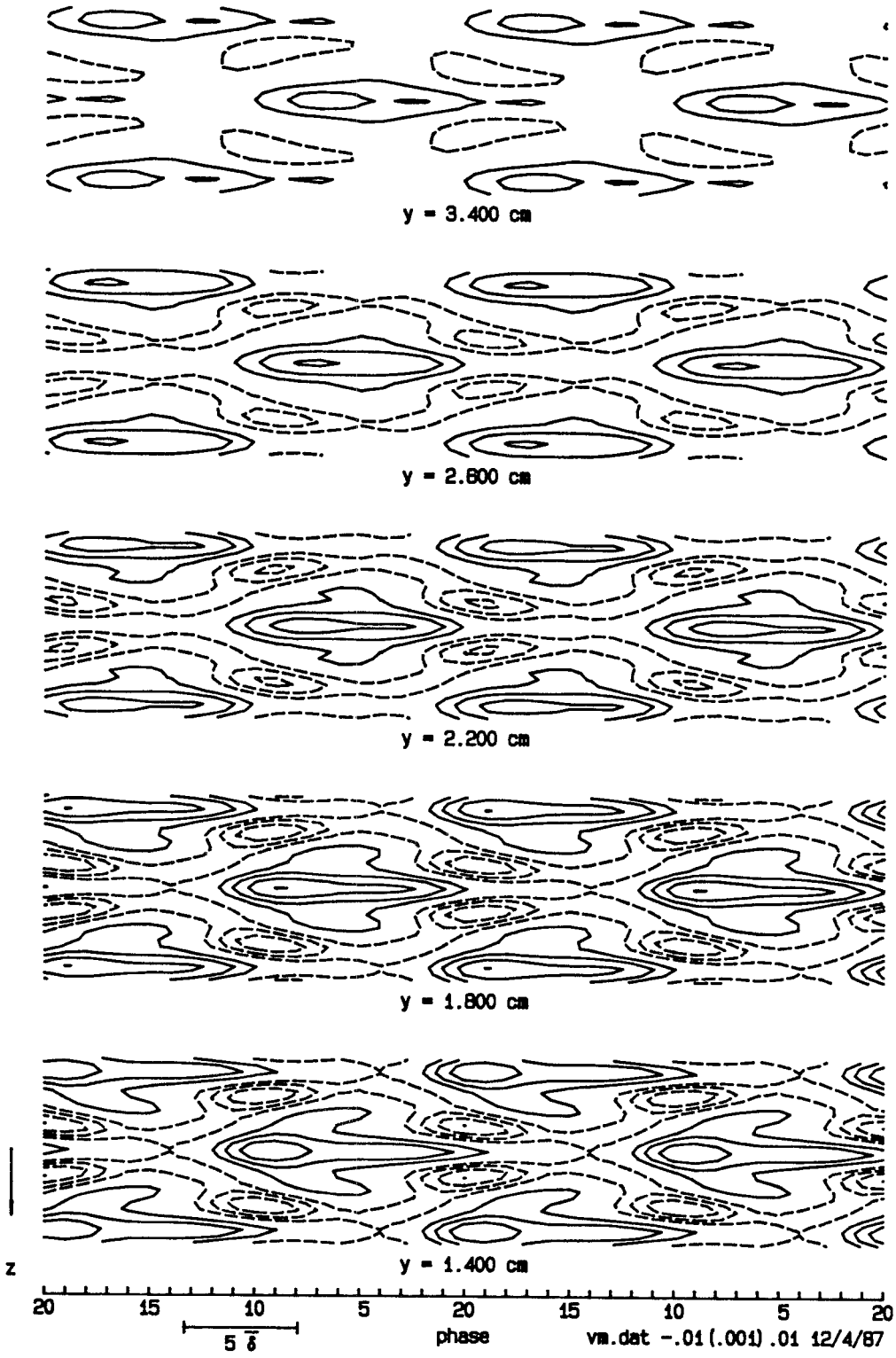

Figure 5.19 (cont'd.). Normal velocity $<v>$ in the $t-z$ plane.

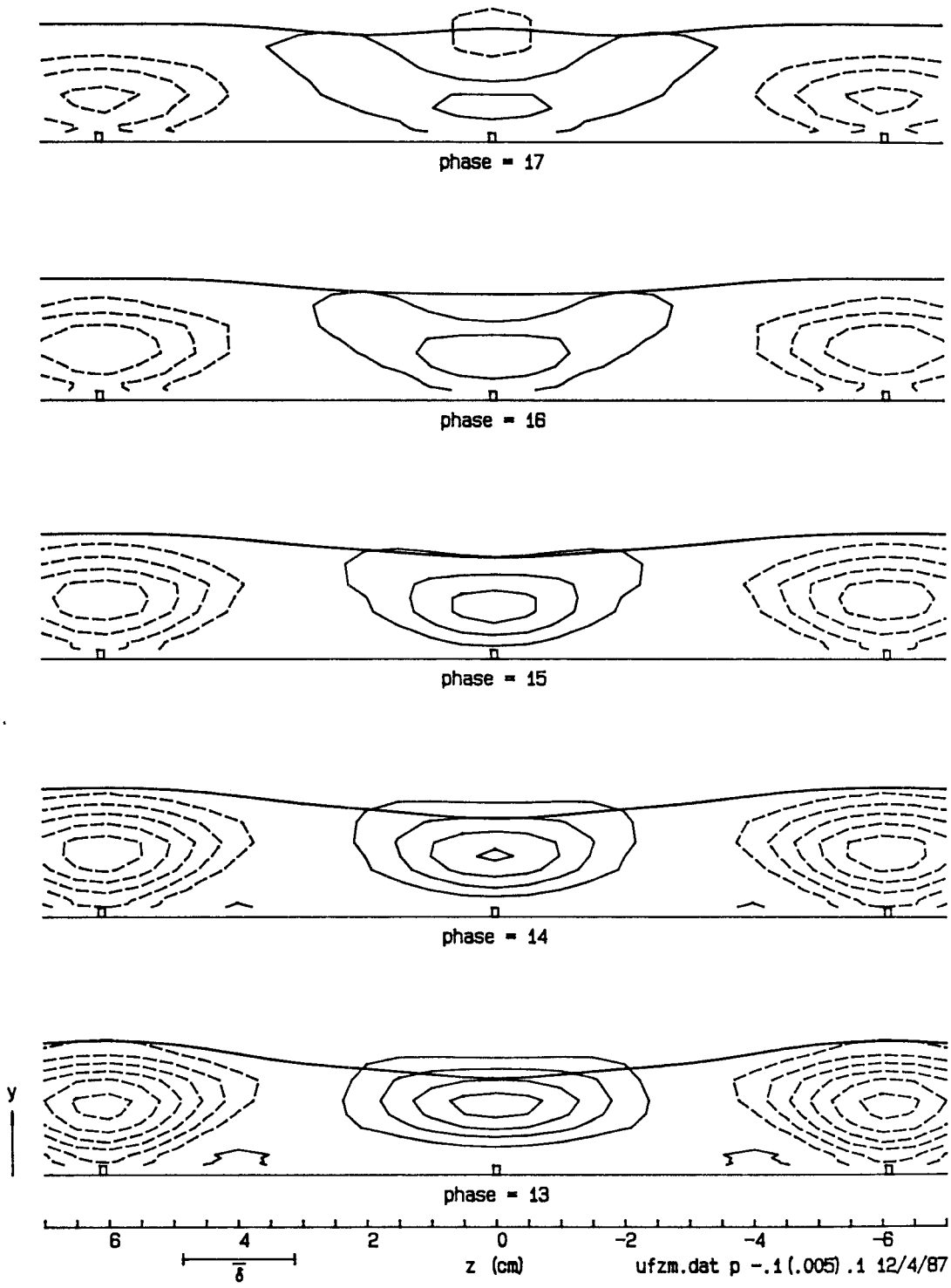

Figure 5.20. Streamwise perturbation velocity $<u> - \bar{u}$ in the $z-y$ plane. Contour interval 0.005.

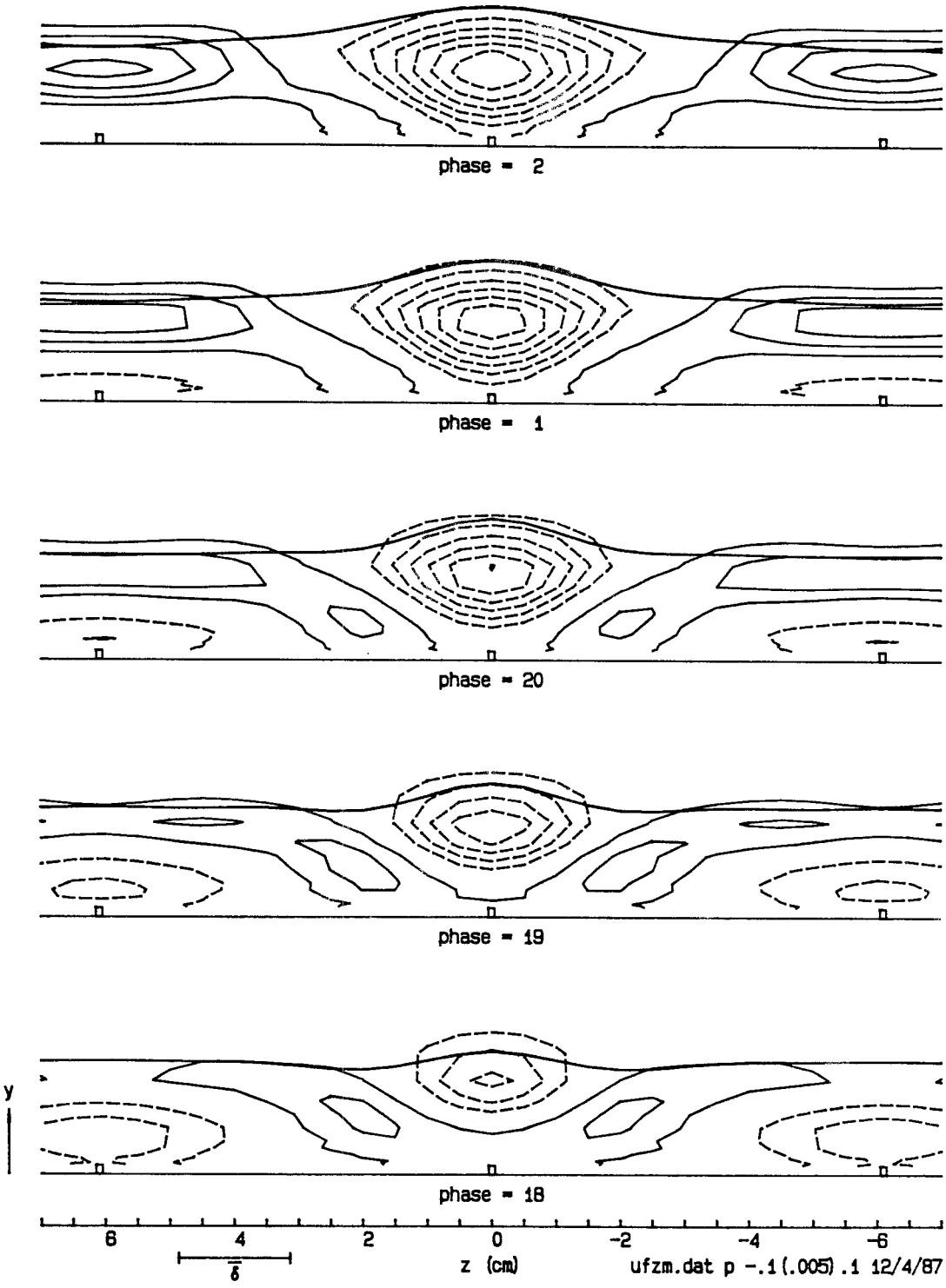

Figure 5.20 (cont'd.). Streamwise perturbation velocity $<u> - \bar{u}$ in the $z-y$ plane.

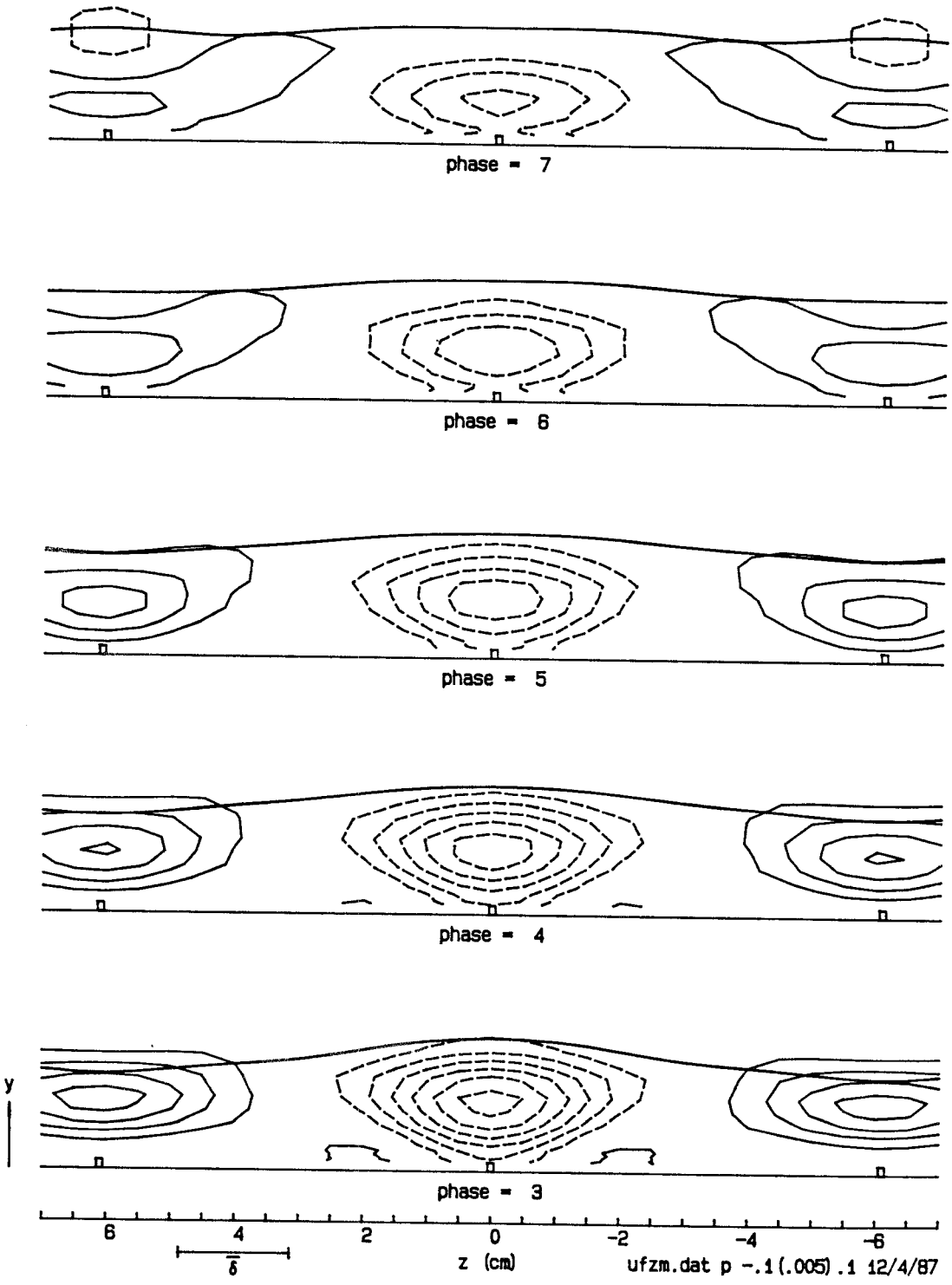

Figure 5.20 (cont'd.). Streamwise perturbation velocity $<u> - \bar{u}$ in the $z-y$ plane.

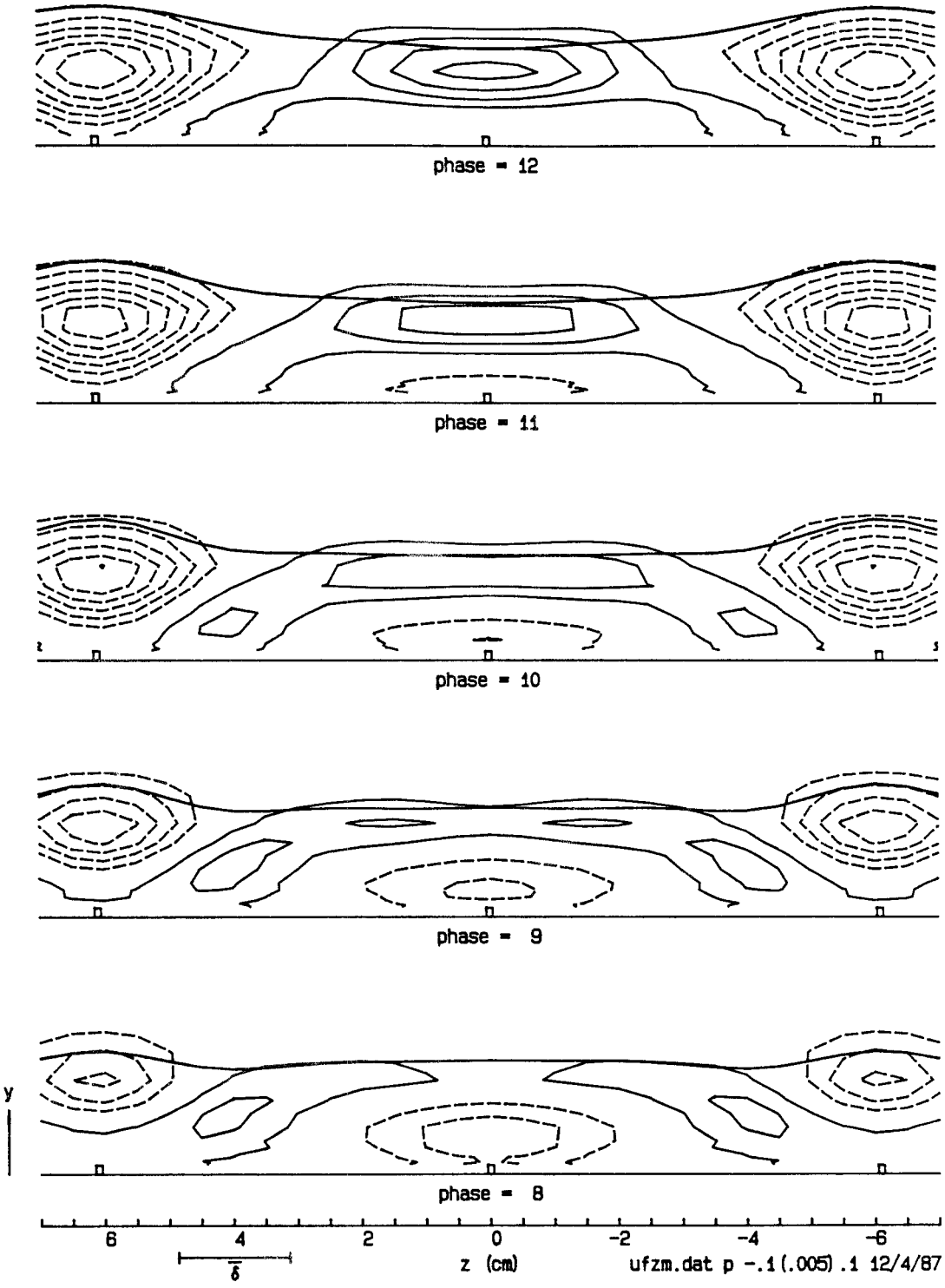

Figure 5.20 (cont'd.). Streamwise perturbation velocity $<u> - \bar{u}$ in the $z-y$ plane.

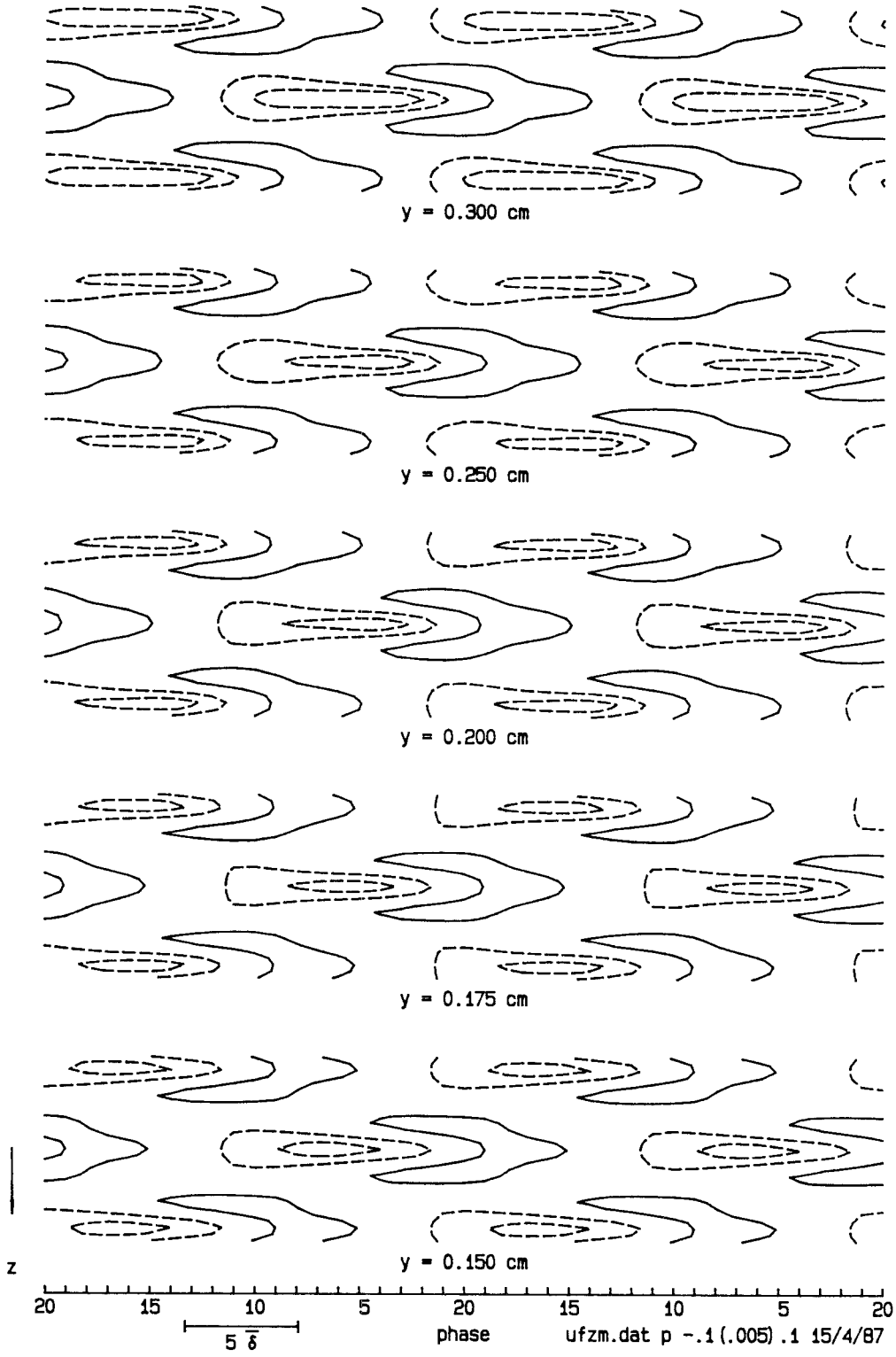

Figure 5.21. Streamwise perturbation velocity $<u> - \bar{u}$ in the $t-z$ plane. Contour interval 0.005.

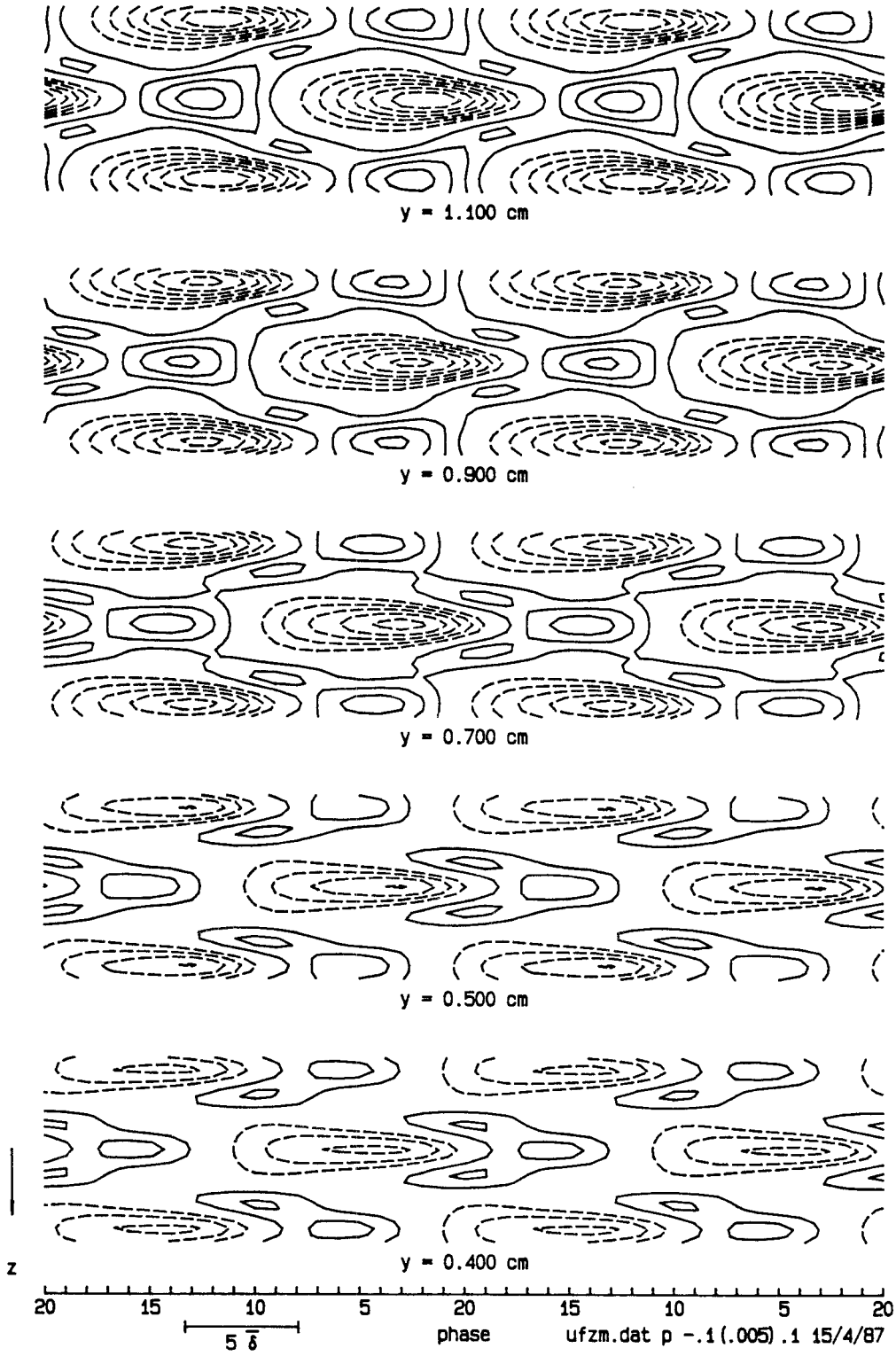

Figure 5.21 (cont'd.). Streamwise perturbation velocity $<u> - \bar{u}$ in the $t-z$ plane.

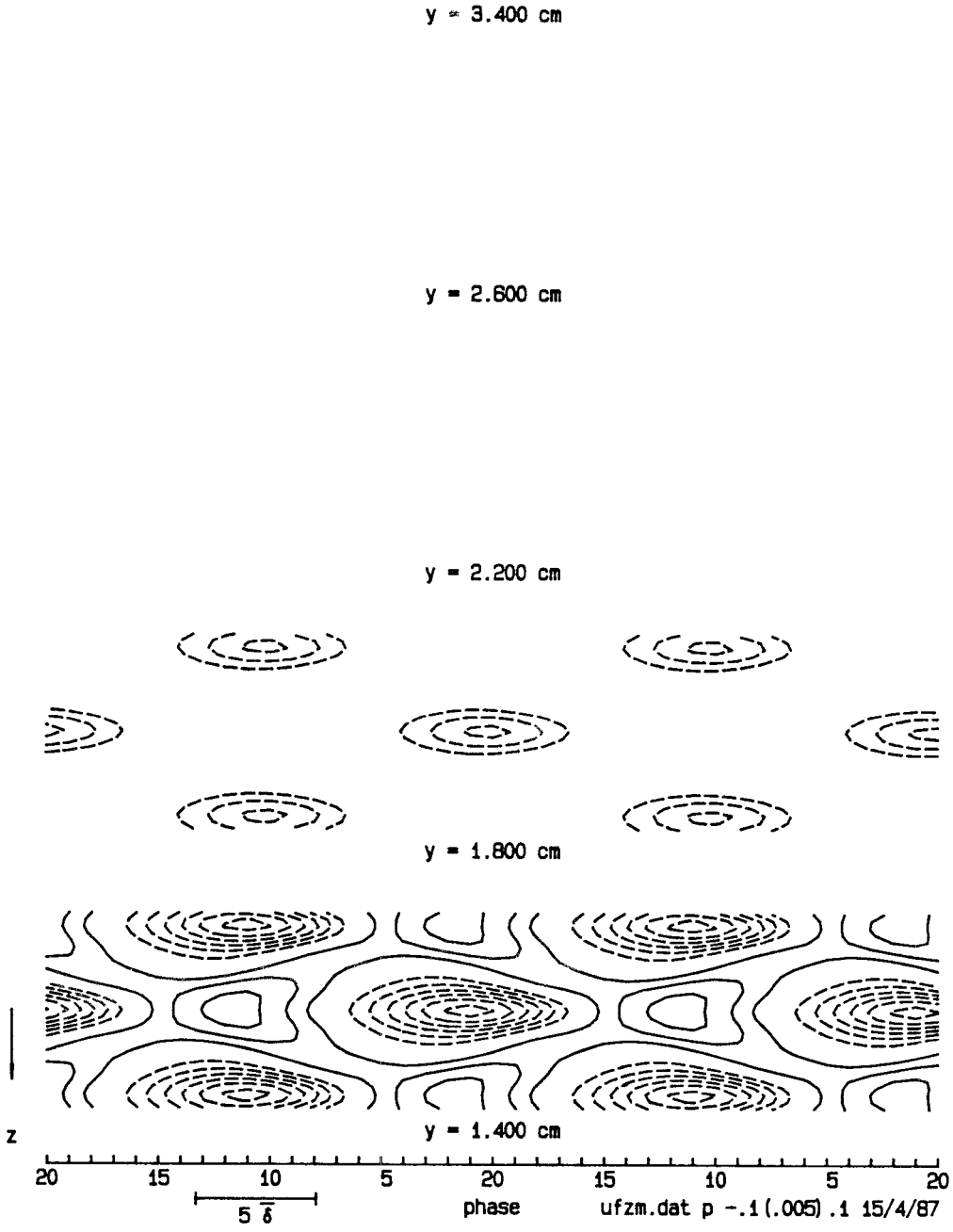

Figure 5.21 (cont'd.). Streamwise perturbation velocity $<u> - \bar{u}$ in the $t-z$ plane.

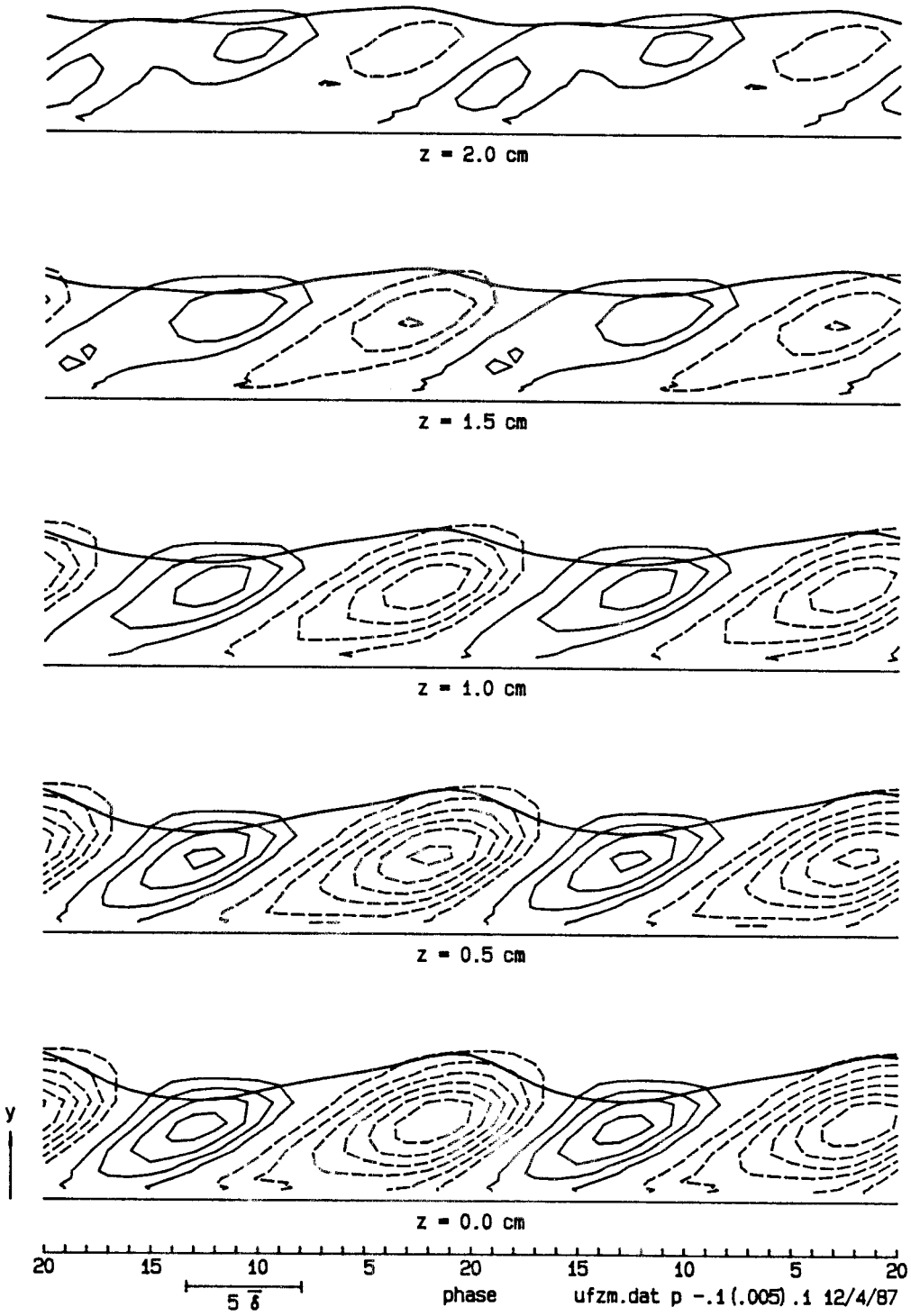

Figure 5.22. Streamwise perturbation velocity $<u> - \bar{u}$ in the t–y plane. Contour interval 0.005.

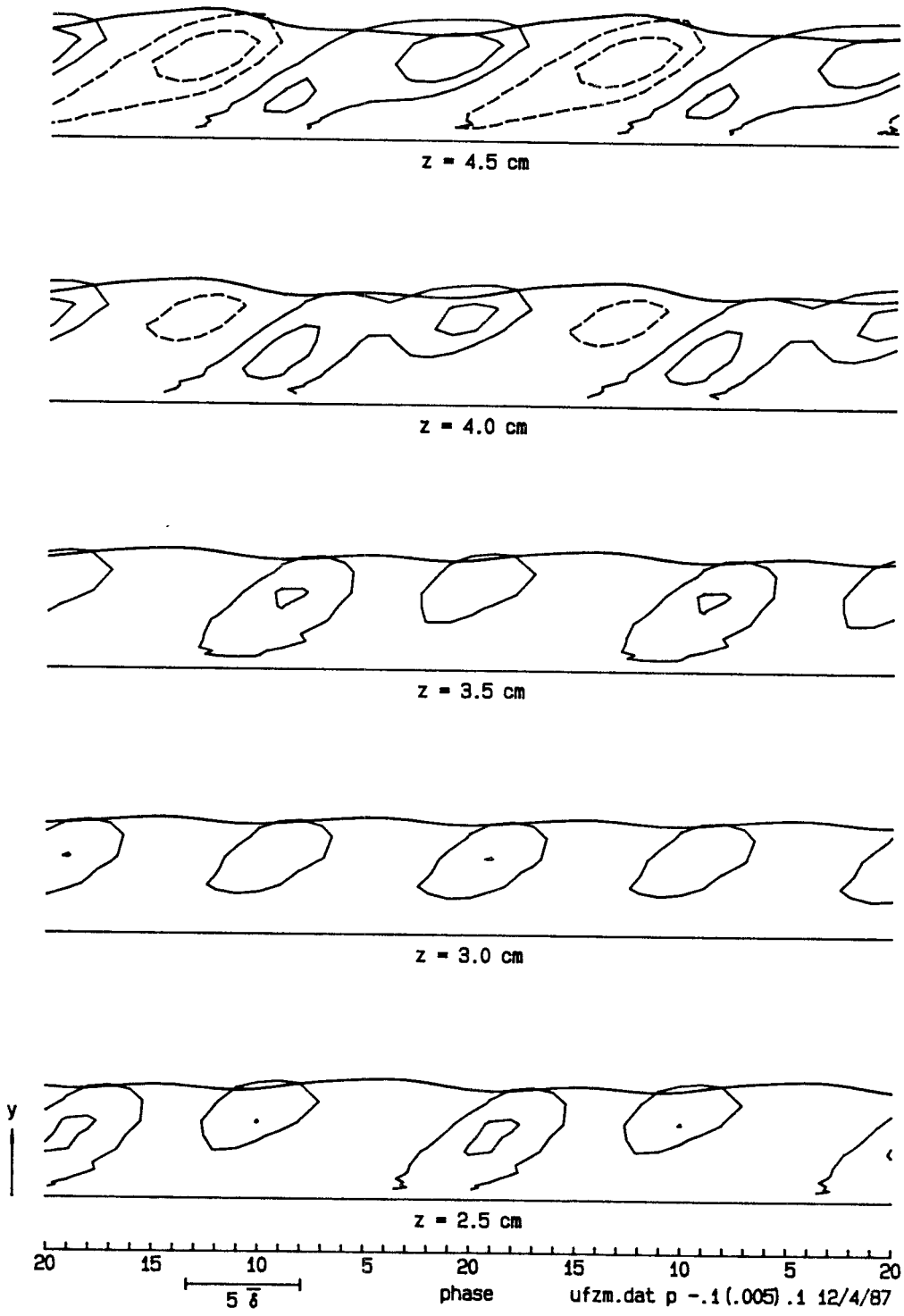

Figure 5.22 (cont'd.). Streamwise perturbation velocity $<u> - \bar{u}$ in the t–y plane.

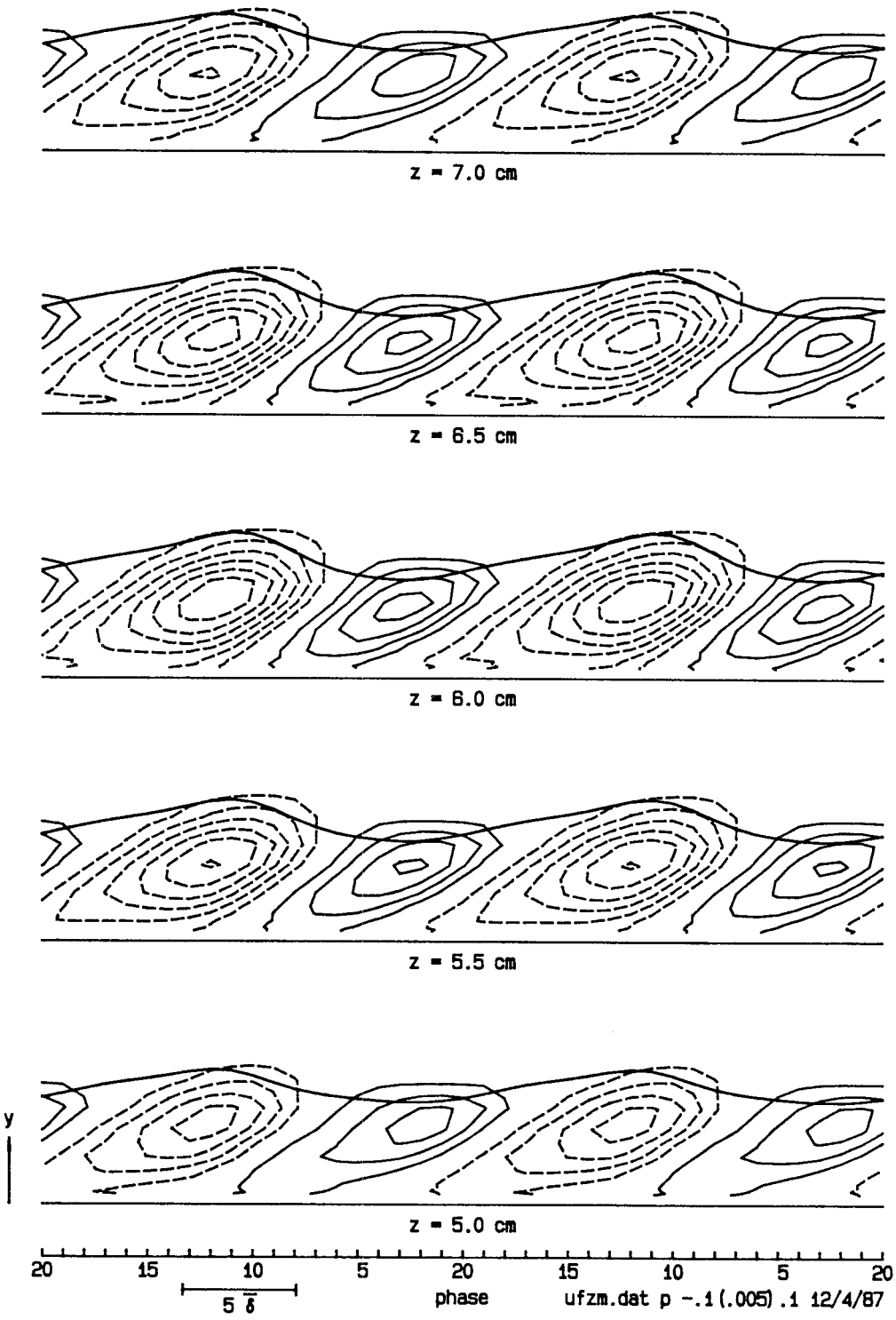

Figure 5.22 (cont'd.). Streamwise perturbation velocity $<u> - \bar{u}$ in the t–y plane.

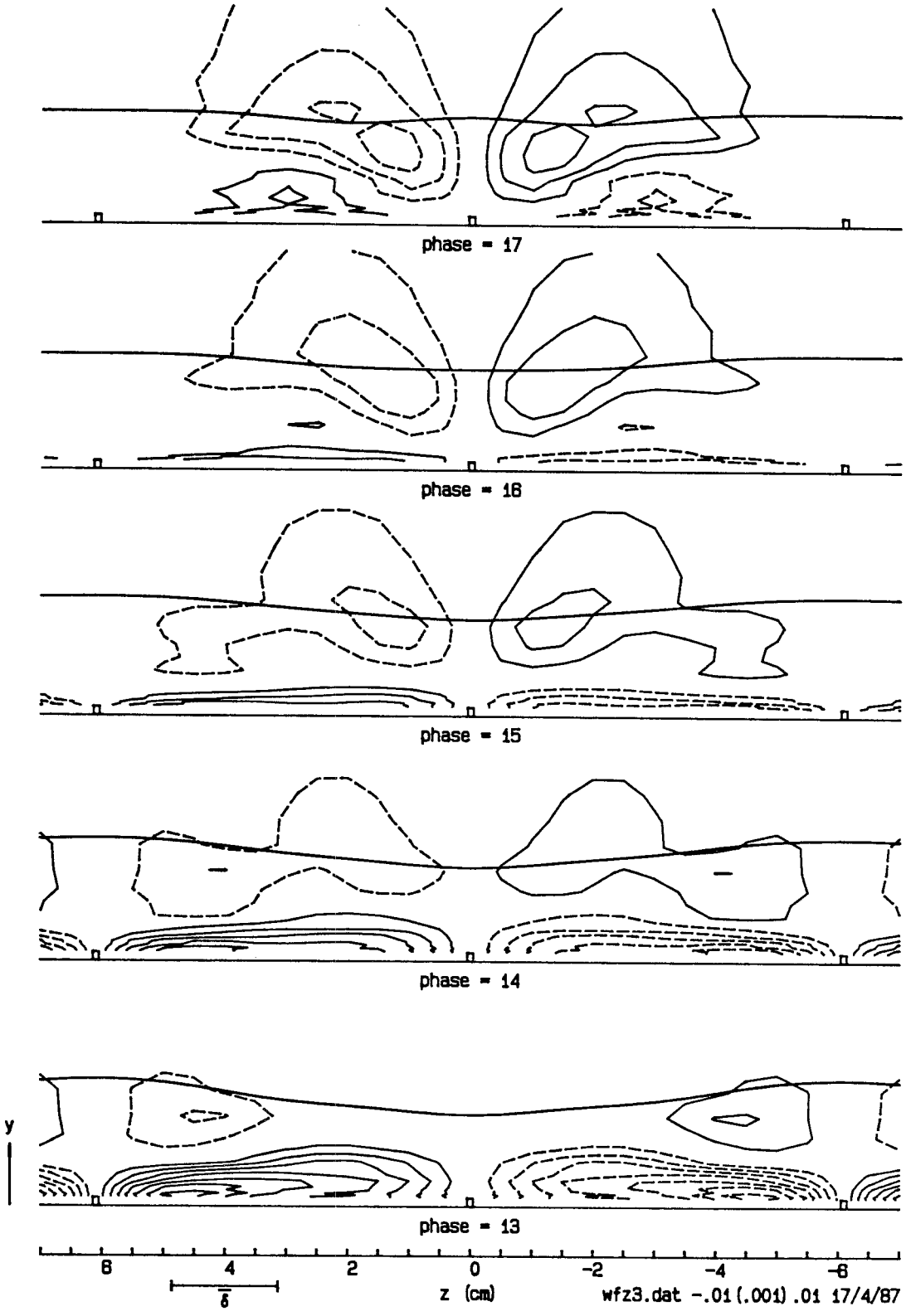

Figure 5.23. Spanwise velocity $<w>$ in the $z-y$ plane. Contour interval 0.001.

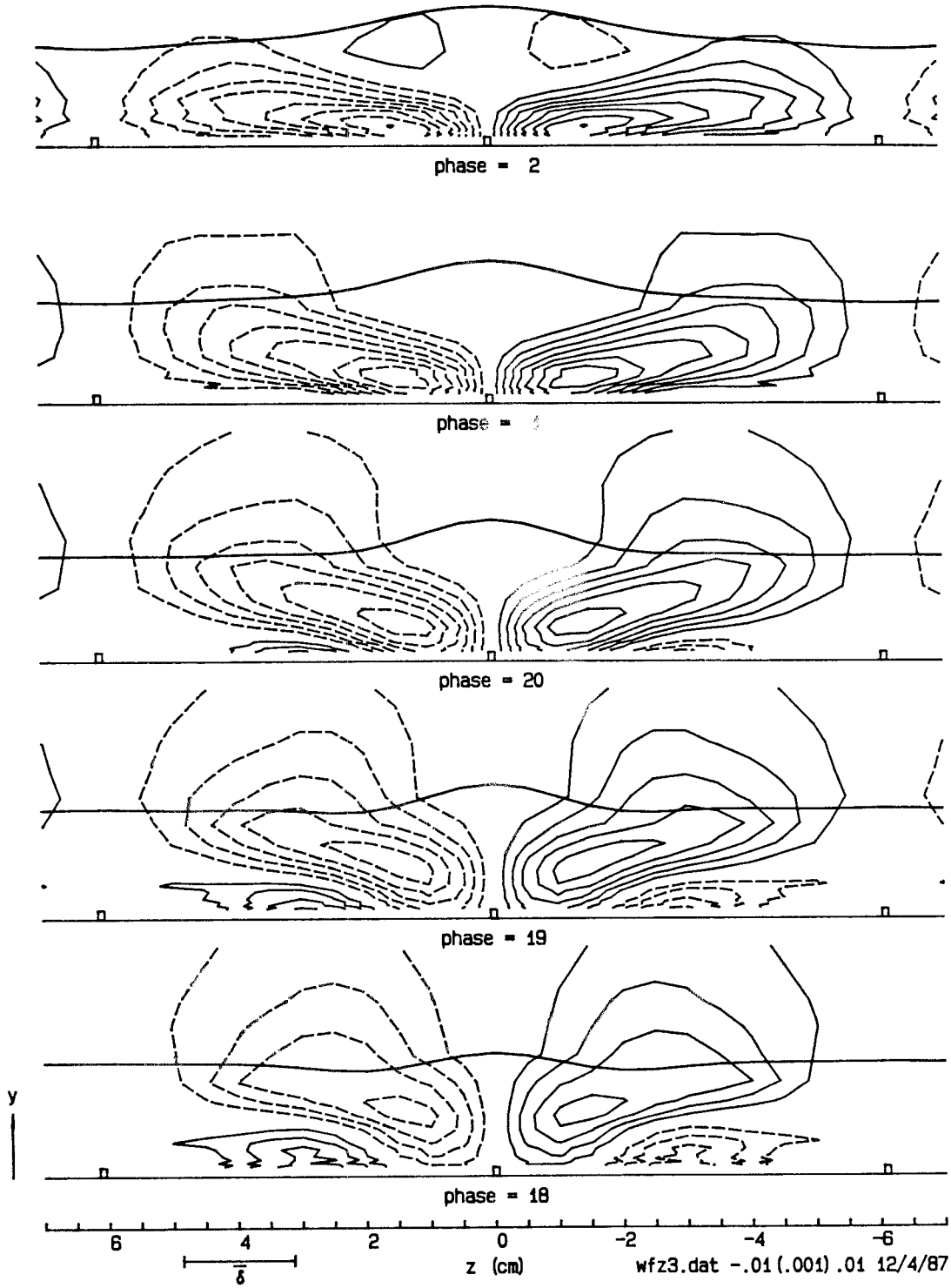

Figure 5.23 (cont'd.). Spanwise velocity $\langle w \rangle$ in the $z-y$ plane.

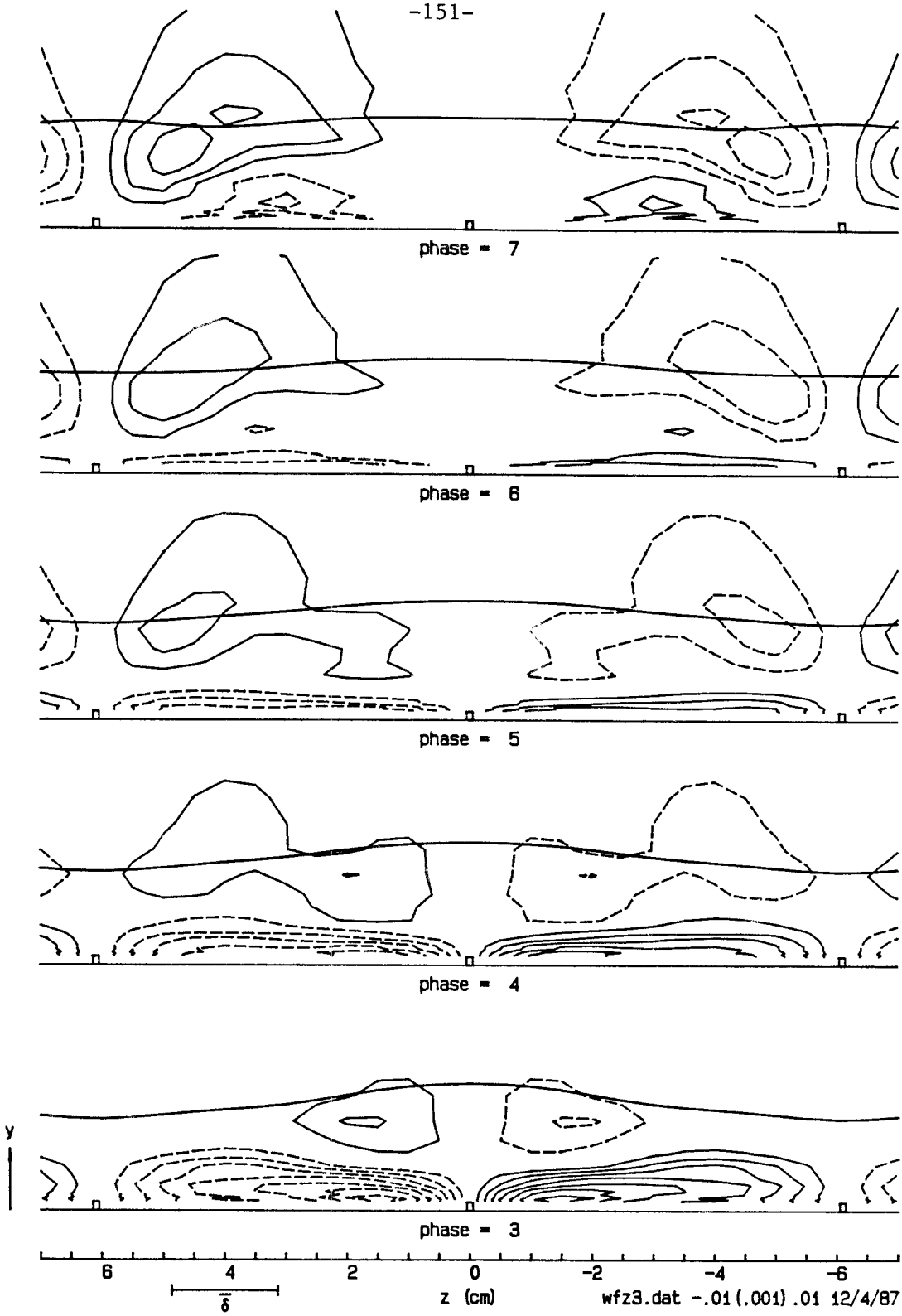

Figure 5.23 (cont'd.). Spanwise velocity $\langle w \rangle$ in the $z-y$ plane.

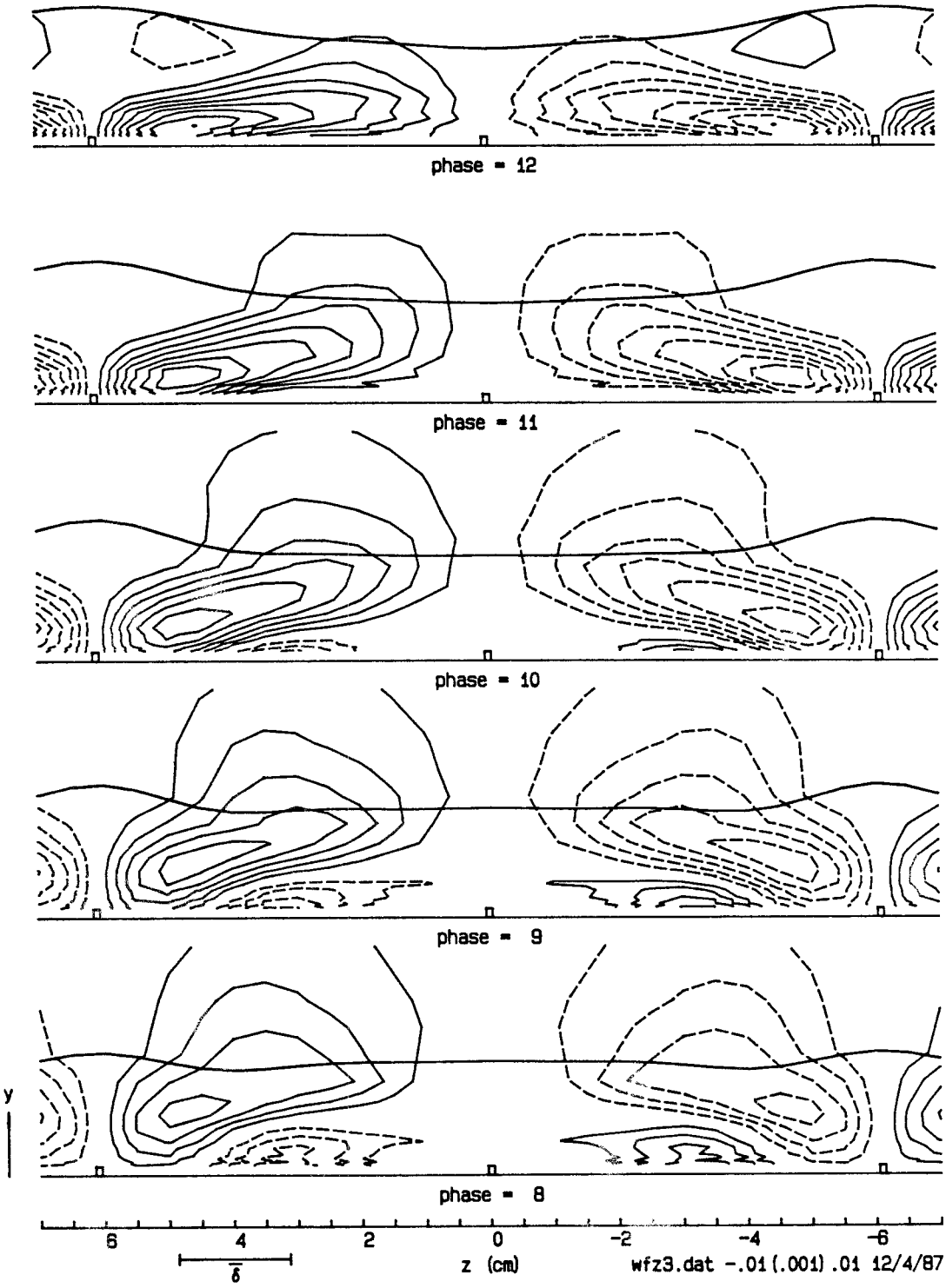

Figure 5.23 (cont'd.). Spanwise velocity $<w>$ in the $z-y$ plane.

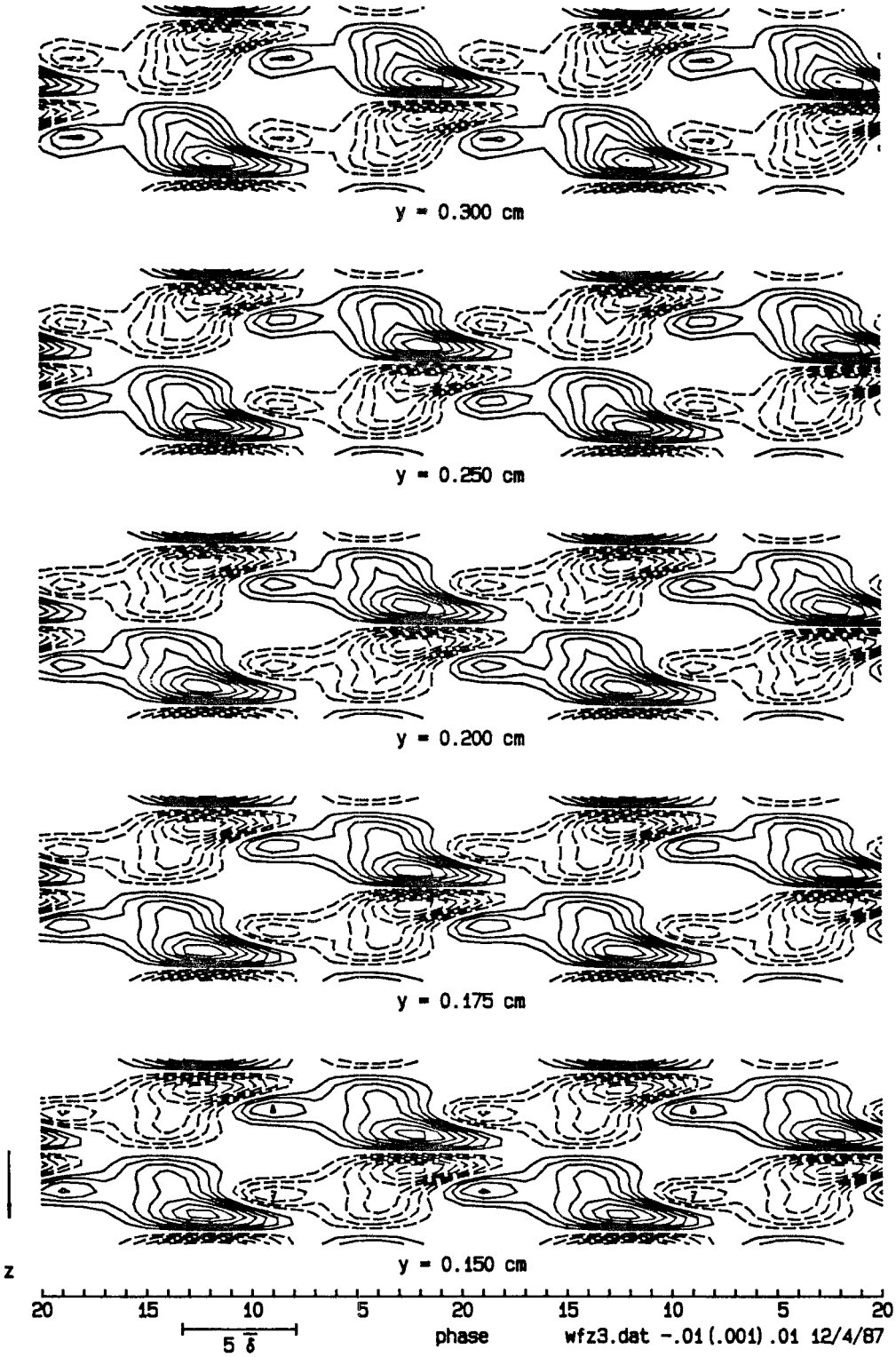

Figure 5.24. Spanwise velocity $\langle w \rangle$ in the t–z plane. Contour interval 0.001.

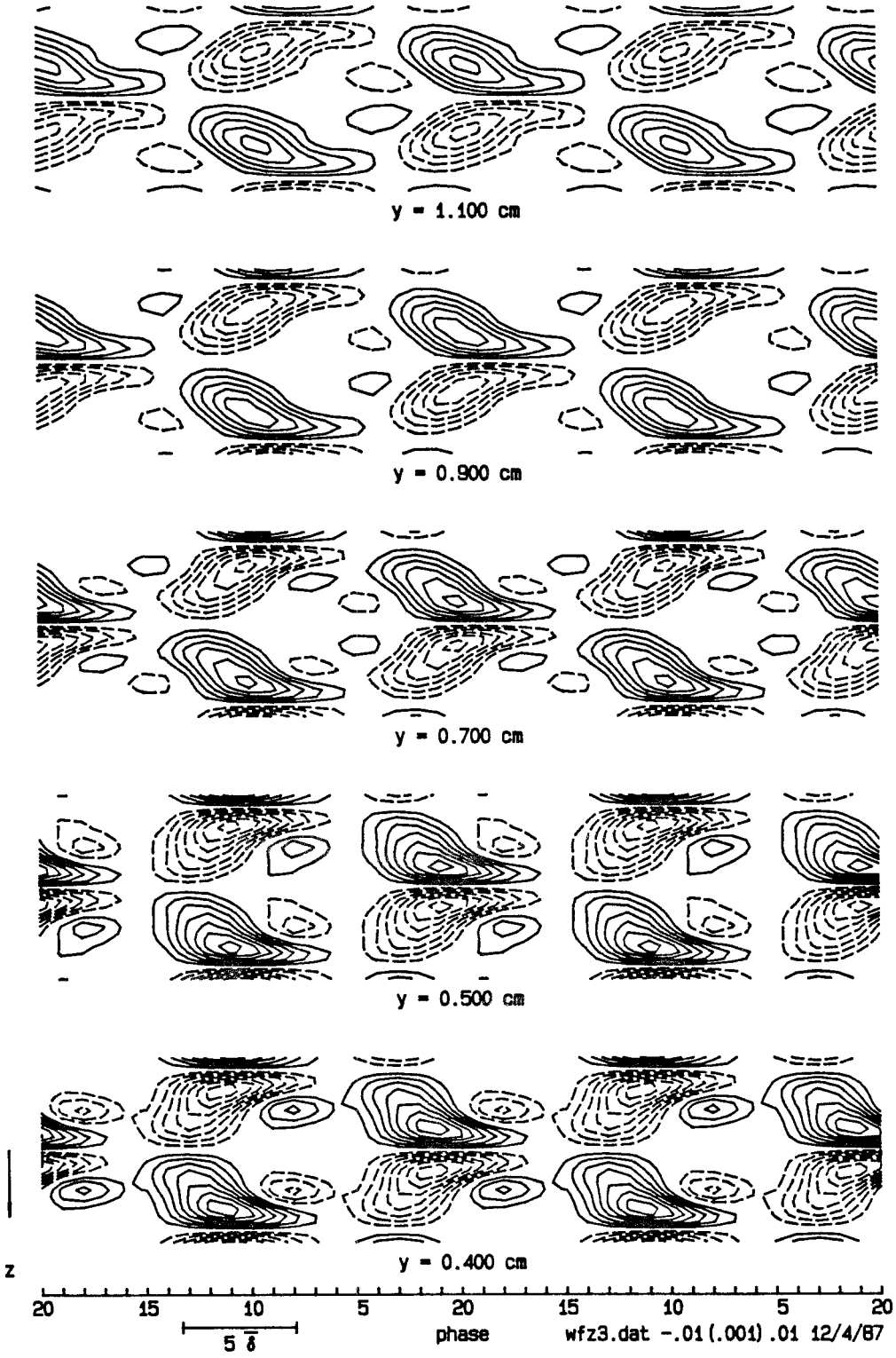

Figure 5.24 (cont'd.). Spanwise velocity $<w>$ in the $t-z$ plane.

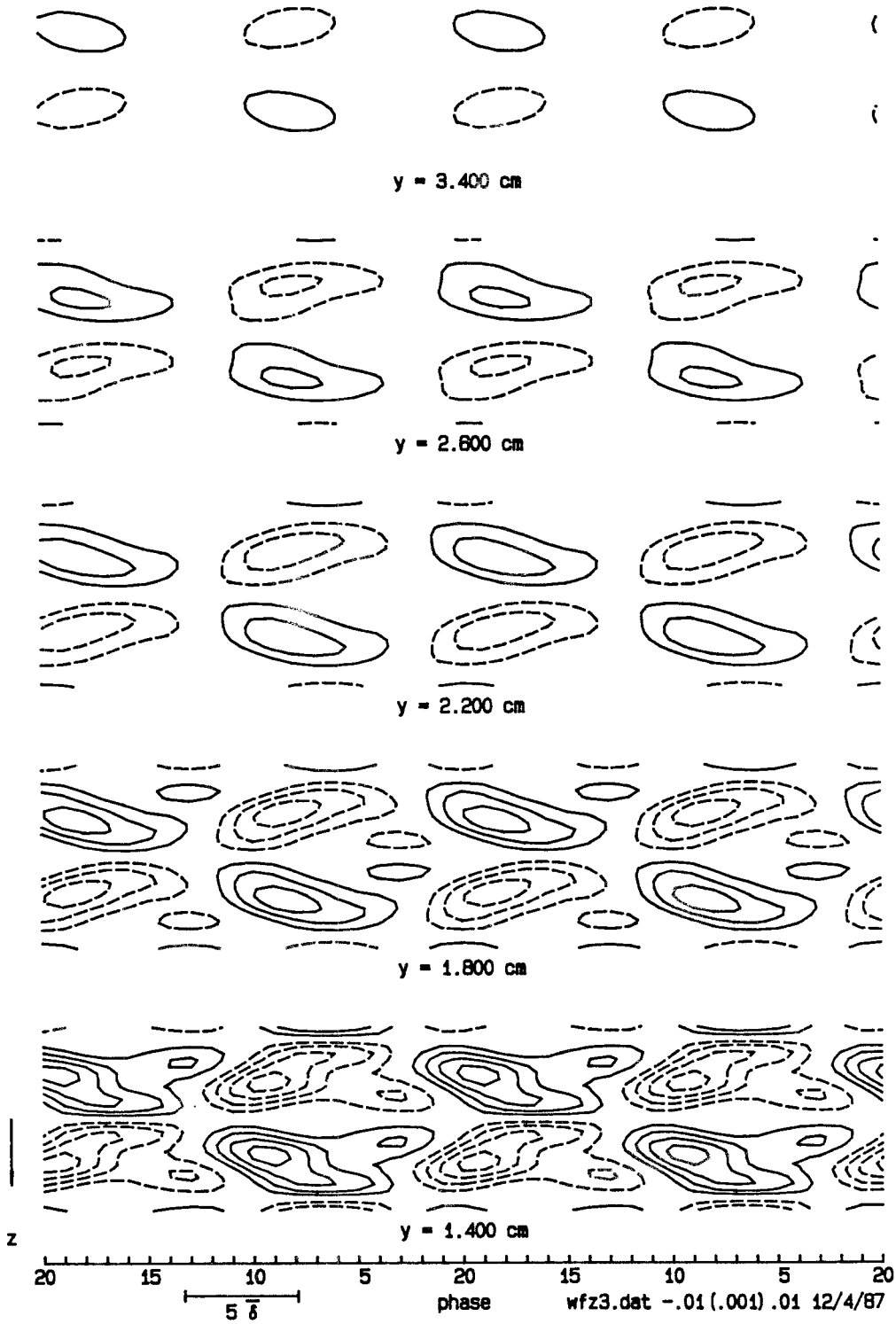

Figure 5.24 (cont'd.). Spanwise velocity $\langle w \rangle$ in the $t-z$ plane.

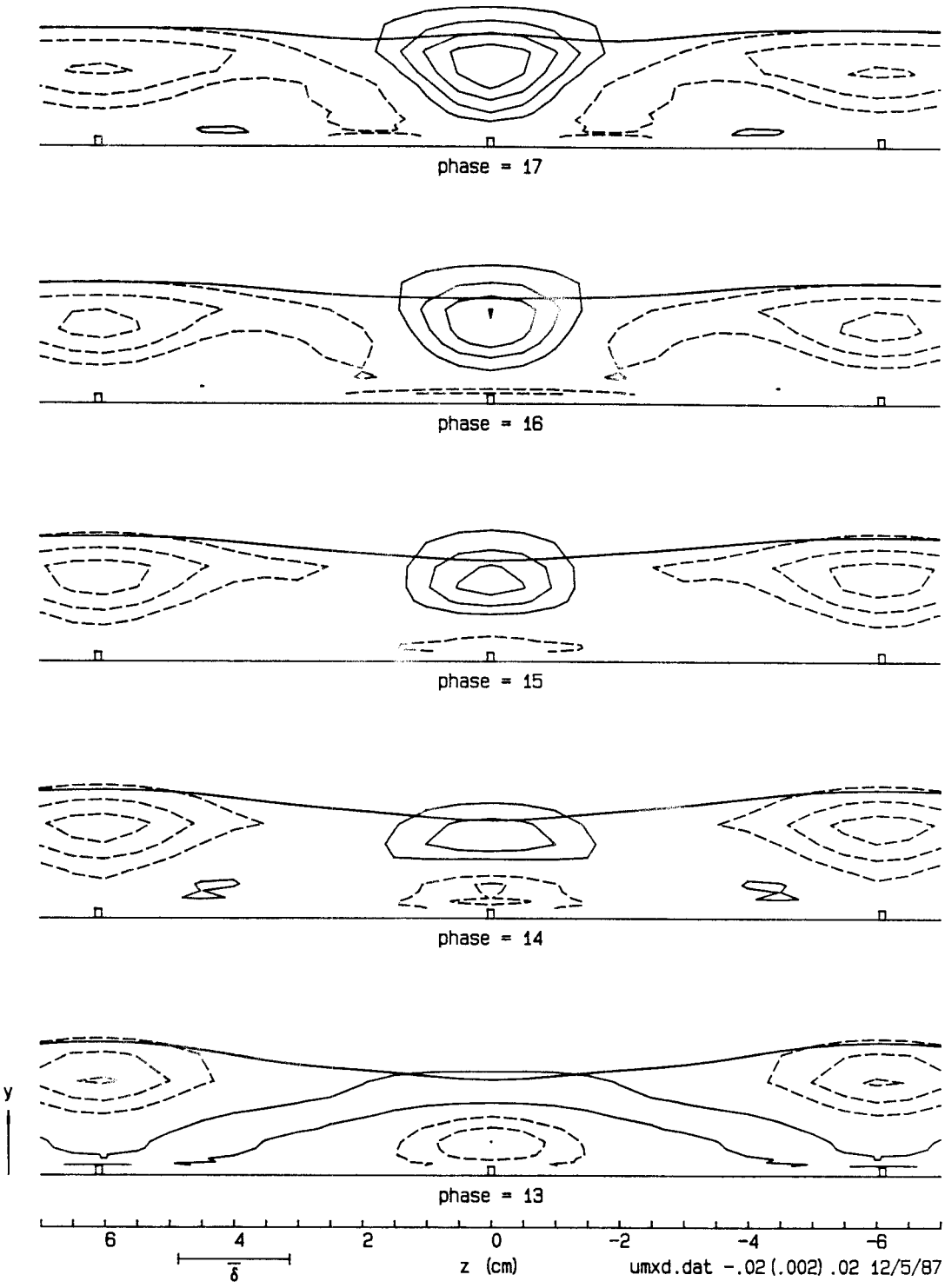

Figure 5.25. Velocity gradient $\partial<u>/\partial x$ in the $z-y$ plane. Contour interval 0.002.

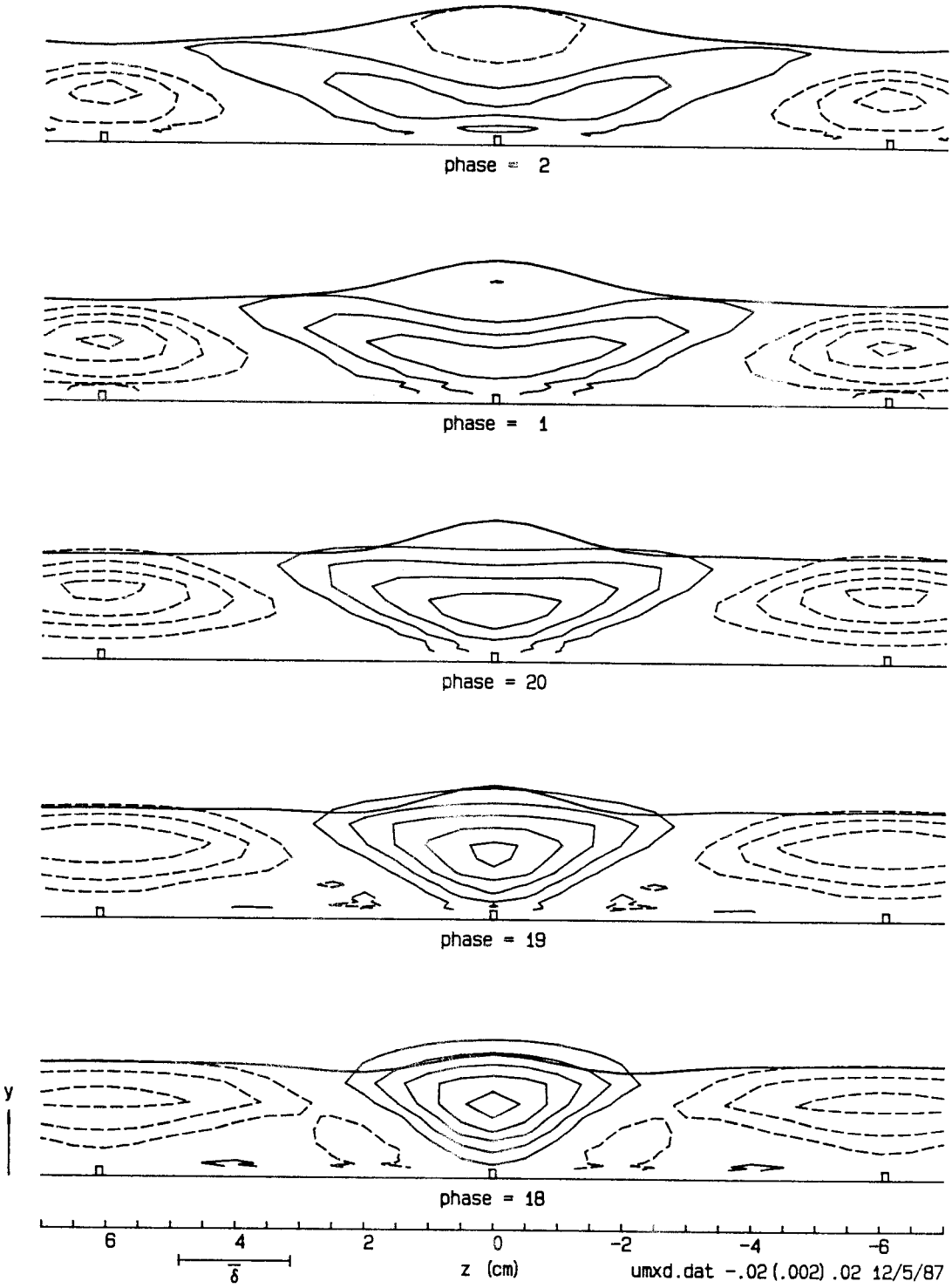

Figure 5.25 (cont'd.). Velocity gradient $\partial<u>/\partial x$ in the $z-y$ plane.

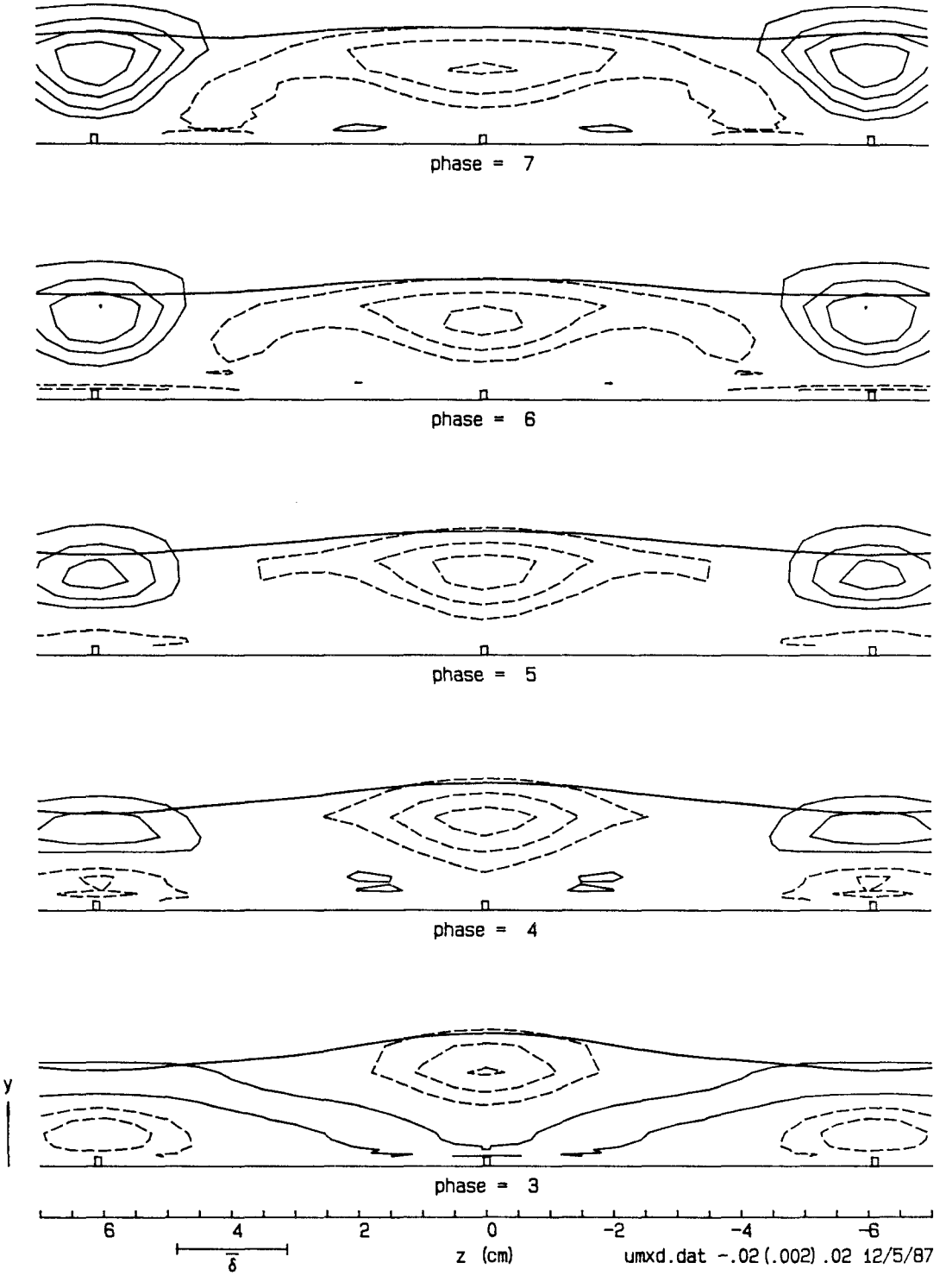

Figure 5.25 (cont'd.). Velocity gradient $\partial<u>/\partial x$ in the $z-y$ plane.

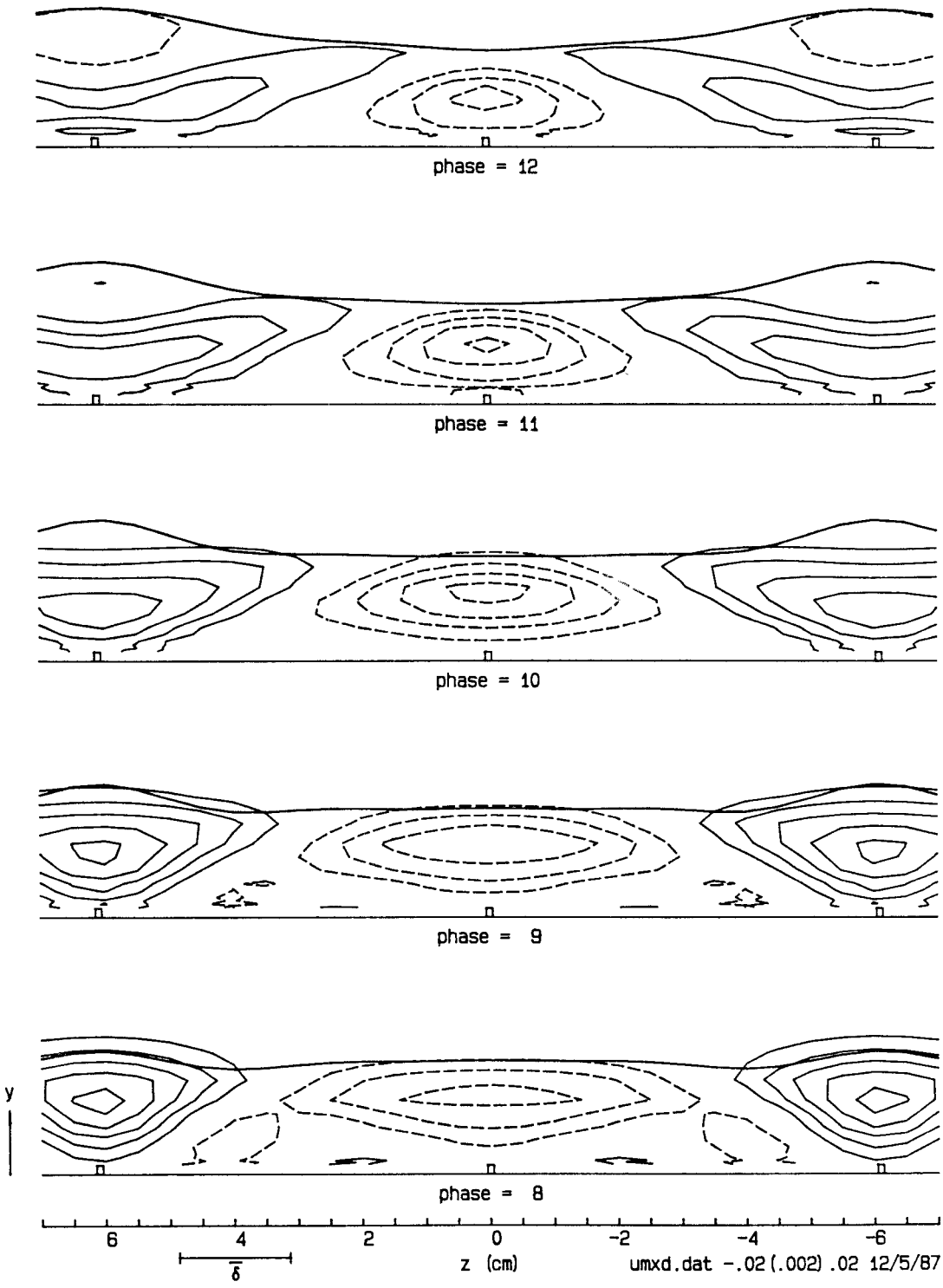

Figure 5.25 (cont'd.). Velocity gradient $\partial<u>/\partial x$ in the $z-y$ plane.

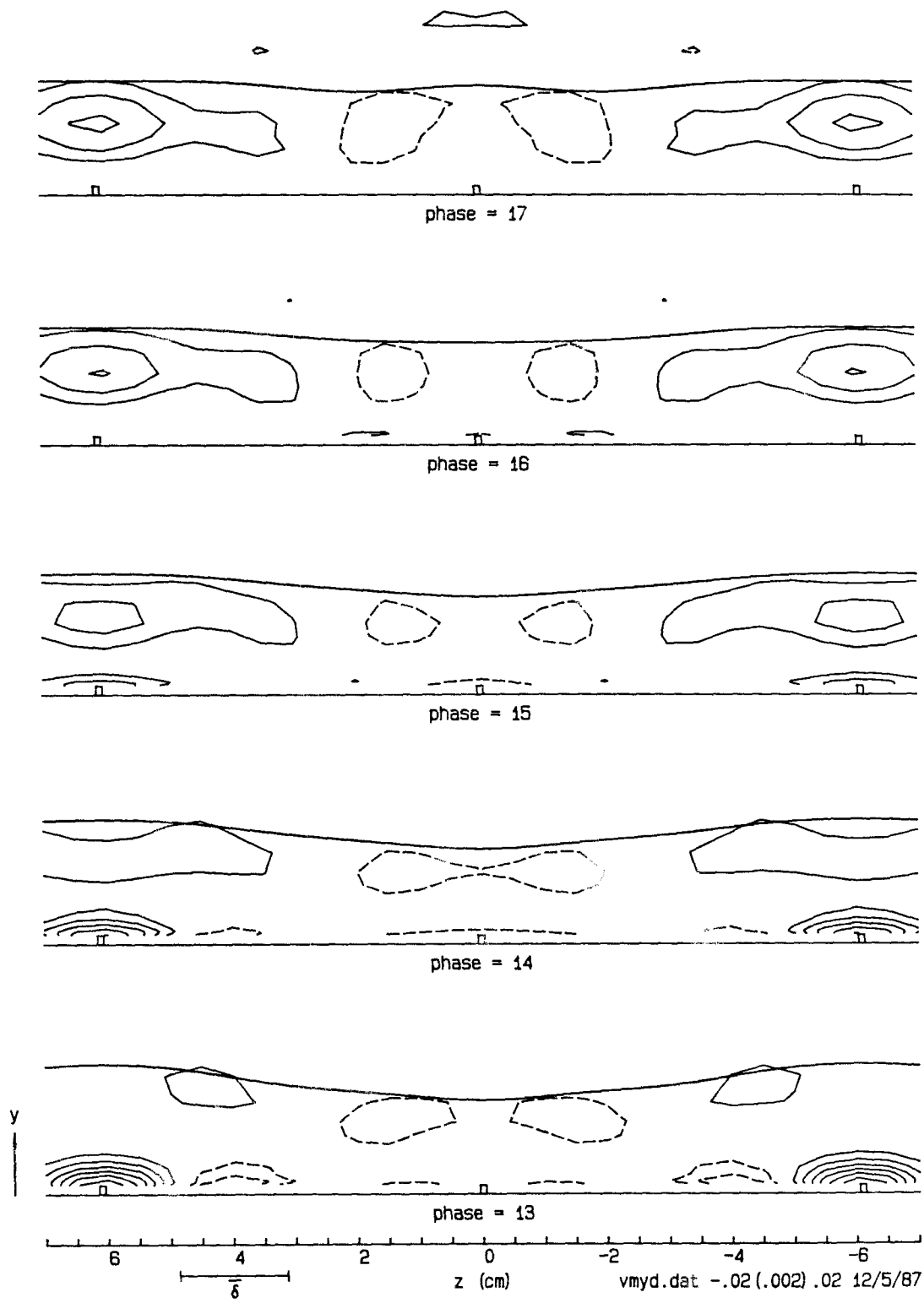

Figure 5.26. Velocity gradient $\partial \langle v \rangle / \partial y$ in the $z-y$ plane. Contour interval 0.002.

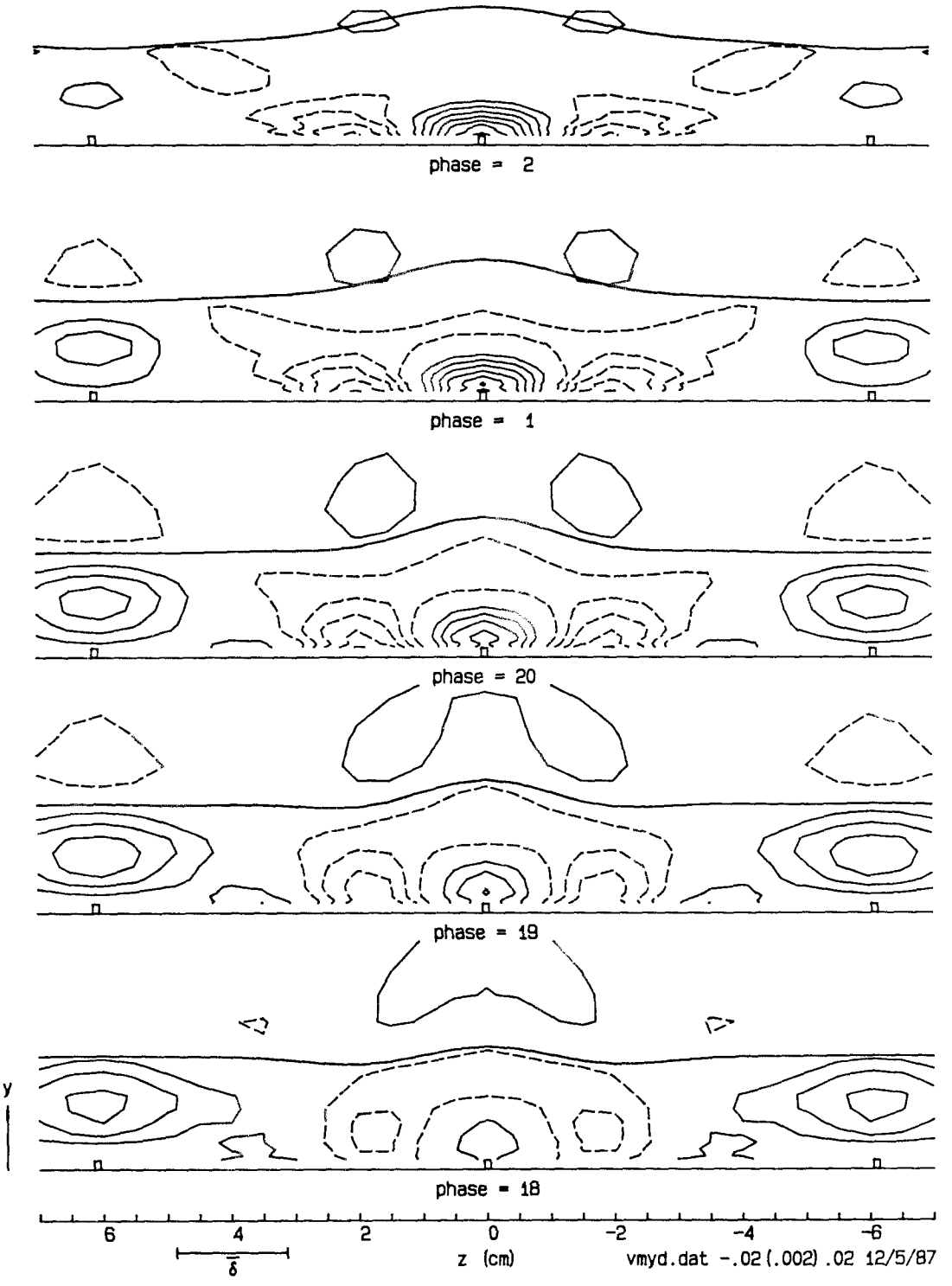

Figure 5.26 (cont'd.). Velocity gradient $\partial\langle v\rangle/\partial y$ in the $z-y$ plane.

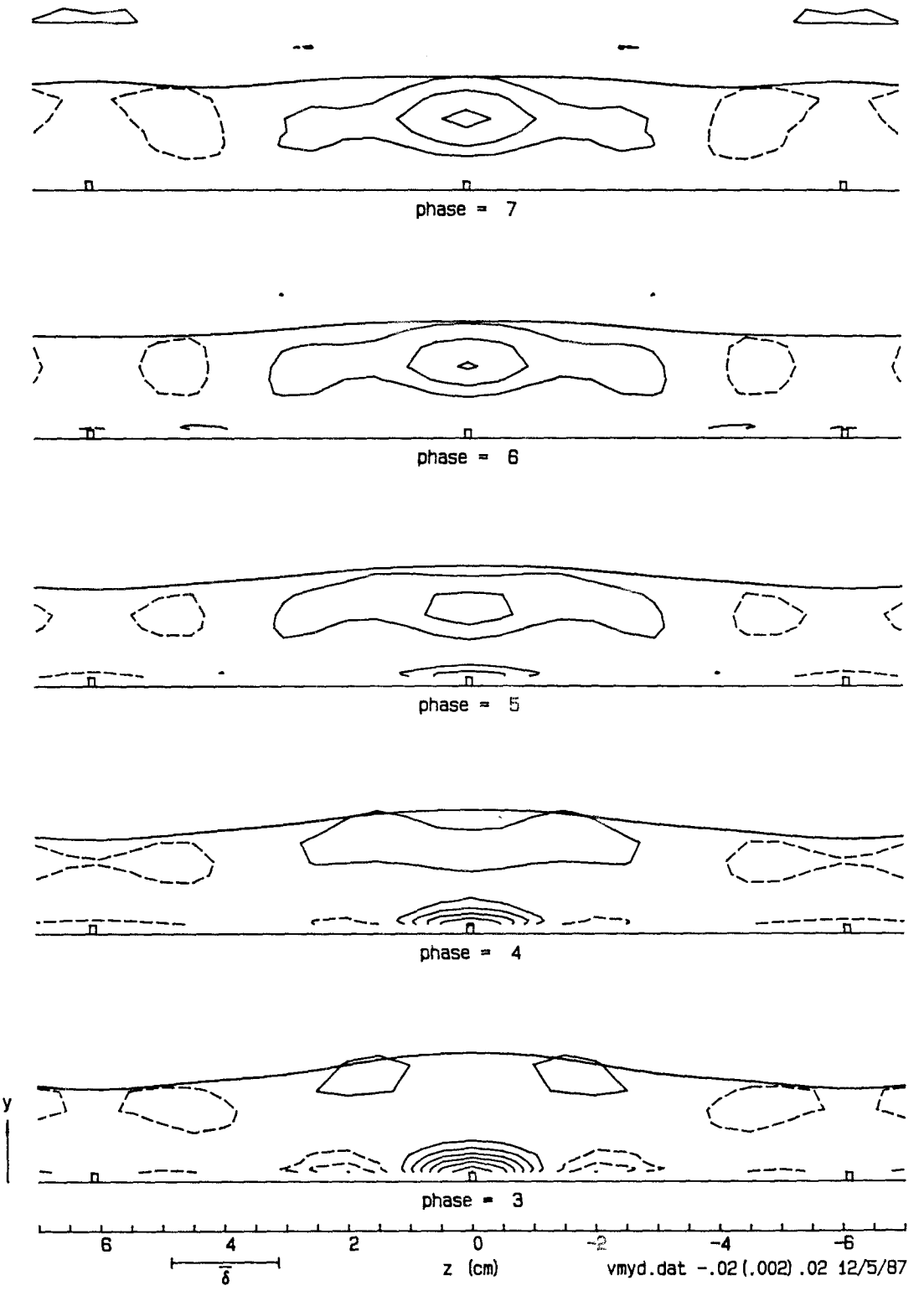

Figure 5.26 (cont'd.). Velocity gradient $\partial\langle v\rangle/\partial y$ in the $z-y$ plane.

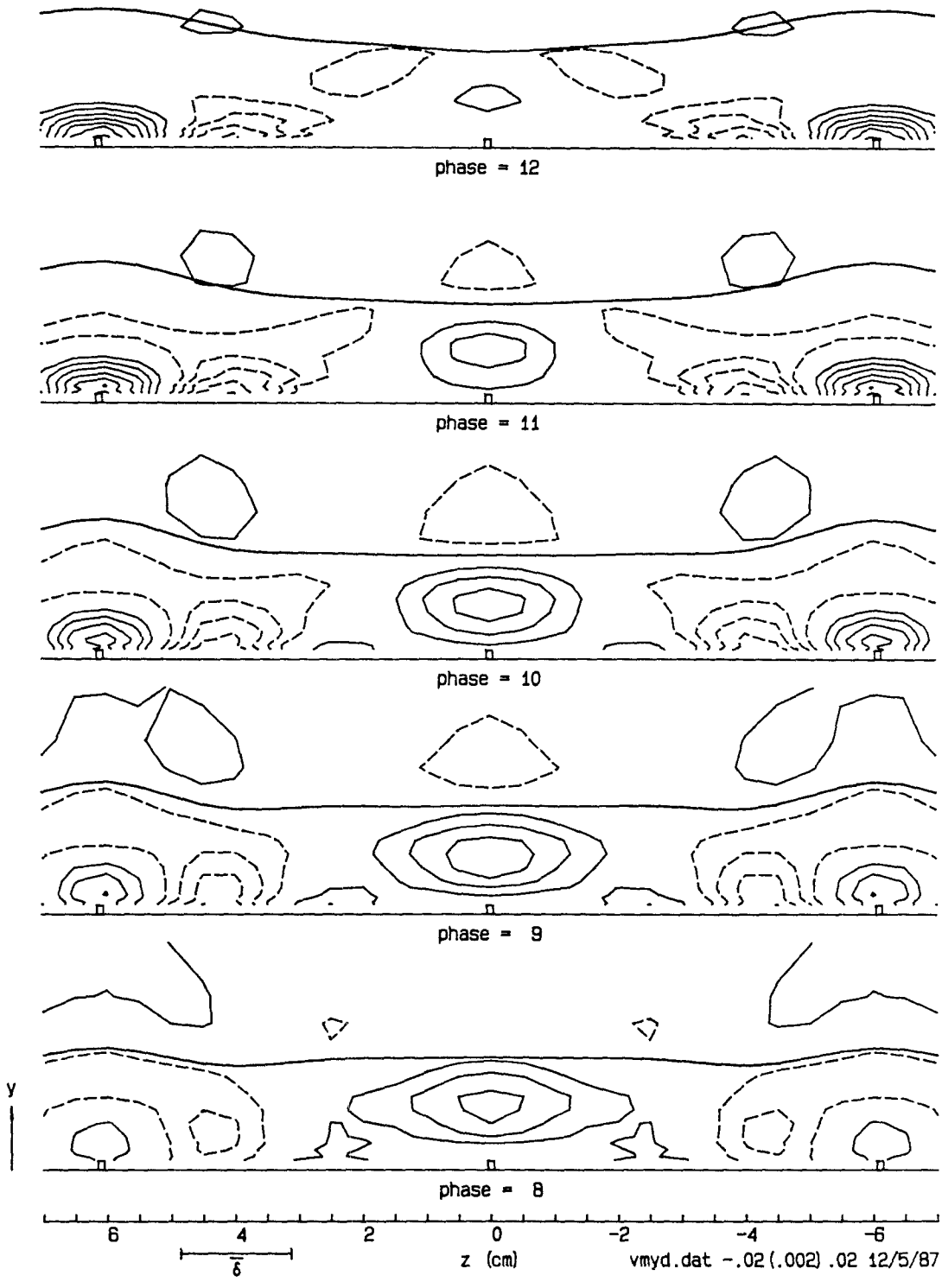

Figure 5.26 (cont'd.). Velocity gradient $\partial\langle v\rangle/\partial y$ in the $z-y$ plane.

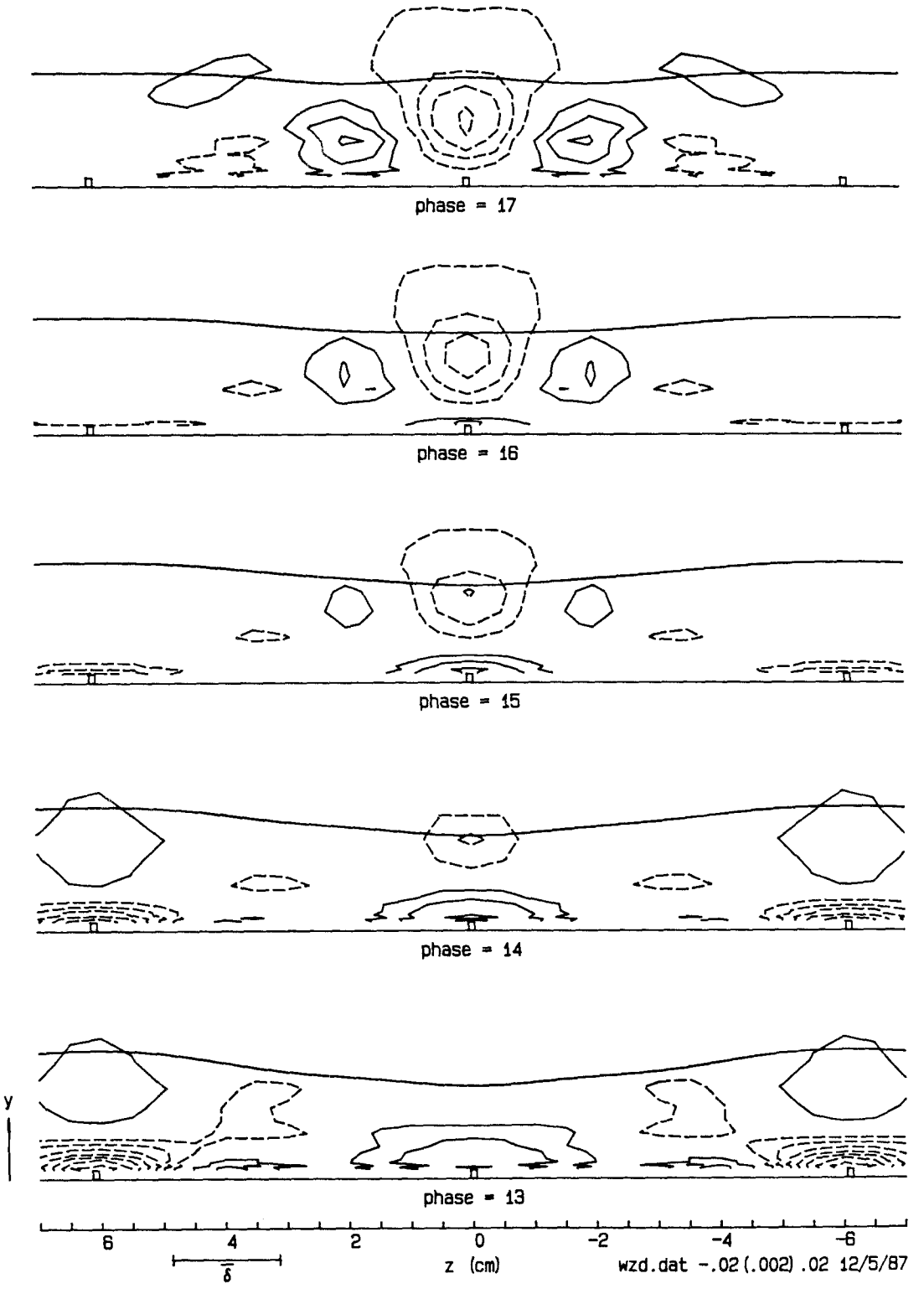

Figure 5.27. Velocity gradient $\partial \langle w \rangle / \partial z$ in the $z-y$ plane. Contour interval 0.002.

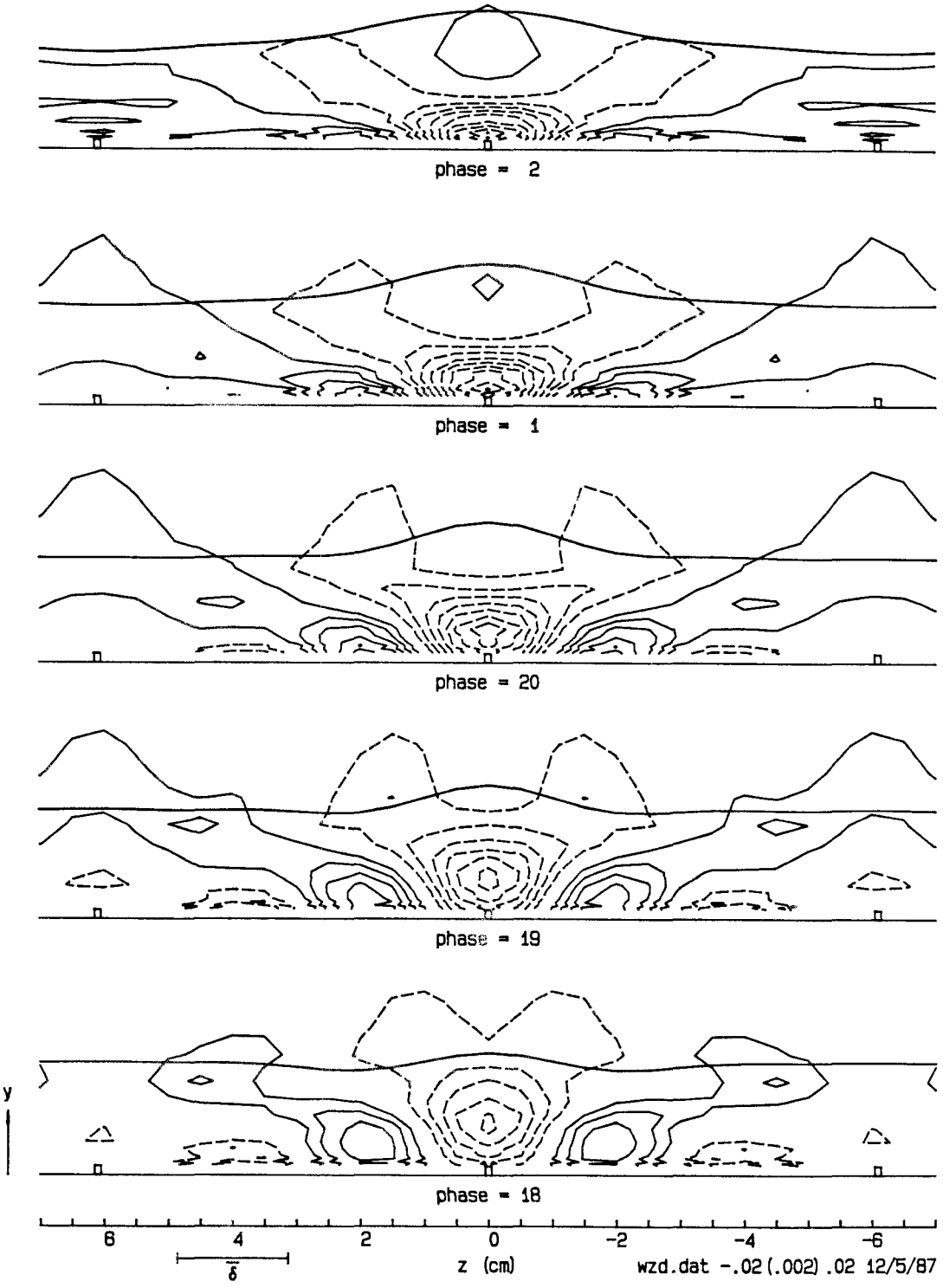

Figure 5.27 (cont'd.). Velocity gradient $\partial \langle w \rangle / \partial z$ in the $z-y$ plane.

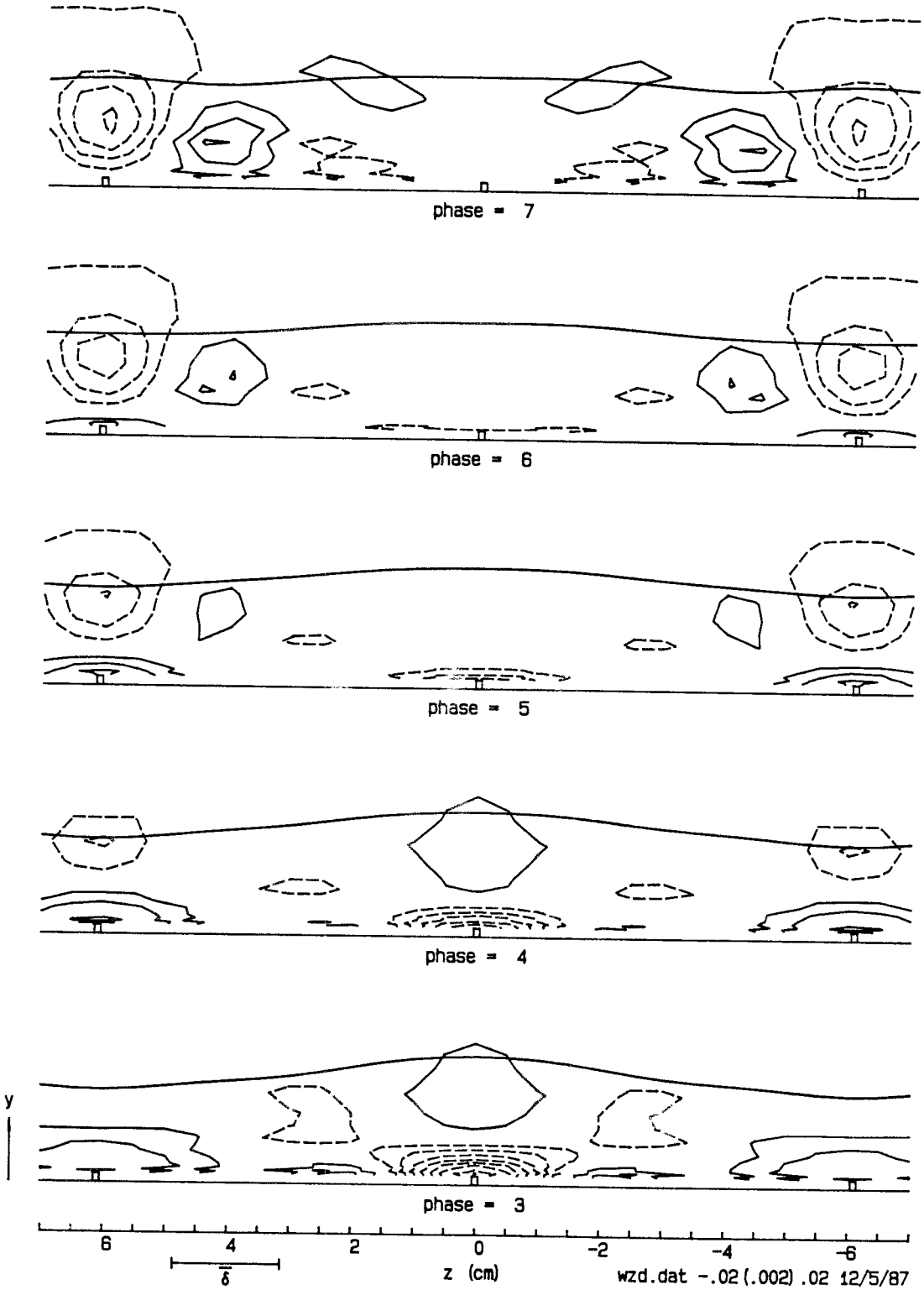

Figure 5.27 (cont'd.). Velocity gradient $\partial \langle w \rangle / \partial z$ in the $z-y$ plane.

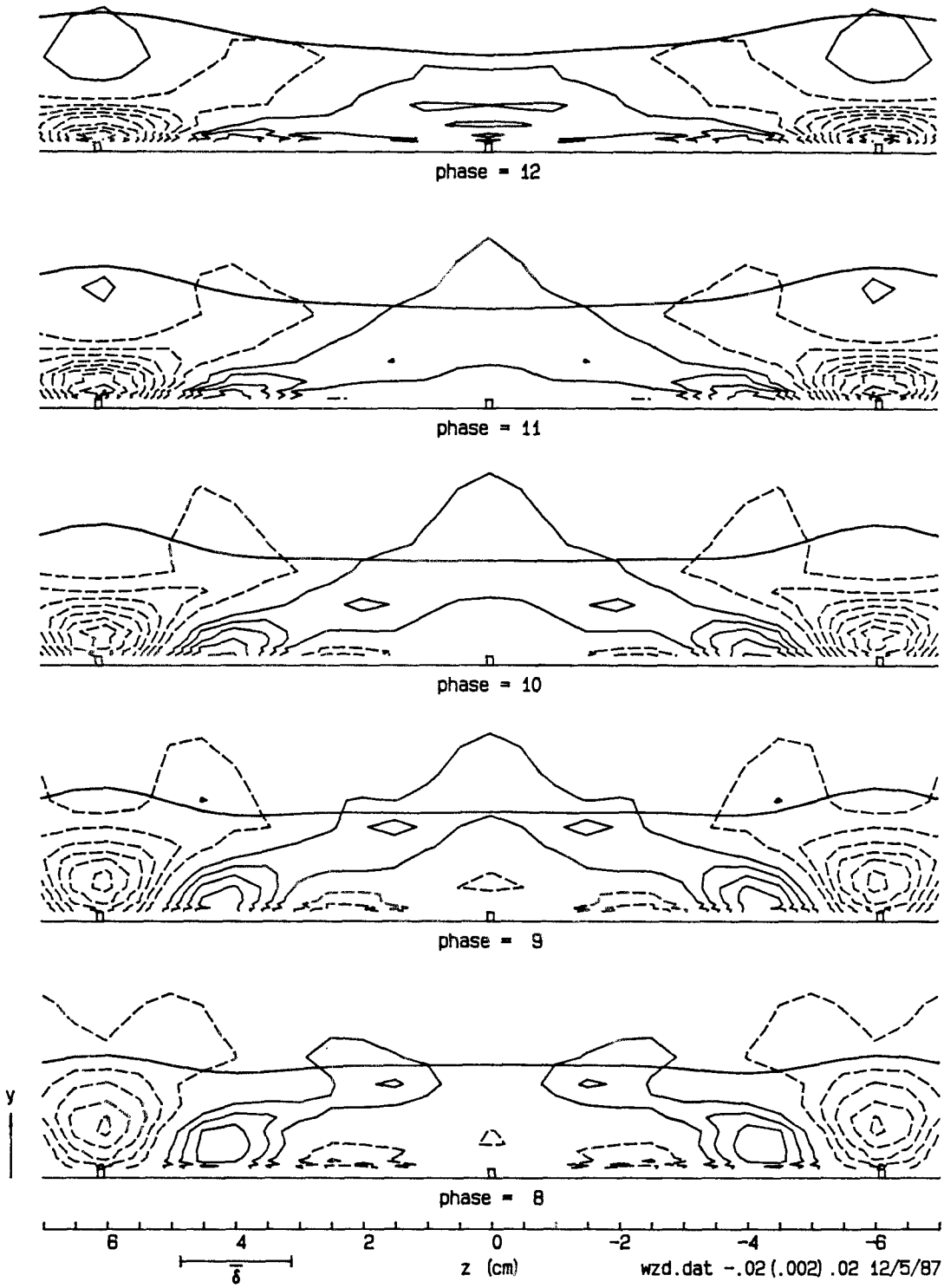

Figure 5.27 (cont'd.). Velocity gradient $\partial \langle w \rangle / \partial z$ in the z–y plane.

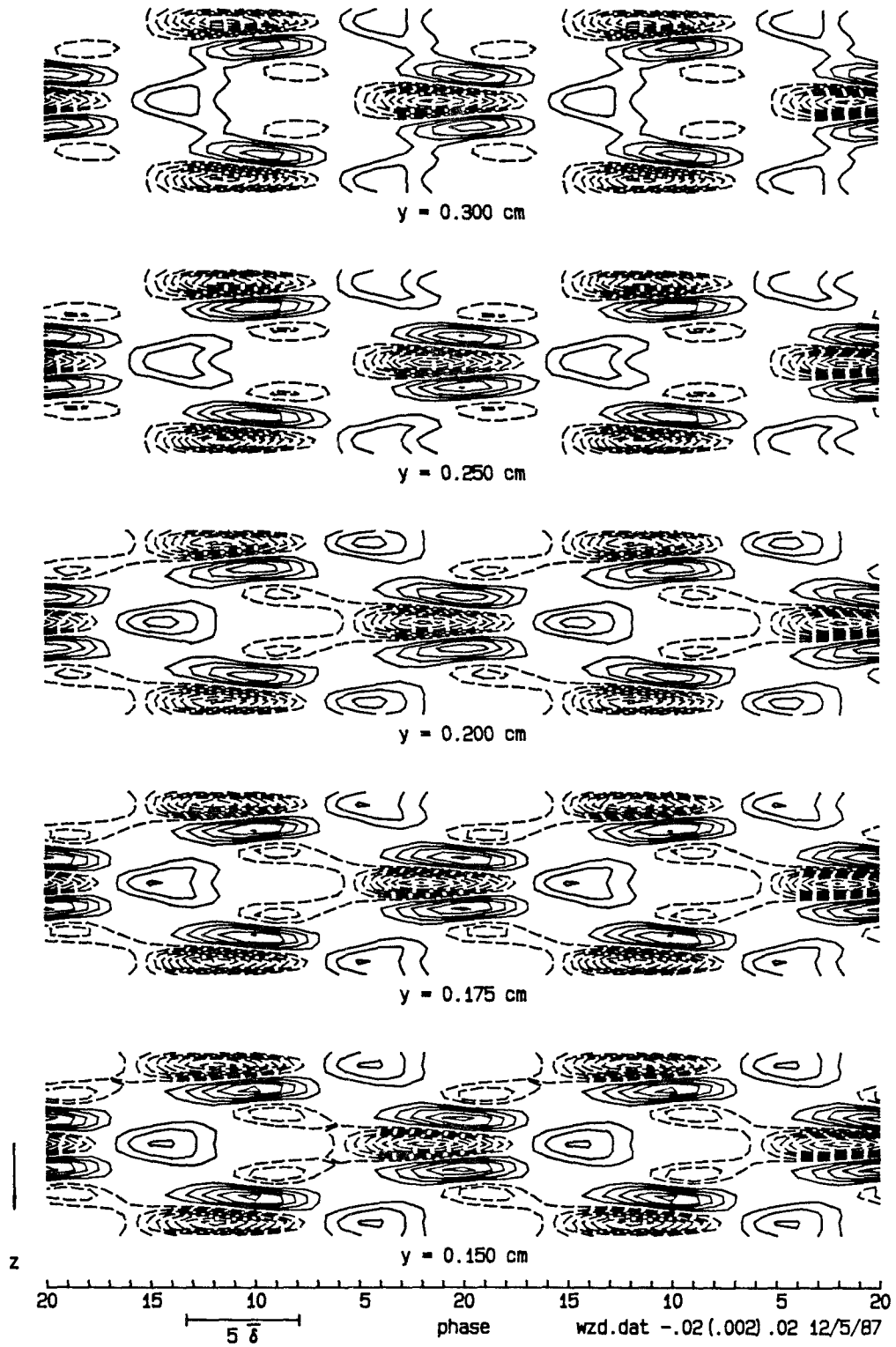

Figure 5.28. Velocity gradient $\partial \langle w \rangle / \partial z$ in the $t-z$ plane. Contour interval 0.002.

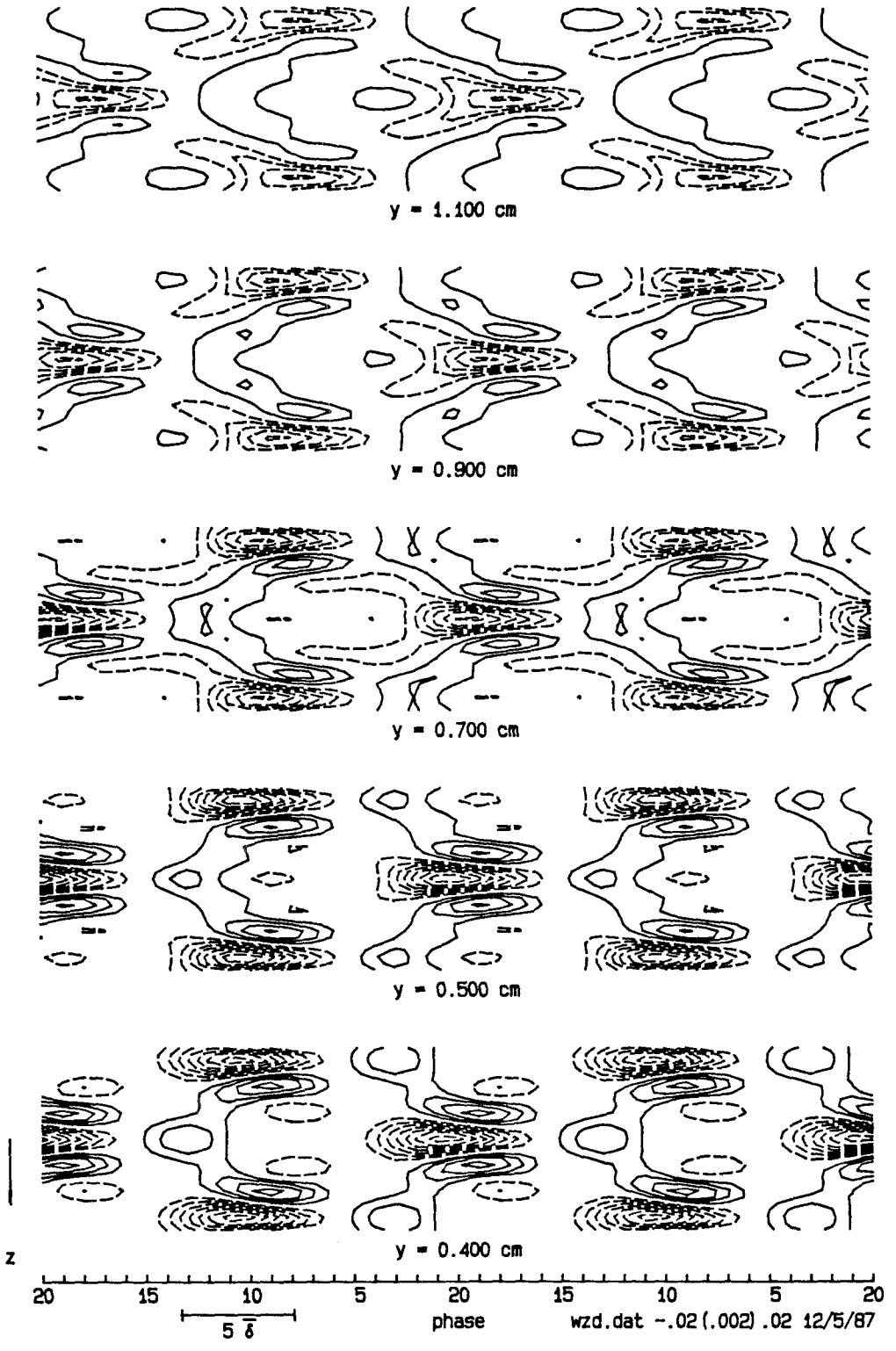

Figure 5.28 (cont'd.). Velocity gradient $\partial \langle w \rangle / \partial z$ in the $t-z$ plane.

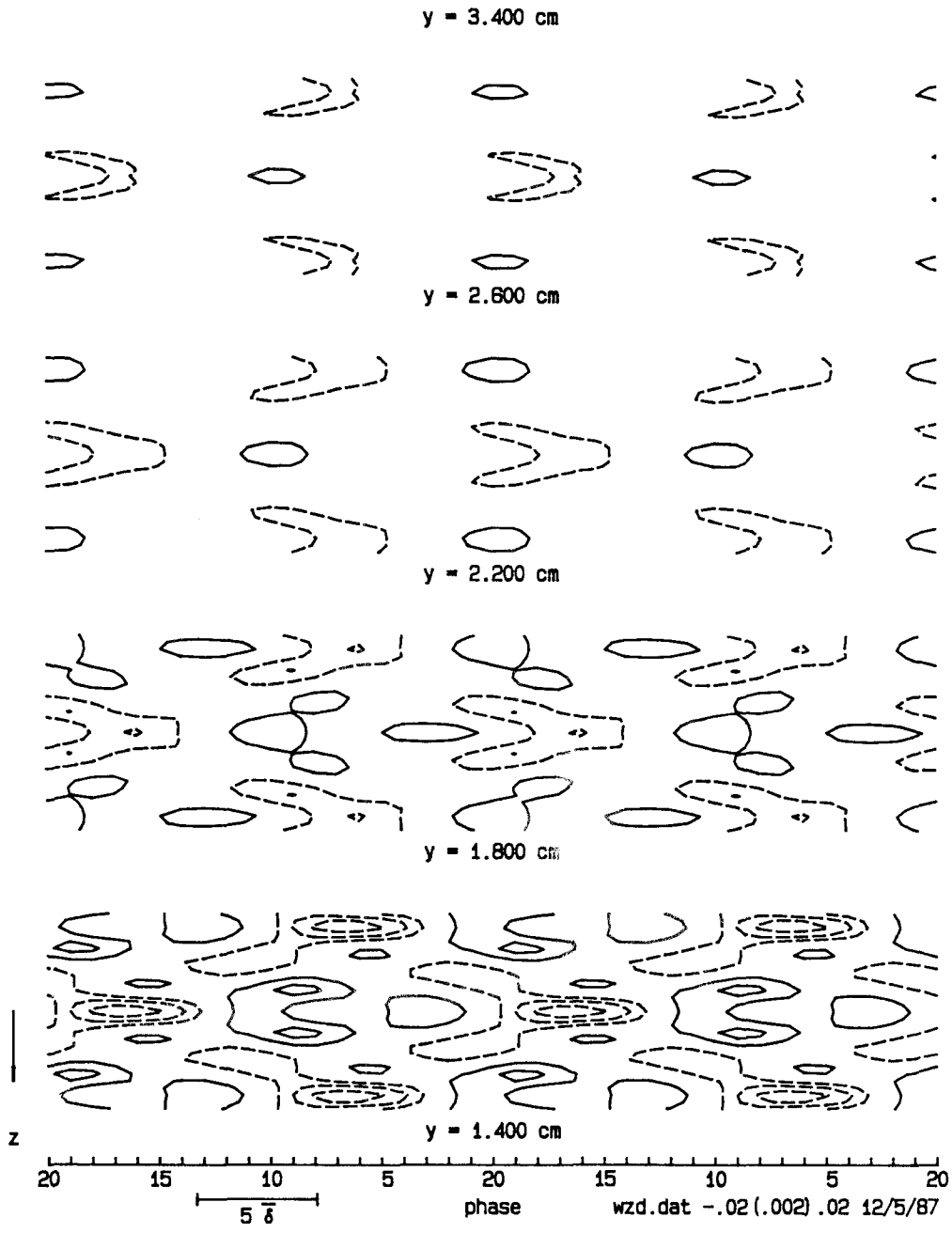

Figure 5.28 (cont'd.). Velocity gradient $\partial \langle w \rangle / \partial z$ in the $t-z$ plane.

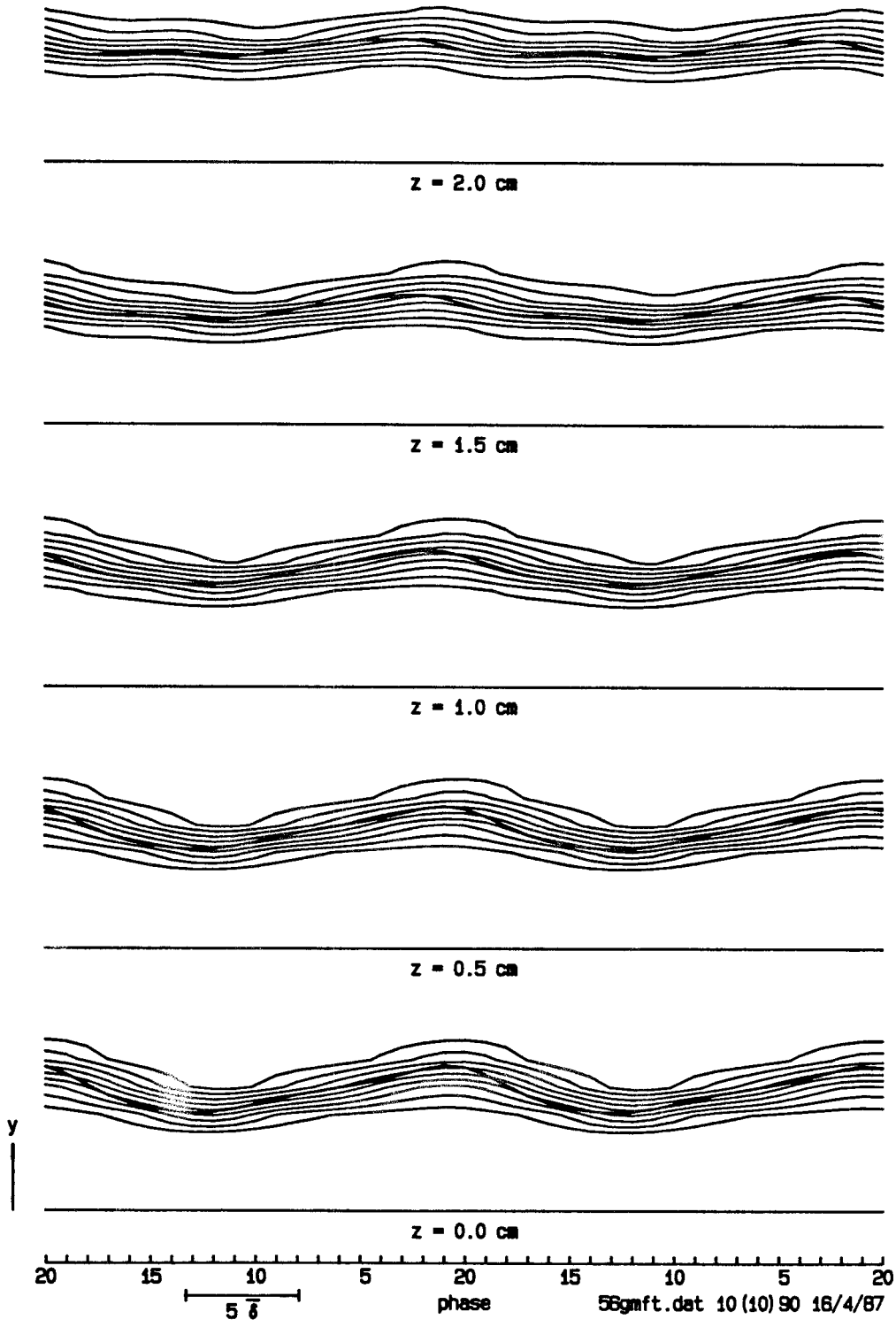

Figure 5.29. Intermittency <γ> in the $t-y$ plane. Contour interval 0.1.

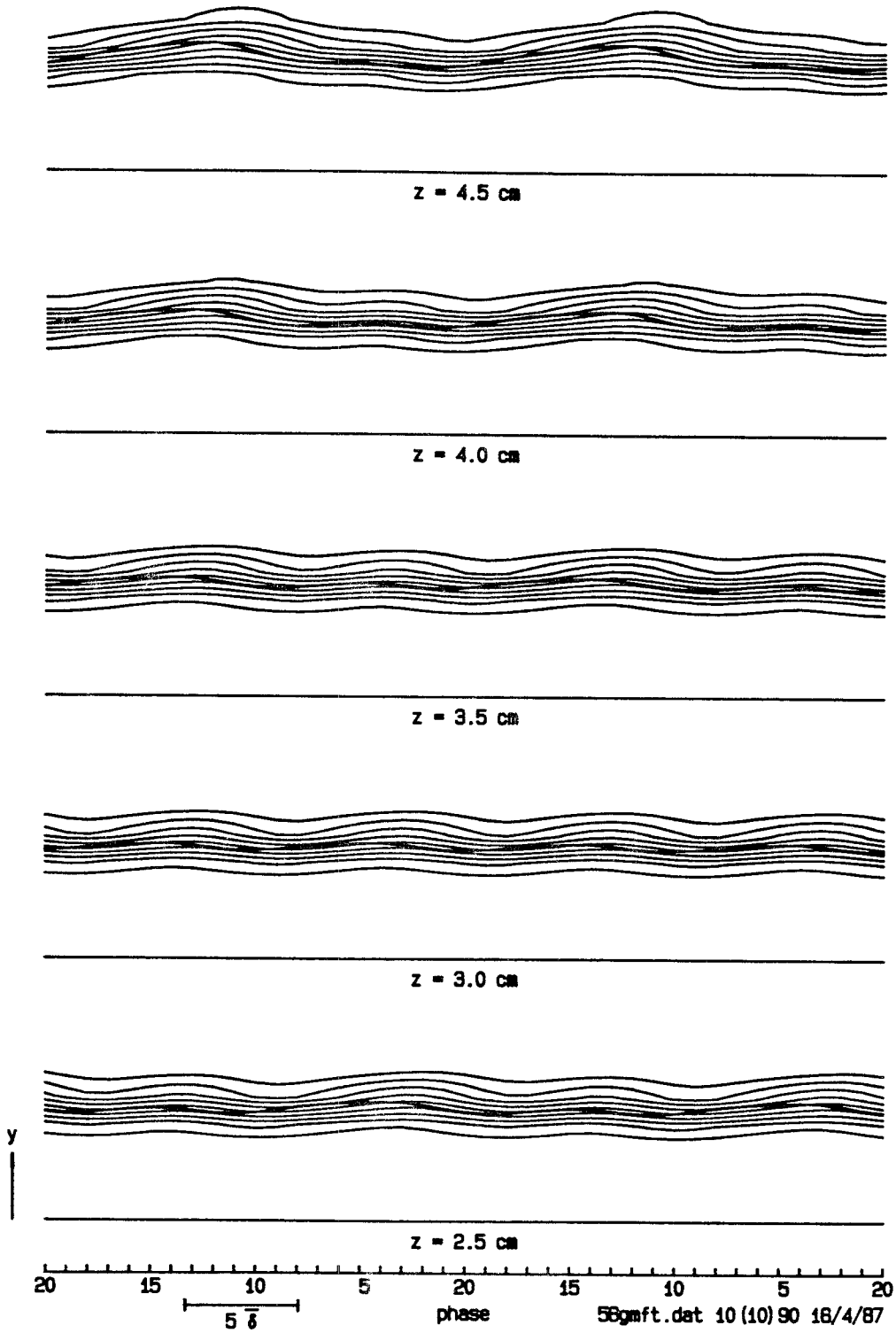

Figure 5.29 (cont'd.). Intermittency $\langle\gamma\rangle$ in the $t-y$ plane.

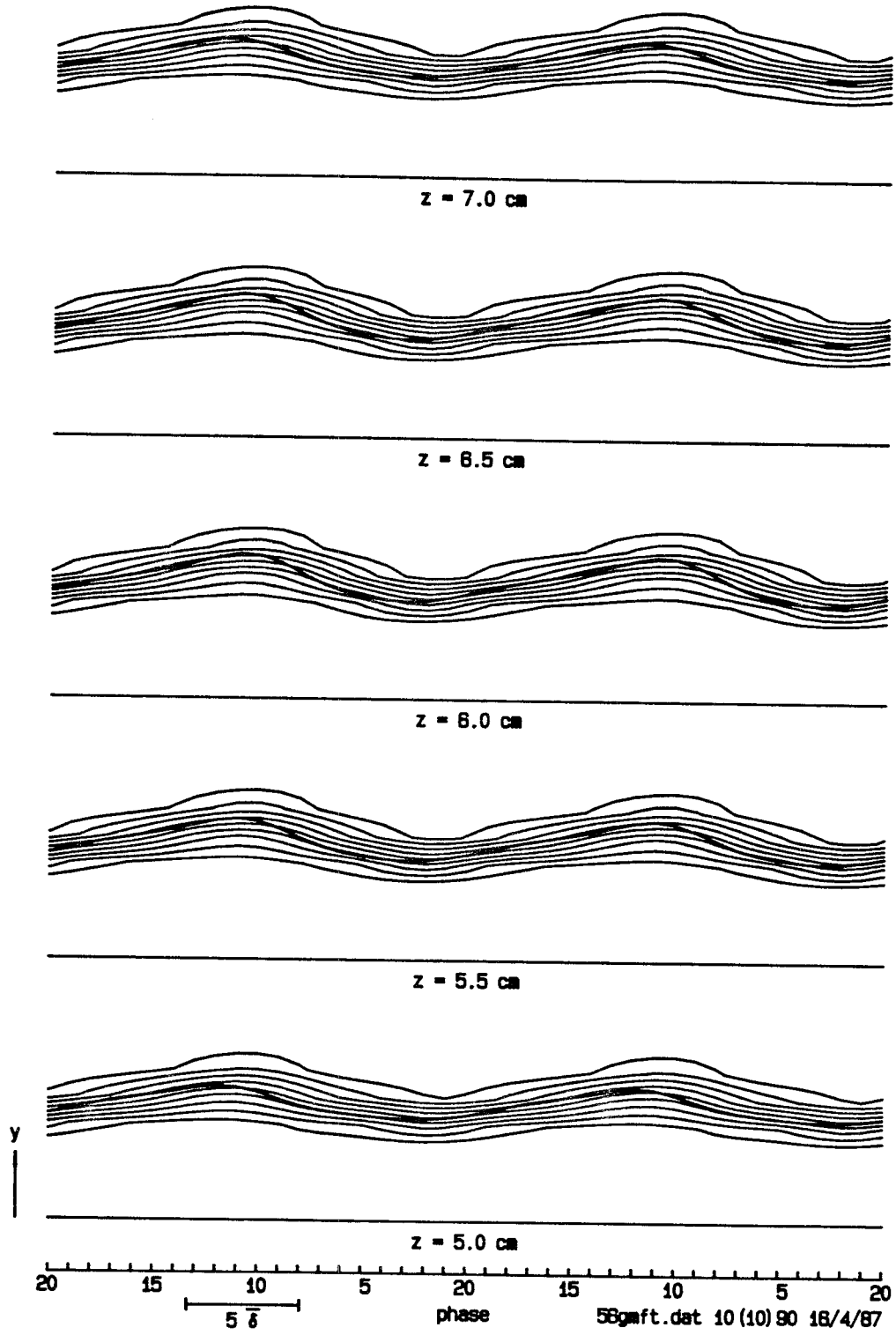

Figure 5.29 (cont'd.). Intermittency $\langle\gamma\rangle$ in the $t-y$ plane.

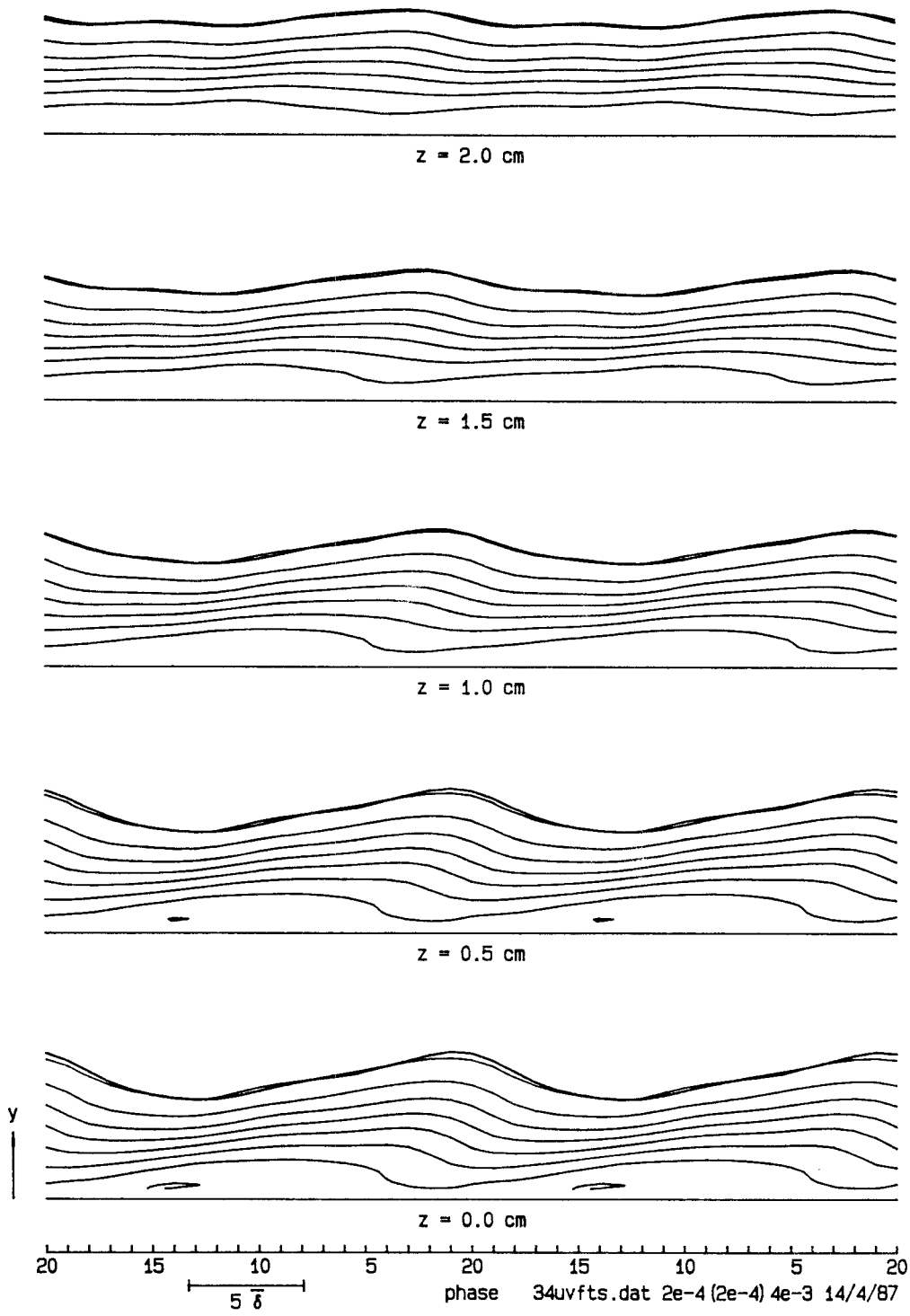

Figure 5.30. Reynolds shearing stress $<u'v'>$ in the $t-y$ plane. Contour interval 0.0002.

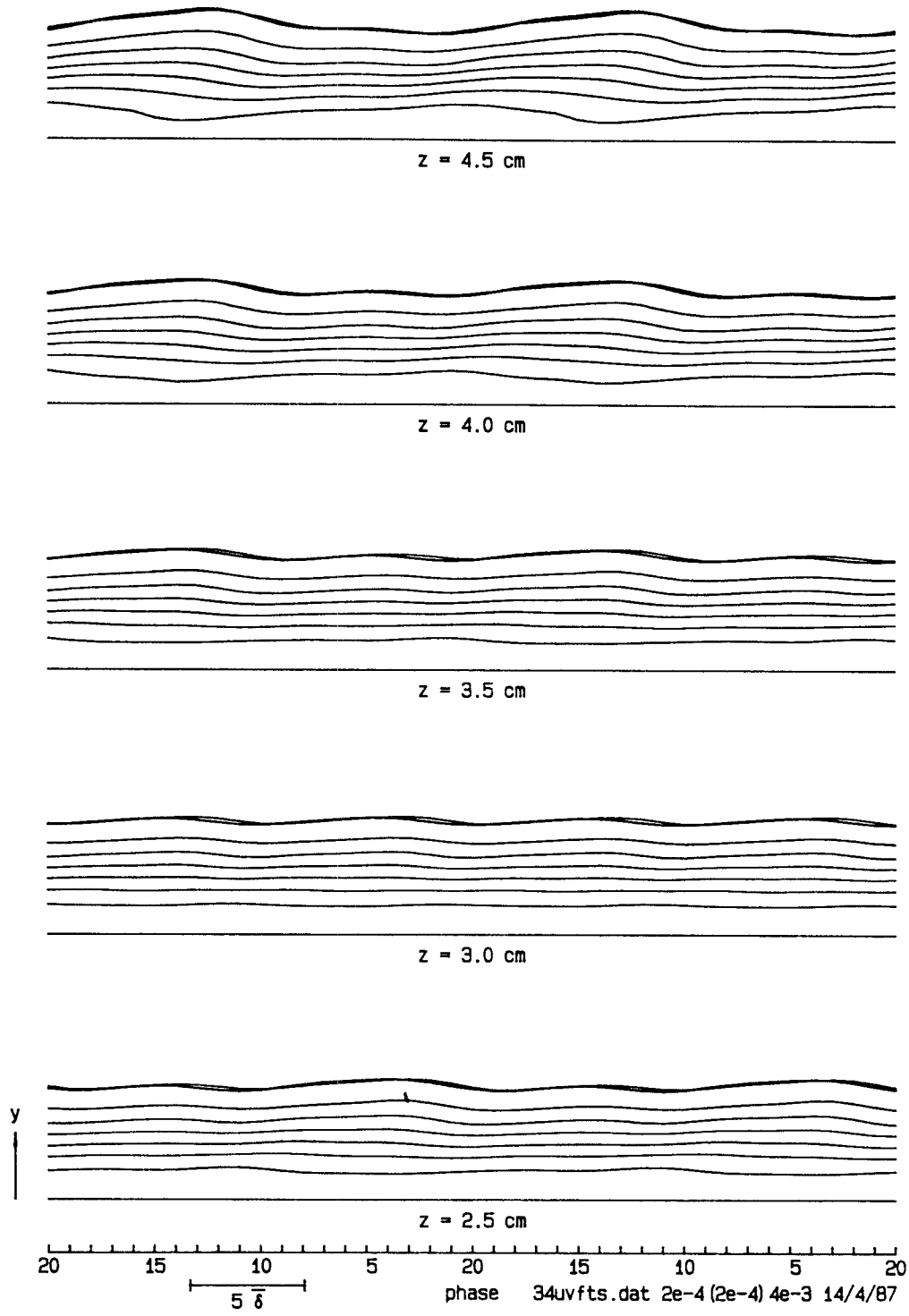

Figure 5.30 (cont'd.). Reynolds shearing stress $<u'v'>$ in the $t-y$ plane.

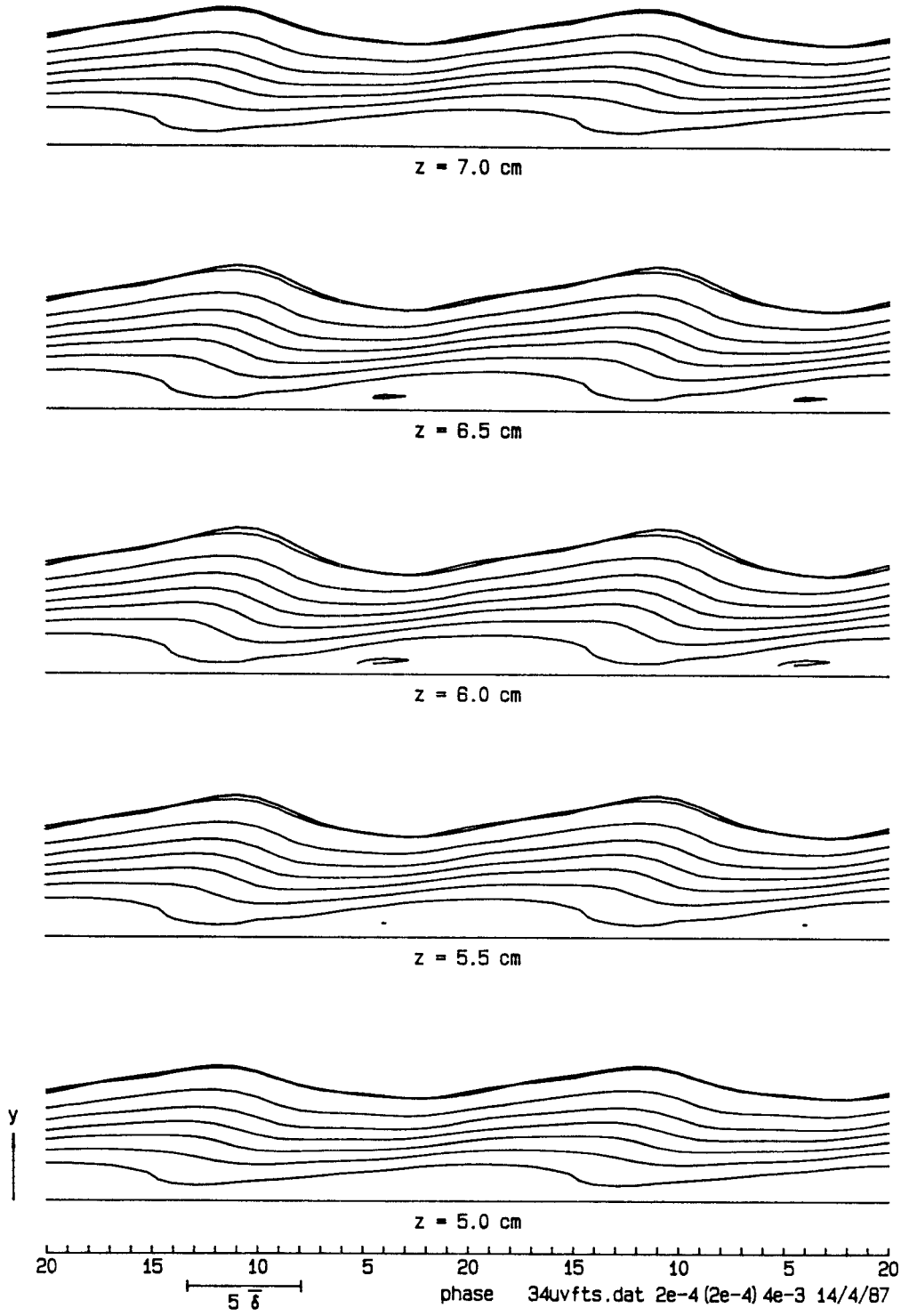

Figure 5.30 (cont'd.). Reynolds shearing stress $<u'v'>$ in the $t-y$ plane.

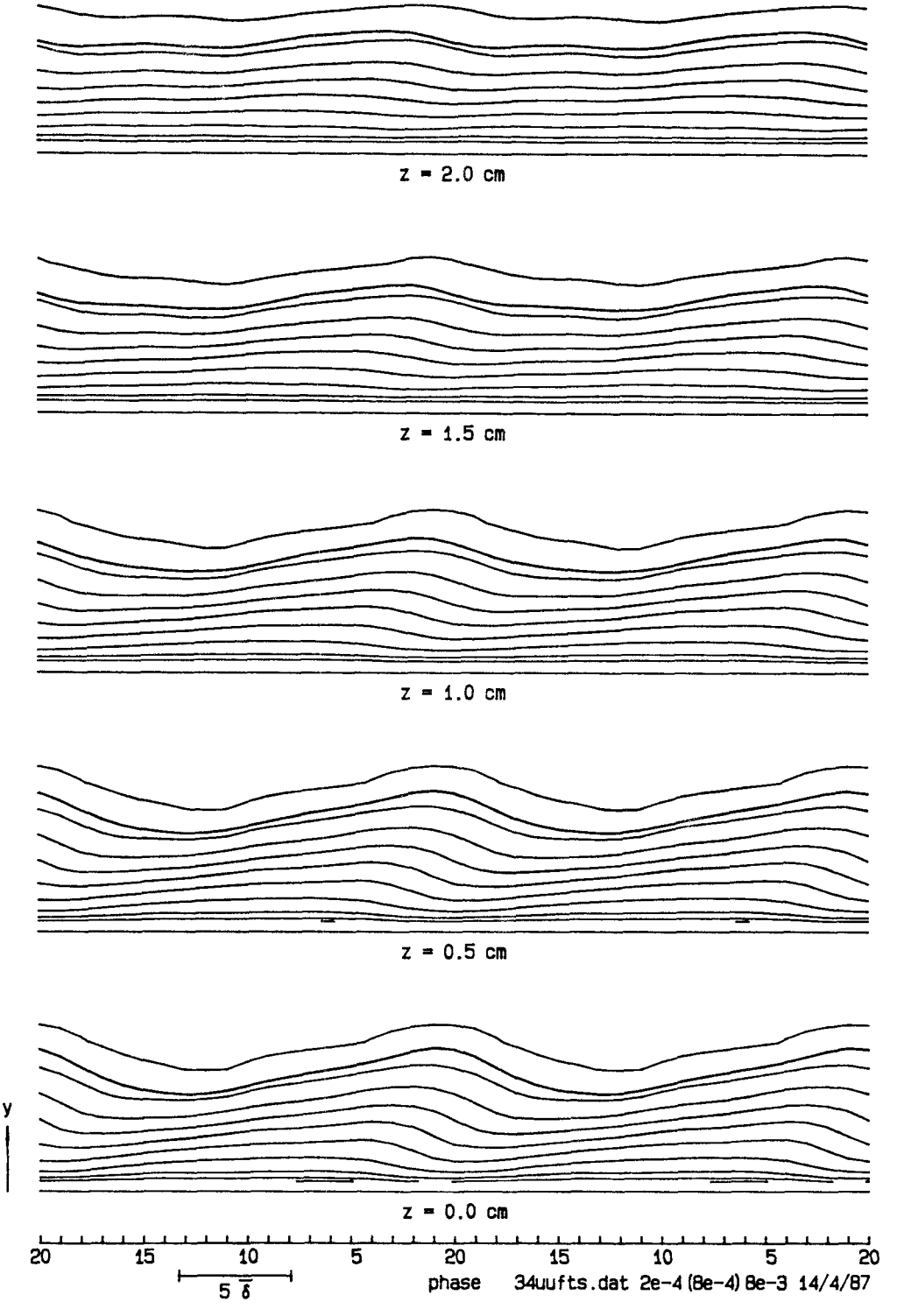

Figure 5.31. Reynolds normal stress $<u'u'>$ in the $t-y$ plane. Contour interval 0.0008.

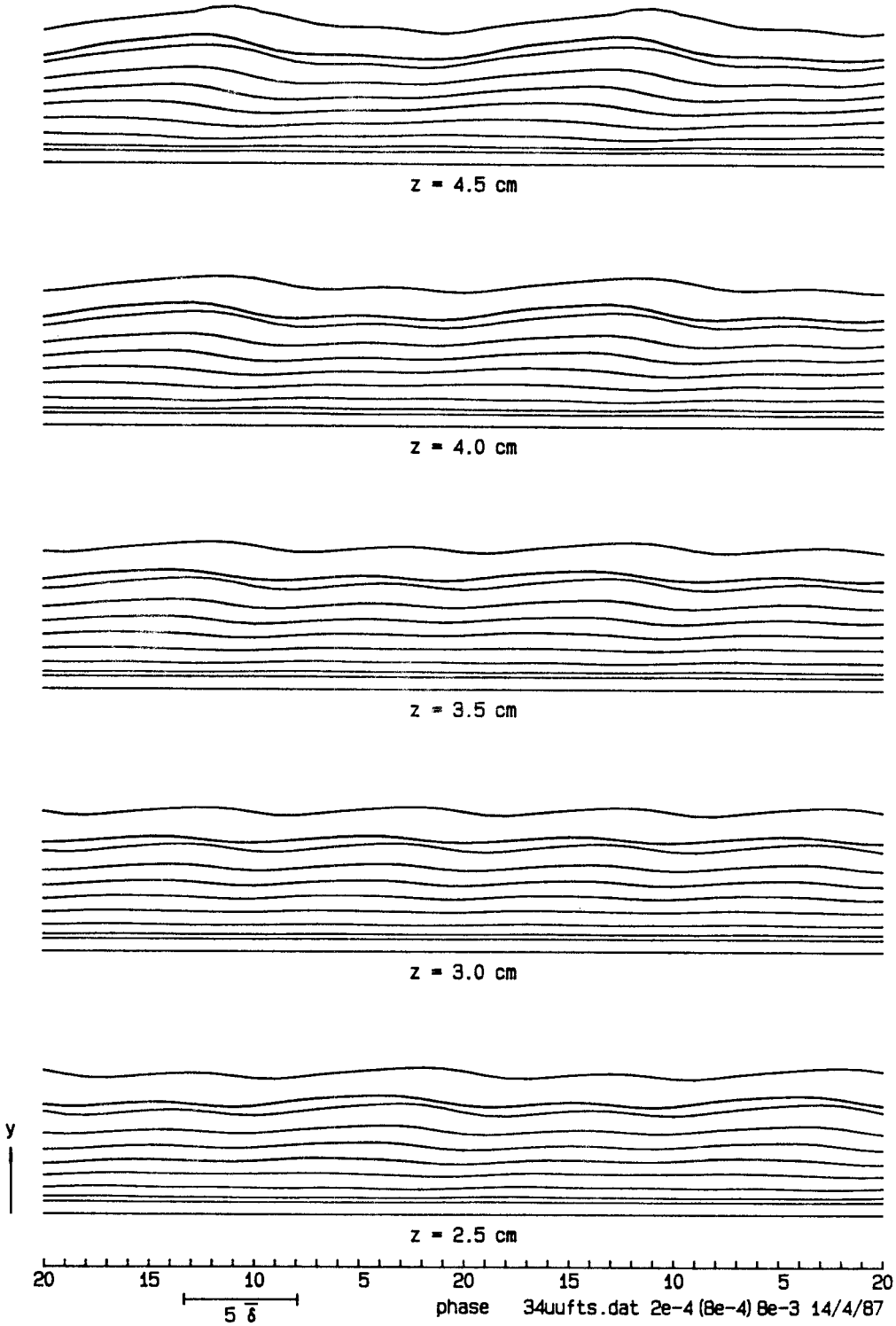

Figure 5.31 (cont'd.). Reynolds normal stress $<u'u'>$ in the $t-y$ plane.

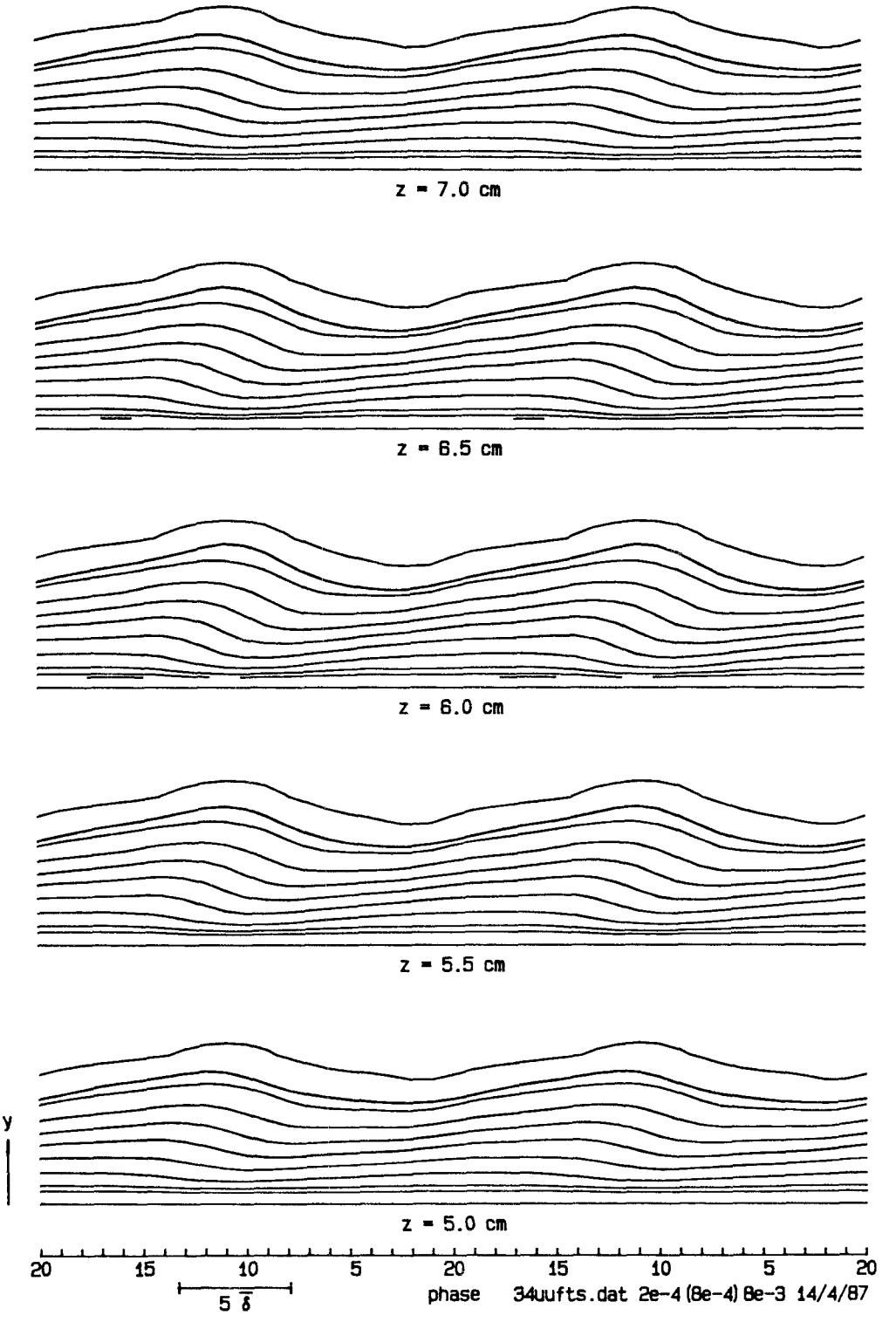

Figure 5.31 (cont'd.). Reynolds normal stress $<u'u'>$ in the $t-y$ plane.

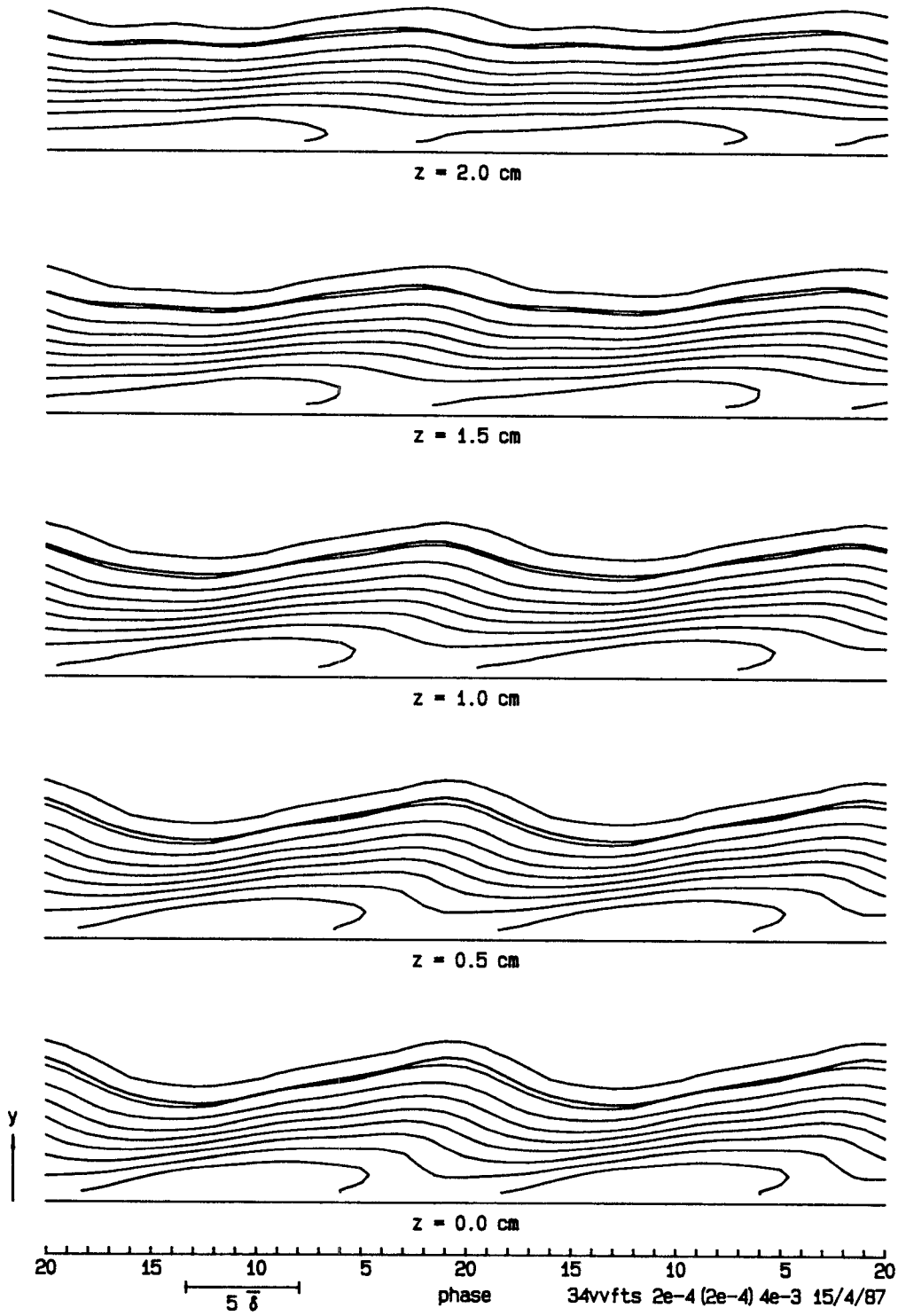

Figure 5.32. Reynolds normal stress $\langle v'v' \rangle$ in the $t-y$ plane. Contour interval 0.0002.

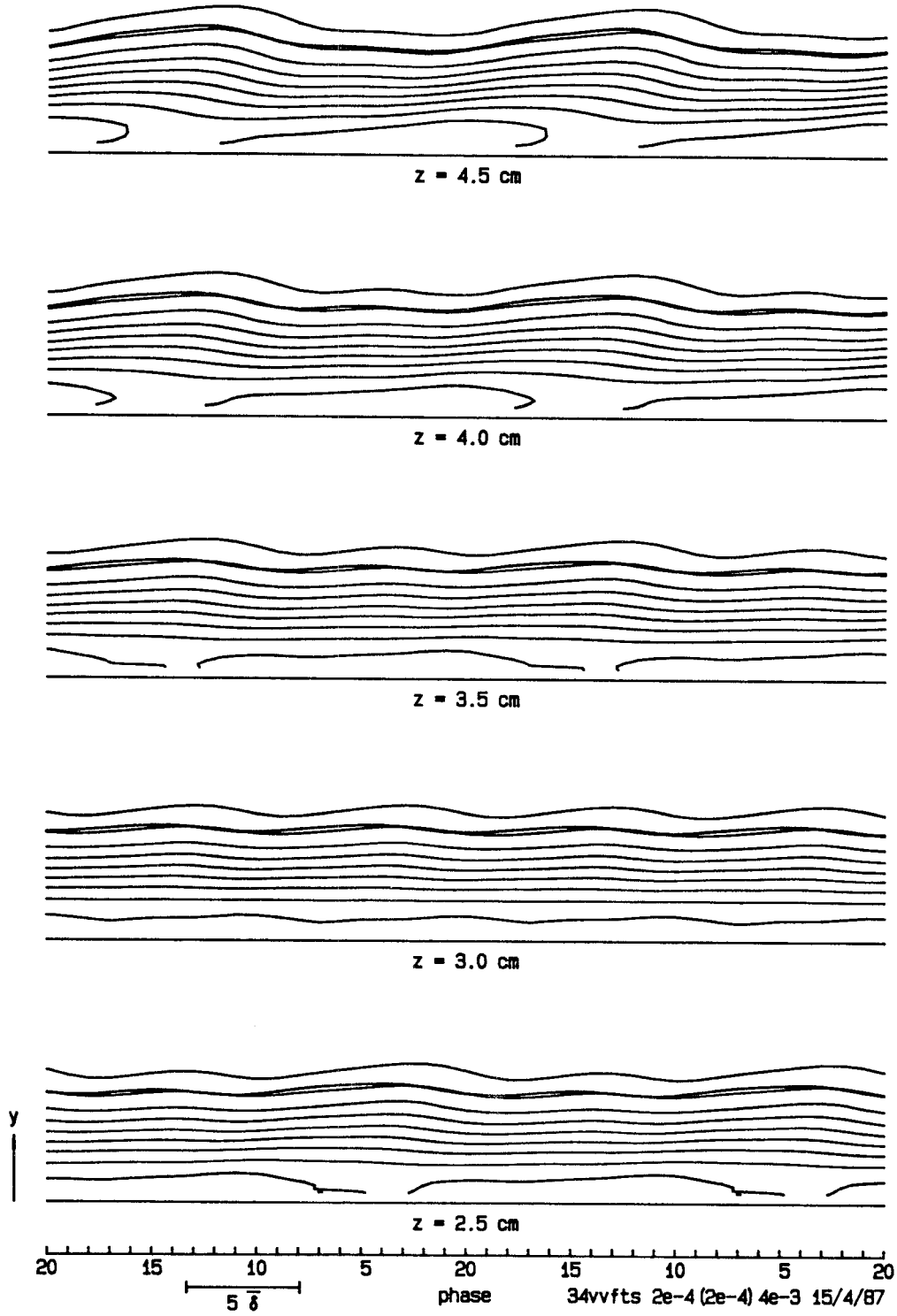

Figure 5.32 (cont'd.). Reynolds normal stress $\langle v'v' \rangle$ in the $t-y$ plane.

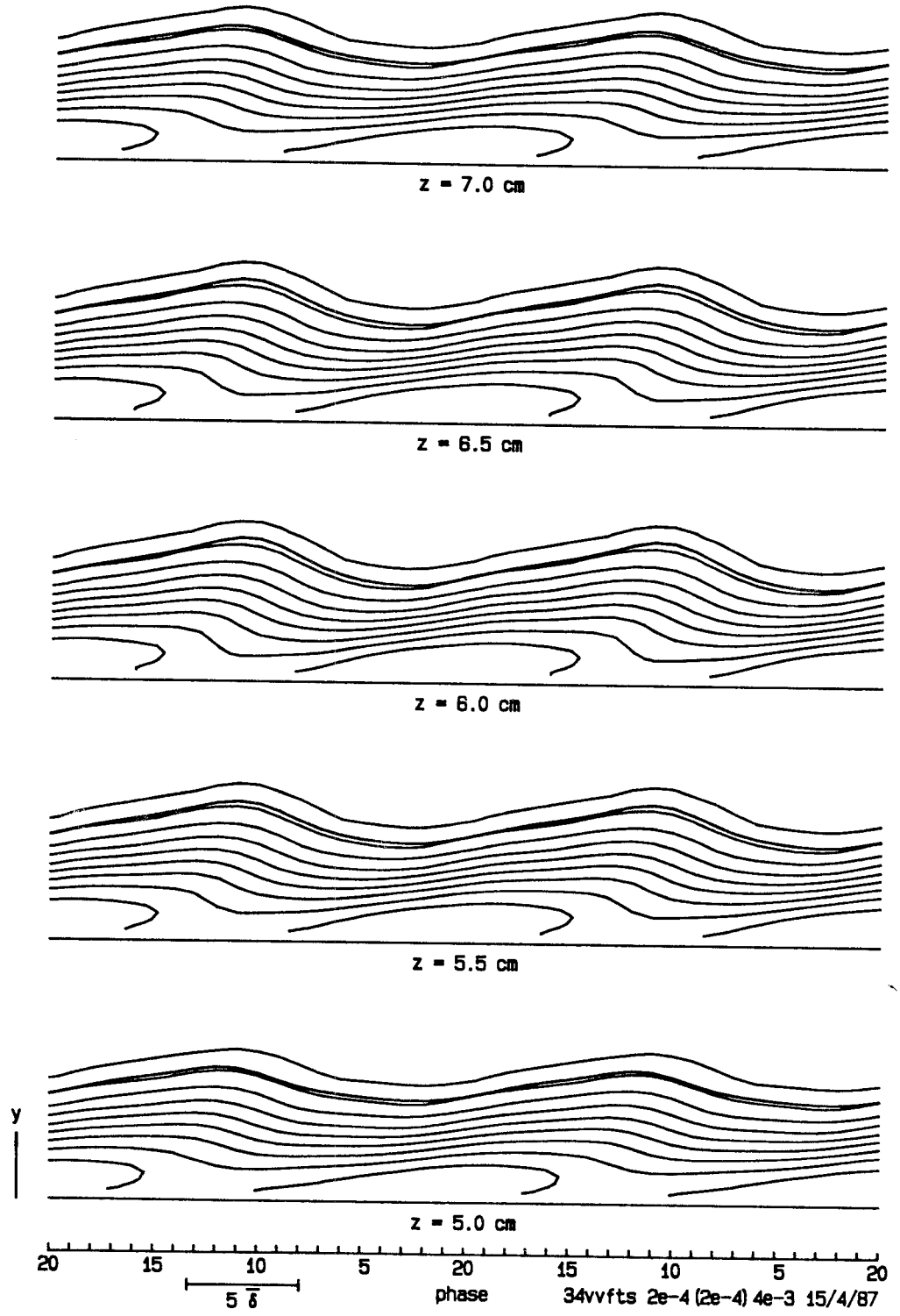

Figure 5.32 (cont'd.). Reynolds normal stress $\langle v'v' \rangle$ in the $t-y$ plane.

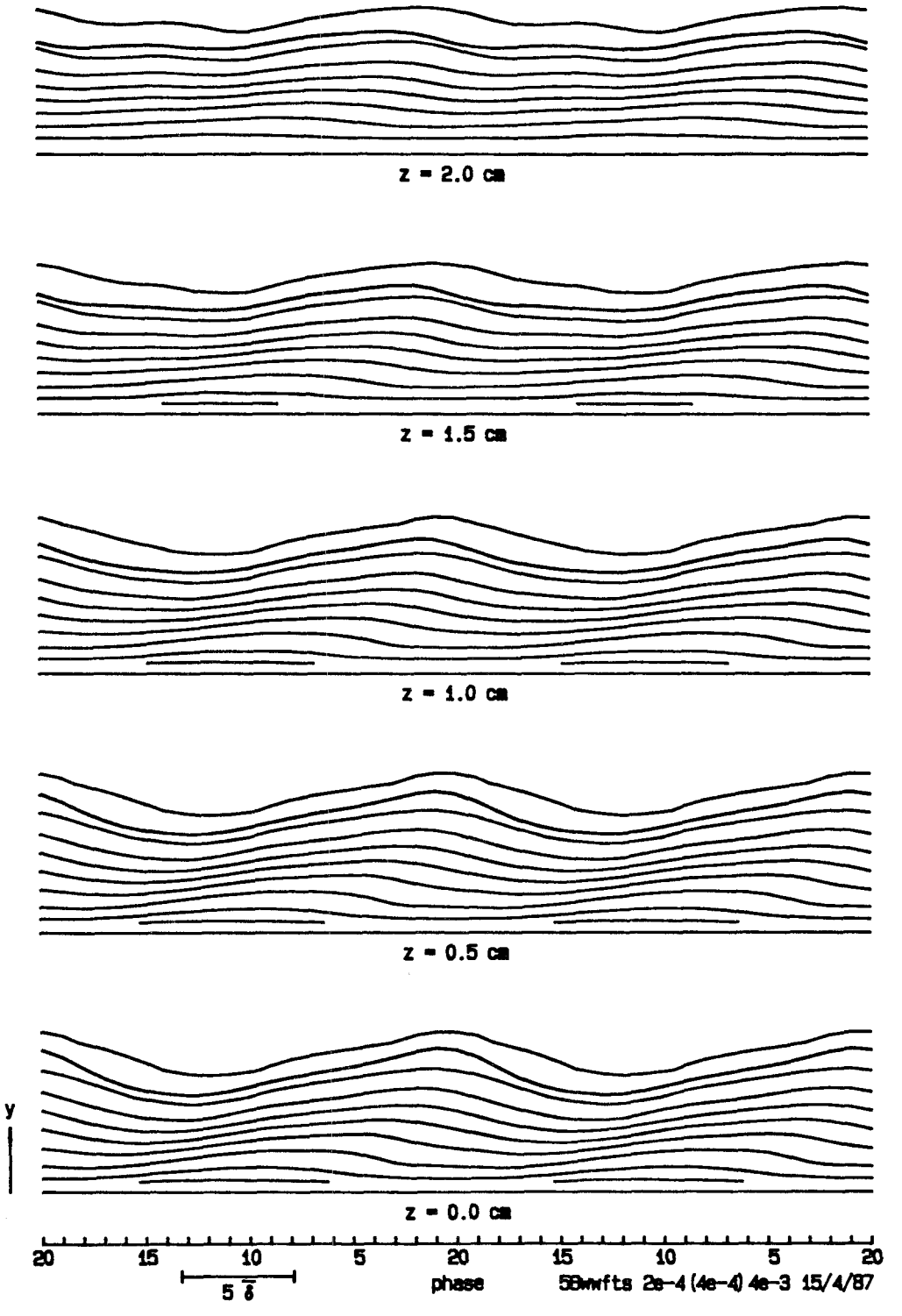

Figure 5.33. Reynolds normal stress $\langle w'w' \rangle$ in the $t-y$ plane. Contour interval 0.0004.

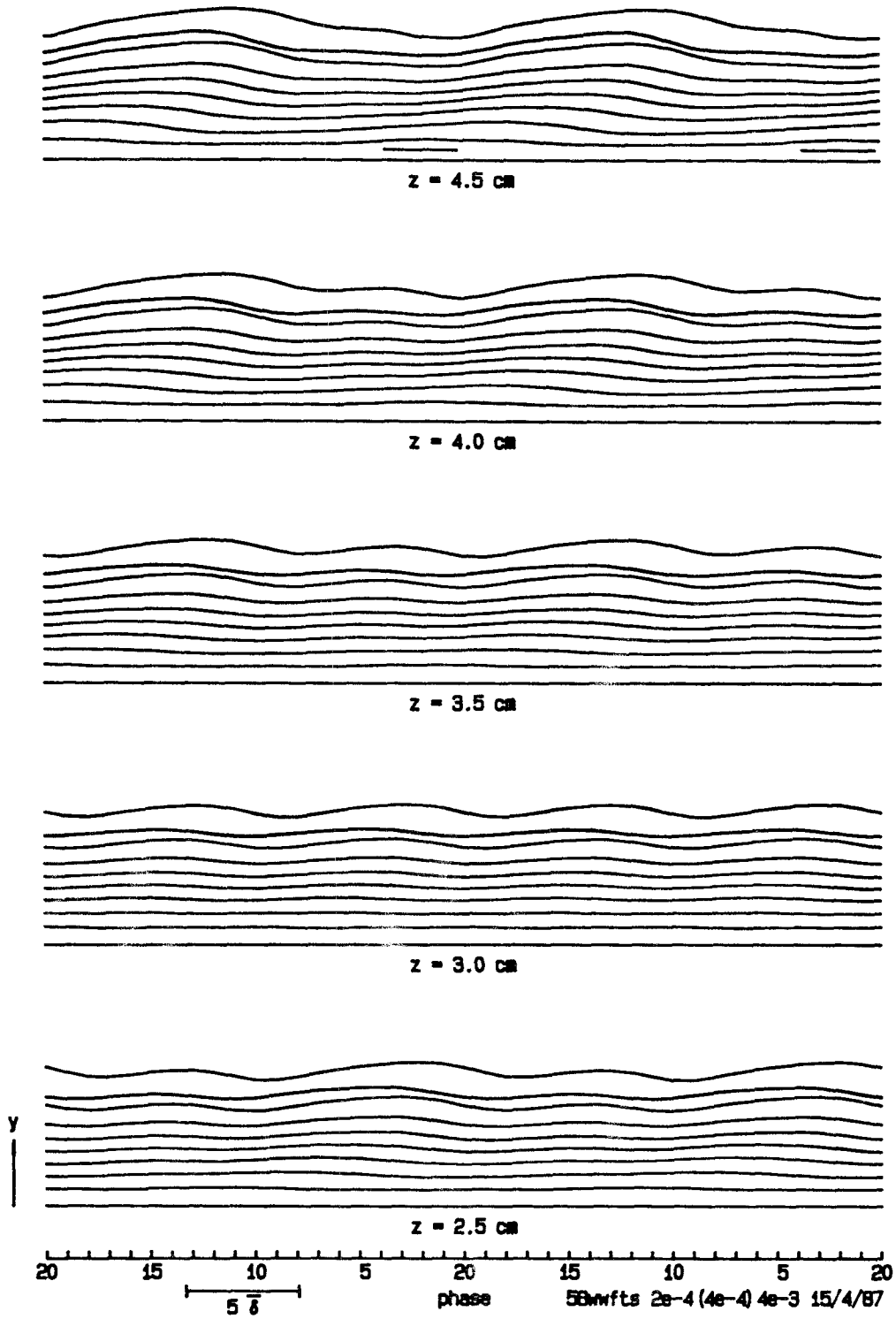

Figure 5.33 (cont'd.). Reynolds normal stress $<w'w'>$ in the $t-y$ plane.

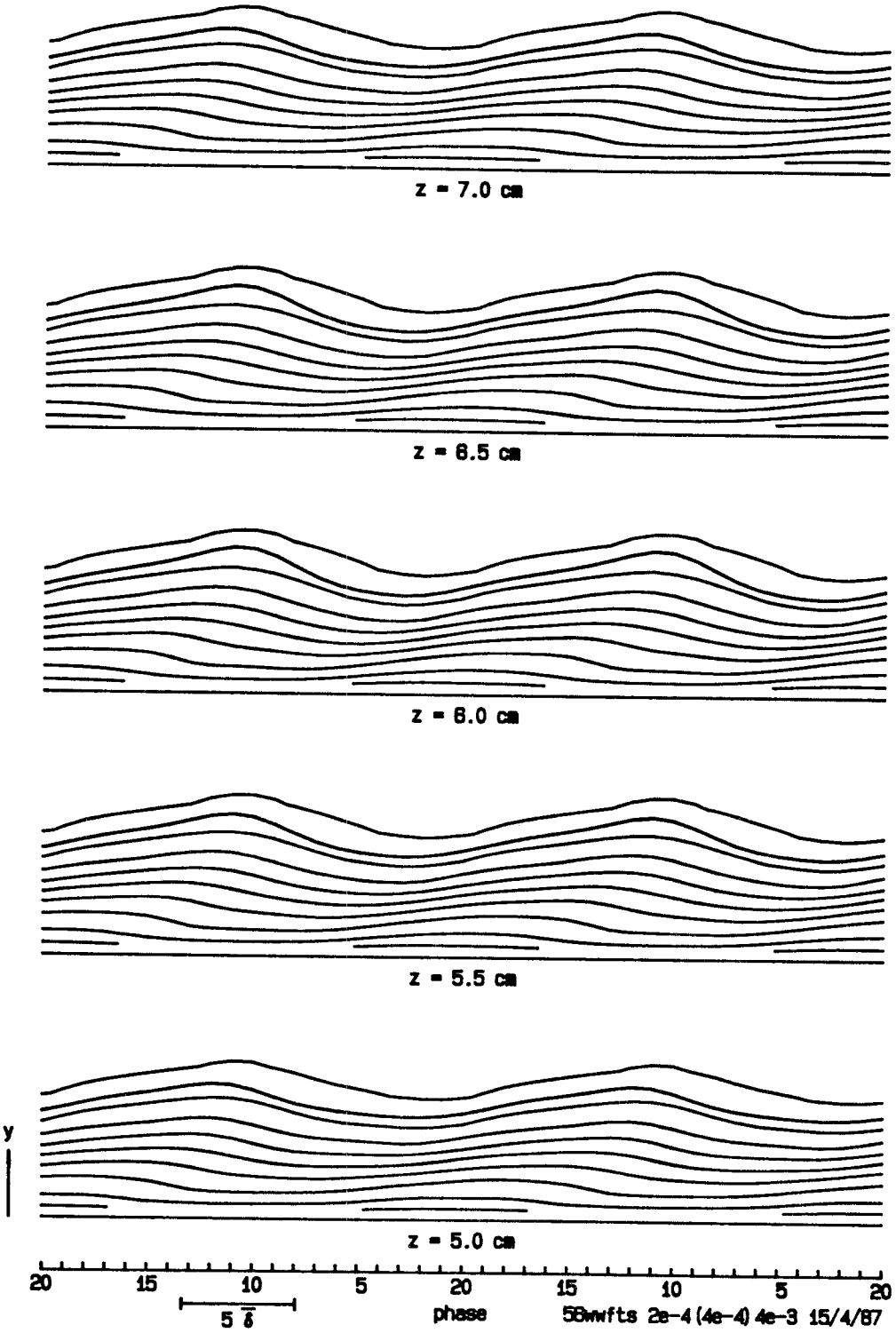

Figure 5.33 (cont'd.). Reynolds normal stress $\langle w'w' \rangle$ in the $t-y$ plane.

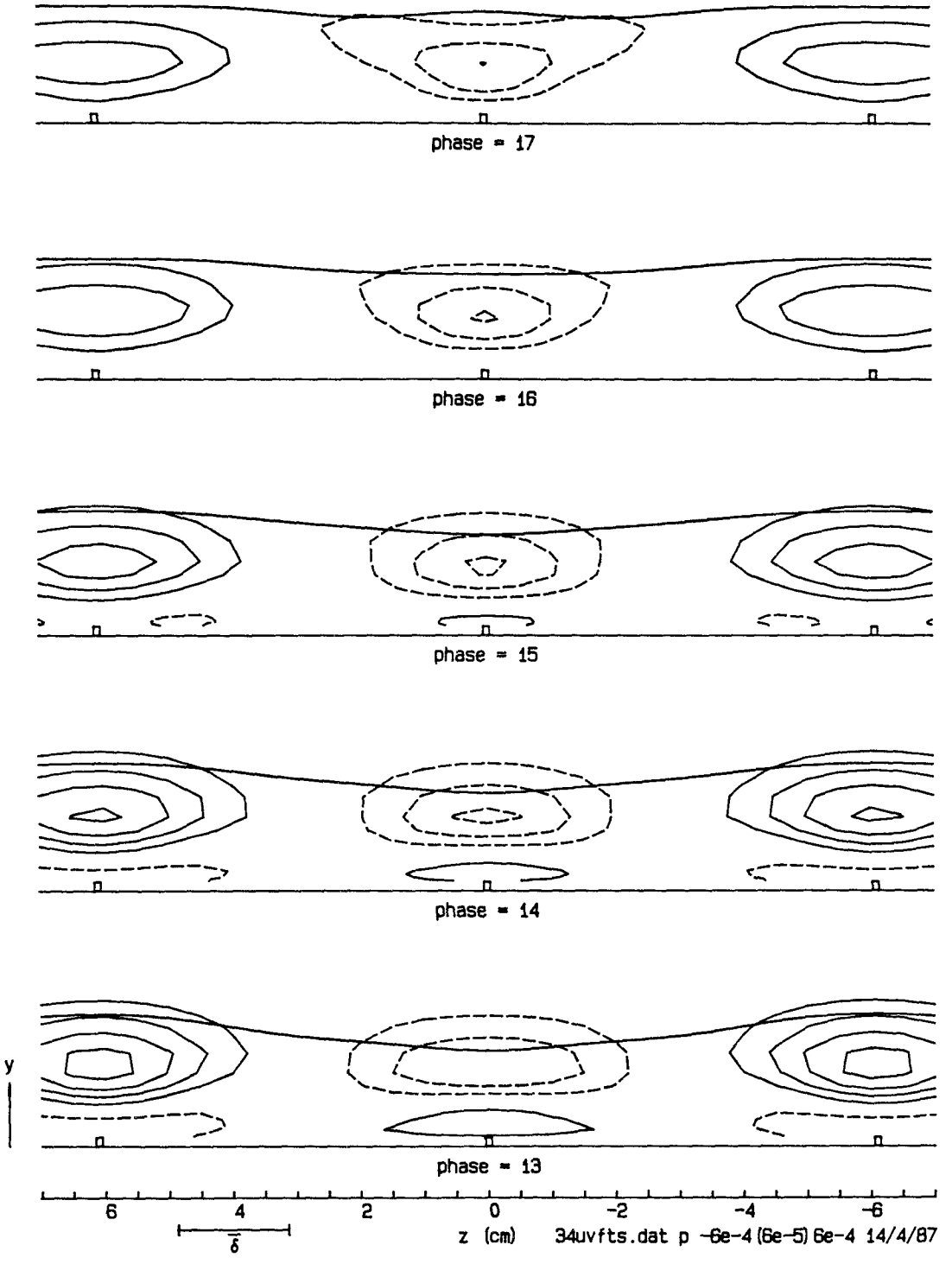

Figure 5.34. Reynolds shearing-stress perturbation $<u'v'> - \overline{u'v'}$ in the $z-y$ plane. Contour interval 0.00006.

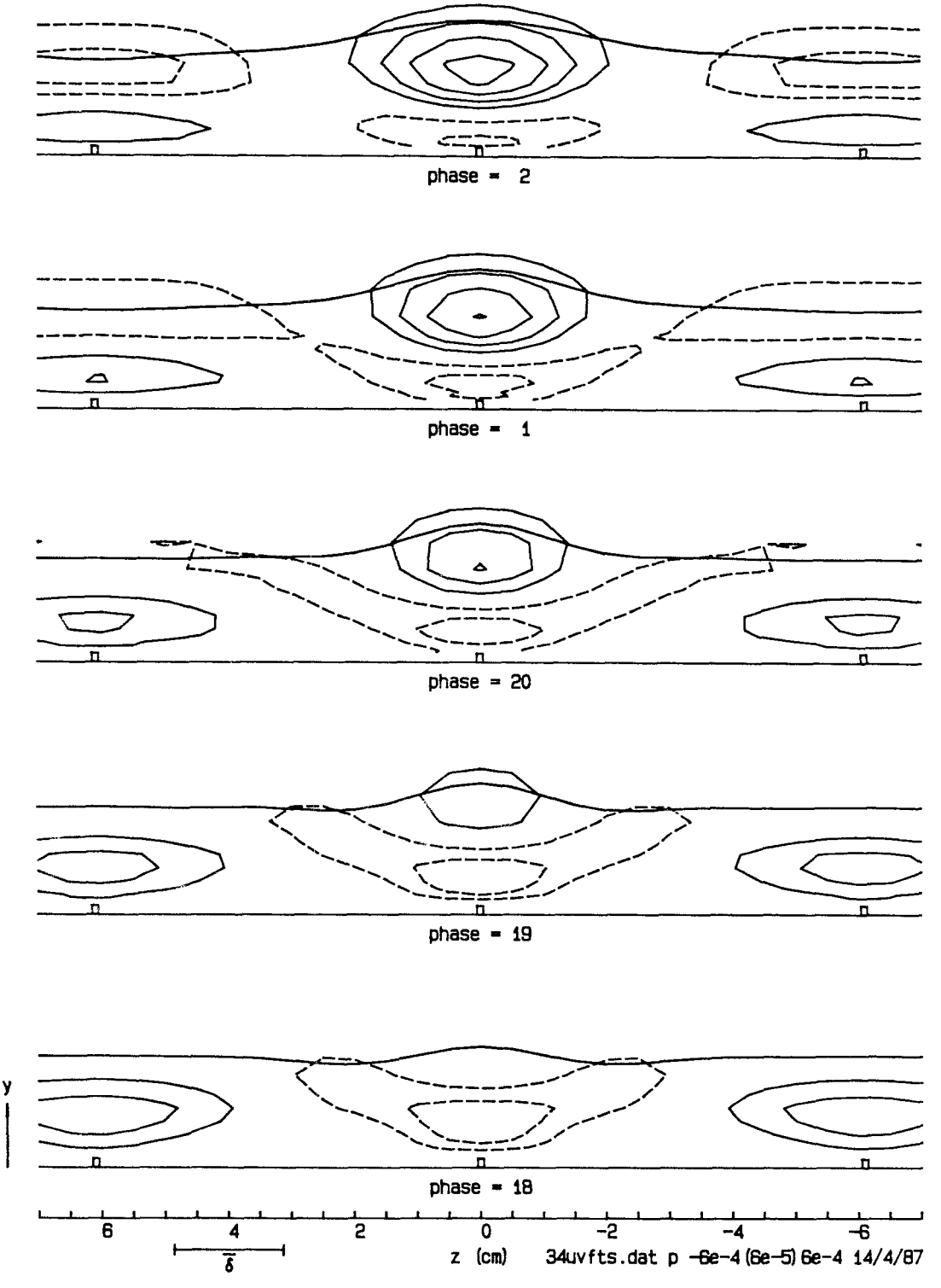

Figure 5.34 (cont'd.). Reynolds shearing-stress perturbation $<u'v'> - \overline{u'v'}$ in the $z-y$ plane.

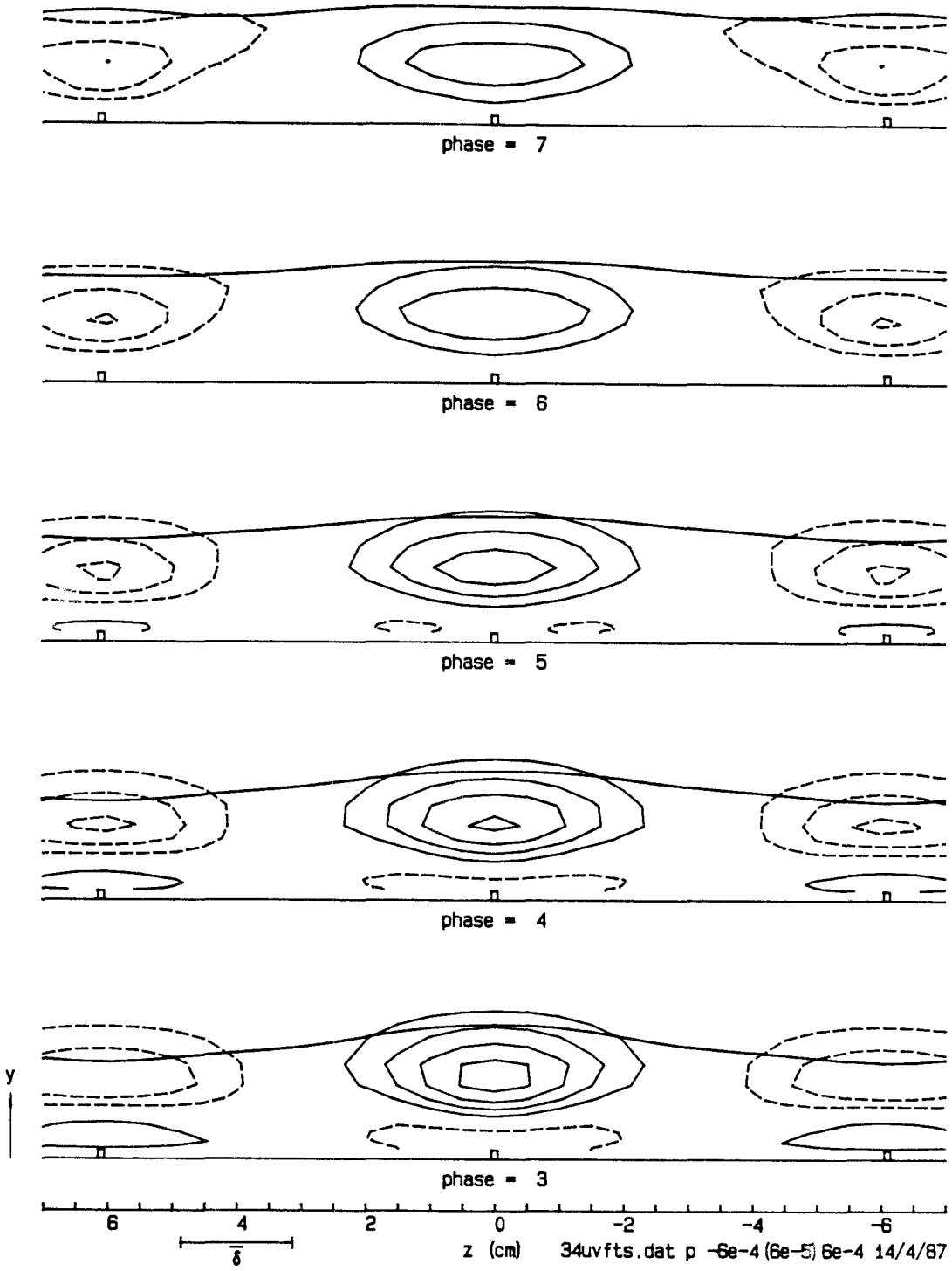

Figure 5.34 (cont'd.). Reynolds shearing-stress perturbation $<u'v'> - \overline{u'v'}$ in the $z-y$ plane.

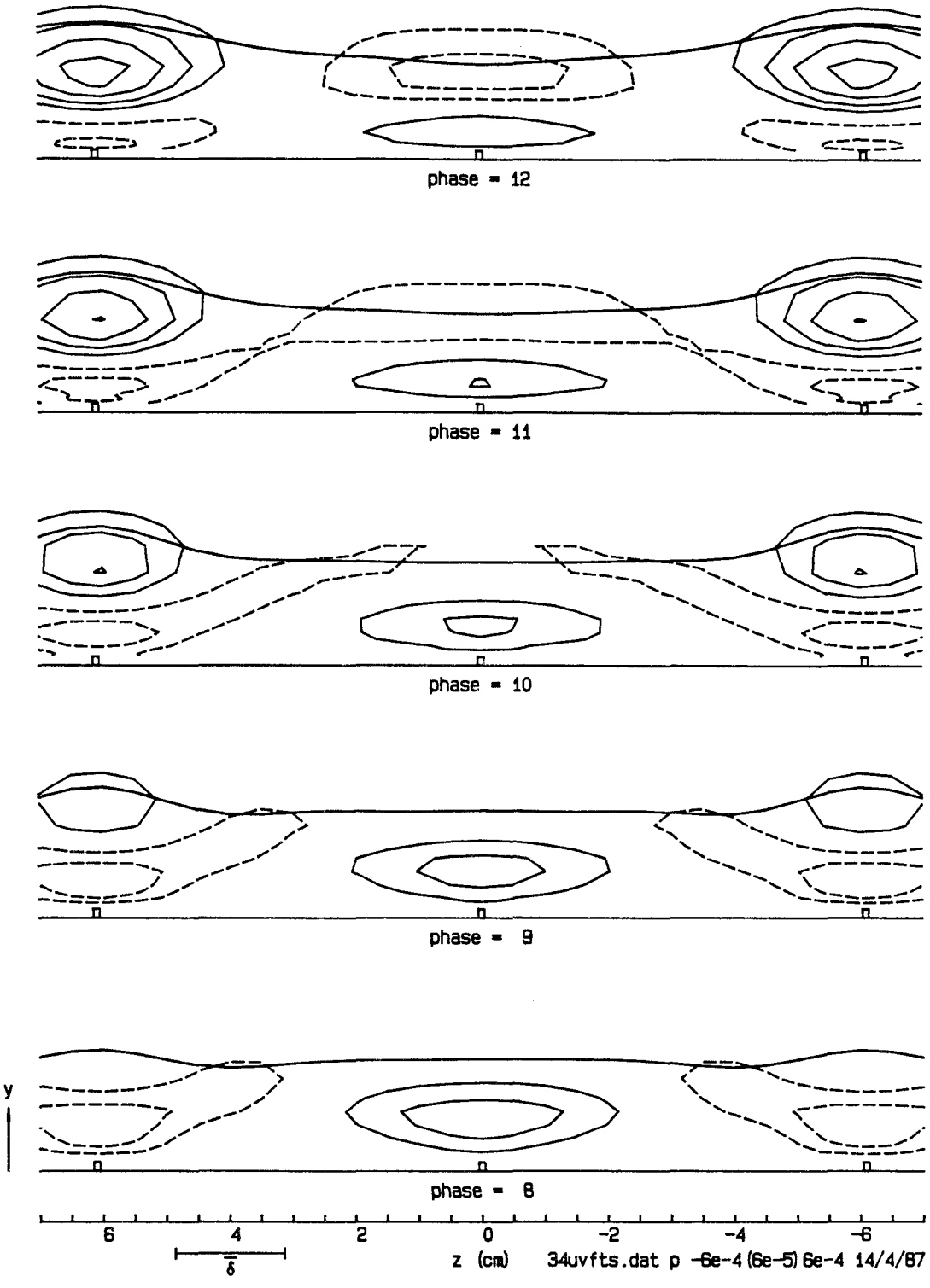

Figure 5.34 (cont'd.). Reynolds shearing-stress perturbation $<u'v'> - \overline{u'v'}$ in the $z-y$ plane.

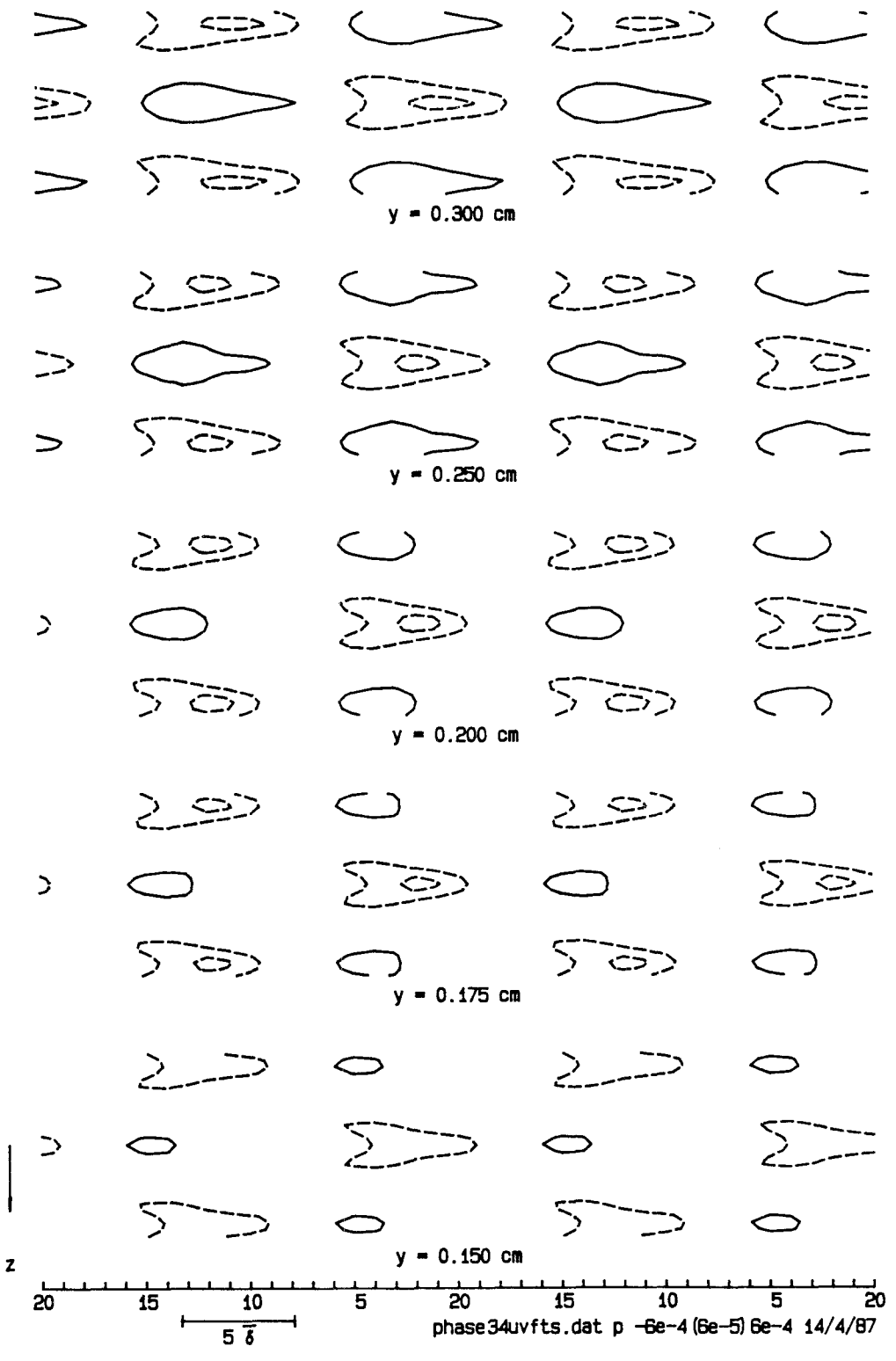

Figure 5.35. Reynolds shearing-stress perturbation $<u'v'> - \overline{u'v'}$ in the $t-z$ plane. Contour interval 0.00006.

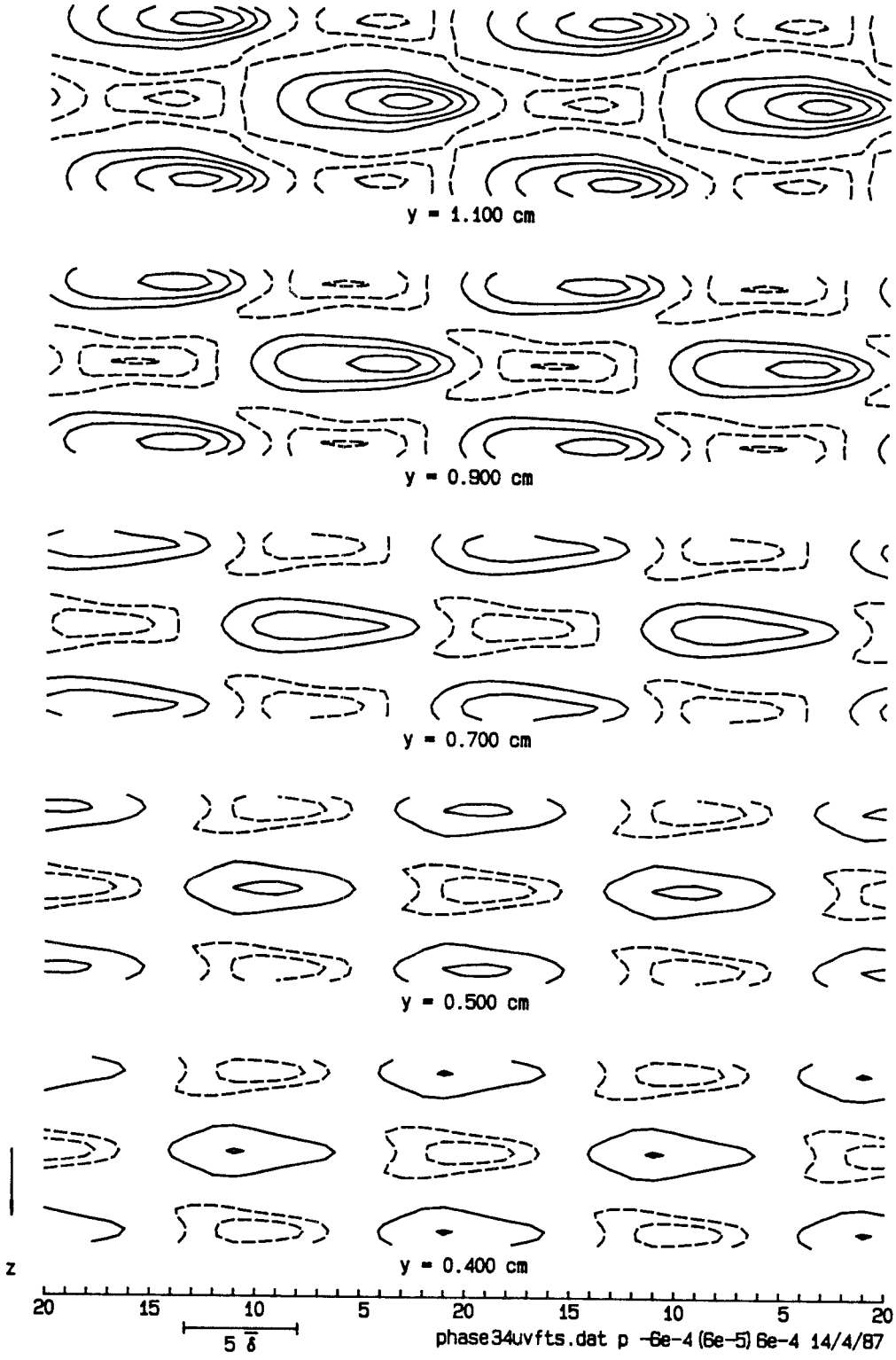

Figure 5.35 (cont'd.). Reynolds shearing-stress perturbation $<u'v'> - \overline{u'v'}$ in the $t-z$ plane.

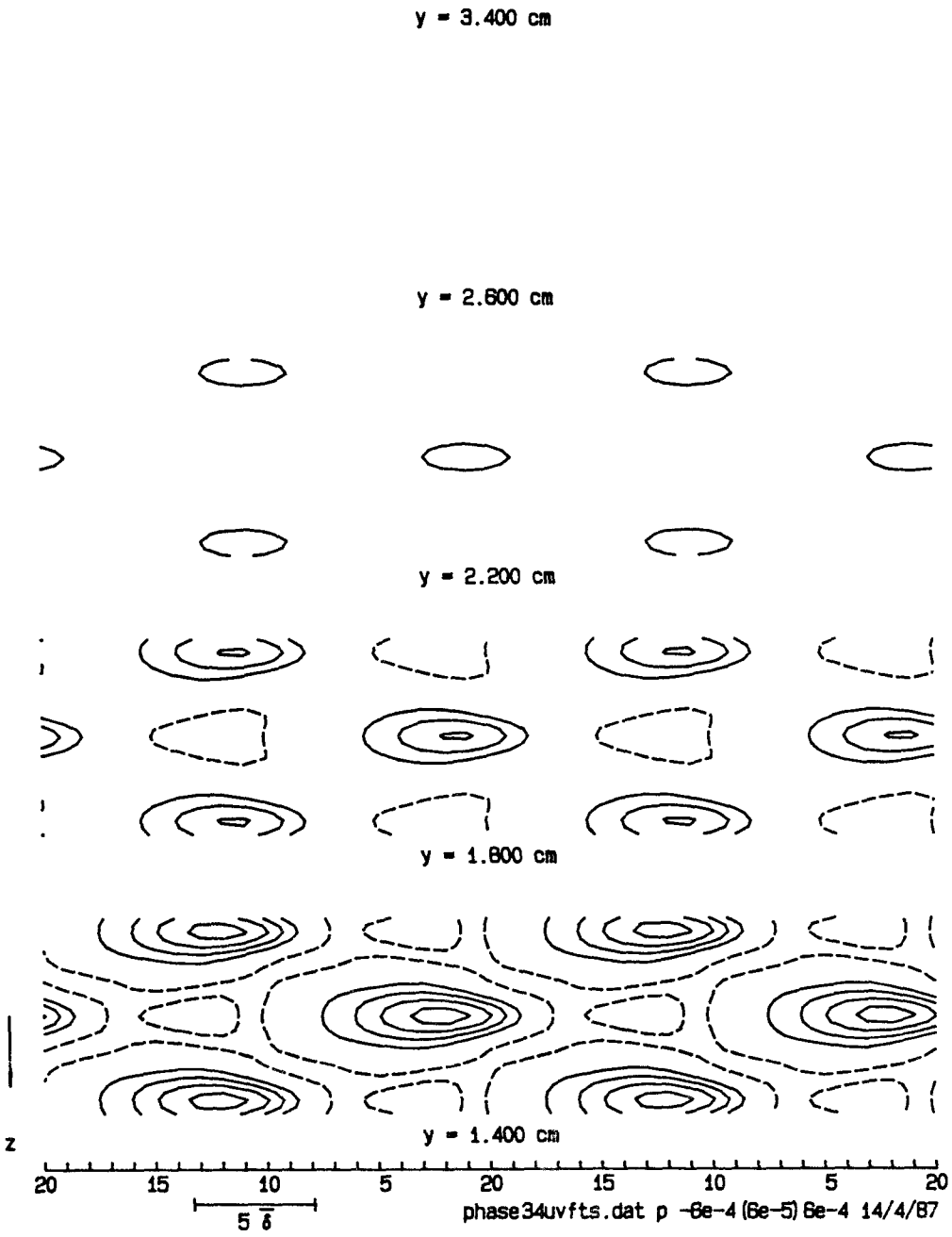

Figure 5.35 (cont'd.). Reynolds shearing-stress perturbation $<u'v'> - \overline{u'v'}$ in the $t-z$ plane.

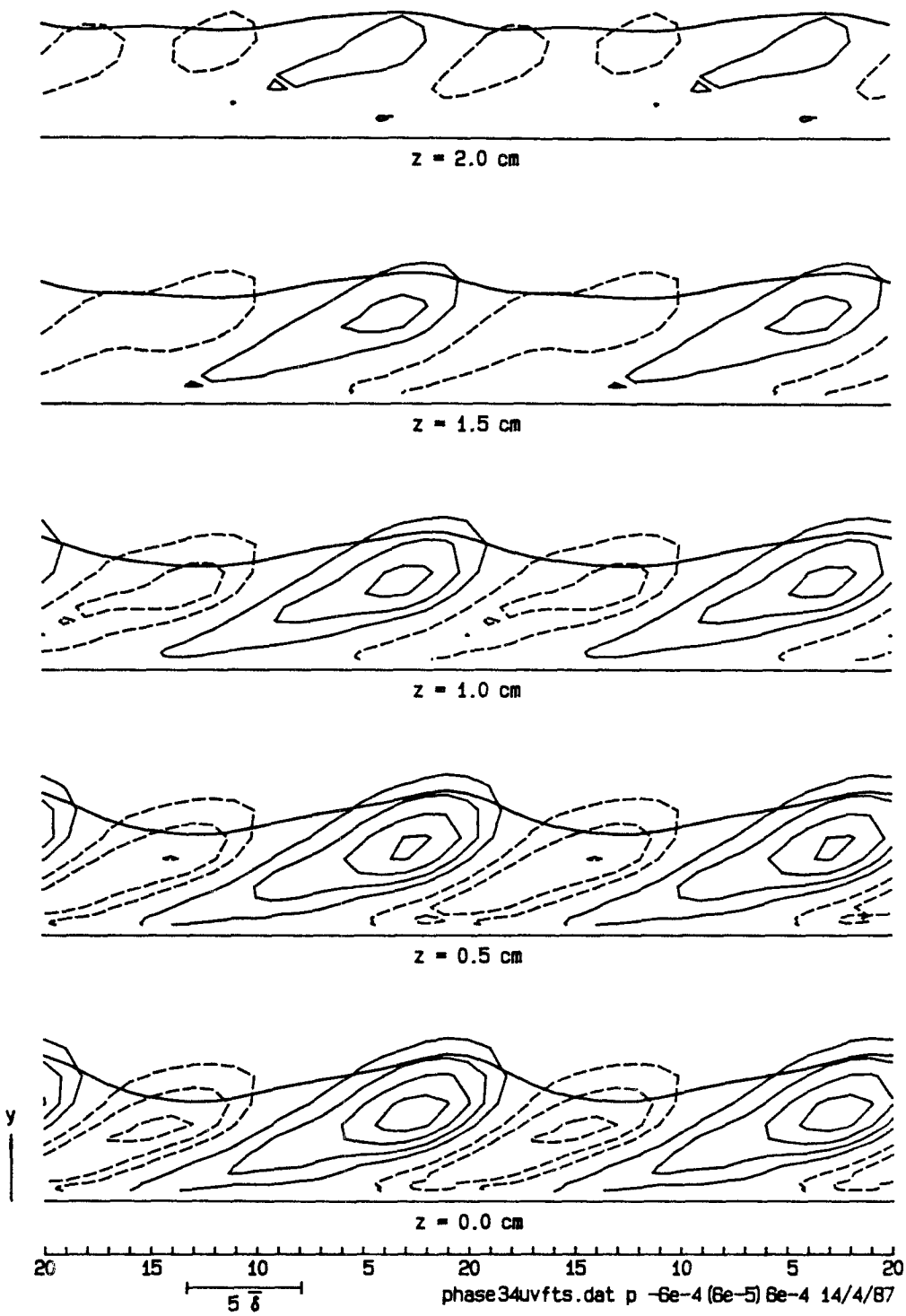

Figure 5.36. Reynolds shearing-stress perturbation $<u'v'> - \overline{u'v'}$ in the $t-y$ plane. Contour interval 0.00006.

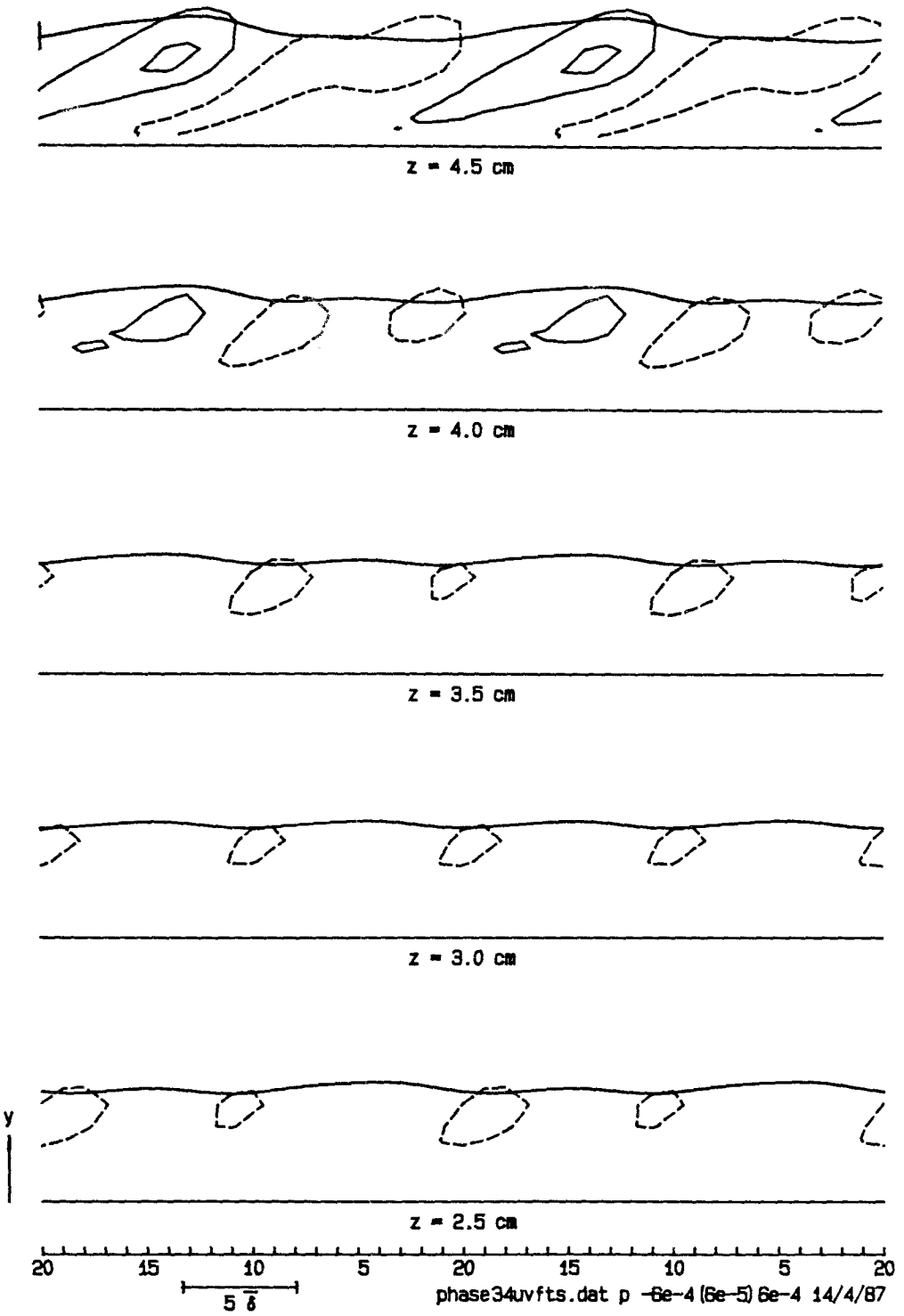

Figure 5.36 (cont'd.). Reynolds shearing-stress perturbation $<u'v'> - \overline{u'v'}$ in the $t-y$ plane.

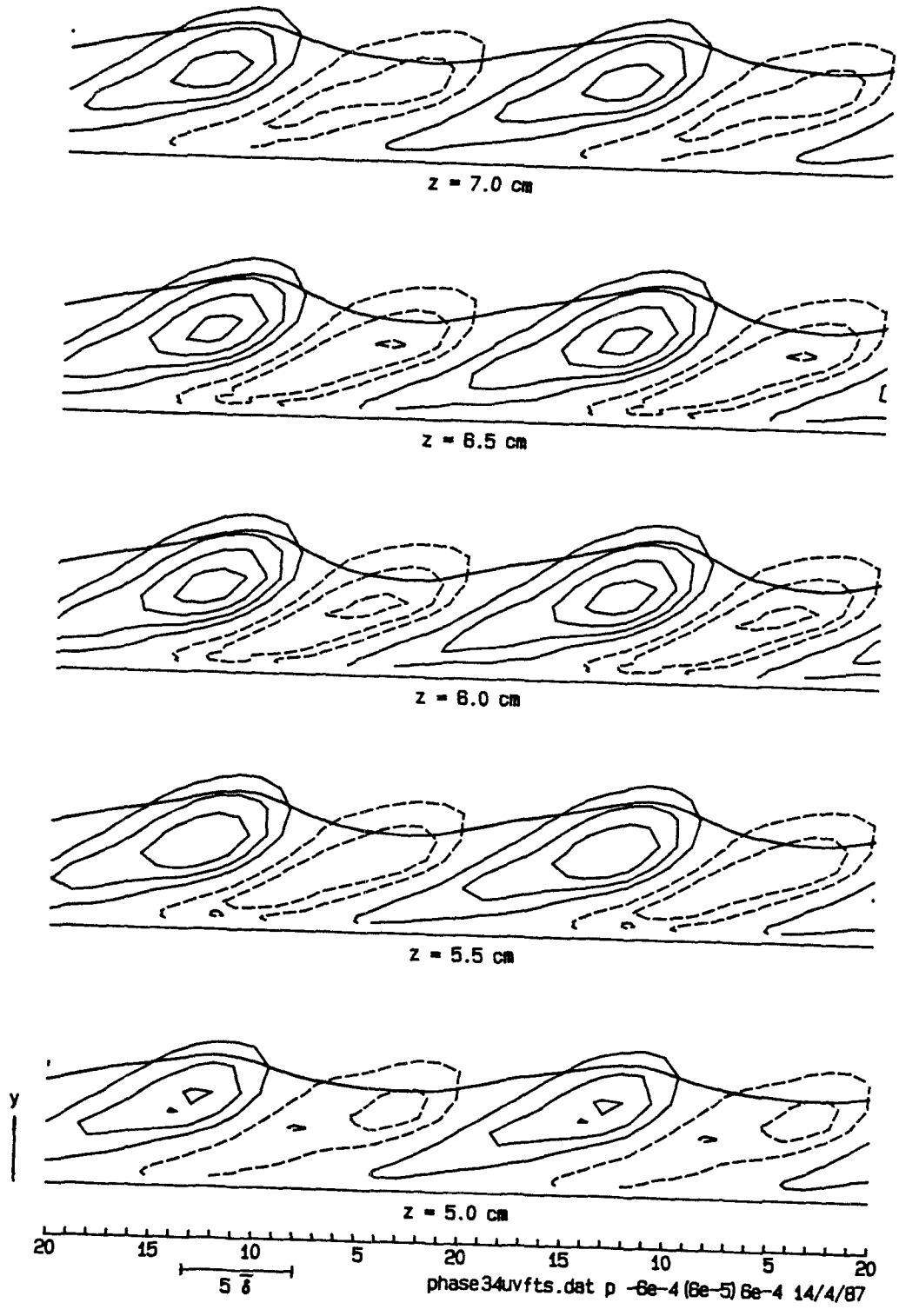

Figure 5.36 (cont'd.). Reynolds shearing-stress perturbation $<u'v'> - \overline{u'v'}$ in the t–y plane.

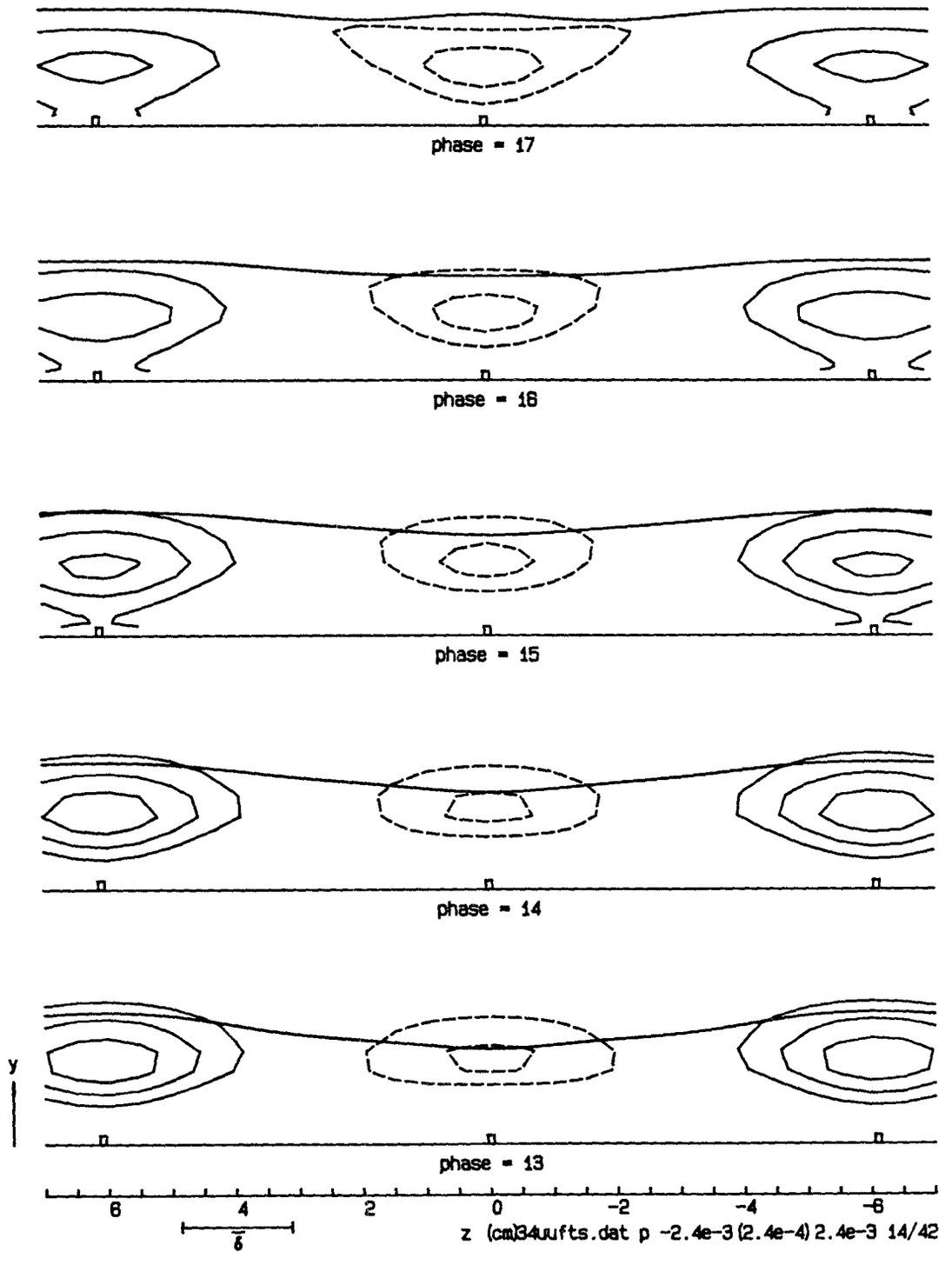

Figure 5.37. Reynolds normal-stress perturbation $<u'u'> - \overline{u'u'}$ in the $z-y$ plane. Contour interval 0.00024.

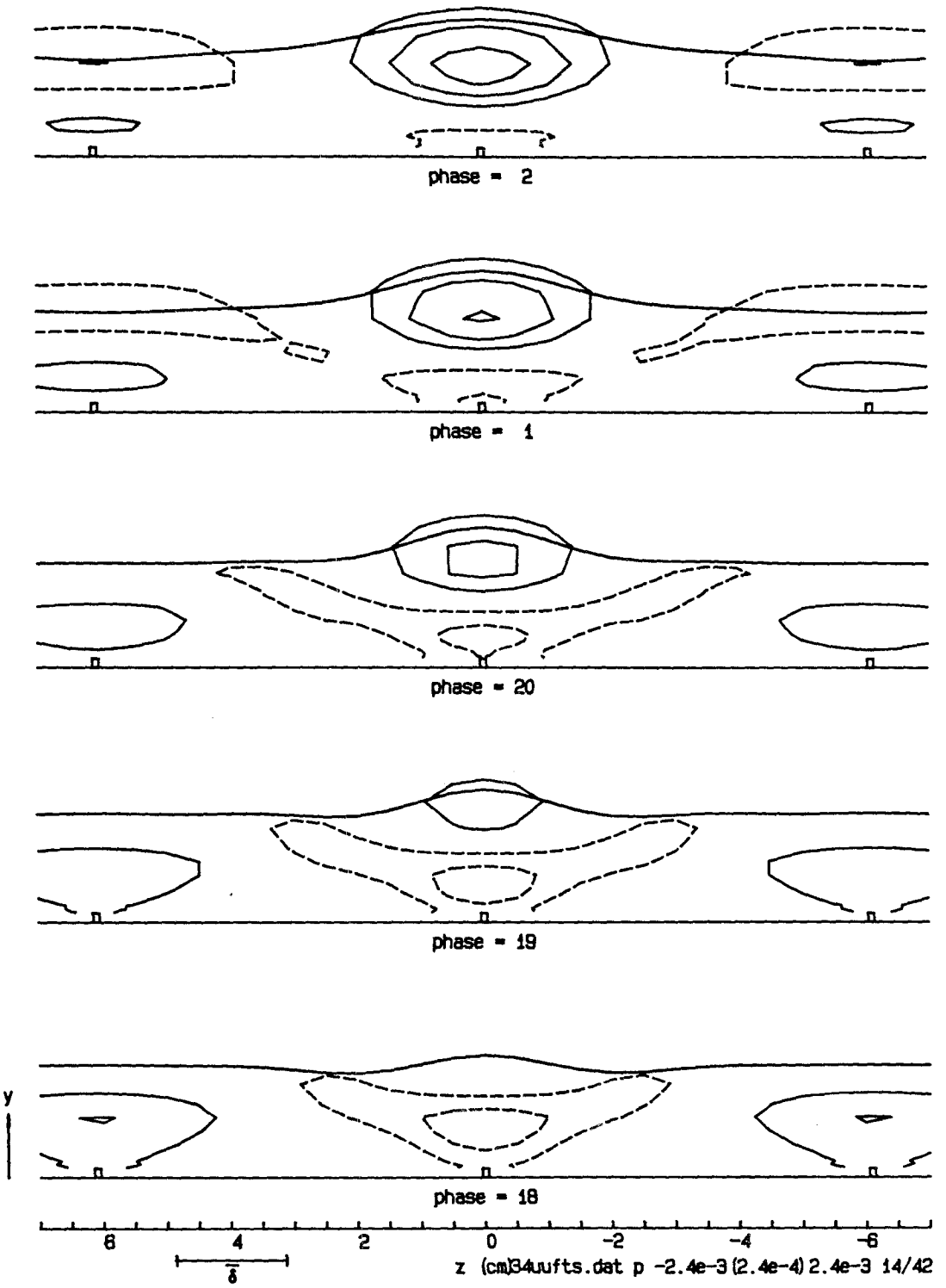

Figure 5.37 (cont'd.). Reynolds normal-stress perturbation $<u'u'> - \overline{u'u'}$ in the $z-y$ plane.

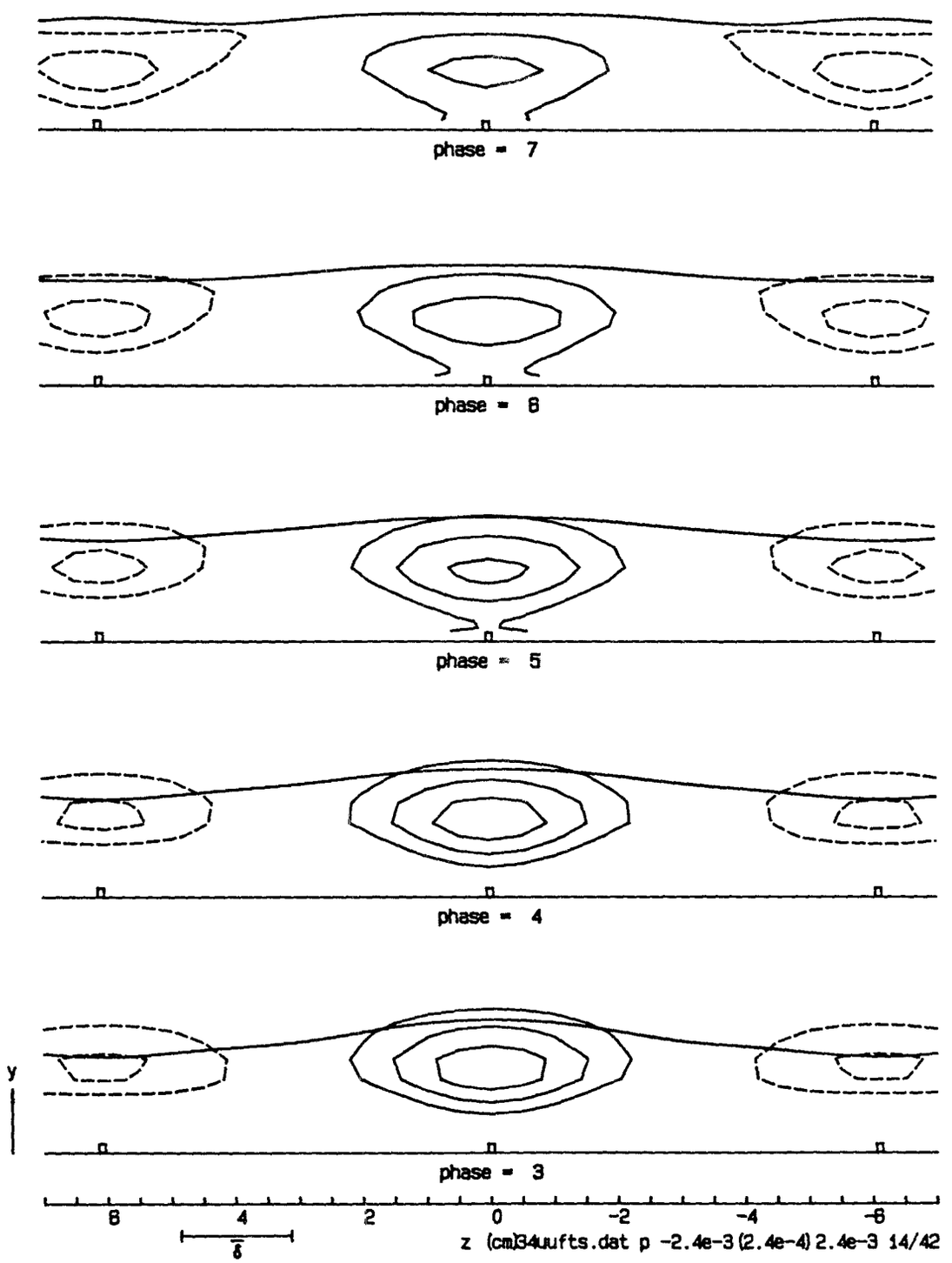

Figure 5.37 (cont'd.). Reynolds normal-stress perturbation $<u'u'> - \overline{u'u'}$ in the $z-y$ plane.

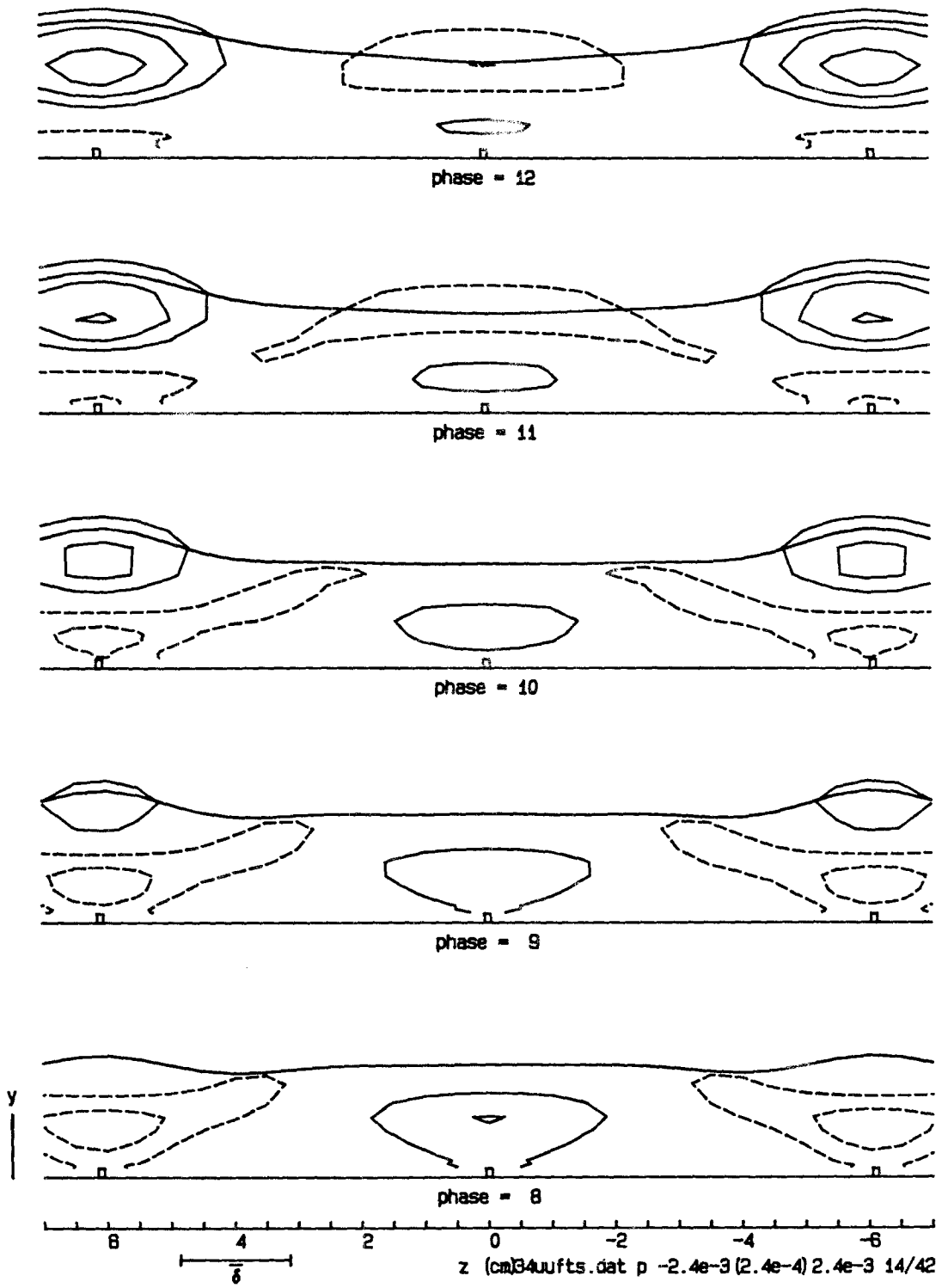

Figure 5.37 (cont'd.). Reynolds normal-stress perturbation $\langle u'u' \rangle - \overline{u'u'}$ in the $z-y$ plane.

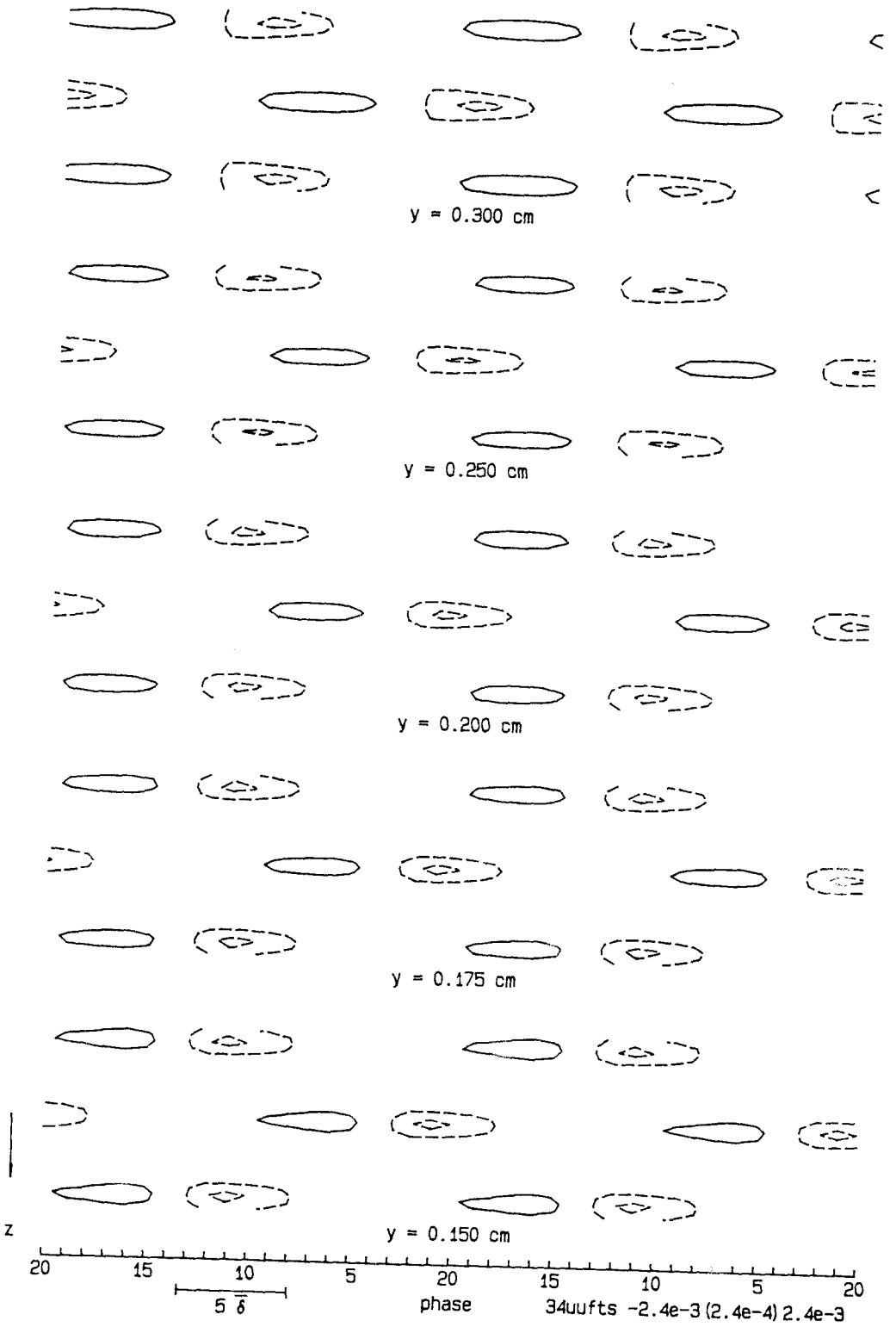

Figure 5.38. Reynolds normal-stress perturbation $<u'u'> - \overline{u'u'}$ in the $t-z$ plane. Contour interval 0.00024.

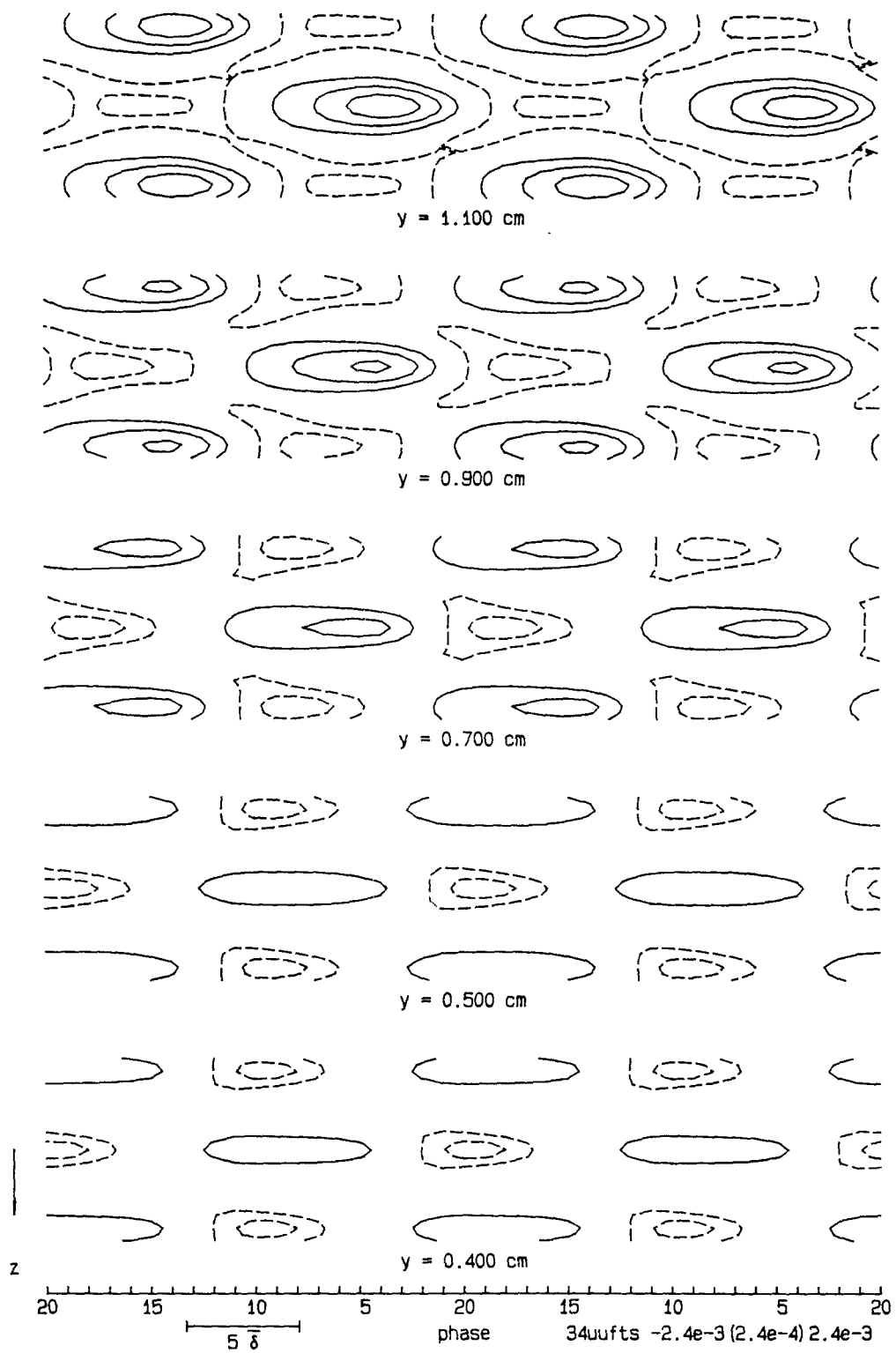

Figure 5.38 (cont'd.). Reynolds normal-stress perturbation $<u'u'> - \overline{u'u'}$ in the $t-z$ plane.

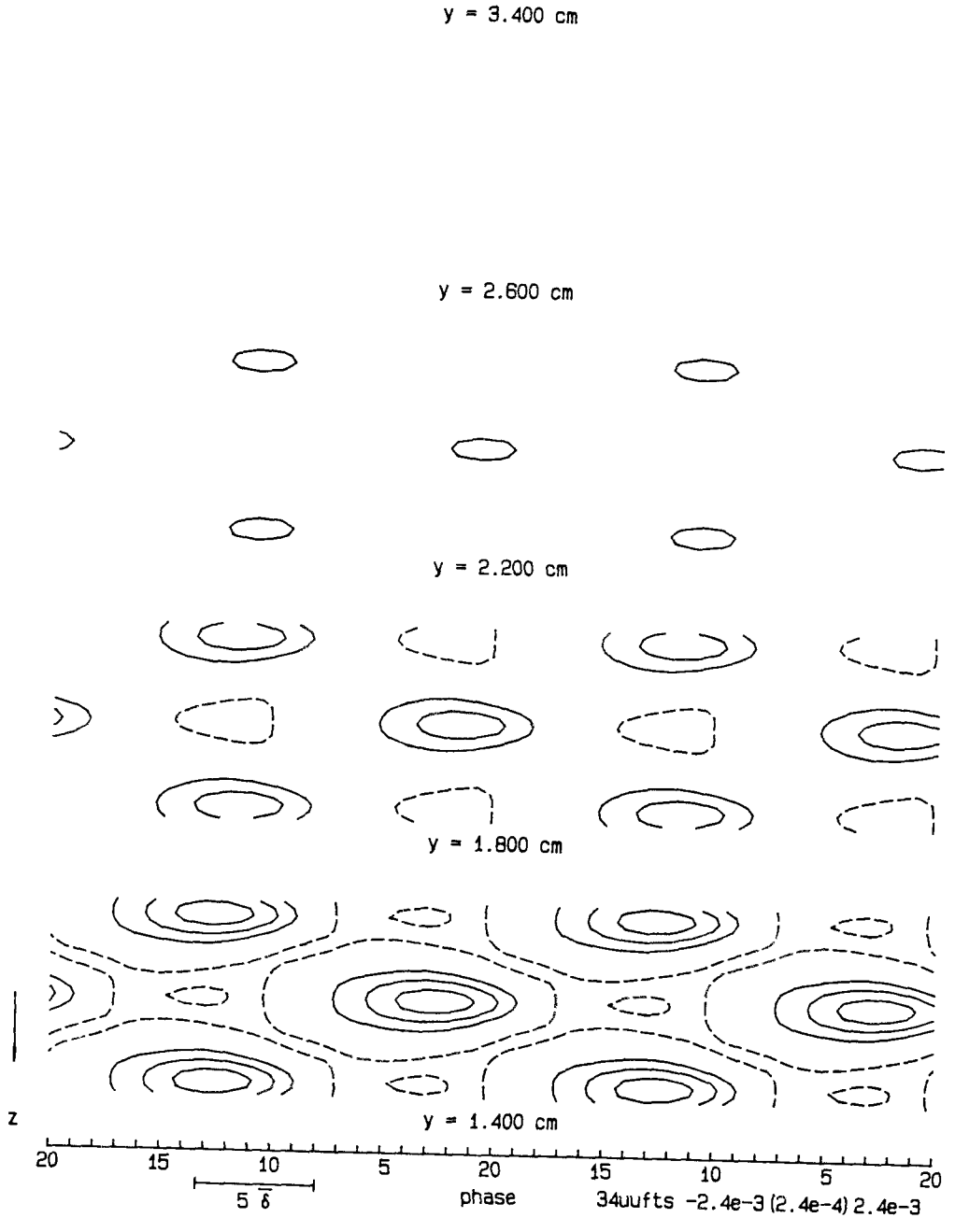

Figure 5.38 (cont'd.). Reynolds normal-stress perturbation $<u'u'> - \overline{u'u'}$ in the $t-z$ plane.

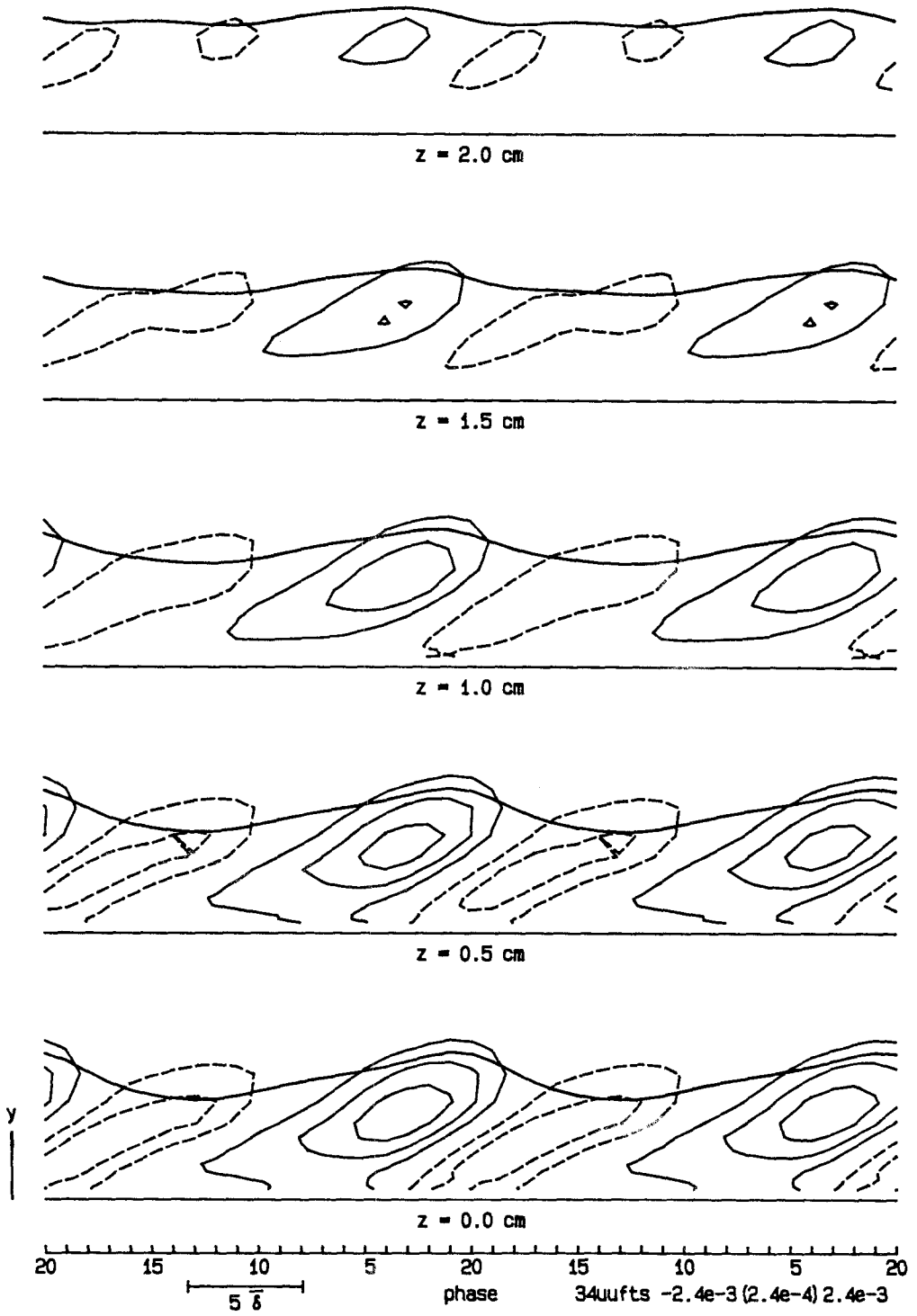

Figure 5.39. Reynolds normal-stress perturbation $<u'u'> - \overline{u'u'}$ in the t–y plane. Contour interval 0.00024.

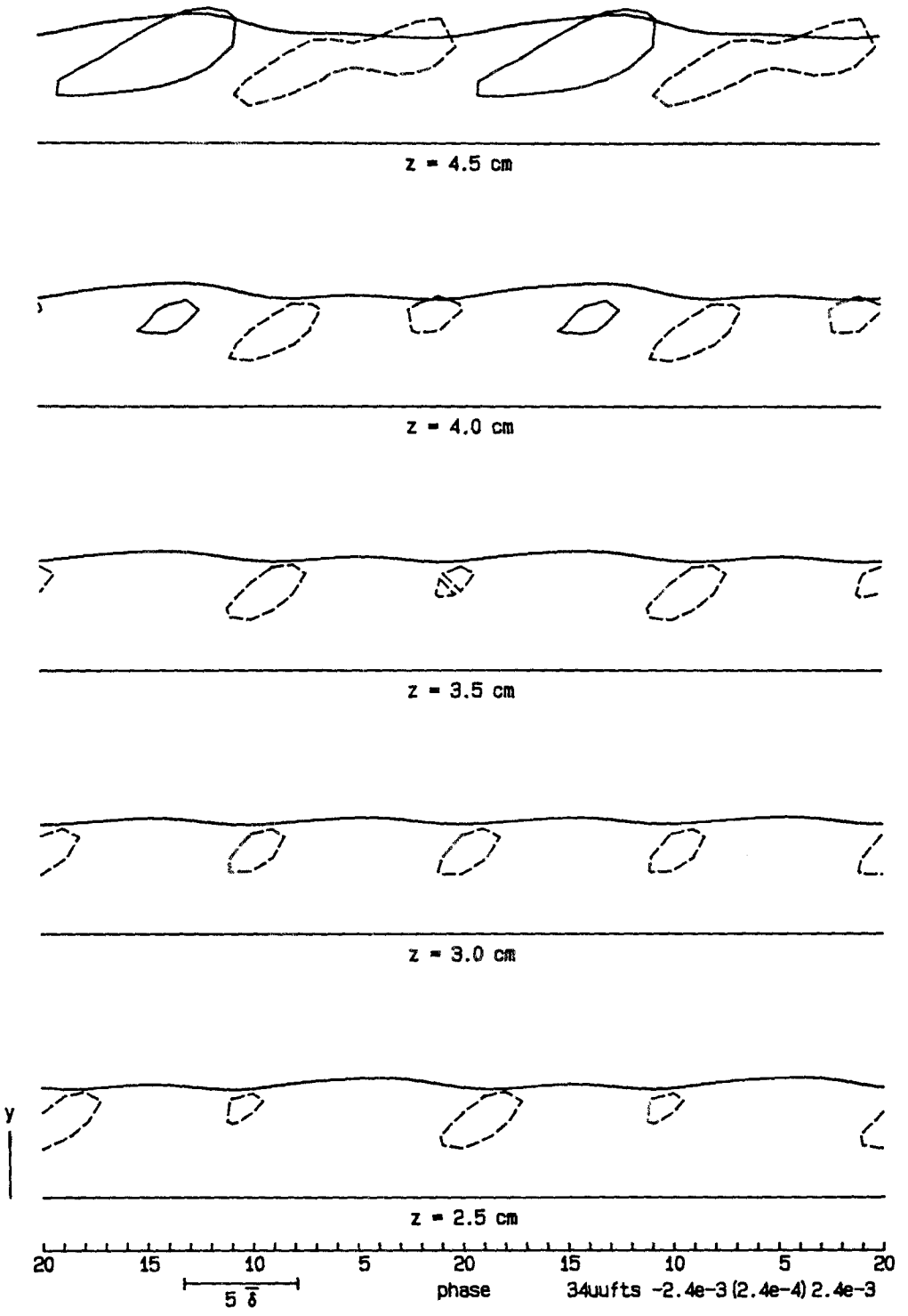

Figure 5.39 (cont'd.). Reynolds normal-stress perturbation $<u'u'> - \overline{u'u'}$ in the t–y plane.

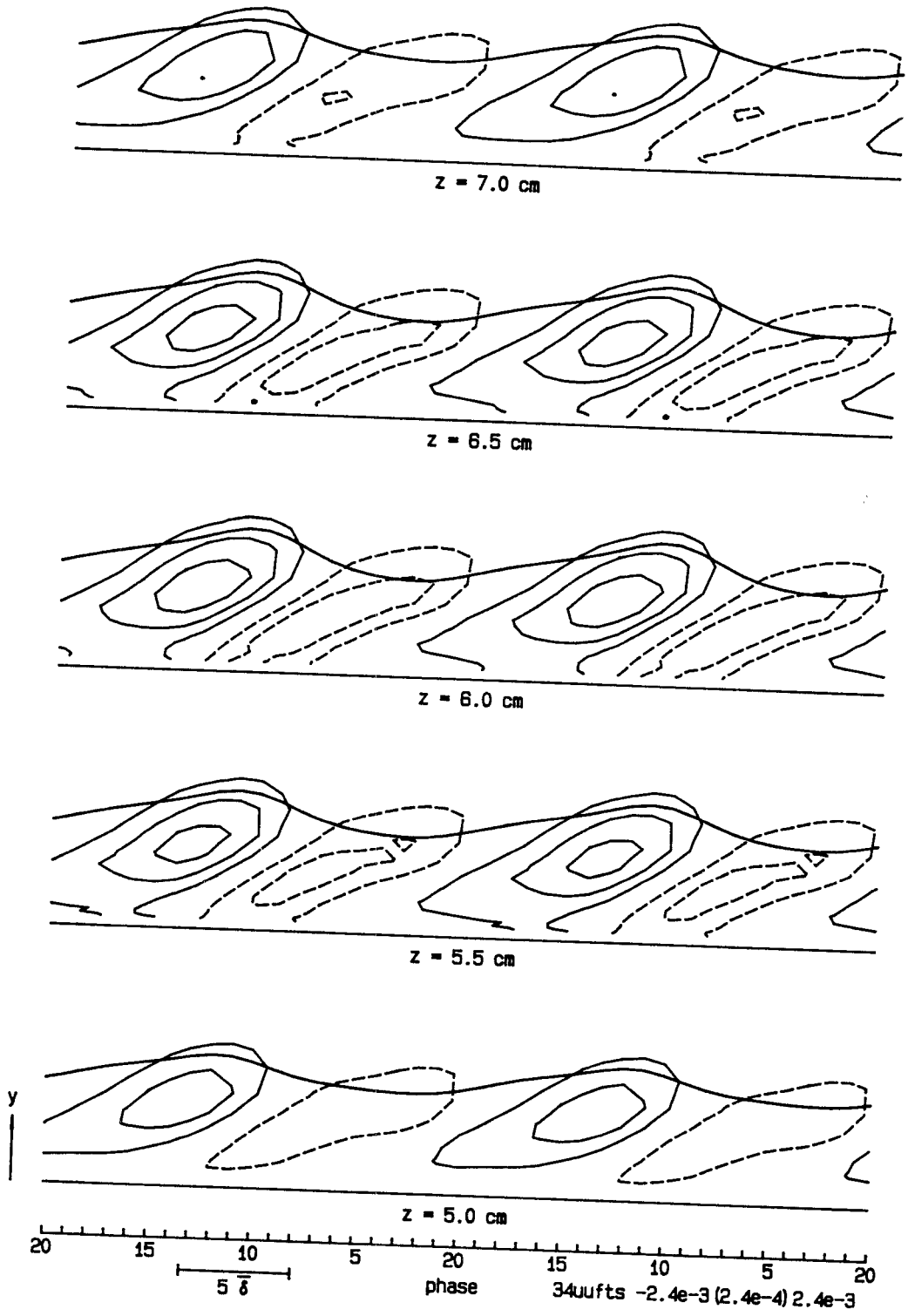

Figure 5.39 (cont'd.). Reynolds normal-stress perturbation $<u'u'> - \overline{u'u'}$ in the $t-y$ plane.

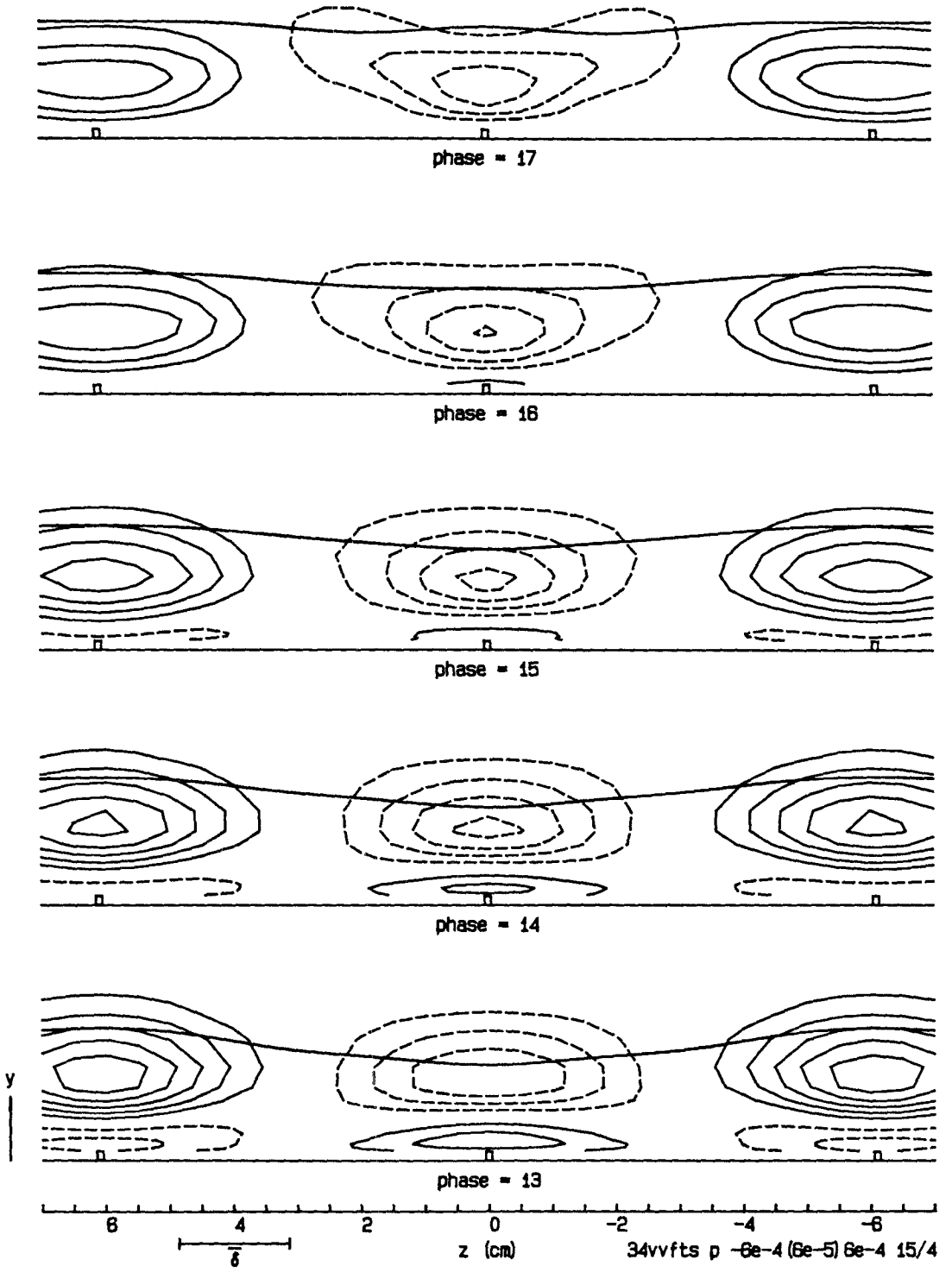

Figure 5.40. Reynolds normal-stress perturbation $\langle v'v' \rangle - \overline{v'v'}$ in the $z-y$ plane. Contour interval 0.00006.

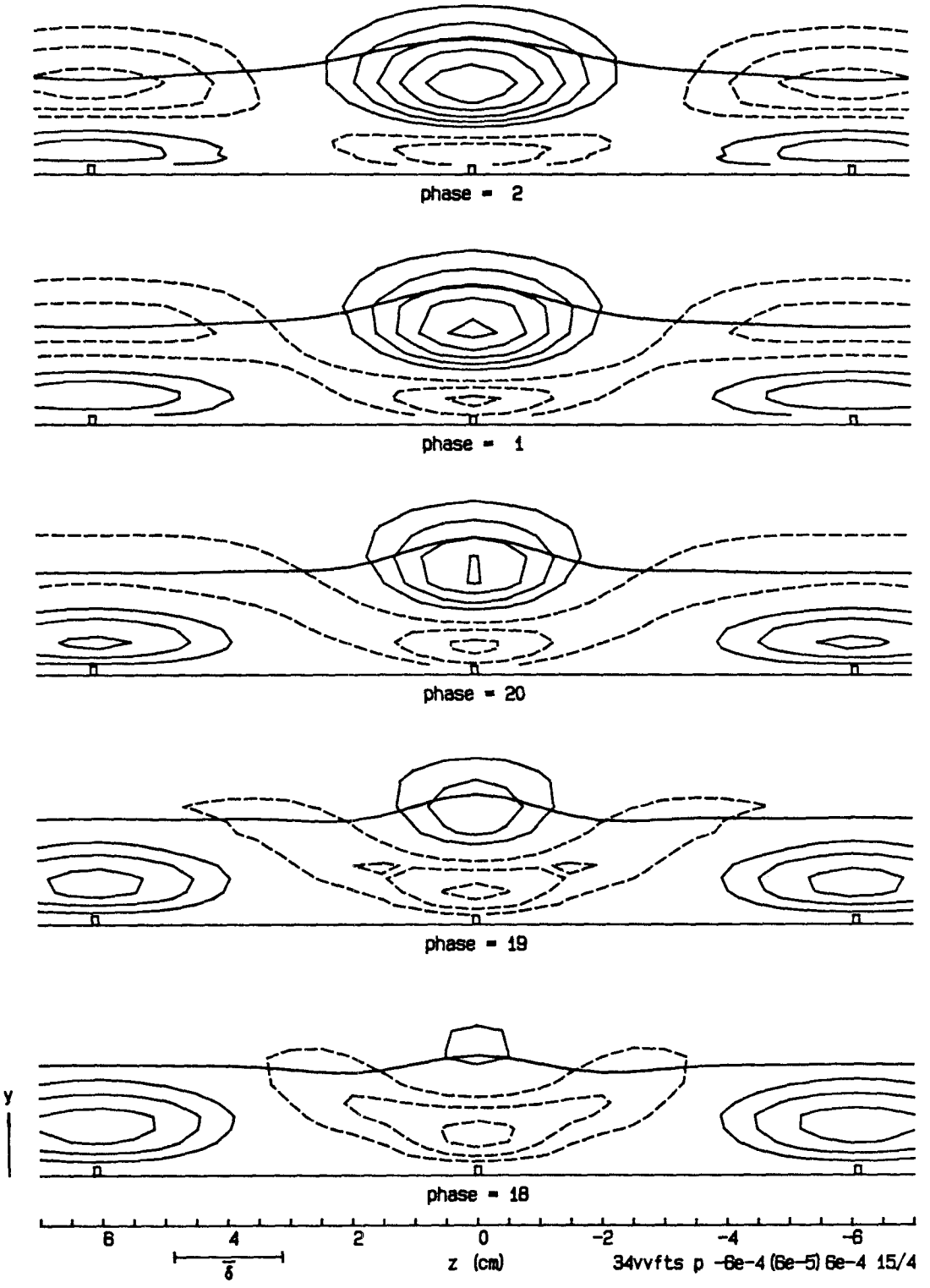

Figure 5.40 (cont'd.). Reynolds normal-stress perturbation $\langle v'v' \rangle - \overline{v'v'}$ in the $z-y$ plane.

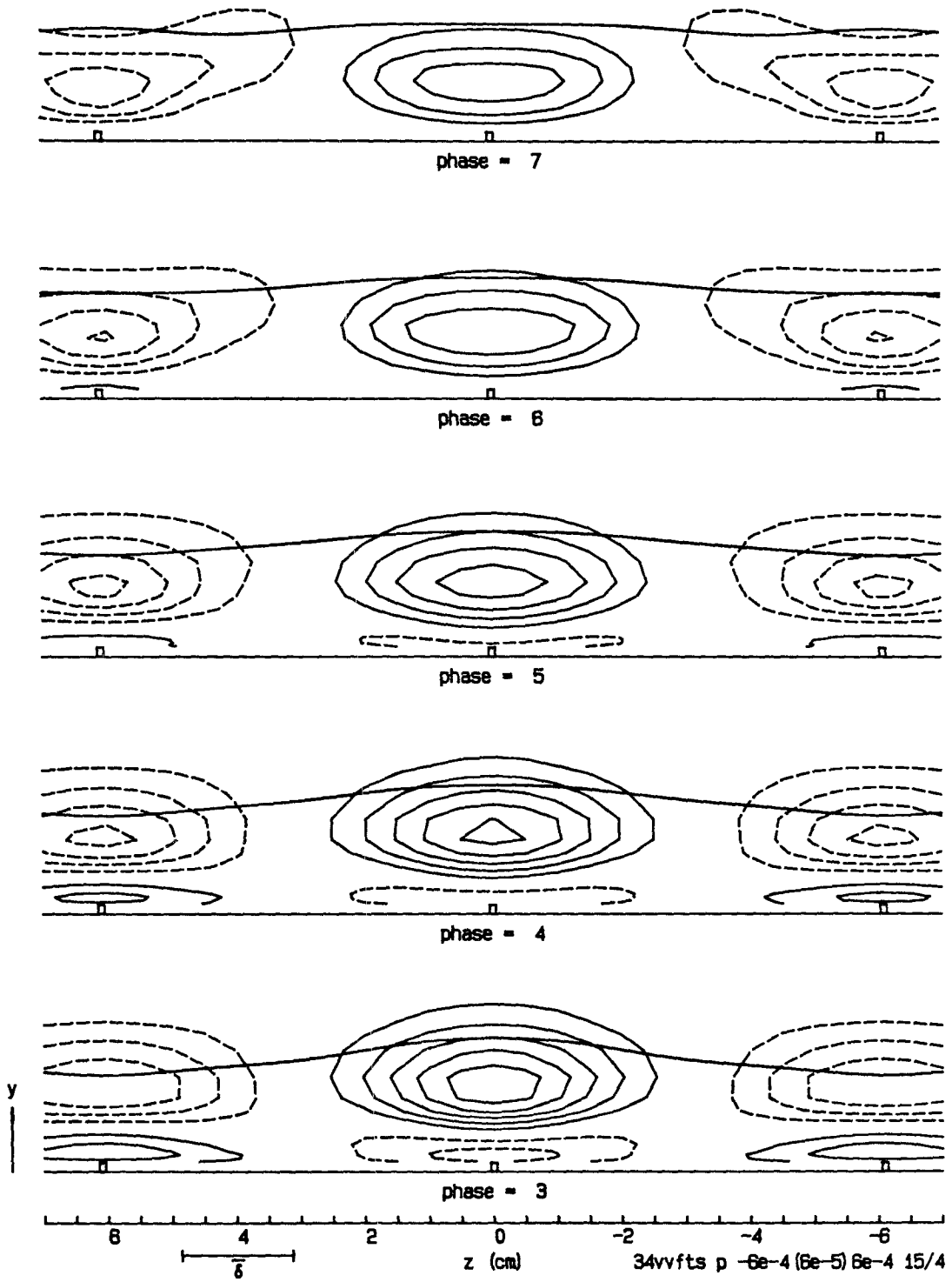

Figure 5.40 (cont'd.). Reynolds normal-stress perturbation $<v'v'> - \overline{v'v'}$ in the $z-y$ plane.

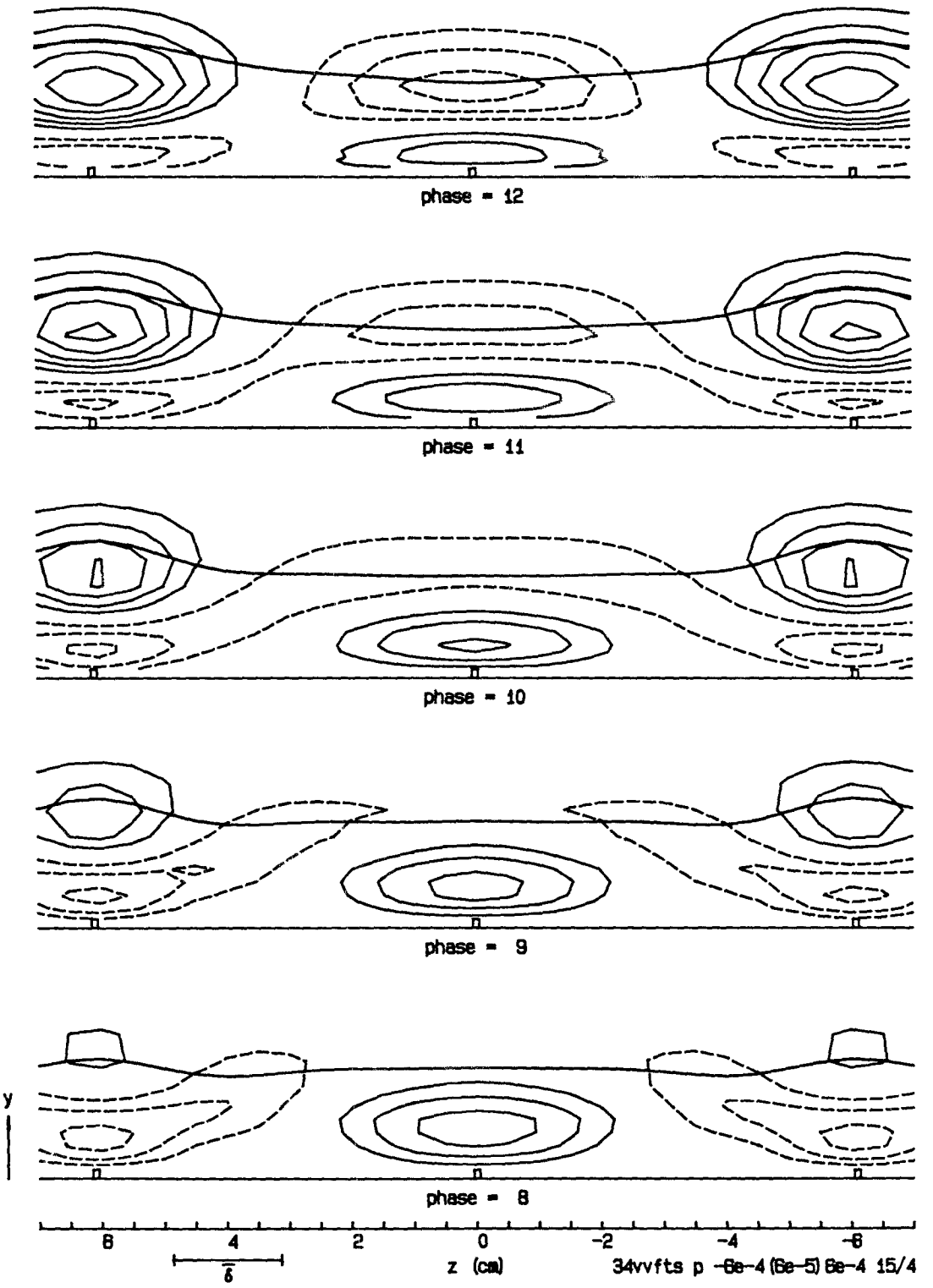

Figure 5.40 (cont'd.). Reynolds normal-stress perturbation $\langle v'v' \rangle - \overline{v'v'}$ in the $z-y$ plane.

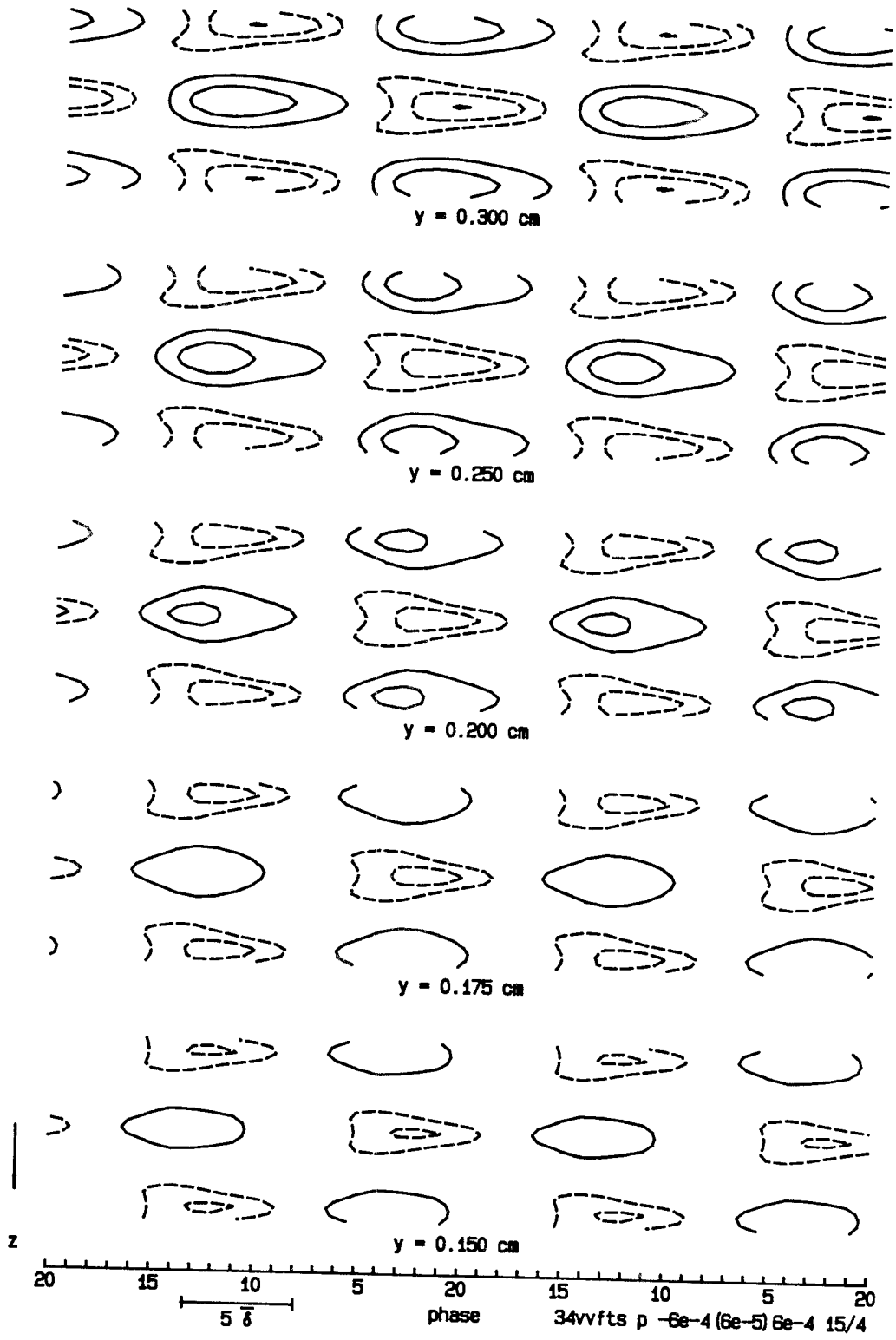

Figure 5.41. Reynolds normal-stress perturbation $\langle v'v' \rangle - \overline{v'v'}$ in the $t-z$ plane. Contour interval 0.00006.

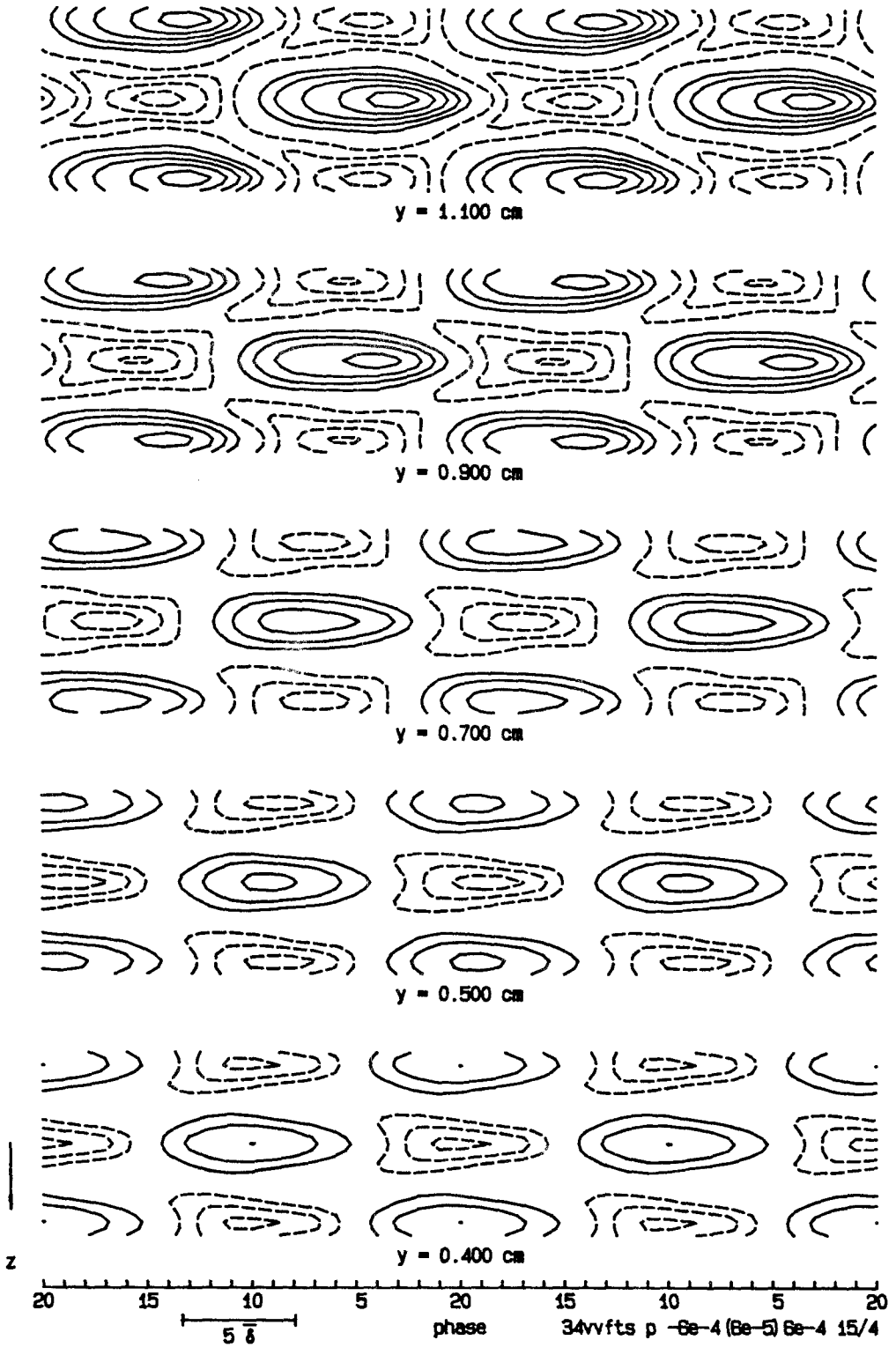

Figure 5.41 (cont'd.). Reynolds normal-stress perturbation $\langle v'v' \rangle - \overline{v'v'}$ in the t–z plane.

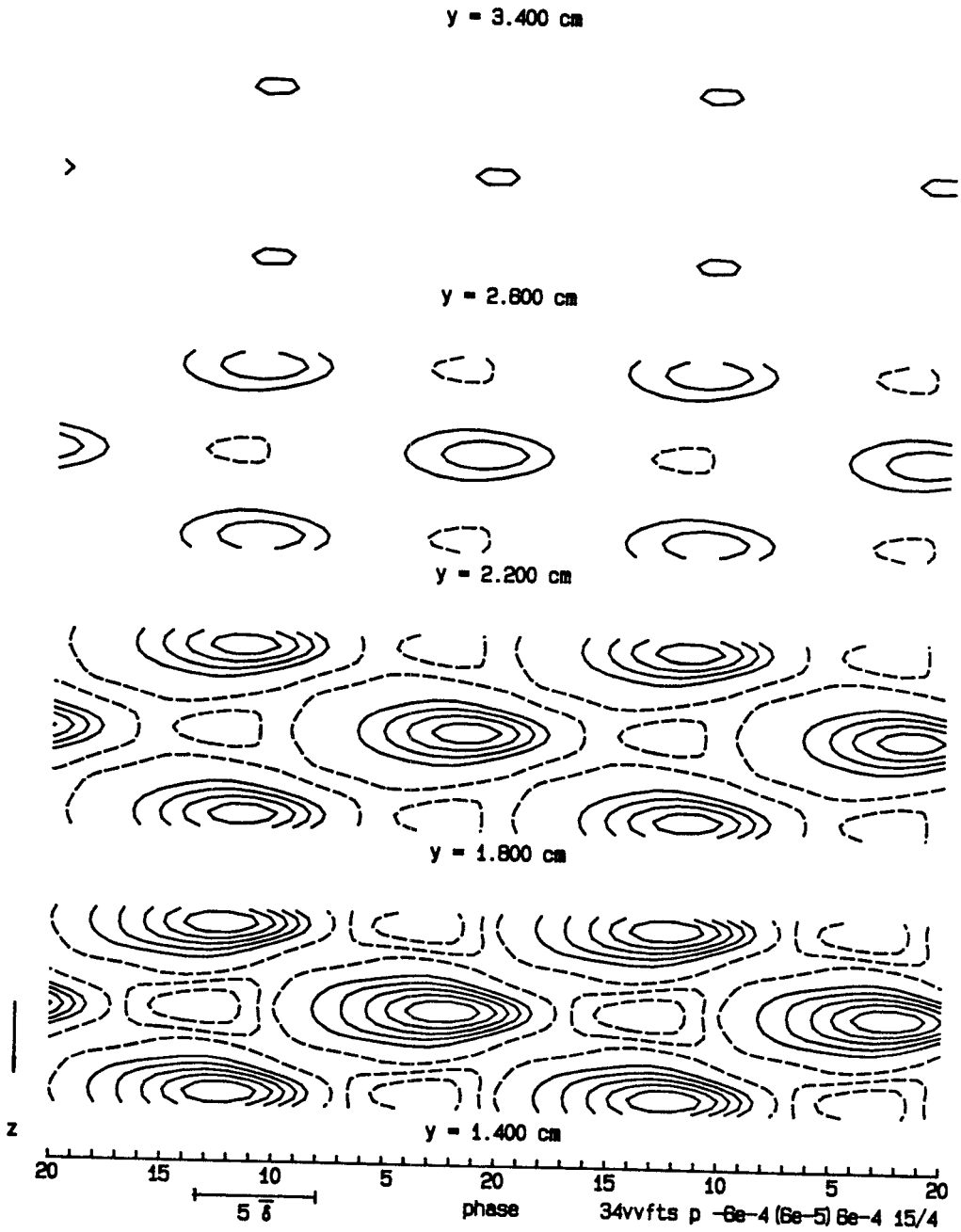

Figure 5.41 (cont'd.). Reynolds normal-stress perturbation $<v'v'> - \overline{v'v'}$ in the $t-z$ plane.

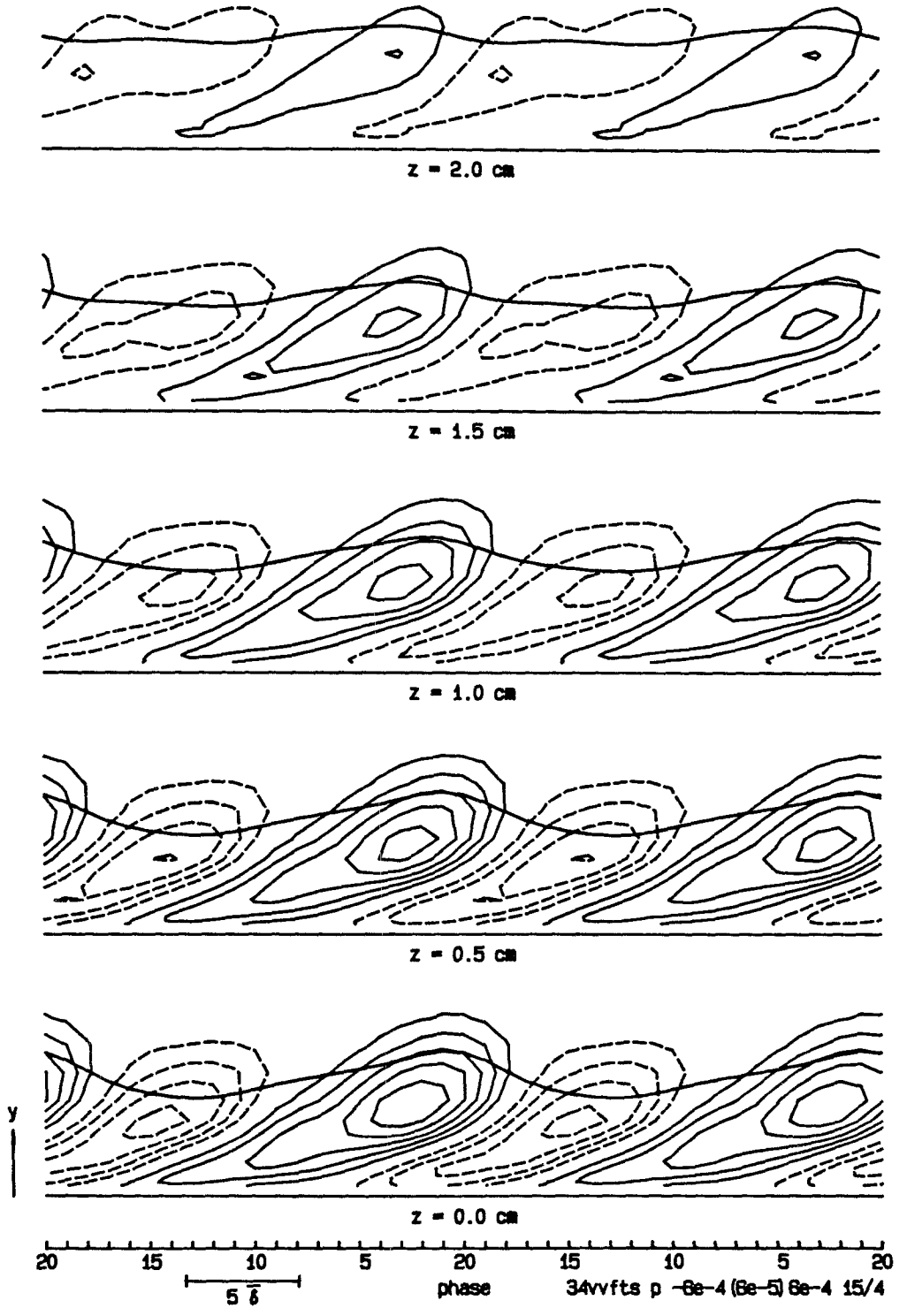

Figure 5.42. Reynolds normal-stress perturbation $\langle v'v' \rangle - \overline{v'v'}$ in the $t-y$ plane. Contour interval 0.00006.

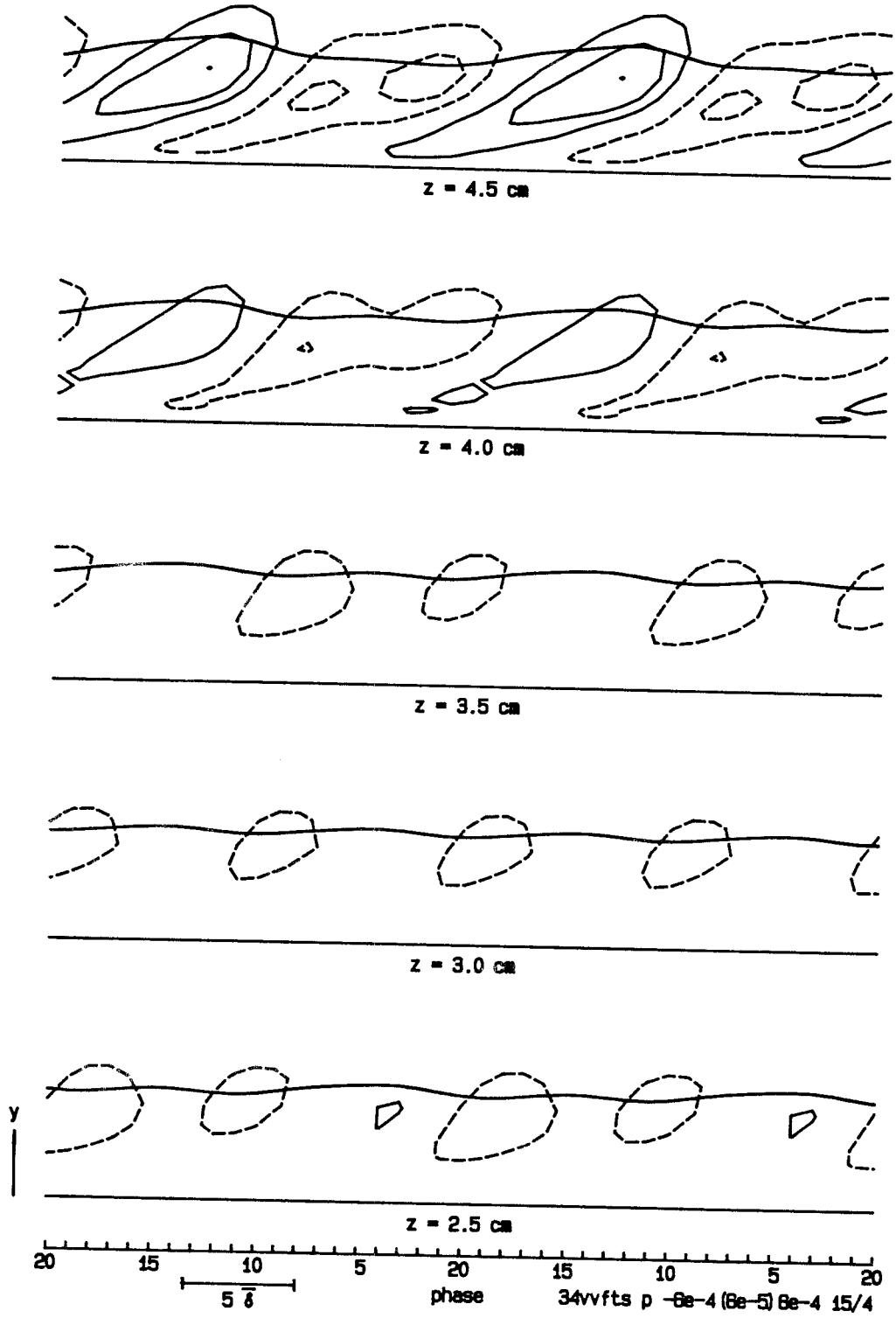

Figure 5.42 (cont'd.). Reynolds normal-stress perturbation $<v'v'> - \overline{v'v'}$ in the $t-y$ plane.

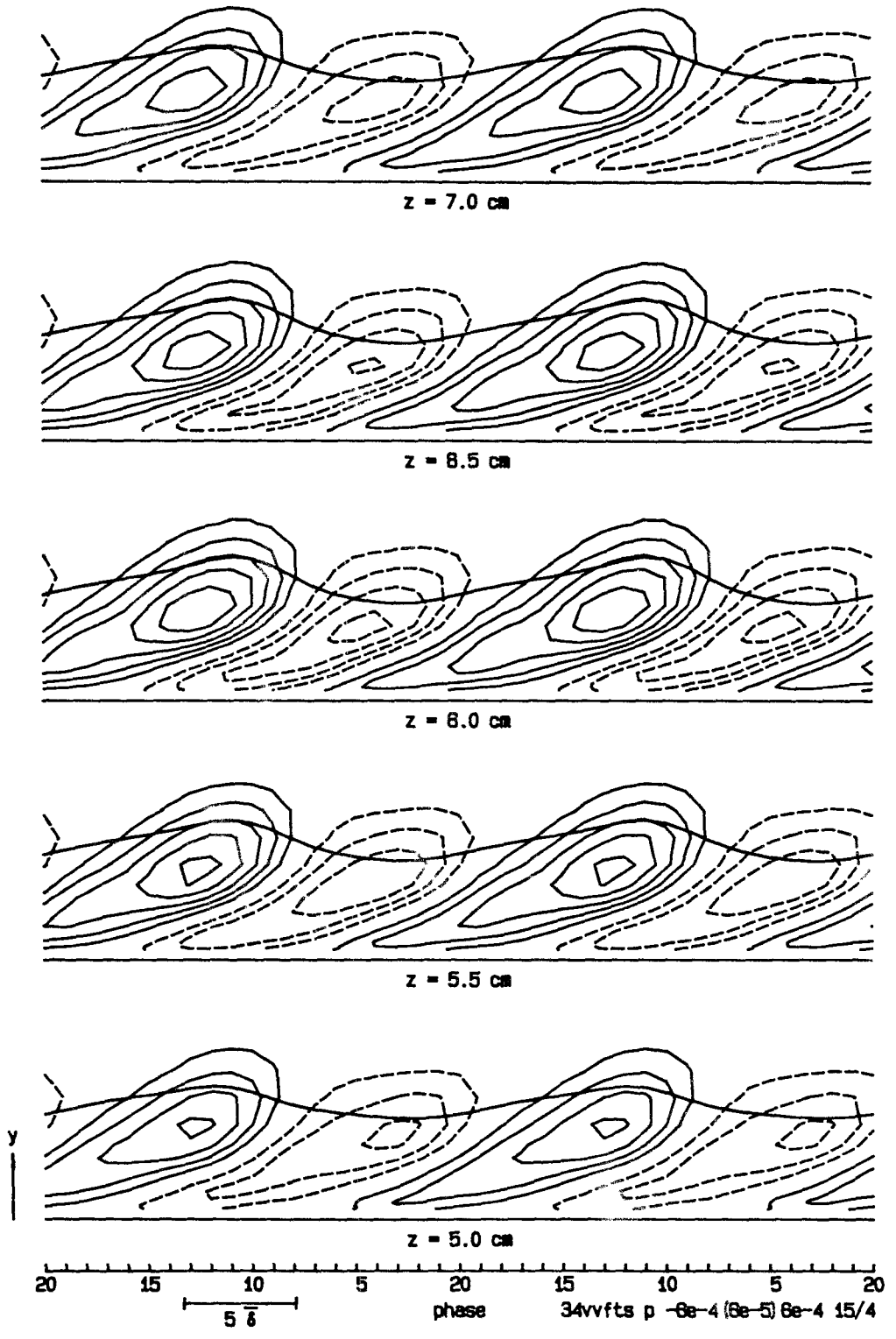

Figure 5.42 (cont'd.). Reynolds normal-stress perturbation $<v'v'> - \overline{v'v'}$ in the $t-y$ plane.

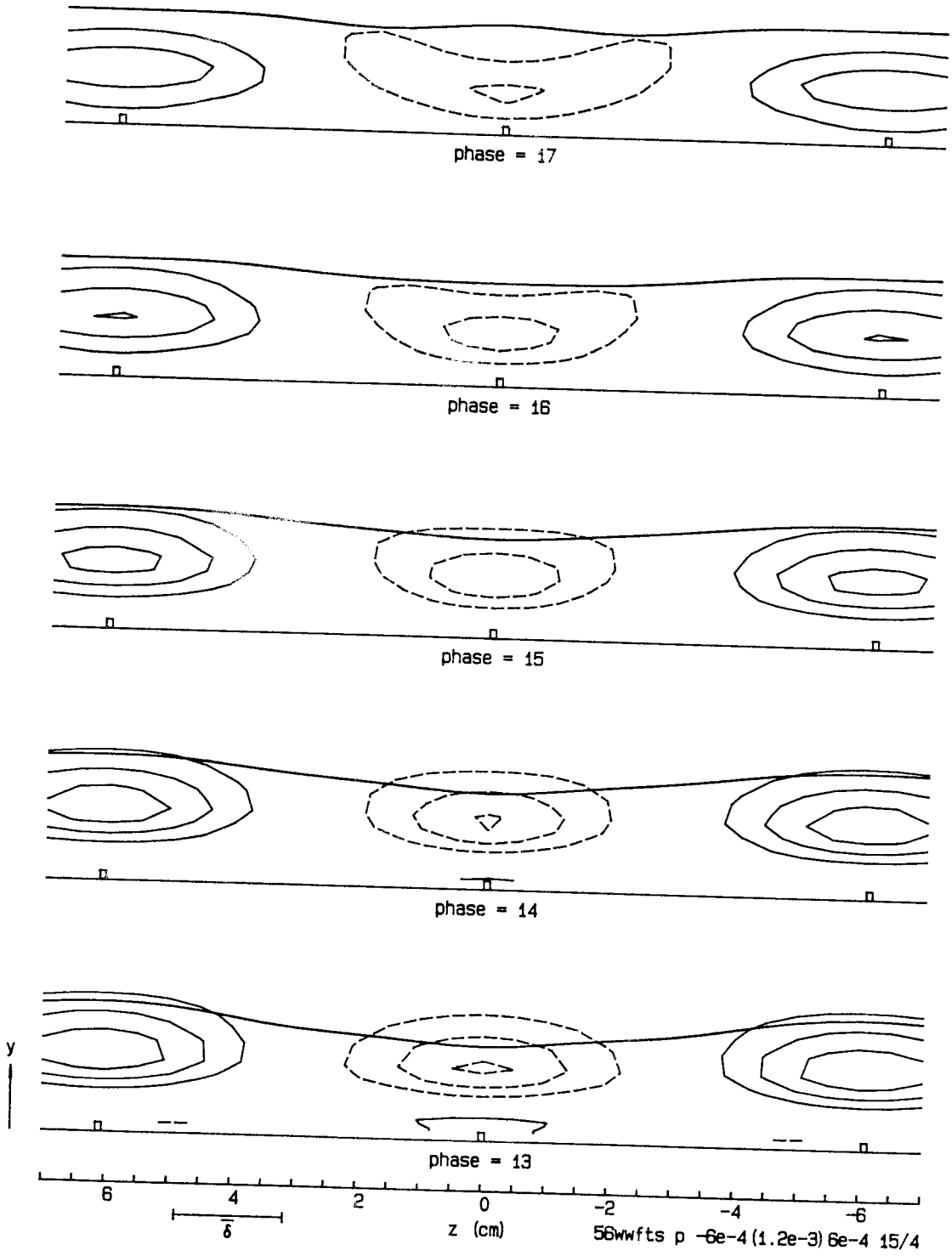

Figure 5.43. Reynolds normal-stress perturbation $<w'w'> - \overline{w'w'}$ in the $z-y$ plane. Contour interval 0.00012.

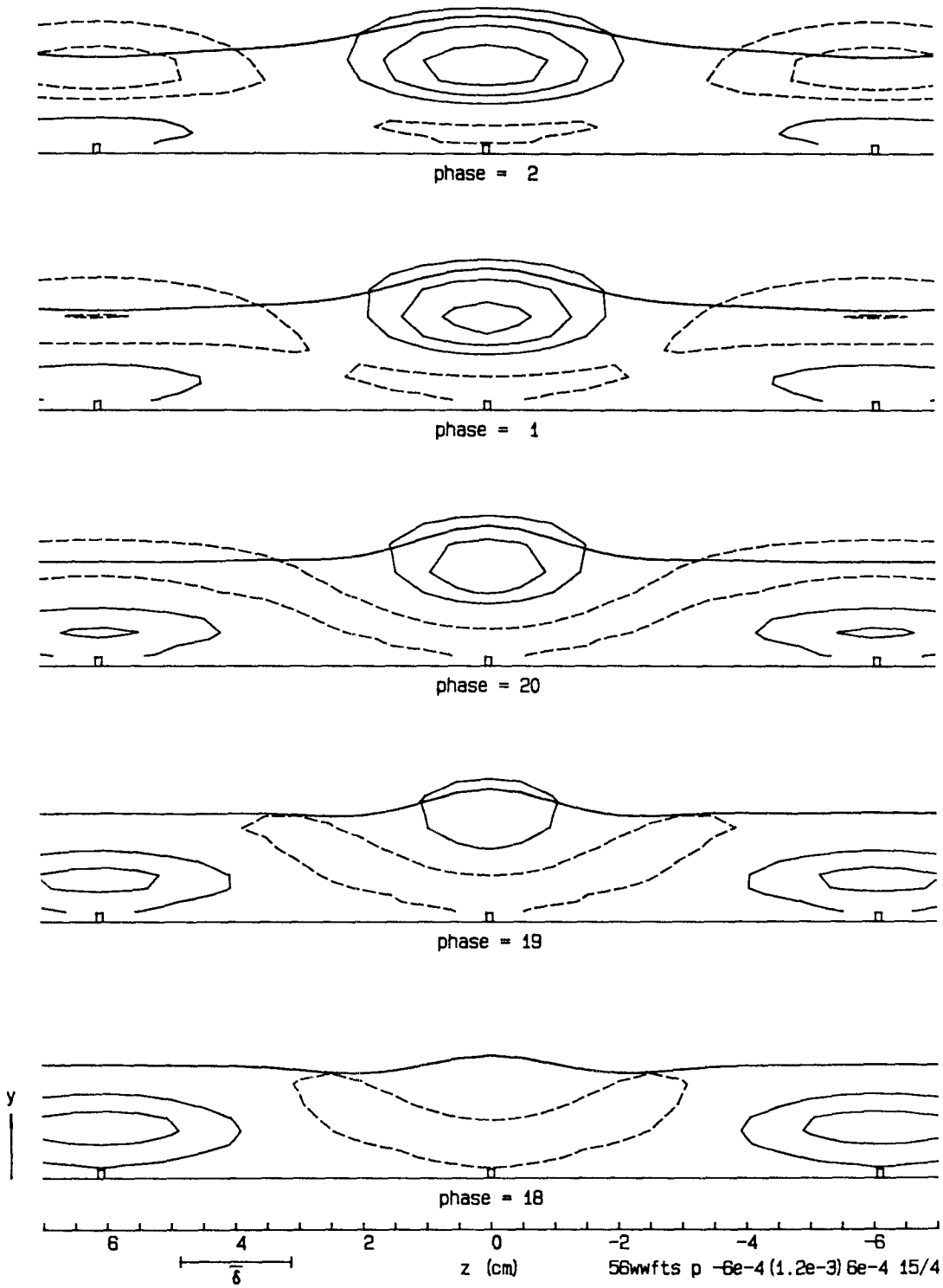

Figure 5.43 (cont'd.). Reynolds normal-stress perturbation $\langle w'w' \rangle - \overline{w'w'}$ in the $z-y$ plane.

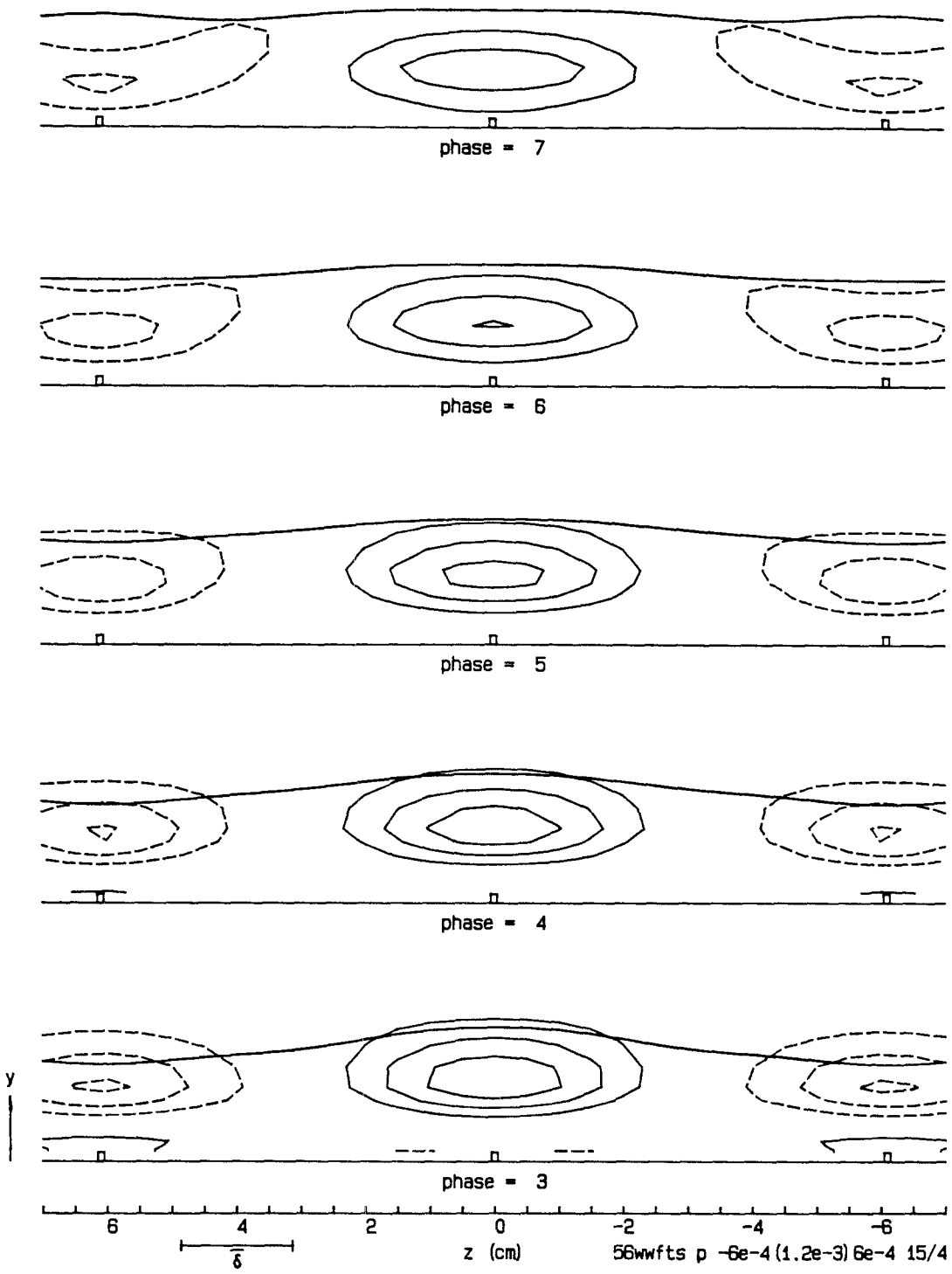

Figure 5.43 (cont'd.). Reynolds normal-stress perturbation $\langle w'w' \rangle - \overline{w'w'}$ in the $z-y$ plane.

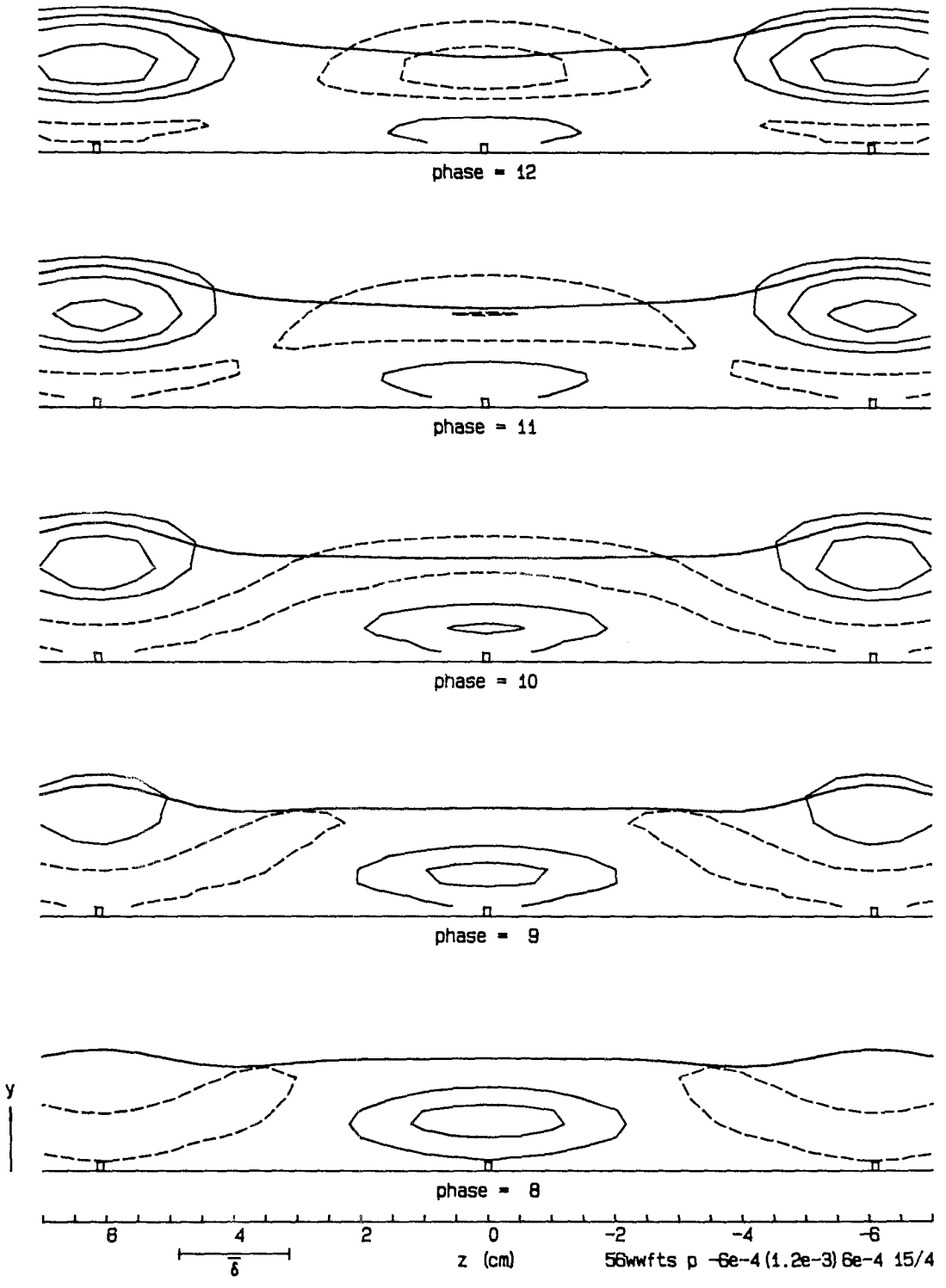

Figure 5.43 (cont'd.). Reynolds normal-stress perturbation $<w'w'> - \overline{w'w'}$ in the $z-y$ plane.

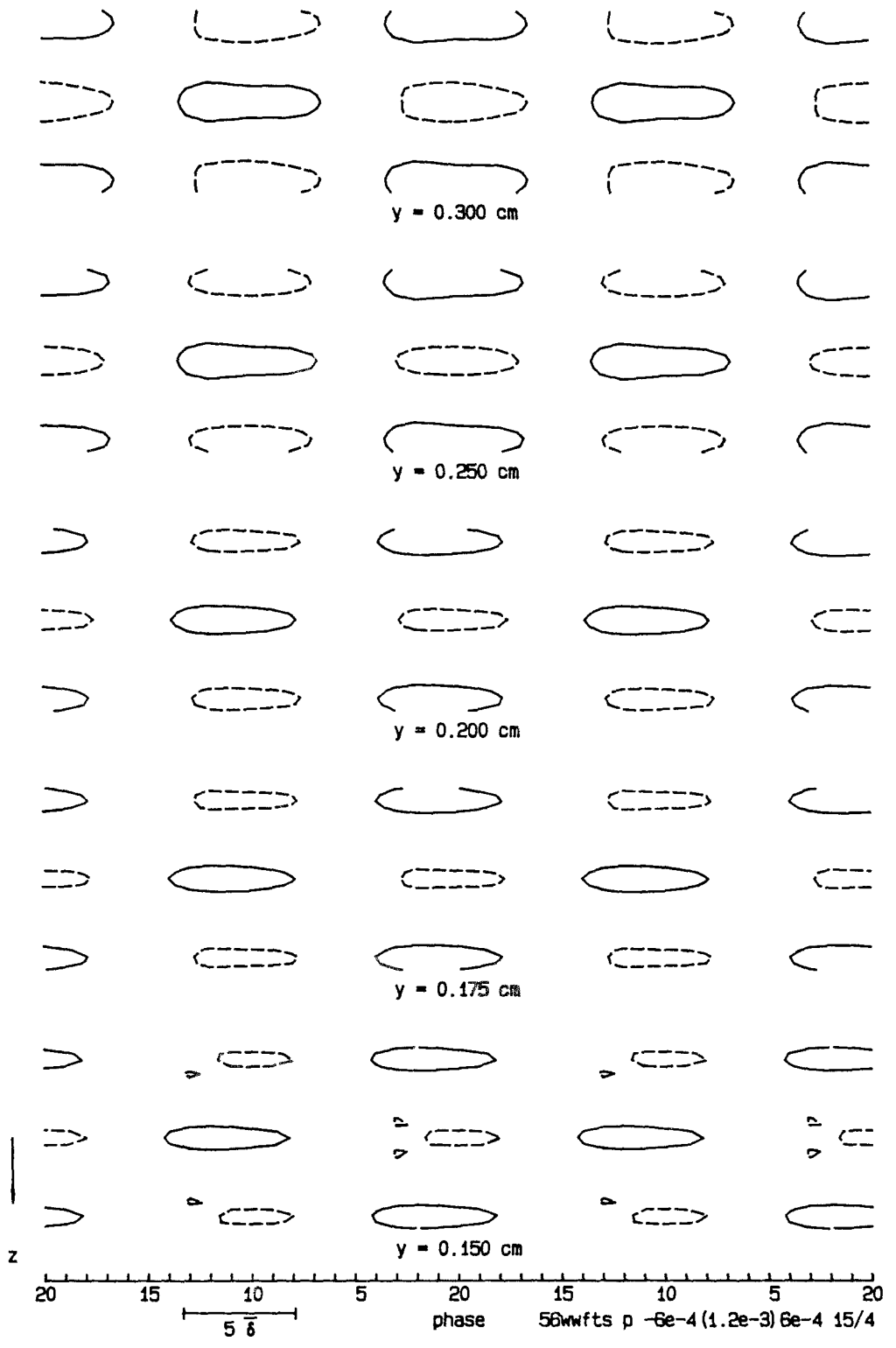

Figure 5.44. Reynolds normal-stress perturbation $\langle w'w' \rangle - \overline{w'w'}$ in the $t-z$ plane. Contour interval 0.00012.

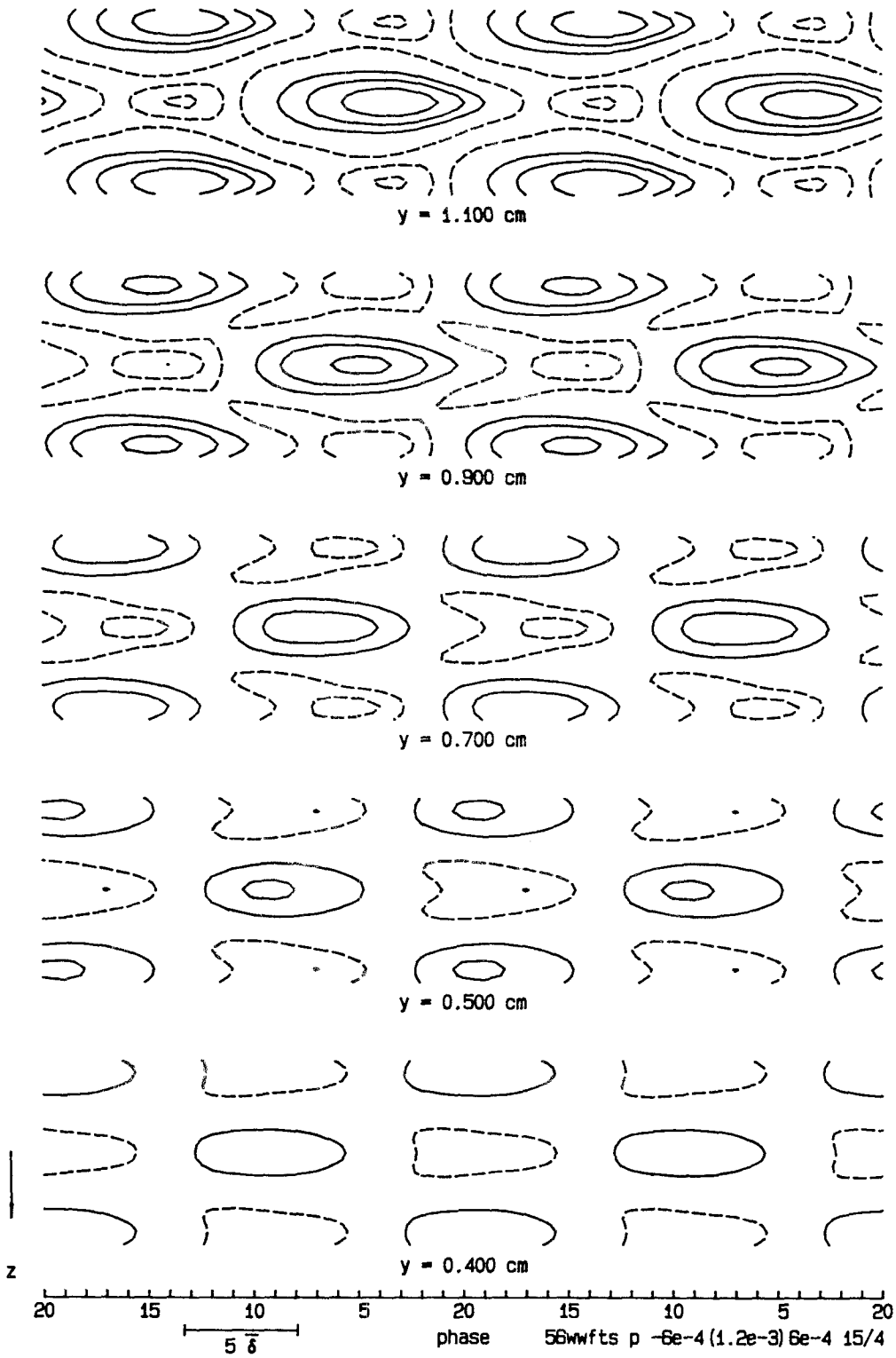

Figure 5.44 (cont'd.). Reynolds normal-stress perturbation $\langle w'w' \rangle - \overline{w'w'}$ in the $t-z$ plane.

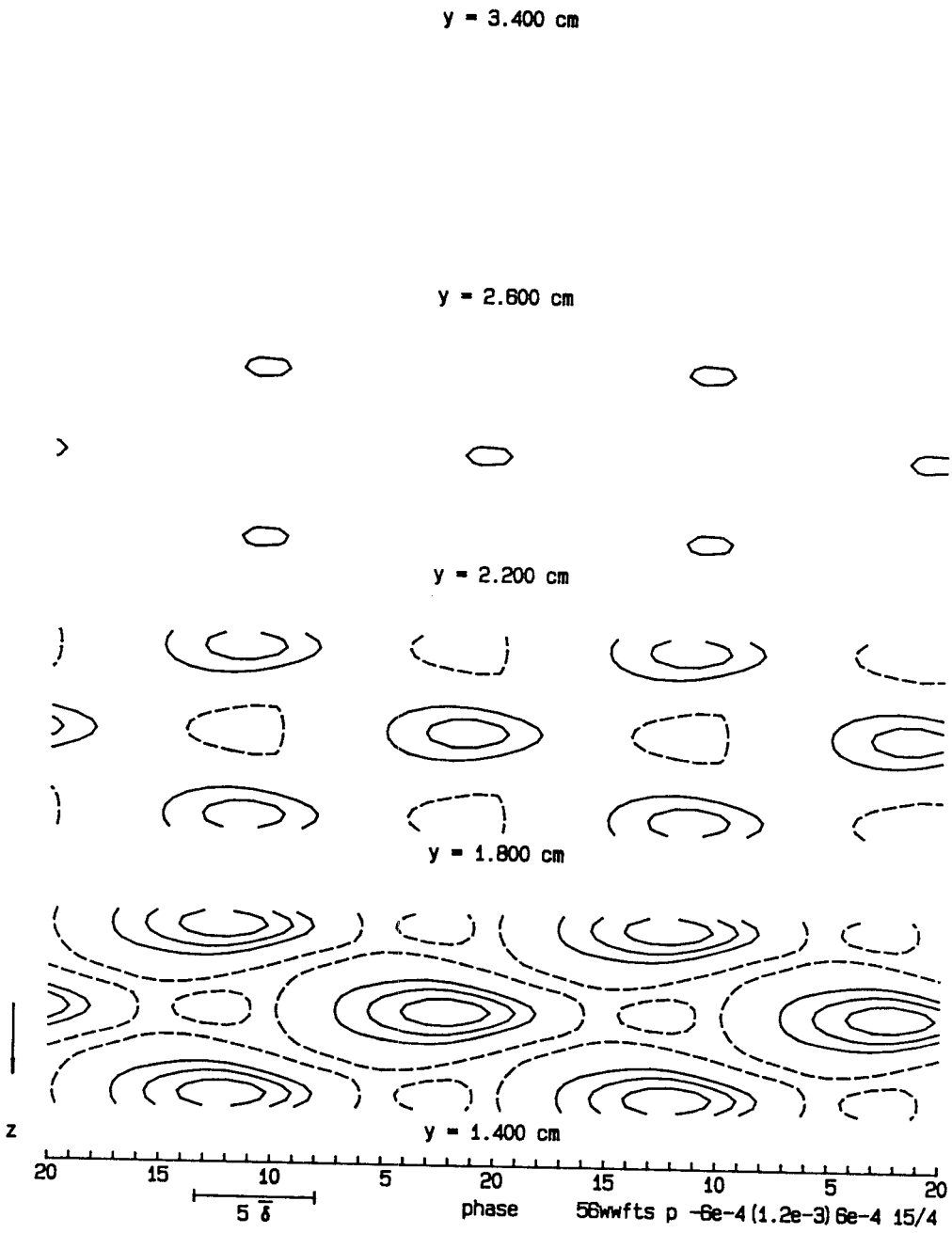

Figure 5.44 (cont'd.). Reynolds normal-stress perturbation $\langle w'w' \rangle - \overline{w'w'}$ in the $t-z$ plane.

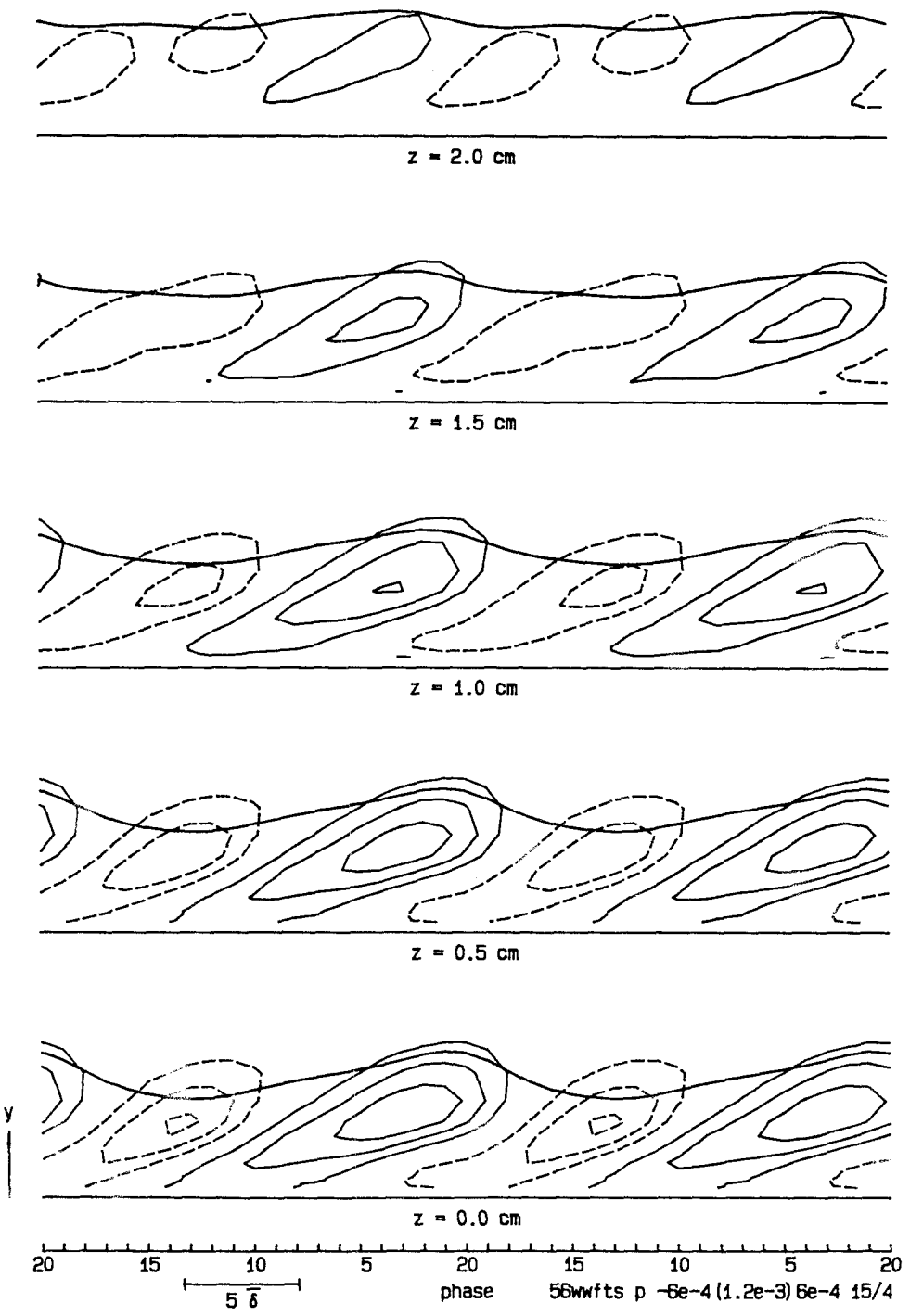

Figure 5.45. Reynolds normal-stress perturbation $\langle w'w' \rangle - \overline{w'w'}$ in the $t-y$ plane. Contour interval 0.00012.

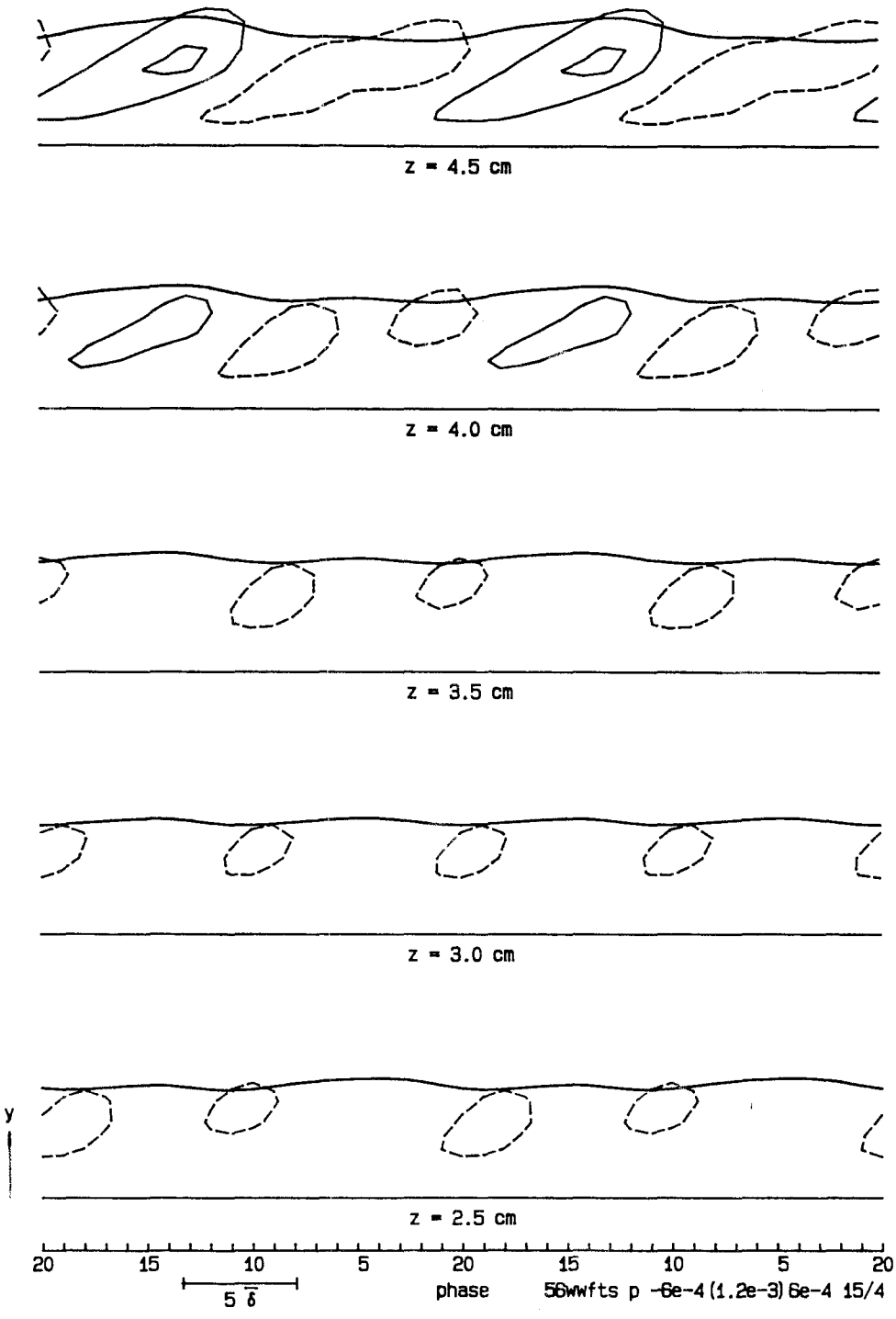

Figure 5.45 (cont'd.). Reynolds normal-stress perturbation $<w'w'> - \overline{w'w'}$ in the $t-y$ plane.

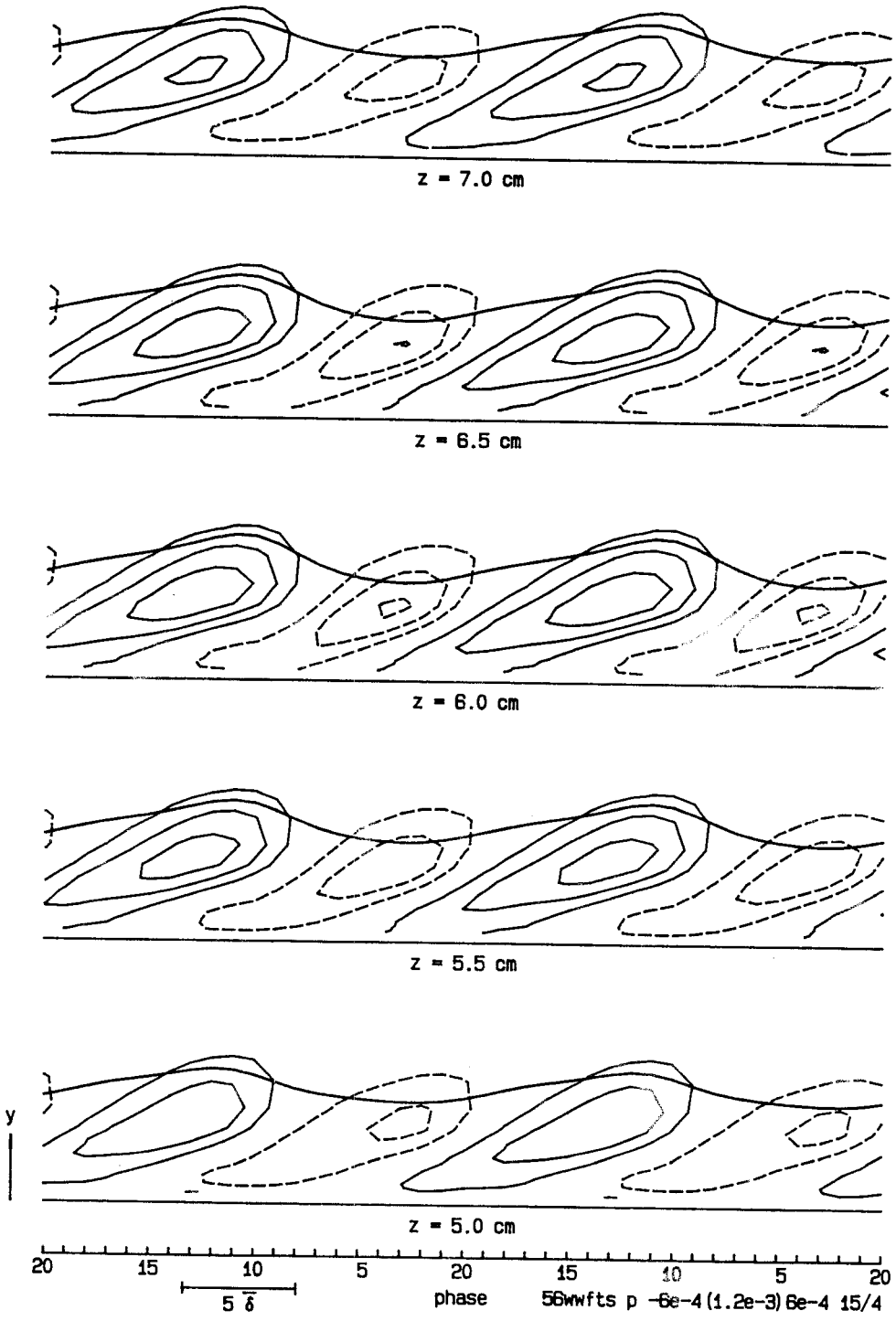

Figure 5.45 (cont'd.). Reynolds normal-stress perturbation $<w'w'>' - \overline{w'w'}$ in the $t-y$ plane.

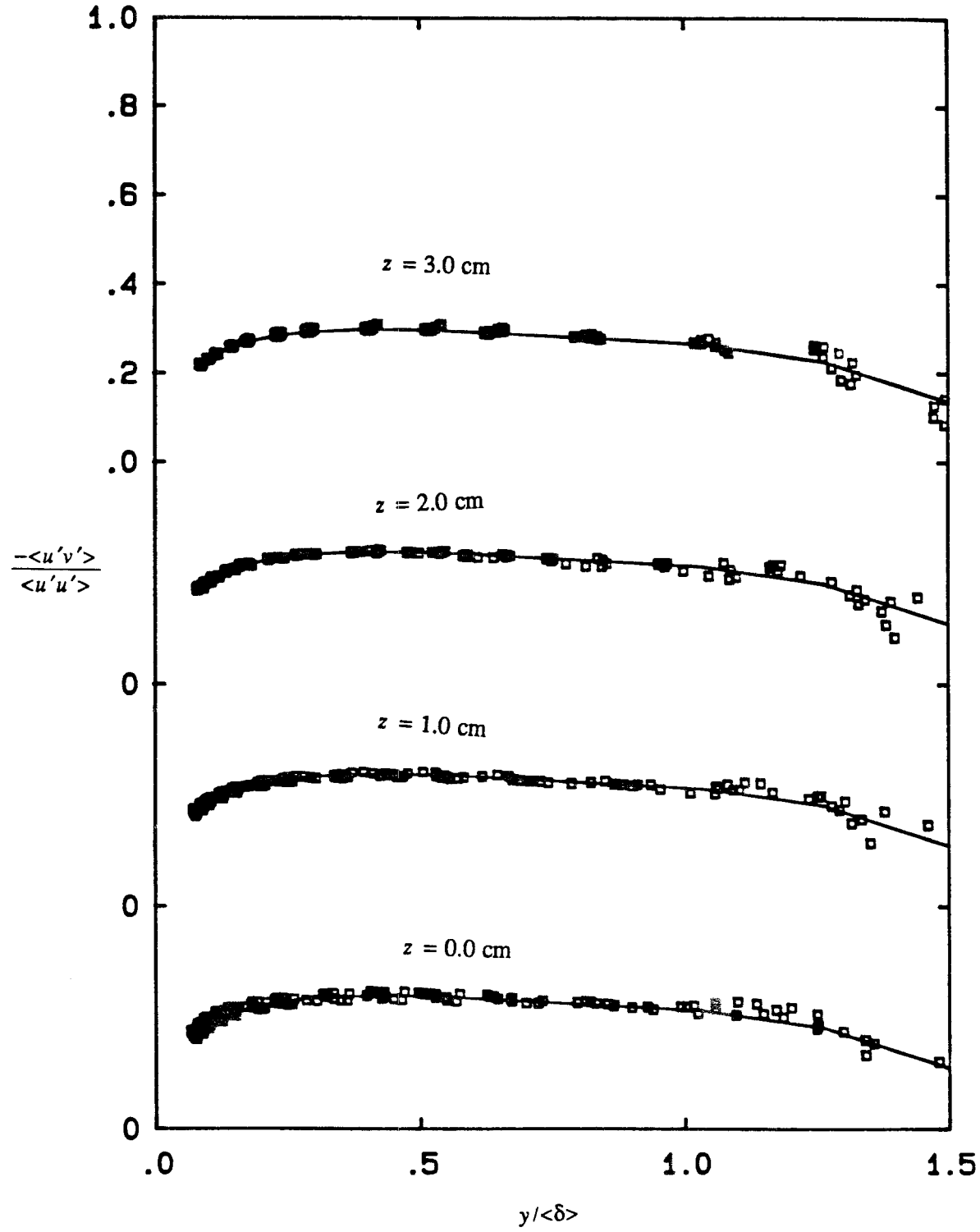

Figure 5.46a. Reynolds-stress ratio $-\langle u'v' \rangle / \langle u'u' \rangle$ against $y/\langle\delta\rangle$ in active region. Phases 16(1)6; z = 0(1)3 cm.

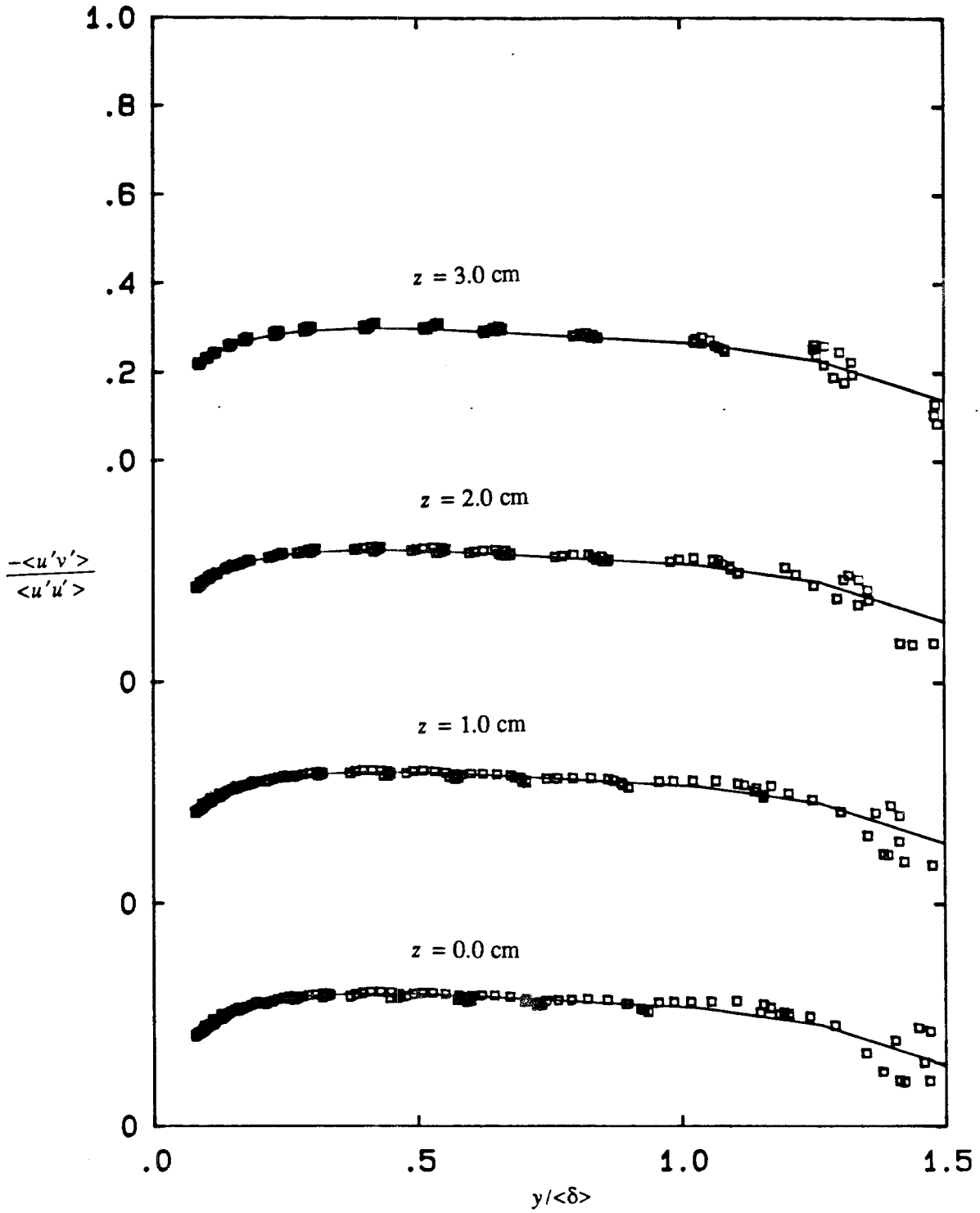

Figure 5.46b. Reynolds-stress ratio $-<u'v'>/<u'u'>$ against $y/<\delta>$ in passive region. Phases 6(1)16; z = 0(1)3 cm.

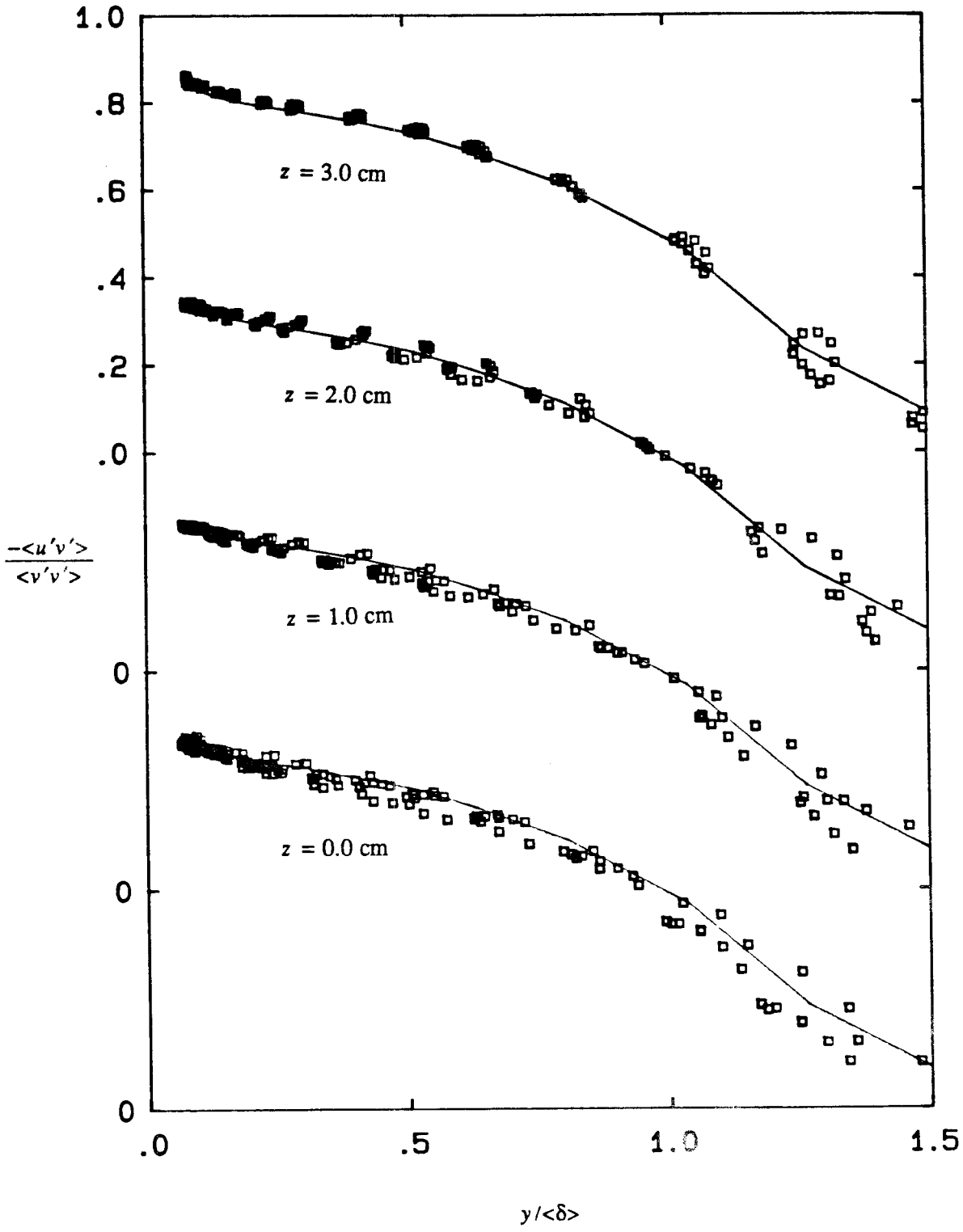

Figure 5.47a. Reynolds-stress ratio $-<u'v'>/<v'v'>$ against $y/<\delta>$ in active region. Phases 16(1)6; z = 0(1)3 cm.

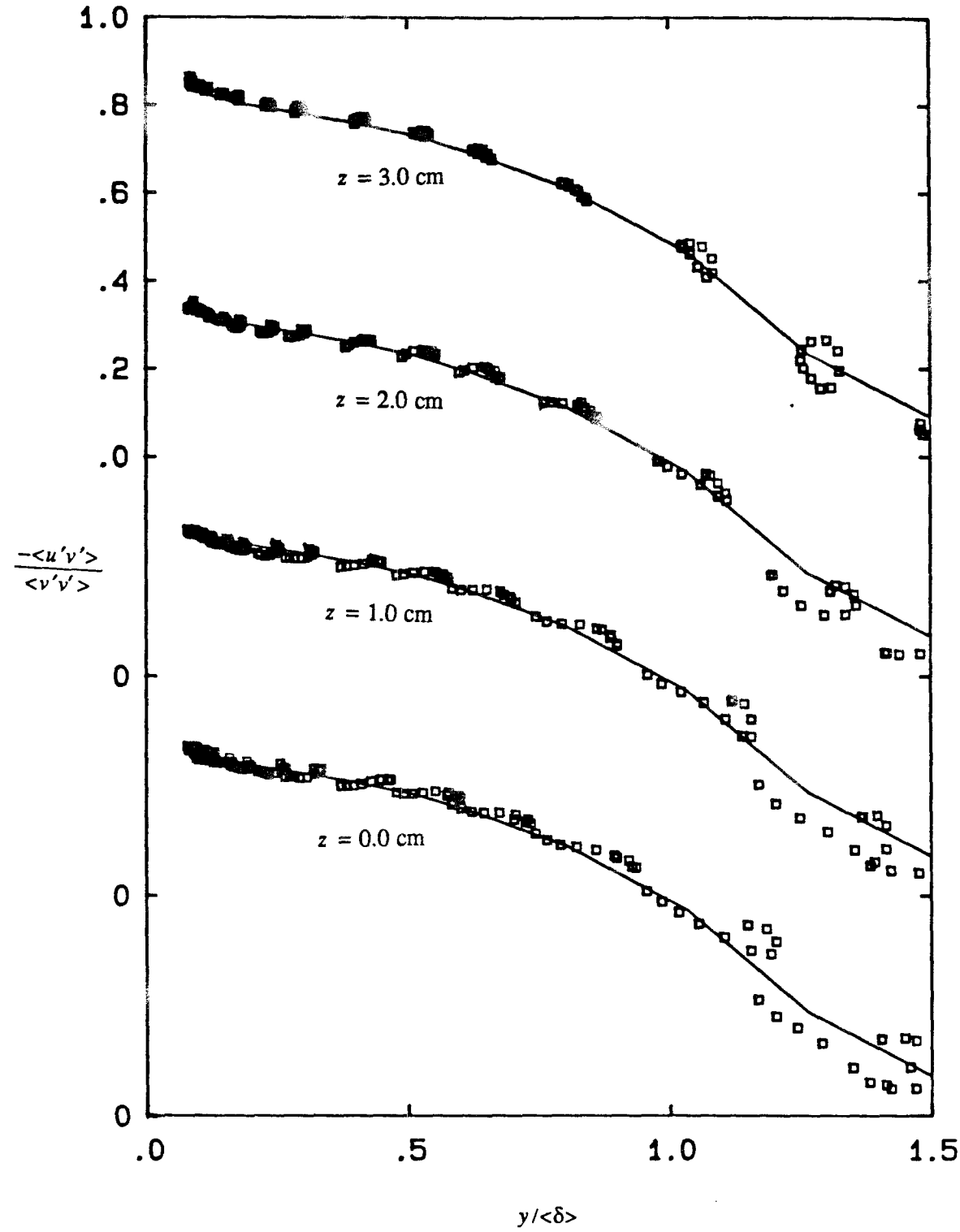

Figure 5.47b. Reynolds-stress ratio $-<u'v'>/<v'v'>$ against $y/<\delta>$ in passive region. Phases 6(1)16; z = 0(1)3 cm.

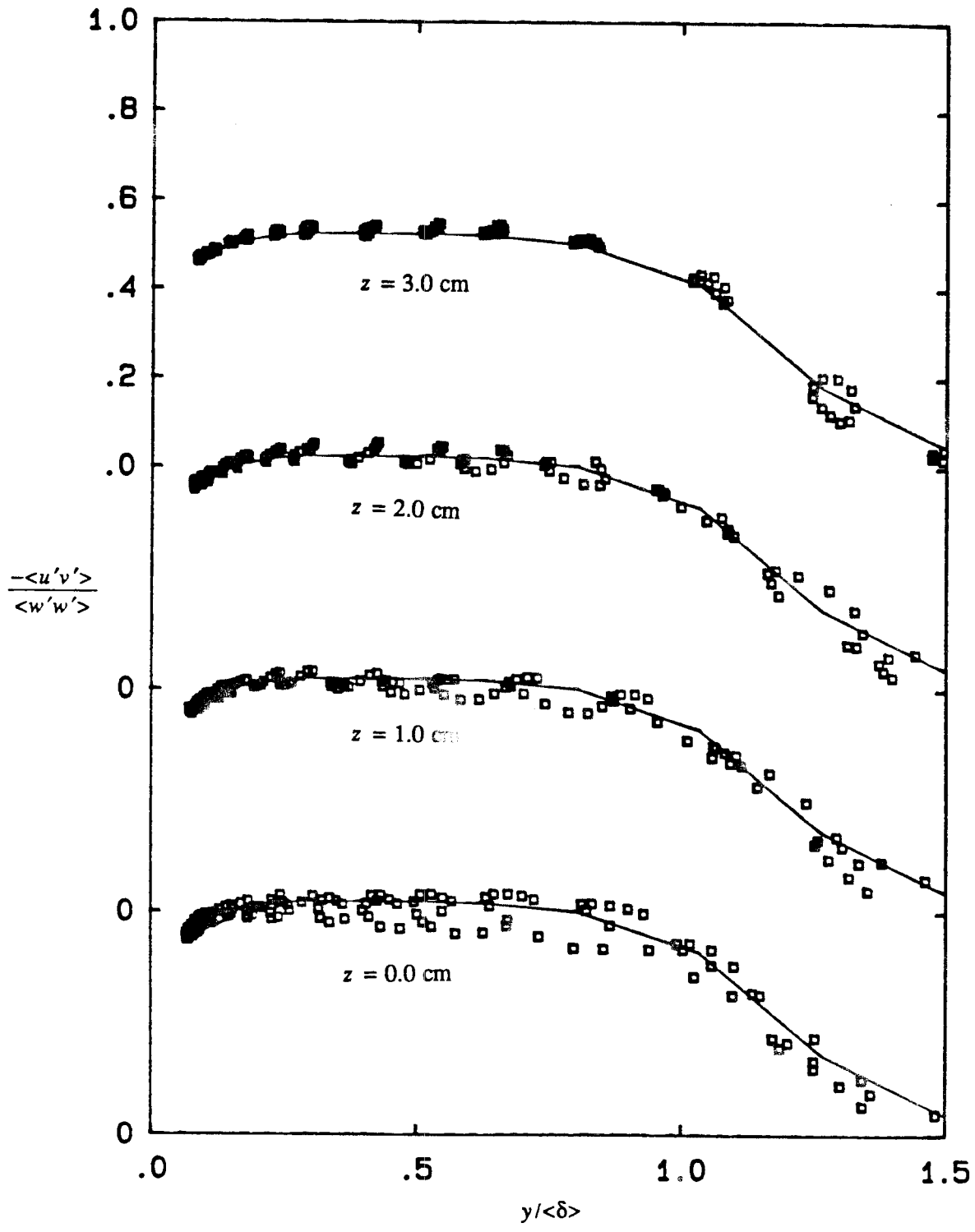

Figure 5.48a. Reynolds-stress ratio $-<u'v'>/<w'w'>$ against $y/<\delta>$ in active region. Phases 16(1)6; z = 0(1)3 cm.

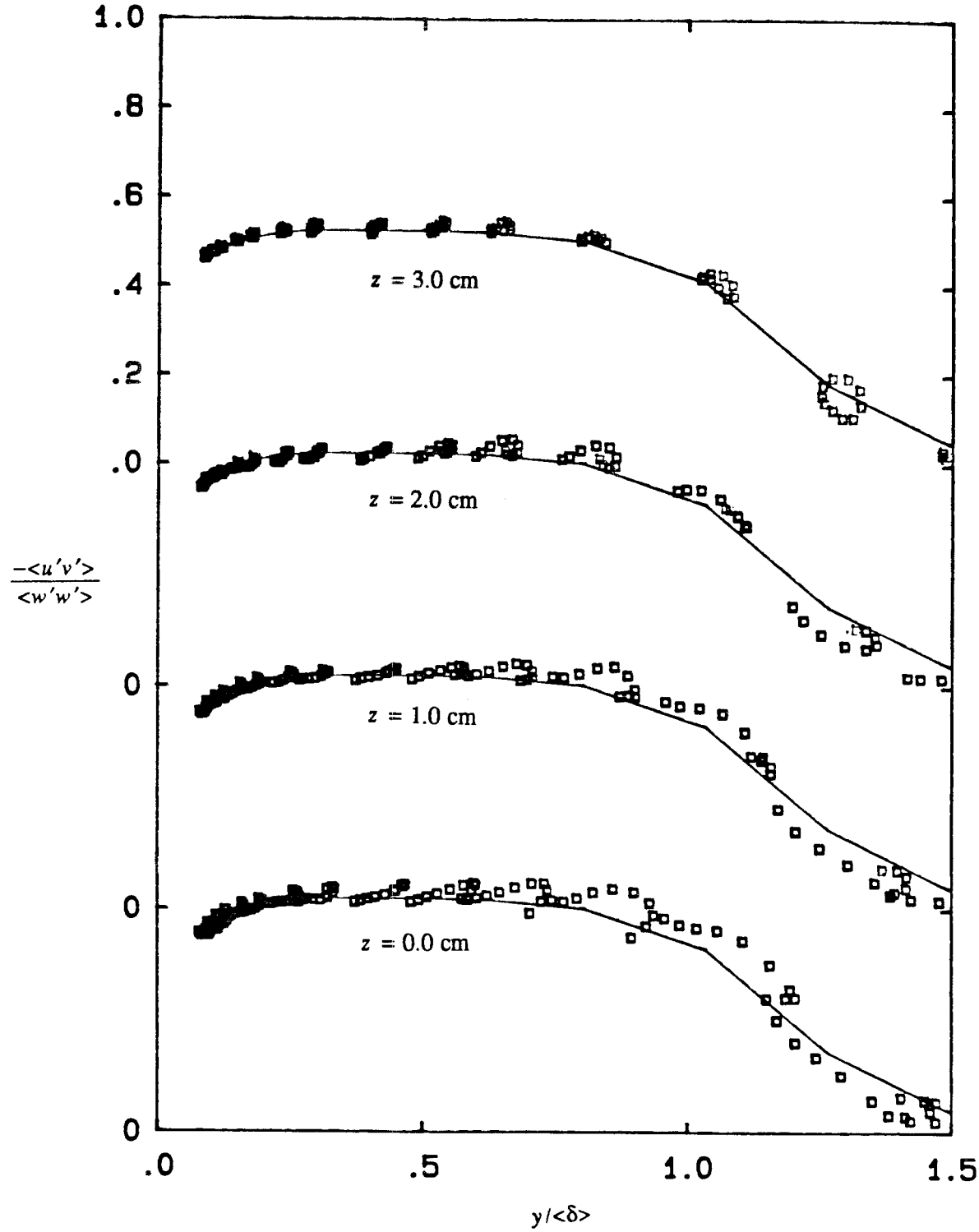

Figure 5.48b. Reynolds-stress ratio $-<u'v'>/<w'w'>$ against $y/<\delta>$ in passive region. Phases 6(1)16; z = 0.(1)3 cm.

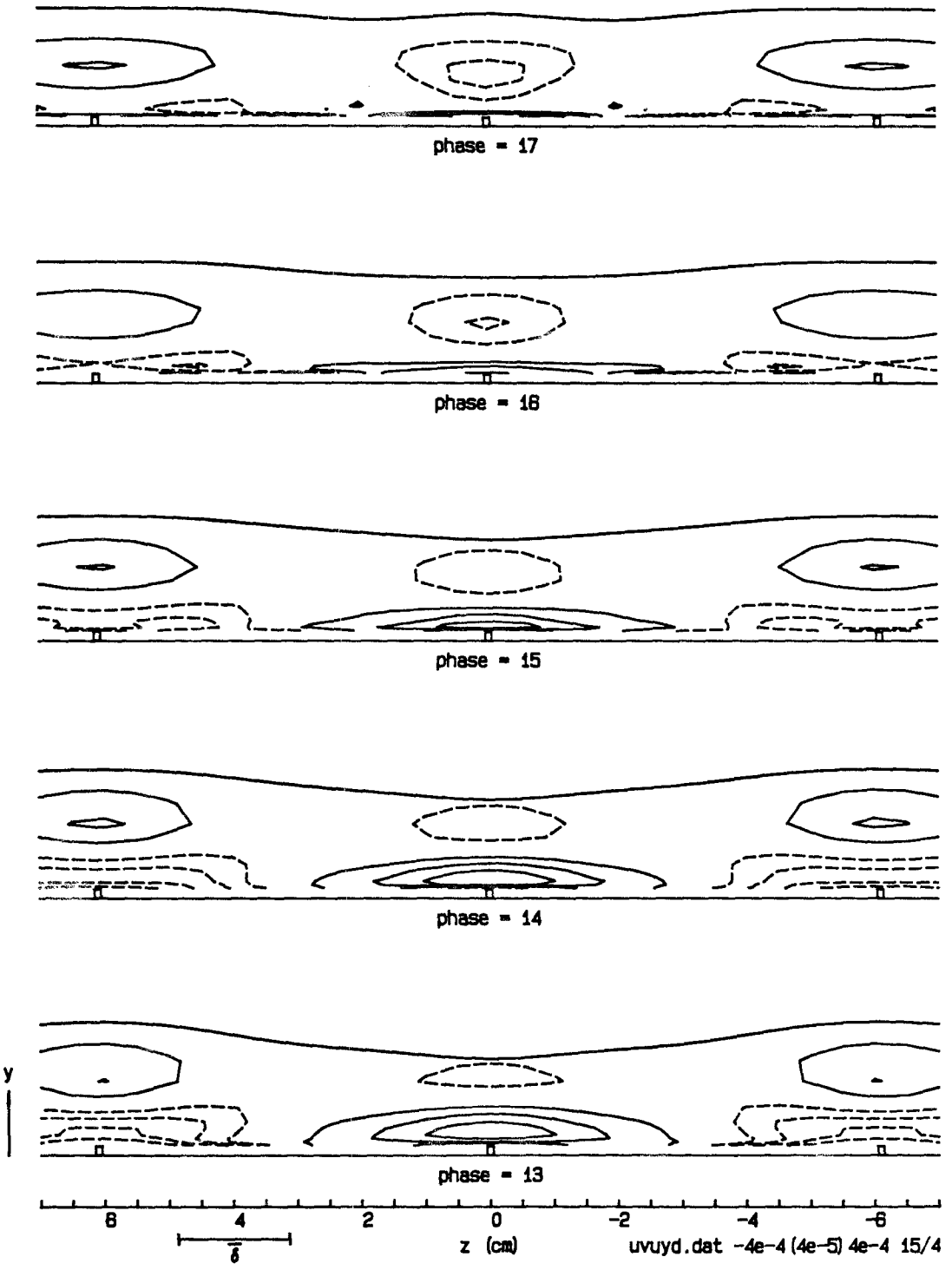

Figure 5.49. Turbulence-production perturbation $-\langle u'v' \rangle \partial \langle u \rangle / \partial y + \overline{\langle u'v' \rangle \partial \langle u \rangle / \partial y}$ in the $z-y$ plane. Contour interval 0.00004.

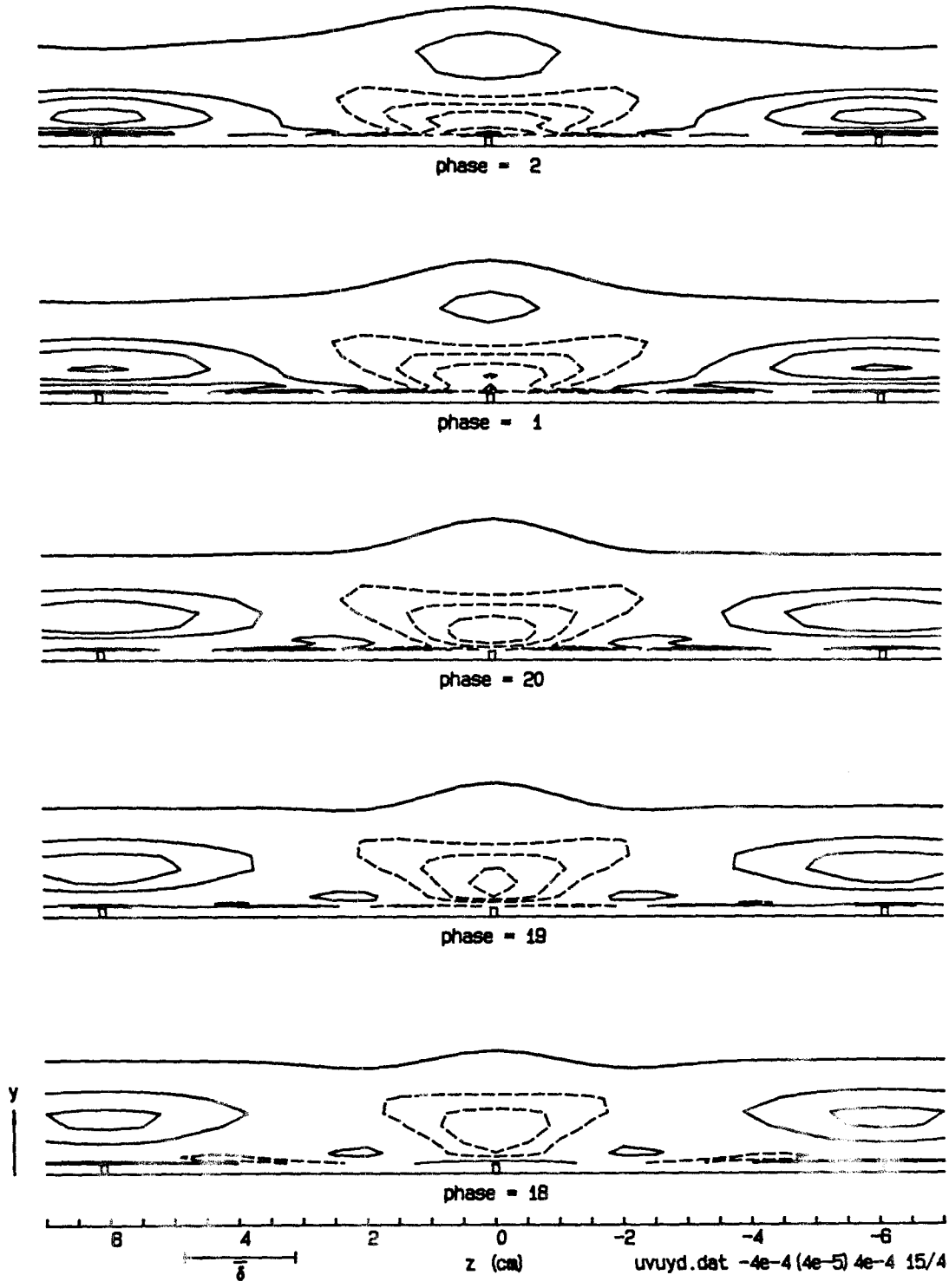

Figure 5.49 (cont'd.). Turbulence-production perturbation $-\langle u'v' \rangle \partial \langle u \rangle / \partial y + \overline{\langle u'v' \rangle \partial \langle u \rangle / \partial y}$ in the $z-y$ plane.

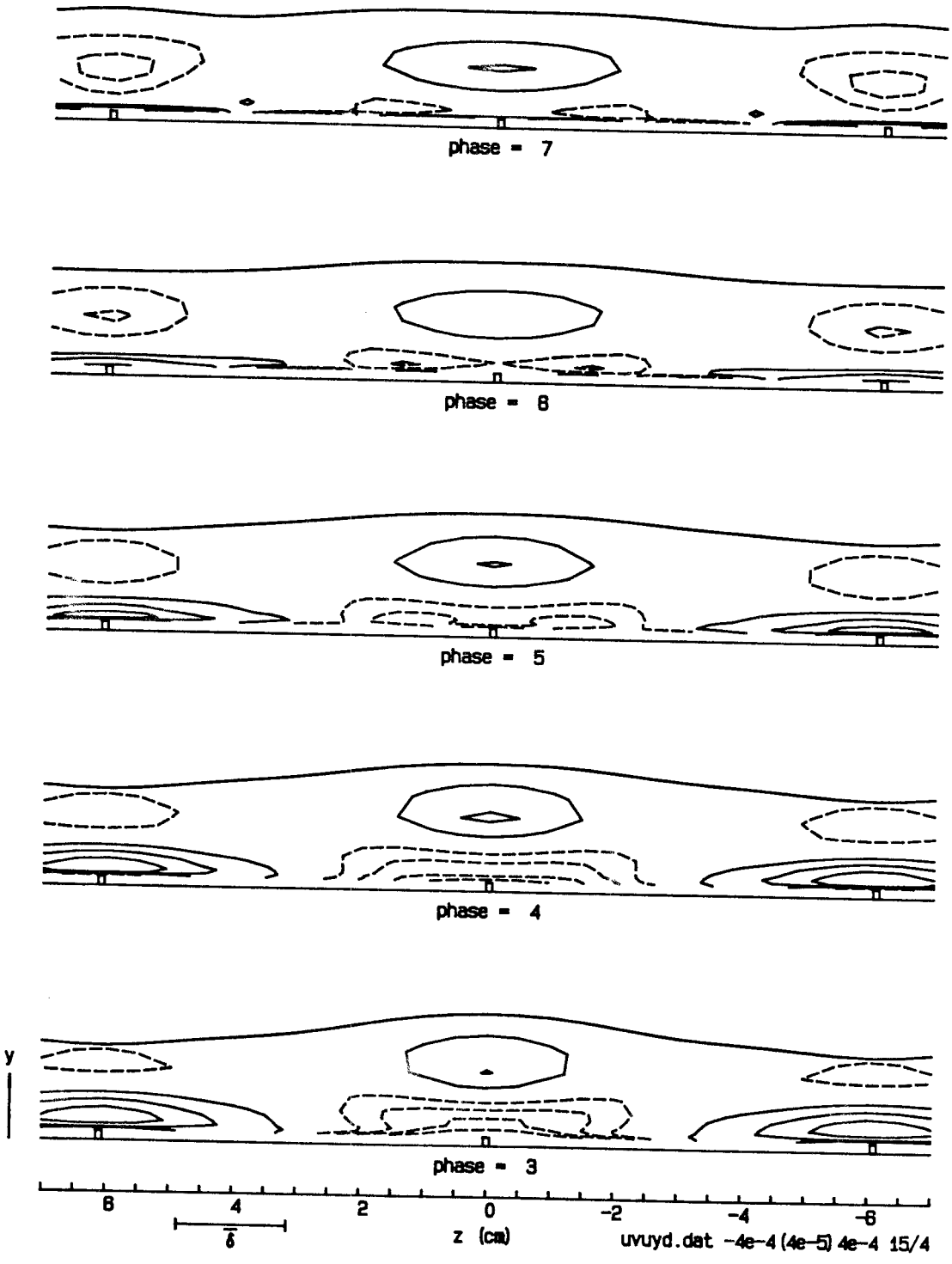

Figure 5.49 (cont'd.). Turbulence-production perturbation $-\langle u'v' \rangle \partial \langle u \rangle / \partial y + \overline{\langle u'v' \rangle \partial \langle u \rangle / \partial y}$ in the $z-y$ plane.

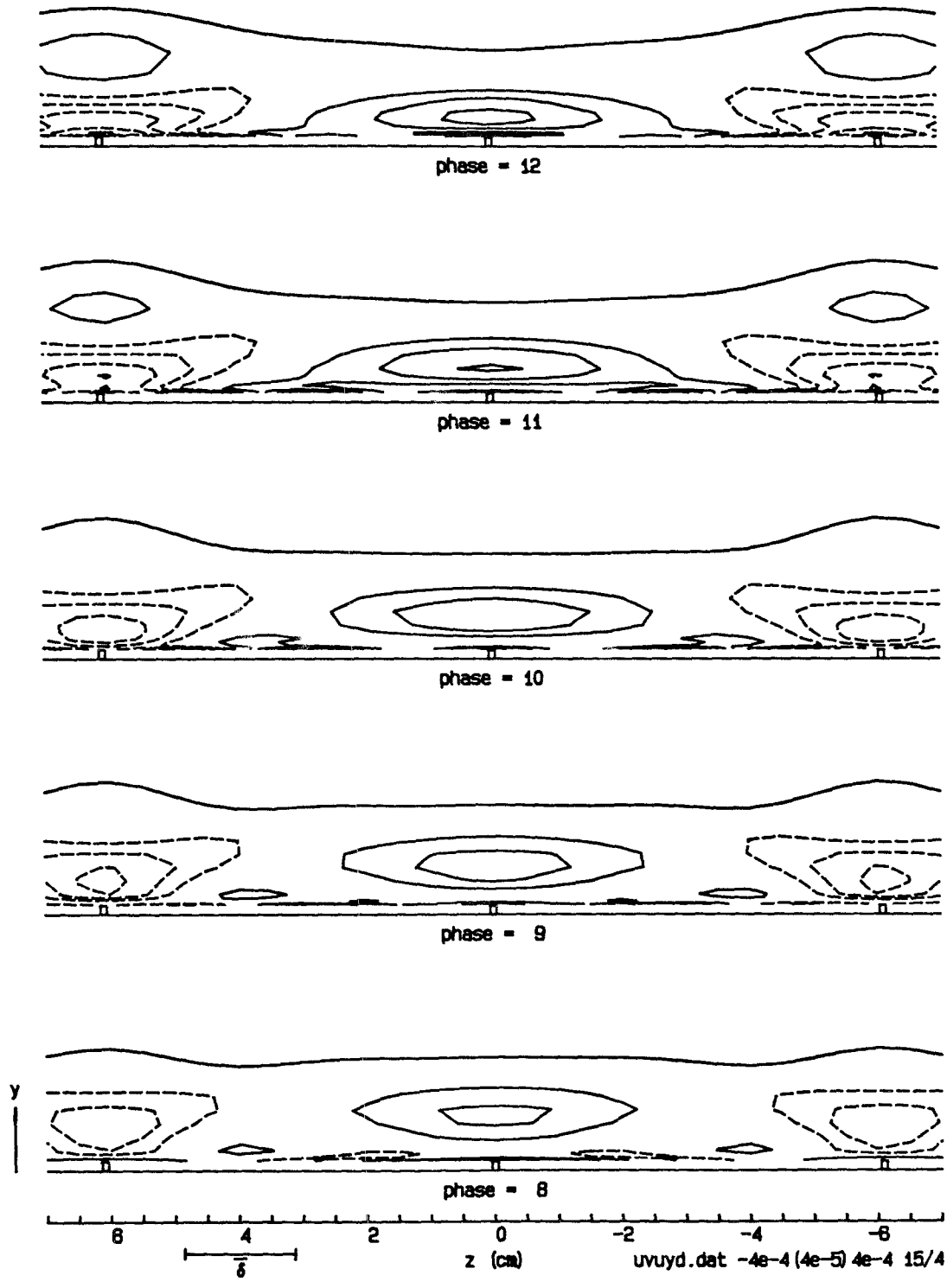

Figure 5.49 (cont'd.). Turbulence-production perturbation $-\langle u'v' \rangle \partial \langle u \rangle / \partial y + \overline{\langle u'v' \rangle \partial \langle u \rangle / \partial y}$ in the $z-y$ plane.

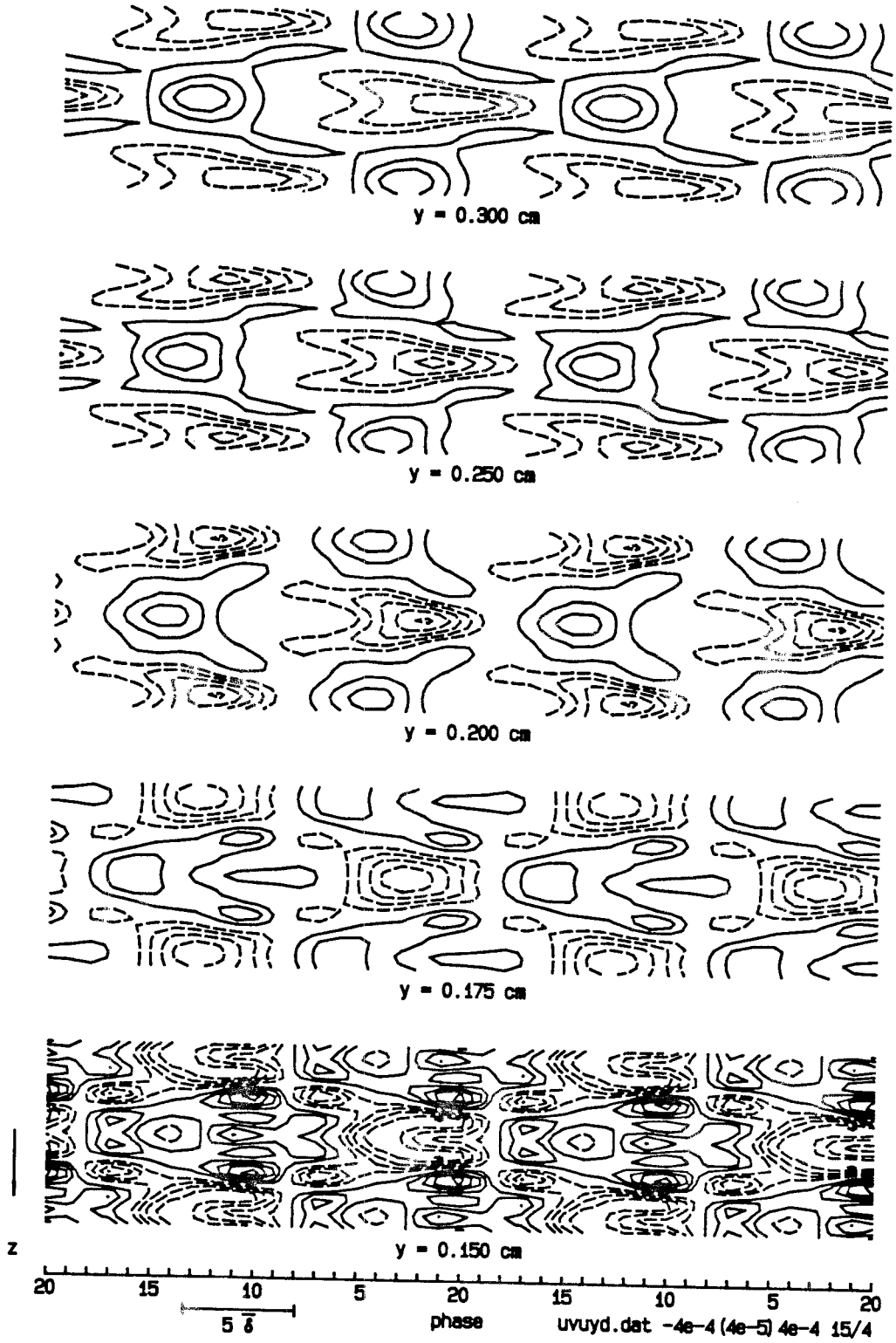

Figure 5.50. Turbulence-production perturbation $-\langle u'v' \rangle \partial \langle u \rangle / \partial y + \overline{\langle u'v' \rangle \partial \langle u \rangle / \partial y}$ in the $t-z$ plane. Contour interval 0.00004.

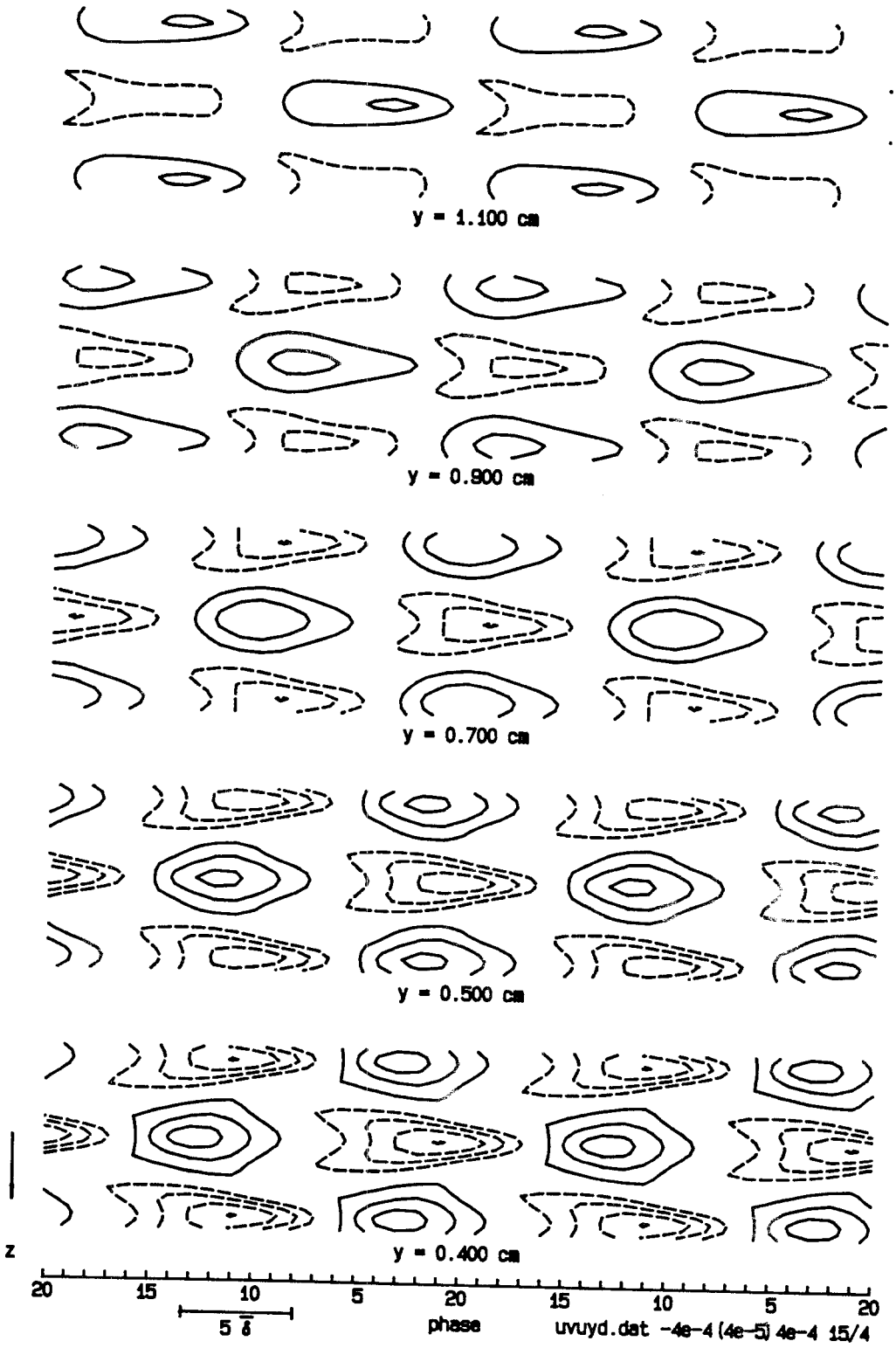

Figure 5.50 (cont'd.). Turbulence-production perturbation $-\langle u'v' \rangle \partial \langle u \rangle / \partial y + \overline{\langle u'v' \rangle \partial \langle u \rangle / \partial y}$ in the $t-z$ plane.

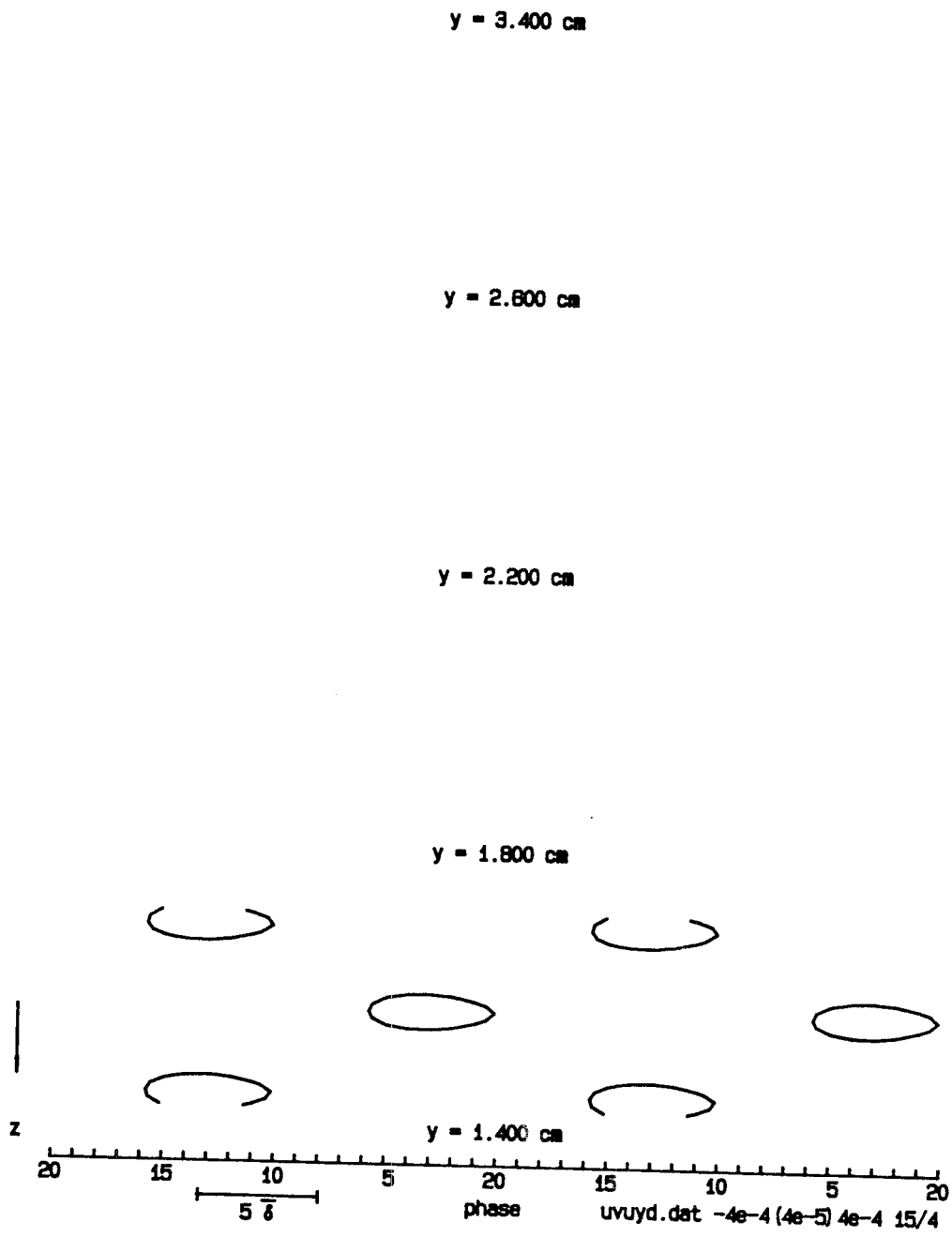

Figure 5.50 (cont'd.). Turbulence-production perturbation $-\langle u'v' \rangle \partial \langle u \rangle / \partial y + \overline{\langle u'v' \rangle \partial \langle u \rangle / \partial y}$ in the t–z plane.

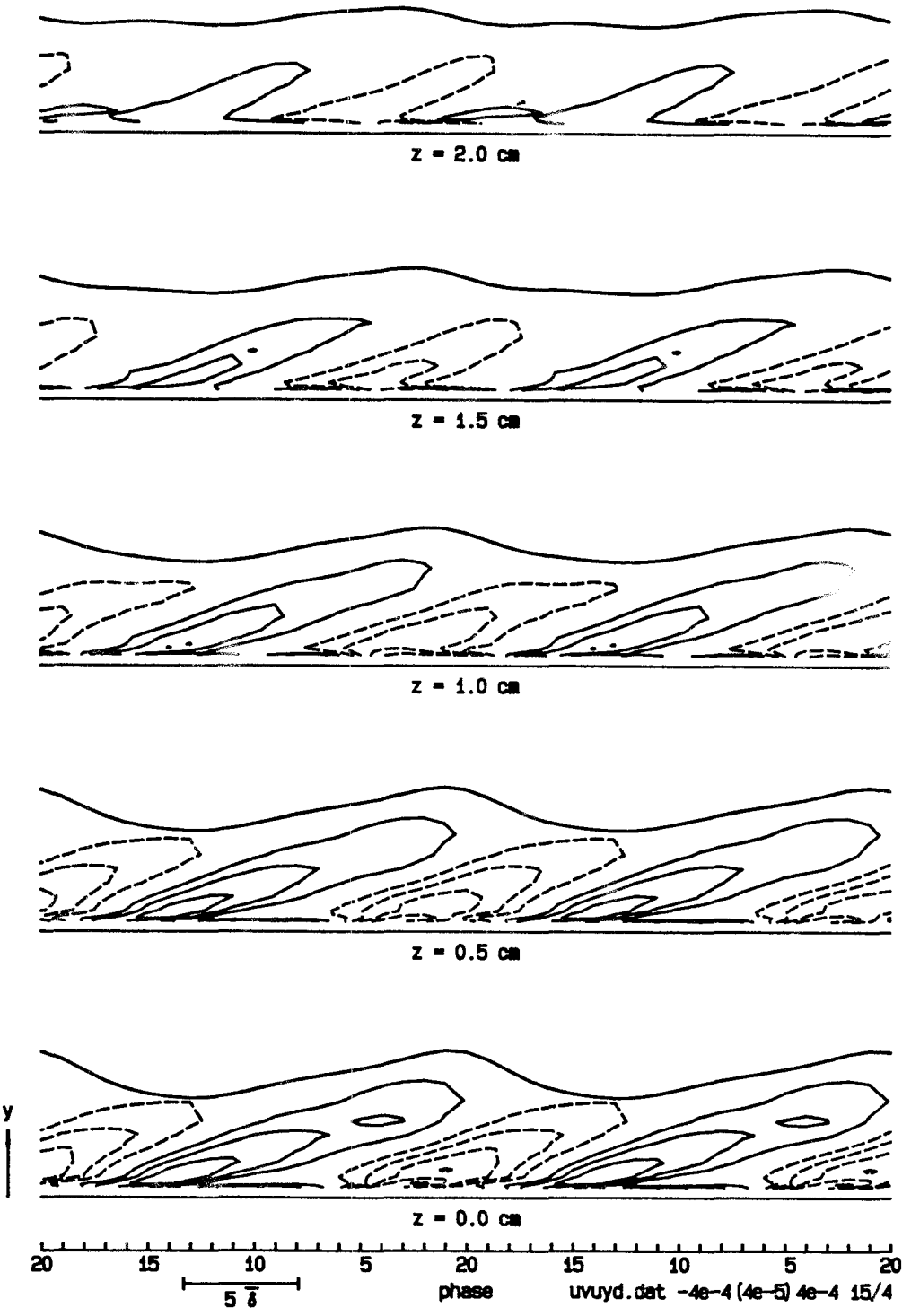

Figure 5.51. Turbulence-production perturbation $-\langle u'v' \rangle \partial \langle u \rangle / \partial y + \overline{\langle u'v' \rangle \partial \langle u \rangle / \partial y}$ in the $t-y$ plane. Contour interval 0.00004.

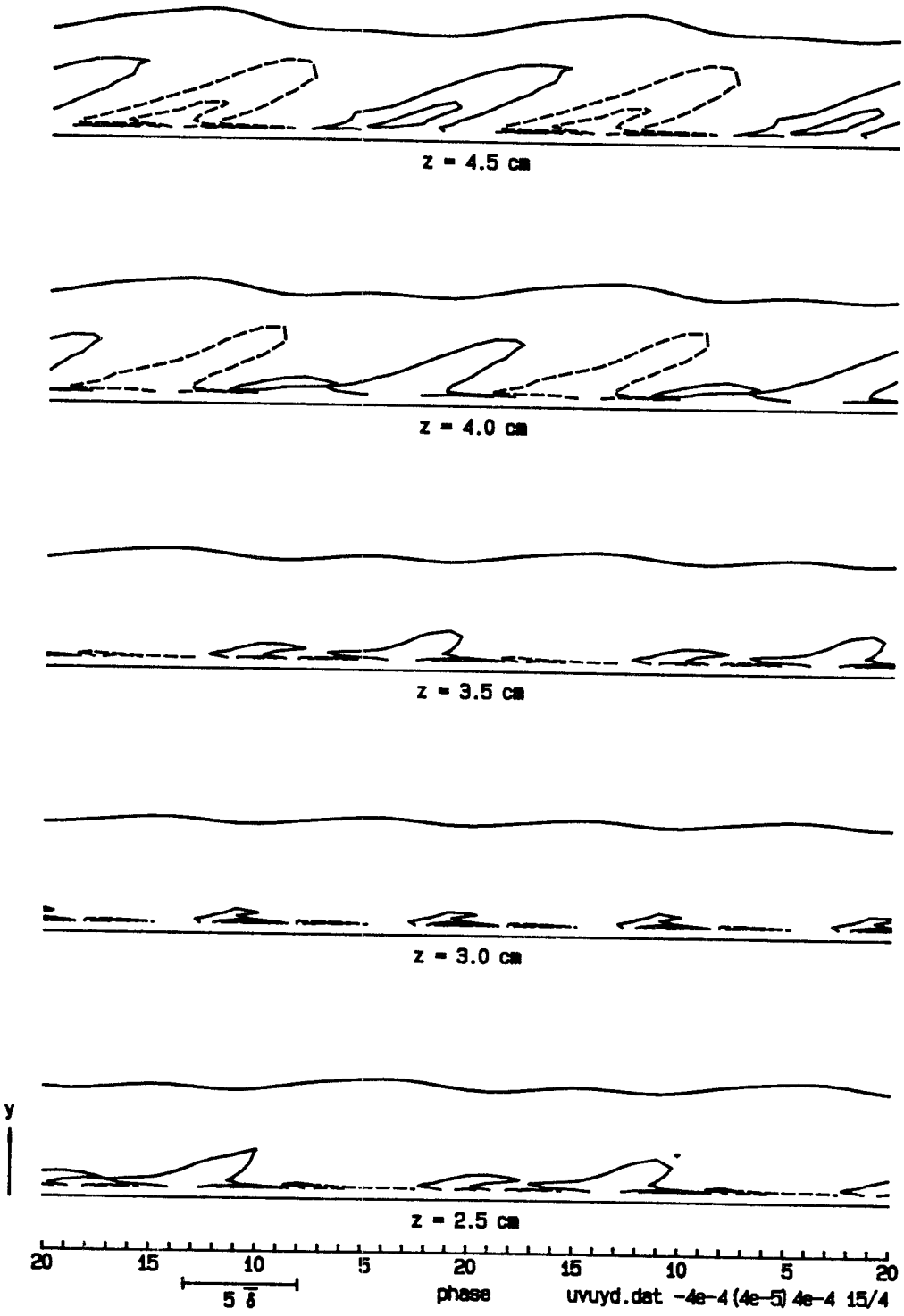

Figure 5.51 (cont'd.). Turbulence-production perturbation $-\langle u'v' \rangle \partial \langle u \rangle / \partial y + \overline{\langle u'v' \rangle \partial \langle u \rangle / \partial y}$ in the t–y plane.

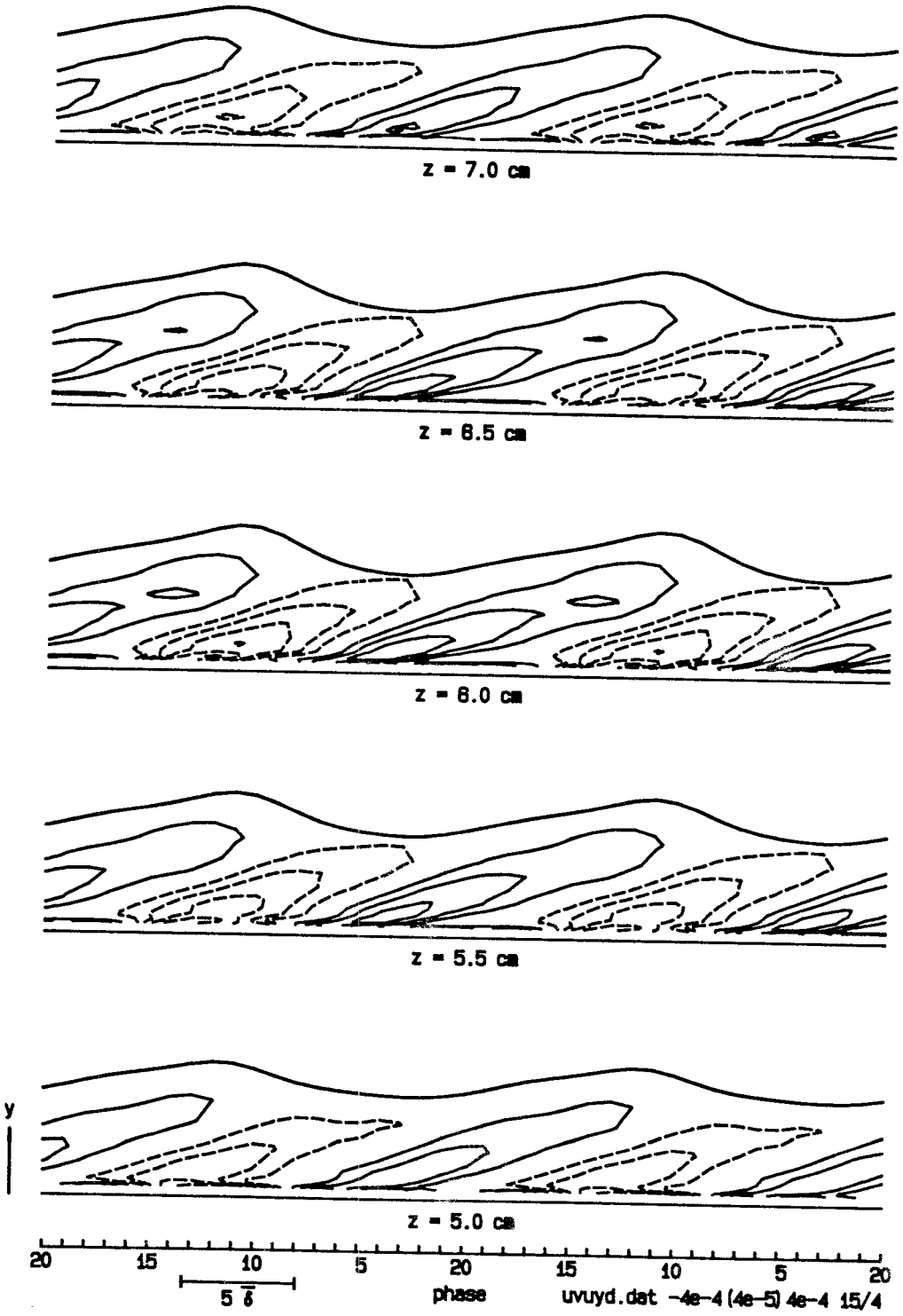

Figure 5.51 (cont'd.). Turbulence-production perturbation $-\langle u'v' \rangle \partial \langle u \rangle / \partial y + \overline{\langle u'v' \rangle \partial \langle u \rangle / \partial y}$ in the t–y plane.

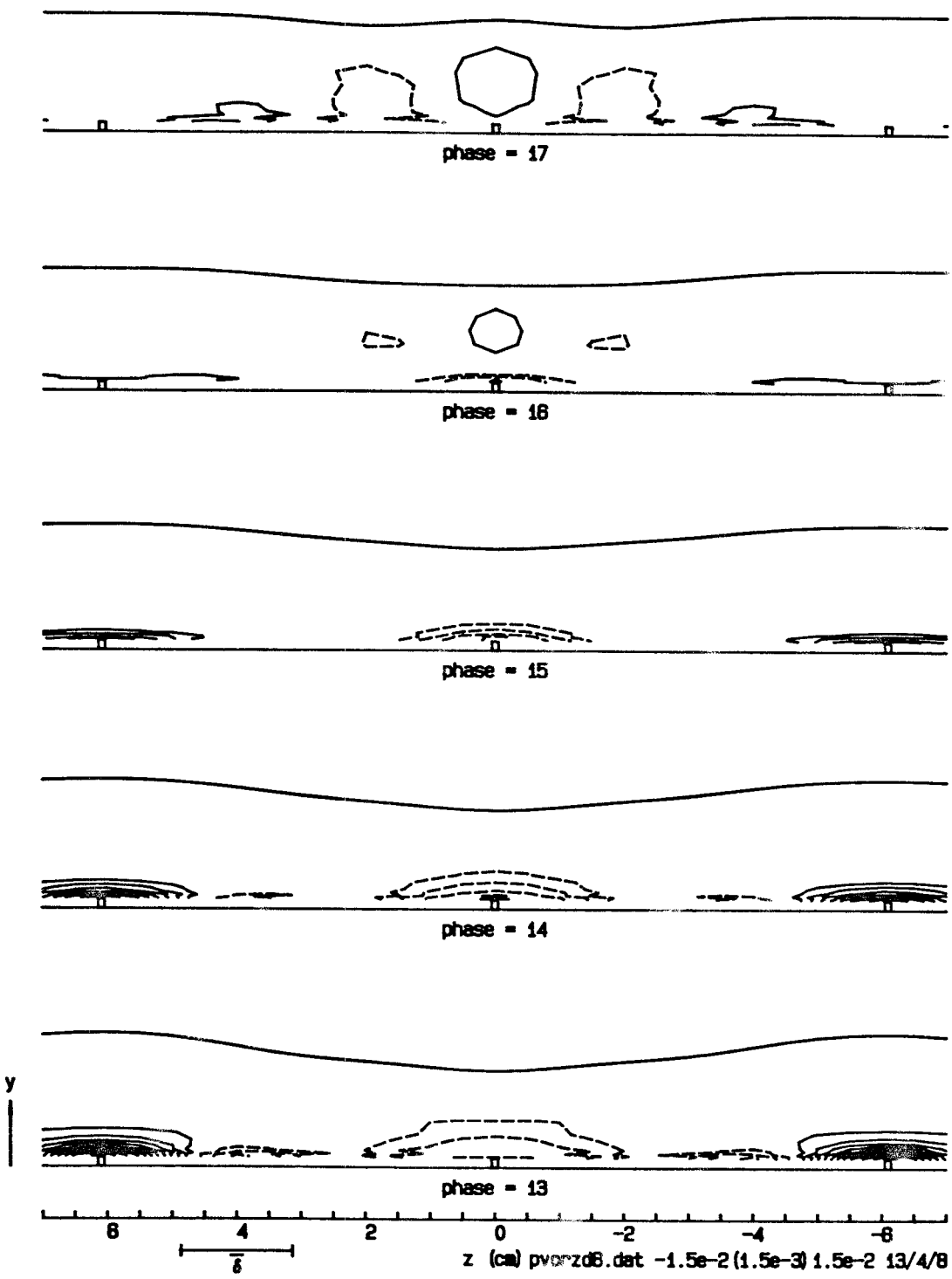

Figure 5.52. Stretching term for $\langle\omega_z\rangle$, $\langle\omega_z\rangle\,\partial\langle w\rangle/\partial z$, in the $z-y$ plane. Contour interval 0.0015.

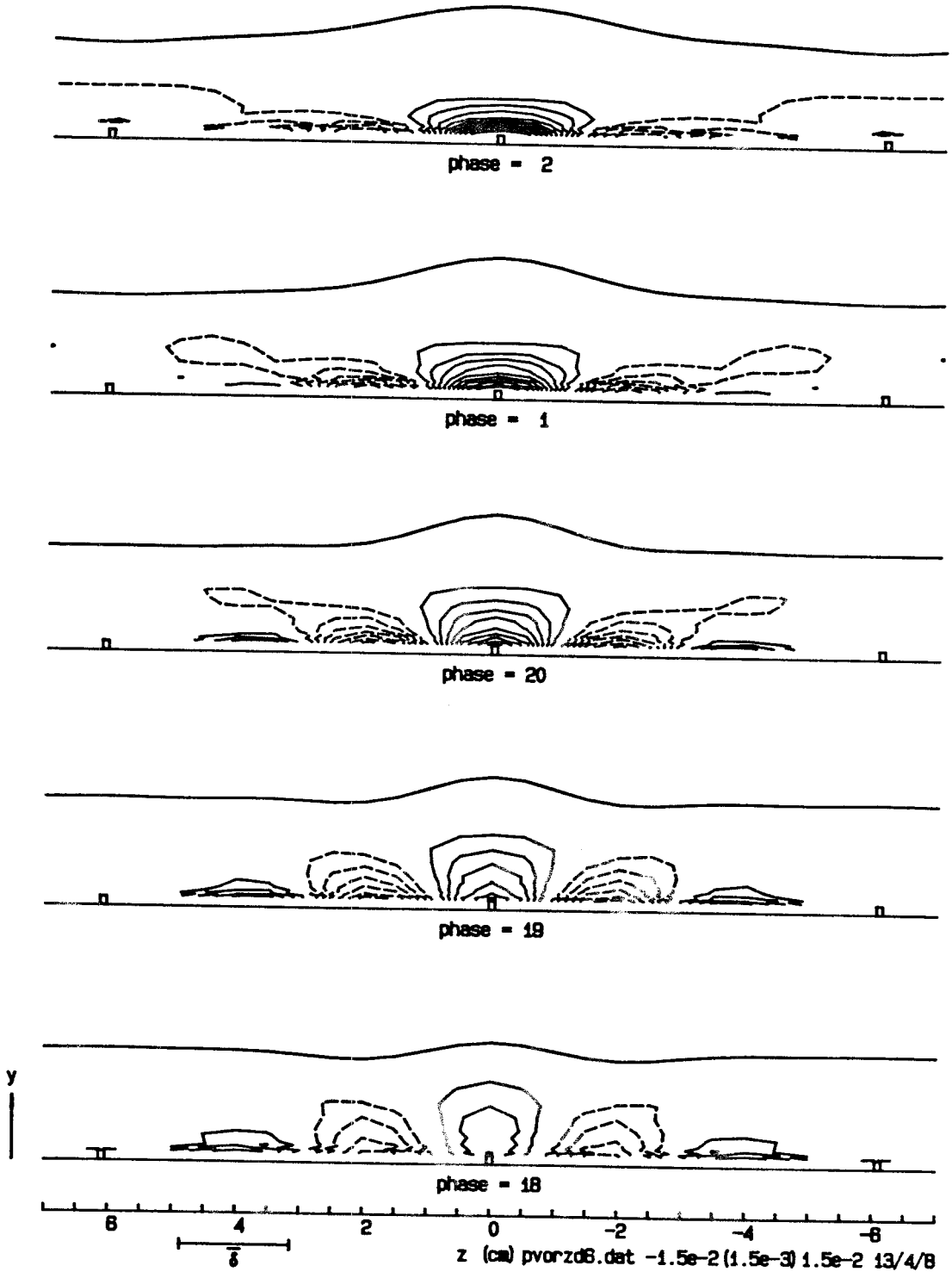

Figure 5.52 (cont'd.). Stretching term for $<\omega_z>$, $<\omega_z>\partial<w>/\partial z$, in the $z-y$ plane.

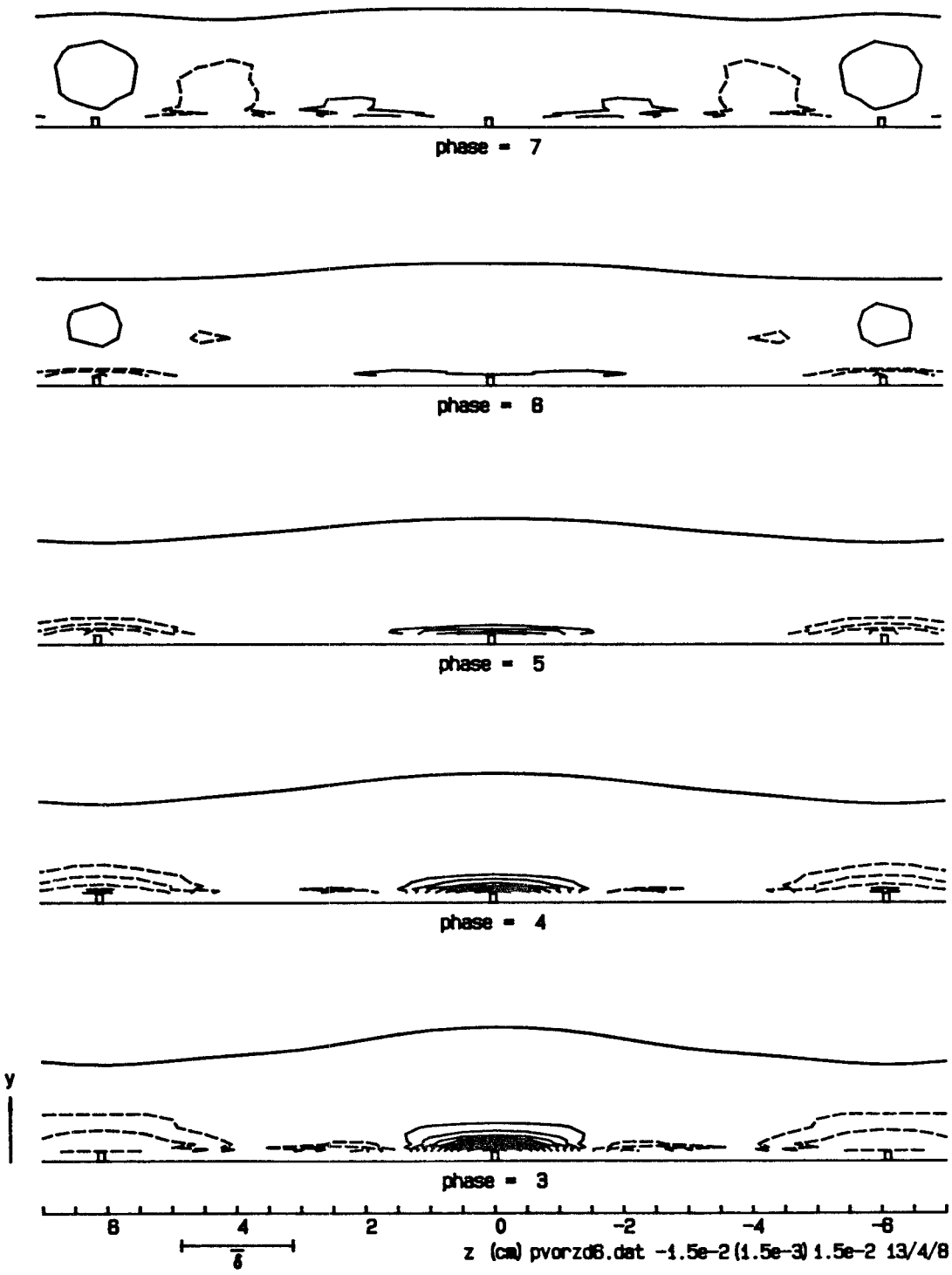

Figure 5.52 (cont'd.). Stretching term for $\langle\omega_z\rangle$, $\langle\omega_z\rangle\,\partial\langle w\rangle/\partial z$, in the $z-y$ plane.

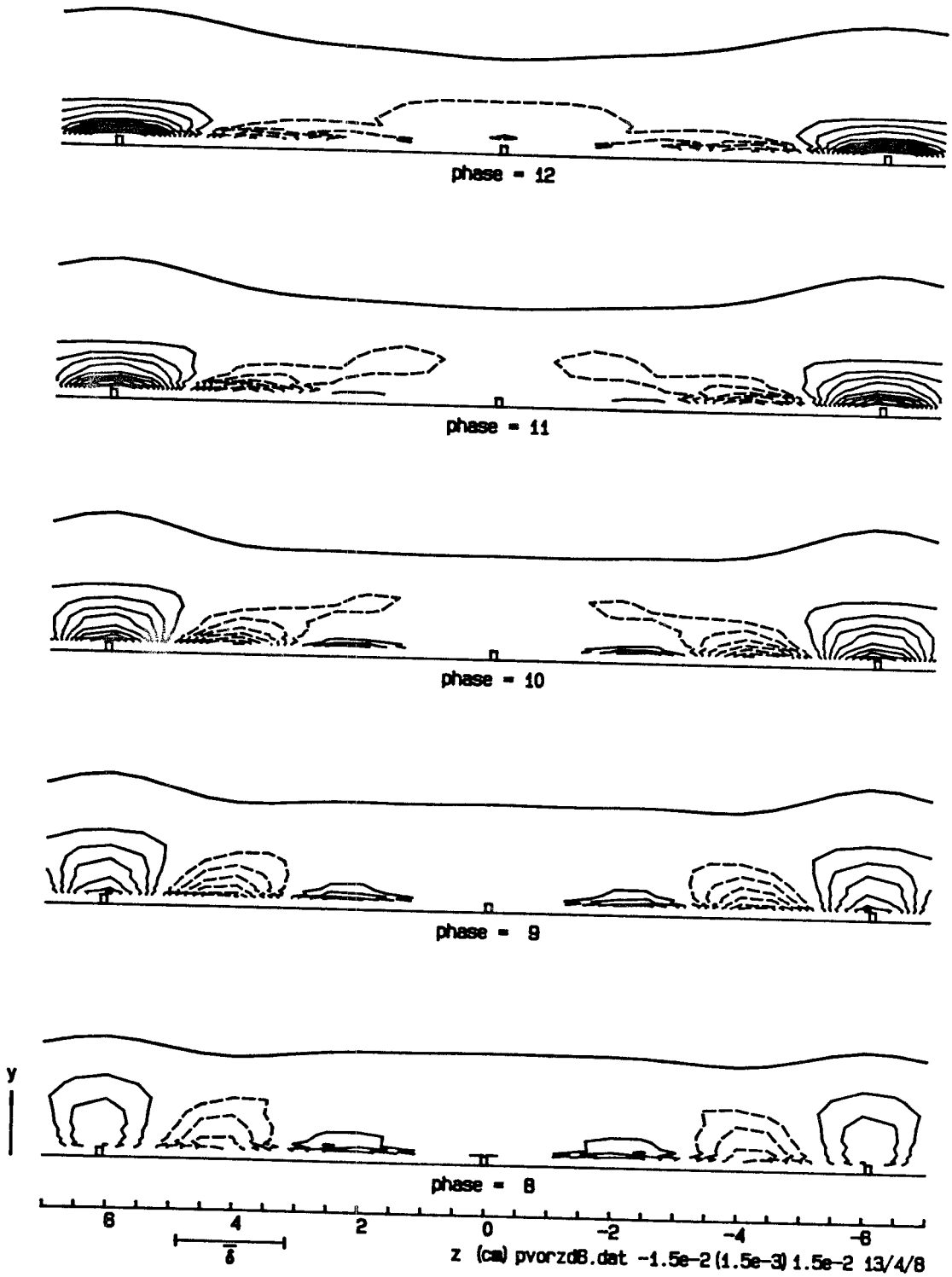

Figure 5.52 (cont'd.). Stretching term for $<\omega_z>$, $<\omega_z>\partial<w>/\partial z$, in the $z-y$ plane.

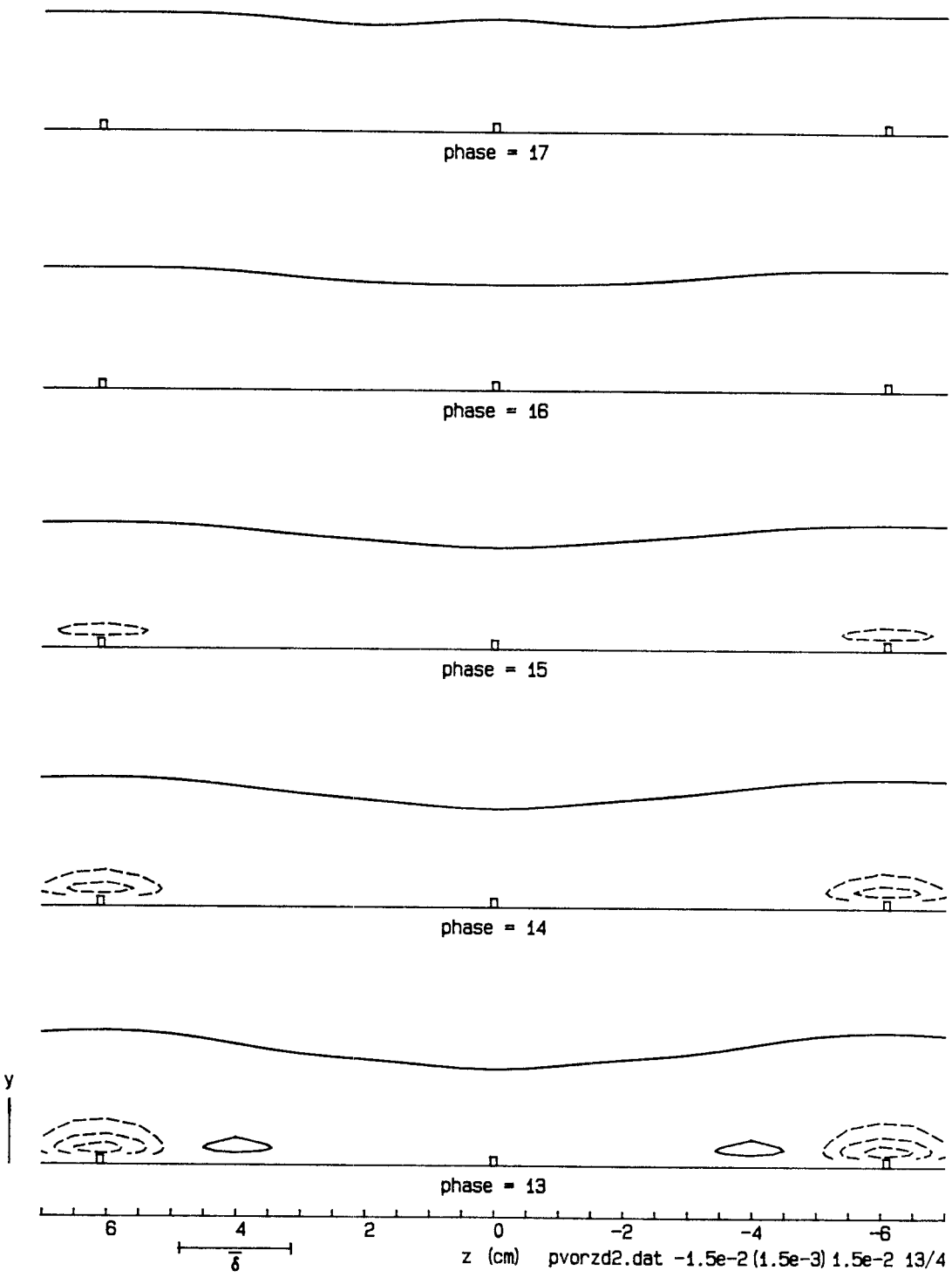

Figure 5.53. Convective term for $<\omega_z>$, $-<v>\partial<\omega_z>/\partial y$, in the $z-y$ plane. Contour interval 0.0015.

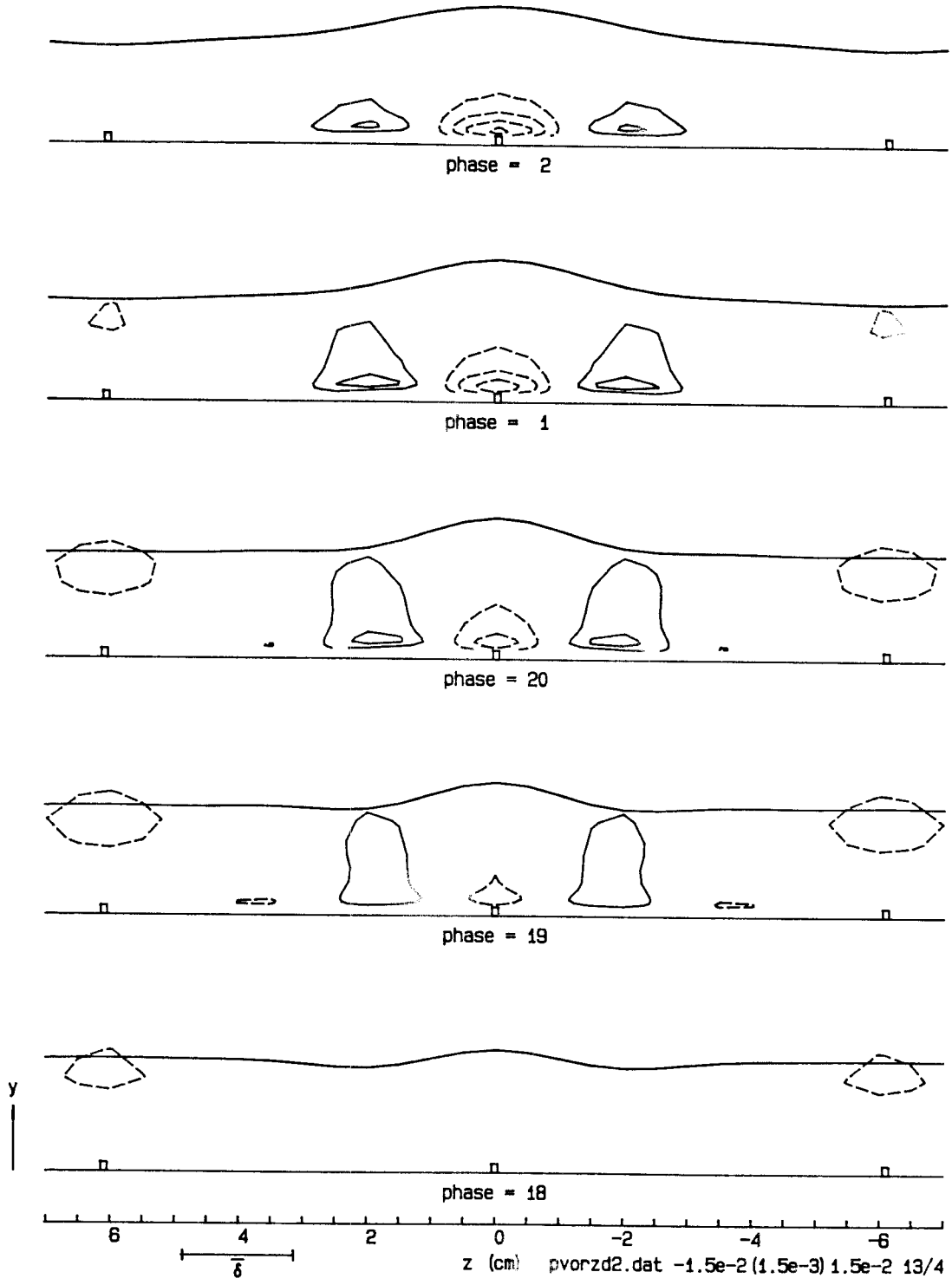

Figure 5.53 (cont'd.). Convective term for $<\omega_z>$, $-<v>\partial<\omega_z>/\partial y$, in the $z-y$ plane.

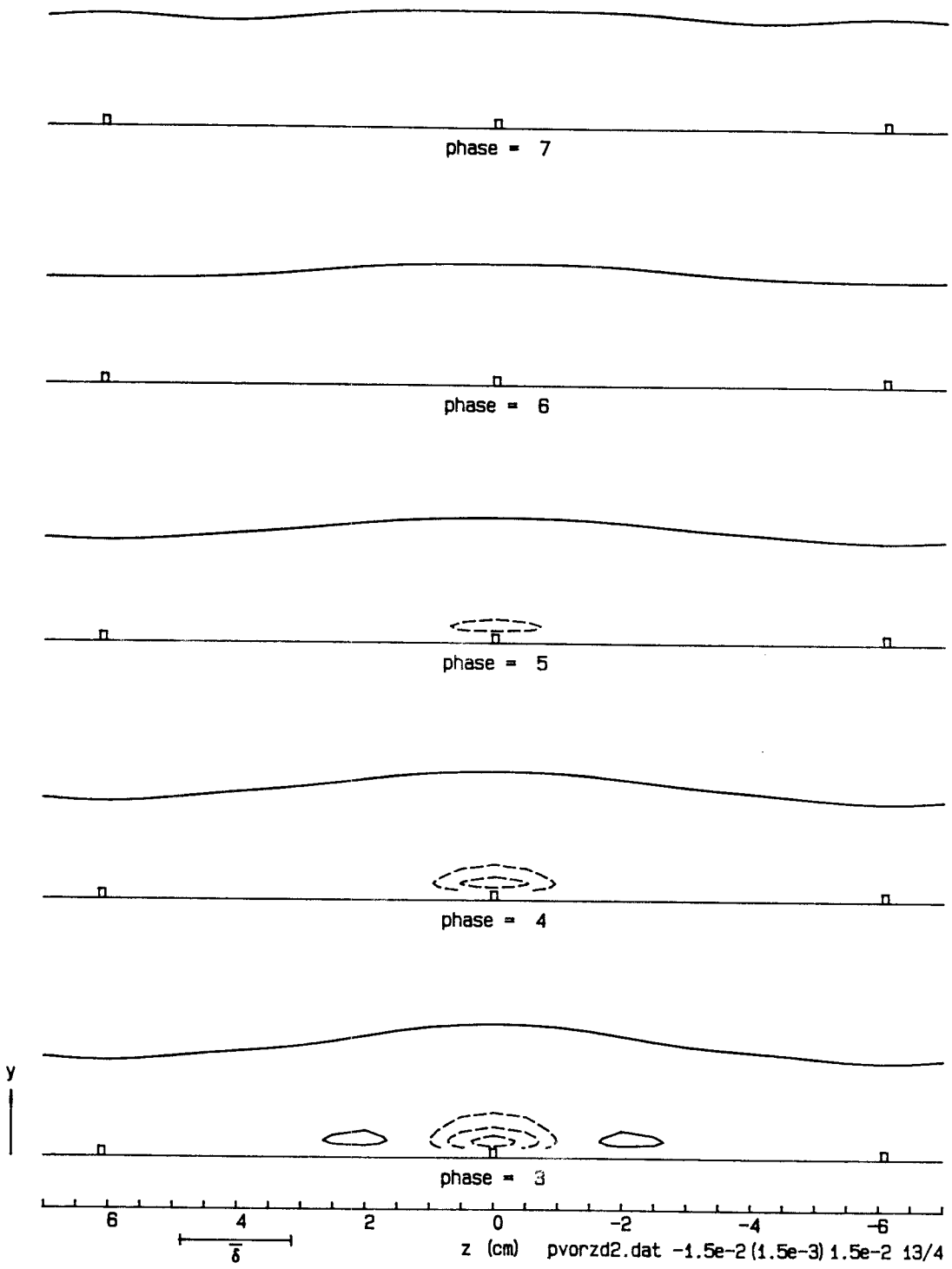

Figure 5.53 (cont'd.). Convective term for $<\omega_z>$, $-<v>\partial<\omega_z>/\partial y$, in the $z-y$ plane.

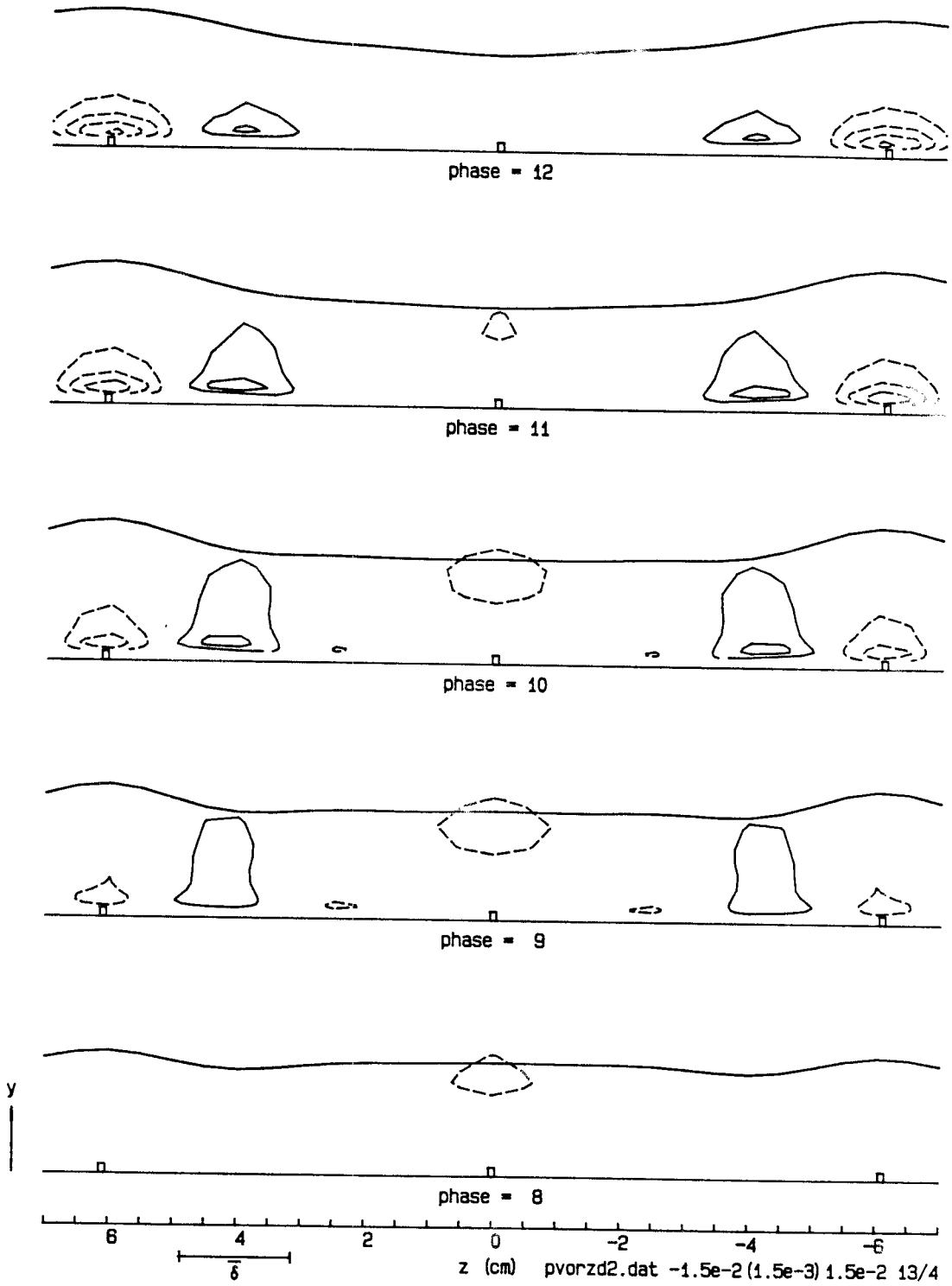

Figure 5.53 (cont'd.). Convective term for $\langle\omega_z\rangle$, $-\langle v\rangle\,\partial\langle\omega_z\rangle/\partial y$, in the $z-y$ plane.

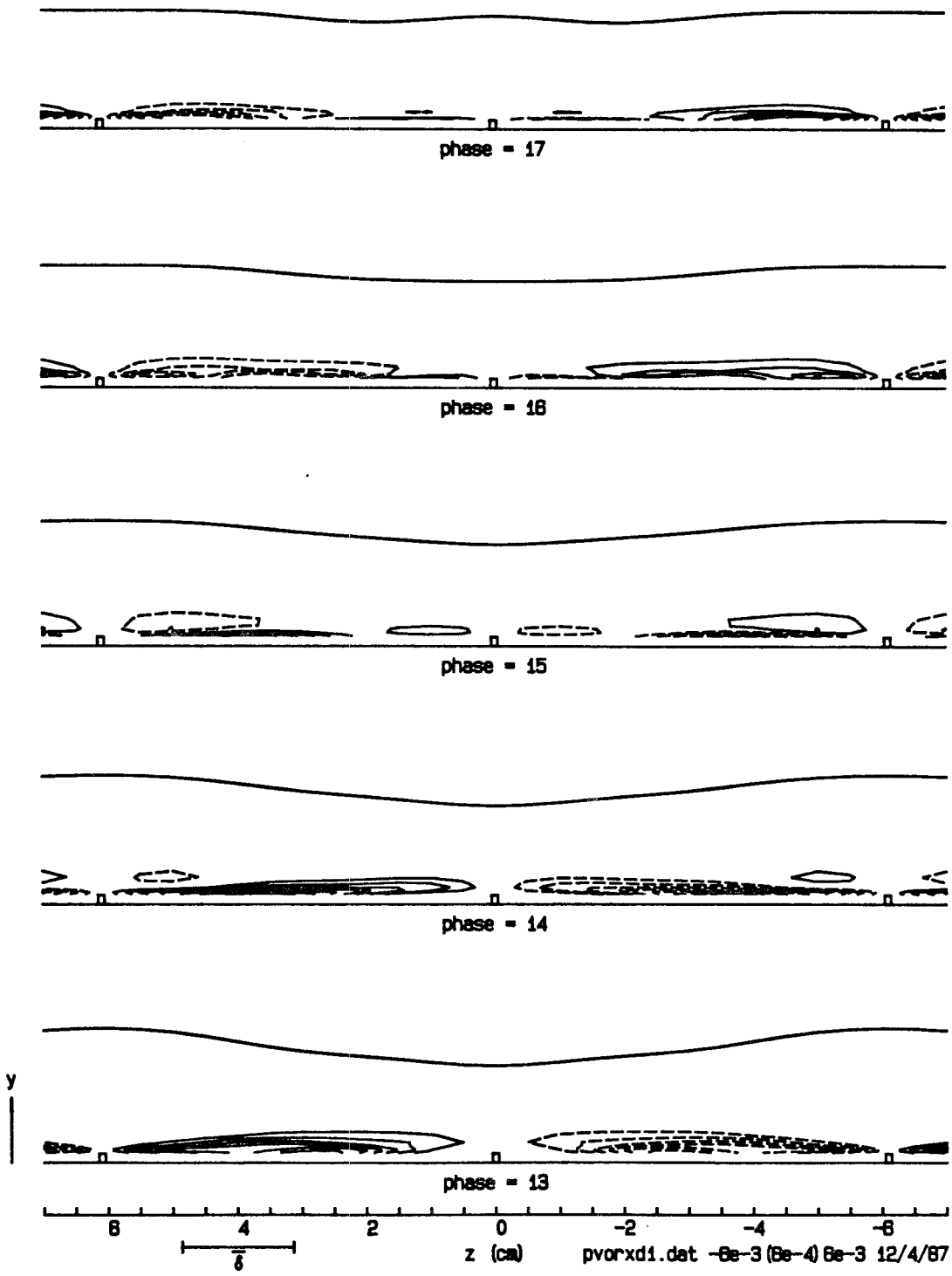

Figure 5.54. Convective term for $<\omega_x>$, $-(<u> - c)\,\partial<\omega_x>/\partial x$ in the $z-y$ plane. Contour interval 0.0006.

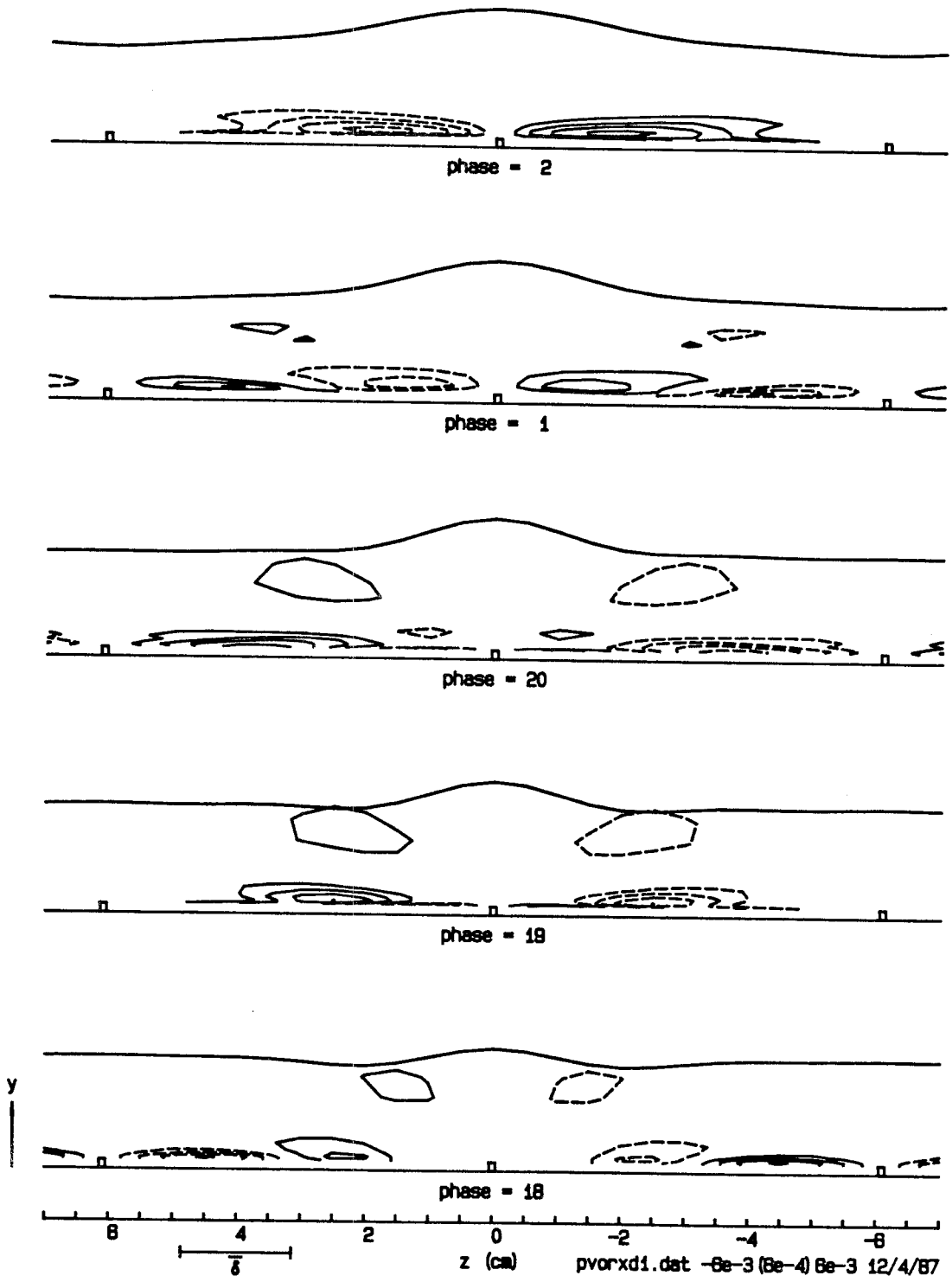

Figure 5.54 (cont'd.). Convective term for $\langle\omega_x\rangle$, $-(\langle u\rangle - c)\,\partial\langle\omega_x\rangle/\partial x$ in the $z-y$ plane.

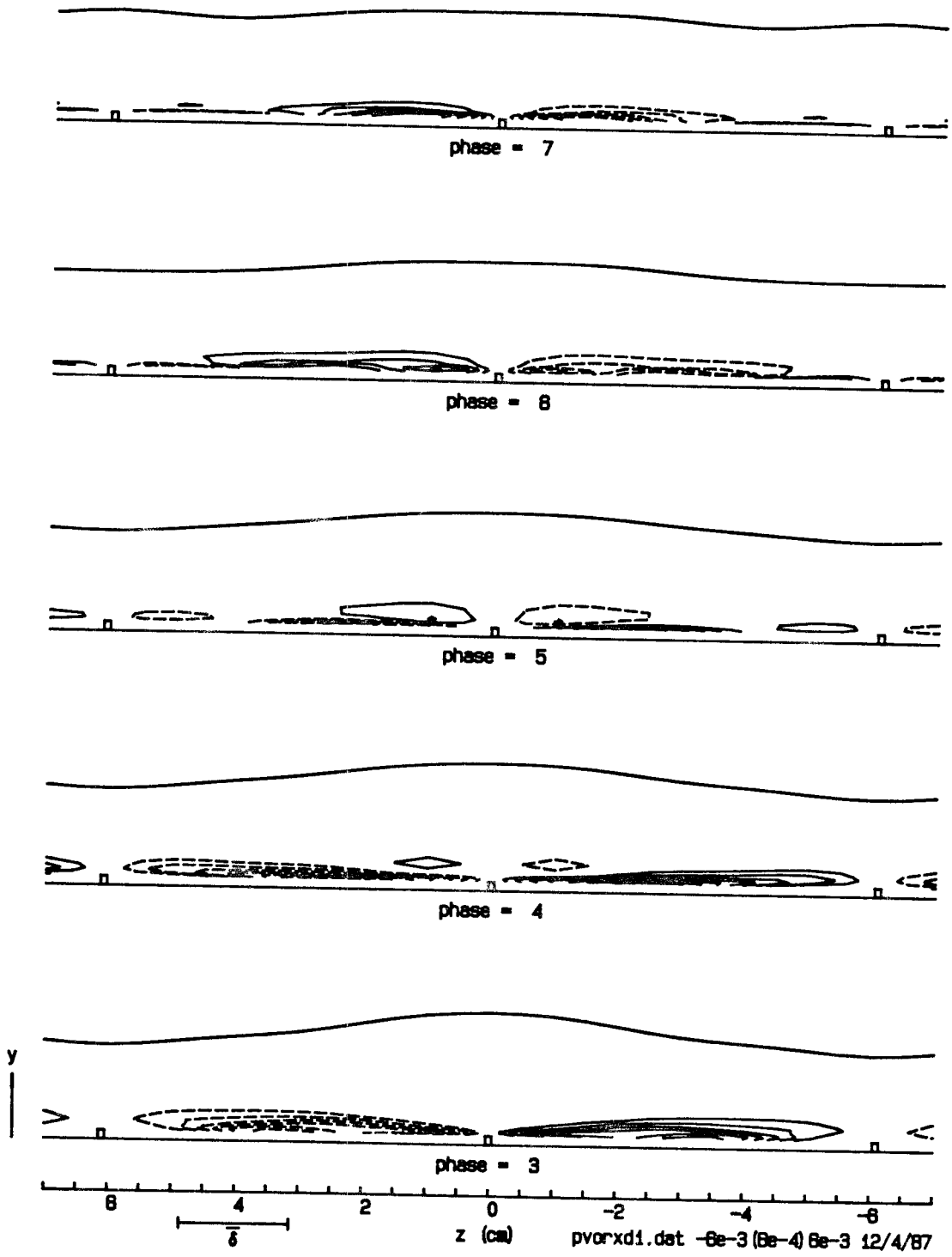

Figure 5.54 (cont'd.). Convective term for $\langle\omega_x\rangle$, $-(\langle u\rangle - c)\,\partial\langle\omega_x\rangle/\partial x$ in the $z-y$ plane.

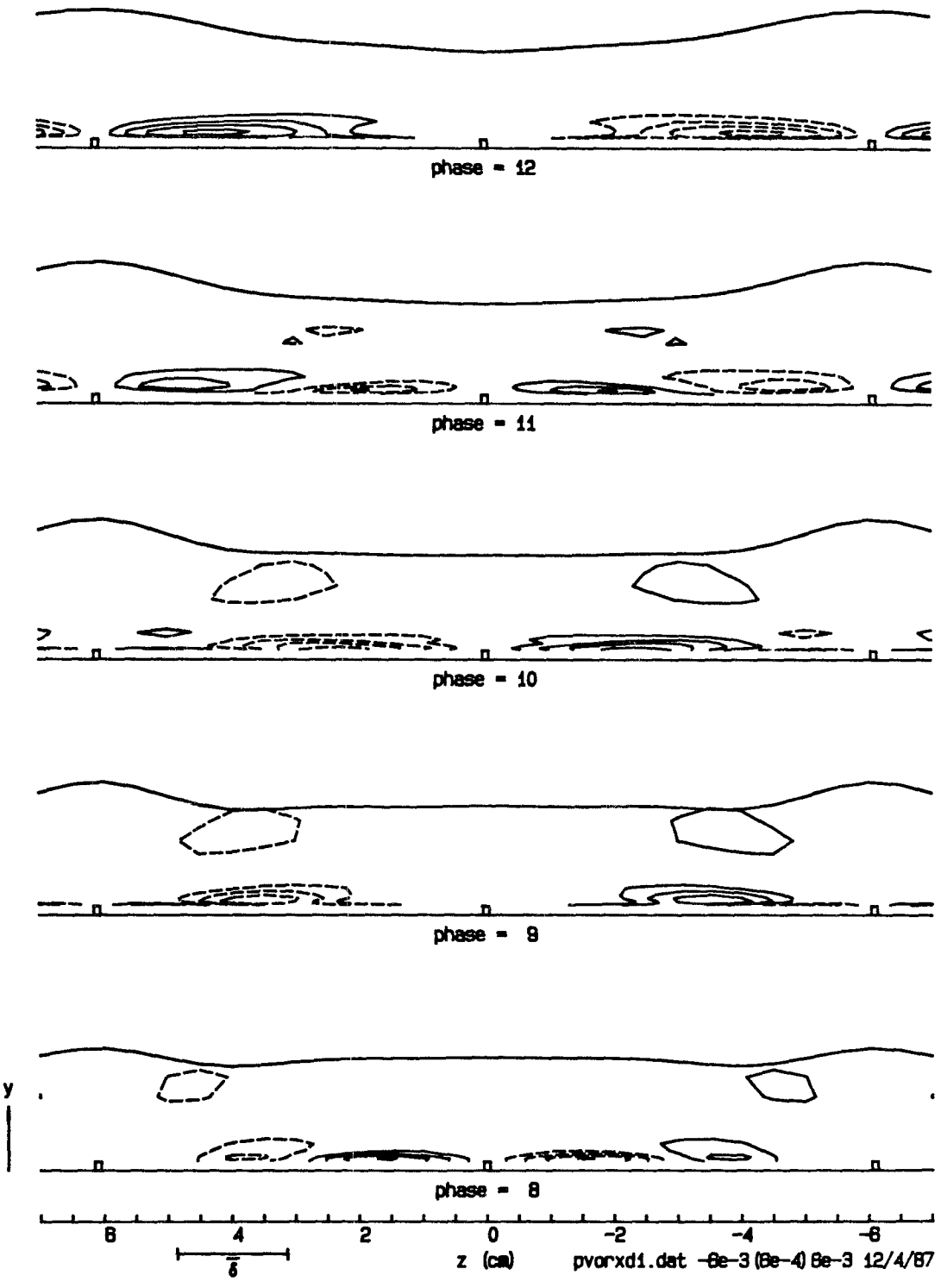

Figure 5.54 (cont'd.). Convective term for $<\omega_x>$, $-(<u> - c)\,\partial<\omega_x>/\partial x$ in the $z-y$ plane.

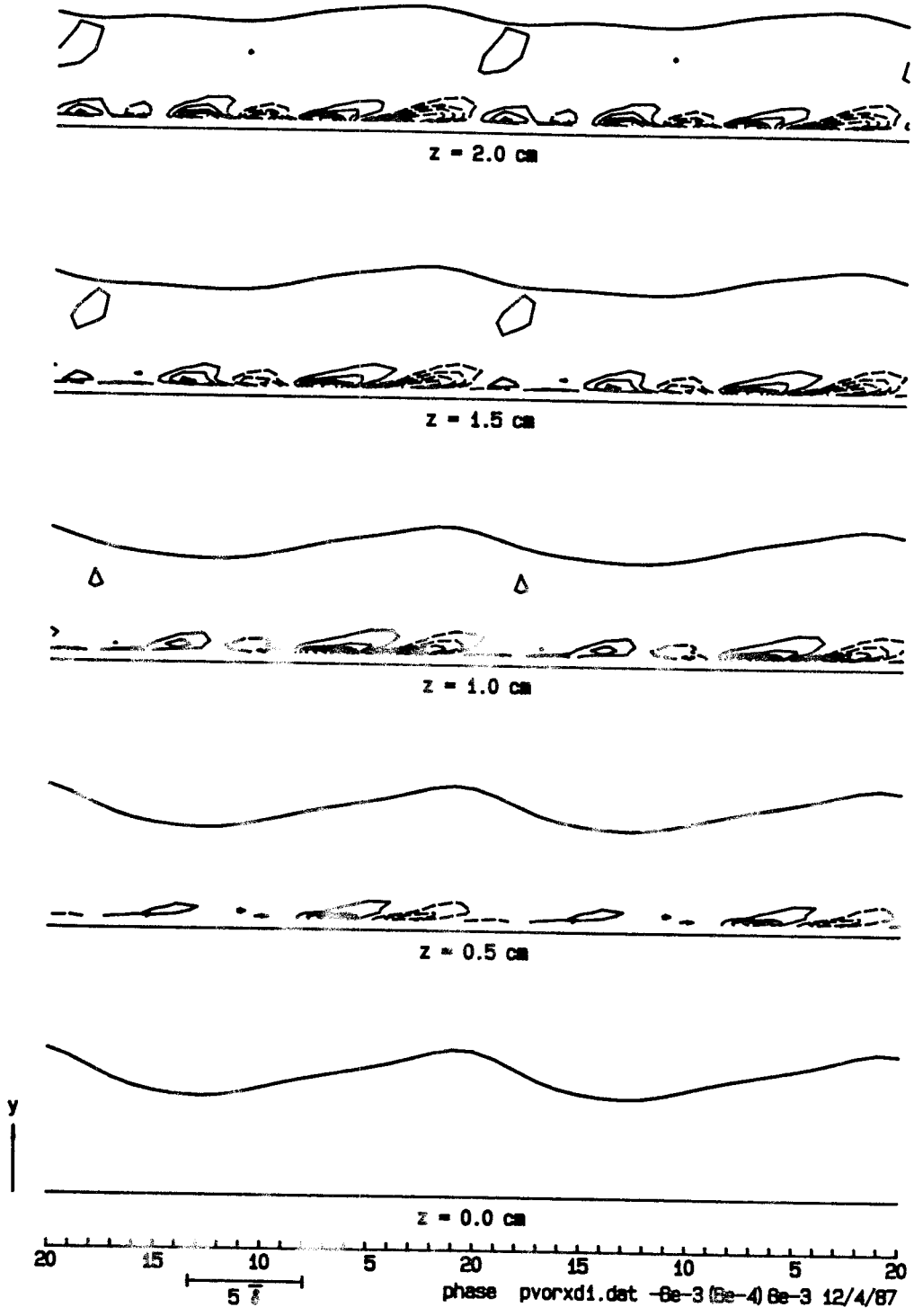

Figure 5.55. Convective term for $\langle\omega_x\rangle$, $-(\langle u\rangle - c)\,\partial\langle\omega_x\rangle/\partial x$, in the t–y plane. Contour interval 0.0006.

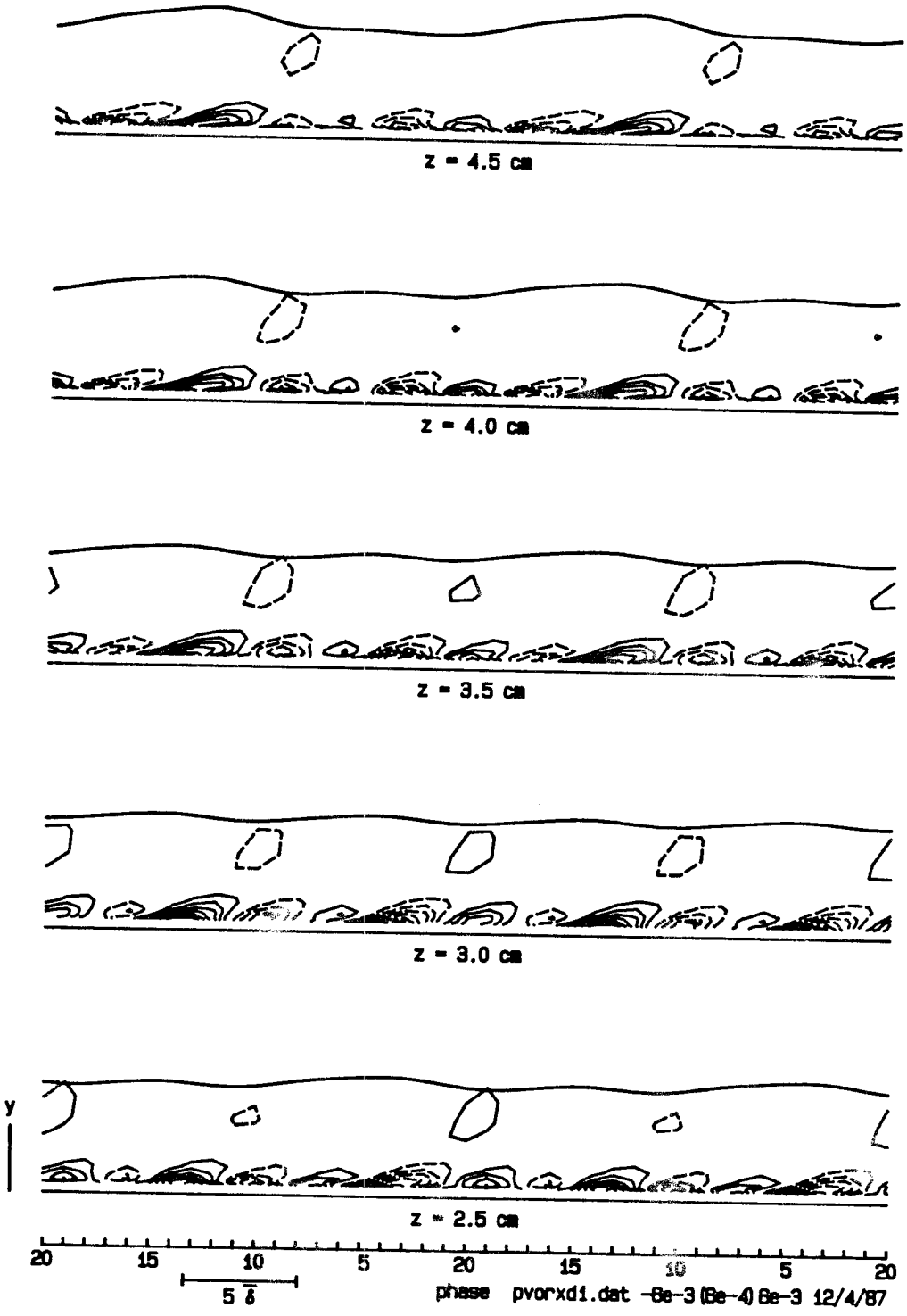

Figure 5.55 (cont'd.). Convective term for $\langle\omega_x\rangle$, $-(\langle u\rangle - c)\,\partial\langle\omega_x\rangle/\partial x$, in the t–y plane.

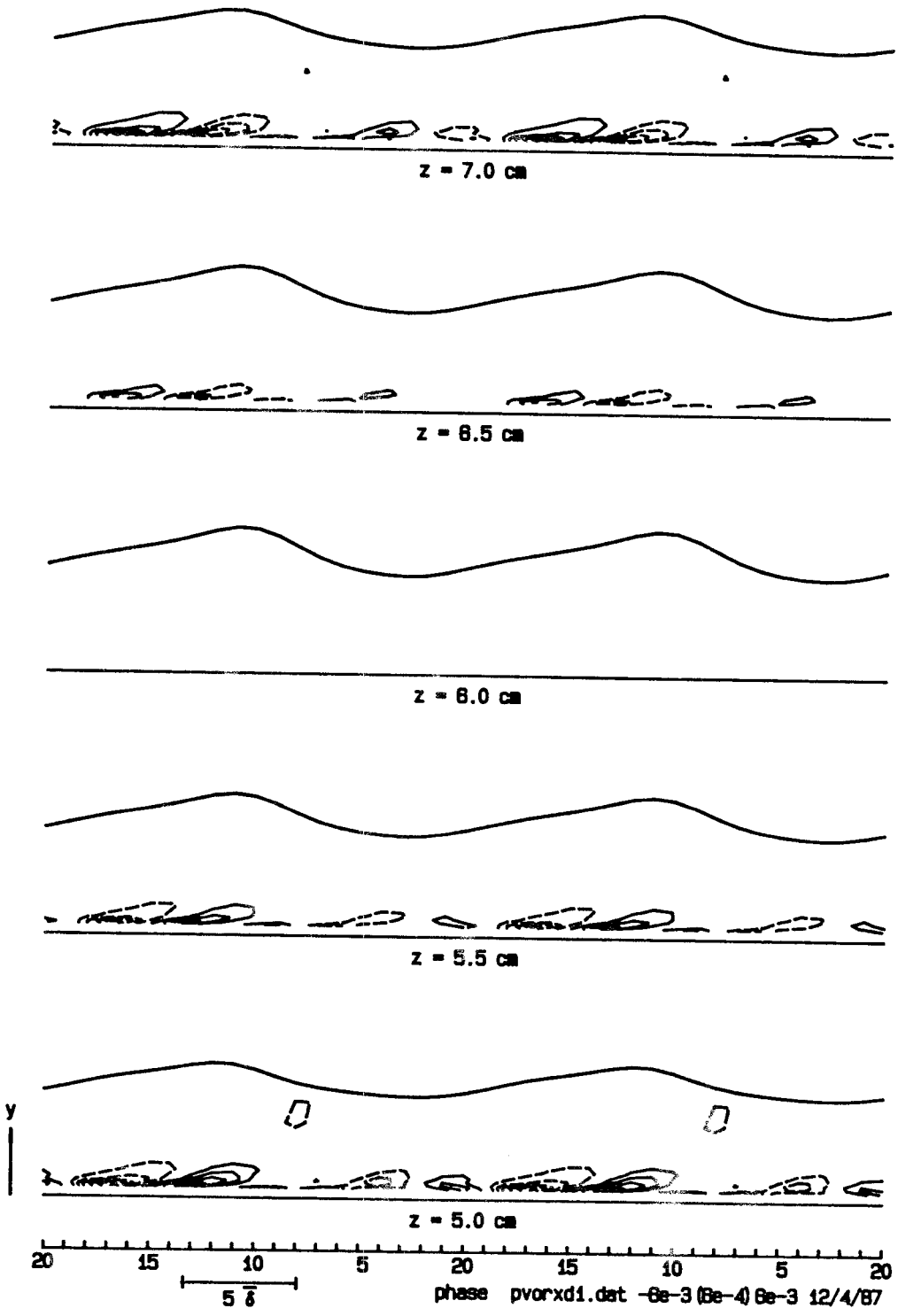

Figure 5.55 (cont'd.). Convective term for $\langle\omega_x\rangle$, $-(\langle u\rangle - c)\,\partial\langle\omega_x\rangle/\partial x$, in the t–y plane.

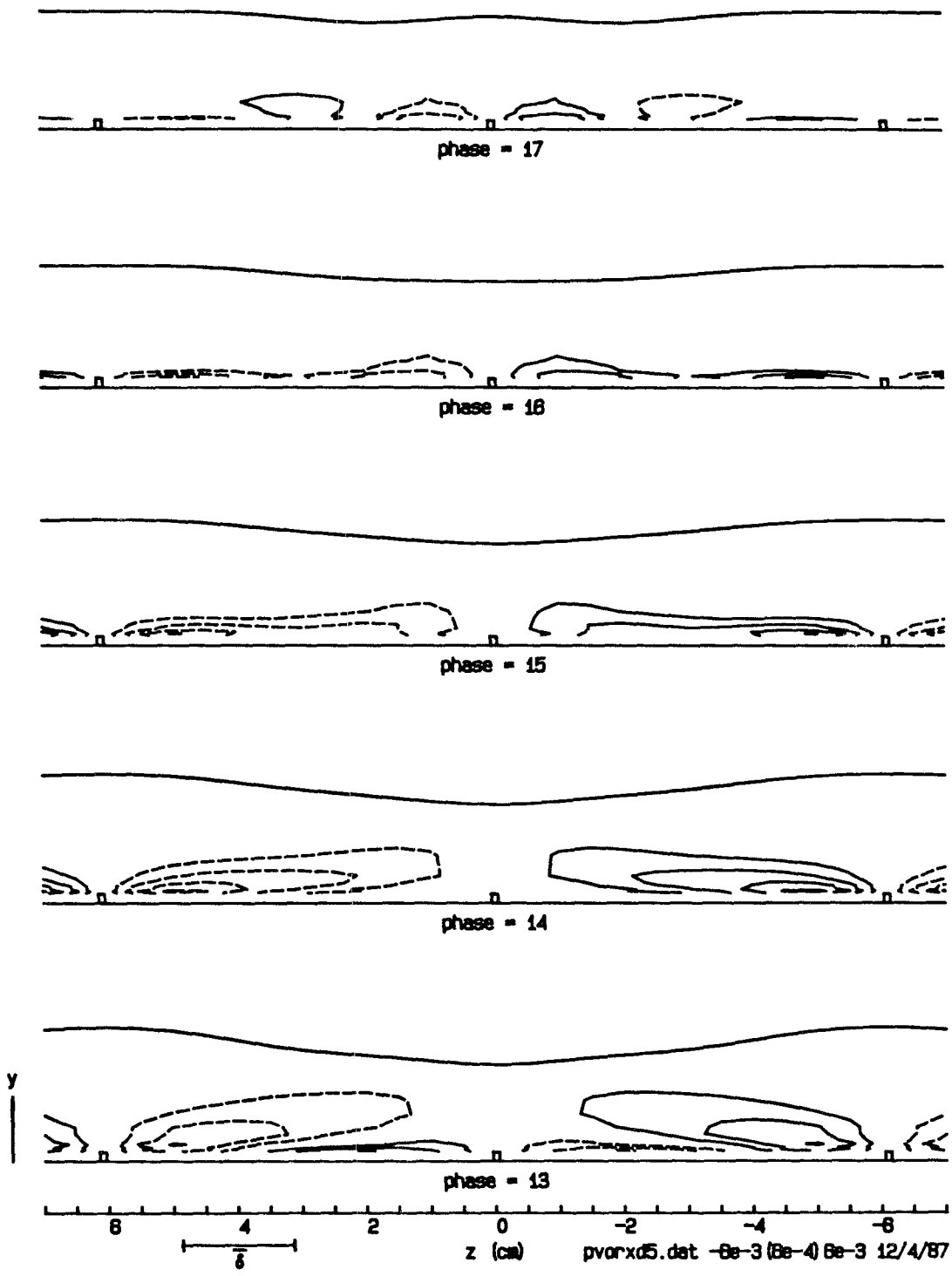

Figure 5.56. Tilting term for $<\omega_x>$, $-(\partial<u>/\partial y)(\partial<w>/\partial x)$, in the $z-y$ plane. Contour interval 0.0006.

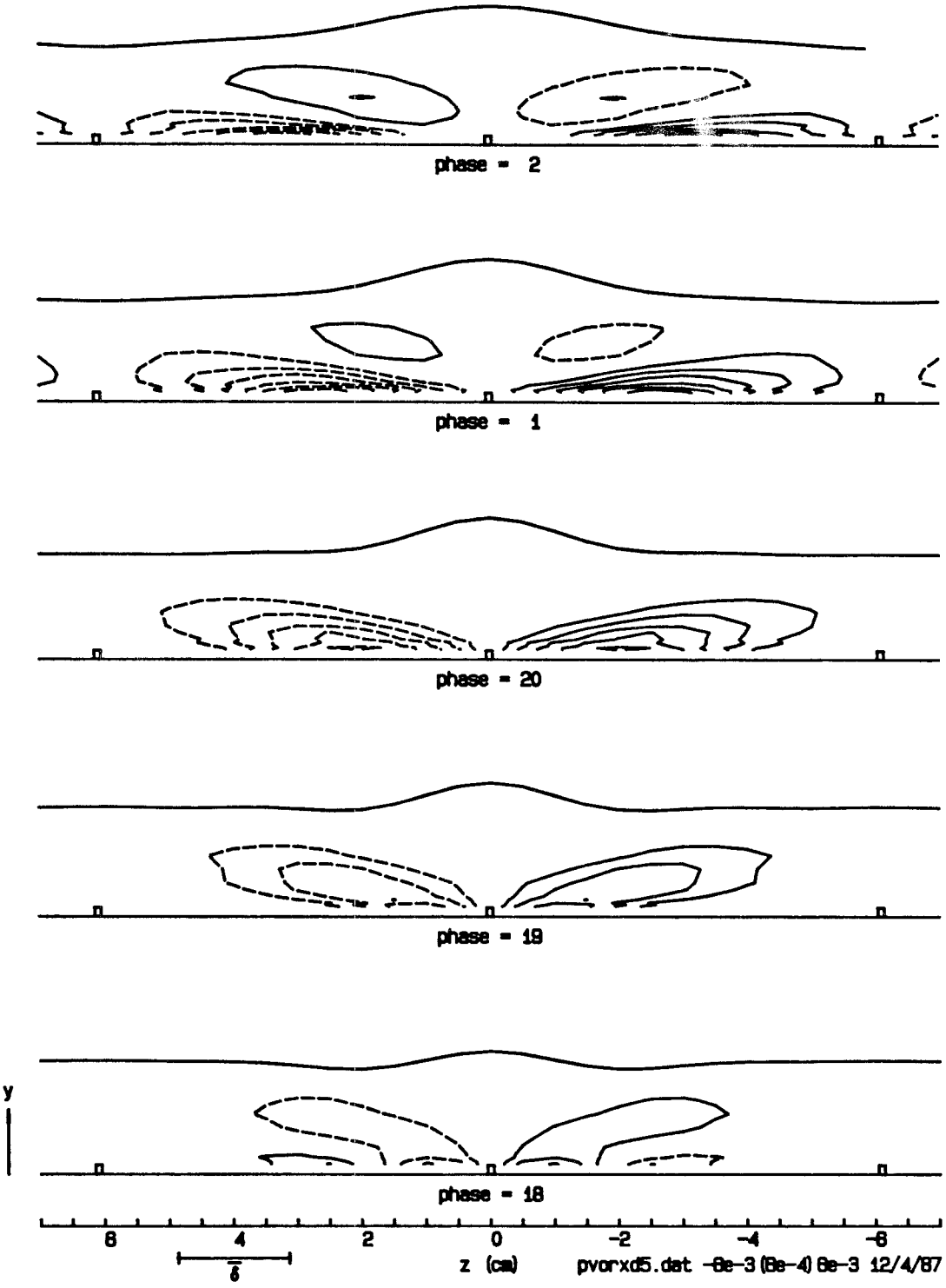

Figure 5.56 (cont'd.). Tilting term for $<\omega_x>$, $-(\partial<u>/\partial y)(\partial<w>/\partial x)$, in the $z-y$ plane.

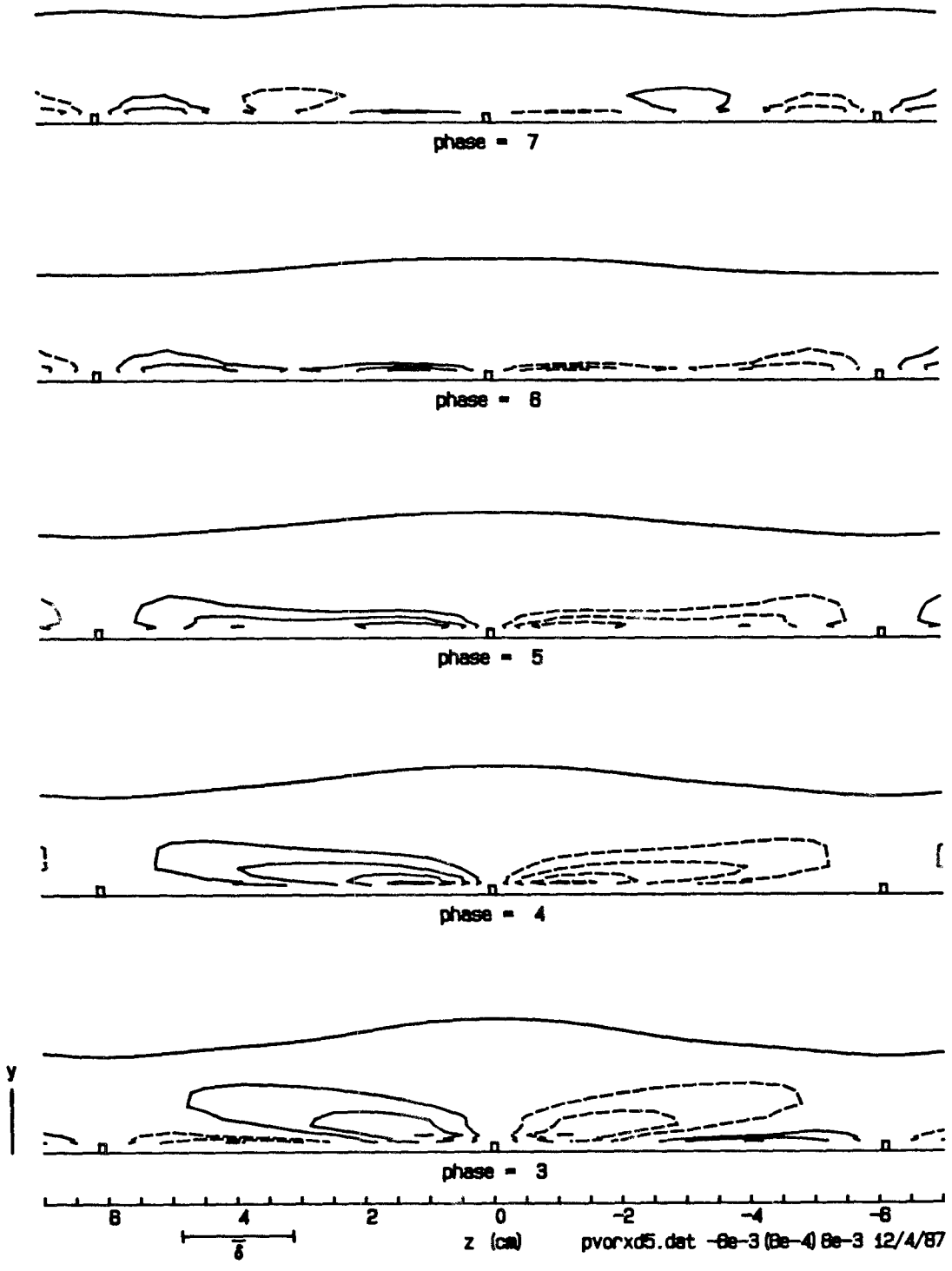

Figure 5.56 (cont'd.). Tilting term for $<\omega_x>$, $-(\partial<u>/\partial y)(\partial<w>/\partial x)$, in the $z-y$ plane.

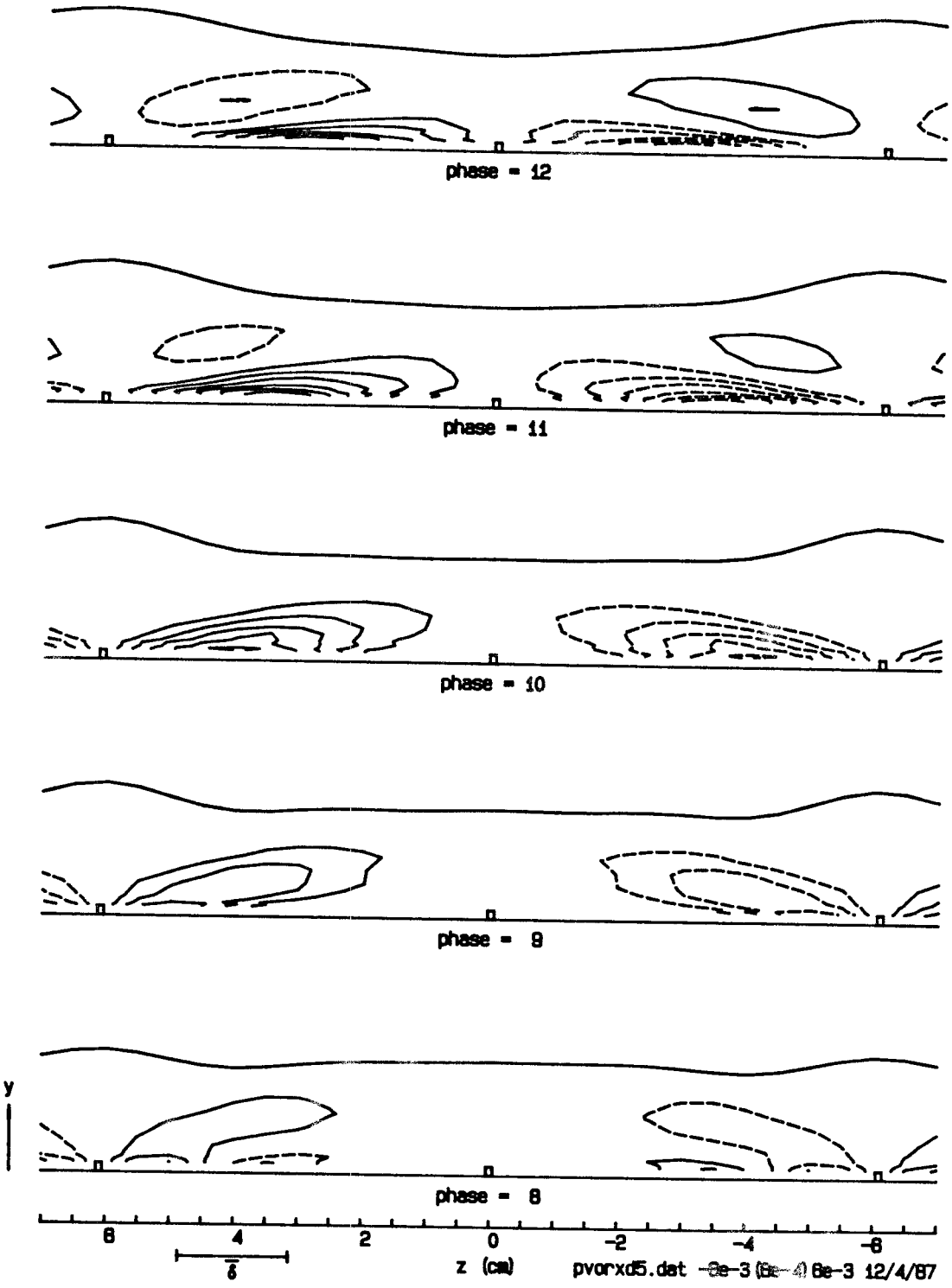

Figure 5.56 (cont'd.). Tilting term for $<\omega_x>$, $-(\partial<u>/\partial y)(\partial<w>/\partial x)$, in the $z-y$ plane.

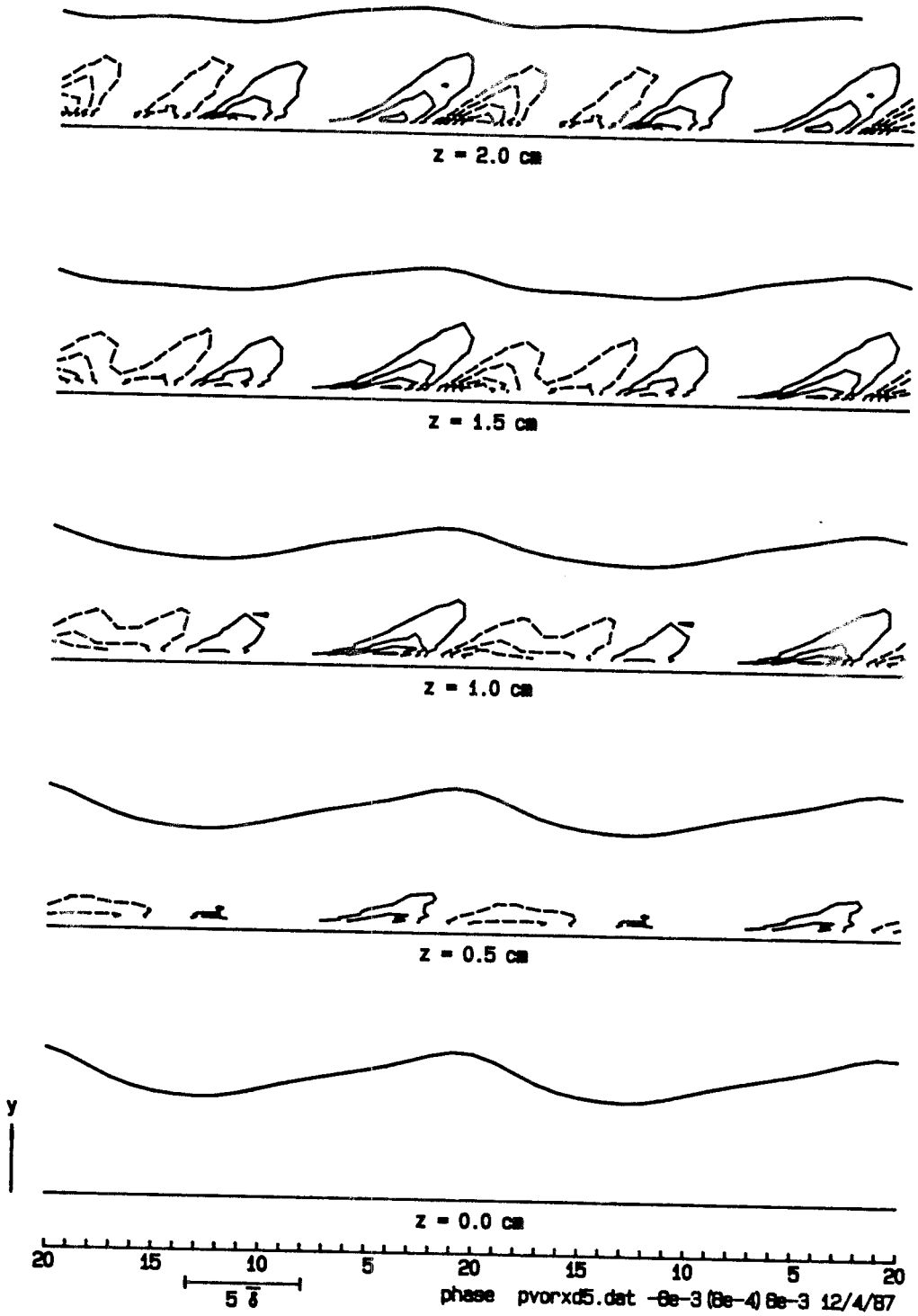

Figure 5.57. Tilting term for $\langle\omega_x\rangle$, $-(\partial\langle u\rangle/\partial y)(\partial\langle w\rangle/\partial x)$, in the t–y plane. Contour interval 0.0006.

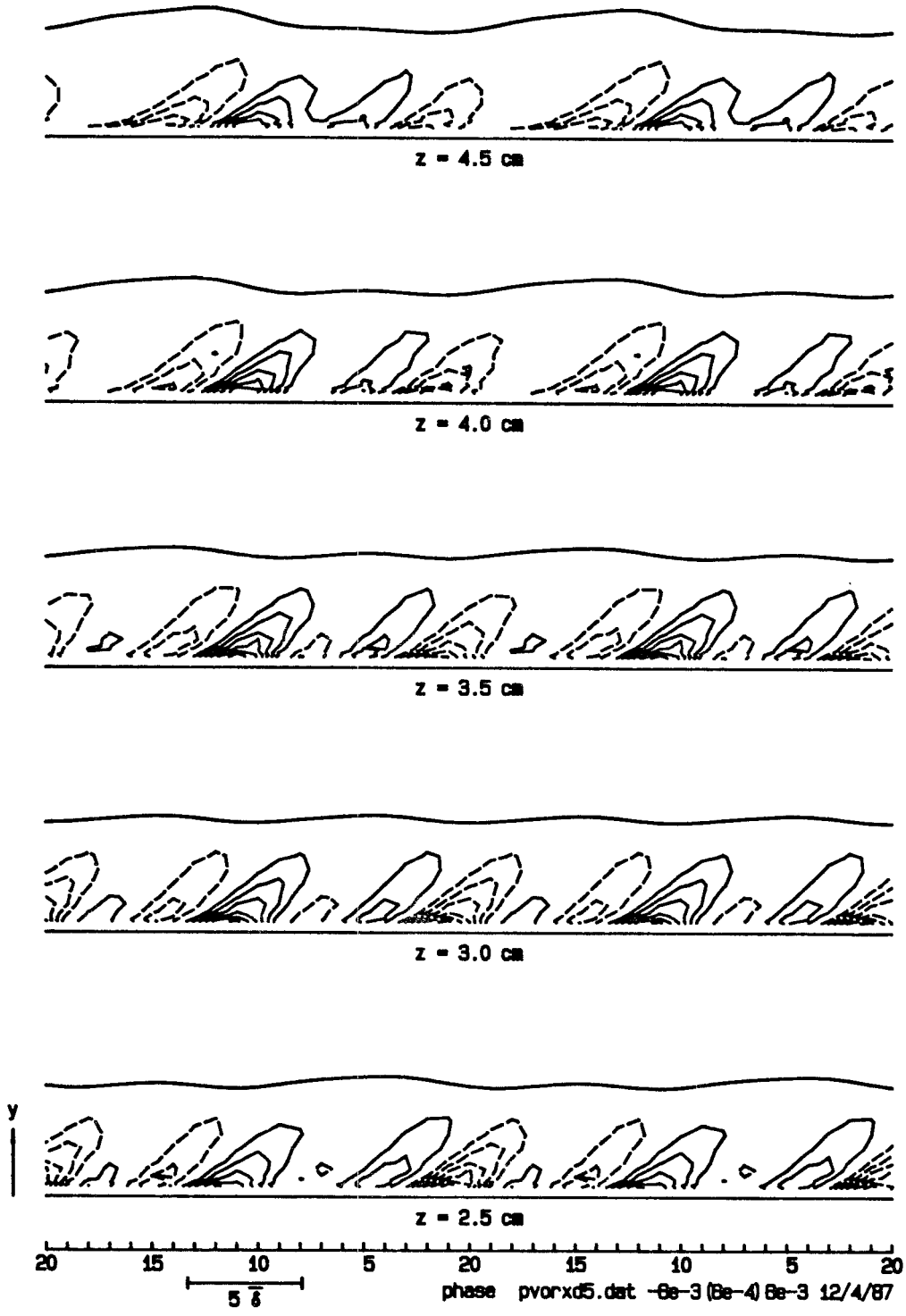

Figure 5.57 (cont'd.). Tilting term for $\langle\omega_x\rangle$, $-(\partial\langle u\rangle/\partial y)(\partial\langle w\rangle/\partial x)$, in the t–y plane.

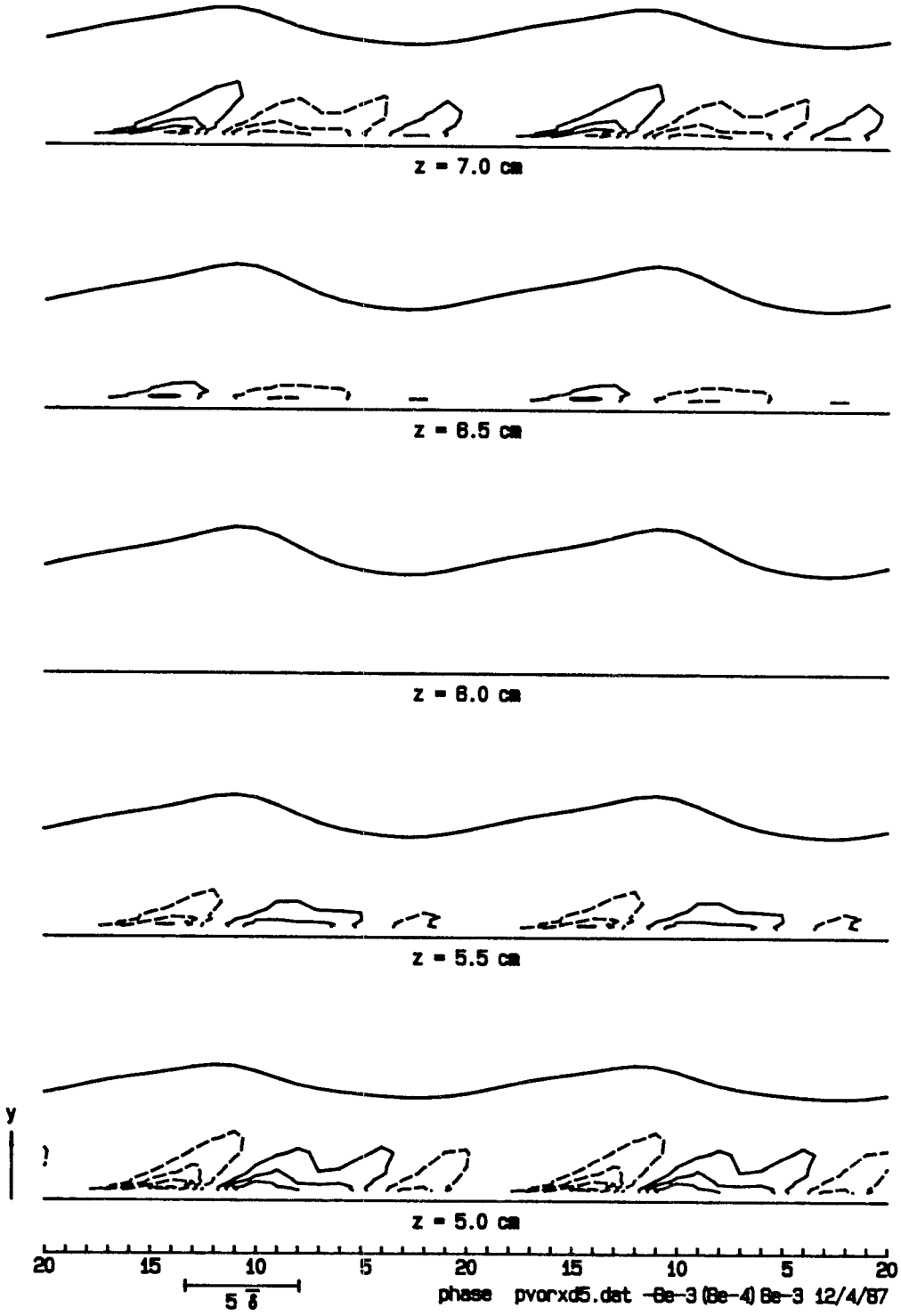

Figure 5.57 (cont'd.). Tilting term for $<\omega_x>$, $-(\partial<u>/\partial y)(\partial<w>/\partial x)$, in the t–y plane.

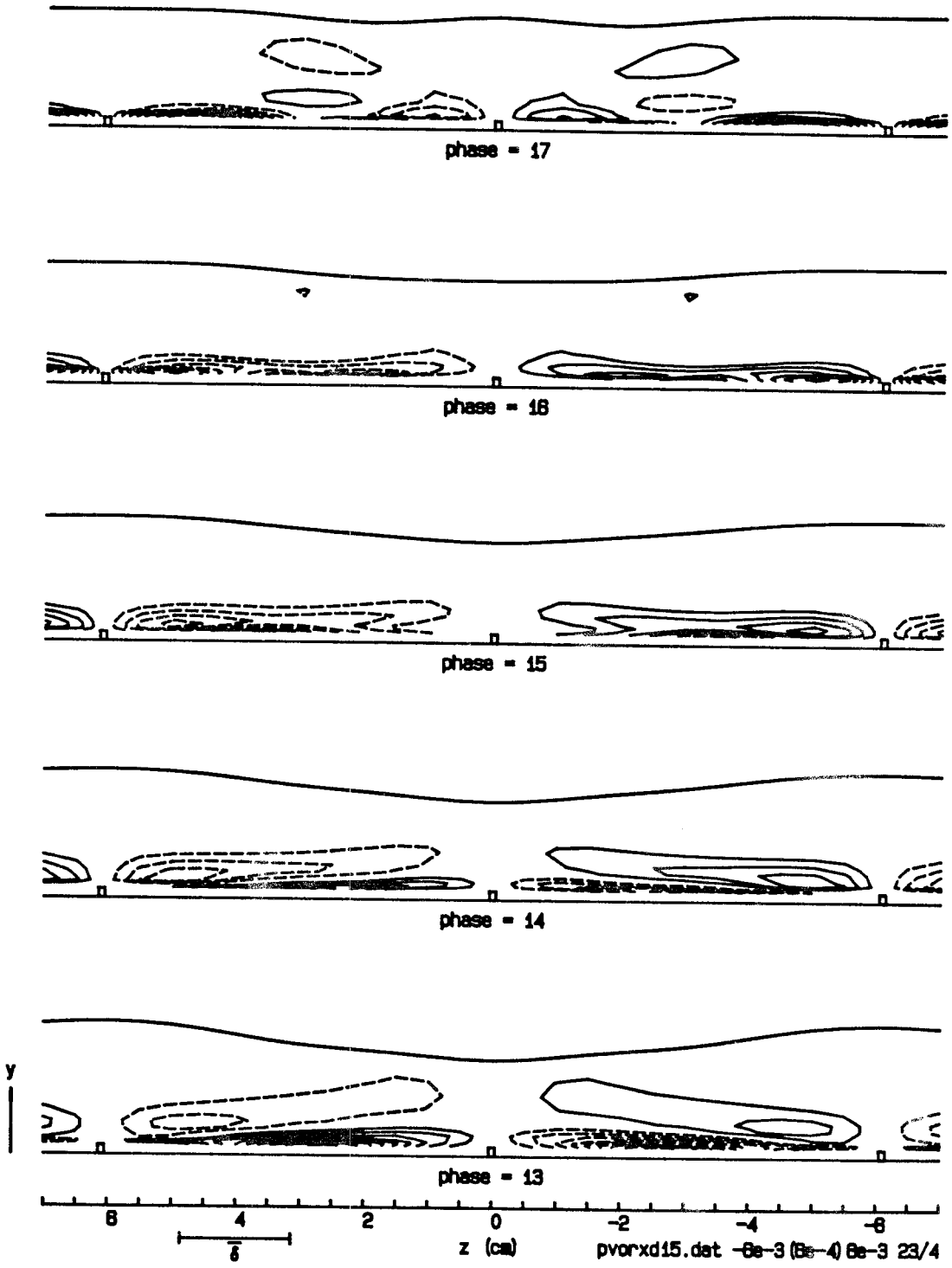

Figure 5.58. Sum of convective and tilting terms for $\langle\omega_x\rangle$ in the $z-y$ plane. Contour interval 0.0006.

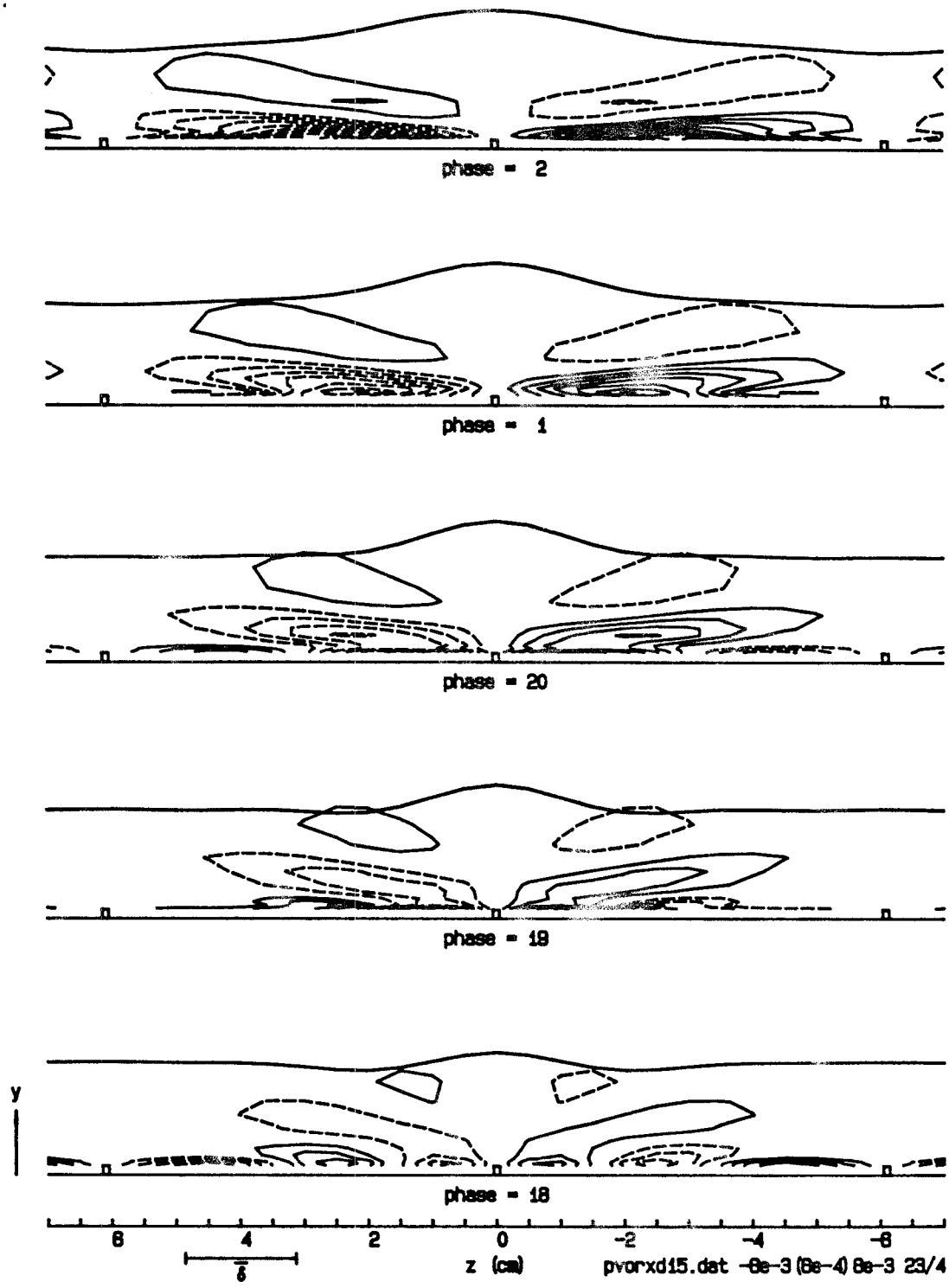

Figure 5.58 (cont'd.). Sum of convective and tilting terms for $<\omega_x>$ in the $z-y$ plane.

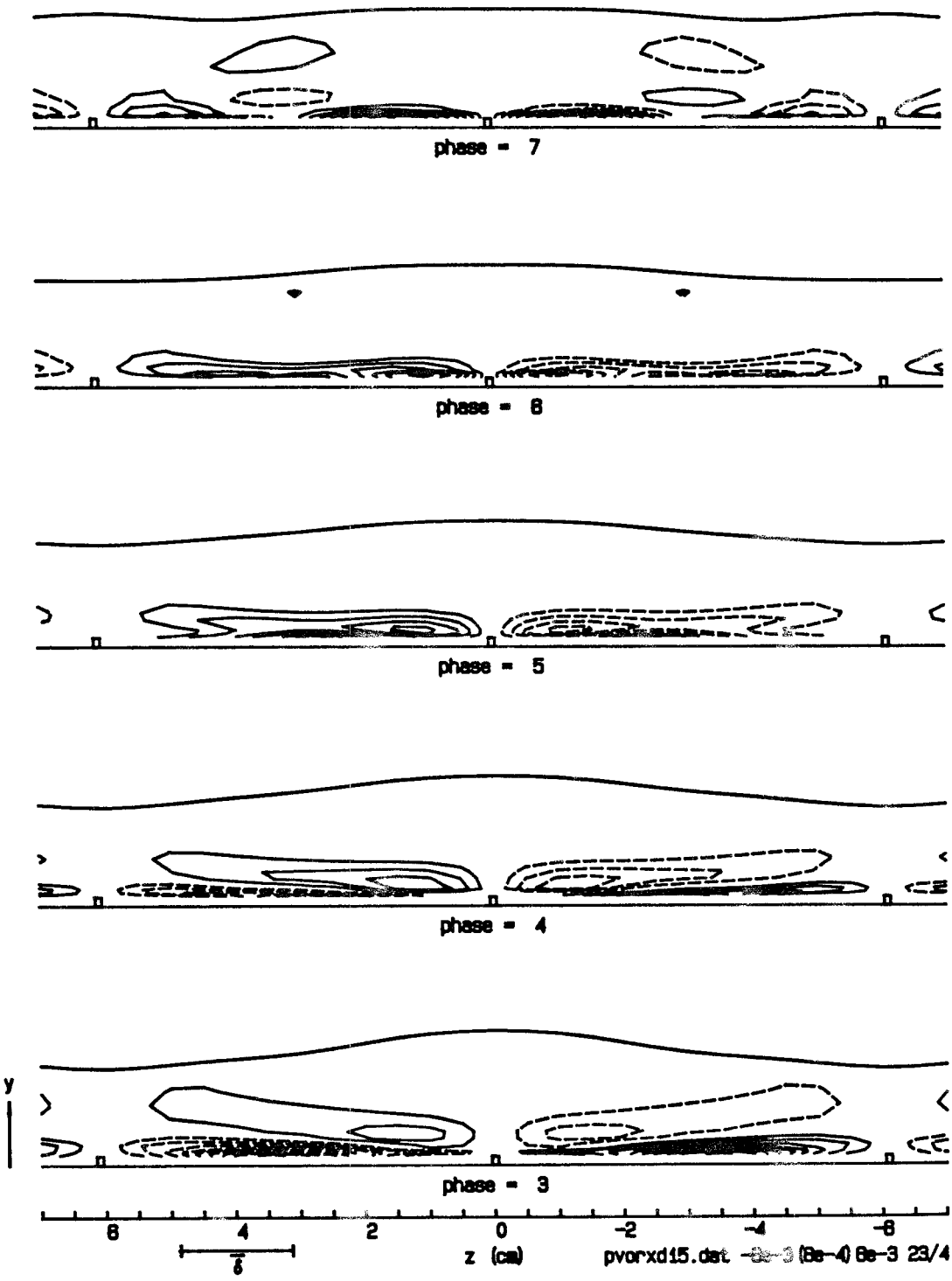

Figure 5.58 (cont'd.). Sum of convective and tilting terms for $<\omega_x>$ in the $z-y$ plane.

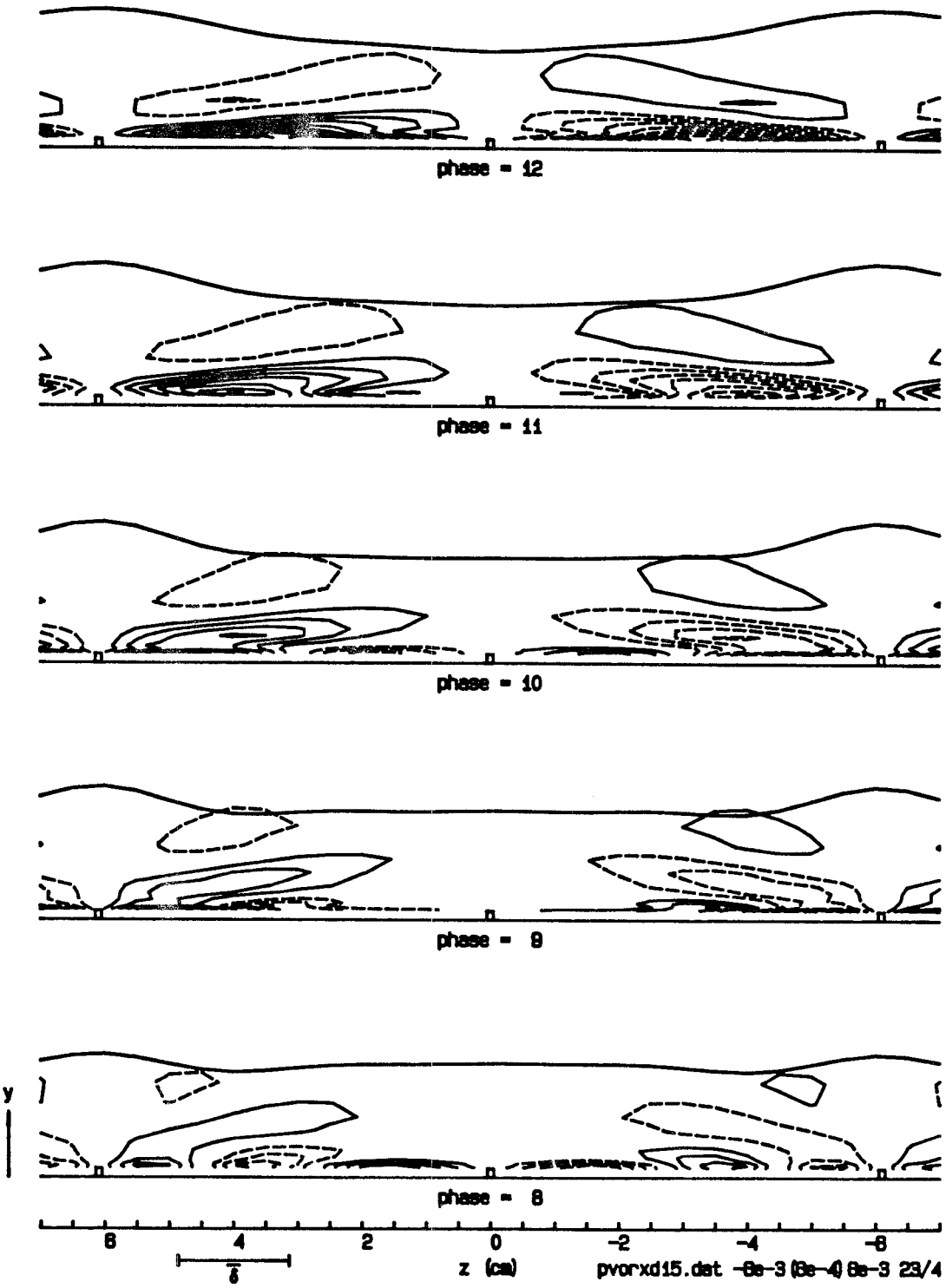

Figure 5.58 (cont'd.). Sum of convective and tilting terms for $<\omega_x>$ in the $z-y$ plane.

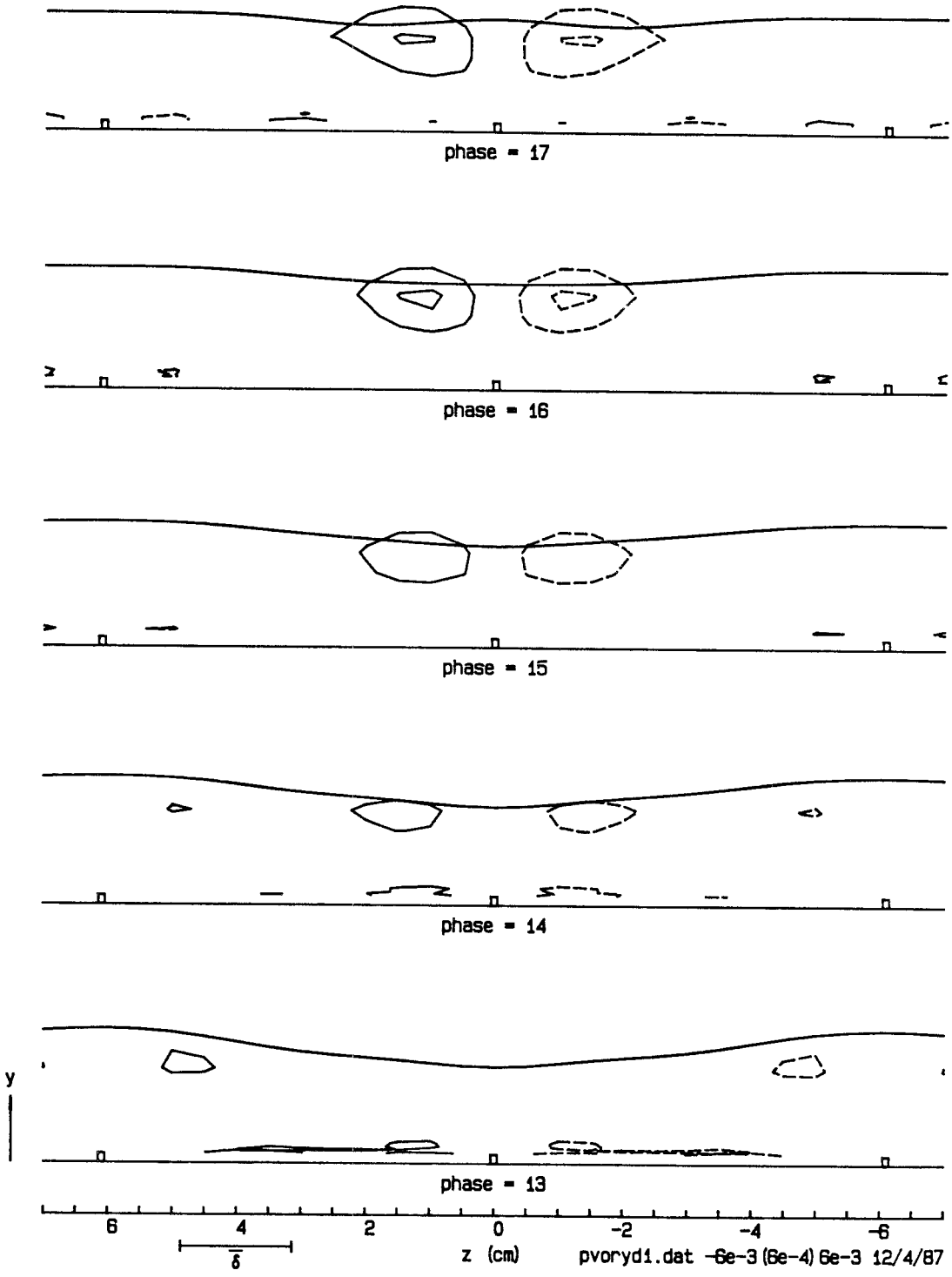

Figure 5.59. Convective term for $\langle\omega_y\rangle$, $-(\langle u\rangle - c)\,\partial\langle\omega_y\rangle/\partial x$, in the $z-y$ plane. Contour interval 0.0006.

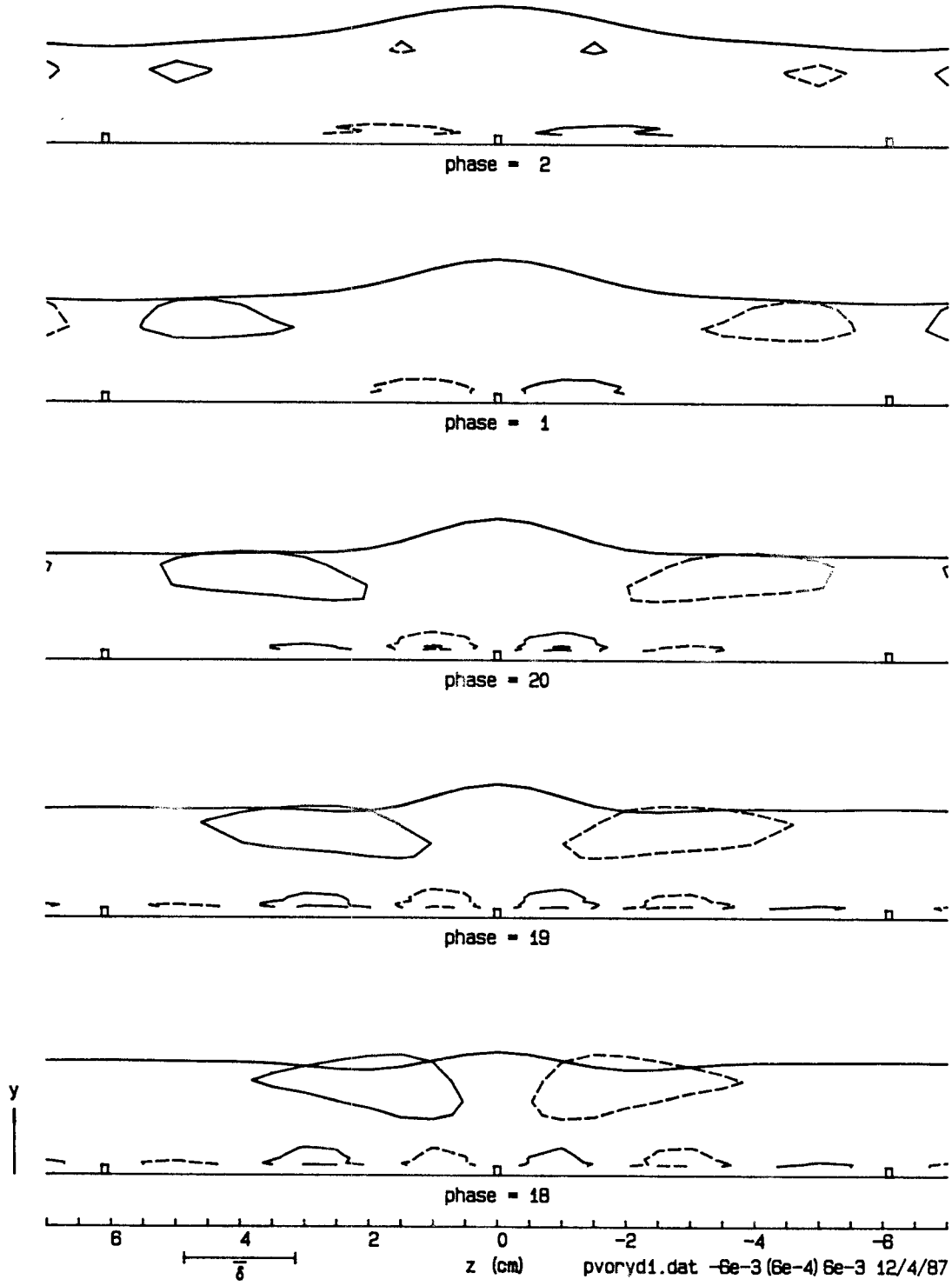

Figure 5.59 (cont'd.). Convective term for $<\omega_y>$, $-(<u> - c)\,\partial<\omega_y>/\partial x$, in the $z-y$ plane.

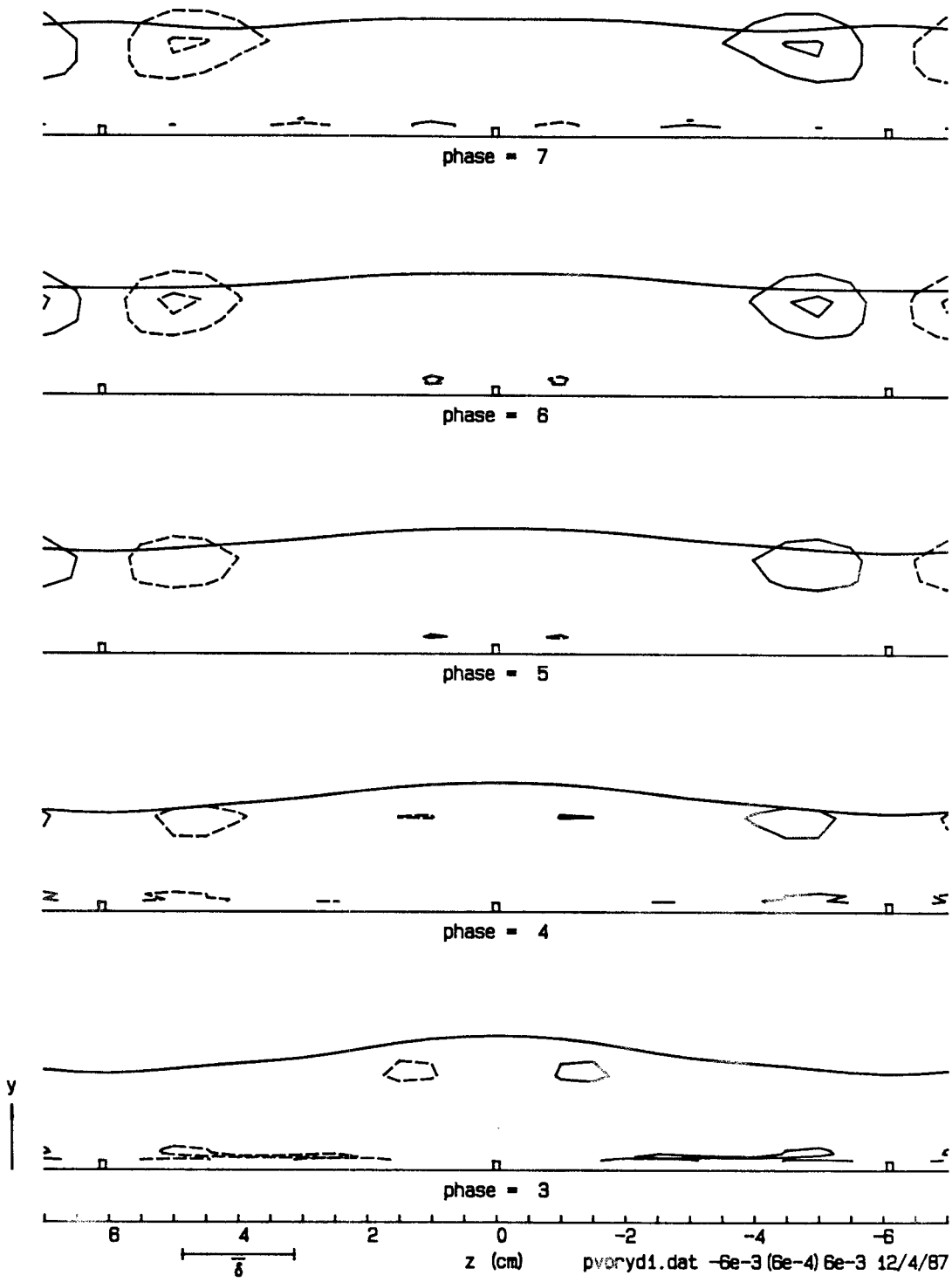

Figure 5.59 (cont'd.). Convective term for $<\omega_y>$, $-(<u>-c)\,\partial<\omega_y>/\partial x$, in the $z-y$ plane.

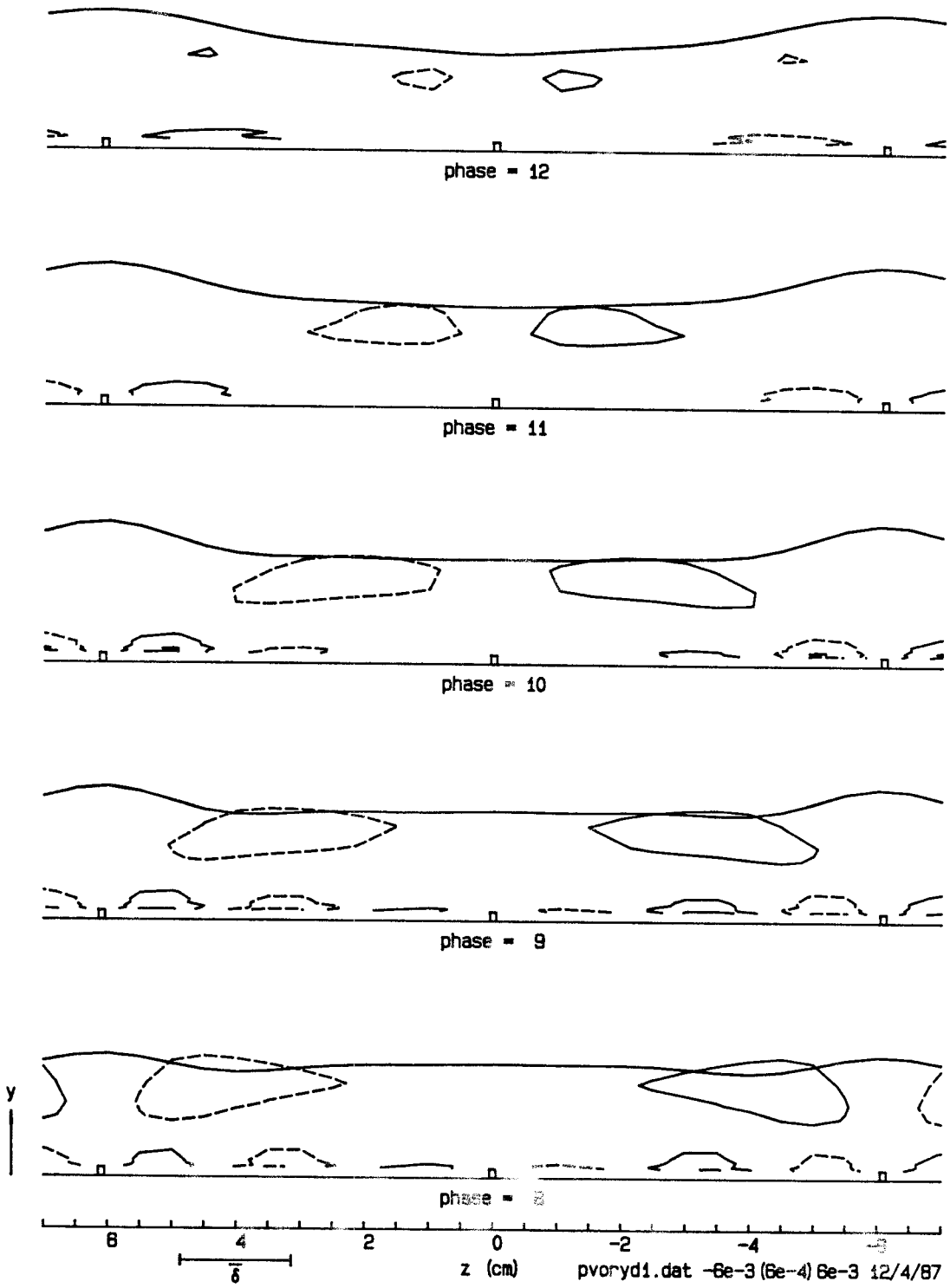

Figure 5.59 (cont'd.). Convective term for $\langle\omega_y\rangle$, $-(\langle u\rangle - c)\,\partial\langle\omega_y\rangle/\partial x$, in the $z-y$ plane.

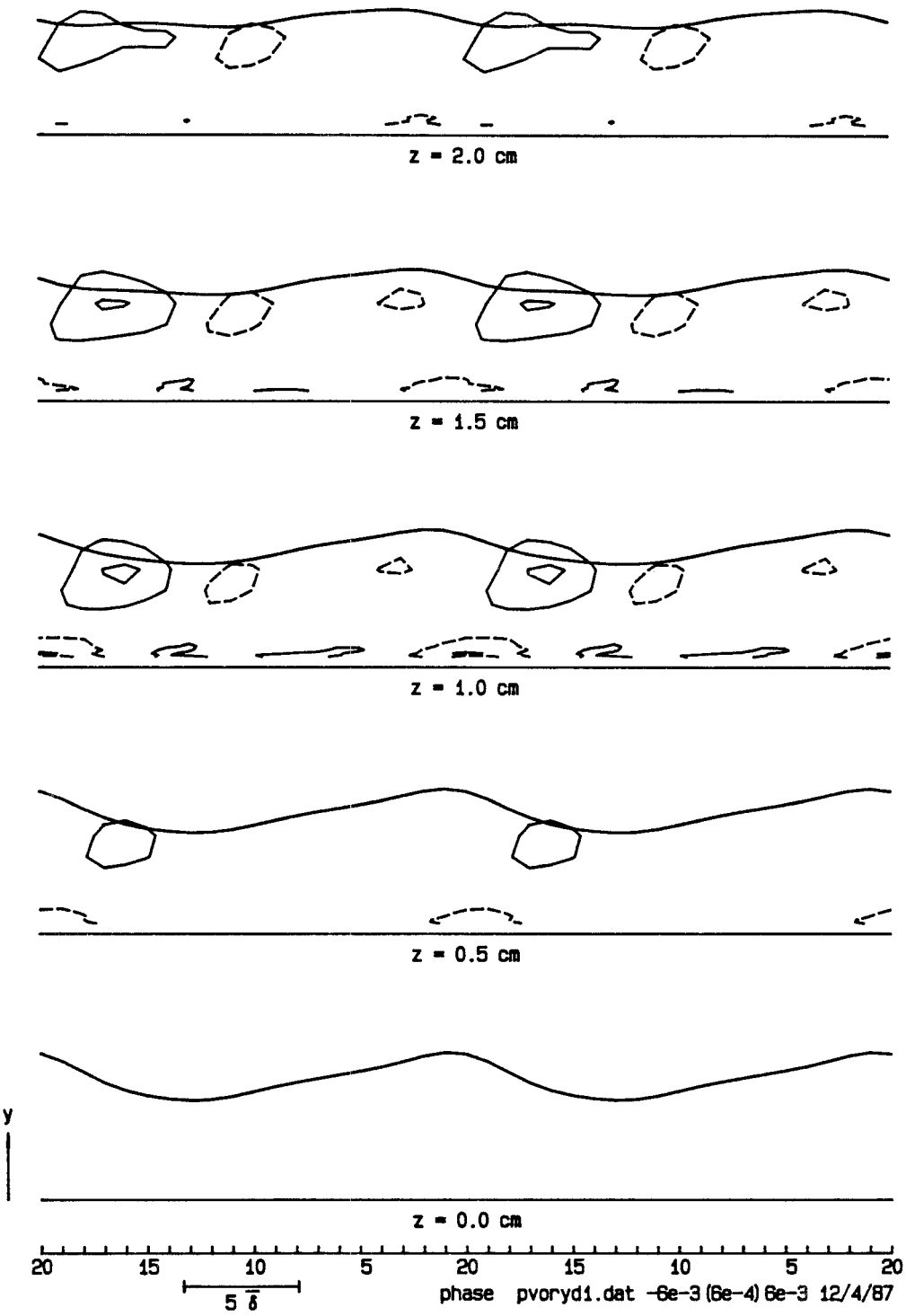

Figure 5.60. Convective term for $<\omega_y>$, $-(<u>-c)\,\partial<\omega_y>/\partial x$, in the t–y plane. Contour interval 0.0006.

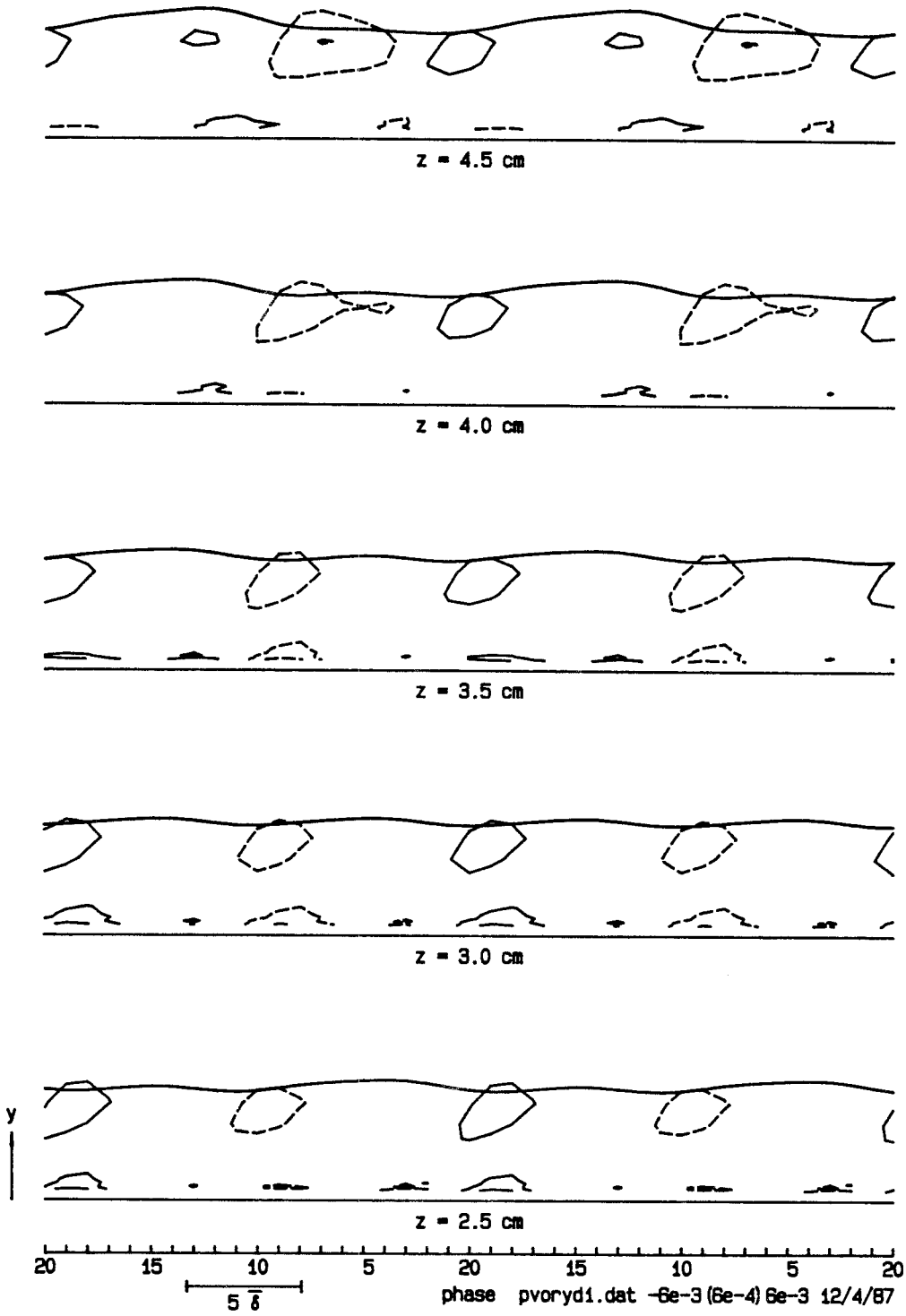

Figure 5.60 (cont'd.). Convective term for $\langle\omega_y\rangle$, $-(\langle u\rangle - c)\,\partial\langle\omega_y\rangle/\partial x$, in the t–y plane.

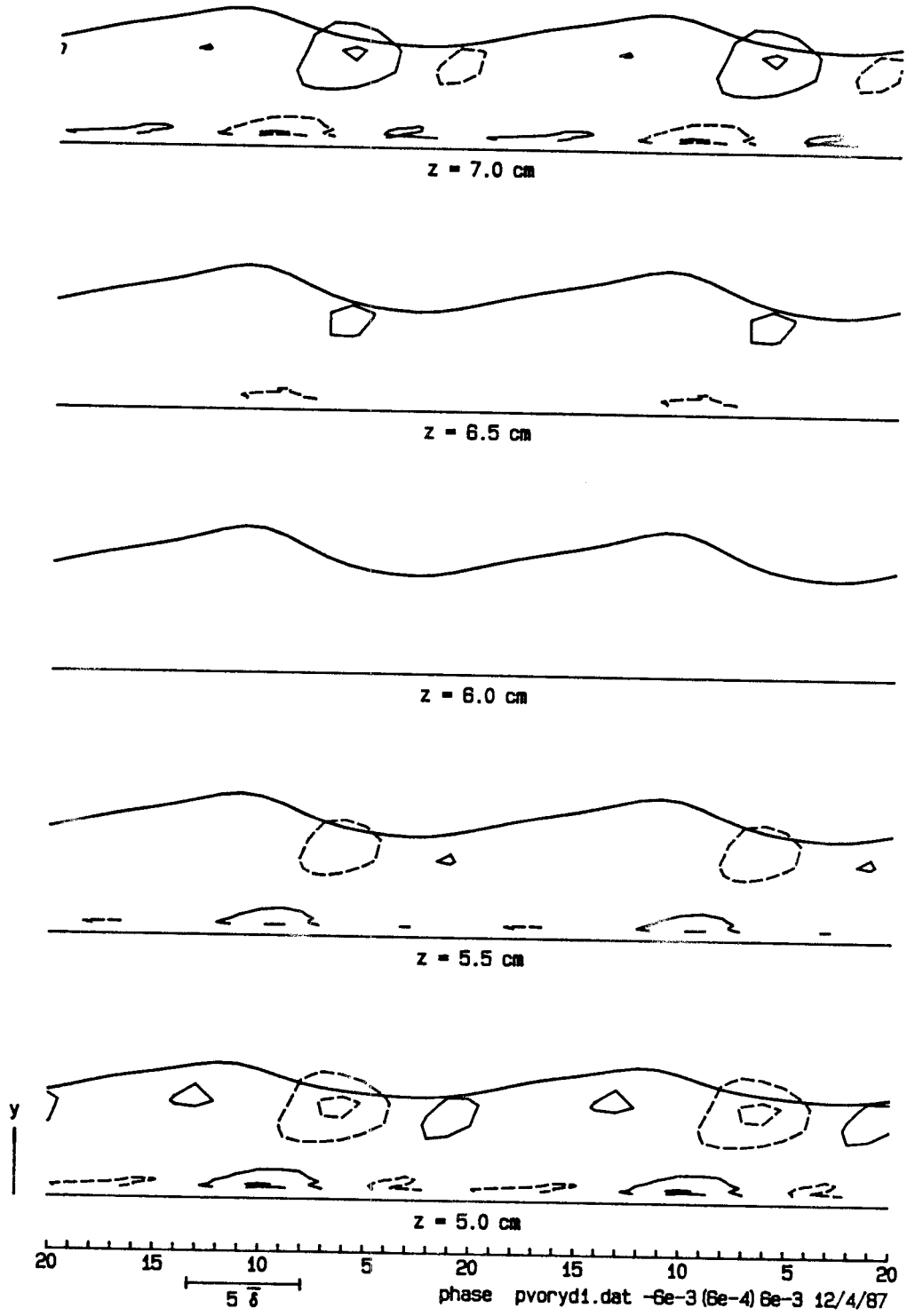

Figure 5.60 (cont'd.). Convective term for $\langle\omega_y\rangle$, $-(\langle u\rangle - c)\,\partial\langle\omega_y\rangle/\partial x$, in the t–y plane.

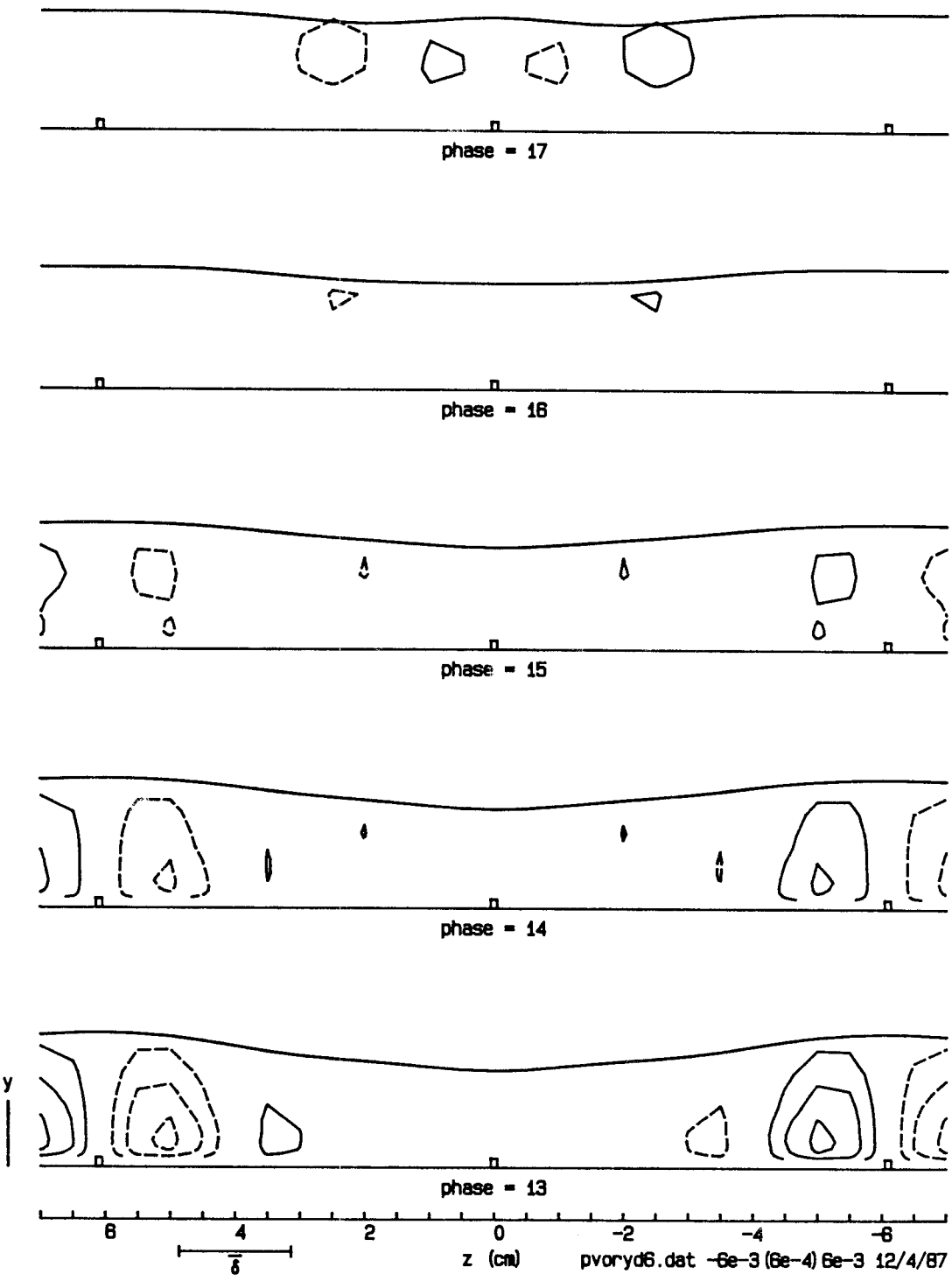

Figure 5.61. Tilting term for $\langle\omega_y\rangle$, $\langle\omega_z\rangle\,\partial\langle v\rangle/\partial z$, in the $z-y$ plane. Contour interval 0.0006.

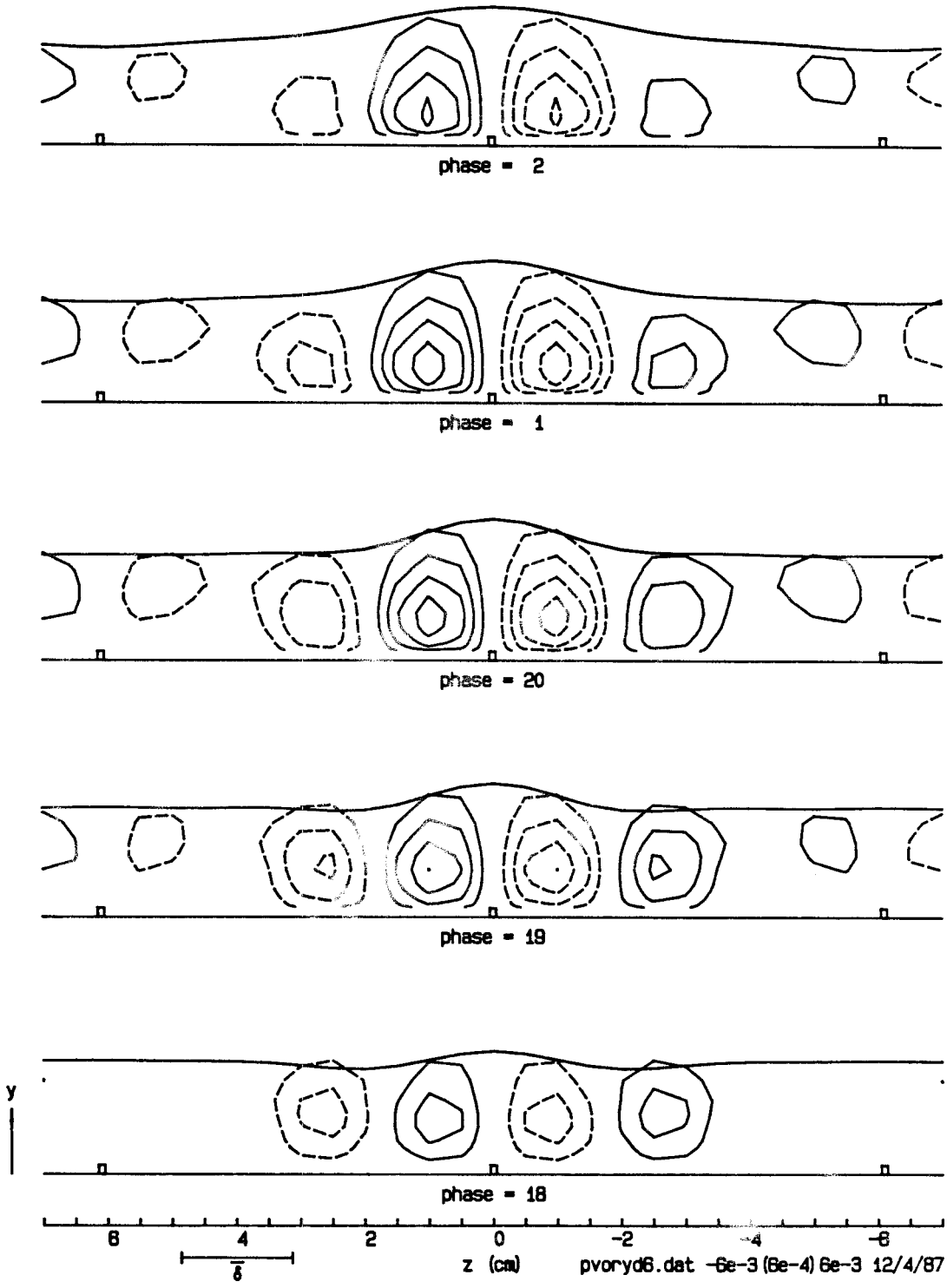

Figure 5.61 (cont'd.). Tilting term for $<\omega_y>$, $<\omega_z>\partial<v>/\partial z$ in the $z-y$ plane.

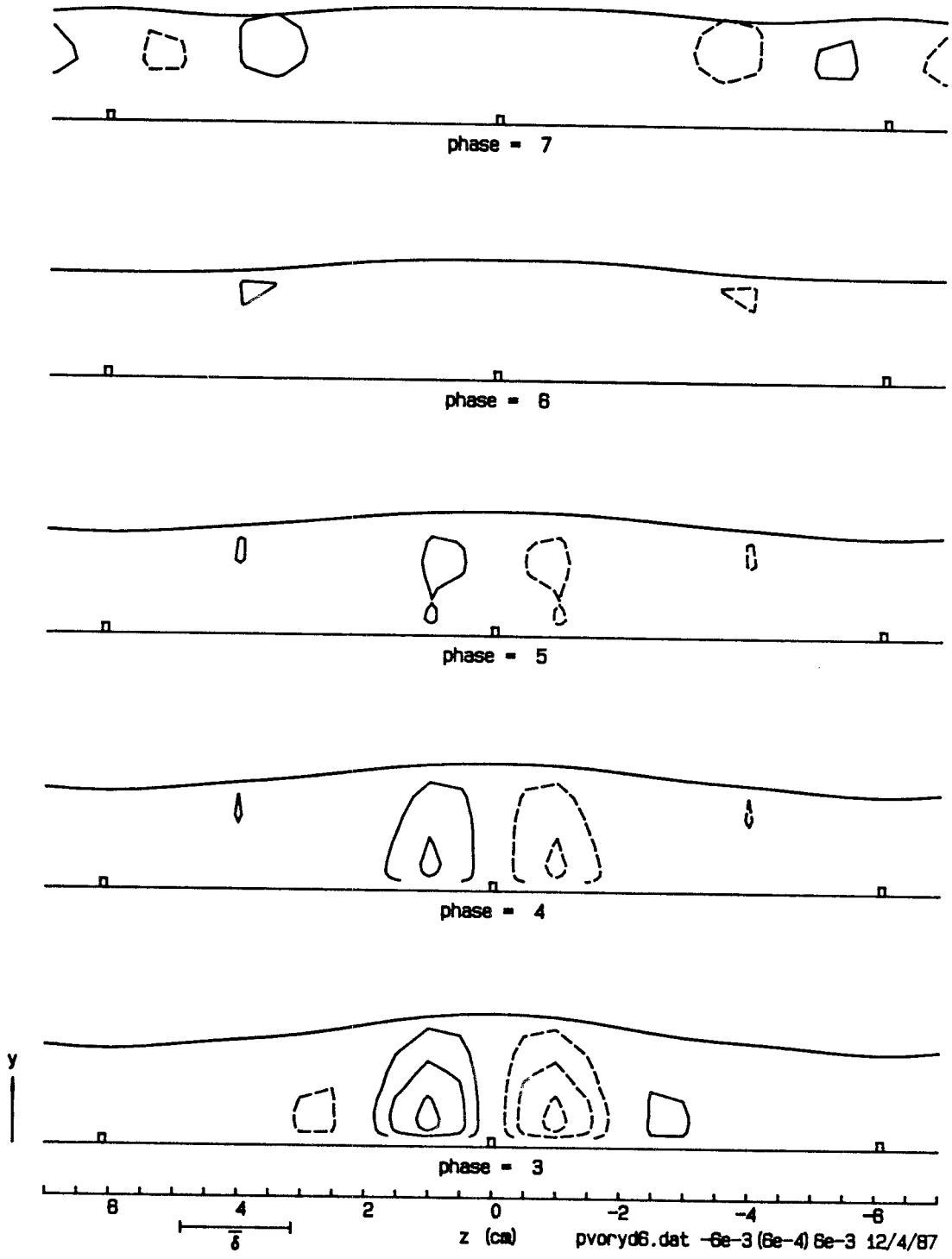

Figure 5.61 (cont'd.). Tilting term for $<\omega_y>$, $<\omega_z>\partial<v>/\partial z$, in the $z-y$ plane.

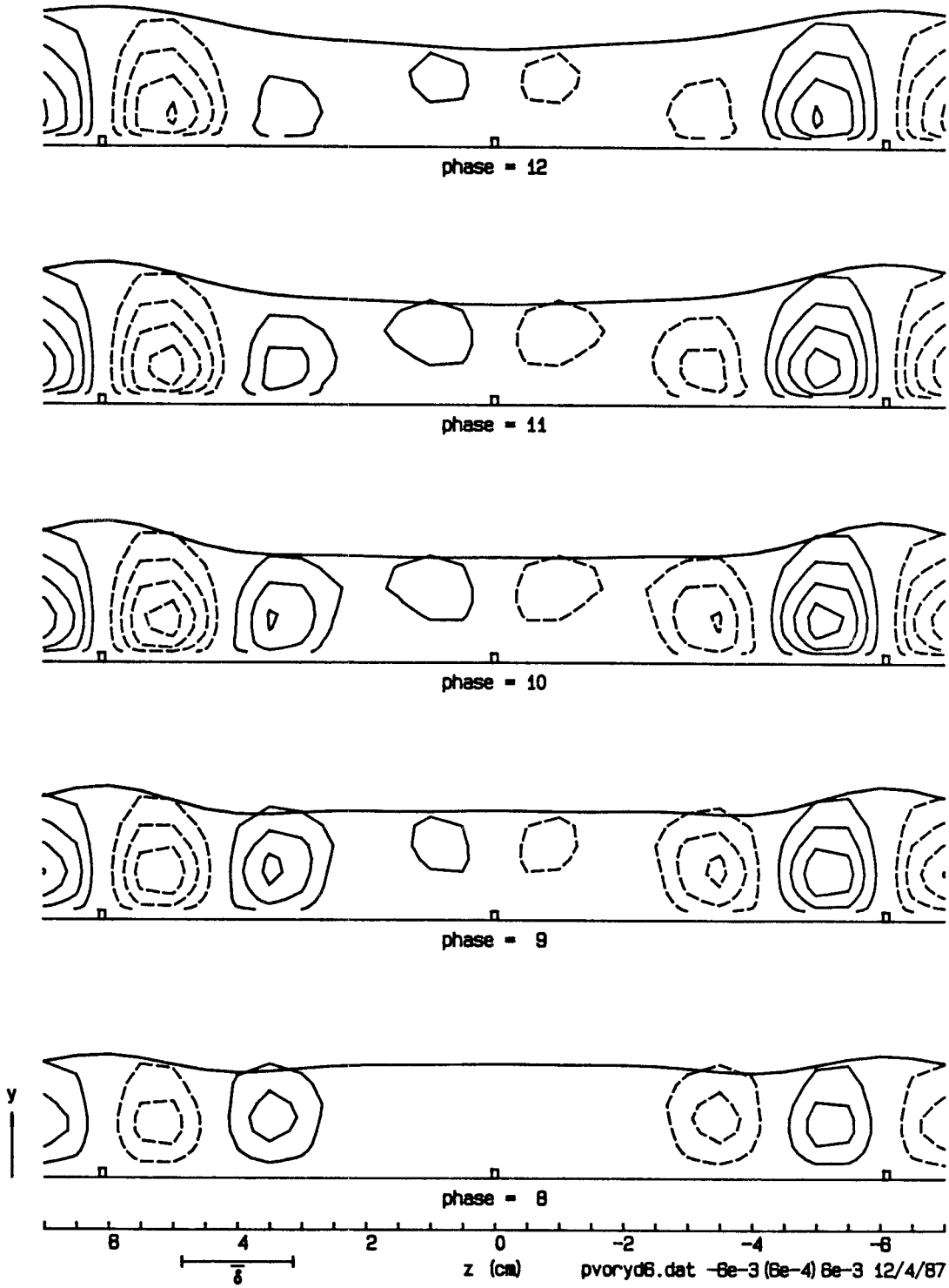

Figure 5.61 (cont'd.). Tilting term for $<\omega_y>$, $<\omega_z>\partial<v>/\partial z$, in the $z-y$ plane.

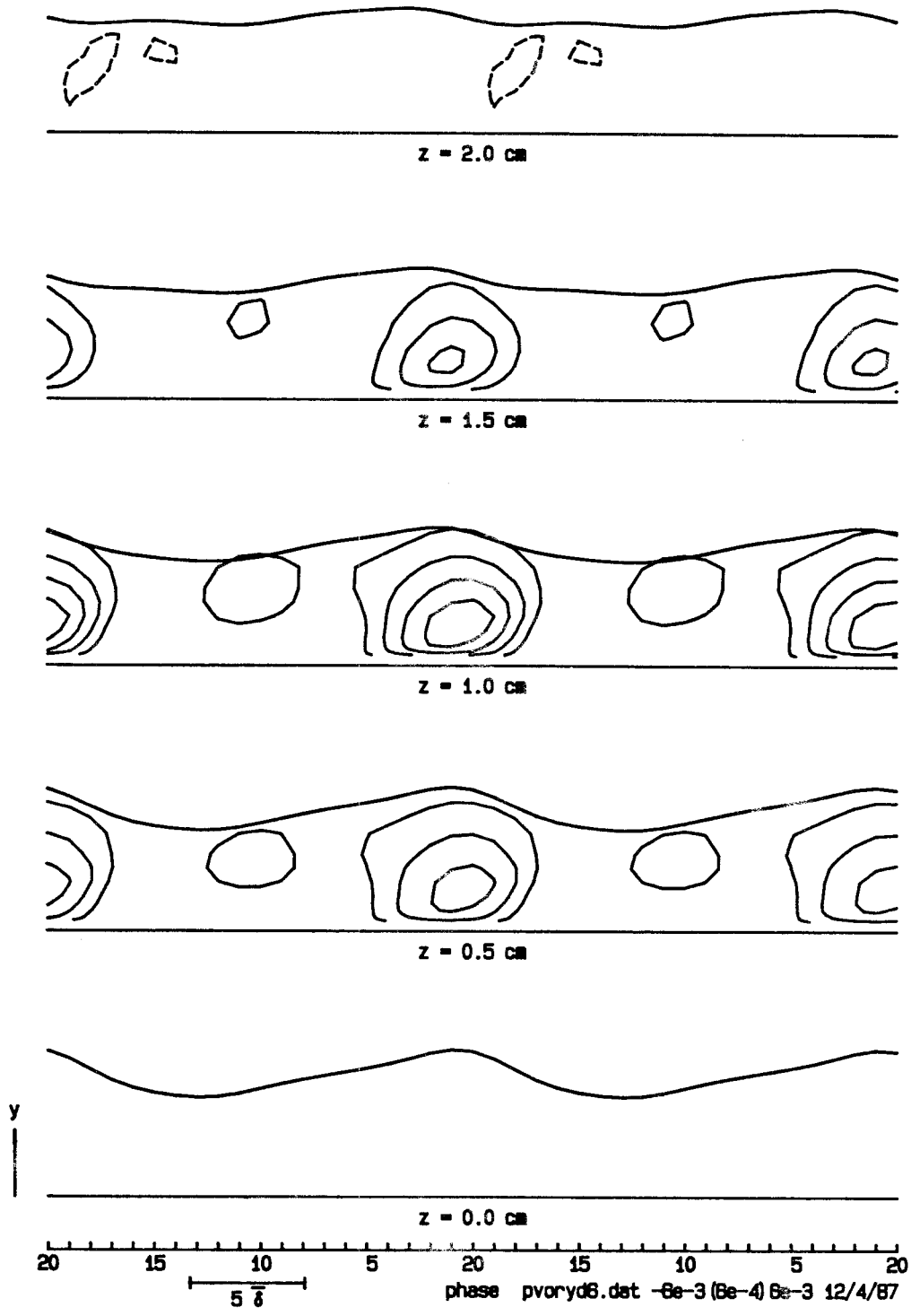

Figure 5.62. Tilting term for $\langle\omega_y\rangle$, $\langle\omega_z\rangle\,\partial\langle v\rangle/\partial z$, in the t–y plane. Contour interval 0.0006.

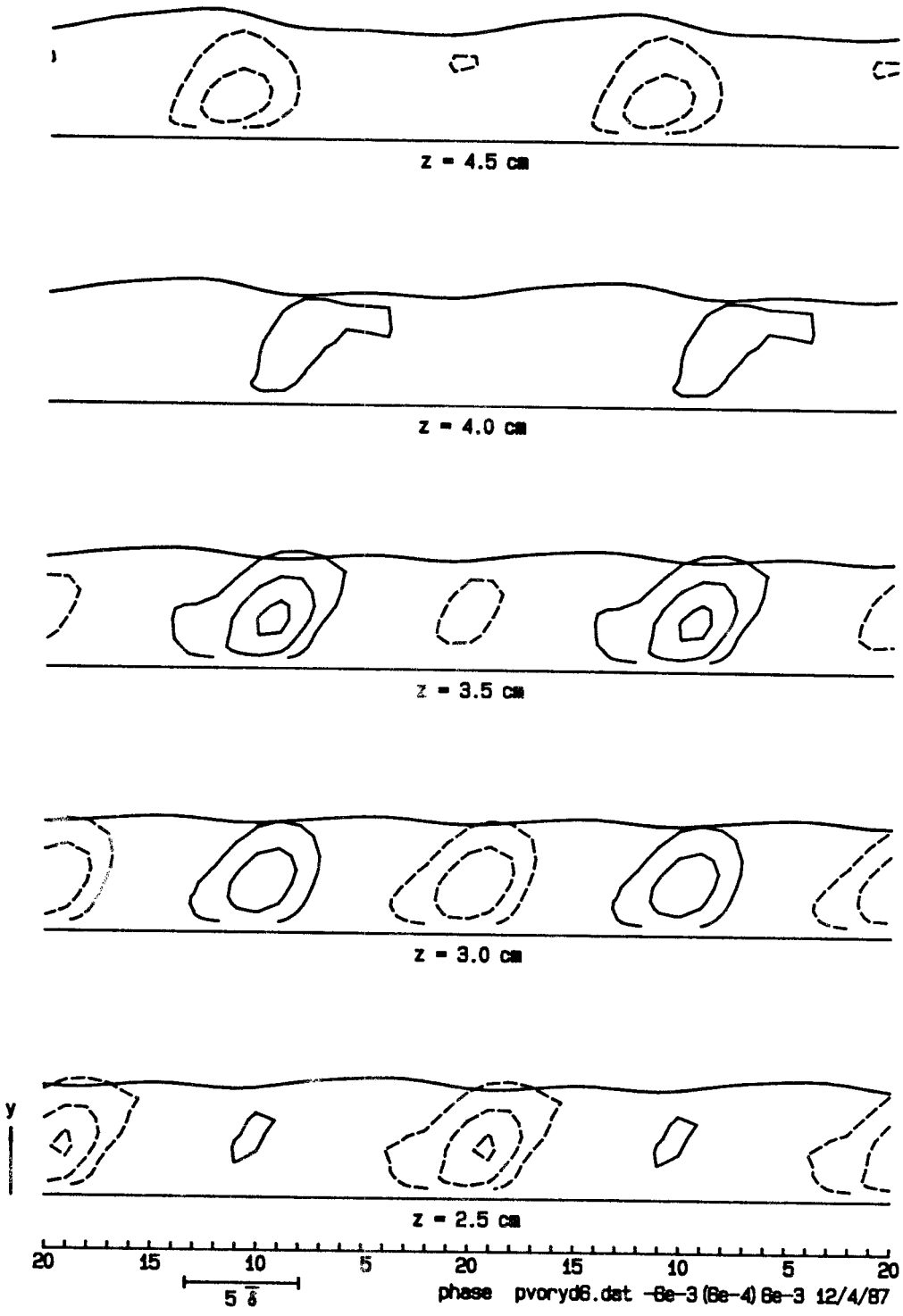

Figure 5.62 (cont'd.). Tilting term for $<\omega_y>$, $<\omega_z>\partial<v>/\partial z$, in the $t-y$ plane.

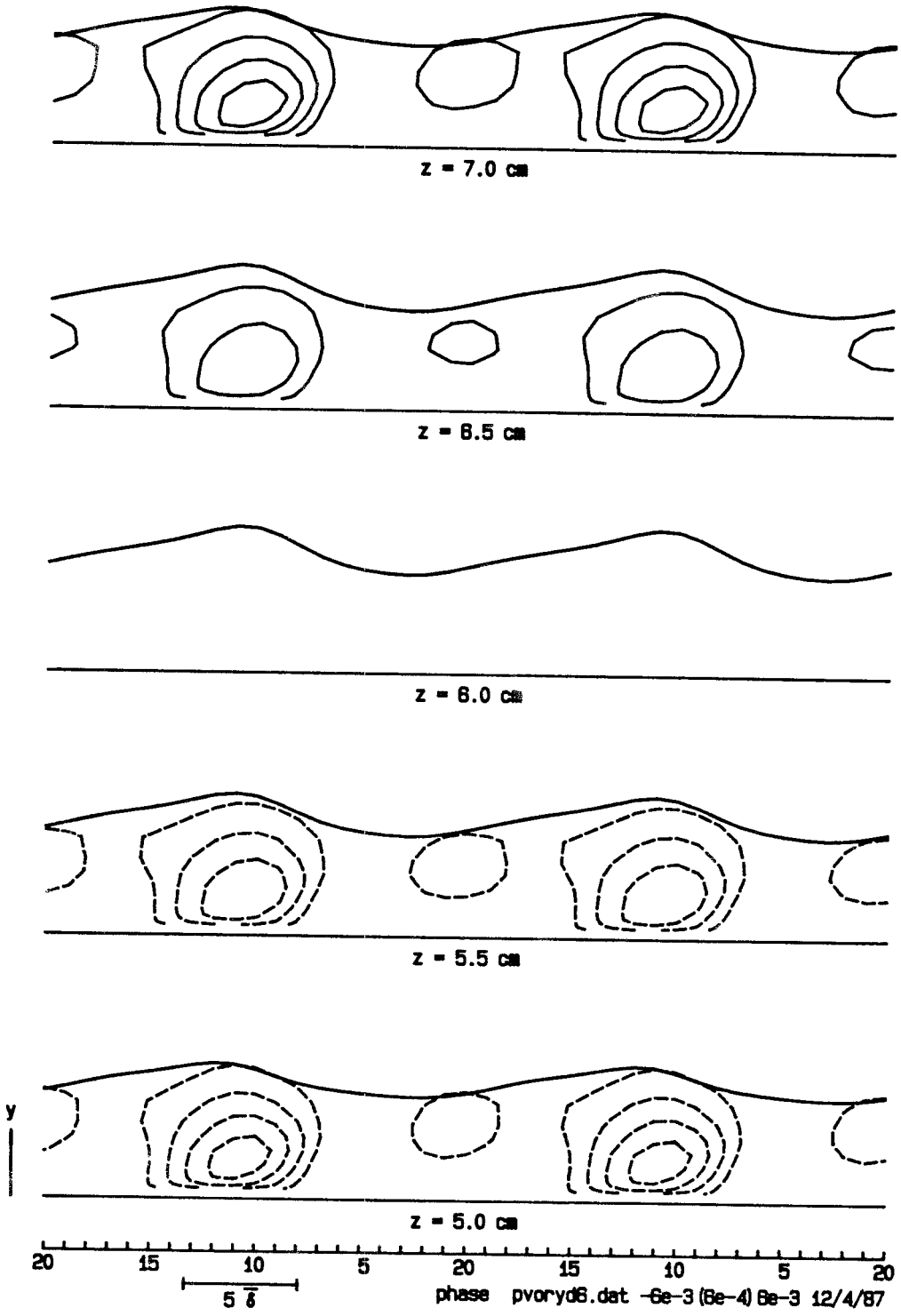

Figure 5.62 (cont'd.). Tilting term for $<\omega_y>$, $<\omega_z> \partial<v>/\partial z$, in the $t-y$ plane.

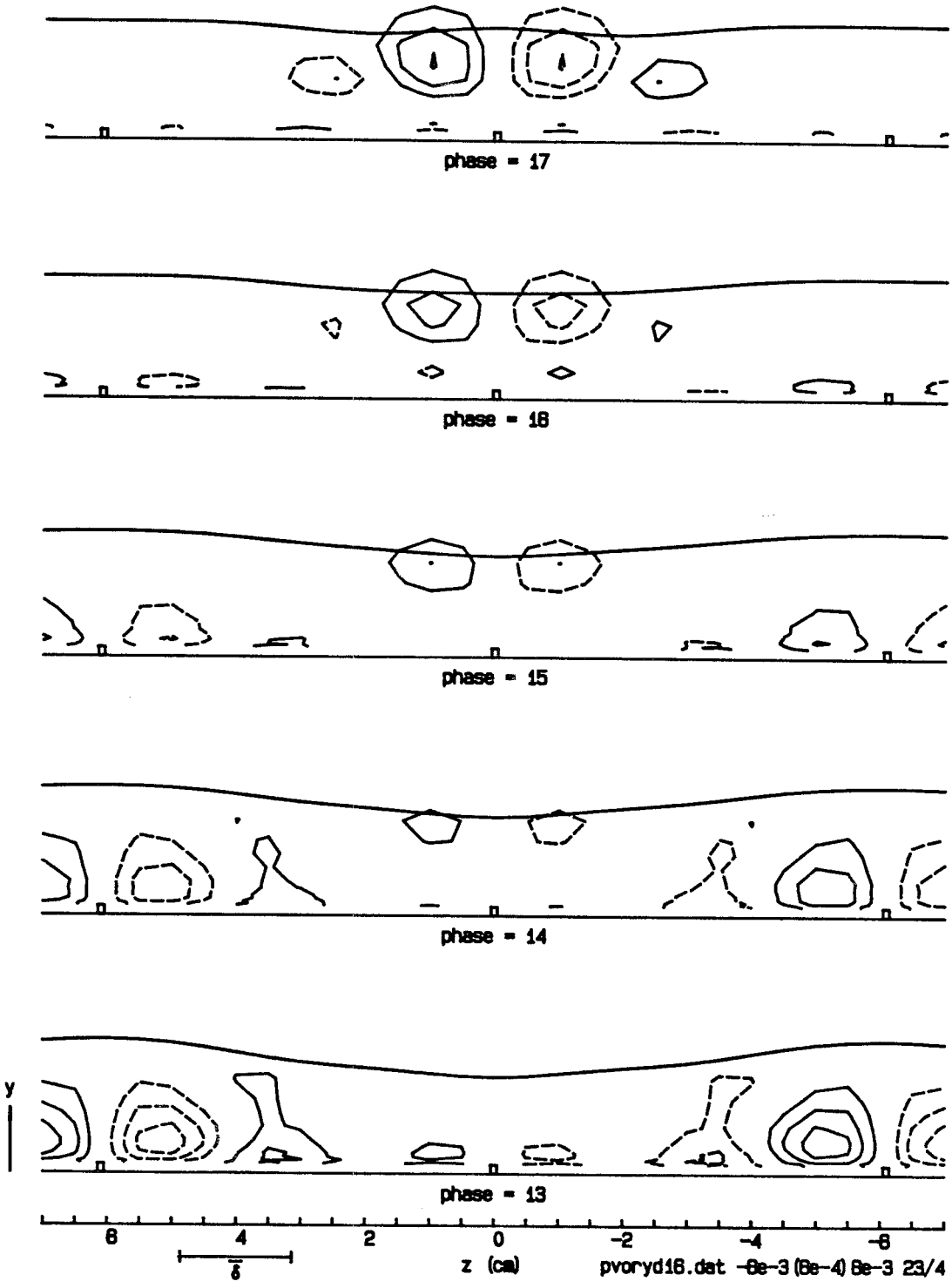

Figure 5.63. Sum of convective and tilting terms for $\langle\omega_y\rangle$ in the $z-y$ plane. Contour interval 0.0006.

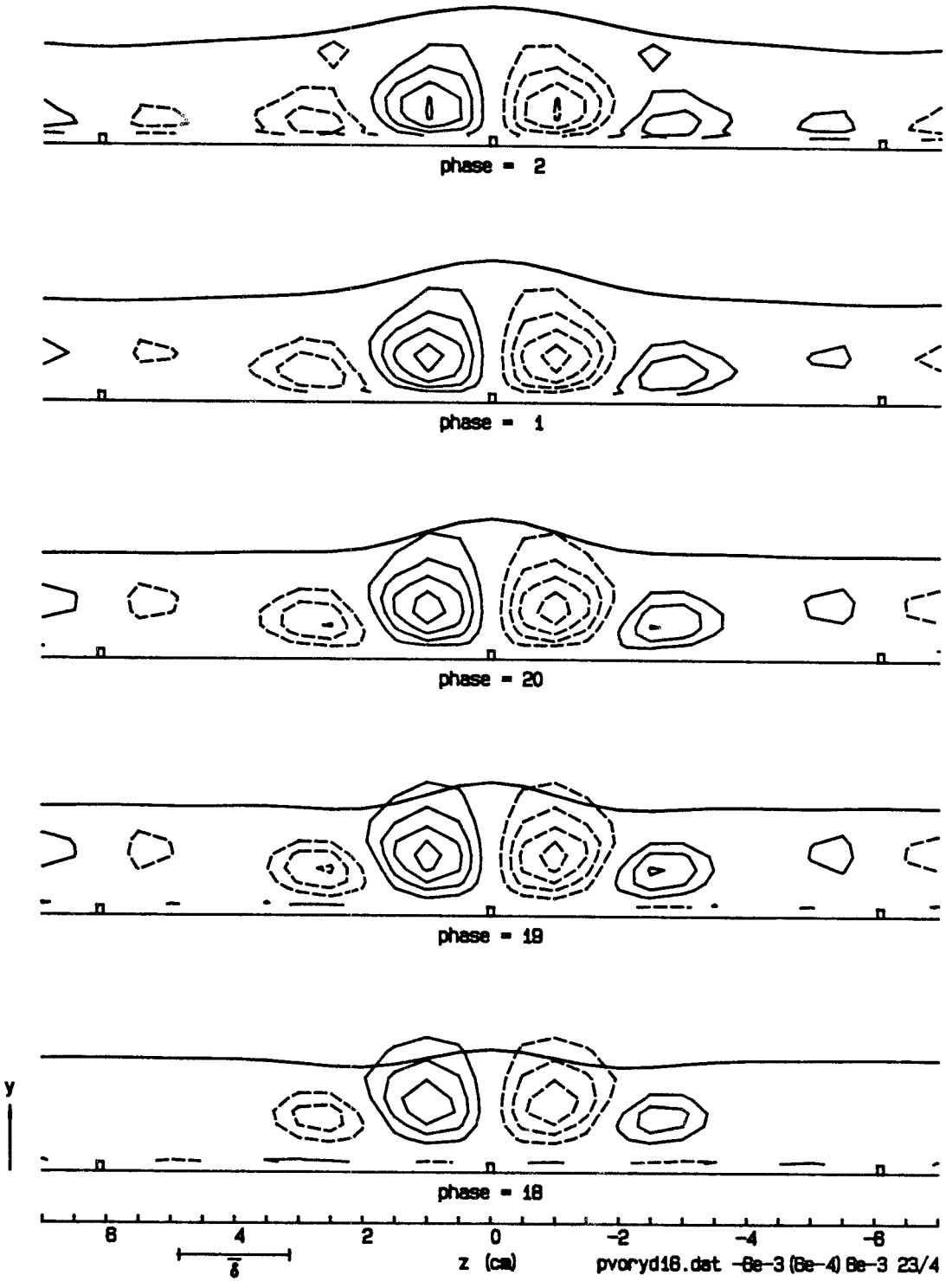

Figure 5.63 (cont'd.). Sum of convective and tilting terms for $<\omega_y>$ in the $z-y$ plane.

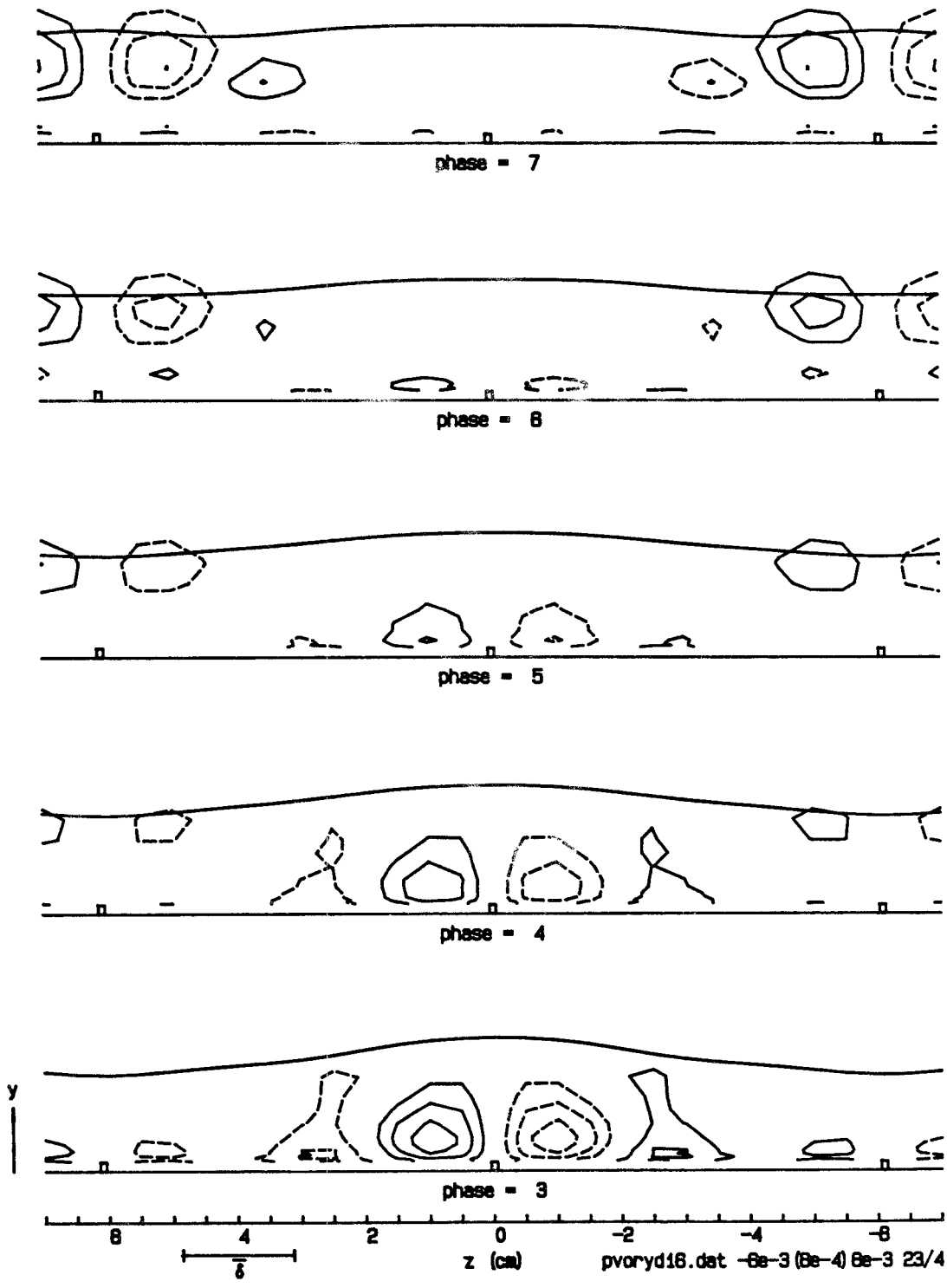

Figure 5.63 (cont'd.). Sum of convective and tilting terms for $<\omega_y>$ in the $z-y$ plane.

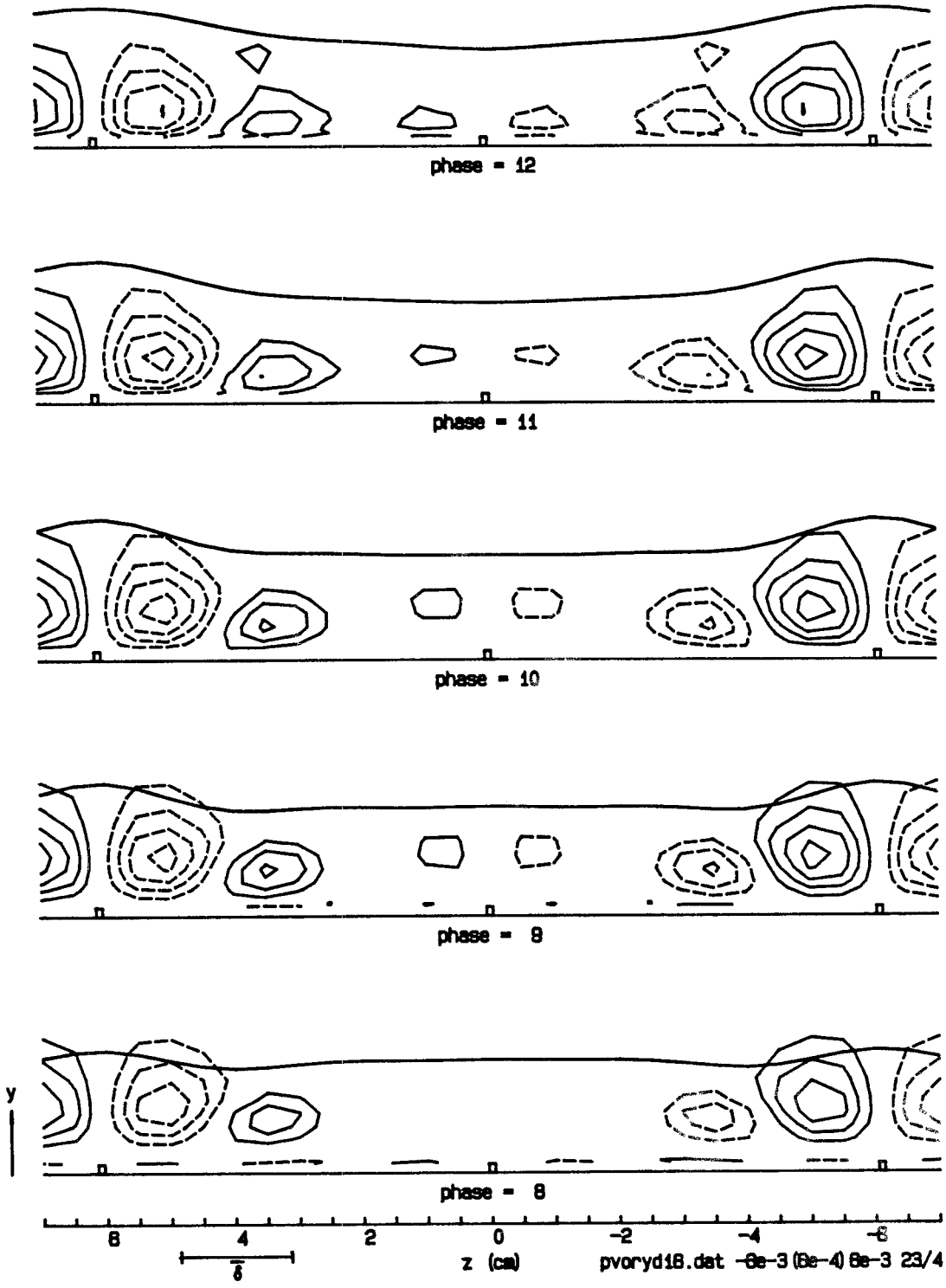

Figure 5.63 (cont'd.). Sum of convective and tilting terms for $<\omega_y>$ in the $z-y$ plane.

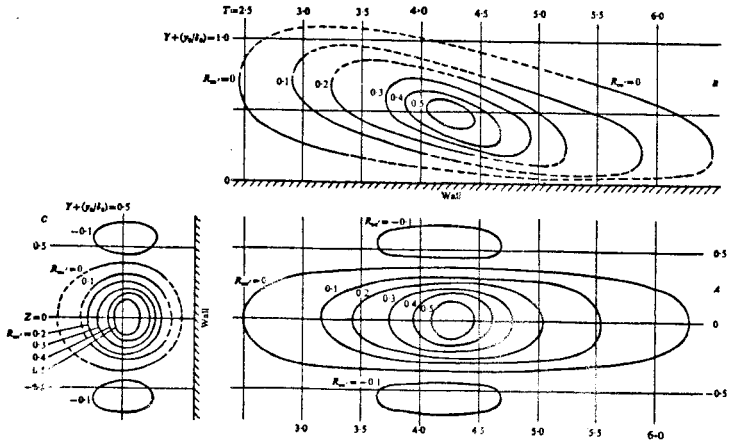

Three-dimensional representation of the space-time auto-correlation of the streamwise velocity fluctuation inside the fully turbulent region, $R_{uu'}(X_0, Y, Z, T)$ at $X_0 = 3{\cdot}8$ and $y_0/\delta_0 = 0{\cdot}5$. Section A: $Y = 0$ plane. Section B: $Z = 0$ plane. Section C: $T = 4{\cdot}27$ plane.

Figure 5.64. Space-time autocorrelation in a natural turbulent boundary layer (from Kovasznay et al. 1970).

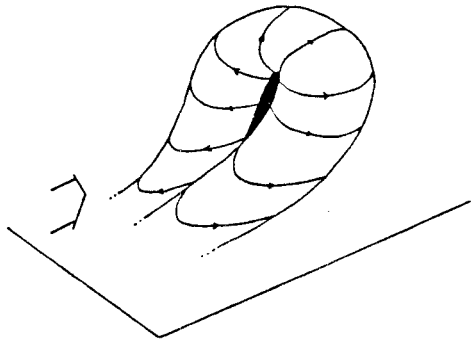

A "horse shoe" vortex.

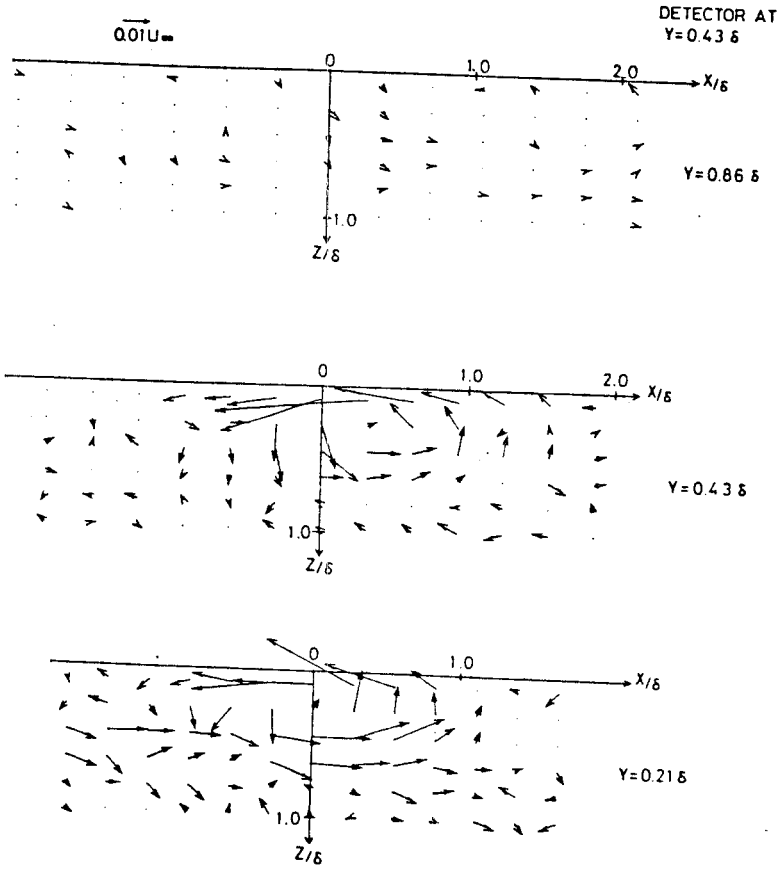

u,w vectors. Detector at Y=0.436,X=Z=0 .

Figure 5.65. Horse-shoe vortex and conditionally averaged perturbation velocity vectors in the $x-z$ plane in a natural turbulent boundary layer (from Fukunishi 1984).

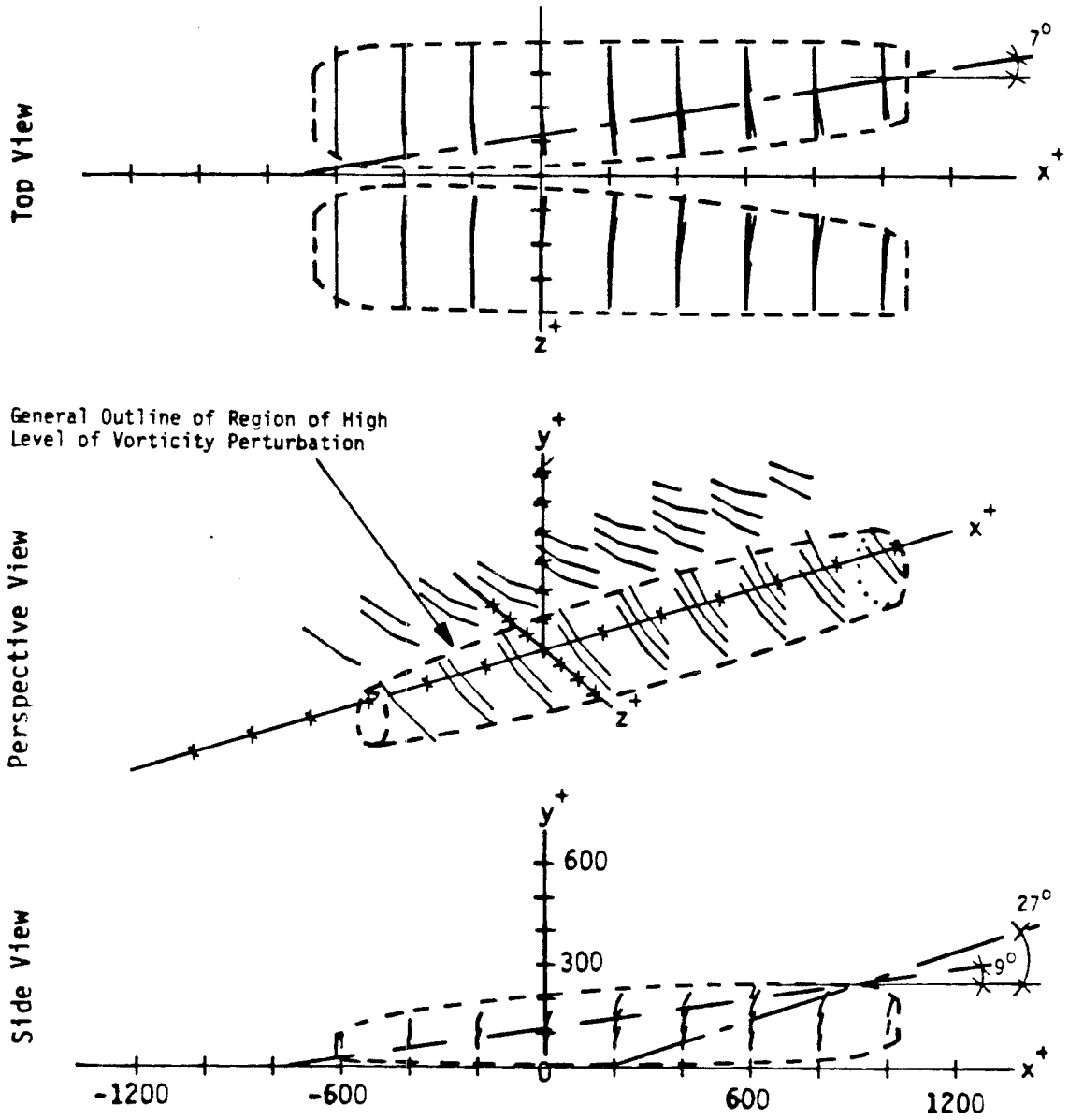

Segments of Vortex Lines Marking Regions of High Levels of Streamwise and Normal Vorticity Associated with Wall-Detected Q2 Events

Figure 5.66a. Eddy structure associated with ejection (Q2) event in a natural turbulent boundary layer (from Guezennec 1985).

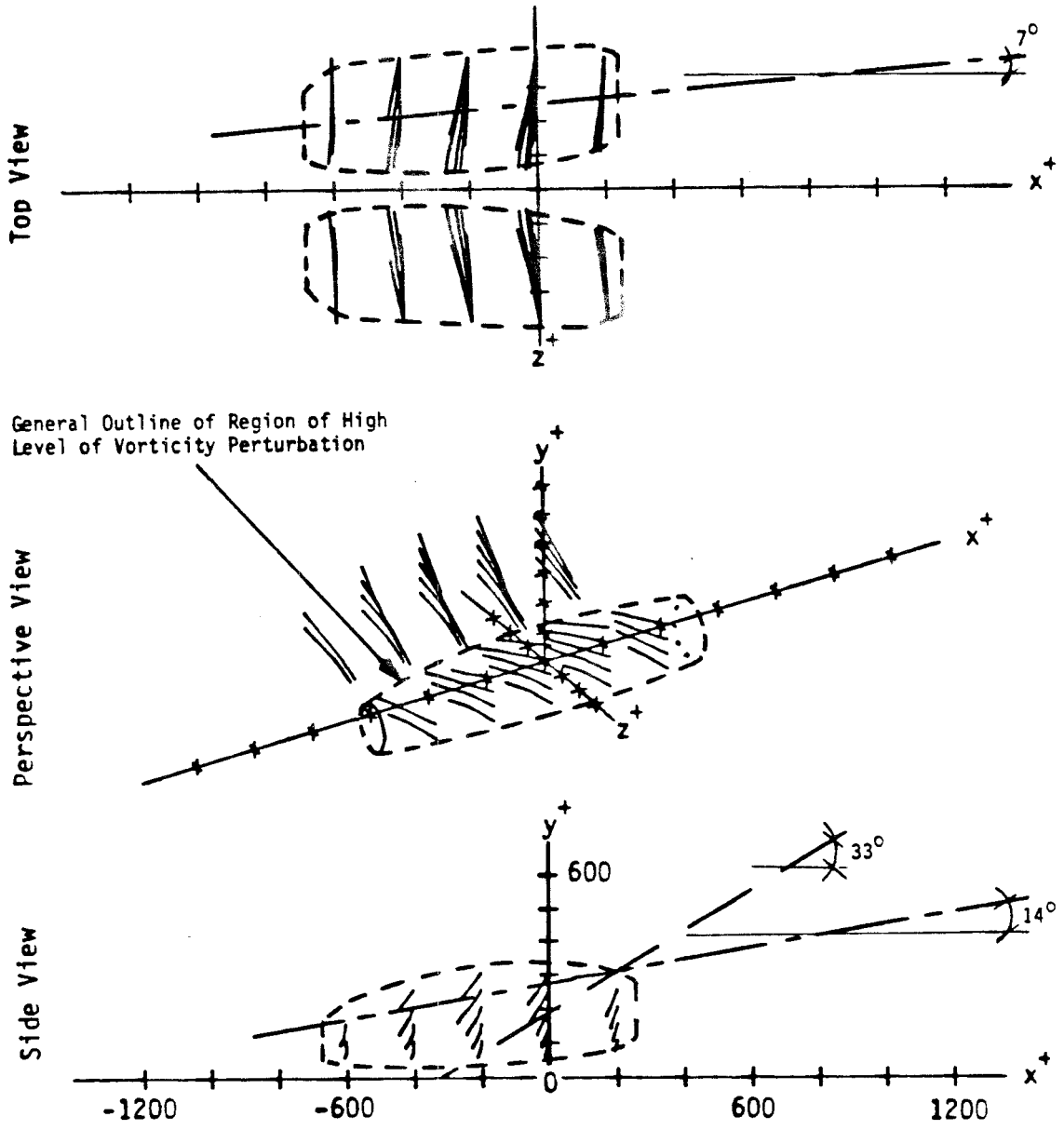

Segments of Vortex Lines Marking Regions of High Levels of Streamwise and Normal Vorticity Associated with Wall-Detected Q4 Events

Figure 5.66b. Eddy structure associated with sweep (Q4) event in a natural turbulent boundary layer (from Guezennec 1985).

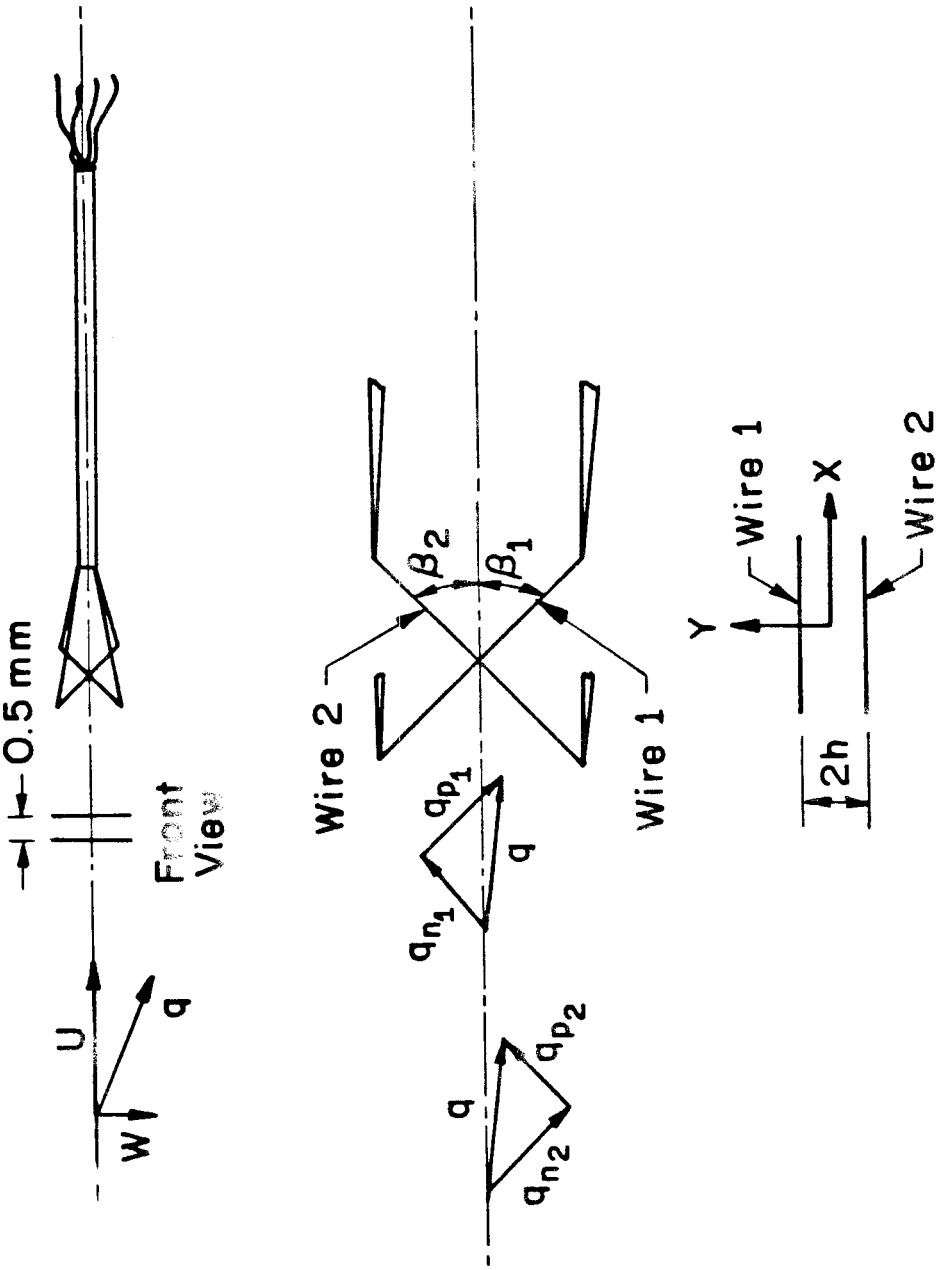

Figure A1. Geometry of X-wire probe.

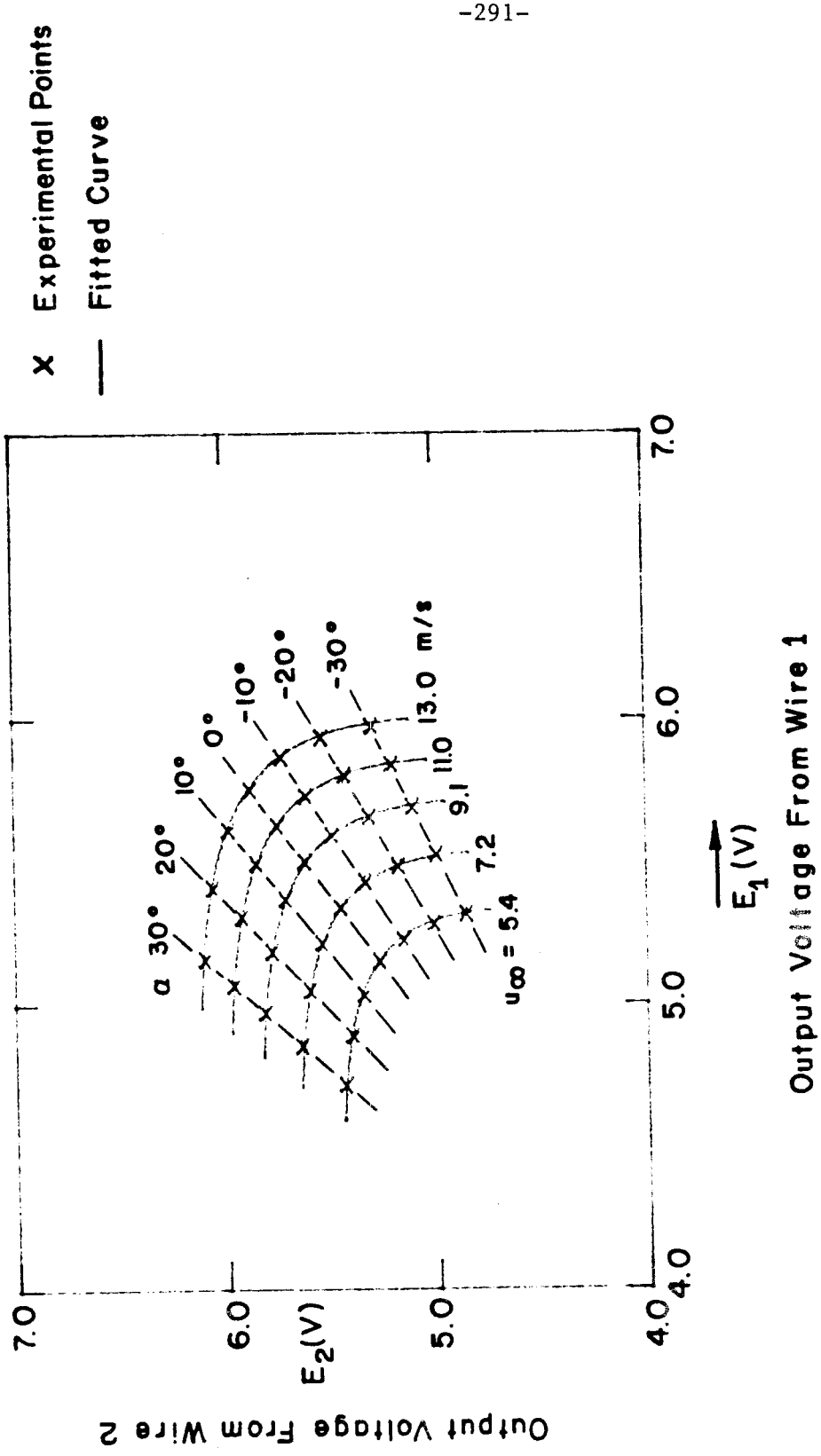

Figure A2. X-wire calibration curve.

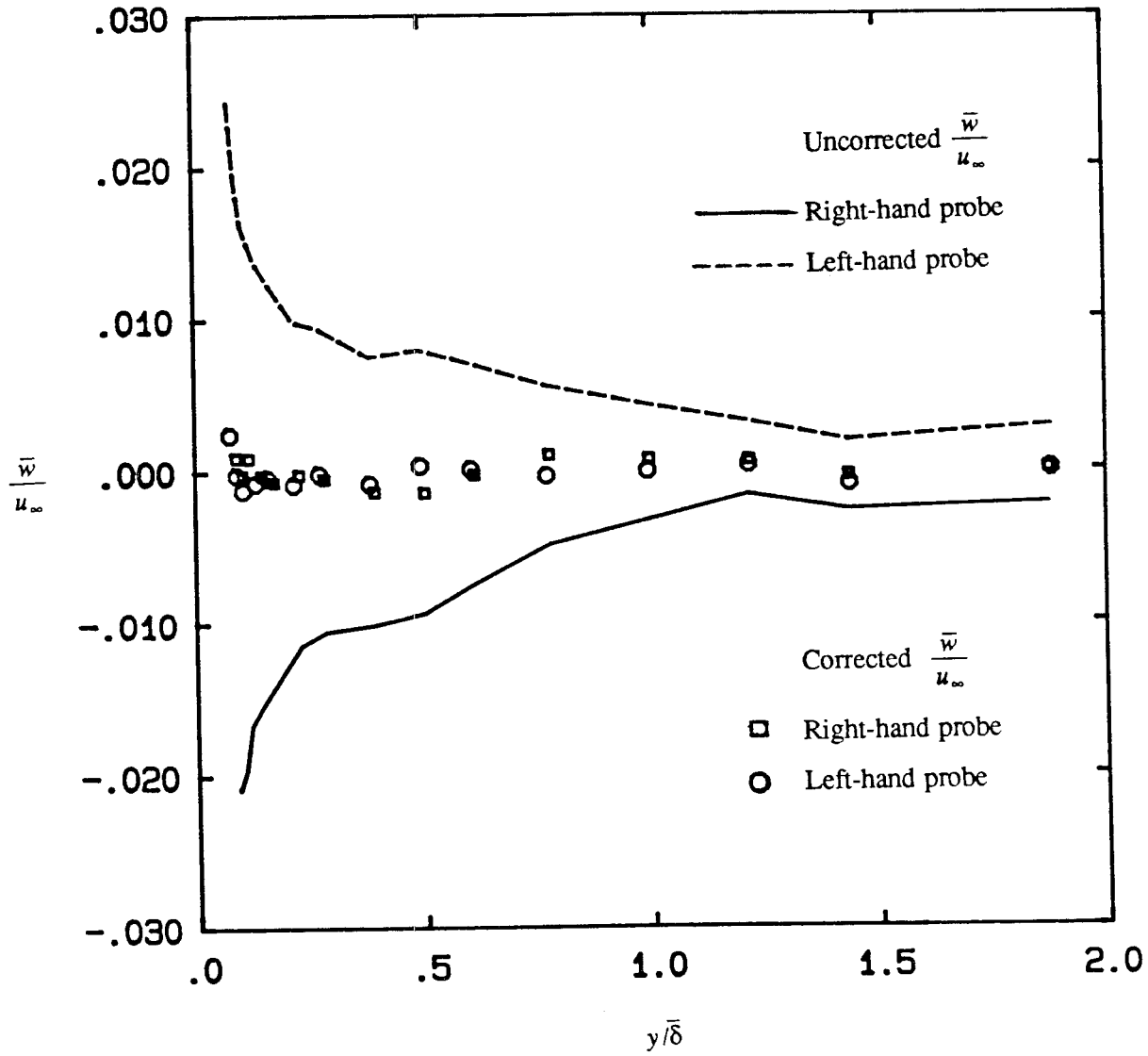

Figure A3. Gradient correction for right-hand and left-hand probes. Values of $\bar{w}$ are time means at x = 117.8 cm, z = 0 cm, and various y.

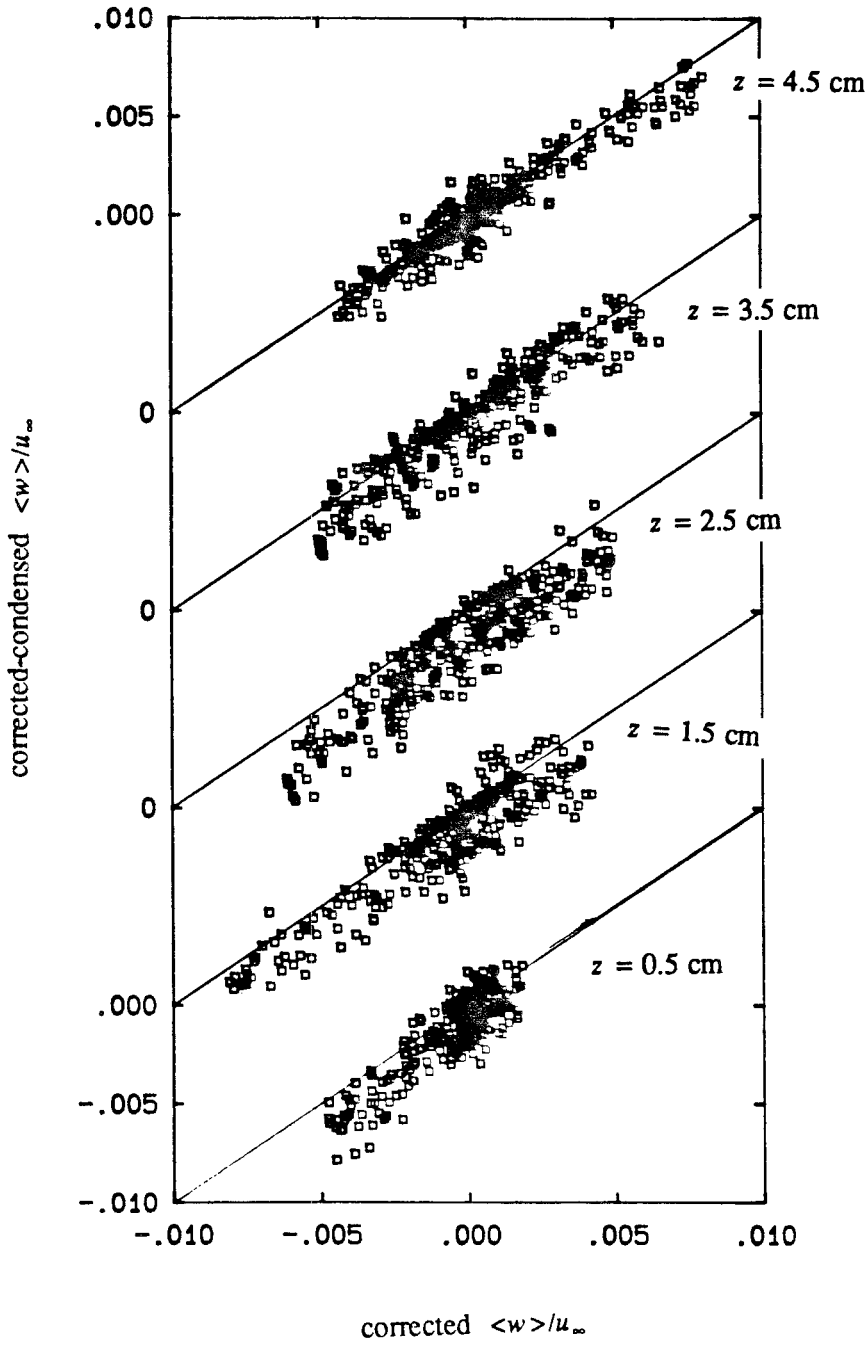

Figure A4. Corrected $\langle w \rangle$ data for several values of z compared with final condensed $\langle w \rangle$.

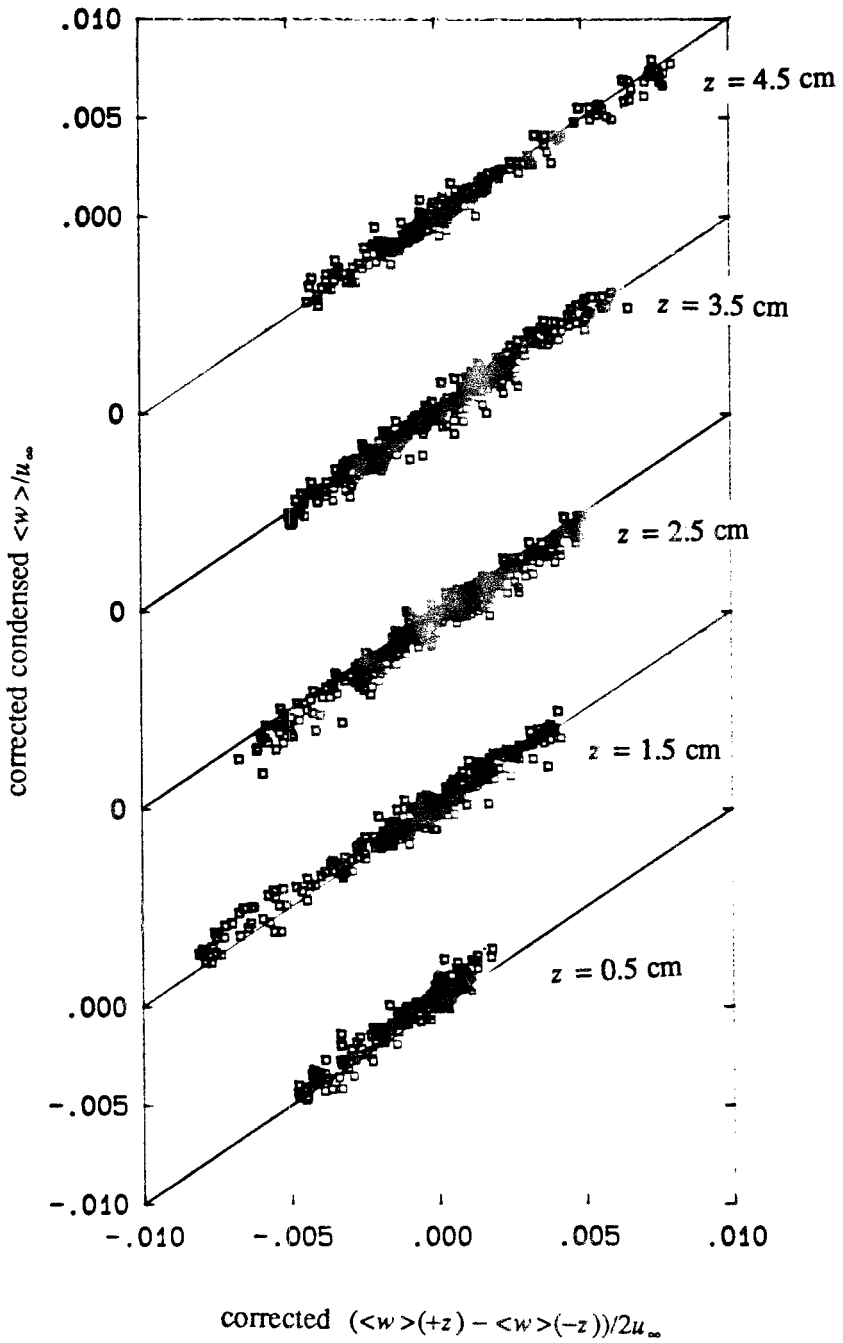

Figure A5. Corrected $\langle w \rangle$ data combined for positive and negative z to eliminate symmetric errors and compared with final condensed $\langle w \rangle$.

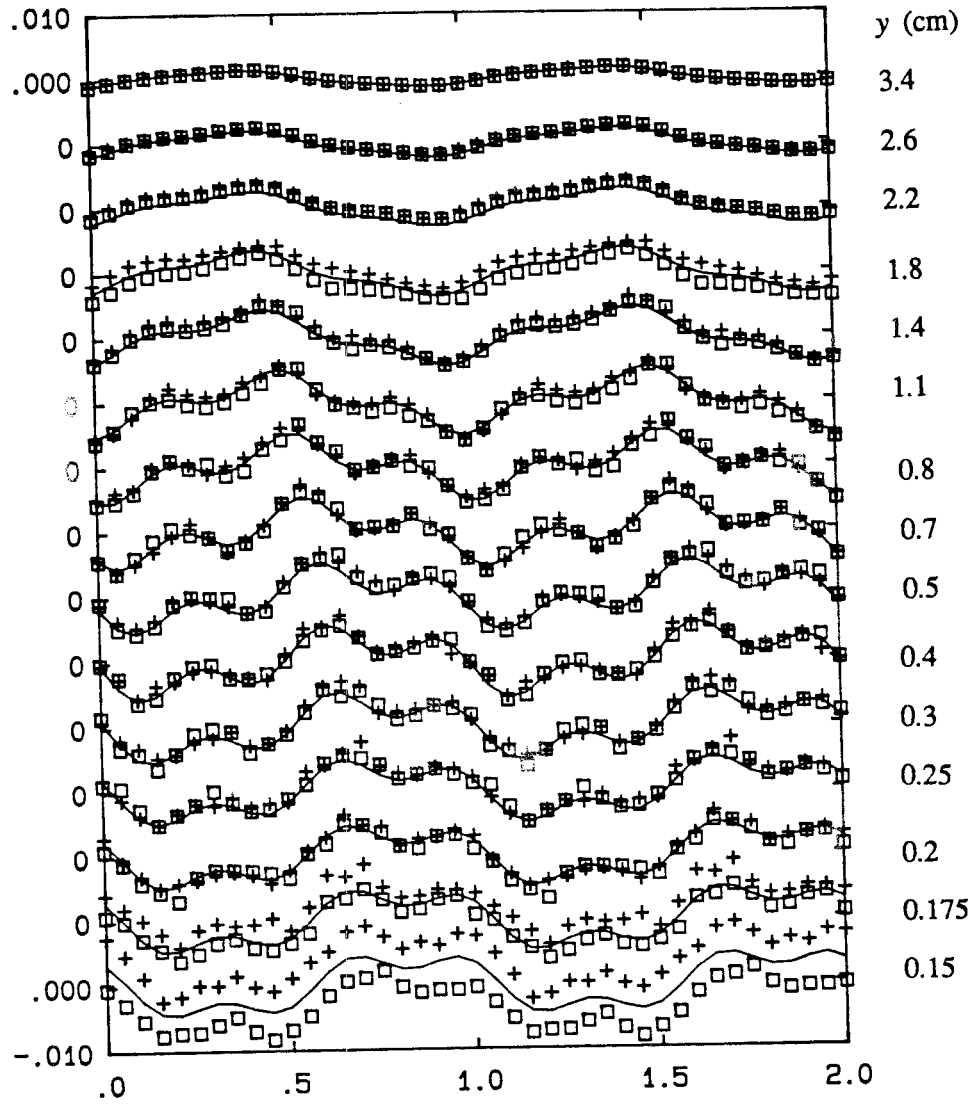

——— Corrected-condensed $\langle w \rangle / u_\infty$ for right-hand probe at z = 3 cm.

\+ Corrected $\langle w \rangle / u_\infty$ for left-hand probe at z = + 3 cm.

□ Corrected $-\langle w \rangle / u_\infty$ for left-hand probe at z = - 3 cm

Figure A6. Comparison of data from left-hand and right-hand probes.